UNIVERSITY OF BELGRADE
FACULTY OF PHYSICS

Aleksandra R. Dimitrievska

Measurement of the W boson mass and the calibration of the muon momentum with the ATLAS detector

DOCTORAL DISSERTATION

Belgrade, 2017

УНИВЕРЗИТЕТ У БЕОГРАДУ
Физички факултет

Александра Р. Димитриевска

Мерење масе W бозона и калибрација импулса миона на детектору АТЛАС

ДОКТОРСКА ДИСЕРТАЦИЈА

Београд, 2017

Ментор:

др Ненад Врањеш, научни сарадник,
Институт за физику у Београду

Чланови комисије:

проф. др Петар Аџић, редовни професор
Физичког факултета Универзитета у Београду

проф. др Маја Бурић, редовни професор
Физичког факултета Универзитета у Београду

др Мартен Бонекамп, старији истраживач,
DSM/IRFU/SPP CEA-Saclay

др Лидија Живковић, научни саветник,
Институт за физику у Београду

др Ненад Врањеш, научни сарадник,
Институт за физику у Београду

Датум одбране:

Measurement of the W boson mass and the calibration of the muon momentum with the ATLAS detector

ABSTRACT

In this thesis measurement of the W-boson mass based on data collected during 2011 in proton–proton collisions at a centre-of-mass energy of 7 TeV with the ATLAS detector at the Large Hadron Collider (LHC) is presented. In the Standard Model, the W-boson mass depends on the top quark mass and the Higgs-boson mass through higher order corrections. Therefore, a precise measurements the mass of the top quark, W- and Higgs-boson, provide a stringent test of the Standard Model. Any observed inconsistency can be an indirect proof of the physics beyond the Standard Model. Previous measurements of the mass of the W boson are performed at the Large electron–positron collider, and at the Tevatron proton–antiproton collider with the CDF and D0 experiments. The current world average value of the W-boson mass is $m_W = 80385 \pm 15$ MeV, while the most precise single measurement with an uncertainty of 19 MeV is performed with the CDF experiment. On the other hand, the indirect constraint on the W-boson mass from the global electroweak fit predicts $m_W = 80358 \pm 8$ MeV.

At hadron colliders, the W-boson mass is determined through its lepton (electron and muon) decays from the Jacobian peaks of the final state kinematic distributions, such as the transverse momentum of the electron and muon, the transverse momentum of the neutrino and the W-boson transverse mass. The W-boson mass is extracted by comparing these mass sensitive distributions in the data to the set of corresponding template distributions generated using the Monte Carlo simulation of the detector response. The mass is determined by means of χ^2 minimisation with statistical and systematics uncertainties accounted for. The measurement of the W-boson mass represents a major challenge, requiring a true understanding of the detector performance (i.e. precise determination of reconstruction efficiency and lepton momentum resolution, as well as the neutrino transverse momentum), and an accurate modeling of the parton distribution functions and the lepton angular distributions.

The conventional approach for determining the neutrino energy is from balancing the detected energy in the transverse plane of all reconstructed particles in the event: jets, electrons, photons, tau-leptons, muons and the energies reconstructed in the calorimeter cells which are not associated with any other object. For the W-boson mass measurement an algorithm based on hadronic recoil is developed, so that the transverse momentum of the neutrino becomes a derived quantity from the vector sum of the hadronic recoil and the lepton transverse momentum. The hadronic recoil is calculated as a vector sum of all of the transverse energy of all reconstructed detector signals in

the calorimeters, excluding the energy deposits associated to the decay electrons and muons. The hadronic recoil calibration exploits the $Z \to \ell\ell$ decays, since the W- and Z-bosons are produced from very similar partonic processes and have similar decay kinematics. The recoil calibration procedure is sensitive to the following sources of systematic uncertainties: the limited statistics of the calibration sample, the differences in the hadronic response between Z- and W-boson events and on pile-up (additional proton–proton interactions).

Muon momentum calibration is based on reference samples of $J/\psi \to \mu\mu$, $Z \to \mu\mu$ and $\Upsilon \to \mu\mu$ decays. The simulated muon momentum is corrected so it matches the measured muon momentum in experimental data. The muon momentum resolution is determined with an uncertainty in ranges from 1.7 % at central pseudorapidity and for transverse momentum $p_{\mathrm{T}} = 10$ GeV, to 4 % at large pseudorapidity and $p_{\mathrm{T}} = 100$ GeV, while the muon momentum scale is known with an uncertainty of 0.05 % to 0.2 % depending on pseudorapidity.

For the W-boson mass measurement, after all selection requirements, there is 7.8×10^6 candidates in the $W \to \mu\nu$ channel and 5.9×10^6 candidates in the $W \to e\nu$ channel. Obtained result for the W-boson mass measurement with the ATLAS experiment is:

$$\begin{aligned} m_W &= 80370 \pm 7\,(\text{stat.}) \pm 11\,(\text{exp. syst.}) \pm 14\,(\text{mod. syst.})\ \text{MeV} \\ &= 80370 \pm 19\ \text{MeV}, \end{aligned}$$

where the first uncertainty is statistical, the second corresponds to the experimental systematic uncertainty, and the third to the physics modelling systematic uncertainty. The experimental uncertainty accounts the uncertainties from electron energy and muon momentum calibration and their reconstruction efficiencies, the hadronic recoil calibration, and background processes. The physics modeling systematic uncertainty comes from inaccurate modeling of the W-boson production and decay processes in proton–proton collisions at the LHC. The W-boson mass measurement is compatible with the current world average value and with the Standard Model prediction. The obtained result is similar in precision to the currently leading measurements performed by the CDF experiment.

Key words: W-boson mass, muon momentum calibration, hadronic recoil, ATLAS, LHC.

Scientific area: Physics

Research area: Experimental High Energy Physics

Мерење масе W бозона и калибрација импулса миона на детектору АТЛАС

РЕЗИМЕ

У овој тези је описано мерење масе W бозона, које се заснива на подацима прикупљеним на детектору АТЛАС током 2011. године у протон–протон сударима на енергији од 7 TeV на Великом сударачу хадрона (ЛХЦ). Према Стандардном моделу маса W бозона зависи од масе топ кварка и масе Хигсовог бозона кроз корекције вишег реда. Прецизним мерењем масе топ кварка, W и Хигсовог бозона могуће је тестирање конзистентности Стандардног модела, и било које неслагање представља индиректан доказ постојања честица изван Стандардног модела. Маса W бозона је претходно измерена на експериментима на Великом елетрон–позитронском сударачу, као и на експериментима ЦДФ и Д0 на протон–антипротон сударачу Теватрон. Тренутна средња вредност измерене масе W бозона износи $m_W = 80385 \pm 15$ MeV, док је најпрецизније мерење остварено на експерименту ЦДФ са неодређеношћу ± 19 MeV. Са друге стране, на основу глобалног фита параметара Стандардног модела предвиђена маса W бозона износи $m_W = 80358 \pm 8$ MeV.

На хадронским сударачима маса W бозона се мери у лептонским (електронском и мионском) каналима распада, користећи опсервабле са оштрим Јакобијанским пиком као што су трансверзални импулс лептона, трансверзални импулс неутрина и трансверзална маса лептон–неутрино система. Маса се добија поређењем одговарајућих расподела, добијених из експерименталних података и Монте Карло симулација, које су засноване на детаљном опису детектора и његовог одговора на интеракцију честица са материјалом детектора. Поређење се врши минимизацијом добијеног χ^2 који укључује статистичке и систематске неодређености. Мерење масе W бозона је веома компликовано и захтева прецизно теоријско моделовање вероватноћа расподела партона у протону, угаоне расподеле лептона који потичу из распада W бозона и трансверзалног импулса W бозона, као и познавање рада детектора при реконструкцији лептона и неутрина (прецизно одређивање ефикасности реконструкције и резолуције импулса миона и трансверзалног импулса неутрина).

На експерименту АТЛАС, трансверзални импулс неутрина се стандардно одређује на основу закона одржања енергије у трансверзалној равни, као векторска сума трансверзалних импулса реконструисаних објеката: џетова,

електрона, фотона, тау лептона, миона и енергије у калориметарским ћелијама које нису асоциране ни са једним другим објектом. За мерење масе W бозона развијен је алгоритам базиран на мерењу хадронског узмака, тако да трансверзални импулс неутрина постаје изведена величина која се добија векторским сабирањем хадронског узмака и трансверзалног импулса лептона. Хадронски узмак представља векторску суму трансверзалних енргија свих кластера у калориметру, осим енергије коју је депоновао лептон. Калибрација хадронског узмака се врши коришћењем $Z \to \ell\ell$ резонанце, због сличног начина продукције и распада са W бозоном. Систематске неодређености на мерење масе W бозона које потичу од калибрације хадронског узмака зависе од статистике калибрационог узорка, разлике хадронског узмака између Z и W бозона, као и од нагомилавања сигнала у детектору који потичу од судара других протона.

Калибрација импулса миона на детектору АТЛАС се заснива на великој статистици добро изучених процеса $J/\psi \to \mu\mu$, $Z \to \mu\mu$ и $\Upsilon \to \mu\mu$ распада. Реконструкција импулса миона у симулираним догађајима је коригована како би се поклопила са скалом и резолуцијом импулса миона измереним у реалним догађајима. Приказана процедура калибрације импулса миона има систематске неодређености на резолуцију у опсегу од 1.7% за мионе са трансверзалним импулсом $p_{\mathrm{T}} = 10$ GeV и псеудорапидитетом $|\eta| < 1$, до 4% за мионе са $p_{\mathrm{T}} = 100$ GeV и псеудорапидитетом $|\eta| > 1$, док систематске неодређености на скалу износе од 0.05 % до 0.2 % у зависности од псеудорапидитета миона.

За мерење масе W бозона селектовано је око 7.8×10^6 $W \to \mu\nu$ догађаја и око 5.9×10^6 $W \to e\nu$ догађаја. Измерена маса W бозона износи:

$$\begin{aligned} m_W &= 80370 \pm 7\,(\text{stat.}) \pm 11\,(\text{exp. sist.}) \pm 14\,(\text{mod. sist.})\ \text{MeV} \\ &= 80370 \pm 19\ \text{MeV}, \end{aligned}$$

при чему прва наведена вредност представља статистичку неодређеност, друга је експериментална, а трећа торијска неодређеност. Експериментална неодређеност потиче од неодређености калибрације импулса и ефикасности реконструкције електрона и миона, калибрације хадронског узмака, као и позавања фонских процеса. Теоријска неодређеност потиче из неодређености познавања процеса продукције и распада W бозона у протон–протон сударима. Добијени резултат је конзистентан са тренутном средњом вредношћу, као и са предвиђањима Стандардног модела. Измерена маса W бозона на експерименту АТЛАС по прецизности одговара најпрецизнијем претходном појединачном мерењу на експерименту ЦДФ.

Кључне речи: маса W бозона, калибрација мерења импулса миона, хадронски узмак, АТЛАС, ЛХЦ.

Научна област: Физика

Ужа научна област: Експериментална физика високих енергија

Contents

Introduction **1**

Chapter 1: The Standard Model and the W-boson Mass Measurement **5**

1.1 The Standard Model of particle physics 5
1.1.1 Electroweak theory 8
1.1.2 Quantum Chromodynamics 10
1.1.3 Electroweak symmetry breaking 12
1.1.4 Limitations of the Standard Model 14

1.2 Motivation for the W-boson mass measurement 15
1.2.1 Electroweak precision observables 18
1.2.2 Importance and role of electroweak fits 19
1.2.3 Previous measurements and LHC prospects 22

1.3 Electroweak bosons at hadron colliders 25
1.3.1 Phenomenology of proton–proton collisions 25
1.3.2 W-boson production and decay 30

1.4 Measurement strategy 34
1.4.1 Challenges in the W-boson mass measurement at hadron colliders 34
1.4.2 Inputs to the W-boson mass measurement 36
1.4.3 Template fit method and propagation of systematics uncertainties 38

Chapter 2: Experimental Setup **41**

2.1 The Large Hadron Collider 41
2.1.1 LHC operation during the period 2010-2012 47
2.1.2 LHC performance for Run-2 and further runs 48

2.2 The ATLAS Detector 50
2.2.1 Definitions and conventions 52
2.2.2 Magnet System 54
2.2.3 The Inner Detector 55
2.2.4 Calorimeters 57
2.2.5 The Muon Spectrometer 60
2.2.6 Trigger System 64
2.2.7 Simulation infrastructure and data preparation 65

Chapter 3: Monte Carlo Event Generation, Detector Simulation and W-boson Reconstruction **67**

3.1 Event Generation 67

3.2 Event Samples 70
3.2.1 Collision data samples 70
3.2.2 Simulated data samples 71

3.3 Modeling of the Z- and W-boson production and decay 73
3.3.1 Electroweak corrections 74
3.3.2 Modeling of Z- and W-boson rapidity distribution 74
3.3.3 Modeling of Z- and W-boson transverse momentum distribution 75

3.4 Object Reconstruction and Identification 77

3.5 W-boson Event Selection 82

Chapter 4: Muon Momentum Calibration **84**

4.1 Muon Reconstruction at ATLAS in Run-1 84

4.2 Muon Energy Loss in the Calorimeters 89

4.3 Muon Momentum studies using J/ψ events 91
4.3.1 Trigger, muon and event selection 93
4.3.2 Mass fits 97
4.3.3 Momentum fits 105
4.3.4 Energy loss corrections 111

4.4 Muon Momentum Calibration in Run-1 115
4.4.1 Muon momentum scale and resolution corrections evaluated from $J/\psi \to \mu\mu$ and $Z \to \mu\mu$ decays 116
4.4.2 Validation of the muon momentum scale and resolution corrections with $J/\psi \to \mu\mu$ decay 121

4.5 Muon momentum uncertainties in the Higgs boson mass measurement 133

Chapter 5: Performance of the Hadronic Recoil Reconstruction **138**

5.1 Introduction 138

5.2 Cluster based hadronic recoil 141

5.3 Other definitions of the hadronic recoil reconstruction 142

5.4 Initial performance of the hadronic recoil 147

5.5 Calibration of the hadronic recoil 148
5.5.1 Pile-up modeling 150
5.5.2 Event activity correction 152

5.5.3 Azimuthal corrections 156
5.5.4 Residual recoil corrections 157

5.6 Validation of the corrected hadronic recoil in Z- and W-boson events 166
5.6.1 Validation with the Z-boson events 166
5.6.2 Validation with the W-boson events 172
5.6.3 Closure test of the hadronic recoil correction procedure 177

5.7 Propagation of the systematics uncertainties to the W-boson mass measurement 184

Chapter 6: Measurement of the W-boson Mass with the 7 TeV data 200

6.1 W-boson events 200
6.1.1 Final experimental and theoretical corrections 201
6.1.2 Z-boson based cross checks 207
6.1.3 Background determination 208
6.1.4 Systematics uncertainties 210
6.1.5 Control distributions 217

6.2 Mass fits 217
6.2.1 Correlation between the fitting observables 223
6.2.2 Combination procedure 225
6.2.3 Results with the initial fitting range 227
6.2.4 Consistency checks 229
6.2.5 Optimisation of the fitting range 229
6.2.6 Final results 231
6.2.7 Discussion 236

6.3 Prospects for the future 239
6.3.1 Prospects for the W-boson mass measurement using 8 TeV and 13 TeV data 239
6.3.2 Direct measurement of the W-boson transverse momentum with low pile-up data 240

Conclusion 242

References 244

Appendix 259

A: Cut-flow tables for the W-boson event selection 259

B: Fitting range scans 262

Introduction

Curiosity is governed people to search for the fundamental answers about the Universe. The most common approach, explaining complicated things in a simple way, is not changed for centuries. With every new model, a more accurate description of nature is obtained. The Standard Model represents a theoretical framework build from observation which describes fundamental particles and their interactions. The electroweak sector of the Model is based on symmetry group $SU(2)_{\mathrm{L}} \otimes U(1)_{\mathrm{Y}}$ and describes the electromagnetic and weak interactions which are mediated via massless photons and three massive intermediate vector bosons, the $W^{\pm}$ and Z^0, respectively. The latest achievement of the Standard Model is the discovery of the Higgs boson by the ATLAS and CMS experiments at the Large Hadron Collider (LHC). The discovery of the Higgs boson and the measurement of its mass allows for the first time to overconstrain Standard Model and test its consistency by precisely measuring the masses of the W boson (m_W), top quark and the Higgs boson. With precision measurements, such as the measurement of the W-boson mass, we are testing our current description of the laws of nature. Constraints on physics beyond the Standard Model are currently limited by the precision of the W-boson mass measurement. Improving the precision of the measurement of m_W is therefore of high importance for testing the overall consistency of the Model.

This thesis presents the measurement of the W-boson mass in proton–proton collisions collected during 2011 at a centre-of-mass energy of $\sqrt{s} = 7$ TeV with the ATLAS experiment at the LHC. The previous measurements are performed at the CERN's Large electron-positron collider (LEP) and at the proton-antiproton collider Tevatron at Fermilab. The current world average value for the W-boson mass measurement is $m_W = 80385 \pm 15$ MeV, while the global electroweak fit gives value of $m_W = 80358 \pm 8$ MeV, which is two times more precise than the most precise direct measurement.

At hadron colliders the W bosons are produced via Drell-Yan quark-antiquark annihilation. The W-boson events are detected through the leptonic decays, in electron and muon channels. The W-boson candidates are selected by requiring exactly one electron or muon with high transverse momentum and the presence of the large missing transverse energy in the event, originating from the neutrino. The missing transverse energy is inferred from the hadronic recoil which represents a vector sum of all of the transverse energy of all reconstructed detector signals in the calorimeters. The mass of the W boson is measured from sensitive observables which have a sharp Jacobian peak: the reconstructed transverse electron and muon momentum, the missing transverse energy and the W-boson transverse mass distribution.

Measurement of the m_W with an accuracy of 8 MeV set by the Standard Model prediction, represents a major challenge for the ATLAS experiment requiring a true understanding of the detector performance and limitations, to be reached via multiple analysis stages. Two main objects that need to be measured precisely are the lepton (electron and muon) and the neutrino for which hadronic activity in the calorimeter needs to be measured. The main theoretical inputs that are needed for this measurement consist of higher order corrections in the perturbative expansion of the strong-coupling constant, non-perturbative quantum chromodynamics effects, parton distribution functions and the lepton angular distribution.

For the W-boson mass measurement described in this thesis, after all selection requirements, there is about eight million W-boson candidates in the muon and six million candidates in the electron channel, which yields a statistical uncertainty smaller than 10 MeV. The selected W-boson sample is larger than the corresponding sample collected at the Tevatron. For the detector calibration, physics modeling and the validation of the analysis strategy, the Z-boson decay in electron and muon channels is used. Selected Z-boson sample contains about two million events in both channels.

In this thesis the muon momentum calibration is also presented. An accurate measurement of muon momentum is crucial for many physics analyses with muons in the final state. In the ATLAS detector, muons are reconstructed independently in the inner detector and in the muon spectrometer. The muon spectrometer is designed to provide muon momentum measurement with a relative resolution better than 3% over a wide range of muon transverse momentum and up to 10% for muons with transverse momentum of about 10 GeV. The reconstruction of muon tracks in the muon spectrometer is biased by several effects, such as muon energy loss in the material upstream of the spectrometer, multiple scattering inside the spectrometer, as well as its precise chambers alignment. The detailed response of the ATLAS detector is simulated in GEANT 4. In order to precisely describe the measurement of the muon transverse momentum in data, additional corrections to the simulated muon transverse momenta are needed to be defined. The procedure of correcting the simulated muon transverse momenta is muon momentum calibration. Muons from the decay of the J/ψ resonance can be used for studying the muon energy loss in the calorimeters. The calibration of the muon momentum is based on large statistics samples of $J/\psi \to \mu\mu$, $Z \to \mu\mu$ and $\Upsilon \to \mu\mu$ decays, after which the muon momentum scale is described to the per-mile level and muon momentum resolution to the percent level. The muon momentum calibration is used for the Higgs-boson mass measurement in the four lepton channel with the ATLAS experiment.

This thesis is structured as follows. Chapter 1 presents a theoretical introduction of the Standard Model, phenomenology of proton–proton collisions, and motivation for the W-boson mass measurement, with an overview of the previous measurements and the measurement strategy with the ATLAS experiment. In Chapter 2 the LHC and the ATLAS detector are described. Chapter 3 presents the data and simulation samples used for the measurement with a summary of the modeling of vector-boson production and decay. In Chapter 4 muon momentum studies with the J/ψ resonance and the energy loss of the muons passing the calorimeters are given, together with the muon

momentum scale and resolution corrections. Chapter 5 describes the performance of the hadronic recoil as well as the calibration procedure with estimation of the systematics uncertainties used for the W-boson mass measurement. Final experimental and theoretical corrections, with their systematics uncertainties are given in Chapter 6, with detailed analysis of the W-boson mass extraction, optimisation procedure and obtained results.

Author's contribution

The measurement of the W-boson mass described in this thesis is a collaborative work performed by the W-boson mass group, which is a part of the Standard Model group at the ATLAS experiment. The author has been involved in the calibration of the muon momentum scale and resolution corrections within the Muon Combined Performance group. The resulting publications:

- L. Chevalier, A. Dimitrievska, N. Vranjes, *Muon performance studies using* $J/\psi \to \mu^+\mu^-$ *at* $\sqrt{s} = 7$ *TeV and* $\sqrt{s} = 8$ *TeV of pp collisions*, ATL-COM- MUON-2013-022 (2013), `https://cds.cern.ch/record/1596789`
- G. Artoni, M. Corradi, A. Dimitrievska, F. Sforza, N. Vranjes, P. Fleischmann, *Muon momentum scale and resolution corrections evaluated with* $Z \to \mu\mu$ *and* $J/\psi \to \mu\mu$ *decays on Run I ATLAS data*, ATL-COM-MUON-2014-001 (2014), Preliminary version of MCP scale and momentum corrections for 2012 data, `https://cds.cern.ch/record/1643495`
- ATLAS Collaboration, *Measurement of the muon reconstruction performance of the ATLAS detector using 2011 and 2012 LHC proton–proton collision data*, Eur. Phys. J. C **74** (2014) 3130, arXiv: 1407.3935 [hep-ex]
- T. Adye, ..., A. Dimitrievska, ..., N. Vranjes, et al., *Higgs mass measurements and uncertainties in 2011 and 2012 data*, ATL-COM-PHYS-2012-1774 (2012), `https://cds.cern.ch/record/1498240`
- ATLAS Collaboration, *Measurement of the Higgs boson mass from the* $H \to \gamma\gamma$ *and* $H \to ZZ^* \to 4\ell$ *channels in pp collisions at center-of-mass energies of 7 and 8 TeVwith the ATLAS detector*, Phys. Rev. D **90** (2014) 052004, arXiv: 1406.3827 [hep-ex]

are part of Chapter 4. In view of the W-boson mass measurement, the author has been involved in the hadronic recoil calibration:

- A. Dimitrievska, N. Vranjes, M. Schott, M. Boonekamp, *Measurement of* m_W *at 7 TeV: Hadronic recoil corrections*, ATL-COM-PHYS-2015-344 (2015), `https://cds.cern.ch/record/2013274`

summarised in Chapter 5, and in the combination and fitting range optimisation of the measurement:

- N. Andari, M. Boonekamp, S. Camarda, A. Dimitrievska, R. Hanna, O. Kivernyk, M. Schott, R. Stroehmer, N. Vranjes, S. Webb, C. Zimmermann, et al., *Measurement of m_W with 7 TeV data: W-boson mass measurement*, ATL- COM-PHYS-2014-1569 (2014), `https://cds.cern.ch/record/1976186`
- ATLAS Collaboration, *Measurement of the W-boson mass in proton–proton collisions at $\sqrt{s} = 7$ TeV with the ATLAS detector*, ATLAS-CONF-2016-113 (2016), `http://cds.cern.ch/record/2238954`

  ATLAS Collaboration, *Measurement of the W-boson mass in pp collisions at $\sqrt{s} = 7$ TeV with the ATLAS detector*, (2017), arXiv: 1701.07240 [hep-ex],

are described in Chapter 6.

1

The Standard Model and the W-boson Mass Measurement

Theoretical framework of all the particles that make the visible matter in the Universe is given by the Standard Model (SM) of particle physics. The three of four fundamental interactions are also included in the SM: electromagnetic, weak and strong. The SM has been successful in predicting a wide range of phenomena with an accurate description of the observed data. The measurement of the W-boson mass plays an essential role in the particle physics since it can provide indirect proof of the physics beyond SM when combining with the precise measurements of the Higgs boson and the top quark masses.

In this chapter a theoretical background of the thesis is described. In the first part a general overview of the SM is given. The motivation for the W-boson mass measurement with the review of previous measurements is described in the following section. Next, a phenomenology of proton–proton collisions with a description of the W-boson production and decay mechanisms at hadron colliders is presented. This chapter concludes with a description of the measurement strategy.

1.1 THE STANDARD MODEL OF PARTICLE PHYSICS

The SM of particle physics is a quantum field theory (QFT) formulated in the late 1960s, describing the fundamental particles of nature and their interactions, with the exception of gravity. The gravity is described by general relativity and in the SM its effects are negligible for energies up to the Planck scale (10^{19} GeV), which is far away from the energies currently reachable at the collider experiments. The SM is based on sets of fundamental spin-1/2 particles called *fermions* which interact through spin-1 particles called *gauge bosons* and spin-0 particle *Higgs boson* responsible for the origin of mass. For each particle there is an antiparticle with the same mass, but opposite charges. Fermions are grouped depending on the electric charge to leptons with integer and quarks with third-numbered electric charges. Quarks (q) carry a *color* charge (r, g, b) and are combined into colorless hadrons, which may be mesons ($q\bar{q}$) or baryons (qqq or $\bar{q}\bar{q}\bar{q}$). There are 12 gauge bosons: eight gluons, g (mediators of the strong interaction), three weak bosons, W^+, W^- and Z (mediators of the weak interaction) and photon, γ (mediator of the electromagnetic interaction). Leptons interact via weak interaction and also via electromagnetic if they are electrically charged. Quarks interact

via all three interactions. Particles are classified by their basic quantum numbers which are related to the invariance of the theory under symmetries. They are grouped in three generations, each generation with the higher mass than the previous. The first generation is formed of particles that are constituents of stable visible matter, while the other two generations are formed of unstable particles. Figure 1.1 shows the fundamental particles of SM of particle physics with their basic properties. Detailed references for this section are the standard textbooks [1–3] and reviews [4, 5].

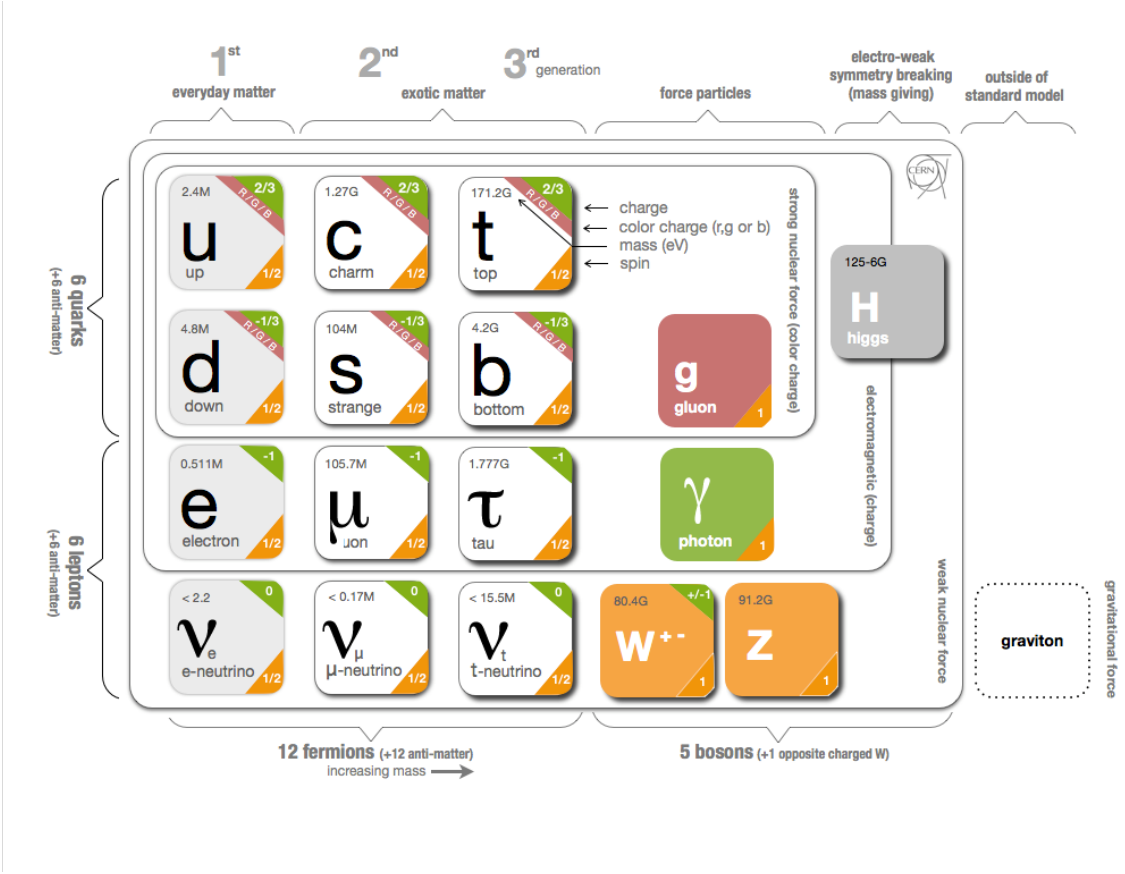

Figure 1.1: Graphical scheme of the particles in the Standard Model with their basic properties [6]. The graviton, a hypothetical mediator of gravity, which is outside of SM is also shown.

QFT [7] gives mathematical framework for construction of fields as quantum mechanical models of systems parametrised by an infinite number of dynamical degrees of freedom. In QFT particles are associated to excited states of fields $\phi_i(x)$ depending on the space-time coordinates x. Description of fermions is given with fermion fields $\psi(x)$, and vector fields $A_\mu(x)$ in case of gauge bosons. The dynamics and kinematics of the theory are given by the Lagrangian densities $\mathcal{L}$ as a function of one or more fields $\phi_i(x)$ and their derivatives $\partial_\mu\phi_i(x)$. The Euler-Lagrange equation of motion, derived from the principle of least action, is:

$$\partial_\mu \left(\frac{\partial \mathcal{L}}{\partial(\partial_\mu \phi)} \right) - \frac{\partial \mathcal{L}}{\partial \phi} = 0. \tag{1.1}$$

for each field in the Lagrangian.

The SM is characterised by a high degree of symmetry. According to the Noether theorem [8], each continuous symmetry is associated to a conserved quantity, thus the dynamics of a physical system can be described by its symmetry. For example, the invariance under space translations corresponds to momentum conservation, invariance under time translation leads to the energy conservation and invariance under rotation gives angular momentum conservation. The field $\phi(x)$ under transformation U gives:

$$\phi(x) \rightarrow \phi'(x) = U\phi(x). \tag{1.2}$$

The transformations U describe a symmetry of the theory if the equations of motion remain invariant. If U is a constant, then the transformation is global (internal), but in case that $U(x)$ is x-dependent then the transformation is local. For each symmetry of the theory, the set of all unitary transformations U form a Lie group [9]. If the symmetry is commutative the group is referred as Abelian, for non-commutative symmetries group is non-Abelian. For instance, the spin and mass of a particle are associated with their representation of the Poincare group (non-Abelian Lie group), which is the symmetry group of space-time and includes translations, rotations and boosts. Electromagnetic interactions respect parity (P) and charge conjugation (C) symmetries, while weak interactions are maximally P and C violating, and violate the combined symmetry CP as well. The combined symmetry, CPT, where T is time reversal, has never been observed to be broken by any force, and is believed to be generally conserved in all Lorentz invariant QFT [7].

A gauge theory is QFT in which the Lagrangian is invariant under local transformations under a gauge group, where gauge refers to the degrees of freedom of the Lagrangian. The SM is non-Abelian gauge theory based on $SU(3)_C$ symmetry group for strong interactions between the quarks and $SU(2)_L \otimes U(1)_Y$ for the electroweak interactions between quarks and leptons. The index C denotes the color charge, index L refers to left-handed, while Y represents the hypercharge. The SM Lagrangian density $\mathcal{L}_{\mathrm{SM}}$ consists from terms for electroweak $\mathcal{L}_{\mathrm{EW}}$ and strong interaction $\mathcal{L}_{\mathrm{QCD}}$, the Yukawa term $\mathcal{L}_{\mathrm{Yukawa}}$ and, as well the Higgs sector term $\mathcal{L}_{\mathrm{Higgs}}$:

$$\mathcal{L}_{\mathrm{SM}} = \mathcal{L}_{\mathrm{EW}} + \mathcal{L}_{\mathrm{QCD}} + \mathcal{L}_{\mathrm{Yukawa}} + \mathcal{L}_{\mathrm{Higgs}}. \tag{1.3}$$

More details are given in the following sections. An important property of SM is its renormalizability, used to address the divergence of integrals in perturbative calculations.Renormalisation restores the predictive power of SM. The SM has 18 free parameters which are all measured by experiments: six quark masses, three lepton masses, four CKM (Cabibbo–Kobayashi–Maskawa [10, 11]) parameters, three gauge couplings, the vacuum expectation value and the mass of the Higgs boson. Since some of the parameters can't be measured directly, like the three gauge constants, it is more convenient to translate them into quantities that can be measured experimentally with extremely high precision. The most precisely measured set of SM parameters consists of the Fermi coupling constant (G_{F}), the strong coupling constant (α_s) and the mass of the Z boson (m_Z). Table 1.1 shows measured values of the free SM parameters. When all free parameters are fixed, amplitudes for scattering processes and decay rates can be calculated using perturbation theory with power series expansion in the dimensionless reduced coupling constants of electromagnetic, weak and strong interaction. SM

has been confirmed by many experiments with very good agreement to the theoretical predictions.

Table 1.1: Measured values of the SM free parameters with their uncertainties [12].

Parameter	Value
Fermion masses	
Electron	$m_e = 510.9989461(31)$ keV
Muon	$m_\mu = 105.6583745(24)$ MeV
Tau	$m_\tau = 1.77686(12)$ GeV
Up quark	$m_u = 2.2^{+0.6}_{-0.4}$ MeV
Down quark	$m_d = 4.7^{+0.5}_{-0.4}$ MeV
Strange quark	$m_s = 96^{+8}_{-4}$ MeV
Charm quark	$m_c = 1.27(3)$ GeV
Bottom quark	$m_b = 4.18^{+4}_{-3}$ GeV
Top quark	$m_t = 173.21(87)$ GeV
Couplings	
Strong coupling constant	$\alpha_s(m_Z) = 0.1181(11)$
Fermi coupling constant	$G_\mathrm{F} = 1.1663787(6) \times 10^{-5}$ GeV^{-2}
Boson masses	
W boson	$m_W = 80.385(15)$ GeV
Z boson	$m_Z = 91.1876(21)$ GeV
Higgs boson	$m_H = 125.09(24)$ GeV
CKM parameters	
Angle	$\varphi_{12} = 13.04(5)^\circ$
Angle	$\varphi_{23} = 0.201(11)^\circ$
Angle	$\varphi_{31} = 2.38(6)^\circ$
Phase	$\delta_{13} = 1.20(8)$ rad

1.1.1 *Electroweak theory*

The first ever defined QFT is the Quantum Electrodynamics (QED) which describes electromagnetic interactions [13, 14]. QED is one of the most successful theories due to its very accurate predictions. The most precisely validated prediction is the anomalous magnetic moment of the electron [12]. QED is an Abelian gauge theory based on $U(1)$ symmetry group. Fermion with mass m is described with Dirac equation for a free fermion field $\psi(x)$:

$$(i\gamma^\mu \partial_\mu - m)\psi(x) = 0, \tag{1.4}$$

where γ^μ are gamma matrices. The Lagrangian density $\mathcal{L}$ for this field is given with:

$$\mathcal{L} = \bar{\psi}(x)\,(i\gamma^\mu \partial_\mu - m)\,\psi(x), \tag{1.5}$$

where the first part in the equation describes the kinetic energy of the free fermion field and the second corresponds to the self interaction. The local gauge transformation of the $U(1)$ group is defined as:

$$\psi(x) \to \psi'(x) = e^{i\alpha(x)}\psi(x), \tag{1.6}$$

where $\alpha(x)$ is a phase transformation (arbitrary continuous function of space-time). In order for Lagrangian density to be gauge invariant under this transformation, covariant derivative must be introduced and defined as:

$$\partial_\mu \rightarrow \mathcal{D}_\mu = \partial_\mu - ieA_\mu(x), \tag{1.7}$$

where $A_\mu(x)$ is vectorial gauge field of the exchanged vector bosons of electromagnetic interaction between fermions and e is the electric charge of the fermion. According to the Noether theorem charge is conserved. The gauge transformation of the vectorial field is defined as:

$$A_\mu(x) \rightarrow A'_\mu(x) = A_\mu(x) - \frac{1}{e}\partial_\mu\alpha(x). \tag{1.8}$$

Therefore, the Lagrangian density becomes:

$$\mathcal{L} = \bar{\psi}(x)\left(i\gamma^\mu\partial_\mu - m\right)\psi(x) - e\bar{\psi}(x)\gamma^\mu A_\mu(x)\psi(x), \tag{1.9}$$

where the second term describes the electromagnetic interaction between the fermion and photon field. A kinetic term for the photon field must be added, since photons are observed as free particles. The kinetic term is defined from field strength tensor $F_{\mu\nu} = \partial_\mu A_\mu - \partial_\nu A_\mu$. Then, the QED Lagrangian density becomes:

$$\mathcal{L}_{\text{QED}} = \bar{\psi}(x)\left(i\gamma^\mu\partial_\mu - m\right)\psi(x) - e\bar{\psi}(x)\gamma^\mu A_\mu(x)\psi(x) - \frac{1}{4}F_{\mu\nu}F^{\mu\nu}. \tag{1.10}$$

Adding a mass term for the photon field in the Lagrangian density would violate local gauge invariance. The QED coupling constant, related to the fine structure constant, $\alpha = e^2/4\pi \approx 1/137$ is very small which allows perturbative calculations.

Analogous to the electromagnetic interaction, the weak interaction was postulated to explain the β decay. Then, after the great success of QED, the idea was to extend the gauge invariance principle to model the weak interactions for non-Abelian symmetries. However, compared to the QED, the theory of weak interactions is more complicated, since these processes involve only left-handed fermions (right-handed anti-fermions), and furthermore, there are charged and neutral current interactions. The charged currents change the flavor of the left-handed fermion fields, whereas neutral currents conserve the flavor. The Yang–Mills gauge theories were the first theories to model the weak interaction based on $SU(2)_L$ symmetry group [15]. All fermions interact via weak interaction. The left- and right-handed fermions are represented with wave functions (spinors), respectively:

$$\psi_L = \frac{1}{2}(1-\gamma^5)\psi \quad \text{and} \quad \psi_R = \frac{1}{2}(1+\gamma^5)\psi, \tag{1.11}$$

where γ^5 is defined with gamma matrices γ^μ, $\gamma^5 = i\gamma^0\gamma^1\gamma^2\gamma^3$. Therefore, fermions appear as families with left-handed doublets of quarks and leptons ($I^2 = 1/2$ and $I_3 = \pm 1/2$) and right-handed singlets of quarks and leptons ($I_3 = 0$):

$$\begin{array}{ccccccc} \begin{pmatrix} u \\ d \end{pmatrix}_L & \begin{pmatrix} c \\ s \end{pmatrix}_L & \begin{pmatrix} t \\ b \end{pmatrix}_L & & \begin{pmatrix} \nu_e \\ e \end{pmatrix}_L & \begin{pmatrix} \nu_\mu \\ \mu \end{pmatrix}_L & \begin{pmatrix} \nu_\tau \\ \tau \end{pmatrix}_L . \\ u_R & c_R & t_R & & e_R & \mu_R & \tau_R \\ d_R & s_R & b_R & & & & \end{array} \tag{1.12}$$

The electroweak model (EW) developed in the 1960s by Glashow, Weinberg and Salam unifies electromagnetic and weak interactions under $SU(2)_L \otimes U(1)_Y$ symmetry group [16–19]. For energies below the electroweak scale, which is around 246 GeV, the symmetry is broken. New quantum number is introduced after unification of this two interactions: the weak hypercharge, Y, defined in a relation:

$$Q = I_3 + \frac{Y}{2}, \tag{1.13}$$

where Q is the electric charge and I_3 is the third component of the weak isospin. The $SU(2)_L$ has three generators with gauge fields: W^1_μ, W^2_μ and W^3_μ, while $U(1)_Y$ group has one generator with gauge field B_μ. Therefore, the EW Lagrangian density is:

$$\mathcal{L}_{EW} = \sum_{j=1}^{3} i\bar{\psi}_j(x)\gamma^\mu D_\mu \psi_j(x) - \frac{1}{4}W^a_{\mu\nu}W^{\mu\nu}_a - \frac{1}{4}B^{\mu\nu}B_{\mu\nu}, \tag{1.14}$$

with vector gauge fields:

$$W^{\mu\nu}_a = \partial^\mu W^\nu_a - \partial^\nu W^\mu_a + g\epsilon_{abc}W^\mu_b W^\nu_c \quad \text{and} \quad B^{\mu\nu} = \partial^\mu B^\nu - \partial^\nu B^\mu, \tag{1.15}$$

and covariant derivative given as:

$$D_\mu = \partial_\mu + ig\frac{\sigma_a}{2}W^a_\mu + i\frac{g'}{2}YB_\mu, \tag{1.16}$$

where g and g' are coupling constants of the weak and electromagnetic interactions, respectively, and σ^a are the Pauli matrices. Linear combination of vector gauge fields yields physical fields W^+_μ and W^-_μ which mediate charged, and Z_μ and A_μ which mediate neutral intaraction. The EW Lagrangian density describes fermions and gauge bosons as massless particles, since additional mass term would break the local gauge invariance. The invariance of the EW Lagrangian density under $SU(2)_L$ leads to weak isospin I conservation, while the invariance under $U(1)_Y$ leads to weak hypercharge Y conservation, according to the Noether theorem.

1.1.2 *Quantum Chromodynamics*

Quantum Chromodynamics (QCD) is non-Abelian gauge theory which describes strong interaction based on $SU(3)_C$ symmetry group [20–23]. Quarks are represented by triplets of fermion fields:

$$\psi_f(x) = \begin{pmatrix} q_r \\ q_g \\ q_b \end{pmatrix}, \tag{1.17}$$

where f denotes the quark flavor and r, g and b represent the three colors conventionally noted as red, green and blue, respectively. The QCD Lagrangian density is:

$$\mathcal{L}_{QCD} = \sum_{j,k} \bar{\psi}_j \left(i\gamma^\mu D_\mu - m\right)_{jk} \psi_k - \frac{1}{4}G^a_{\mu\nu}G^{\mu\nu}_a, \tag{1.18}$$

where j and k go through all flavors. The covariant derivative D_μ is defined with eight generators of $SU(3)$ symmetry group given by Gell–Mann matrices λ_a:

$$D_\mu = \partial_\mu - ig_s G^a_\mu(x)\lambda_a. \tag{1.19}$$

The first term in the Lagrangian density represents kinetic term for quarks and their interaction with gluons, while the second one is the kinetic term for the gluon field. The field strength tensor $G^a_{\mu\nu}$ is defined as:

$$G^a_{\mu\nu} = \partial_\mu G^a_\nu - \partial_\nu G^a_\mu - g_s f_{abc} G^b_\mu G^c_\nu, \tag{1.20}$$

where f_{abc} are the structure constants of $SU(3)$ group defined from commutation relations of the Gell-Mann matrices $[\lambda^a, \lambda^b] = if_{abc}\lambda^c$, g_s is the strong coupling constant and $G^a_\mu(x)$ represents the gluon vector fields. The last term in the field strength tensor represents the self-interaction of the gluon field. Since there is no gauge invariant mass term in the Lagrangian density (as for QED), gluons are massless.

One of the fundamental parameters of QCD is the renormalised coupling constant $\alpha_s = g_s^2/2\pi$ which depends on the energy scale Q involved in the interaction process. The coupling constant decreases as the energy scale increases. When a coupling constant α_s is known at some energy scale μ_R, i.e. *renormalisation scale*, the dependence on Q is calculated using the perturbation theory. Figure 1.2 shows the running of the strong coupling constant α_s as a function of the energy scale Q with a comparison between the theoretical predictions and measurements from different experimental sources. As a consequence QCD shows two characteristic behaviours of quarks and

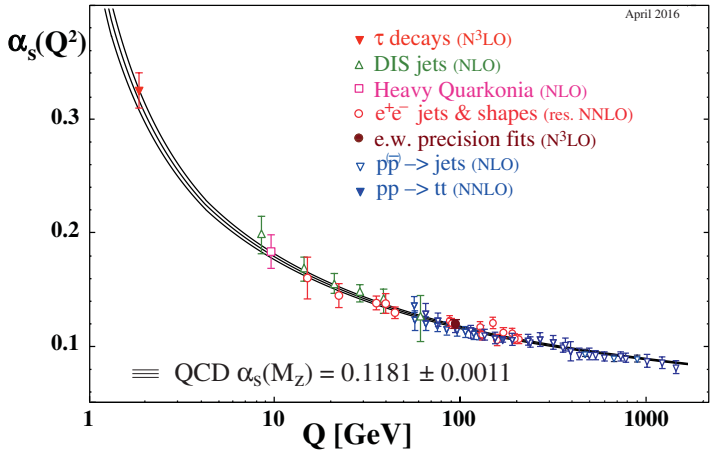

Figure 1.2: Summary of measurements of the running strong coupling constant α_s as a function of the energy scale Q [12].

their interactions: asymptotic freedom and confinement. Confinement represents the fact that quarks and gluons cannot be observed as isolated states, they are only observed as color singlet states of hadrons that have integer electric charge and zero color charge. Asymptotic freedom represents decrease of interaction strength at short

distances. As a consequence at short distances colored particles (gluons and quarks) interact very weakly, i.e. behave as free particles. As a consequence of QCD confinement and asymptotic freedom, perturbation theory can be used to describe high-energy processes, but not in the low energy regime. Further, colored particles undergo so-called hadronization, before they could possibly be observed. In the process of hadronization, the colored objects are grouped into color singlet objects - baryons and mesons. A collimated jet of such baryons and mesons is detected in the detector, if the initial quark or gluon is generated with high momentum and it originates from a hard-scattering process.

1.1.3 *Electroweak symmetry breaking*

The EW theory (described in Section 1.1.1) predicts massless vector bosons and fermions which is in strong disagreement with experimental data. The solution of this problem was proposed by group of scientists Higgs, Brout, Englert, Guralnik, Kibble, and Hagen in 1960s who developed a mechanism for spontaneous symmetry breaking via the addition of a complex scalar doublet to the SM [9, 17, 24–28]. The concept of spontaneous symmetry breaking is derived from phase transition in solid state physics observed by Heinserberg in 1928 [29].

For a complex scalar doublet $\Phi(x)$ with four degrees of freedom:

$$\Phi(x) = \begin{pmatrix} \Phi^+ \\ \Phi^0 \end{pmatrix} = \frac{1}{\sqrt{2}} \begin{pmatrix} \Phi_1 + i\Phi_2 \\ \Phi_3 + i\Phi_4 \end{pmatrix}, \tag{1.21}$$

the simplest possible potential that will respect SM symmetry is:

$$V(\Phi\Phi^\dagger) = \mu^2\Phi^\dagger\Phi + \lambda(\Phi^\dagger\Phi)^2, \tag{1.22}$$

with $\lambda > 0$. There are two possibilities for the sign of μ^2 term: for $\mu^2 > 0$ the potential V is a concave function of the field Φ with an absolute minimum in the origin of the axis and the minimal energy of the field is unique and can't break the symmetry; for $\mu^2 < 0$ the minimum is not unique and corresponds to the circumference centred in the origin. Figure 1.3 shows the Higgs potential projection $V(\Phi)$ with both possibilities for the sign of μ^2 term. Then, the EW Lagrangian density with kinetic term which is invariant under local $SU(2) \times U(1)$ transformation is:

$$\mathcal{L} = (D_\mu\Phi)^\dagger(D^\mu\Phi) - V(\Phi\Phi^\dagger), \tag{1.23}$$

with covariant derivative defined as in Equation 1.16. The stable minimum of the potential can be derived from:

$$\Phi\Phi^\dagger = \frac{-\mu^2}{2\lambda}, \tag{1.24}$$

which represents equation of 4-dimensional sphere. There are infinite number of solutions with different phase. Each choice of Φ_0 that breaks a symmetry, generates a mass for a gauge boson. On the other hand, the invariant choice of Φ_0, under gauge

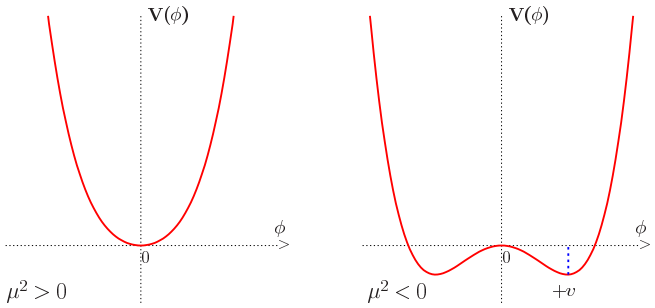

Figure 1.3: The projection of the Higgs potential $V(\Phi)$.

transformation will create massless gauge bosons (Goldstone bosons). Therefore, the chosen field is:

$$\Phi_0 = \frac{1}{\sqrt{2}} \begin{pmatrix} 0 \\ \upsilon \end{pmatrix}, \tag{1.25}$$

where υ is the vacuum expectation value, defined as $\upsilon = \sqrt{-\mu^2/\lambda}$.

When the Lagrangian density, Equation 1.23, is rewritten in terms of the scalar complex doublet field Φ, requiring the symmetry to be local, the EW gauge fields are written in terms of B_μ and W^i_μ fields. The corresponding particles of EW fields are the $W^\pm$ and Z bosons and the photon, defined as:

$$W^\pm_\mu = \frac{1}{\sqrt{2}} \left(W^1_\mu \mp W^2_\mu \right), \tag{1.26}$$

$$Z_\mu = -B_\mu \sin\theta_W + W^3_\mu \cos\theta_W, \tag{1.27}$$

$$A_\mu = B_\mu \cos\theta_W + W^3_\mu \sin\theta_W, \tag{1.28}$$

where θ_W is the Weinberg's angle $\tan\theta_W = g'/g$ and electric charge $e = g'\cos\theta_W = g\sin\theta_W$. The masses of the bosons also arise from the Lagrangian:

$$(D_\mu\Phi)^\dagger(D^\mu\Phi) = \frac{\upsilon^2 g^2}{4} W^+_\mu W^{-\mu} + \frac{1}{2}\frac{\upsilon^2(g^2+g'^2)}{4} Z_\mu Z^\mu + ... \tag{1.29}$$

The photon is massless, while masses of W and Z bosons are:

$$m_W = \frac{1}{2} g\upsilon \quad \text{and} \quad m_Z = \frac{1}{2}\upsilon\sqrt{g^2+g'^2}. \tag{1.30}$$

Therefore, the Lagrangian density describes two massive gauge bosons with mass m_W, one massive boson field with mass m_Z, one massless gauge field and one scalar field with mass $m_H = \sqrt{2\lambda\upsilon^2}$, usually called Higgs boson, where the massless Goldstone bosons disappeared. The fermion masses are generated by introducing an interaction term, so called Yukawa term, between the lepton field and the Higgs field in the Lagrangian density. The acquired fermion mass is $m_f = g_l\upsilon/\sqrt{2}$, where g_l is the coupling parameter of the scalar field to the fermions. The Higgs mechanism introduces arbitrary coupling parameters for each fermion mass.

After almost 50 years of search for the Higgs boson, in 2012 was discovered by the ATLAS [30] and CMS [31] experiments at the Large Hadron Collider (LHC).

1.1.4 *Limitations of the Standard Model*

The SM has been tested in many ways, especially during the past 30 years at lepton (LEP, SLC), lepton-hadron (HERA) and hadron colliders (Tevatron, LHC). It is one of the most successful theories that precisely predicted a wide variety of phenomena (i.e. the existence of Z, $W^{\pm}$ bosons). The predictive power of the SM is preserved beyond tree-level computations and allows probing the quantum effects. Thus, the result of the calculation is a clear prediction of the model which has been tested at the per mille level. The SM has accurately predicted and matched cross section measurements over 10 orders of magnitude. Figure 1.4 shows the comparison of the latest measurements of different SM production cross sections with the ATLAS experiment to the theoretical predictions with an impressive agreement over many orders of magnitude. Therefore, one can conclude that the SM describes the data up to the highest energies achieved experimentally.

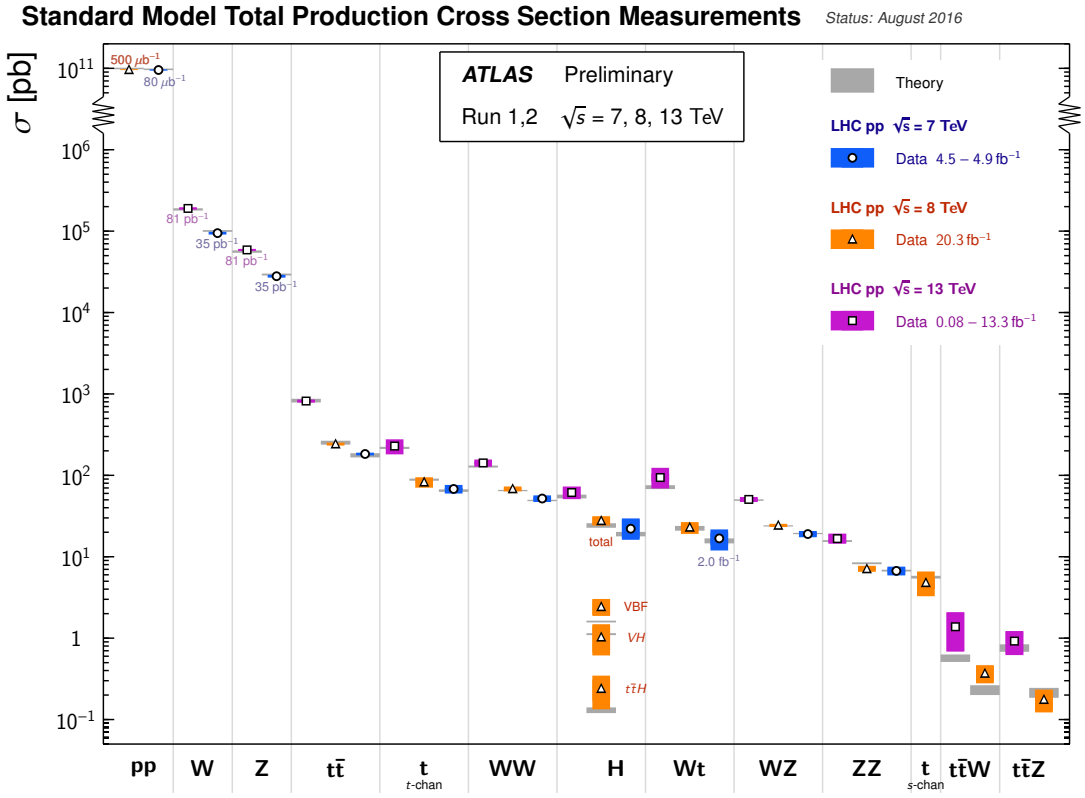

Figure 1.4: Summary of several SM total production cross section measurements performed by ATLAS experiment, compared to the corresponding theoretical expectations [32].

Despite the broad success of SM, there are still a number of theoretical and experimental limitations to the theory [33]:

- Gravity is not included in the SM, therefore it is considered that SM is valid up to the Planck scale 10^{19} GeV where gravity becomes important.

- Dark matter and dark energy occupy almost 23% and 72% of the Universe, respectively, and still these phenomena are unexplained. Within SM there is no dark matter candidate with properties expected from experimental observations.
- There is 16 orders of magnitude difference between the electroweak and the Planck scale, which is referred as the hierarchy problem. Thus, an unnatural fine-tuning of the quadratically divergent quantum corrections for the mass of the Higgs boson is needed.
- Within the SM there is no mass term for neutrinos, however the finite neutrino masses are experimentally confirmed from neutrino oscillations.
- The matter-antimatter asymmetry in the Universe is unexplained, since they were created in equal amounts after the Big Bang.

These open questions motivate further search for the physics beyond the SM. One of the most considered theories as an extension of the SM is Supersymmetry (SUSY) [34]. SUSY is based on a principle that there is a supersymmetric fermion (boson) partner for every SM boson (fermion). SUSY partners are not yet experimentally observed, therefore SUSY must be a broken symmetry at some energies. However, the masses of the SUSY partners must not be too large, no more than a few TeV in order to solve the hierarchy problem. SUSY provides solutions for some of the issues with the SM: the lightest neutral particle is a candidate for dark matter, coupling constants unify to exactly one at some energy scale, providing the unification of the fundamental interactions. There are many ways to extend SM with SUSY, and the minimal supersymmetric SM extension (MSSM) is the minimal phenomenologically possible SUSY extension of SM with with minimal particle content.

1.2 MOTIVATION FOR THE W-BOSON MASS MEASUREMENT

SM predicts relations between the W-boson mass m_W, the Z-boson mass m_Z, the fine structure constant α and the Fermi constant G_F. After replacing the terms for coupling constants g and g' in Equation 1.30 one gets:

$$m_W^2 \left(1 - \frac{m_W^2}{m_Z^2}\right) = \frac{\pi\alpha}{\sqrt{2}G_\mathrm{F}}. \tag{1.31}$$

When using the most precise measurements for the Fermi constant, Z-boson mass and the fine structure constant (see Table 1.1), the predicted W-boson mass from Equation 1.31 is $m_W \approx 80.9$ GeV which is 37σ away from the current world average value [12]. In order to precisely explain the experimental data, inclusion of radiative corrections Δr is needed [35]:

$$m_W^2 \left(1 - \frac{m_W^2}{m_Z^2}\right) = \frac{\pi\alpha}{\sqrt{2}G_\mathrm{F}}(1 + \Delta r). \tag{1.32}$$

The radiative corrections describe contributions from the quantum fluctuations of the vacuum and they are represented by loops. Significant contributions are coming from

loops involving the top quark and the Higgs boson:

$$\Delta r = \Delta r_{\mathrm{H}} + \Delta r_{\mathrm{t}}. \tag{1.33}$$

The contribution from the $t\bar{b}$ loop, Δr_{t}, is large due to the large mass difference between the t and b quarks:

$$\Delta r_{\mathrm{t}} = \frac{3G_{\mathrm{F}}m_t^2}{8\sqrt{2}\pi^2}\left(\frac{\cos\theta_W}{\sin\theta_W}\right)^2, \tag{1.34}$$

where m_t is top quark mass. The contribution from the Higgs loop Δr_{H} is:

$$\Delta r_{\mathrm{H}} = \frac{11G_{\mathrm{F}}m_W^2}{24\sqrt{2}\pi^2}\left(\ln\frac{m_H^2}{m_W^2} - \frac{5}{6}\right), \tag{1.35}$$

where m_H is the Higgs boson mass. Therefore, the radiative corrections depend on m_t^2 and $\ln m_H^2$. They also depend on the m_W itself, so iterative procedure is needed for m_W calculation. Corrections from one-loop diagrams have a contribution of about $\Delta r \approx 0.03$. Figure 1.5 shows the Feynman diagrams for W-boson mass with one-loop correction.

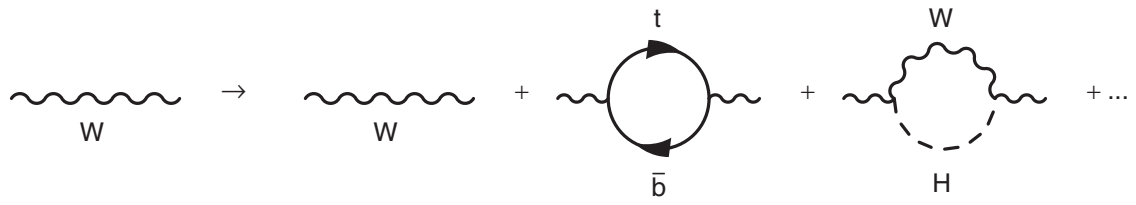

Figure 1.5: W-boson mass propagator with loop corrections from top and bottom quarks and Higgs boson.

Currently, the most accurate prediction for the W-boson mass in the SM is obtained by combining the complete two-loop calculation with the known higher-order QCD and EW corrections, which yields to an uncertainty of $\delta m_W^{theo} \approx 4$ MeV [36]. The dominant theoretical uncertainty on the m_W prediction is from the parametric uncertainty caused by the experimental uncertainty on the top quark mass. An experimental uncertainty on top quark mass of $\delta m_t = 1$ GeV generates a parametric uncertainty on m_W of $\delta m_W \approx 6$ MeV. The parametric uncertainty from the current experimental uncertainty on the hadronic contribution to the shift in the fine structure constant is $\delta m_W = 2$ MeV, while the experimental uncertainty on the Z-boson mass measurement gives $\delta m_W = 2.5$ MeV. The experimental uncertainty on the Higgs boson mass causes much smaller parametric uncertainty on the m_W prediction, $\delta m_W \approx 0.2$ MeV. The calculated theoretical uncertainty, $\delta m_W^{theo} \approx 4$ MeV, is much smaller than the present experimental error on the m_W measurement $\delta m_W^{exp} = 15$ MeV [12]. The future projected theoretical uncertainty is expected to be $\delta m_W^{theo} \approx 1$ MeV from three-loop calculations [37].

If there is physics beyond the SM, then it contributes to the radiative corrections via virtual effects of yet undiscovered particles. Depending on the model, there are different possible contributions to the radiative corrections. In MSSM, the prediction

of the m_W depends on the masses, mixing angles and couplings of all MSSM particles. Dominant contribution to the radiative corrections is coming from the superpartners of top and bottom quarks, similar to the top-bottom loop corrections in the SM [38]. The dependence of m_W on m_t is shown in Figure 1.6. The green area shows allowed area of the m_W and m_t taking into account the MSSM parameter space with the limits from the Higgs searches at LEP, Tevatron and LHC, not the observed signal at about $m_H = 125.6 \pm 0.7$ GeV. The red strip indicates the region where the MSSM prediction for m_W overlaps with the SM prediction, with $m_H = 125.6 \pm 0.7$ GeV. The grey ellipse shows the 68% confidence limit of the current experimental results for m_W and m_t (taken from [12]). A non-zero SUSY contribution tends to increase the prediction for m_W compared to the SM case. Figure 1.6 shows that the ellipse is fully contained in the MSSM area, also the region with the best agreement between the MSSM prediction for m_W and the experimental result corresponds to relatively light masses of SUSY particles. For example, very light superpartners of leptons (sleptons), just above the LEP limit, could induce a shift in m_W of about 60 MeV, while light charged superpartners of bosons (charginos) can give corrections of up to 20 MeV [38].

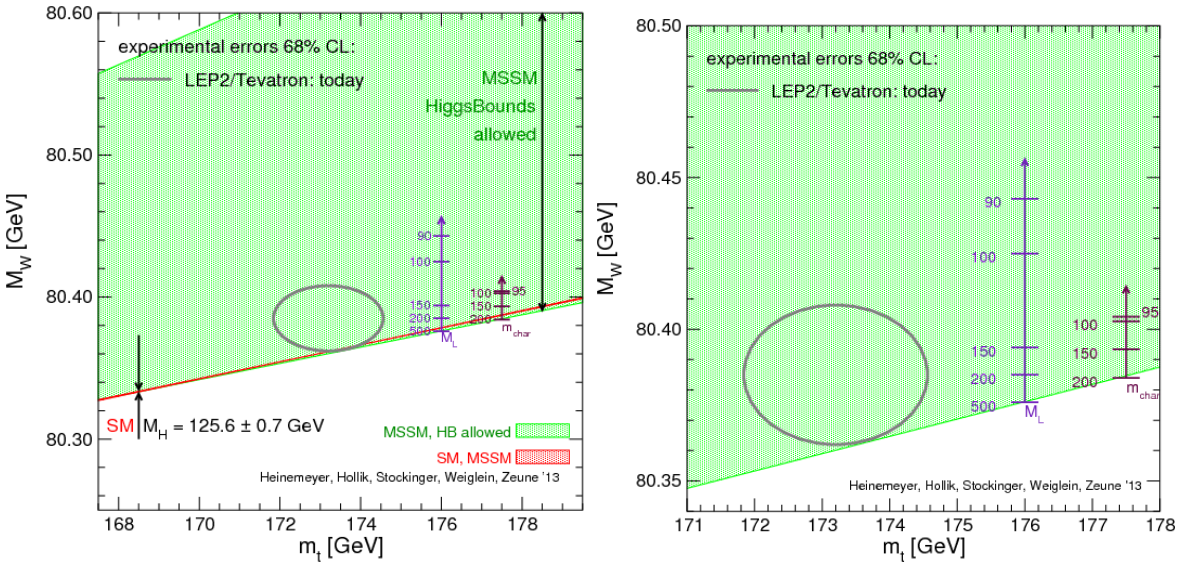

Figure 1.6: m_W as a function of m_t [38]. The green region shows the m_H bound allowed region for the MSSM m_W prediction. The red strip indicates the overlap region of the SM and the MSSM, with $m_H = 125.6 \pm 0.7$ GeV. The two arrows indicate the possible size of the contributions of the SUSY particles as explained in the text. Plot on the right is zoom into the most relevant region, with the SM area omitted.

A precise measurement of the m_W is of great importance since it is highly sensitive and probes the radiative corrections allowing the consistency test of the SM, as well as testing the existence of the physics beyond SM. The direct searches for the physics beyond the SM have not found any signal up to now, and in order to enhance the sensitivity for discriminating between different models, it is useful to compliment them with the precise measurement of m_W.

1.2.1 *Electroweak precision observables*

After the Higgs boson discovery, the SM is over-constrained and all parameters of the SM have been determined from direct measurements. Electroweak precision data provide a very powerful check of the internal consistency of the SM. The effects of the loop corrections are small, usually less than 1%, so they are significant only for observables which can be measured with an equally high precision. Many observables have been precisely measured at electron-positron colliders (LEP and SLC) and hadron colliders (Tevatron and LHC).

The list of electroweak precision observables comprise of: mass and decay width of the Z boson, m_Z and Γ_{Z}, mass and decay width of the W boson, m_W and Γ_{W}, the top quark mass, m_t, the Higgs-boson mass, m_H, forward-backward asymmetries, A_{FB} in specific Z-boson decay channels and the hadronic contribution to the running fine-structure constant evaluated at the Z-boson mass, $\Delta\alpha_{\mathrm{had}}(m_Z^2)$ [39].

Observables determined from the Z-boson lineshape [40, 41] are: number of light neutrino flavors contributing to the invisible Z-boson decay width: $N_\nu = 2.9841 \pm 0.0083$, mass and decay width of the Z boson, forward-backward asymmetry and effective weak mixing angle. Mass of the top quark has bean measured at Tevatron and LHC, with a combined value of $m_t = 173.34 \pm 0.76$ GeV [42], the latest measurement with the ATLAS experiment yields $m_t = 172.84 \pm 0.70$ GeV [43], while the most recent CMS combination for top quark mass measurements gives $m_t = 172.44 \pm 0.49$ GeV [44]. The Higgs boson mass is measured by the ATLAS [30] and CMS [31] experiments at the LHC, with the combined value of $m_H = 125.09 \pm 0.24$ GeV [45]. The strong coupling constant is measured at LEP with low energies, HERA, Tevatron and LHC, as shown in Figure 1.2. The Fermi coupling constant is extracted from muon lifetime and is one of the most precise measured parameters with a relative uncertainty of 500 parts-per-billion (10^{-9}) [12]. Measured values of these parameters with their experimental uncertainties are given in Table 1.1.

Mass and decay width of the W boson have been precisely measured at LEP and Tevatron, more details about these measurements will be given in Section 1.2.3. Current experimental accuracy of the m_W measurement is $1.8 \cdot 10^{-4}$ [12]. The importance of m_W as a precision observable relies on its accurate determination, both experimentally and theoretically. The mass of the W boson is related to the masses of the top quark and the Higgs boson as shown in Equation 1.32, and it is of great importance to measure these quantities as precisely as possible.

The progress in experimental accuracy is much slower for m_W measurement than for m_t and m_H because of its complexity. Further experimental improvements are expected at the LHC [39]. With a large dataset and sufficient time to understand and improve systematic uncertainties, the measurement of the m_H, m_W and m_t is expected at the level of: $\delta m_H = 100$ MeV, $\delta m_W = 10$ MeV (with the final combination of Tevatron measurements), $\delta m_t = 0.6$ GeV.

1.2.2 *Importance and role of electroweak fits*

The EW fits of the SM compare the precision measurements of electroweak observables with accurate theoretical predictions calculated at multi-loop level. In the beginning, the EW fits were used to test the validity of SM and to indirectly constrain remaining free SM parameters before the direct discovery of remaining particles.

Before the Higgs boson discovery, the electroweak precision measurements allowed stringent constraints on its mass with indirect determination. The indirect determination of the Higgs boson mass was derived from radiative corrections to precision observables measured at LEP and SLC, processed by LEP Electroweak Working Group [41]. For the W-boson mass and width the combination of LEP and Tevatron results were used, while for the mass of the top quark Tevatron result was used. The statistical model, from which the constraints on m_t and m_H were determined, was based on an estimate of higher-order corrections to m_W, with complete fermionic and bosonic two-loop corrections, and it was made with the ZFitter package [46]. The remaining theoretical uncertainties due to missing higher order corrections had been estimated to be 4 MeV on m_W and $4.9 \cdot 10^{-5}$ on $\sin\theta_W$ and thus negligible compared to the experimental uncertainty or theoretical uncertainties from the light quark component of the vacuum polarisation term. The result for the predicted Higgs boson mass was 89^{+35}_{-26} GeV, with χ^2 of 17.3/13 (χ^2 probability of 19%) [41].

The GFitter group has made studies of global EW fit to electroweak precision data [39, 47]. The full list of used theoretical and experimental inputs is given in [39], which for the first time provides a consistent set of calculations at next-to-next-to leading order (NNLO) for all relevant input observables, together with the two-loop calculations of the W-boson mass and the effective weak mixing angle. The global EW fit gives $\chi^2_{min} = 17.8$ for 14 free parameters, this result shows good internal consistency of the SM. Figure 1.7 shows a comparison of the global fit results with the direct measurements, as well as with the indirect determinations for each observable. All pull values, defined as deviations from the indirect determinations, are smaller than 3σ. The biggest difference is observed for forward-backward asymmetry A_{FB} in specific Z decay channels. After including the m_H in the fit, an improvement in the prediction of the m_W, m_t and $\sin\theta_W$ is observed. Besides the m_t, other predictions have smaller uncertainties than the ones from direct measurements. The SM fit with minimal input corresponds to the input of minimal set of parameters: m_H, all fermion masses, $\alpha_s(m_Z^2)$ and and three parameters defining the electroweak sector and its radiative corrections (m_Z, G_{F} and $\Delta\alpha_{\mathrm{had}}(m_Z^2)$). In order to test the sensitivity of the SM fit to the various input observables, each of the observables is disabled in the fit and a log-likelihood scan of the disabled observable is performed. In that way, an indirect determination of the disabled observable is obtained. The result of the indirect determination is shown in Figure 1.8, as the $\Delta\chi^2$ profile as a function of m_W (grey band) compared to the $\Delta\chi^2$ profile of the fit including the measurement of the m_H (blue curve), and the experimentally measured value is represented with a red point. The obtained value

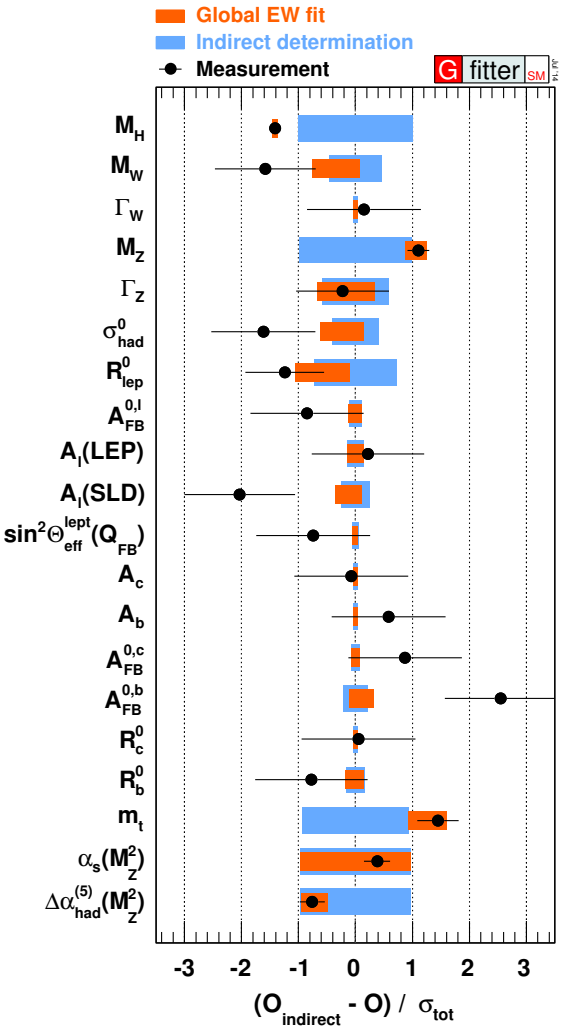

Figure 1.7: Comparison of the fit results (orange bars) with indirect determinations (blue bars) and direct measurements (data points): pull values for the SM fit defined as deviations to the indirect determinations [39]. The total error is taken to be the error of the direct measurement added in quadrature with the error from the indirect determination.

from indirect determination of the m_W from the fit is:

$$\begin{aligned} m_W = 80358.4 \pm 4.6_{m_t} \pm 3.0_{\delta^{theo}m_t} \pm 2.6_{m_Z} \pm 1.8_{\Delta\alpha_{\rm had}} \\ \pm 2.0_{\alpha_s} \pm 0.1_{m_H} \pm 4.0_{\delta^{theo}m_W} \text{ MeV}, \end{aligned} \tag{1.36}$$

where the uncertainties of m_W correspond to the experimental or theoretical uncertainty of the observable given in subscript. The final result gives:

$$m_W = 80358 \pm 8 \text{ MeV}. \tag{1.37}$$

The predicted m_W value differs by 1.8σ from the direct measurement, and the uncertainty is smaller by a factor of two. The largest uncertainties on the m_W prediction are due to experimental and theoretical uncertainty on m_t, followed by the theoretical uncertainty on m_W and experimental uncertainty on m_Z. The theoretical uncertainty

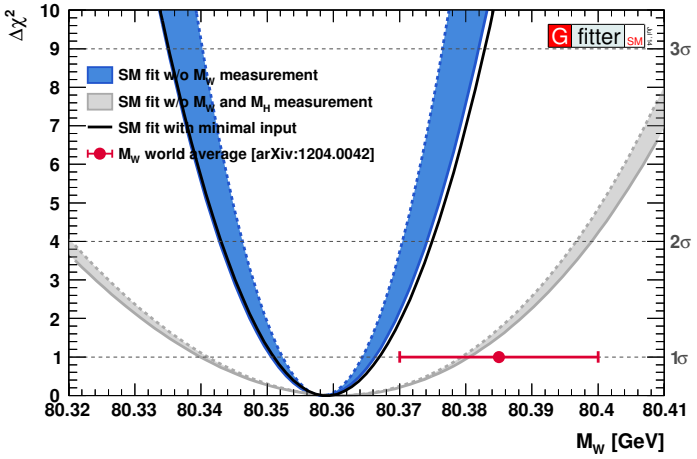

Figure 1.8: $\Delta\chi^2$ profiles as a function of m_W [39]. The blue band corresponds to the result of the fit without the m_W measurement. Grey band corresponds to the fit result without m_W and m_H measurements. The SM fit with minimal input is shown as a black line. The experimental world average of m_W is indicated by a red point with 1σ error bars.

on m_W comes from unknown higher order contributions, estimated by assuming that the perturbation series follow a geometric growth. The dominant sources are $\mathcal{O}(\alpha^2\alpha_s)$ terms beyond the known contribution of $\mathcal{O}(G_F^2\alpha_s m_t^4)$, $\mathcal{O}(\alpha^3)$ electroweak three-loop corrections and $\mathcal{O}(\alpha_s^3)$ [36]. Comparison among m_W, m_t and m_H gives an important consistency test of the SM. Figure 1.9 illustrates the scans of the confidence level profile of m_W versus m_t for various Higgs boson mass hypotheses. This result demonstrates good internal consistency of the SM.

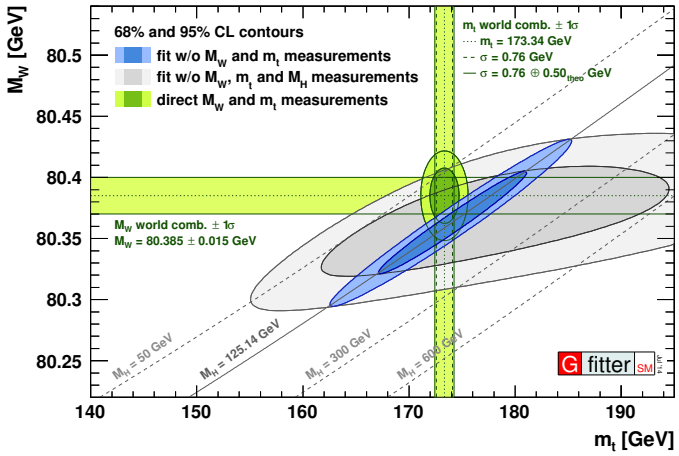

Figure 1.9: Contours at 68% and 95% CL obtained from scans of m_W versus m_t compared to the direct measurements for different m_H hypotheses where the direct m_H measurement is included in the fit (blue area) or not (grey area) [39].

The fit of EW precision observables has been recently performed with an alternative implementation by the HEPfit group [48]. The indirect determination of the m_W yields $m_W = 80362 \pm 8$ MeV, which is consistent with the result from the GFitter group.

1.2.3 *Previous measurements and LHC prospects*

The $W^{\pm}$ and Z bosons were discovered in 1983 on UA1 and UA2 experiments at CERN's SPS proton–antiproton collider. The measured values for the W-boson mass were $m_W = 81 \pm 5$ GeV and $m_W = 80^{+10}_{-6}$ GeV on UA1 [49] and UA2 [50], respectively. Since then, many experiments measured the mass of the W boson as precisely as possible. Figure 1.10 shows how the precision of m_W changed with time since the discovery.

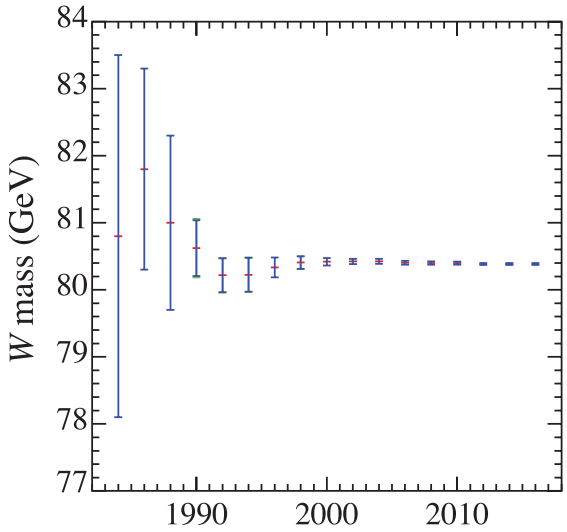

Figure 1.10: Change of the precision of m_W changed with time [12]. Different measurements of the W-boson mass are represented by points on y-axis, while on the x-axis is the year when the (result of) measurement is published.

The W boson has been studied and its mass measured at the LEP (CERN), by 4 experiments ALEPH [51] , DELPHI [52], L3 [53] and OPAL [54]. The W bosons were produced in the reaction $e^+e^- \to W^+W^-$. Compared to very precisely measured Z-boson mass, the W-boson mass was more difficult to measure since the W bosons can not be produced individually because of the charge conservation and also because their leptonic decay channel includes a neutrino. The dependence of W^+W^- pair production cross section on m_W is large near the threshold of 161 GeV, allowing a direct measurement of m_W at these energies. At higher energies, $172 - 209$ GeV this dependence is weaker, therefore, the mass of the W boson has to be determined as the invariant mass of its decay products. The m_W was measured by reconstructing the W boson which decays hadronicaly into quark pairs ($W \to q\bar{q}$) or leptonicaly into a lepton and a neutrino ($W \to \ell\nu$, $\ell = e, \mu, \tau$). The combined measured mass at LEP is [55]:

$$m_W = 80376 \pm 33 \text{ MeV}. \tag{1.38}$$

The uncertainty is dominated by the statistical component of 22 MeV, while the two dominant systematical uncertainties come from the hadronization processes of the hadronic W-boson decay (14 MeV) and the measurement of the LEP beam energy (9 MeV).

The W boson has also been studied at proton-antiproton collider at Tevatron by CDF [56] and D0 [57] experiments. At hadron colliders the W-boson mass is measured through the leptonic decays $W \to \ell\nu$ ($\ell = e, \mu$) only. The main difficulty in the measurement of the m_W at the Tevatron arises from the fact that the initial energy is unknown since W bosons are produced from the valence quarks inside the protons, and due to the presence of the neutrino in final state which disables the direct reconstruction of the W-boson invariant mass. The measured values at CDF and D0 are $m_W = 80389 \pm$ 19 MeV and $m_W = 80383 \pm 23$ MeV, respectively. The CDF experiment measured the m_W in both, electron and muon channels with only 20% of the available data, while the D0 experiment published results only in electron channel with approximately 50% of the available data. By combining results from the Tevatron experiments the m_W determination becomes very precise [58]:

$$m_W = 80387 \pm 16 \text{ MeV}. \tag{1.39}$$

In both CDF and D0 measurements the dominant experimental systematics is due to the lepton energy scale (7 MeV at CDF), while the dominant theoretical uncertainty of 10 MeV is due to the parton distribution functions (PDF) which describe the probability of extracting a parton of a given flavor with a fraction of the total energy of the proton. Tables 1.2 and 1.3 show the full list of uncertainties for the m_W measurement at the D0 and CDF experiments, respectively.

Table 1.2: The uncertainties of the m_W measurement at the CDF experiment [58].

Source	**Uncertainty** [**MeV**]
Lepton energy scale and resolution	7
Recoil energy scale and resolution	6
Lepton removal	2
Backgrounds	3
Experimental subtotal	10
$p_{\mathrm{T}}(W)$ model	5
PDF	10
QED radiation	4
Production subtotal	12
Total systematics	15
Statistics	12
Total	19

Combination of LEP and Tevatron results yields an average value of:

$$m_W = 80385 \pm 15 \text{ MeV}, \tag{1.40}$$

which is dominated by the Tevatron measurements. Figure 1.11 shows measurements of the W-boson mass by the LEP and Tevatron experiments with current world average value.

The current measurements are mostly limited by statistical uncertainties, either directly through limited W-boson samples or indirectly through limited calibration samples. In proton–proton collisions at the LHC, an improvement of the W-boson mass

Table 1.3: The uncertainties of the m_W measurement at the D0 experiment [58].

Source	**Uncertainty** [**MeV**]
Electron energy calibration	16
Electron resolution model	2
Electron shower modeling	4
Electron energy loss model	4
Recoil energy scale and resolution	5
Electron efficiencies	2
Backgrounds	2
Experimental subtotal	18
$p_T(W)$ model	2
PDF	11
QED radiation	7
Production subtotal	13
Total systematics	22
Statistics	13
Total	26

measurement is foreseen. Initial estimates of the expected statistics and systematics suggest that the measurement of the W-boson mass with a precision of the order 7 MeV per lepton channel could be reached [59]. The future expected experimental improvement of m_W is foreseen at the ILC $\delta m_W^{\text{exp}} = 3{-}4$ MeV, the FCC $\delta m_W^{\text{exp}} = 1$ MeV, and the CEPC $\delta m_W^{\text{exp}} = 3$ MeV colliders (more details about future colliders is given in Chapter 2) [39].

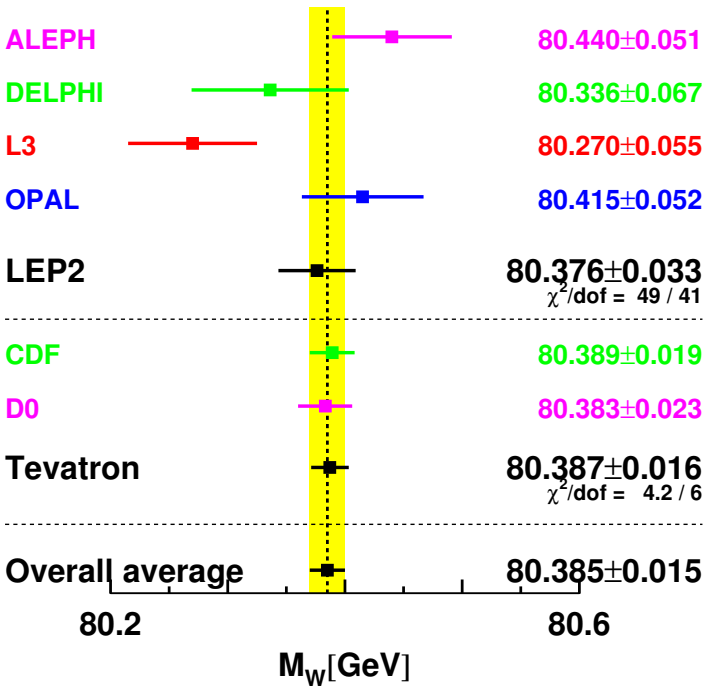

Figure 1.11: The measurements of the W-boson mass by the LEP and Tevatron experiments [12].

1.3 ELECTROWEAK BOSONS AT HADRON COLLIDERS

One major advantage of hadron colliders is in abundant production of W and Z bosons via Drell-Yan (DY) process [60]. Since hadrons are composite objects, the actual interaction happens among its constituents, which makes the study of processes in hadron collisions complicated.

Protons consist of three valence quarks, two u and one d quark, which are exchanging gluons between themselves. Gluons can create virtual pairs of a quark and its anti-quark, commonly known as sea of quarks and gluons. The phenomenological formulation for describing processes inside the proton, known as the *parton* model, was proposed by Feynman in 1969 in order to analyse high-energy hadron collisions [61]. Thus, protons are described as collections of point-like particles, partons, bound together by their interactions. All objects inside the proton are called partons: gluons, valence- and sea-quarks. This nomenclature derives from the first observations of elementary particles inside protons in deep inelastic scattering (DIS) experiments [61].

In the next part a phenomenology of the proton–proton collisions is described, followed by the W-boson production and decay in proton–proton collisions.

1.3.1 *Phenomenology of proton–proton collisions*

The scattering processes in general can be classified as:

- *Elastic scattering*: represents collisions of particles in which the total kinetic energy of the particles is conserved, the colliding particles remain intact and momentum transfer is small.
- *Inelastic scattering*: occurs when the total kinetic energy of the colliding particles is not conserved, and one or both of the colliding particles may dissociate into a system of particles. Inelastic scattering, depending on the momentum of produced particles, can be further separate into:
  - *Soft scattering*, where one or two of the protons dissociate into a system of particles with low momenta. One can distinguish diffractive and non diffractive (also called *minimum bias*) events characterised by production of a high number of charged particles events. Soft processes are dominated by non perturbative QCD effects, which are not well modeled by the event simulation, as described later.
  - *Hard scattering*, where one or two of the protons dissociate into a system of particles with high momenta, like DY processes. In a hard scattering processes the quarks and gluons behave as free particles (due to asymptotic freedom), and the perturbative QCD can be used for accurate predictions [62]. Usually, the hard scattering processes are accompanied by soft interactions with effects which are included in phenomenological models up

to some degree of accuracy. A typical hard scattering process is shown in Figure 1.12. This process contains particles that originate from the two outgoing partons and remaining particles after a parton is knocked out of each of the initial two beams of hadrons, i.e. beam-beam remnants. The resulting partons lose energy through the *parton shower*, where soft and collinear quarks and gluons are radiated off until confinement starts to dominate. The recombination of partons into color neutral hadrons is called *hadronisation*. These hadrons may subsequently decay into other hadrons, neutrinos, or leptons, resulting in a shower of particles. Apart from the hard scattering, a hard gluon (or a photon) can be radiated off the scattering partons. This is collectively referred to as *initial* or *final state radiation* (ISR or FSR). The proton remnants which do not participate in the hard scattering are colored states and due to the confinement they interact mostly via soft scattering among each other and to the hard scattering remnants to form color neutral states. This hadronisation leads typically to soft jets along the direction of the beam, but can also enter the detector. This is referred to as the *underlying event* (UE).

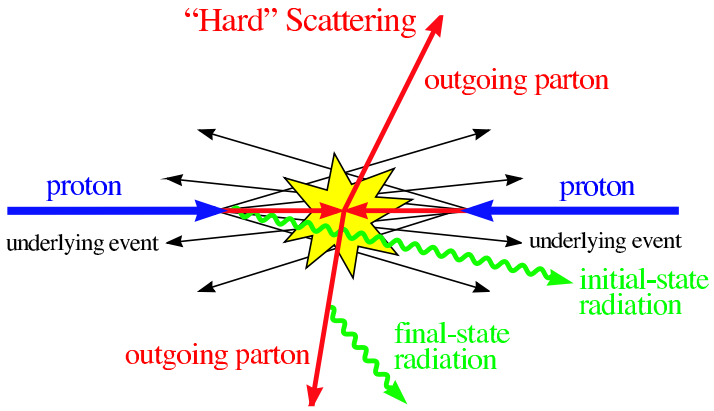

Figure 1.12: Schematic diagram of a hard scattering process [62].

In a hard scattering event, the momentum of the proton P is distributed among its constituent's partons: every parton i carries a fraction x_i of the protons momentum, p_i defined as $x_i = p_i/P$. The squared momentum transfer in the process is so called energy scale Q^2. The longitudinal momentum of the interacting parton–parton system is unknown, since it depends on the known four-momenta of the colliding protons and also on the unknown momentum fractions x_1 and x_2 of the two colliding partons. The probability of finding a parton of a given flavor i with a momentum fraction x_i of the total proton momentum at the energy scale Q^2, is described by parton distribution functions (PDF) $f_i(x_i, Q^2)$. The PDFs are solutions of the Dokshitzer-Gribov-Lipatov-Altarelli-Parisi (DGLAP) equations, which determine their evolution with the scale Q, but the x dependence can't be calculated analytically [63–65].

The x dependence of the PDFs is determined from a global fit to experimental data originating from various sources. The DIS cross section measurements, both from fixed target lepton-nucleon experiments (electrons, muons and neutrinos scatter off

hydrogen, deuterium and nuclear targets), constrain quark and gluon PDFs at high x, while the electron-proton collisions at HERA constrain them at low x. Yet, the DIS measurements mostly determine information about the valence quarks. To probe the sea (anti)quarks and gluon PDFs, other datasets are used as well, such as: fixed target DY data to constrain high x sea quarks, single jet inclusive production cross section at the Tevatron and LHC contributing to the high x gluon PDFs, and the Z- and W-boson production cross sections at the Tevatron and the LHC, which are sensitive to up and down quark distributions, and their anti-quark counterparts. The PDFs obtained from these fits depend on a large number of parameters, which, apart from the assumptions about the PDFs, originate from the choice of dataset, the specifics of the perturbative QCD calculation, the correlation between α_s and the PDFs, the treatment of the heavy quarks and the uncertainty treatment. As each group differs for each of these points, the resulting PDFs will differ as well. Figure 1.13 shows the $Q^2 - x$ map probed with the different experiments, with the area that corresponds to Z- and W-boson production at LHC clearly marked.

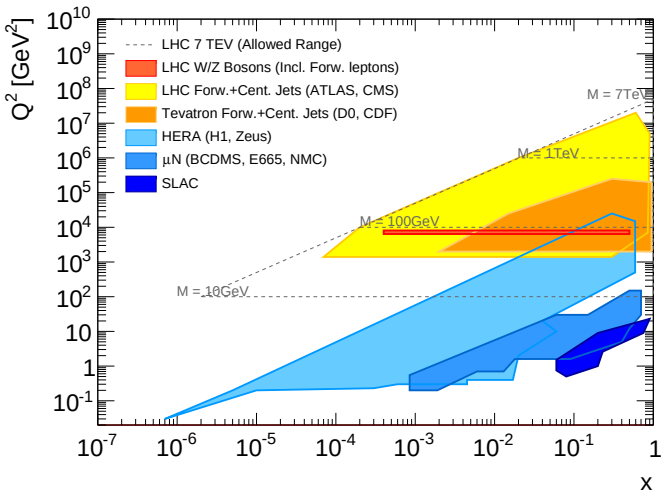

Figure 1.13: Dependence of the squared momentum transfer Q^2 as a function of the momentum fraction x of a parton on the proton momentum [66]. Areas probed by the experiments are marked as shaded areas.

Each of the parameters used in the fit to experimental data has a corresponding uncertainty. The minimisation techniques applied in the determination of PDFs are usually based on the Hessian method [67]. This method leads to a best fit value for each of the parameters, with a corresponding χ^2 distribution. For every parameter of PDFs, the deviation is determined given a certain tolerance in the change in χ^2. This tolerance in different parameters gives a set of eigenvectors which describe the complete parameter set including the given confidence ranges (68% or 90%).

There are several collaborations that provide complete sets of PDFs, which have different number of parameters of the fit model and different experimental data used to fit the processes of interest. The most common sets are CTEQ [68], MSTW [69] and NNPD F[70]. An example of a PDF sets from CTEQ is CT14 for different values

of the Q^2 scale is shown in Figure 1.14. The probability of finding a parton of a given flavor inside the proton diverges at low x since it corresponds to virtual partons with a low energy for which the splitting of gluon to quark-antiquark pair is more likely. The bulk of the momentum fraction of the proton is carried by its valence quarks, and not by the sea. With the increase of the momentum transfer Q^2, the gluon contribution also increases.

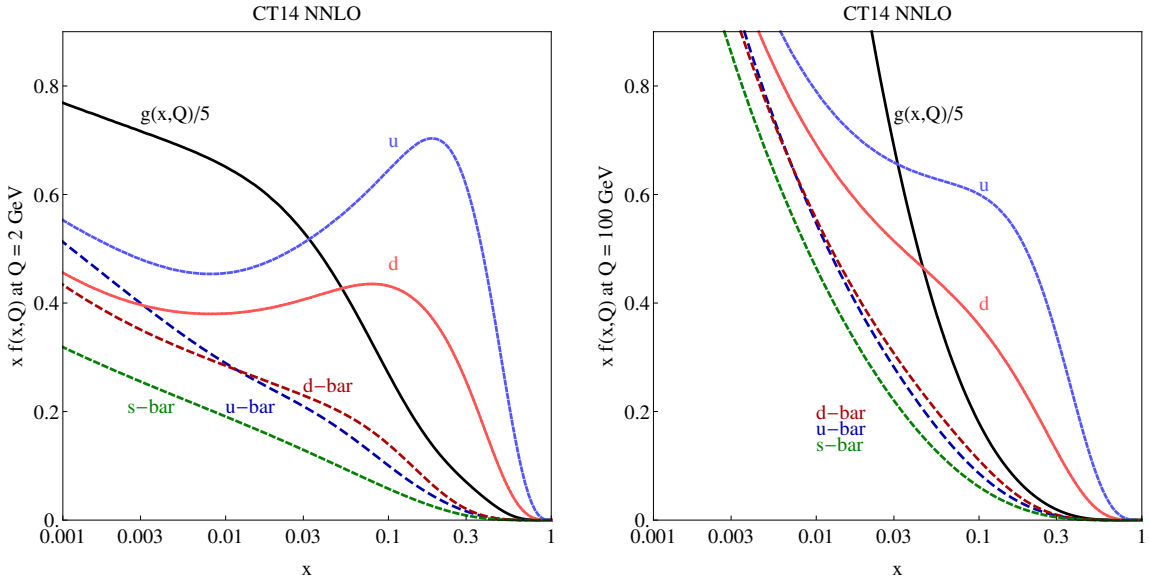

Figure 1.14: CT14 PDFs sets for u, $\bar{u}$, d, $\bar{d}$, s quarks and gluons for two fixed values of the scale: $Q = 2$ GeV and $Q = 100$ GeV [71].

Figure 1.15 shows the schematic diagram of a proton–proton collision, where only partons a and b participate in the interaction. To quantify the interaction rate between the two hadrons, it is common to use a hadronic cross section. The relation between the hadronic and partonic cross section is given with:

$$\sigma_{A+B\to X}(\mu_{\mathrm{F}}, \mu_{\mathrm{R}}) = \sum_{a\in A, b\in B} \int dx_a dx_b f_{a/A}(x_a, \mu_{\mathrm{F}}) f_{b/B}(x_b, \mu_{\mathrm{F}}) \hat{\sigma}_{ab\to X}(\mu_{\mathrm{F}}, \mu_{\mathrm{R}}), \qquad (1.41)$$

where a and b represent partons within protons A and B with momentum fractions x_a and x_b, respectively, and $\hat{\sigma}_{ab\to X}$ is the hard scattering cross section for those partons. The sum runs over all parton flavours contributing to the process. Interacting quarks can radiate off gluons where the probability of emitting a (collinear) gluon increases for decreasing momentum of the radiated gluon, resulting in divergent integrals in the cross section calculation. Divergent integrals can be managed by separating the divergent part from the finite terms at a factorisation scale, μ_{F}. The divergent terms are absorbed into the PDFs using the factorisation theorem [72], leading to an infrared safe expression of the partonic cross section, which can still be calculated perturbatively. The μ_{F} is usually taken as the mass of the outgoing system of particles ($\mu_F \approx m_{\mathrm{X}}$). The μ_{R} is the renormalisation scale which defines the QCD running coupling and the renormalisation α_s. In the computation of observables such as the cross sections, only a finite number of terms can be calculated, which all depend on μ_{R}. The renormalisation scale is usually

chosen to be equal to the energy scale of the interaction, as this choice eliminates large logarithms in the loop diagrams, and therefore optimises the convergence of the perturbative expansion [72]. However, choice of the μ_{R} represents the source of an uncertainty in the calculation. It is also common to choose the factorisation to be the same as renormalisation scale ($\mu_{\mathrm{F}} = \mu_{\mathrm{R}}$).

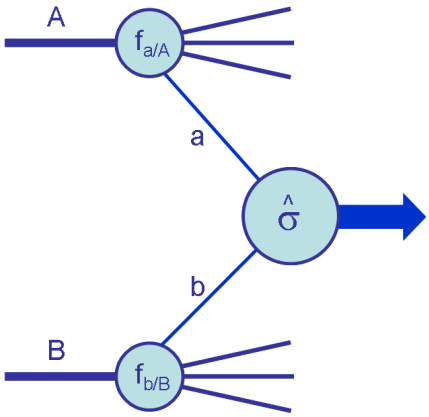

Figure 1.15: Schematic diagram of a proton–proton collision, labeled A and B, where partons a and b participate in hard interaction [62].

The parton level hard scattering cross section is calculated using perturbative QCD as a power series expansion of α_s:

$$\hat{\sigma}_{ab\to X} = \hat{\sigma}_0 + \alpha_s(\mu_R^2)\hat{\sigma}_1 + \alpha_s^2(\mu_R^2)\hat{\sigma}_2 + \mathcal{O}(\alpha_s^3), \tag{1.42}$$

where the first term represents the cross section calculated at leading order (LO), and each subsequent term will add higher order calculations, i.e. the second term adds next-to-leading order (NLO), and the third term adds next-to-next-to-leading order (NNLO). Thus, for processes calculated at LO, no radiative corrections are added to the initial or final states and only the matrix element computation is present. In NLO calculations, real emissions (extra partons) or virtual corrections are included, each of them carrying a proportionality to α_s. In the case when the perturbative series does not converge because of the presence of large logarithms coming from the phase-space integration of soft and collinear gluon singularities, the so-called logarithmic resumation technique is used. This technique involves a definition of another convergent function in which the individual terms of the original functions are rescaled and summed to the fixed order contribution to restore the convergence. The first term of the series represents the leading-log (LL) contribution, the second one the next-to-leading-log (NLL) and so on.

The production cross section of main SM processes in proton–proton collisions at the LHC and proton-antiproton collisions at the Tevatron as a function of centre of the mass energy $\sqrt{s}$ is shown in Figure 1.16. The production of W and Z bosons is more abundant at the LHC than at the Tevatron.

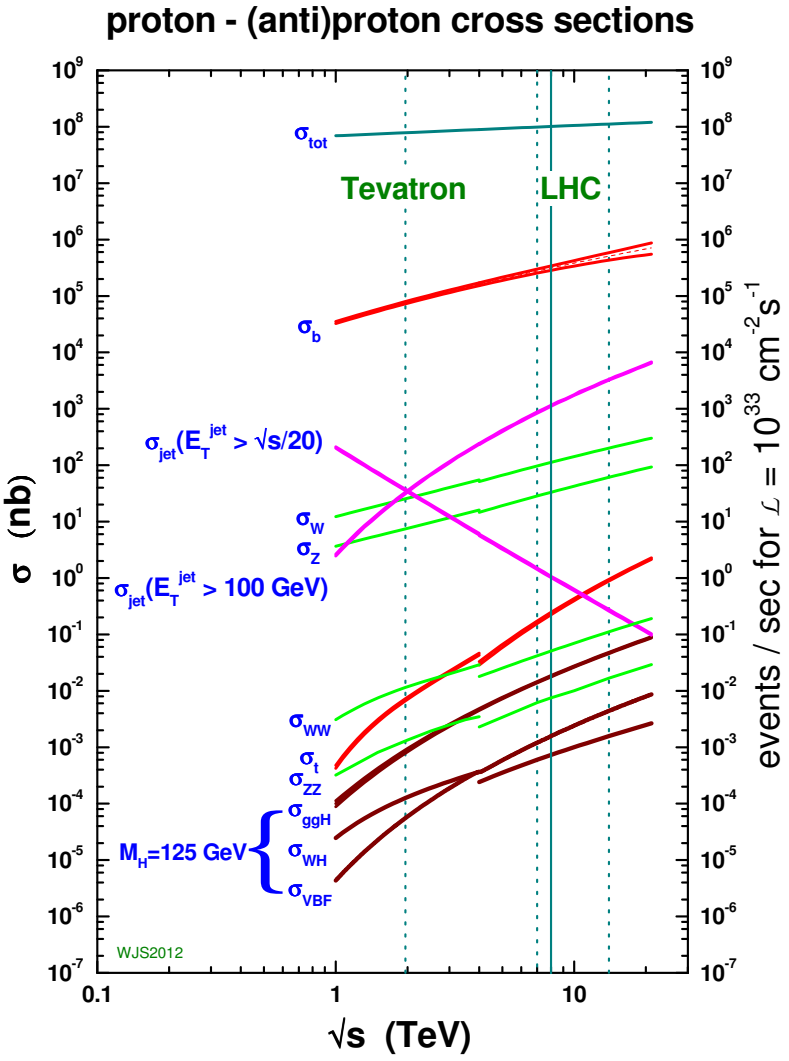

Figure 1.16: Production cross sections for various processes as a function of the centre of mass energy in hadron collisions [69].

1.3.2 *W-boson production and decay*

In proton–proton collisions, the W bosons at LO are produced in the DY process of quark-antiquark annihilation. At the LHC, W^+ boson is produced with valence u and sea $\bar{d}$ quarks and W^- boson from valence d and sea $\bar{u}$ quarks. Since protons consist of two u and one d valence quark, in proton–proton collisions at the LHC, the total number of produced W^+ bosons is larger. The next largest contribution for W-boson production is from sea c and s quarks, contributing with 17% for W^+ and 23% for W^- bosons. Although these are sea-sea processes, they dominate the Cabibbo suppressed process from u and s valence-sea contribution [73]. The flavor decomposition for W production at LO is shown in Figure 1.17. Table 1.4 shows a summary of contributing processes to the W-boson production at LO, NLO and NNLO.

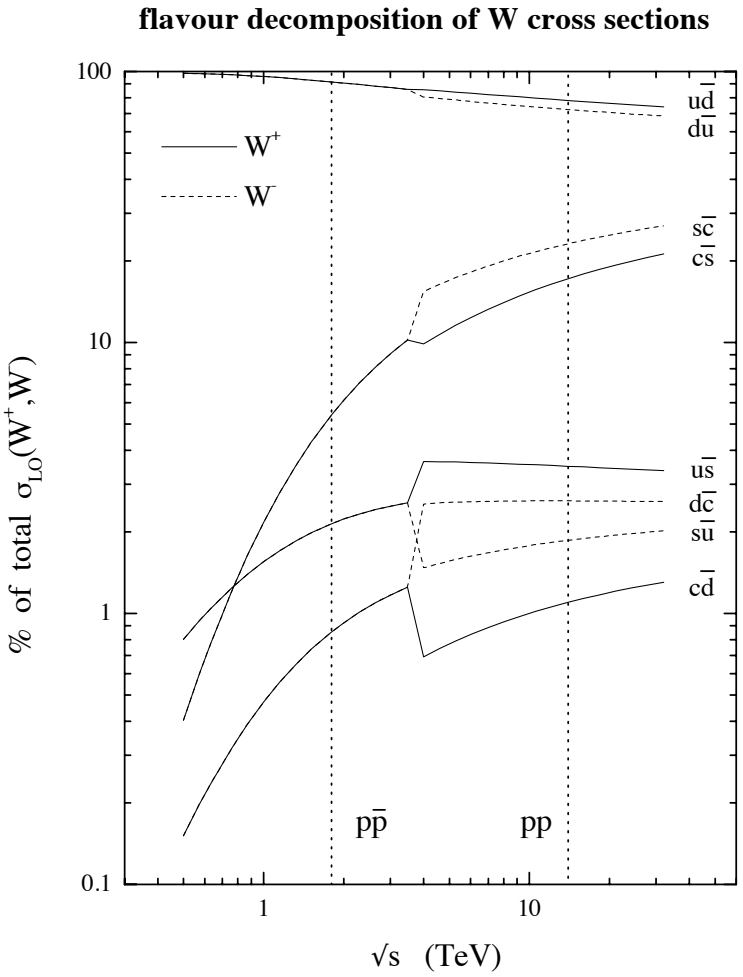

Figure 1.17: Parton decomposition of the W^+ (solid line) and W^- (dashed line) total cross sections in proton–proton and proton-antiproton collisions as a function of $\sqrt{s}$ at LO. Individual contributions are shown as a percentage of the total cross section in each case. In proton-antiproton collisions the decomposition is the same for W^+ and W^- bosons [73].

The four-momenta of the interacting partons for the W-boson production at LO (Born level), is given by:

$$p_1^\mu = \frac{\sqrt{s}}{2}(x_1, 0, 0, x_1) \quad \text{and} \quad p_2^\mu = \frac{\sqrt{s}}{2}(x_2, 0, 0, x_2). \tag{1.43}$$

where the parton masses are neglected, assuming that the partons are exactly collinear with the colliding protons. The sum of the four momenta of the W-boson decay products is defined as:

$$\hat{s} = (p_1^\mu + p_2^\mu)^2 = s x_1 x_2. \tag{1.44}$$

Then the mass of the W boson is:

$$\hat{s} = m_W^2. \tag{1.45}$$

Thus, assuming $x_1 \sim x_2$, the typical momentum fraction involved in the W-boson production is $x \approx m_W/\sqrt{s}$. The produced W boson has energy and longitudinal

Table 1.4: The different contributing processes to the W-boson production at LO, NLO and NNLO.

Order	Process
α_s^0 (LO)	$q + \bar{q} \to W$
α_s^1 (NLO)	$q + \bar{q} \to W$ (one-loop corrections) $q + \bar{q} \to W + g$ $q(\bar{q}) + g \to W + q(\bar{q})$
α_s^2 (NNLO)	$q + \bar{q} \to W$ (two-loop corrections) $q + \bar{q} \to W + g$ (one-loop corrections) $q + \bar{q} \to W + g + g$ $q(\bar{q}) + g \to W + q(\bar{q})$ (one-loop corrections) $q(\bar{q}) + g \to W + q(\bar{q}) + g$ $q + \bar{q} \to W + q + \bar{q}$ $q(\bar{q}) + \bar{q}(q) \to W + q(\bar{q}) + \bar{q}(q)$ $g + g \to W + q + \bar{q}$

momentum given by:

$$E = \frac{\sqrt{s}}{2}(x_1 + x_2) \quad \text{and} \quad p_{\mathrm{L}}^{\mathrm{W}} = \frac{\sqrt{s}}{2}(x_1 - x_2). \tag{1.46}$$

The total partonic cross section, from Equation 1.42, is calculated from the matrix element of the process [12]:

$$\hat{\sigma}(\hat{s}) \propto \left(\frac{G_{\mathrm{F}} m_W^2}{\sqrt{2}}\right)^2 \frac{\hat{s}}{(\hat{s} - m_W^2)^2 - m_W^2 \Gamma_{\mathrm{W}}^2}, \tag{1.47}$$

where the last fraction corresponds to the relativistic Breit-Wigner resonance distribution, which depends on $\hat{s}$. The Breit-Wigner resonance is a peak distribution at m_W with width Γ_{W}.

The W-boson decay modes are shown in Table 1.5. The decays are distributed nearly equally between the three lepton flavors. Since the dijet cross section at hadron colliders is several orders of magnitude larger than the W-boson cross section, as shown in Figure 1.16, the hadronic decay modes of W bosons are not usable for the W-boson mass measurement, although the branching ratio is much higher than for the leptonic decays. The $W \to \tau\nu$ decays are also not used for the W-boson mass measurement, since τ decays have a neutrino in the final state and the momentum measurement of a τ lepton is not as precise as that of an electron or muon. Therefore, for precision m_W measurement only two decay modes are used: electron and muon.

As mentioned before, colliding partons carry only a fraction of the proton energy, thus the total initial energy in longitudinal direction is not known, which is a difficulty for the precision W-boson mass measurement at hadron colliders. The other reason for complexity of this measurement is the existence of the neutrino in the final state in the electron and muon decay channels.

Table 1.5: The W-boson decay modes [12].

Decay mode	Branching ratio [%]
$W \to e\nu$	10.71 ± 0.16
$W \to \mu\nu$	10.63 ± 0.15
$W \to \tau\nu$	11.38 ± 0.21
$W \to$ hadrons	67.41 ± 0.27

The lepton momentum in the transverse plane is given with:

$$p_{\mathrm{T}}^{\ell} = \frac{m_W}{2} \sin\theta, \tag{1.48}$$

where θ is the angle between the lepton and the parton direction, and $p_{\mathrm{T}}^{\ell} \leq m_W/2$. The lepton transverse momentum can be transformed into:

$${p_{\mathrm{T}}^{\ell}}^2 = \frac{\hat{s}}{4} \sin^2\theta = \frac{\hat{s}}{4}(1 - \cos^2\theta). \tag{1.49}$$

The dependence of the W-boson production as a function of the lepton transverse momentum is given by:

$$\frac{d\sigma}{dp_{\mathrm{T}}^{\ell}} = \frac{d\sigma}{d\cos\theta} \frac{d\cos\theta}{dp_{\mathrm{T}}^{\ell}}, \tag{1.50}$$

where the second term can be calculated from Equation 1.49:

$$\frac{d\cos\theta}{dp_{\mathrm{T}}^{\ell}} = \frac{4p_{\mathrm{T}}^{\ell}}{\hat{s}} \left(1 - \frac{4p_{\mathrm{T}}^{\ell}}{\hat{s}}\right)^{-1/2}. \tag{1.51}$$

The last term has a singularity for $p_{\mathrm{T}}^{\ell} = \sqrt{s}/2 \propto m_W/2$, causing the characteristic maximum (commonly denoted as Jacobian peak) visible in the transverse momentum distribution of the W-boson decay products. By measuring the location of the Jacobian peak, the m_W can be measured. The same peak is observed in the neutrino transverse momentum distribution, which can be experimentally measured with the missing transverse energy as discussed in Section 3.4, and in the transverse mass distribution, more details on these distributions is given in Section 1.4.2. The first term in Equation 1.50 is describing the angular distribution of the W-boson decay products:

$$\frac{d\sigma}{d\cos\theta} \sim (1 - \lambda q \cos\theta)^2, \tag{1.52}$$

where q is the charge of the lepton and λ is a parameter that depends on helicity. At LO, the W bosons are produced in the direction of one of the protons, thus the helicity is $\lambda = +1$ if $x_1 > x_2$ and $\lambda = -1$ if $x_1 < x_2$. The parton with higher x gives a longitudinal boost to the W boson and defines its direction of motion. As explained previously, the electroweak interactions couples only to left-handed fermions and right-handed anti-fermions. In the high energy limit, the helicity is a conserved quantum number and only negative helicity fermions and positive helicity anti-fermions are involved.

When higher-order terms in QCD are considered the differential DY cross section can be parametrised as:

$$\begin{aligned}\frac{d\sigma}{dp_{\mathrm{T}}^2\, d\phi\, d\cos\theta} \propto & (1+\cos^2\theta) + A_0(1-3\cos^2\theta) \\ & - A_1 q \sin 2\theta \cos\phi + \frac{1}{2} A_2 \sin^2\theta \cos 2\phi \\ & + A_3 \sin\theta \cos\phi + A_4 q \cos\phi \\ & + A_5 \sin^2\theta \sin 2\phi + A_6 q \sin 2\theta \sin\phi \\ & + A_7 \sin\theta \sin\phi, \end{aligned} \tag{1.53}$$

where p_{T} and q are the transverse momentum and charge of the boson, A_i are p_{T}-dependent coefficients where the effects of QCD are folded, and ϕ and θ are the azimuthal and polar angles of the lepton produced in the decay in the Collins-Soper frame [74]. The Collins-Soper frame corresponds to the rest frame of the W boson where the plane of the incoming quarks defines the xz-plane and the y-axis is perpendicular to it. The azimuth and polar angles are defined by the lepton decaying from the W boson.

1.4 MEASUREMENT STRATEGY

The W boson has been studied in great detail at the LEP and the Tevatron colliders, as well as at the LHC. Previous measurements of the m_W are described in Section 1.2.3. Currently, the most precise measurement is from Tevatron's CDF experiment with a total uncertainty of $\delta m_W = 19$ MeV.

This section provides an overview of the strategy for the W-boson mass measurement at the LHC with the ATLAS detector. First, the challenges of the m_W measurement at hadron colliders are described, emphasising the differences between the Tevatron and the LHC. Then, the definition of the variables that are used for extraction of the m_W is given, concluding with the description of the fitting procedure and the methodology used for evaluation of the systematic uncertainties.

1.4.1 *Challenges in the W-boson mass measurement at hadron colliders*

The W-boson events are detected through their leptonic decays in electron and muon channels. The W-boson candidates are selected by requiring exactly one lepton (electron or muon) with high transverse momentum and the presence of large missing transverse energy in the event, originating from the neutrino. The neutrino in the event cannot be directly reconstructed, therefore the neutrino energy is determined by balancing the detected energy in the transverse plane with respect to the beam position.

Measurement of the m_W with a desired accuracy represents a major challenge for

the ATLAS experiment at the LHC. It requires a true understanding of the detector's performance and limitations, and that is reached via multiple analysis stages. Two main objects that need to be measured precisely are the lepton (electron and muon) and the neutrino. The main theoretical inputs needed for this measurement consist of higher order corrections in the perturbative expansion of the strong-coupling constant α_s, non-perturbative QCD effects, PDFs and the lepton angular distribution [75, 76].

Comparing to the Tevaton measurements, at LHC there are:

- *Much higher number of additional proton–proton interactions (pile-up)*
  Beside the proton–proton interaction of interest, there are other collisions which happen at the same time since the LHC is colliding two bunches of protons (around 10^{11} protons per bunch). Therefore, events from the other interactions are detected which degrades the resolution of the measurement of the hadronic activity.
- *Different production mechanisms*
  W-boson production has a larger contribution from sea quarks at the LHC than at the Tevatron. At the LHC, the W-boson production that involves charm and strange quarks is approximately 25% of the inclusive production rate. While, at the Tevatron, only 5% of the inclusive W-boson production rate involves charm and strange quarks. The PDFs of both charm and strange quarks are currently very poorly constrained [75]. Due to the enhanced contribution of heavy flavor in W-boson production at the LHC with respect to the Tevatron, an improved knowledge of the PDFs is required [75].
- *Higher statistics samples*
  At the LHC, the W-boson production cross section is roughly an order of magnitude higher than at the Tevatron (Figure 1.16). Therefore, higher cross section for the production of W and Z bosons and higher integrated luminosity at the LHC compared to the Tevatron allows for higher statistics samples of W-boson events which will improve the statistical sensitivity. Also, at the LHC, there are higher statistics calibration samples $J/\psi \to \ell\ell$ and $Z \to \ell\ell$ ($\ell = e, \mu$), used for reducing the systematic uncertainties [59].

Experimental calibration of the detector is performed by exploiting the well defined Z-boson resonance in electron and muon channels. Lepton momentum is calibrated using precisely measured mass of the Z boson [77–79], while the hadronic activity in the calorimeter is calibrated using the expected momentum balance with the reconstructed Z-boson transverse momentum. Tag-and-probe method is employed for the charged lepton identification and reconstruction efficiency corrections. Finally, the experimental calibration is validated with the W-boson like events created from the Z-boson events by treating one of the charged leptons as a neutrino.

Expected uncertainties that can be achieved at the LHC with the data corresponding to an integrated luminosity of 10 fb^{-1} at $\sqrt{s} = 14$ TeV according to [59] are: statistical 2 MeV for each channel, lepton energy scale 4 MeV and resolution 1 MeV per channel, efficiency 4.5 MeV for electron and 1 MeV for muon channel, recoil scale and resolution 5 MeV per channel. The estimated theoretical uncertainties are: PDFs

20 MeV, $p_{\mathrm{T}}^{\mathrm{W}}$ modeling 3 MeV. These uncertainties can be compared at the Tevatron experiments [58]:

$$\delta m_W^{\mathrm{stat.}} \approx \delta m_W^{\mathrm{exp.}} \approx \delta m_W^{\mathrm{theo.}},$$

and at the LHC:

$$\delta m_W^{\mathrm{stat.}} < \delta m_W^{\mathrm{exp.}} < \delta m_W^{\mathrm{theo.}}.$$

In conclusion, at the LHC, compared to the Tevatron measurement, the statistical sensitivity is better, the experimental level of accuracy is similar while the theoretical uncertainties are higher.

Expected dominant source of systematical uncertainty on m_W measurement at the LHC is PDF. It can be reduced by selecting only lower part of the W-boson transverse momentum distribution which makes the Jacobean peak of the p_{T}^{ℓ} distribution steeper and it suppresses the contribution from quark-gluon scattering [75].

1.4.2 *Inputs to the W-boson mass measurement*

Observables which are used for the m_W measurement are defined in the transverse plane. The mass of the W boson is measured from sensitive observables, i.e. those that have a sharp Jacobian peak at the m_{W} or $m_{\mathrm{W}}/2$. There are three mass-sensitive observables:

- *Lepton transverse momentum* p_{T}^{ℓ}, the lepton momentum in the transverse plane with Jacobian peak at $m_W/2$. The Jacobian peak for p_{T}^{ℓ} distribution is smeared down by the W-boson transverse motion (non-zero $p_{\mathrm{T}}^{\mathrm{W}}$). The advantage of p_{T}^{ℓ} distribution is that it is the best measured quantity in the event. The p_{T}^{ℓ} distribution is sensitive to the lepton energy calibration, the modeling of the transverse momentum of the W boson and the PDFs [59].

- *Neutrino transverse momentum* p_{T}^{ν}, the neutrino momentum in the transverse plane with Jacobian peak at $m_W/2$. This distribution is less sensitive to the modeling of transverse momentum of the W boson, but it is largely affected by the multiple interactions per bunch crossing which results in very poor resolution and it is not used in this measurement.

- *Transverse mass of the W boson* m_{T}, defined as:

$$m_{\mathrm{T}} = \sqrt{2p_{\mathrm{T}}^{\ell}p_{\mathrm{T}}^{\nu}(1-\cos\Delta\phi)}, \tag{1.54}$$

  where $\Delta\phi$ is the azimuthal angle between the lepton and the neutrino. The transverse mass has the form of an invariant mass but without any information from the longitudinal direction with a Jacobian peak at m_W. This observable is at first order insensitive to $p_{\mathrm{T}}^{\mathrm{W}}$, but depends on the poor resolution of the missing transverse momentum (originating from the neutrino) and additional proton–proton interactions.

At LO, in the rest frame of the W boson the charged lepton and the neutrino are back-to-back, therefore p_{T}^{ℓ} and $E_{\mathrm{T}}^{\mathrm{miss}}$ have a sharp Jacobian peaks at exactly $m_W/2$, while the m_{T} distribution has a sharp peak at m_W. At higher orders, the $p_{\mathrm{T}}^{\mathrm{W}}$ is non zero, due to the initial gluon radiation off the interacting quarks and the initial transverse momentum of the interacting quarks, leading to the smearing of the Jacobian peak. Therefore, when a W boson is not produced with zero momentum, the lepton transverse momentum vector is (to the first order in the ratio of the $p_{\mathrm{T}}^{\mathrm{W}}$ and W boson energy):

$$\vec{p}_{\mathrm{T}}^{\,\ell} \approx \vec{p}_{\mathrm{T}}^{\,\ell\ \mathrm{rest}} + \frac{1}{2}\vec{p}_{\mathrm{T}}^{\,\mathrm{W}}, \tag{1.55}$$

where $\vec{p}_{\mathrm{T}}^{\,\ell\ \mathrm{rest}}$ is the lepton transverse momentum in the rest frame of the W boson, and the $\vec{p}_{\mathrm{T}}^{\,\mathrm{W}}$ is the transverse momentum of the W boson. The magnitude of the lepton transverse momentum is (to the first order of $p_{\mathrm{T}}^{\mathrm{W}}/p_{\mathrm{T}}^{\ell\ \mathrm{rest}}$):

$$p_{\mathrm{T}}^{\ell} \approx p_{\mathrm{T}}^{\ell\ \mathrm{rest}} + \frac{1}{2}p_{\parallel}^{\mathrm{W}}, \tag{1.56}$$

where $p_{\parallel}^{\mathrm{W}}$ is the $\vec{p}_{\mathrm{T}}^{\,\mathrm{W}}$ projected along the lepton axis. On the other hand, the transverse mass has a second order dependence of the $p_{\mathrm{T}}^{\mathrm{W}}$, by combining the W-boson transverse momentum $\vec{p}_{\mathrm{T}}^{\,\mathrm{W}} = \vec{p}_{\mathrm{T}}^{\,\ell} + \vec{p}_{\mathrm{T}}^{\,\nu}$ with the Equation 1.54:

$$\frac{1}{2}m_{\mathrm{T}} \approx p_{\mathrm{T}}^{\ell} - \frac{1}{2}p_{\parallel}^{\mathrm{W}}. \tag{1.57}$$

After comparing the last equation with Equation 1.56, the result is:

$$\frac{1}{2}m_{\mathrm{T}} \approx p_{\mathrm{T}}^{\ell\ \mathrm{rest}}. \tag{1.58}$$

Therefore, at first order, m_{T} does not depend on the transverse momentum of the W boson and the Jacobean peak of m_{T} is not smeared by non-zero $p_{\mathrm{T}}^{\mathrm{W}}$.

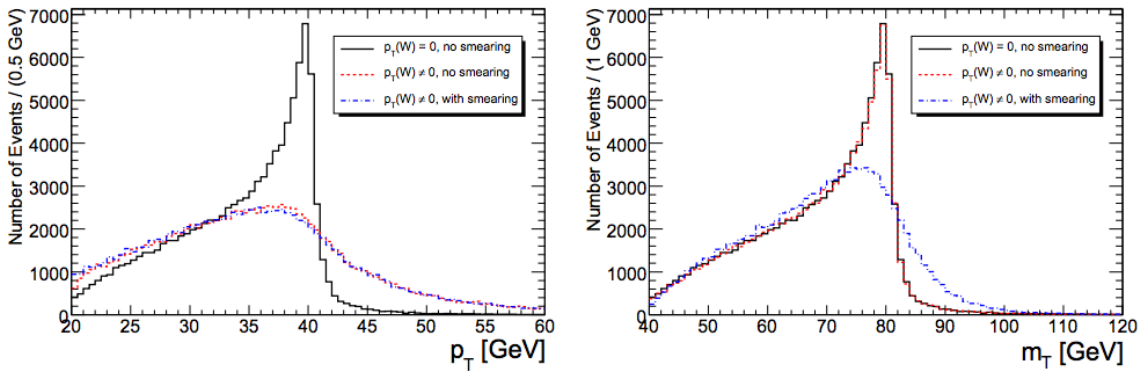

Figure 1.18: Mass sensitive distributions: p_{T}^{ℓ} (left) and m_{T} (right) showing the Jacobian edge and the effect of smearing due to non-zero $p_{\mathrm{T}}^{\mathrm{W}}$ and detector resolution. The black line represents the shape of the distribution with $p_{\mathrm{T}}^{\mathrm{W}} = 0$, the red dashed line is for non-zero $p_{\mathrm{T}}^{\mathrm{W}}$, while blue dashed line shows the shapes of the distributions including the effect of detector resolution and response [76].

The detector resolution also smears the Jacobian peak. The precision with which the Jacobian peak can be reconstructed determines the precision of the m_W measurement. Figure 1.18 shows p_{T}^{ℓ} and m_{T} distributions from Monte Carlo simulation (details about the simulation is given in Chapter 3) and the effect of the smearing of the Jacobian peak, the lepton resolution is about 2%, while the accuracy of $E_{\mathrm{T}}^{\mathrm{miss}}$ determination has a resolution of about 20-30% [76]. The smearing of the Jacobian peak due to non-zero $p_{\mathrm{T}}^{\mathrm{W}}$ is larger for the p_{T}^{ℓ} than for the m_{T} distribution (as expected from Equations 1.56 and 1.58).

The measurement of the m_W at the 10 MeV precision level requires understanding of the shape of the p_{T}^{ℓ} distribution at the 1 per mill level or better. In order to show the sensitivity of p_{T}^{ℓ} and m_{T} observables, examples of these distributions at ATLAS experiment with 50 MeV shifts around the m_W peak are shown in Figure 1.19.

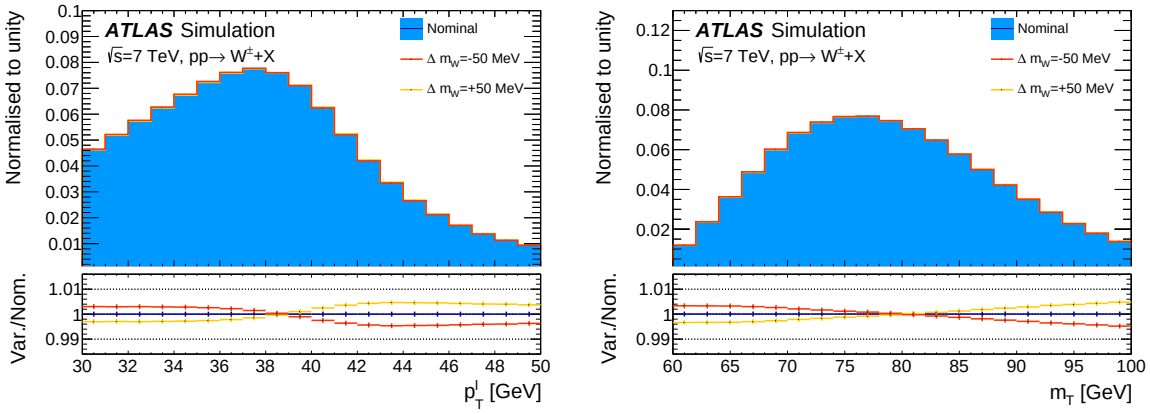

Figure 1.19: Examples of p_{T}^{ℓ} and m_{T} distributions with 50 MeV shifts around the m_W peak [80].

1.4.3 *Template fit method and propagation of systematics uncertainties*

For the determination of the m_W, the correlation between the W-boson mass and the kinematic peaks of its decay products is used. This is so-called *template fit* approach, it was used for previous m_W measurements by D0 and CDF experiments. The advantage of the template fit method is the possibility to study in details the impact of different experimental and model dependent systematic uncertainties. Predictions for different m_W (*templates*) are obtained from a single simulated reference sample, by reweighting the W-boson invariant mass distribution according to the Breit-Wigner parameterisation (Equation 1.47). The reweighting is performed analytically, using the `LineShapeTool` code [81]. The W-boson width is scaled according to $\Gamma_{\mathrm{W}} \propto m_W^3$. In order to verify the accuracy of this reweighting procedure, the reweighted resonance is compared to the distributions explicitly generated by setting the W-boson mass, as shown in Figure 1.20.

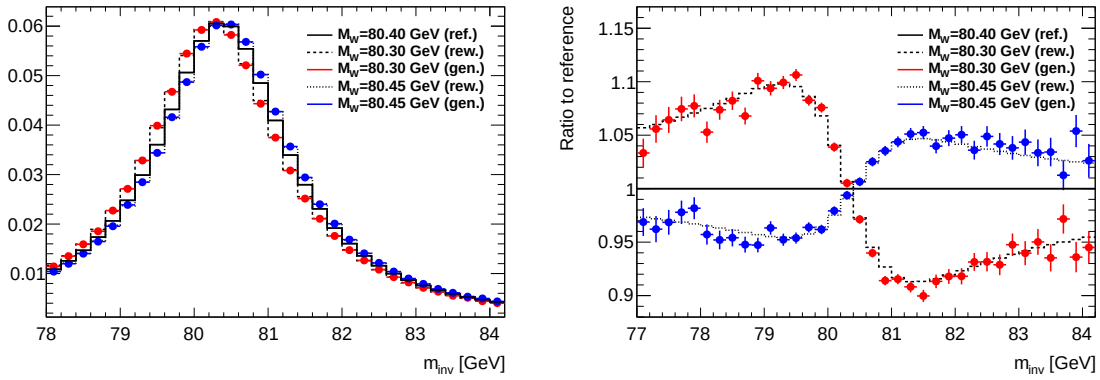

Figure 1.20: Comparison of reweighted and generated invariant mass distributions, for several values of m_W. The full line represents the main sample with the reference mass, and the dashed lines are the results of the reweighting to $\Delta m_W = -100$ MeV and $\Delta m_W = +50$ MeV. The points represent the result of event generation runs setting $m_W = 80300$ MeV and $m_W = 80450$ MeV on input. Plots taken from [81].

The templates are compared to the observed distributions, and χ^2 compatibility is calculated for each template:

$$\chi^2 = \sum_{i=1}^{N} \frac{(f_{1,i} - f_{2,i})^2}{\sigma_{f_{1,i}}^2 + \sigma_{f_{2,i}}^2}, \tag{1.59}$$

where the summation runs over the distribution bins, $f_{1,i}$ is the number of entries in bin i of the first distribution, $f_{2,i}$ is the number of entries in bin i of the second distribution, $\sigma_{f_{1,i}}$ and $\sigma_{f_{2,i}}$ correspond to the uncertainties on bin i in the first and second distribution, respectively. The mass is determined from the minimum of fitted parabola to the χ^2 profile as a function of the m_W used in the templates, as shown in Figure 1.21.

In order to test the detector calibration and the physics modeling, the m_W fits are performed for W^+ and W^- in electron and muon decay channels. Any inconsistency in m_W between electron and muon channel would point to a problem in detector calibration, while consistent charge dependency would point to a problem of the underlying physics model. A detailed description of the different measurement categories is given in Chapter 6.

The total statistical uncertainty is estimated from the width of the χ^2 parabola. Systematic uncertainties are evaluated by comparing the nominal template with pseudodata produced from the nominal template by varying each source of uncertainty. Then, the difference in the values of the m_W extracted from the nominal template and pseudodata is used to estimate the uncertainty. After the estimation of all sources of uncertainties, an optimisation of the fitting range is performed by minimising the total expected measured uncertainty.

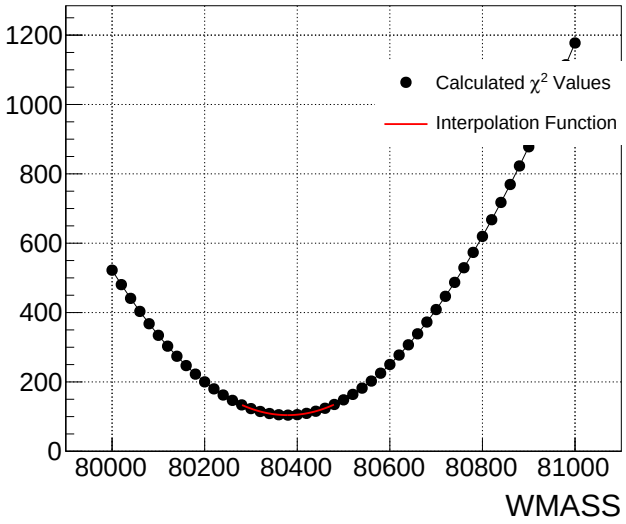

Figure 1.21: Example of the fitted parabola (red line) used to extract the global minimum of the χ^2 function [81].

In order to ensure unbiased measurement of the m_W, templates are blinded. The blinding procedure is based on shifting of the reweighting target mass by a random value from a uniform distribution with a width of ± 100 MeV centred around the nominal mass value. The same blinding shift is used for W^+- and W^--boson processes. The blinding is removed when the overall consistency between different measurement categories is observed.

2 *Experimental Setup*

Progress in modern particle physics is governed by the development of accelerators and construction of complex detectors. By the middle of the XX century the cosmic rays were the basic sources of particles in experimental particle physics. The particle accelerator is a device that accelerates beams of charged particles to increasingly higher energies. The advent of particle accelerators introduced controlled experimental conditions and allowed for particle physics to prosper further. The first accelerators relayed on electrostatic principles and accelerated ions up to energies of only few tens of keV. Progress in particle accelerators can be achieved by increasing the energy of the particles and by increasing the beam intensity. The most common choice for particles which are used in accelerators are electrons and protons as well as their anti-particles. Today, the world's largest particle accelerator is the Large Hadron Collider (LHC) which is designed to accelerate protons up to energies of 7 TeV in order to search for answers to fundamental questions in particle physics.

The development of particle detectors is the other key ingredient for progress in particle physics. From the first small and primitive detectors (x-ray films) to the large multipurpose detector systems which exploit the fact that particles can be distinguished through their interaction with matter.

This chapter introduces experimental framework of the thesis. The first part contains an overview of the LHC and its main designed and operational parameters. The description of the ATLAS detector with the basic definitions and geometry, together with more detailed overview of its sub-systems is presented in the following section. The last part of the section is focused on an overview of the ATLAS trigger system, simulation infrastructure and data preparation.

2.1 THE LARGE HADRON COLLIDER

CERN (Conseil Européen pour la Recherche Nucléaire) is a European research organisation with the largest high energy physics laboratory, located at the French–Swiss border near Geneva established in 1954 by 12 European countries. The first accelerator *Synchrocyclotron* (SC) at this location was built in 1957 accelerated ions up to energies of 600 MeV. The next accelerator was built in 1959, the *Proton Synchrotron* (PS) accelerated protons in 628 m ring up to energies of 28 GeV. Anti-deuteron was the first anti-nuclei observed with the PS in 1965. The first underground accelerator was

the *Super Proton Synchrotron* (SPS), built in 1971 and accelerated protons and ions in 6.9 km ring up to energies of 400 GeV. With help of the SPS as a proton–antiproton collider, the W and Z bosons were discovered in 1983. The next project was the design and construction of the *Large Electron–Positron Collider* (LEP). The LEP accelerated electrons and positrons in 26.659 km circular tunnel 100 m underground up to energies of 45 GeV. The PS and the SPS were redesigned for acceleration of electrons and positrons and were used for their acceleration before injecting them to the LEP. Later, the LEP was upgraded up to energies of 100 GeV. The electron energy at the LEP was limited by synchrotron radiation. The electron energy loss ΔE is proportional to $E^4 m^{-4} R^{-1}$, where E is electron energy, m is its mass and R is radius of the LEP tunnel. Small mass of the electron results in large energy losses, for instance after just one round in the tunnel, the 104.6 GeV electron looses around 3.5 GeV, with higher energies the looses are also higher.

After LEP reached its maximum energy, the next generation accelerator should be exploited. Differences between lepton and hadron colliders should be taken into account when deciding about next generation of colliders, lepton colliders are considered as a "precision", while hadron as "discovery" machines, since hadrons are composite objects (the event structure at hadron colliders is more complex then at lepton colliders and multi-particle calculations are needed in order to fully describe the final state) and hadron colliders provide higher values for the centre-of-mass energy then the lepton colliders. A characteristic quantity for colliders is its centre-of-mass energy $\sqrt{s}$ which is the total energy of the colliding system. CERN decided to reuse the LEP tunnel and construct a hadron collider [82]. The LHC project was approved in 1994 and the construction began in 2001. There are other high energy colliders which were build outside of CERN. The Tevatron [83], a 6.86 km proton–anti-proton collider with $\sqrt{s} = 1.96$ TeV located in Fermilab near Chicago, operated from 1987 until 2011. The Tevatron was the first synchrotron which used superconducting magnets [12]. Limiting factor to the number of collisions per unit of time at the Tevatron was the production of anti-protons. The production rate of anti-protons is $\sim 5{\cdot}10^4$ times smaller then protons. The HERA [84] was the first high-energy lepton–hadron collider which operated from 1992 to 2007 at DESY complex in Germany. HERA's proton beams had maximum energy of 920 GeV, while lepton beams (electrons or positrons) had maximum energy of 27.5 GeV. Some proposals for future high-energy colliders are: international electron–positron linear collider in Japan (ILC [85]), circular electron–positron collider in China (CEPC/SPPC [86]) and in Europe (FCC [87]). There are also some proposals for linear colliders: electron–positron collider at CERN (CLIC [88]) and muon collider [89]. The selection on future projects relies on the balance between the physics reach and their feasibility.

The LHC is a proton–proton collider designed with a nominal centre-of-mass energy of $\sqrt{s} = 14$ TeV, it can accelerate heavy ions also, exploiting lead–lead and proton–lead collisions. The main physics motivation for the LHC is to search for answers on fundamental questions in particle physics: the origin of mass and the relations between masses and symmetry breaking mechanism, the origin of different flavors and quark and lepton families, the nature of matter-antimatter asymmetry in the Universe, study the physical properties of the quark-gluon plasma, search for physics beyond the

SM. To fulfill the rich physics programme at the LHC, the proton energy of 7 TeV is needed, in order to reach the 1 TeV range for the search of the Higgs boson and the physics beyond the SM. Since the processes of interest have small production cross-sections (as shown in Figure 1.16), the high luminosity is also required for the LHC, the designed value is 10^{34} $cm^{-2}s^{-1}$, the definition of luminosity is given later in this section. The design values of the LHC parameters are listed in Table 2.1. Although the LHC is primary designed for discoveries rather then the precision measurements, its excellent performance combined with perfect knowledge of the ATLAS detector allows precision measurements of fundamental SM parameters. This measurements are expected improve the previous measurements at the LEP and the Tevatron colliders. The design and operation of the LHC in detail can be found in References [90–93] while in this chapter only a basic overview is given.

The schematic view of the CERN accelerator complex is shown in Figure 2.1. The source of protons is a bottle of hydrogen gas. The protons are extracted from hydrogen molecules by stripping the electrons in high electric field. The acceleration of protons starts in linear accelerator (LINAC 2) up to energies of 50 MeV. Then the protons enter into the PS booster which accelerates them up to 1.4 GeV. Next is the PS where the protons reach energies of 25 GeV. After PS, the protons are entering SPS where their energy is increased up to 450 GeV. The final step is injection of the protons in two separate rings of the LHC where they circulate in opposite directions until the colliding energy is reached. Approximately 20 minutes are needed to accelerate the protons from the source to the LHC with the colliding energy. Under normal operating conditions the protons can circulate for many hours inside the LHC, the longest one lasted for almost 37 hours in 2016.

Protons are accelerated in radio frequency cavities (RF) which were developed for LEP (by speeding up slower particles and slowing down the faster particles), the frequency is equal to an integer number of the revolution frequency so that protons are accelerated by the same electric field each time they pass through. The LHC ring consists of eight straight sectors, where the 400.8 MHz RF cavities are, each cavity provides 2 MV electric field, with an integrated accelerating field of 5 MV/m.

The LHC has to control the proton trajectory within the 27 km tunnel with a complex magnet system. For the designed beam energy, a 8.36 T magnetic field is required. In order to achieve such magnetic fields, a superconducting dipole magnets from niobium-titanium coils are used which operate at 1.9 K (using superfluid helium-4) with a current of 11850 A. The limiting factor for the LHC beam energy is the strength of the dipole magnetic field for bending the proton trajectory. Since in the LHC, the two proton beams circulate in two vacuum chambers in opposite directions at horizontal distance of 194 nm, the opposite magnetic fields are needed to direct each beam. This is accomplished by two-in-one (twin-bore) system where separate magnets have common cryogenic system and support structure (this magnets has to be identical, relative variation of the magnetic field can't exceed 10^{-4} in order for LHC to work properly). The LHC consists of over 9000 magnets: 1232 dipole magnets for bending, 392 quadrupole magnets for focusing the beam (to a transverse size of 15 μm) and 688 sextuple magnets for decreasing the proton energy spread.

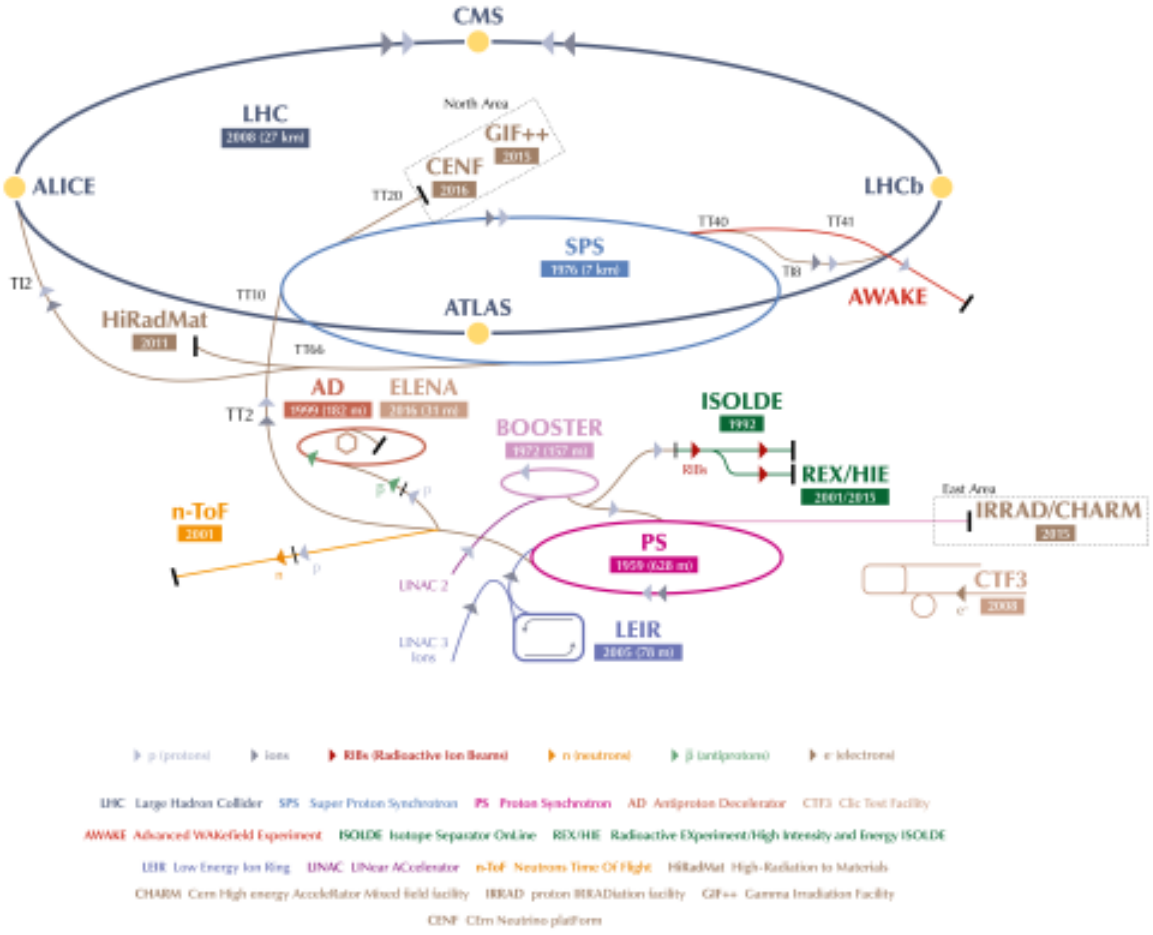

Figure 2.1: The CERN accelerator complex [94].

The LHC proton beam is made from sequences of proton bunches, because of complexity with accelerating, controlling and monitoring continuous beam of protons. Each bunch consists of around 10^{11} protons which are formed in PS booster. The protons are kept in bunches with RF cavities because protons have different acceleration due to different electric field. The designed space between the bunches is 24.95 ns (corresponds to 7.5 m), which gives maximum of 3564 places for bunches inside the LHC ring. The designed number of bunches is 2808 (39 sequences of 72 bunches) which is smaller from the maximum number due to limitations such as: 38 empty bunches are needed due to transfers from SPS to LHC, also 8 bunches are empty because of the transfers from PS to SPS and 119 empty bunches are needed after the last bunch for beam dump.

One of the most important parameter of an accelerator is its *luminosity* which is measuring the number of collisions per unit time. The number of particles N created in a collision is given as a product of a production cross section σ of the process of interest and integrated luminosity L, where L is integral of instantaneous luminosity

$\mathcal{L}$ over time [12]:

$$N = \sigma L = \sigma \int dt \mathcal{L}(t). \tag{2.1}$$

The instantaneous luminosity is directly proportional to the number of protons in each bunch and inversely proportional to the beam size:

$$\mathcal{L} = \frac{1}{4\pi} \nu \frac{N_\mathrm{b} n_1 n_2}{\sigma_\mathrm{x} \sigma_\mathrm{y}} F, \tag{2.2}$$

where ν is the revolution frequency (approximately 11245 Hz), N_b is number of bunches, n_1, n_2 are the number of protons in the bunches, σ_x and σ_y characterise the transverse beam size in horizontal and vertical directions respectively and F is geometrical reduction factor (because of non zero crossing angle between beams at the interaction point). For Gaussian beam distribution the transverse beam size is given by $\sigma = \sqrt{\epsilon \beta^*}$, where ϵ is beam emittance (average spread of the beam particles in phase space) and β^* betatron function at interaction point (which measures the distance between the interaction point and the place where the transverse beam size doubles). Finally, instantaneous luminosity is given by [93]:

$$\mathcal{L} = \frac{1}{4\pi} \nu \frac{N_\mathrm{b} n_1 n_2}{\epsilon_\mathrm{n} \beta^*} F \gamma, \tag{2.3}$$

where $\epsilon_\mathrm{n} = \gamma \epsilon$ is normalised emittance and γ is relativistic factor.

The value of the highest possible instantaneous luminosity is limited by:

- The mean number of inelastic interactions per bunch crossing which is characterising the amount of activity in the detector. Higher instantaneous luminosity increases the number of simultaneous collisions per bunch crossing.
- Non-zero crossing angle which is required to prevent collisions between bunches away from the nominal one.
- Loss of protons from collisions is degrading the beam intensity, therefore there is an exponential decrease of an instantaneous luminosity with time.

The luminosity is measured by detecting the number of interactions for each bunch crossing [95]:

$$\mathcal{L} = \frac{\mu_\mathrm{vis} N_\mathrm{b} \nu}{\sigma_\mathrm{vis}}, \tag{2.4}$$

where μ_vis is the number of visible interactions per bunch crossing and σ_vis is the visible cross section. ATLAS monitors the delivered luminosity by measuring the observed interaction rate per bunch crossing (μ_vis). The calibration of σ_vis is achieved using dedicated beam-separated scans, know as van der Meer scans [96], where the absolute luminosity can be inferred from direct measurements of the beam parameters.

Due to high total proton–proton inelastic cross section at LHC ($\sigma_{pp} \sim 70$ mb) and large number of protons per bunch, multiple proton–proton interactions are happening

simultaneously when two bunches collide at the interaction point. Therefore, at nominal instantaneous luminosity, at the same time as the hard-scattering event of interest, there are approximately 25 additional inelastic interactions. In addition, there are interactions from other bunches contributing to the same event. This phenomenon is called *pile-up*. Higher pile-up additionally degrades performance of the detector. The pile-up can be divided into two: in-time pile-up originating from interactions coming from the collisions inside the same bunch, and out-of-time pile-up originating from the interactions between subsequent or preceding bunches. The mean number of inelastic proton–proton interactions per bunch crossing $< \mu >$ depends on the total proton–proton inelastic cross section and the instantaneous luminosity per bunch:

$$< \mu >= \sigma_{\mathrm{pp}} \cdot \mathcal{L}. \tag{2.5}$$

The pile-up affects the reconstruction of the physics objects important for the measurement of the W-boson mass which will be described in detail in Chapter 5.

There are seven experiments which are designed to analyse the data from the LHC:

- ALICE (**A** **l**arge **i**on **c**ollider **e**xperiment) [97] is a detector specialised in heavy ion physics which studies the physics of strongly interacting matter and the quark-gluon plasma.
- ATLAS (**A** **t**oroidal **L**HC **a**pparatu**s**) [98] is a general purpose detector located at Point 1 (IP1), for studying proton–proton (and ion–ion) collisions (more details will be given in the Section 2.2).
- CMS (**C**ompact **m**uon **s**olenoid) [99] is a general purpose detector, located at Point 5, for studying proton–proton (and ion–ion) collisions with a same physics program as ATLAS detector.
- LHCb (**LHC** **b**eauty experiment) [100] is dedicated for precision measurements of CP violation and rare decays of B hadrons. It has particular geometry covering only forward region where the probability to observe B meson decay is maximal.
- LHCf (**LHC** **f**orward experiment) [101] is dedicated to the measurement of neutral particles emitted in the very forward region of the LHC collisions, to study the LHC as a source of cosmic rays in laboratory conditions in order to calibrate and interpret cosmic ray experiments.
- MoEDAL (**Mo**nopole and **e**xotics **d**etectors **a**t the **L**HC) [102] is designed to search for highly ionizing avatars of new physics such as magnetic monopoles or massive (pseudo-)stable charged particles.
- TOTEM (**Tot**al **e**lastic and diffractive cross section **m**easurement) [103] is designed to measure the total proton–proton cross section with the luminosity-independent method and study the elastic and diffractive scattering at the LHC.

The four main experiments (ALICE, ATLAS, CMS and LHCb) are build around interaction points. ALICE and LHCb are low luminosity experiments.

Powering tests for the LHC started in 2008, while the first beams successfully circulated on September 10, but on September 19, a quench developed in a region between two magnets, damaging the magnets and support structures along 700 m of the tunnel, which delayed the first collisions. It was decided that until further repairs and upgrades are not done, the LHC operates at smaller energies. The first collisions happened in November 2009 with beam energy of 450 GeV, later the beam energy was increased to 1.18 TeV.

The first period of data-taking, i.e. Run-1, started in 2009 and ended in beginning of 2013. After 2 years of shut down with upgrades of the LHC machine and the detectors, Run-2 started in 2015 and it is planed to last until the end of 2018. The designed beam energy is planed to be reached during further runs.

In the following sections, the LHC performance will be described, focusing only on proton–proton collisions. Typical values of the main LHC parameters during Run-1 and Run-2 compared to the designed ones are summarised in Table 2.1.

Table 2.1: The LHC parameters during Run-1, Run-2 and its design values for proton–proton collisions [104]. The values of luminosity, crossing angle, number of colliding bunches and mean number of interactions per bunch crossing are referring to IP1 (ATLAS).

Parameter	Design	2010	2011	2012	2015	2016
Beam Energy [TeV]	7.0	3.5	3.5	4.0	6.5	6.5
Protons per bunch [10^{11}]	1.15	1.0	1.3	1.5	1.1	1.1
Bunches per beam	2808	368	1380	1380	2244	2076
Revolution frequency [Hz]	11245	11245	11245	11245	11245	11245
Transverse emittance [μm]	3.75	2.6	2.4	2.4	3.5	3.4
β^* at IP [m]	0.55	2.5-3.5	1.0-1.5	0.6	0.8	0.4
Half crossing angle at IP [μrad]	143	100	120	146	145	185
Bunch spacing [ns]	25	150	75/50	50	50/25	25
Peak instantaneous luminosity [10^{34} cm^{-2}s^{-1}]	1	0.021	0.36	0.77	0.51	1.37
Delivered integrated luminosity [fb^{-1}]	-	0.048	5.5	22.8	4.2	38.9
Recorded integrated luminosity [fb^{-1}]	-	0.045	5.1	21.3	3.9	36.0
Mean number of interactions per bunch crossing	-	4.0	9.1	20.7	13.7	24.2

2.1.1 *LHC operation during the period 2010-2012*

From the beginning of Run-1, the beam parameters slowly evolved until the end of 2012. The beam energy in 2010 and 2011 was half of the designed one, while in 2012 it was 4 TeV. The number of bunches per beam increased from 368 to 1318, while the bunch spacing decreased from 150 ns to 50 ns and the pile-up increased from 4 to approximately 21, with the mean number of interactions was $< \mu >= 9.1$ in 2011, while in 2012, the pile-up increased to $< \mu >= 20.7$. The total integrated luminosity as a function of time and the luminosity weighted distribution of the mean number of interactions per bunch crossing are shown in Figure 2.2.

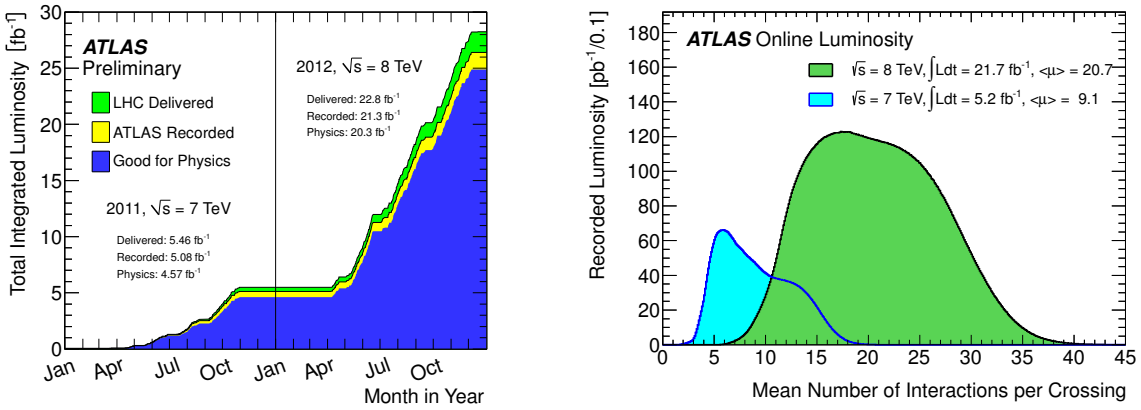

(a) **(b)**

Figure 2.2: The total integrated luminosity as a function of time (a) and the luminosity weighted distribution of the mean number of interactions per bunch crossing (b) during 2011 and 2012 [105].

In Figure 2.2(a) three luminosities are shown, the green area shows the delivered luminosity during stable beams collisions, while the yellow area represents the recorded luminosity with the ATLAS detector, the blue area, marked as "good for physics", represents the luminosity which is accepted for physics analyses with all detector components fully operational. The delivered integrated luminosity for proton–proton collisions at centre-of-mass energy of $\sqrt{s} = 7$ TeV is 5.46 fb^{-1} and at $\sqrt{s} = 8$ TeV is 22.8 fb^{-1}, while the ATLAS recorded luminosity is 5.08 fb^{-1} and 21.3 fb^{-1} in 2011 and 2012, respectively. The uncertainty on the luminosity determination with the ATLAS detector is 1.8 % and 1.9 % in 2011 and 2012, respectively [106, 107].

2.1.2 *LHC performance for Run-2 and further runs*

After the two year long shutdown, Run-2 started in June 2015 with the beam energy of 6.5 TeV and the bunch spacing of 50 ns at the beginning and then decreased to 25 ns later in the year. In 2016 the beam energy remained the same. The total integrated luminosity and the number of interactions per crossing during 2015 and 2016 are shown in Figure 2.3. When comparing to Run-1, the collected data in Run-2 is much higher, only in 2016 it was recorded 36.0 fb^{-1} of data with $< \mu >= 24.2$, while reached peak instantaneous luminosity is 1.37 times larger then the designed one.

Run-2 is expected to finish at the end of 2018 after which another long shut-down is expected when the LHC machine and the detectors will be upgraded. During this time the magnet system will be revised to stabilise operation at the design energy. Run-3 is expected to start in 2021 and by the 2023 when it will finish it is expected to collect around 300 fb^{-1} of data. The schematic view of the long term LHC schedule is shown in Figure 2.4. In order to increase the LHC's discovery potential, the next project,

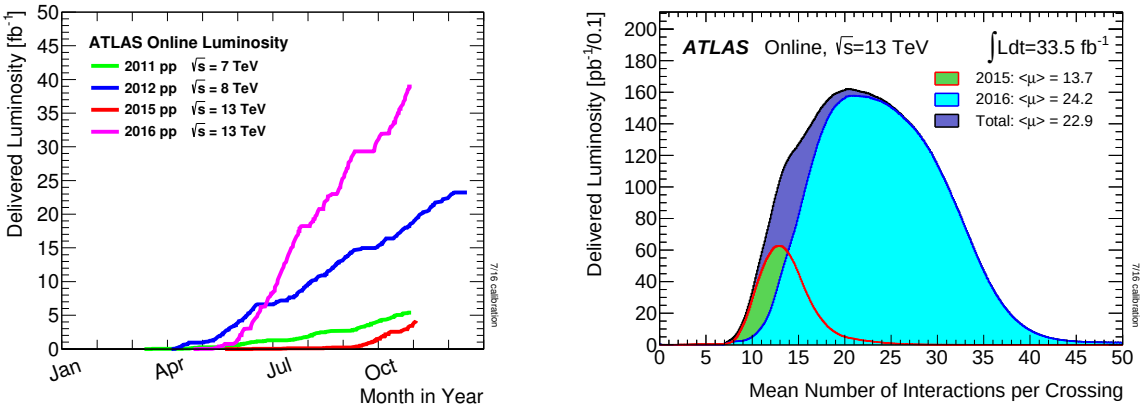

(a) (b)

Figure 2.3: The total integrated luminosity versus time delivered to the ATLAS detector during stable proton–proton beams for 2011-2016 (a) and the luminosity weighted distribution of the mean number of interactions per bunch crossing during 2015 and 2016 (b) [108].

after 2024, is the High Luminosity LHC (HL-LHC) [109]. The HL-LHC is expected to collect around 3000 fb^{-1} of data during 12 years of operation, with this luminosity 140 to 200 proton–proton collisions per bunch are expected. The experiments will also be upgraded so they can maintain their good performance in such harsh environment. With this increased luminosity it is feasible to study rear processes which are below the sensitivity of the LHC.

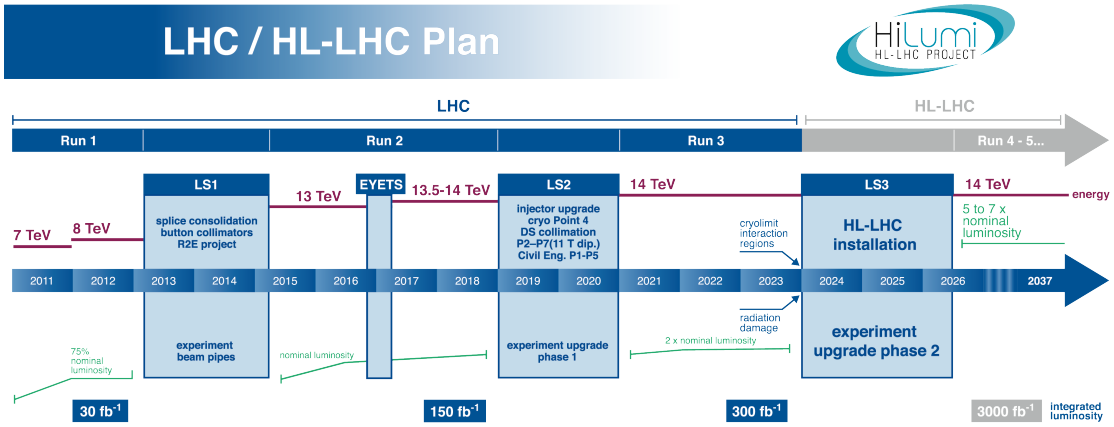

Figure 2.4: The long term LHC schedule [110].

2.2 THE ATLAS DETECTOR

The ATLAS detector [76, 98] is general purpose particle detector at the LHC, located around one of the four interaction points (IP1) in a cavern 95 m below the surface. The ATLAS collaboration founded in 1992, which operates the ATLAS detector, currently consists of over 5000 scientist from 180 institutions in 38 countries.

A LHC detector has to satisfy following requirements, in order to maintain harsh LHC conditions. Fast response with short dead time of the detector is needed in order to collect data at high luminosities. High detector granularity is required for distinguishing particles as well as for separating interesting from the pile-up events. Large acceptance in pseudorapidity with full azimuth coverage is necessary for full event reconstruction, especially for missing energy determination. Resistance to radiation is essential for obtaining good detector performance over a long period of time.

As a general purpose detector, the ATLAS detector, has to investigate a variety of different physics phenomena at the LHC. It measures the energy and momenta of particles produced in the collisions provided by the LHC. The physics programme of the ATLAS detector includes: measurements of the SM processes (precise measurement of masses of the W boson and the top quark, high precision tests of the QCD, electroweak interactions and flavor physics), search of the Higgs boson is a primary physics goal and measurement of its properties (search in wide range of possible masses and measure its mass, couplings, spin, parity), search for the physics beyond SM (search of heavy gauge bosons W' and Z', CP violation, lepton flavour violation in $\tau \to 3\mu$ or $\tau \to \gamma\mu$, measurement of $B_s^0 \to \mu\mu$, search of anomalous triple and quadratic gauge couplings, search of SUSY particles, dark matter candidates and extra dimensions).

The ATLAS detector is a complex detector system consisting of different types of sub-detectors ordered concentrically in layers around the beam axis with forward-backward symmetric cylindrical geometry and almost a full coverage in the solid angle around the collision point. The schematic view of the ATLAS detector is shown in Figure 2.5 with it's components. It is the largest particle detector, with 46 m long and 25 m in diameter and weights around 7000 t. ATLAS detector consists of a cylindrical barrel region with two end-cap disks at each end. The first layer of the ATLAS detector is the inner detector (ID) which measures the momentum of charged particles in a 2 T magnetic field produced by a surrounding solenoid magnet. The next system is the electromagnetic and hadronic calorimeter for detection of electrons, photons and hadrons and measurement of their energy via electromagnetic or hadronic showers. The outer layer is the muon spectrometer (MS) for high-precision tracking of muons in a approximately 4 T toroidal magnetic field. The design performance requirements for the ATLAS detector and coverage of its sub-detectors are summarised in Table 2.2, more detailed description for each subsystem is given in Sections 2.2.3, 2.2.4 and 2.2.5.

Figure 2.6 illustrates passage of different types of particles in the transverse plane of the ATLAS detector. Charged particles are identified by bending their trajectories in a magnetic field so their momentum and charge can be measured. Photons and

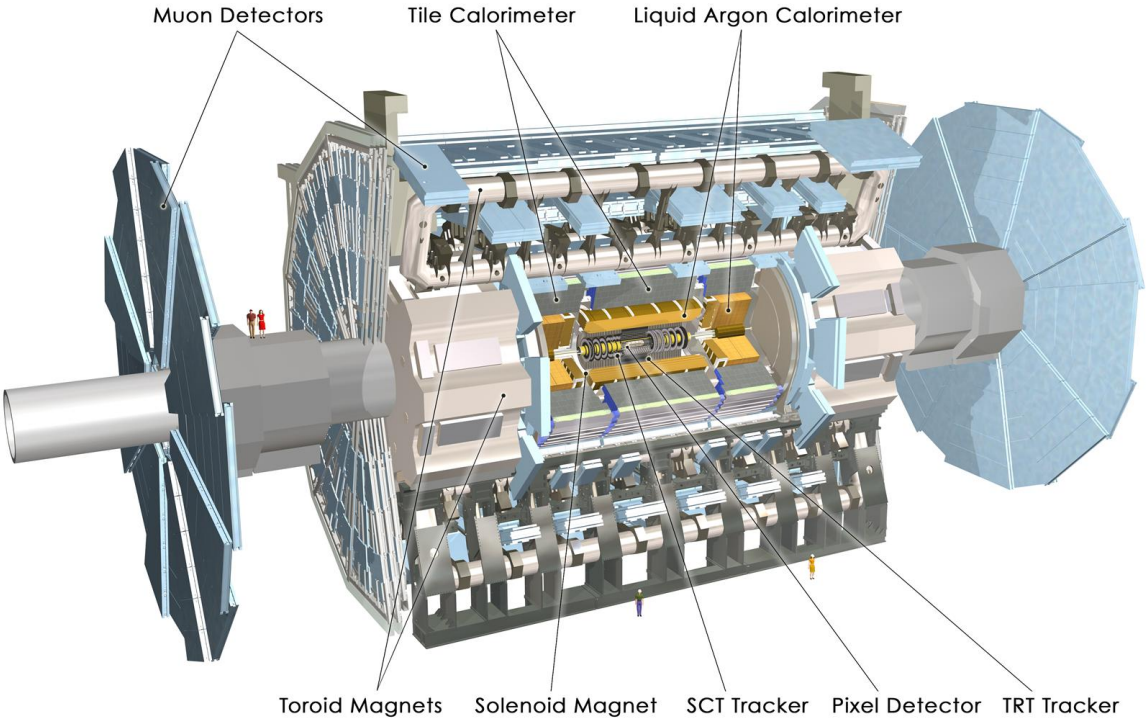

Figure 2.5: The ATLAS detector [111].

Table 2.2: The design performance requirements for the ATLAS detector and coverage of its sub-detectors [98]. The units for E and p_{T} are given in GeV.

Sub-detector	Resolution	Coverage for measurement	Coverage for L1 trigger
ID	$\sigma_{p_{\mathrm{T}}}/p_{\mathrm{T}} = 0.05\%\ p_{\mathrm{T}} \oplus 1\%$	$\lvert\eta\rvert < 2.5$	–
Electromagnetic calorimeter	$\sigma_{\mathrm{E}}/E = 10\%/\sqrt{E} \oplus 0.7\%$	$\lvert\eta\rvert < 3.2$	$\lvert\eta\rvert < 2.5$
Hadronic calorimeter			
barrel and end-cap	$\sigma_{\mathrm{E}}/E = 50\%/\sqrt{E} \oplus 3\%$	$\lvert\eta\rvert < 3.2$	$\lvert\eta\rvert < 3.2$
forward	$\sigma_{\mathrm{E}}/E = 100\%/\sqrt{E} \oplus 10\%$	$3.1 < \lvert\eta\rvert < 4.9$	$3.1 < \lvert\eta\rvert < 4.9$
MS	$\sigma_{p_{\mathrm{T}}}/p_{\mathrm{T}} = 10\%$ at $p_{\mathrm{T}} = 1$ TeV	$\lvert\eta\rvert < 2.7$	$\lvert\eta\rvert < 2.4$

electrons both deposit their energy in the electromagnetic while hadrons are deposit their energy in the hadronic calorimeter. The difference between neutral and charged particles is that later leaves tracks in the ID. Muons and neutrinos are the only particles traversing the detector entirely, while muons form tracks in the MS, neutrinos escape from the detector without any interaction. Therefore, neutrinos can't be detected directly and only the missing energy can be measured for them, but this is also the case for some BSM particles (like dark matter candidates). Only the balance in the transverse plane can be used for the calculation of the missing energy. The total energy in the transverse plane is considered to be zero before the collision because the protons are traveling along the beam axis.

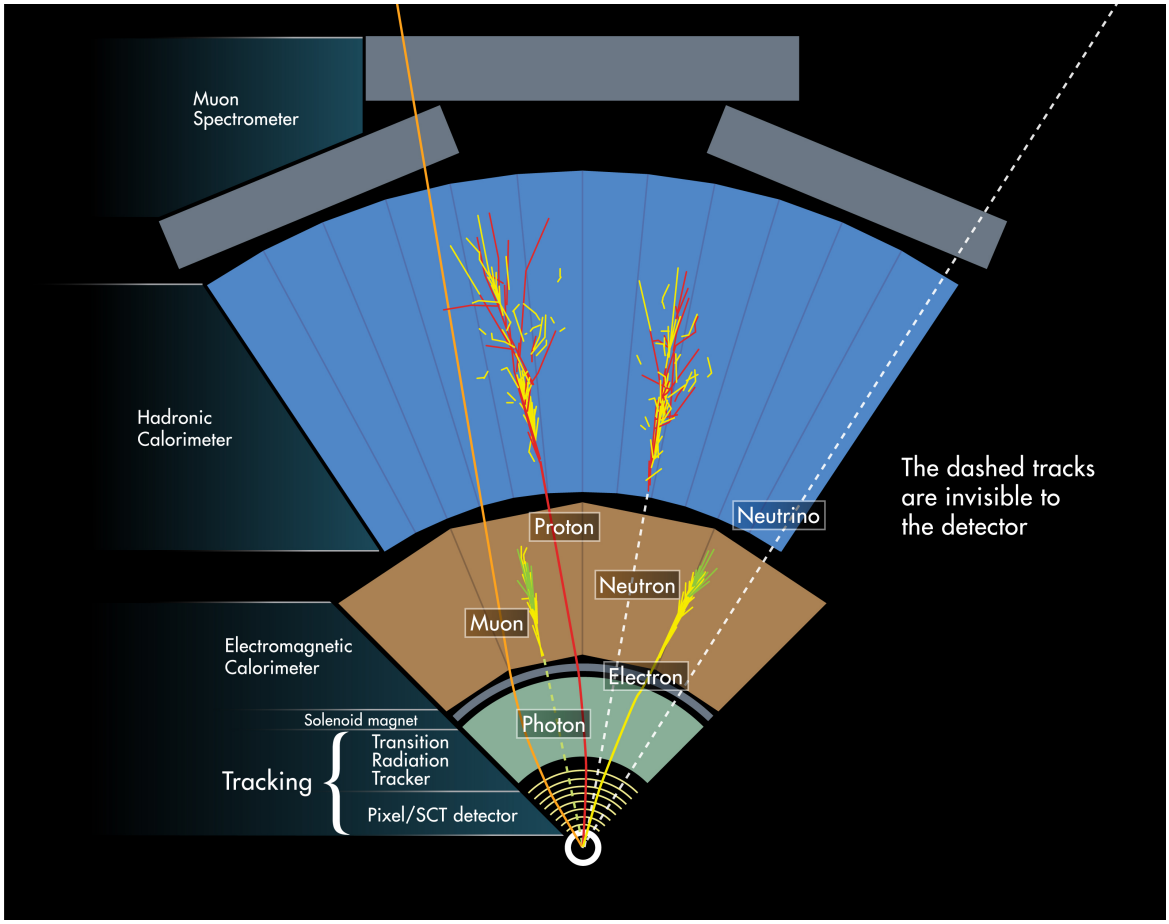

Figure 2.6: The principle of particle detection in the transverse plane of the ATLAS detector [112].

2.2.1 *Definitions and conventions*

The common coordinate system used in ATLAS is a right-handed Cartesian coordinate system with the nominal interaction point in the centre of the detector defined as its origin, as shown in Figure 2.7. The z-axis is the beam line and the x-y plane is transverse to the beam direction, with the positive x-axis pointing to the centre of the LHC ring and the positive y-axis pointing upwards. The cylindrical coordinates are defined with the azimuthal angle φ defined around the beam line in the transverse plane measured from the x-axis, the polar angle θ defined with respect to the positive z-axis and the radial distance r from the beam line, as follows:

$$\varphi = \arctan\frac{y}{x}, \quad \theta = \arctan\frac{z}{\sqrt{x^2+y^2}}, \quad r = \sqrt{x^2+y^2}. \tag{2.6}$$

Side A of the detector corresponds to $z > 0$ $(0 < \theta < \pi/2)$ and side C to $z < 0$ $(\pi/2 < \theta < \pi)$, the upper part of the detector refers to $\varphi > 0$.

The Lorentz invariant variables along the beam line (z-axis) are typically used, i.e.

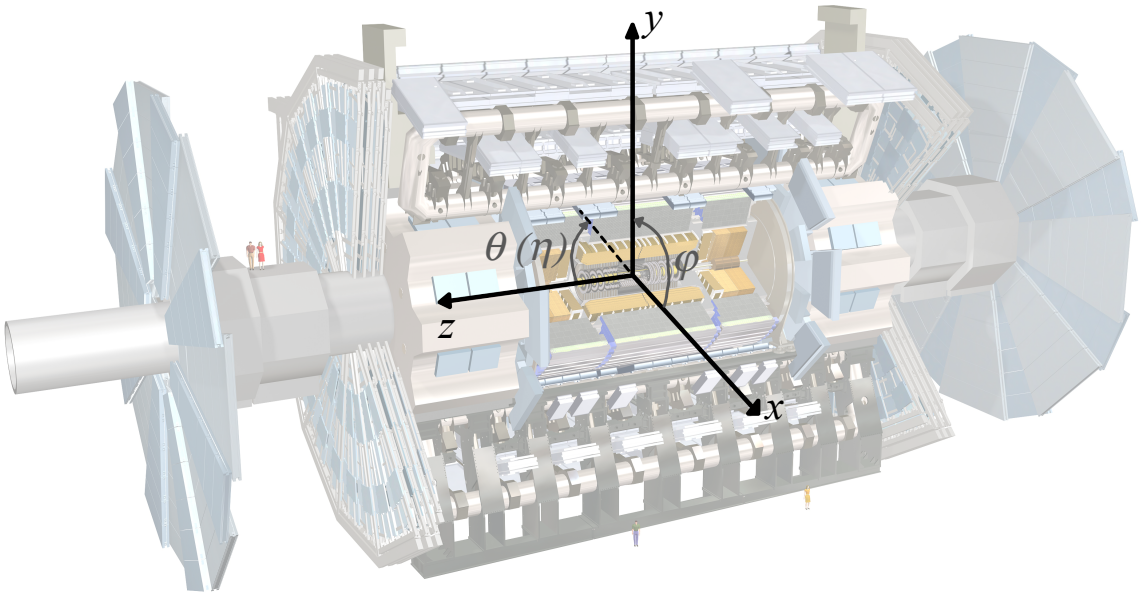

Figure 2.7: The ATLAS coordinate system.

the rapidity:

$$y = \frac{1}{2} \ln \frac{E + p_z}{E - p_z}, \tag{2.7}$$

where E is the energy of the particle and p_z is its longitudinal momentum. For massless particles ($E >> m$) the rapidity is equal to pseudorapidity:

$$\eta = -\ln \tan \frac{\theta}{2}, \tag{2.8}$$

which depends only on the polar angle, $\eta = 0$ corresponds to the transverse plane and $\eta = \pm\infty$ is along the beam line. The angular distance between two measured objects in the detector in (η, φ) plane is defined as:

$$\Delta R = \sqrt{\Delta\eta^2 + \Delta\varphi^2}. \tag{2.9}$$

Two more parameters for the reconstructed tracks of the charged particles should be defined: the longitudinal impact parameter z_0 which is the z position of the track at the point of closest approach and the transverse impact parameter d_0 defined as the distance in the transverse plane of the closest approach (perigee) to the z-axis of the helix produced by the particle. Observables in the transverse plane, for example the energy of the particle (similarly for the particle momentum), are defined as:

$$E_{\mathrm{T}} = E \sin\theta = \frac{E}{\cosh\eta}, \quad E_x = E_{\mathrm{T}} \cos\varphi, \quad E_y = E_{\mathrm{T}} \sin\varphi. \tag{2.10}$$

2.2.2 *Magnet System*

The magnet system of the ATLAS detector [113–115] consists of two sub-systems for ID and MS. These systems have orthogonal magnetic fields enabling two independent measurements of the muon momentum. In total, the detector has four main magnets: one solenoid and three toroids, with 22 m in diameter, 16 m in length and a stored energy of 1.6 GJ. The diagram of the ATLAS magnet system is shown in Figure 2.8.

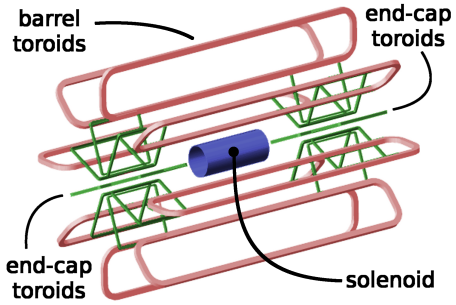

Figure 2.8: Schematic diagram of the magnet system of the ATLAS detector [98].

The solenoid magnet provides a 2 T axial magnetic field to the ID, aligned with the beam axis. Since it is located in front of the electromagnetic calorimeter, the material for the solenoid layout has to be optimised in order to achieve the desired calorimeter performance. Therefore, the calorimeter and the solenoid share one vacuum vessel, the solenoid coil is as thin as possible and the steel of the hadronic calorimeter is used for returning the flux of the magnet, this configuration contributes to 0.66 radiation lengths. The solenoid coil consists of 1154 turns made from superconducting NbTi allay which are stabilised in aluminium matrix and liquid helium is used for maintaining the temperature at 4.5 K, the nominal current of 7.73 kA. The solenoid length is 5.8 m, with inner and outer diameter of 2.46 m and 2.56 m, respectively. The total mass is 5.4 t with a stored energy of 40 MJ, which gives a light-weighted structure with the stored-energy-to-mass-ratio of 7.4 kJ/kg.

The toroidal system produces a magnetic field for the MS and consists of one barrel and two end-cap toroids, each made from eight coils arranged radially and symmetrically around the beam axis as shown in Figure 2.8. The coils are made of aluminium stabilised NbTI allay cooled with liquid helium with 120 and 116 turns for barrel and end-cap, respectively. The nominal current is 20.5 kA producing the peak field of 4 T. The size of the barrel toroid is 25.3 m in length, with inner and outer diameters of 9.4 m and 20.1 m, respectively. The end-cap toroids are 5 m in length, with inner and outer diameters of 1.65 m and 10.7 m, respectively. It is very difficult to generate completely homogenous magnetic field since the toroids cover so large volume, which varies from 0.15 T to 2.5 T in barrel and 0.2 T to 3.5 T in end-caps. The end-cap toroids are rotated by 22.5° compared to the barrel toroid in order to optimise the field between them. The bending power of the magnet is given by the field integral over the track length within the tracking volume $\int Bdl$, which is 1.5 to 5.5 Tm in barrel ($0 < |\eta| < 1.4$) and 1 to 7.5 Tm in end-caps ($1.6 < |\eta| < 2.7$).

2.2.3 *The Inner Detector*

The ID [116, 117] is designed for precise determination of momentum resolution and reconstruction efficiency of charged particles with $p_{\mathrm{T}} > 0.1$ GeV within the range of $|\eta| < 2.5$. It is located the closest to the beam line and consists of three separate parts: pixel detector, semiconductor tracker (SCT) and transition radiation tracker (TRT). In the barrel the layers are concentric cylinders around the beam axis, while in the end-caps the layers are disks in the transversal plane, as shown in Figure 2.9. ID is required to have high granularity and made from radiation-tolerant materials in order to maintain high particle density from the collisions in high pile-up environment. The charged particles are bent by 2 T axial magnetic field in the transverse plane with the bending power of 2 to 0.5 Tm for $\eta = 0$ to $|\eta| = 2.5$, for the forward region the inhomogeneous magnetic field is taken into account with a magnetic field map in reconstruction and simulation. The ID's designed momentum resolution ($\sigma_{p_{\mathrm{T}}}$), as shown in Table 2.2, is:

$$\frac{\sigma_{p_{\mathrm{T}}}}{p_{\mathrm{T}}} = 0.05\%\ p_{\mathrm{T}} \oplus 1\%, \tag{2.11}$$

where the first term is the intrinsic resolution which is dominant for high p_{T} tracks, the second term is from the multiple scattering dominant for the low p_{T} and the operation is defined as $a \oplus b = \sqrt{a^2 + b^2}$. ID also provides reconstruction of primary and secondary vertices (origins of the hard scatter and other proton–proton interactions, more details will be given in Chapter 3), as well as identification of the b-jets and τ leptons.

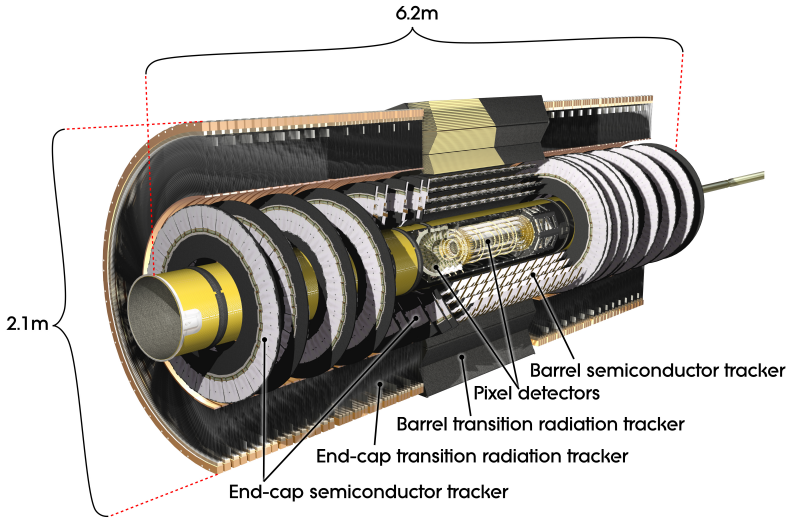

Figure 2.9: Schematic diagram of the ATLAS inner detector [118].

The pixel detector [119, 120] is the most granular part of the ID. It is a solid-state detector and consists of three cylindrical layers between 50.5 and 122.5 mm from the beam axis in barrel and three end-cap disks at each end, which provide three hits for each charged particle track. The high granularity is achieved with 1744 50×400 μm silicon pixel elements 250 μm thick, with 7232 pixels on each element, which gives about 80.4 million readout channels (almost 90% of the total readout channels in the ATLAS detector). This gives an accuracy of the charged track position of about 12 μm in transverse plane and 66 μm and 77 μm in the z direction for barrel and end-cap

regions, respectively. The elements are made from n-type silicon wafers, after a charged particle passes through them, it creates electron-hole pairs which are separated by the electric field and collected at each pixel. The first layer of the pixel detector is called b-layer because of its role in the reconstruction of secondary vertices for the b-jet tagging where the B meson decays away from the IP. Furthermore, it is also used to identify the difference between electrons and converted photons, since converted photons are not expected before the b-layer.

The SCT [121–123] is the next sub-detector in the ID, similar to the pixel detector but with coarser granularity. SCT consists of four barrel layers between 299 and 514 mm from the beam axis and nine end-cap disks on each side which give at least four hits for charged particle track. There are 4088 modules which consist of two pairs of silicon micro-strip planes glued together back-to-back, with an opening angle of 40 mrad between the planes. Each module has 1536 silicon strips 12.6 cm long and 80 μm. This double layer configuration allows for reduction of the global number of readout channels to approximately 6.3 million and measurements along the length of a strip with two dimensional track reconstruction. The spatial resolution for SCT modules is 17 μm in transverse direction and 580 μm in longitudinal direction.

The TRT [124–126] exploits different detector technology compared to the other parts of the ID and covers region up to $|\eta| < 2$. It is made of layers of straw drift tubes filled with gas mixture of xenon, carbon-dioxide and oxygen 70:27:3. Inside the 4 mm diameter tube is a gold-plated tungsten wire (anode) with 30 μm in diameter. The tubes are made of two polyimide films coated on one side with a thin aluminium layer (cathode) and bonded back-to-back using a polypropylene layer, with a total thickness of 70 μm. In the barrel there are approximately 50000 144 cm long tubes aligned with the z-axis, while the end-caps contain around 320000 radial tubes 37 cm long, which in total gives 350 thousand readout channels. When a charged particle passes through the tubes, it ionises the gas which creates an electric signal along the wire. When a relativistic charged particle traverses between the tubes (two materials with different dielectric constants: air and polypropylene) it emits transition radiation photons with probability proportional to E/m of the particle. Those photons are absorbed by the xenon gas and increase the intensity of the signal. There are two readout thresholds, one for the passage of the generic charged particle through the tubes (low threshold $E < 0.5$ keV for tracking hits) and one for relativistic charged particle passage (high threshold $E > 6$ keV for transition-radiation hits). At the same momentum, electron will emit more transition radiation photons then charged hadron, thus, TRT is used to distinguish electrons from charged hadrons, like pions. There are approximately 35 to 40 hits per track. The spatial resolution in the transverse plane is 130 μm and there is no segmentation in the longitudinal direction.

After Run-1 a new sub-detector was added in front of the pixel detector, insertable b-layer (IBL) [127, 128], in order to protect the other parts of the ID from the radiation damage in high pile-up conditions. Installation of the IBL required a reduction of the diameter of the beam pipe, also the IBL sensors had to be smaller and thiner compared to the pixel detector. The IBL should improve b-tagging efficiency and vertex identification during Run-2 [129, 130].

2.2.4 *Calorimeters*

The ATLAS calorimeter system [131–133] is located between the ID and MS and precisely measures the energies of charged and neutral particles up to region of $|\eta| < 4.9$. It has to be hermetic in order to measure the missing energy for the neutrino and reconstruct forward jets. The calorimeter system is composed of two parts: electromagnetic (EM) for electron and photon identification and measurement and hadronic (HAD) calorimeter for accurate jets and missing transverse energy measurements, as shown in Figure 2.10. Both of them are sampling calorimeters, with alternate layers of passive absorbing material, which induce particle showers, and active (sampling) measurement medium, which measures the energy of the particles in the shower. The electromagnetic shower consists of consecutive bremsstrahlung and pair production processes, while the hadronic shower is based on several processes (strong decays, weak decays and electromagnetic showers, ...). The depth of the calorimeters has to be large enough to contain all the electromagnetic and hadronic showers before they reach the MS (punch-through). A characteristic quantity of the length of electromagnetic shower is radiation length X_0 which corresponds to a traveled distance inside the medium when particle looses $1/e$ of its energy, where e is mathematical constant. In case of hadronic showers, absorption length λ_0 is used with similar definition. Typically, hadronic showers are longer and broader compared to the electromagnetic, thus the HAD calorimeters are located after the EM.

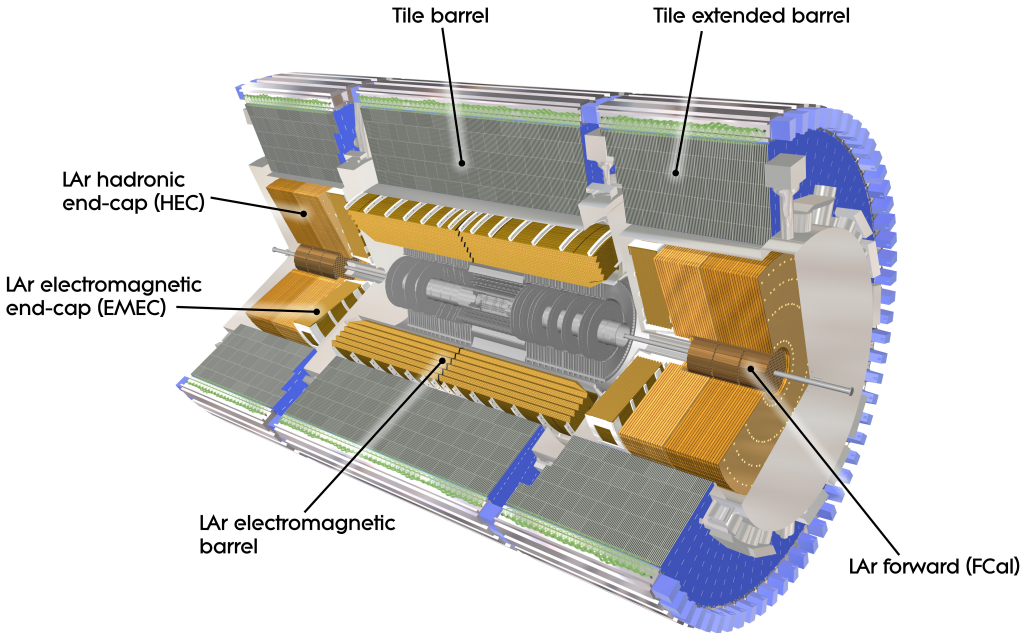

Figure 2.10: Schematic diagram of the ATLAS calorimeter system [134].

The EM calorimeter is designed for precise energy measurement of electromagnetically interacting particles (electrons and photons) and exploits liquid argon (LAr) as

active material and lead as an absorber. LAr was chosen because of its linear response and radiation hardness. The EM calorimeter consists of two half barrels ($|\eta| < 1.475$) and inner ($1.375 < |\eta| < 2.5$) and outer ($2.5 < |\eta| < 3.2$) end-caps. The region $1.37 < |\eta| < 1.52$ has a lot of dead material (cables, services, support, ...) which reduces the calorimeter performance, it is referred as the crack region. The EM calorimeter is constructed with accordion geometry, the barrel accordion waves are axial and run in azimuth while in the end-caps the waves are radial and run axially. This configuration allows uniform performance through the detector, a good energy and spatial resolution, low electronic noise and high radiation resistance, however the response time is long (400 ns). The schematic view of a module of the barrel EM calorimeter is shown in Figure 2.11(a), each half-barrel consists of seven rings with sixteen modules. There are three longitudinal layers up to $|\eta| < 2.5$ and two for region $2.5 < |\eta| < 3.2$. The first barrel layer has the highest granularity made of thin $\Delta\eta \times \Delta\varphi = 0.0031 \times 0.098$ strips which provide good position measurement of the shower and improves particle identification. The second and the third layer have bigger modules of sizes 0.025×0.0245 and 0.05×0.0245, respectively, most of the electromagnetic shower is contained inside the second layer, while its tail is contained inside the third layer. LAr is ionised by the shower particles and the signal is collected at the electrodes (three copper plates separated by polyimide insulator). In total, the electromagnetic calorimeter has more then 170 thousand readout channels. The EM calorimeter was optimised for resolution and efficiency measurement of photons in $H \to \gamma\gamma$ and electrons in $H \to 4\ell$ channel. The EM designed energy resolution, as shown in Table 2.2, is:

$$\frac{\sigma_{\mathrm{E}}}{E} = \frac{10\%}{\sqrt{E}} \oplus 0.7\%, \tag{2.12}$$

where E is the energy of the incoming particle in GeV, the first term is stochastic and describes the statistical fluctuations of the fraction of the shower energy deposited in the sampling medium (LAr) and the fraction deposited in the absorber (lead), the second is the constant term accounting for calibration-related effects, mechanical and electrical inhomogeneities, energy loss due to non-instrumented regions. The spatial resolution is $50\ \mathrm{mrad}/\sqrt{E}$ in η. The total thickness of the EM calorimeter is larger then 22 X_0 in barrel and larger then 24 X_0 in end-cap region which enables containing the electromagnetic showers, but there are also about 2 interaction lengths (λ_0) therefore some parts of jets energy can be deposited in them.

The HAD calorimeter measures the energy of particles which interact via strong interaction by exploiting two different technologies. It consists of four parts: a central barrel tile ($|\eta| < 1$), two tile end-caps ($0.8 < |\eta| < 1.7$), two LAr end-caps ($1.5 < |\eta| < 3.2$) and a forward calorimeter ($3.1 < |\eta| < 4.9$). The tile calorimeter is made from alternate layers of steel plates (absorber) and scintillating tiles (active medium) orthogonal to the z-axis, divided azimuthally into 64 modules, illustrated in Figure 2.11(b). When a charged particle crosses the active medium, an ultraviolet scintillation light is produced, collected and converted into visible light by a wavelength-shifting optical fibre. The signal is measured from the photomultiplier where the optical fibre is connected. The granularity of the three-layer tile calorimeter is $\Delta\eta \times \Delta\varphi = 0.1 \times 0.1$ for the first layer and 0.2×0.1 for the other two layers, which is much worse than the EM calorimeter. The total depth of the tile calorimeter is about 7 λ_0. The relative

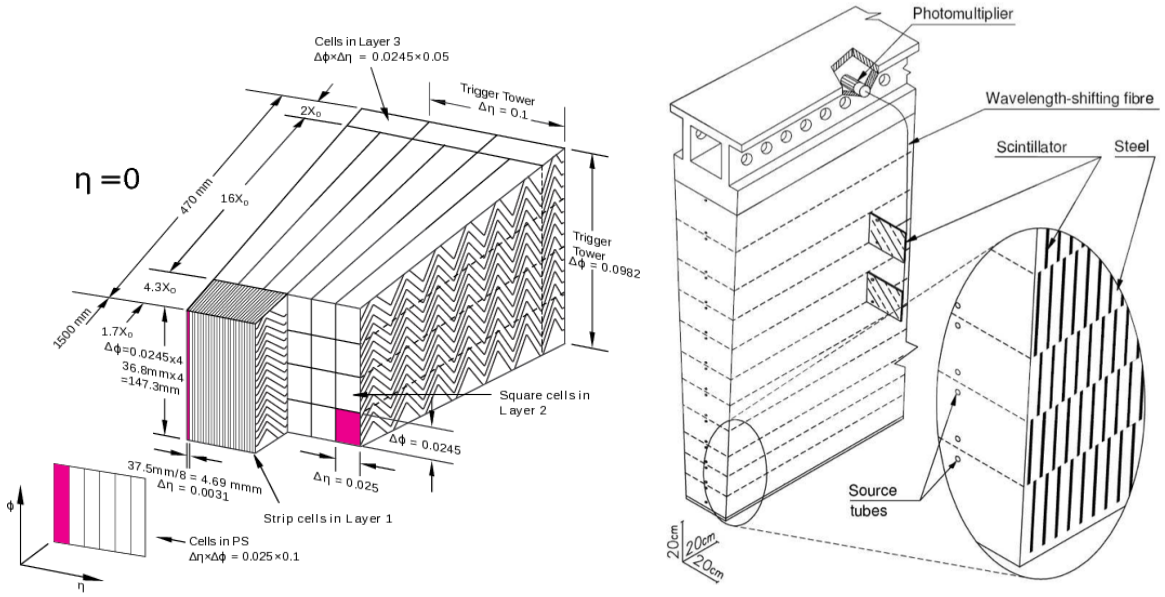

(a) **(b)**

Figure 2.11: Schematic diagram of a EM barrel calorimeter module (a) and a tile calorimeter module (b) [98].

energy resolution of the hadronic tile and end-cap calorimeter is:

$$\frac{\sigma_{\mathrm{E}}}{E} = \frac{50\%}{\sqrt{E}} \oplus 3\%, \tag{2.13}$$

where E is the energy of the incoming particle in GeV. The LAr end-cap HAD calorimeter uses LAr as an active medium and copper plates for the absorbers, divided azimuthally into 32 modules, because of the increased radiation from the beam pipe. The granularity is $\Delta\eta \times \Delta\varphi = 0.1 \times 0.1$ for $|\eta| < 2.5$ and 0.2×0.2 for other region. The total depth of the end-cap calorimeter is about 12 λ_0.

The forward calorimeter covers the region $3.1 < |\eta| < 4.9$ with three layers: an EM that is closest to the interaction point and two HAD calorimeters. LAr is used as an active material while for the absorbing media, copper is used in the EM and tungsten is used in the HAD layers. The forward HAD calorimeter is very dense, with depth of about 9 λ_0 over small longitudinal space. The granularity is $\Delta\eta \times \Delta\varphi = 0.2 \times 0.2$. The relative energy resolution of the forward HAD calorimeter is:

$$\frac{\sigma_{\mathrm{E}}}{E} = \frac{100\%}{\sqrt{E}} \oplus 10\%, \tag{2.14}$$

where E is the energy of the incoming particle in GeV. The forward calorimeter is exposed to large radiation dose because of its proximity to the beam line. The total thickness of the HAD calorimeter is about 11 λ_0 at $|\eta| = 0$ (1.5 λ_0 from outer support is included) which is sufficient to reduce the punch-through. In conclusion, the HAD calorimeters have good resolution for high energy jets and allow good measurement of the missing energy.

2.2.5 *The Muon Spectrometer*

The MS [135] performs muon identification and precision measurement of the muon momentum for a wide range of muon momentum, from 3 GeV to 3 TeV. It uses four detector technologies up to region of $|\eta| < 2.7$ in toroid magnetic field. The configuration of the magnets is chosen in such a way that magnetic field is mostly orthogonal to a muon trajectory, and, at the same time, degradation of the resolution of the measurement due to multiple scattering is minimal. While passing through the calorimeter muons loose a small amount of energy, around 3 GeV for muons with energies up to 100 GeV. Higher energy muons lose energy mostly through radiative energy losses, which may lead to "catastrophic" energy loss comparable to the total muon energy. The layout of the MS is illustrated in Figure 2.12. MS consists of monitored drift tube chambers (MDT) and cathode strip chambers (CSC) for precision tracking measurements, and resistive plate chambers (RPC) and thin gap chambers (TGC) for triggering in barrel and end-cap, respectively. There are three barrel layers located at 5 m, 7.5 m and 10 m from the beam line and four end-cap disks arranged at 7.4 m, 10.8 m, 14 m and 21.5 m from the IP. The schematic view of the MS in the x-y and z-y planes is shown in Figure 2.13. Precise independent measurement of the muon momentum up to few TeV is allowed in the MS for high rapidity region, not covered by the ID. The designed resolution for the MS is $\leq 10\%$ for muon tracks of $p_{\mathrm{T}} = 1$ TeV.

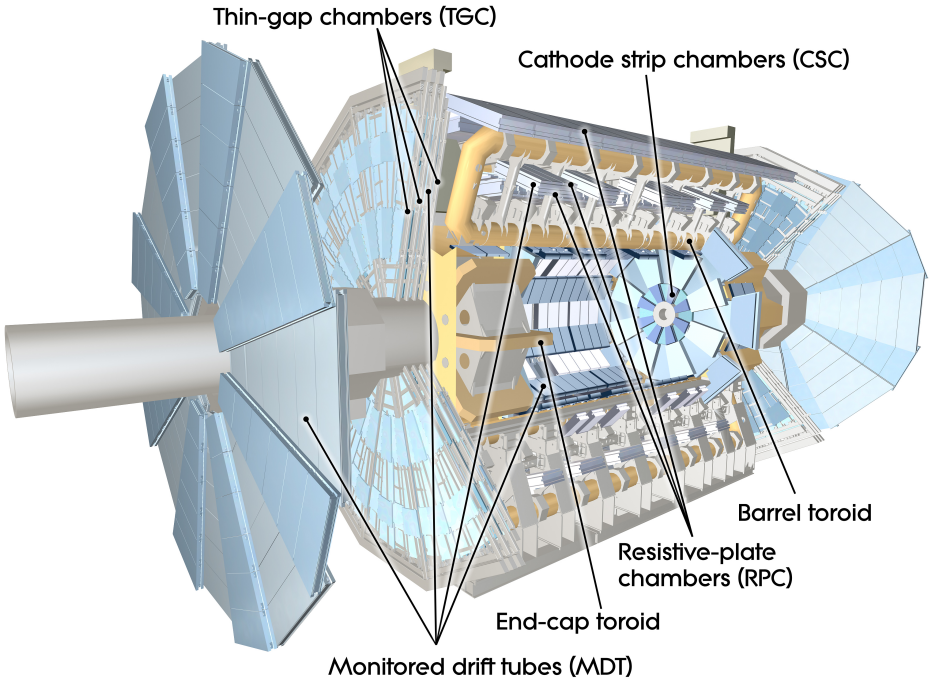

Figure 2.12: Schematic diagram of the ATLAS MS system [136].

The MDT [137] consists of 3 cm in diameter aluminium tubes filled with gas mixture of argon and carbon-dioxide (93:7) with a pressure of 3 bar. The 50 μm in diameter gold-plated tungsten-rhenium wire is in the centre of the tube. Muon momentum meas-

urement is similar to the method used for the TRT. Traversing charged particle ionises the gas inside the tube and ions drift to the wire in electric field. Fine position resolution is enabled by determination of the drift time. Each chamber contains several layers of tubes, in total there is about 400000 tubes in 1194 chambers. Average resolution per tube is 80 μm with a maximal drift time of 700 ns, the combined resolution of a chamber is 30 μm. To achieve this precision the position of the tubes has to be known with less then 80 μm, therefore four optical alignment rays are installed inside each chamber to monitor the position of the chamber within a few μm. There is also optical alignment which monitors relative position of the chambers with its neighbours. The tubes are aligned along the azimuth with precision measurement in pseudorapidity. The MDT cover range up to $|\eta| < 2.7$, except in the first layer in the end-caps where the range is up to $|\eta| < 2.0$.

The CSC [138] cover the first layer in the end-caps in range $2.0 < |\eta| < 2.7$ where the interaction rates are very high (higher than 1150 Hz/cm^2). The CSC are multiwire proportional chambers aligned radially, eight large and eight small trapezoid chambers have full azimuth coverage. The chambers are filled with gas mixture of argon and carbon-dioxide (80:20), with two types of segmented cathode strips allowing measurement in both η and φ directions. The spatial resolution of 40 μm is obtained in the wire direction (pseudorapidity measurement), while resolution in azimuth is only 5 mm which is enough for the momentum direction measurement. Typical drift time is approximately 30 ns.

The MDT and the CSC are arranged so that muons traverse the three layers, providing three precise position measurements. The central rapidity region $|\eta| < 0.1$ is only partially covered with chambers because of the services for the ID and calorimeters, causing loss of the muon acceptance in this region.

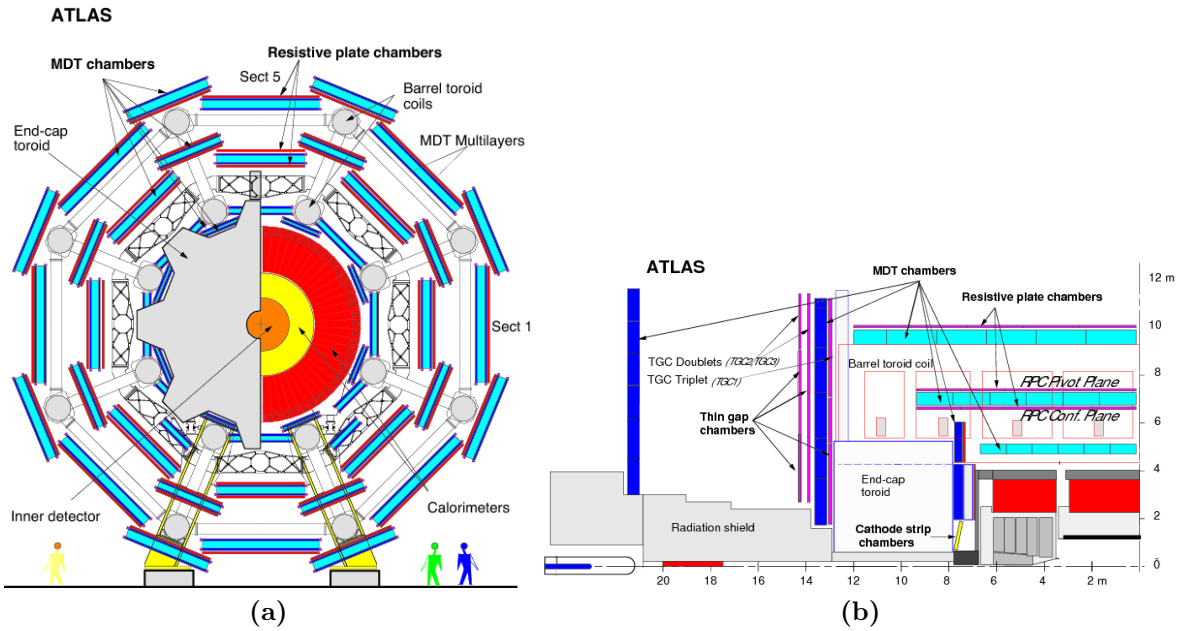

Figure 2.13: Schematic view of the MS in x-y (a) and z-y (b) projections [139].

The RPC [140] are gaseous detectors covering the region up to $|\eta| < 1.05$. It consist of two resistive plates on a 2 mm distance, filled with gas mixture of $C_2H_2F_4$, Iso-C_4H_{10}, and SF_6 (94.7:5:0.3). Muons traveling the gas induce an avalanche towards the anode and thin gas gap allows quick response time which is ideal for triggering. There are 544 RPCs arranged in three layers (two layers are located on either side of the middle MDT layer and the third on the inner or outer side of the outer MDT layer, for the small and large sectors, respectively), referred as three trigger stations, allowing for threshold set up in low and high p_{T} trigger. Each station has two independent layers which provides η and φ measurements, resulting in six possible measurements for muon passing the three stations. The trigger thresholds for inner layers is between 6 and 9 GeV, while for outer layers it is in range 9 and 40 GeV. The RPC have a spatial resolution of 10 mm in z and φ with approximately 1.5 ns time resolution.

The TGC [141] are multiwire proportional chambers with the smaller wire-to-cathode distance (1.4 mm) then the wire-to-wire distance (1.8 mm). The TGC are filled with mixture of carbon-dioxide and n-pentane in high electric field for good time resolution. The operational principle is similar to the CSC. In the end-caps they are located in the inner and middle layer and have a dual application: as a trigger system and for azimuth coordinate measurement. There are nine TGC disks concentrically installed so that cover regions $1.05 < |\eta| < 1.92$ and $1.92 < |\eta| < 2.4$. The small wire-to-wire distance and high electric field near the anode wires contribute to a good timing resolution of 4 ns.

In the barrel the muon chambers are arranged in three cylindrical layers around the beam axis that are called BI (Barrel Inner), BM (Barrel Middle), and BO (Barrel Outer), also it can be separated into small and large sectors. Figure 2.14 illustrates the chamber naming and the numbering of the sectors. The approximate azimuth segmentation of the small (that include the magnet coils) and large (which are between two coils) sectors is shown in Table 2.3. The end-cap muon chambers are arranged in four disks on each side of the interaction point perpendicular to the beam axis, called EI (End-cap Inner), EE (End-cap Extra), EM (End-cap Middle), and EO (End-cap Outer). An auxiliary set of chambers, called BEE (Barrel End-cap Extra), are installed on the cryostats of the end-cap toroids, they are constructed like barrel chambers although functionally they serve in the end-cap system [142]. The pseudorapidity segmentation of the MS is shown in Figure 2.15.

Table 2.3: The small and large sectors azimuth segmentation in MS.

No. MS sector	φ [rad]	No. MS sector	φ [rad]
1	$(-0.235, 0.235)$	9	$(2.905, 3.14) \cup (-3.14, -2.905)$
2	$(0.235, 0.55)$	10	$(-2.905, -2.59)$
3	$(0.55, 1.02)$	11	$(-2.59, -2.12)$
4	$(1.02, 1.335)$	12	$(-2.12, -1.805)$
5	$(1.335, 1.805)$	13	$(-1.805, -1.335)$
6	$(1.805, 2.12)$	14	$(-1.335, -1.02)$
7	$(2.12, 2.59)$	15	$(-1.02, -0.55)$
8	$(2.59, 2.905)$	16	$(-0.55, -0.235)$

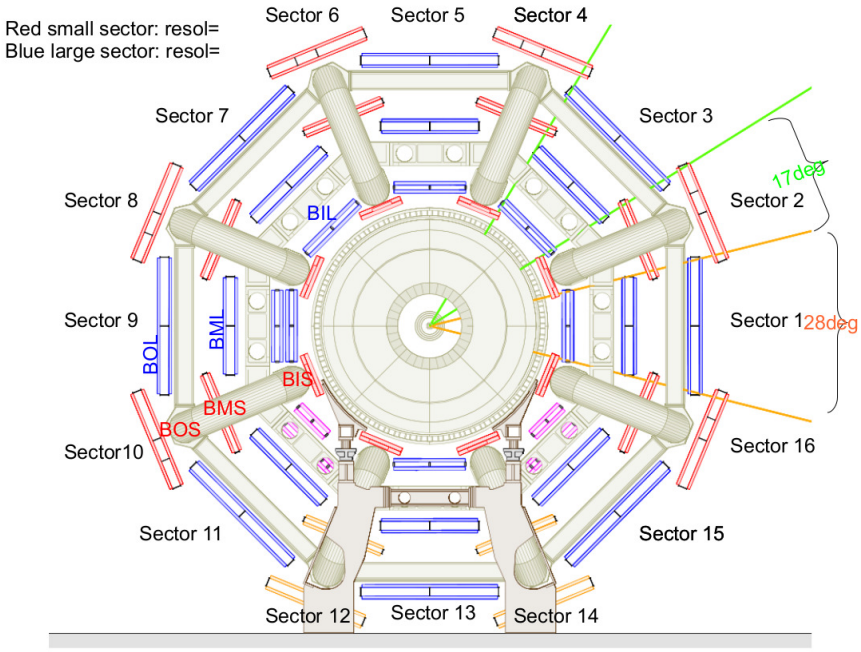

Figure 2.14: Cross-sectional view of the barrel MS perpendicular to the beam axis, the MDT chambers in the small sectors are shown in red, the MDT chambers in the large sectors are shown in blue, with light grey the eight coils of the toroid magnet system are shown [135].

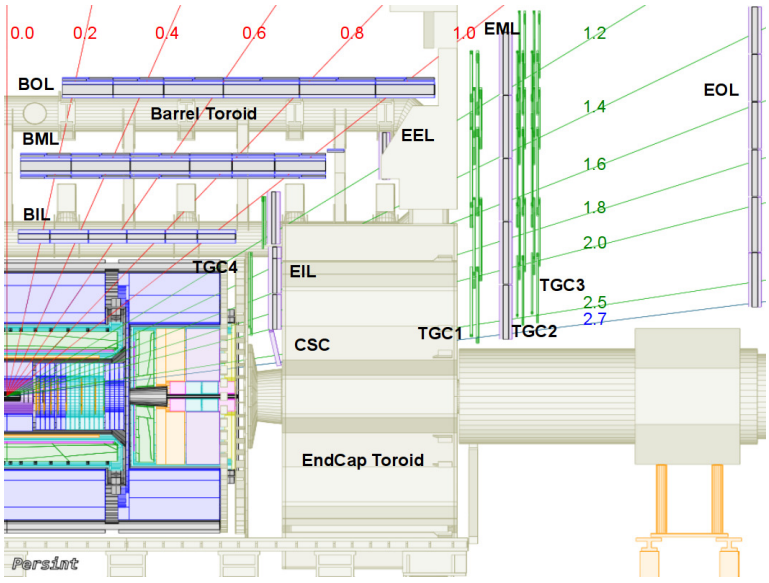

Figure 2.15: Schematic view of the MS in z-y projection with pseudorapidity segmentation [135].

2.2.6 *Trigger System*

The ATLAS detector is required to have fast and efficient trigger system in order to reject background and pile-up events for achieving acceptable trigger rate for physics processes of interest. At the LHC designed luminosity, the event rate is approximately 1 GHz, which require storing about 60 TB of data per second and event data recording is limited to 200 Hz. The ATLAS trigger system [143] selects interesting events in order to reduce the amount of stored data and in Run-1 it was based on three level selection system, where each level refines previous decisions and applies additional selection criteria. Figure 2.16 illustrates the design of the ATLAS trigger system with different trigger rates. The trigger system has to reduce initial bunch crossing rate of 40 MHz to an average recording rate of a few hundred Hz for permanent storage. During Run-1 average event rate was 200 Hz, with a peak of 1000 Hz during 2012, while for Run-2 average event rate is 1 kHz with maximal rate of 1.4 kHz [144, 145]. The first lever trigger is hardware, while the other two are software based.

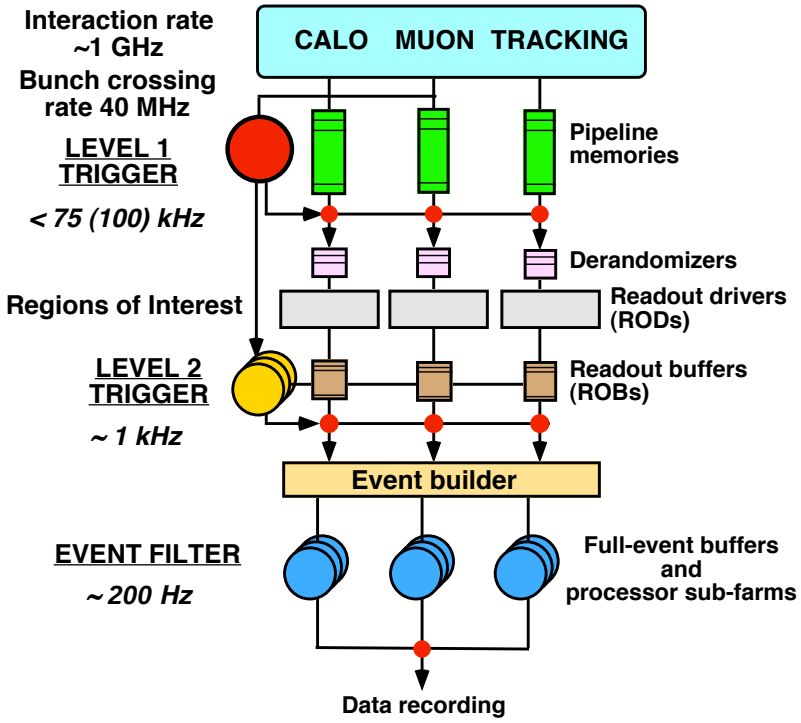

Figure 2.16: Schematic diagram of the ATLAS Trigger system [144].

The first level trigger (L1) selects event within 2.5 μs using limited detector information and reduces the rate to about 75 MHz. The L1 searches for events with muons, electrons, photons, jets, and τ leptons decaying into hadrons, as well as large missing and total transverse energy using the information from the calorimeters and the MS. Muons are identified using the RPC and the TGC trigger chambers in the MS (described in Section 2.2.5). Information from the calorimeters is based on reduced granularity of $\Delta\eta \times \Delta\varphi = 0.1 \times 0.1$, where the L1 maps regions of interest (RoI) with identified interesting features and records information about the type of the particle.

The second level trigger (L2) is designed to reduce event rate to 1 kHz within 40 μs. The L2 uses L1 defined RoI with full granularity and precision of all the available detector data within the RoI and rebuilds the objects.

The final event selection is the event filter (EF) which reduces the event rate to 200 Hz. The EF reconstructs the entire event using the same algorithms used for the offline analysis. It is applied in offline analysis procedures with the average processing time of 4 s. Since more time is allowed per event than at L2, for EF more complicated algorithms are able to run.

A trigger selection can also be prescaled when only a fraction of the events that would pass the trigger selection is kept, to further reduce the event rate and avoid overloading the data taking system.

During Run-2, the L2 and the EF are combined into the high-level trigger (HLT). The HLT runs a more complete event reconstruction on a read-out of the whole detector, and results in a trigger acceptance rate up to 700 Hz. After 2016, the HLT tracking algorithms include a new fast hardware based tracking system (FTK) which increased the rate up to 1 kHz, during 2017 only 50% of the FTK system will be available for testing [145].

2.2.7 *Simulation infrastructure and data preparation*

The run control system monitors the ATLAS data-taking by combining the information from all detector components. The data-taking run starts when all ATLAS systems are ready and there are stable beams in LHC. Usually data-taking run corresponds to single LHC fill and have a unique run number. Runs are further divided into luminosity blocks (LB) where instantaneous luminosity is approximately constant and which usually last a minute. In case of some problems with the detector components, only affected LB can be excluded. Good run list (GRL) lists all LB where all detector parts of the ATLAS experiment that are important for physics analyses are running correctly. The runs are grouped in periods labeled alphabetically with a typical length of few weeks.

The ATLAS detector has to have good data acquisition system (DAQ) to save and store all the information from the detector. The accepted events from the trigger system are transferred to the DAQ for permanent storage and further processing in RAW data format on magnetic tapes in the CERN computer centre (Tier0). They are assigned to different streams according to the type of detected signature. The EGamma stream has events with an important activity in the EM calorimeter, that are electron and photon-like objects that passed the trigger selection. The Muon stream contains events with the activity in the MS. The JetTauEtMiss stream is refers to events with the activity in the HAD calorimeters or large missing transverse energy. The CosmicCalo stream is with events when there were no collisions. There is also a debugging stream which stores events which could not be evaluated in time for the trigger system. The express express and the calibration streams are used for offline monitoring and detector

calibration. One event can be stored in multiple streams.

Large Computing Grid (LGC) [146] is a network of many computer clusters and is used for further processing and reprocessing of data from Tier0. The RAW data is transferred to Tier1 (set of 13 computer centres) when the LHC is not running. After reprocessing the data is stored at Tier2 (local computing systems). The Tier0 RAW data is in form of bytes collected in the different streams. In order to reduce the amount of information (size) data is processed in different formats. Event Summary Data (ESD) stores the whole detector level information transformed into object level information which are distributed to Tire1 centres (together with one additional copy of them). Analysis Object Data (AOD) are derived from ESD which contains only the information about certain physics objects needed for analysis, like electrons, muons, jets or photons. Derived Physics Data (DPD) are taken from AOD conversion after some event selection and reduction of event information. DPD is suitable for final physics analyses. DPD are transferred to Tire2 systems. The data used in this thesis is stored in D3PD format which is derived from DPD so that it can be easily accessed by standard tools (ROOT analysis framework [147]). In Run-2 a new data format procedure has been used, xAOD, modified AOD so that it can be accessed by ROOT framework.

ATLAS has implemented detailed detector simulation in order to understand detector effects in data. Athena [148] is the common ATLAS software framework which uses Geant4 [149] simulation toolkit [146]. The simulation procedure includes event generation and full simulation of the particle interactions produced in the collision with the detector components as well as of the electronics response of the detectors, followed by the same reconstruction algorithms used for collision data.

3 *Monte Carlo Event Generation, Detector Simulation and W-boson Reconstruction*

In order to interpret the data collected by the ATLAS detector a precise prediction of the detector output is necessary. The Monte Carlo (MC) programs are widely used in experimental and theoretical high energy physics to simulate events or to calculate total and differential cross section of a given physics process. A comparison of the experimental data with the MC simulation allows to test the predictions of the underlying theory, as well as to understand the measured data in order to calibrate the detector.

There are several steps in the simulation chain for the ATLAS experiment [146]: *event generation* using a MC generator for initial proton-proton collision and immediate decays, *simulation* of the ATLAS detector geometry and material properties, *digitisation* which converts the hits produced by the core simulation into detector response, and *reconstruction* of the objects in the detector. Both, the real data and the output of the simulation chain use the same ATLAS trigger and reconstruction software packages.

In this chapter an overview of the MC generators used to simulate the signal and background samples is presented. A summary of the modeling of the vector boson production and decay is also given, since achieving the best possible modeling of the physics processes is one of the key aspects of this analysis, and therefore several corrections to the MC predictions are presented. Then, the description of the object reconstruction is given. This chapter concludes with W-boson event reconstruction.

3.1 EVENT GENERATION

The generation of events using the MC programs covers all aspects of particle evolution described in Section 1.3.1. It starts with the simulation of the hard interaction, by calculating the parton level cross section $\hat{\sigma}$ at a fixed order in perturbation theory using incoming parton momenta taken from a chosen PDF set. Then, the parton shower algorithms are used to simulate the effect of soft and collinear radiation from partons leaving the hard interaction. This process gives rise to the transverse momentum of the hard interaction. The gluon radiation simulated in the parton shower is neglecting the spin interactions and interference effects, but this effects are calculated in the

matrix element of the hard interaction. The effects of loop diagrams can only be calculated with the matrix element, but these effects are less significant compared to the radiative effects implemented in the parton showering algorithms. The parton shower algorithms do not provide a good description of the processes with energetic partons, compared to the matrix element calculations. In order to obtain a good description for the hard interaction processes, the parton showers must be merged with fixed order calculations. The transition between the treatment of partons in the matrix element and in the parton shower is difficult to model and different MC generators have different approaches. The next step in the simulation chain is hadronisation of the remaining partons into colorless hadrons, which may then subsequently decay further. The phenomenological models designed to describe non-perturbative physical effects, such as UE which includes the additional activity coming from the proton remnants and multiple parton interactions, have to be tuned using experimental data.

Different MC event generators have different strategies in the event simulation. In the following, a brief description of the most commonly used MC programs in studies of the Z- and W-boson production at hadron colliders is given.

Pythia [150] is a general purpose LO event generator, consisting of all previously described elements. The simulation of the hard scattering is performed for the processes with two incoming and one or two outgoing partons. The hadronisation is done with a string model which describes the color dynamics between quarks and gluons in terms of strings. Pythia uses parton shower algorithm interfaced to matrix element calculation with a full spin correlations between initial and final states.

Herwig [151] is another general purpose LO event generator. The main difference compared to the Pythia is in the use of a different hadronisation algorithm referred to as cluster model based on the pre-confinement property of the shower. The UE is modeled via multiple parton interactions implemented in another program Jimmy [152], which is interfaced to Herwig.

Powheg (POsitive Weight Hardest Emission Generator) [153] is a NLO matrix element generator that does not depend on the subsequent shower MC program. Thus, it can be easily interfaced to either Pythia or Herwig for the parton shower step of the event generation.

MC@NLO [154] is another NLO matrix element generator, with electroweak diagrams calculated at LO. The higher order approximations of the parton shower and hadronisation are obtained using the Herwig generator.

FEWZ (Fully Exclusive W and Z Production) [155] is specialised MC program for calculation of the fully differential production of lepton pairs through the DY process in hadron collisions, with NNLO calculation of the strong coupling constant.

MCFM [156] is, like FEWZ, MC program for calculating predictions for DY processes with the inclusion of NNLO QCD corrections in the strong coupling constant. MCFM includes the decays of the unstable gauge bosons, for the production of Z, W and H boson, as well as HZ, HW and $\gamma\gamma$ in proton–proton collisions.

DYNNLO [157] is a parton-level MC program for calculating the cross section for vector boson production in proton–proton and proton–antiproton collisions, at NNLO level for QCD corrections. The calculation includes the $\gamma - Z$ interference, finite-width effects, the leptonic decay of the vector bosons and the corresponding spin correlations. The advantage of DYNNLO is that allows the user to apply arbitrary kinematical cuts on the final state leptons and the associated jet activity, and to compute the corresponding distributions in the form of binned histograms. DYNNLO explicitly decomposes the calculation of the cross section in the different pieces of the p_{T}-subtraction formalism, and allows the computation of statistically correlated PDF variations.

DYRES [158] is another MC program for calculation of the cross section for vector boson production in proton–proton and proton–antiproton collisions. It combines the calculation of the cross section up to NNLO with the resummation of the logarithmically-enhanced contributions at small transverse momenta up to NNLL in QCD perturbation theory. The program includes the $\gamma - Z$ interference, finite-width effects and the leptonic decay of the vector boson with the corresponding spin correlations. The calculation contains the full kinematics of the vector boson and of its decay products. Like DYNNLO, DYRES allows the user to apply arbitrary cuts on the final state kinematical variables, and to plot the corresponding distributions in the form of binned histograms.

ResBos [159, 160] is a MC program that generates predictions for differential spectra of p_{T} and rapidity of particles produced in proton–proton and proton–antiproton collisions. It is based on a resummed cross section which contains NLO perturbative contributions matched with a sum of large logarithmic terms.

MiNLO (Multi-scale improved NLO) [161] provides predictions of the factorisation and renormalisation scales in hadron collider processes with associated jet production, at NLO. It is used as an NLO extension of the matrix element reweighting procedure employed in LO matrix element parton shower merging algorithms.

Correct simulation of the photon FSR is of great importance for the measurement of the m_W, since it affects the p_{T}^{ℓ} distribution. Photos [162] is a MC program used for calculating QED multiple photon radiative corrections from external leptons in decays of particles and resonances. In order to simulate the effect of QED FSR, other generators are interfaced to Photos. For the Z- and W-boson production at LHC the precision of QED FSR effects with Photos is 0.2 %. Photos generates photon emissions starting from already generated events (with no QED radiations) and modifies the final state lepton kinematics accordingly. The emission of each photon is calculated according to the corresponding QED matrix element, the algorithm is applied iteratively, updating the available phase space after each emission and using the same perturbative accuracy for each iteration. The iteration ends when the photon energy is smaller than 10^7 times the energy of the parent, in the decay rest frame. Other programs that incorporate EW corrections are: Winhac [163] which is a MC event generator for DY processes in proton–proton, proton–antiproton and nucleus–nucleus collisions, with multi photon radiation correction in Z- and W-boson production processes at NLO in the perturbative expansion of the electromagnetic coupling constant

and SANC (Support for Analytic and Numeric Calculations for experiments at colliders) [164] which implements calculations of complete NLO QCD and EW corrections for the DY processes.

Multiple simultaneous interactions (pile-up) are modeled by overlaying independent minimum bias (inelastic) events on top of the hard-scatter event, accounting only for the in-time pile-up. Out-of-time pile-up is modeled in the same way, but there is an offset in time in the simulation to allow for an accurate model of the signal processing. The number of such collisions is modeled to match the pile-up level in data.

The MC generated events are the passed through a full simulation of the ATLAS detector geometry and material properties is based on the GEANT4 package, in order to simulate the interactions of particles as they propagate through the ATLAS detector [149]. The detector description includes maps of the magnetic field as well as measured misalignments of the tracking detectors. For all particles that are passing through the material, multiple scattering, energy loss and charge deposition in the detector material is calculated. In order to obtain a realistic behaviour of particles showering in the calorimeters, nuclear reactions are also simulated. The next step in the simulation is the digitisation, when the energy deposits and hits in the detector are converted into the voltages and currents, as in the detector.Then, the physics objects are reconstructed using identical algorithms for simulated and data events. The object reconstruction is described in Section 3.4.

3.2 EVENT SAMPLES

In this section, collision and simulated data samples which are used in this thesis are described.

3.2.1 *Collision data samples*

The W-boson mass measurement described in this thesis is based on proton-proton collision data recorded in 2011 at the centre of mass energy of $\sqrt{s} = 7$ TeV with the ATLAS detector at the LHC. After application of data quality requirements, ensuring that all detector parts are operational, including the ID, the calorimeters and the MS, as well as the magnet system is operating with nominal fields, the total integrated luminosity corresponds to 4.6 fb^{-1}. For the muon channel, smaller integrated luminosity is used 4.1 fb^{-1}, since a part of the data had to be discarded due to a timing problem in RPC which affected the muon trigger efficiency, leading to the loss of about 12% of the data. The relative uncertainty on the integrated luminosity is 1.8% [106].

The muon momentum studies described in Chapter 4 are based on proton-proton collision data recorded in 2011 and 2012 at the centre of mass energy of $\sqrt{s} = 7$ TeV and $\sqrt{s} = 8$ TeV, respectively. Application of data quality requirements, ensures

that all ID (pixel, SCT and TRT) and MS (MDT, CSC, RPC and TGC) parts are operational, as well as that the magnet system is operating with nominal fields. The total integrated luminosity corresponds to 4.6 fb^{-1} and 20.4 fb^{-1} for 2011 and 2012 datasets, respectively.

3.2.2 *Simulated data samples*

As a baseline for the Z- and W-boson production and decay in electron, muon and tau channels, the POWHEG MC samples are used. However, POWHEG is interfaced with PYTHIA 8 for modeling of the parton shower, hadronisaton and UE, with parameters set up according to the AZNLO tune [165]. The AZNLO tune is designed to describe the Z-boson p_{T} distribution by modeling parton shower parameters. The CT10 [166] PDF set is used for the hard scattering processes, and the CTEQ6LI [167] PDF set is used for the parton shower. The effect of QED FSR is simulated with PHOTOS. Decays of the tau leptons are handled by PYTHIA 8 taking into account polarisation effects. The masses of the Z- and W-bosons are set to $m_W = 80399$ MeV[1] and $m_Z = 91187$ MeV respectively for the nominal simulations. The top background samples are produced using MC@NLO generator interfaced with HERWIG and JIMMY. There is one sample for top quark pair production and several for single top quark production depending on the top quark decay into W boson and lighter quarks (b, s and d). Gauge boson pair production WW, WZ and ZZ is simulated with HERWIG. Only samples with semileptonic decays of top and boson pair production are used. Background samples of heavy flavour multijet events (with $\bar{b}b$ and $\bar{c}c$), were simulated with PYTHIA 8 in order to validate the data-driven methods used to estimate backgrounds with non-prompt leptons in the final state. For the signal samples of Z- and W-boson production and decay in electron and muon channels no filter is applied. For the simulated $W \to \tau\nu$ samples, the lepton filters at the generator level are applied requiring at least one electron or muon with $p_{\text{T}} > 20$ GeV and $|\eta| < 2.8$. Corresponding filtering efficiencies are $\approx 14.6\%$ for the W^+-boson and $\approx 12.7\%$ for the W^--boson sample. Similar filter is applied in the $Z \to \tau\tau$ sample leading to the efficiency of the applied filter of $\approx 26.3\%$. The pile-up is simulated with PYTHIA 8 using A2 tune [168].

Table 3.1 summarises used MC samples for the W-boson mass measurement with the respective cross sections, initial number of events and corresponding integrated luminosity of each sample. The W- and Z-boson samples are normalised according to their measured cross sections [169]. The $t\bar{t}$ samples are normalised to the measured cross section [170], while the single top samples are normalised according to a cross sections calculated using MC@NLO program. The gauge-boson pair production is normalised to the NLO predictions calculated with MCFM [171]. The total number of simulated events, i.e. signal and background, is normalised to the data, after the selection requirements, with subtracted multijet background which was estimated from a data-driven method.

[1]The world average value for the W-boson mass before 2012 was $m_W = 80399 \pm 23$ MeV, this value is used in the MC generators as a parameter.

Table 3.1: MC samples used in the W-boson mass measurement, with the respective cross sections, initial number of events and corresponding integrated luminosity of each sample.

Process	Generator	$\sigma \times BR$[pb]	N_{evt}	L_{int}[fb^{-1}]
Signal Samples				
$W^+ \to \mu^+\nu$	Powheg+Pythia8	6344.9	$9.544{\cdot}10^7$	15.042
$W^- \to \mu^-\nu$	Powheg+Pythia8	4376.5	$6.517{\cdot}10^7$	14.891
$W^+ \to e^+\nu$	Powheg+Pythia8	6344.9	$9.376{\cdot}10^7$	14.778
$W^- \to e^-\nu$	Powheg+Pythia8	4376.5	$6.592{\cdot}10^7$	15.062
Background Samples				
$W^+ \to \tau^+(e^+,\mu^+)\nu$	Powheg+Pythia8	930.04	$1.488{\cdot}10^7$	16.000
$W^- \to \tau^-(e^-,\mu^-)\nu$	Powheg+Pythia8	603.63	$9.990{\cdot}10^6$	16.550
$Z \to \mu^+\mu^-$	Powheg+Pythia8	990.3	$2.949{\cdot}10^7$	29.784
$Z \to e^+e^-$	Powheg+Pythia8	990.3	$2.952{\cdot}10^7$	29.808
$Z \to \tau^+\tau^-(e,\mu)$	Powheg+Pythia8	260.42	$5.871{\cdot}10^6$	22.543
WW	Herwig	20.86	$2.457{\cdot}10^6$	11.781
ZZ	Herwig	1.54	$2.478{\cdot}10^5$	160.883
WZ	Herwig	6.97	$9.920{\cdot}10^5$	142.332
$t\bar{t}$	MC@NLO	101.51	$1.146{\cdot}10^7$	112.950
$st\_tchan\_e\nu$	MC@NLO	6.83	$1.758{\cdot}10^5$	25.737
$st\_tchan\_\mu\nu$	MC@NLO	6.82	$1.755{\cdot}10^5$	25.731
$st\_tchan\_\tau\nu$	MC@NLO	6.81	$1.748{\cdot}10^5$	25.670
$st\_schan\_e\nu$	MC@NLO	0.46	$2.512{\cdot}10^5$	546.170
$st\_schan\_\mu\nu$	MC@NLO	0.46	$2.513{\cdot}10^5$	546.370
$st\_schan\_\tau\nu$	MC@NLO	0.46	$2.514{\cdot}10^5$	546.608
st_Wt	MC@NLO	14.37	$7.897{\cdot}10^5$	54.954

For the crosscheck of the hadronic recoil corrections described in Chapter 5 an alternative set of samples for Z- and W-boson production is used, so that for each Powheg+Pythia6 sample a corresponding Powheg+Herwig sample is used. The crosscheck samples are generated with Powheg interfaced to Herwig for the modelling of the parton shower and to Jimmy for the underlying event, as summarised in Table 3.2.

Table 3.2: MC samples used for the crosscheck of the hadronic recoil corrections, with number of analysed events for each sample.

Process	Generator	N_{evt}
$W^+ \to \mu^+\nu$	Powheg+Pythia6	$2.300 \cdot 10^7$
$W^- \to \mu^-\nu$	Powheg+Pythia6	$1.699 \cdot 10^7$
$Z \to \mu^+\mu^-$	Powheg+Pythia6	$1.998 \cdot 10^7$
$W^+ \to \mu^+\nu$	Powheg+Herwig	$1.593 \cdot 10^7$
$W^- \to \mu^-\nu$	Powheg+Herwig	$1.199 \cdot 10^7$
$Z \to \mu^+\mu^-$	Powheg+Herwig	$9.928 \cdot 10^6$

For the muon momentum studies described in Chapter 4, MC samples of muon decays from J/ψ and Z-boson are used, as summarised in Table 3.3. The FSR is not included in the J/ψ production. Photos generator is not included in the 2011

MC simulation of J/ψ, while built-in QED radiation that is switched on for the 2012 MC production is ineffective since PYTHIA 6 does not have a machinery for photon radiation in ordinary hadronic decays. As a consequence of the FSR convoluted with the detector resolution, position of the mass peak is shifted with respect to the world average value of J/ψ by amount of about 3 MeV toward lower values. For these samples the FSR was modeled by hand. More details about the MC samples used for muon momentum studies will be given in Chapter 4.

Table 3.3: MC samples used for the muon momentum studies, with number of analysed events for each sample.

Process	Generator	N_{evt}
$J/\psi \to \mu^+\mu^-$	PYTHIA6	$4.343 \cdot 10^7$
$Z \to \mu^+\mu^-$	POWHEG+PYTHIA6	$1.998 \cdot 10^7$
$J/\psi \to \mu^+\mu^-$	PYTHIA8	$6.630 \cdot 10^7$
$Z \to \mu^+\mu^-$	POWHEG+PYTHIA8	$2.996 \cdot 10^7$

3.3 MODELING OF THE Z- AND W-BOSON PRODUCTION AND DECAY

A detailed description of the physic modeling is beyond the scope of this thesis and can be found in [172] and [80].

The baseline POWHEG+PYTHIA 8 simulated samples are not describing the Z- and W-boson production and decay precisely enough for the measurement of the W-boson mass. The Z- and W-boson simulated samples are reweighted to include the effects of higher-order QCD and EW corrections, as well as the results of fits to the measured distributions. The correction procedure is based on the factorisation of the fully-differential leptonic DY cross section [60] into four terms:

$$\frac{\mathrm{d}\sigma}{\mathrm{d}p_1\,\mathrm{d}p_2} = \left[\frac{\mathrm{d}\sigma(m)}{\mathrm{d}m}\right]\left[\frac{\mathrm{d}\sigma(y)}{\mathrm{d}y}\right]\left[\frac{\mathrm{d}\sigma(p_\mathrm{T},y)}{\mathrm{d}p_\mathrm{T}\,\mathrm{d}y}\left(\frac{\mathrm{d}\sigma(y)}{\mathrm{d}y}\right)^{-1}\right] \left[(1+\cos^2\theta)+\sum_{i=0}^{7}A_i(p_\mathrm{T},y)P_i(\cos\theta,\phi)\right], \tag{3.1}$$

where p_1 and p_2 are the lepton and anti-lepton four-momenta; m, p_T, and y are the invariant mass, transverse momentum, and rapidity of the dilepton system; θ and ϕ are the polar angle and azimuth of the lepton in any given rest frame of the dilepton system; A_i are angular coefficients; and P_i are spherical harmonics of order zero, one and two. The first term represents the differential cross section as a function of the invariant mass. The second one is the differential cross section as a function of boson

rapidity. The third term corresponds to the boson transverse momentum at a given rapidity. And the forth term represents the angular coefficients, as shown in Equation 1.53. The W- and Z-boson resonances are parametrised according to Equation 1.47 with running-width Breit-Wigner function, which is consistent with the use of the world average value for the boson masses. The third term is modeled with PYTHIA 8 generator. The second and fourth term are modeled with perturbative QCD fixed-order predictions. After these corrections, there is an improved agreement of lepton kinematic distributions with the data.

Measurements of the Z- and W-boson production properties are used to validate and constrain the modelling of the fully-differential leptonic DY cross section. The modelling of the differential cross section as a function of boson rapidity, is validated by comparing to the W- and Z-boson rapidity measurements at $\sqrt{s} = 7$ TeV [169]. The QCD parameters of the parton shower model were determined by fits to the transverse-momentum distribution of the Z boson measured at 7 TeV [165]. The modelling of the angular coefficients is validated by comparing the theoretical predictions to the corresponding measurement using the high statistics $Z \to \ell\ell$ sample collected during 2012 data-taking at $\sqrt{s} = 8$ TeV [173].

3.3.1 *Electroweak corrections*

The baseline MC signal samples used in this analysis are POWHEG+PYTHIA8, which is a LO in the electroweak couplings, therefore the parameterisation of the W and Z resonances has to be corrected. The real photon emission corrections are applied with PHOTOS to the LO MC. Other sources of electroweak corrections, which consist of the interference between ISR and FSR QED corrections, pure weak corrections due to virtual-loop and box diagrams, and final-state emission of lepton pairs [80], are not included in the simulated sample, and their effects are considered as systematic uncertainties.

3.3.2 *Modeling of Z- and W-boson rapidity distribution*

At LO W and Z bosons are produced with zero transverse momentum, and the angular distribution of the decay leptons depends only on the polar angle of the lepton in the boson rest frame. The higher-order corrections give rise to sizeable boson transverse momentum, and to azimuthal asymmetries in the angular distribution of the decay leptons. For the calculation of the differential cross section as a function of boson rapidity and the angular coefficients as a function of the transverse momentum and rapidity of the boson, an optimised version of DYNNLO [157] is used. The rapidity distributions of the vector bosons, and the angular distributions of decay leptons, are reweighted such that they agree with the predictions from the NNLO, using the CT10NNLO PDF set [174].

The values of the angular coefficients predicted by the POWHEG+PYTHIA 8, differ significantly from the corresponding NNLO predictions. In particular, large differences are observed in the predictions of A_0 at low values of boson transverse momentum. Other coefficients, such as A_1 and A_2, are significantly affected by the NNLO corrections. For the Z-boson production, A_3 and A_4 are sensitive to the vector couplings between the Z boson and the fermions, and are predicted assuming the measured value of the effective weak-mixing angle [80].

3.3.3 *Modeling of Z- and W-boson transverse momentum distribution*

The higher-order corrections to the production of the W boson with low p_{T} (for $p_{\mathrm{T}} \ll m_W$) are dominated by multiple soft or almost collinear parton emissions. Contrary, in the events with high p_{T} (for $p_{\mathrm{T}} \gg m_W$) higher order corrections are dominated by emission of one or more hard partons and perturbative QCD is used for calculation of the differential cross section. In order to have a full theoretical picture and a consistent result for full boson p_{T} range the resummed cross section has to be matched with the perturbative QCD prediction.

The modelling of the transverse-momentum spectrum of vector bosons is based on the PYTHIA 8 parton shower MC generator. The predictions of vector-boson production in the PYTHIA 8 MC generator employ LO matrix elements for the $q\bar{q}' \to W, Z$ processes and include a reweighting of the first parton shower emission to the LO V+jet cross section. The resulting prediction of the boson p_{T} spectrum is comparable in accuracy to those of a NLO plus parton shower generator setup such as POWHEG+PYTHIA 8, and of resummed predictions at NLL order [80].

The values of the QCD parameters used in PYTHIA 8 were determined from fits to the Z-boson transverse momentum distribution measured with the ATLAS detector at a centre-of-mass energy of $\sqrt{s} = 7$ TeV [165]. The resulting values of the PYTHIA 8 parameters constitute the AZ tune, and are used to predict the $p_{\mathrm{T}}^{\mathrm{W}}$ spectrum. In order to validate the results of the AZ tune, the predicted differential cross section W-to-Z ratio is compared to the corresponding ratio of the ATLAS measurements of vector-boson transverse momentum [165, 175]. The comparison is shown in Figure 3.1 where kinematic requirements on the decay leptons are applied according to the experimental acceptance. The measured Z-boson p_{T} distribution is rebinned to match the coarser bins of the W-boson p_{T} distribution, which was measured using only 30 pb^{-1} of data. The theoretical prediction is in agreement with the experimental measurements for the region with $p_{\mathrm{T}}^{\mathrm{V}} < 30$ GeV, which is relevant for the measurement of the W-boson mass.

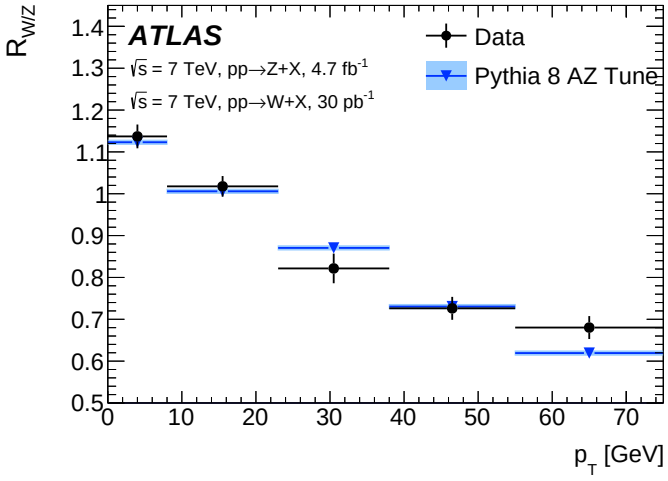

Figure 3.1: The ratio of the differential cross sections $R_{W/Z}(p_{\mathrm{T}})$ as a function of the boson p_{T} [165, 175]. The measured cross sections are compared to the predictions of the Pythia 8 AZ tune. The error bars show the total experimental uncertainties. The plot is taken from [80].

Reweighting procedure

The described physics model is applied to the Powheg+Pythia 8 simulated samples through an event-by-event reweighting. The reweighting procedure is performed in several steps. First the rapidity distribution is reweighted according to the NNLO QCD predictions evaluated with DYNNLO [157]. Then, at a given boson rapidity, the vector boson transverse momentum shape is reweighted to the Pythia 8 prediction with the AZ tune. This procedure provides the transverse momentum distribution of vector bosons predicted by Pythia 8, preserving the rapidity distribution at NNLO. Finally, the angular variables are reweighted according to:

$$w = \frac{1 + \cos^2\theta + \sum A'_i P_i(\cos\theta\phi)}{1 + \cos^2\theta + \sum A_i P_i(\cos\theta\phi)} \tag{3.2}$$

where A_i are angular coefficients of the nominal Powheg+Pythia 8 samples, while A'_i are the angular coefficients evaluated at $\mathcal{O}(\alpha_2^2)$.

The resulting theoretical prediction is tested by comparing the predicted differential cross section as a function of Z-boson rapidity, and W-boson differential cross section as a function of lepton pseudorapidity, to the corresponding ATLAS measurement, as shown in Figure 3.2, which also includes the experimental uncertainties and the PDF uncertainties of the CT10NNLO PDF set. A very good agreement between experimental measurements and theoretical predictions is observed. A χ^2 compatibility test is performed for the three distributions simultaneously, including the correlation between uncertainties. The compatibility test yields a χ^2/dof value of 45/34.

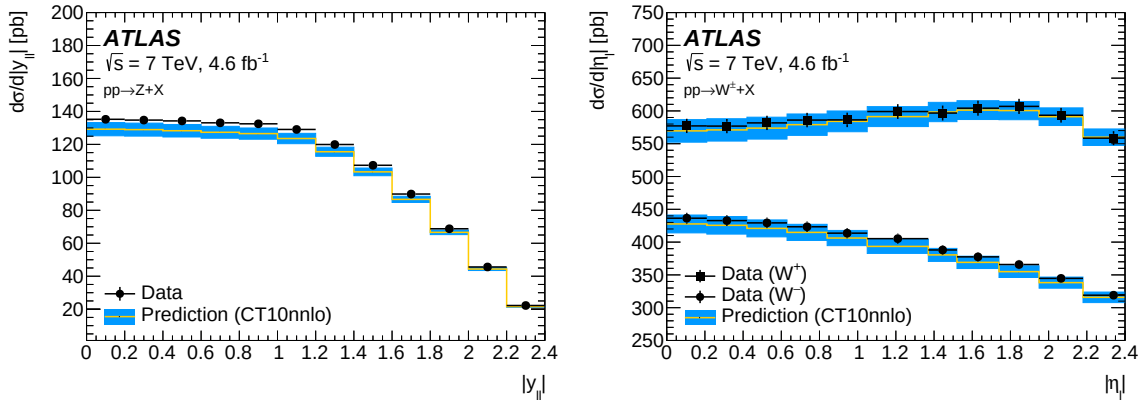

(a) **(b)**

Figure 3.2: (a) Differential Z-boson cross section as a function of boson rapidity, and (b) differential W^+ and W^- cross sections as a function of charged decay-lepton pseudorapidity at $\sqrt{s} = 7$ TeV [169]. The measured cross sections are compared to the POWHEG+PYTHIA 8 predictions, corrected to NNLO using DYNNLO with the CT10NNLO PDF set. The error bars show the total experimental uncertainties, including luminosity uncertainty, and the bands show the PDF uncertainties of the predictions [80].

3.4 OBJECT RECONSTRUCTION AND IDENTIFICATION

The reconstruction and identification of each object is achieved by combining the information from several sub-detectors. The ATLAS reconstruction software uses information about particle trajectories and momenta from the ID and the MS, and energy deposited in the calorimeters in order to build a physics object corresponding to a particle. Good identification and reconstruction performance is crucial for the measurement of the W-boson mass. The W-boson candidates are selected as events with at least one electron or muon candidate and large missing transverse energy, as illustrated in Figure 3.3 in Section 3.5. This section describes the techniques used to define, reconstruct and identify the objects used in the thesis.

Track and vertex reconstruction

Tracks produced by the charged particles traversing the ATLAS detector are reconstructed using a series of algorithms based on hits in the ID [176, 177]. There are two complementary inside-out and outside-in pattern recognition algorithms for track reconstruction. The final track candidates are required to fulfill a set of quality criteria based on the number of hits in the ID as well as longitudinal impact parameter (z_0) and transverse impact parameter (d_0). The impact parameters are determined with respect to the nominal beam-line.

The correct determination of the primary vertex of the proton–proton interaction, i.e. the place where the hard scattering occurred, is extremely important in high pile-up conditions [176]. Primary vertices are reconstructed employing an iterative vertex finding algorithm where vertex seeds are calculated from the z position at the beam line of the various reconstructed tracks. In order to remove fake instances, each track carries a weight measuring its compatibility with the fitted vertex based on a χ^2 fit. When a track is displaced more than 7σ from its vertex, it is assigned to another vertex. Secondary vertices arise from other processes like hadron decays or photon conversions.

Electron reconstruction and identification

Electrons are identified using the information from the ID and the EM calorimeter [77]. The energy of the electron candidate is taken from the clusters of energy deposited in the EM calorimeter, while the charge and momentum direction of the electron are derived from the associated track. In the case that the track is reconstructed from a low number of hits in the high precision ID modules, the direction is determined by the position of the barycentre of the calibrated EM cluster. When the trajectory of a track in the ID is matched to the position of a cluster in the calorimeter, a reconstructed electron candidate is found. Then, the electron clusters are rebuild, using 3×7 in the barrel and 5×5 in the end-caps EM calorimeter cells, within the acceptance of the ID. In order to compute the tower energy, the energy of the cells in all longitudinal layers is summed. The reconstruction algorithm searches clusters of longitudinal towers with total energy above 2.5 GeV, then larger cluster windows are formed.

When the reconstructed candidate electron is found, an identification criteria is applied in order to suppress backgrounds from sources like misidentified hadronic jets, prompt photons and photon conversions, as well as electrons from hadron decays. The identification criteria relies on the shape of electromagnetic shower in the calorimeter as well as on tracking and track-to-cluster matching quantities. The identification can be based either on independent cuts on these quantities or on a single cut on the output of a likelihood function taking as inputs these quantities. Three reference sets of cuts have been defined with increasing background rejection power: loose, medium and tight [77]. The loose selection criteria provides excellent identification efficiency, but low background rejection. The medium selection improves the background rejection by 3-4 times, but also reduces the identification efficiency by 10%. The tight selection uses all of the particle identification tools available for electrons and requires the largest possible rejection of non-isolated electrons. For the tight selection, additional cuts are applied on the number of TRT hits, the ratio of the EM cluster energy to the track momentum, and also there is a veto on reconstructed photon conversion vertices which are associated with the cluster. The tight selection reduces the efficiency to 80% for Z-boson events. These criteria were re-optimised at the end of Run-1 to the plus-plus menu, i.e. loose^{++}, medium^{++} and tight^{++}, which are defined with improved performance over the standard ones for a higher pile-up environment.

A multivariate regression algorithm, developed and optimised on simulated events, is used to calibrate the energy reconstruction [78]. The reconstructed electron energy is corrected to account for the energy deposited in front of the calorimeter and outside the cluster, as well as for variations of the energy response as a function of the impact point of the electromagnetic shower in the calorimeter. The energy calibration algorithm takes as inputs the energy collected by each calorimeter layer, including the presampler, the pseudorapidity of the cluster, and the local position of the shower within the cell of the second layer, which corresponds to the cluster centroid. For the W-boson mass measurement additional calibration is needed, which is based on Z-boson events and depends on electron η and φ, as explained in Section 6.1.1. More details can be found in [178] and [80].

For the W-boson mass measurement, electron candidates are required to have $p_{\mathrm{T}} > 15$ GeV and $|\eta| < 2.4$ and to fulfill a set of tight^{++} identification requirements [77]. The pseudorapidity range $1.2 < |\eta| < 1.82$ is excluded from the measurement, since the amount of passive material in front of the calorimeter and its uncertainty is largest in this region [78]. In this way an inaccurate description of the non-Gaussian tails in the electron energy response is prevented. Additional isolation requirements, applied on the nearby activity in the ID and the calorimeter, are imposed to improve the background rejection. These isolation requirements are implemented by requiring small scalar sum of the p_{T} of tracks in a cone of $\Delta R < 0.4$ around the electron ($p_{\mathrm{T}}^{\mathrm{cone40}}$) and small transverse energy deposited in the calorimeter within $\Delta R < 0.2$ around the electron ($E_{\mathrm{T}}^{\mathrm{cone20}}$). The contribution from the electron candidate itself is excluded. The specific criteria are optimised as a function of electron p_{T} and η, maintaining a uniform isolation efficiency of 97% for track- and 98% for calorimeter-based variables across a wide range of p_{T} and η. In general, these requirements vary in the range from 2.0 to 3.0 GeV for $p_{\mathrm{T}}^{\mathrm{cone40}}$, and from 2.5 to 4.5 GeV for $E_{\mathrm{T}}^{\mathrm{cone20}}$.

Muon reconstruction and identification

Muon reconstruction and its performance will be discussed in detail in Chapter 4. Here some information relevant for the W-bososn mass measurements are given. Muons are reconstructed and identified using the information from the ID and the MS, accompanied by small energy deposits in the calorimeters along their trajectory. A combined muon candidate is formed from a combination of a MS track with an ID track, based on the statistical combination of the track parameters, so called STACO algorithm [179]. For the purpose of the W-boson mass measurement kinematics properties (p_{T}, η and θ) of the muon candidates are defined using only track parameters measured by the ID. This allows a simpler calibration procedure, ignoring muon energy loss in the calorimeters and momentum measurement of the tracks reconstructed in the MS. The downside of this choice is a loss of precision in the measurement of the W-boson mass due to degradation of the muon momentum resolution especially in the region $|\eta| > 2.0$ which is not covered by the TRT [98]. This loss of precision is however negligible for the overall result.

The ID tracks associated with the muons must satisfy quality requirements on the number of hits recorded by each sub-detector [79]:

- expected b-layer hit:
  $N_{\text{pixel}} \geq 1$,

where N_{pixel} is the number of pixel hits,

- expected pixel hits:
  $N_{\text{pixel}} + N_{\text{dead pixel sensors}} > 1$

where $N_{\text{dead pixel sensors}}$ is the number of crossed dead pixel sensors,

- expected SCT hits:
  $N_{\text{SCT}} + N_{\text{dead SCT sensors}} > 5$

where N_{SCT} is the number of SCT hits and $N_{\text{dead SCT sensors}}$ is the number of crossed dead SCT sensors,

- ID Si holes:
  $N_{\text{pixel holes}} + N_{\text{SCT holes}} < 3$,

where $N_{\text{pixel holes}}$ and $N_{\text{SCT holes}}$ are number of pixel and SCT holes, respectively,

- TRT quality cuts:
  for $|\eta| < 1.9$: $N_{\text{TRT}} + N_{\text{TRT outliers}} > 5$ and $\frac{N_{\text{TRT outliers}}}{N_{\text{TRT}}+N_{\text{TRT outliers}}} < 0.9$,
  for $|\eta| \geq 1.9$: $N_{\text{TRT}} + N_{\text{TRT outliers}} > 5$ if $\frac{N_{\text{TRT outliers}}}{N_{\text{TRT}}+N_{\text{TRT outliers}}} < 0.9$,

where N_{TRT} is the number of TRT hits on the muon track and $N_{\text{TRT outliers}}$ is the number of TRT outliers on the muon track.

In addition, muon candidates are required to have a longitudinal impact parameter $|z_0| < 10$ mm, in order to reduce muons arising from cosmic and other non-collision backgrounds. Muon candidates are required to have $p_{\text{T}} > 20$ GeV and $|\eta| < 2.4$. The rejection of multijet background is increased by applying an isolation requirement: the scalar sum of the p_{T} of tracks in the ID in a cone of $\Delta R < 0.2$ around the muon candidate is required to be less than 10% of the muon p_{T}, where the track are required to have $p_{\text{T}} > 1$ GeV and originate from the primary vertex.

Jet reconstruction and identification

Topological clusters [180], i.e. topo-clusters, formed by hadronic deposits, are extracted in the hadronic calorimeter using neighbouring cells with significant energy deposit over the noise. A topological cluster starts with a calorimeter cell for which the signal-to-noise ratio exceeds four, where the noise is the typical ambient energy flux. From this starting cell additional cells are added iteratively if they have a signal-to-noise ratio of at least two. Then reconstructed topological clusters are fed into a jet clustering algorithm which creates the actual jet physics objects.

Jet reconstruction represents characterising of the stream of particles as a whole by identifying jet candidates, instead of measuring the kinematic properties of each individual particle [181]. Since the stream consists mostly of neutral and charged hadrons, jets are characterised by focused energy deposits in the calorimeter system with a significant fraction in the hadronic calorimeter in conjunction with many nearby tracks. In ATLAS, jets are reconstructed with the anti-k_T algorithm [181] with a distance parameter $\Delta R = 0.4$ or 0.6.

Missing transverse energy reconstruction

Missing transverse energy is defined as the momentum imbalance in the plane transverse to the beam axis. Standard approach developed in the ATLAS experiment is an object-based one. The reconstruction of the missing transverse energy allows to benefit from optimised energy calibration schemes for different particle types which is leading to a better resolution [182]. The energies are mostly determined from calorimeter measurements, except for muons. To avoid using calorimeter energy deposits multiple times, the algorithm assigns energy to deposits to a single object according to a strict order: electrons are identified first, followed by photons, hadronically decaying τ leptons, jets, and muons. Finally, topological clusters and tracks not assigned to physics objects are included in the calculation as the so-called soft term. The missing transverse energy is given by its x and y components:

$$E_{x(y)}^{\text{miss}} = -\left(E_{x(y)}^{e} + E_{x(y)}^{\gamma} + E_{x(y)}^{\tau} + E_{x(y)}^{\mu} + E_{x(y)}^{\text{jets}} + E_{x(y)}^{\text{soft}}\right), \tag{3.3}$$

where each term represents the total momentum of the reconstructed objects in the x or y directions. The measured $E_{\text{T}}^{\text{miss}}$ receives contributions from sources besides invisible particles, including calorimeter noise, particles falling in insensitive regions of the detector, energy miss-measurements, and pile-up interactions. Particles falling outside the detector acceptance contribute irreducibly to the $E_{\text{T}}^{\text{miss}}$ resolution. For physics objects like electrons or jets, the noise and pile-up contributions are suppressed by the reconstruction algorithms and identification cuts. To reduce the noise and pile-up contributions to the soft term, the cells are grouped into topological clusters. In order to calibrate $E_{\text{T}}^{\text{miss}}$, all involved physics objects have to be calibrated independently. Therefore, the calibration of this quantity is relatively complicated, as the individual uncertainties have to be treated in a coherent way.

Missing transverse energy based on hadronic recoil is derived quantity from *hadronic recoil* which is used for the m_W measurement. The hadronic recoil $\vec{u}_{\text{T}}$ in the transverse plane is reconstructed from the vector sum of the transverse energy of all topo-clusters[2] reconstructed in the calorimeters $\vec{E}_{\text{T}}^{\,\text{cluster}}$, excluding energy deposits associated to the decay leptons (electrons and muons):

$$\vec{u}_{\text{T}} = \sum \vec{E}_{\text{T}}^{\,\text{cluster}}. \tag{3.4}$$

The transverse energy vector of a cluster has a magnitude $E_{\text{T}} = E/\cosh\eta$ with E being the energy deposit of the cluster and η its pseudorapidity. The azimuth φ of the transverse energy vector is defined from the coordinates of the cluster in the transverse plane. For Z- and W-boson events, $-\vec{u}_{\text{T}}$ provides an estimate of the boson transverse momentum. The parallel projection of the recoil $u_{\parallel}^{Z}$ onto the Z-boson transverse momentum reconstructed from the decay lepton pair $\vec{p}_{\text{T}}^{\,\ell\ell}$ can be compared to the $-\vec{p}_{\text{T}}^{\,\ell\ell}$ and probes the detector response to the recoil in terms of linearity and resolution, while the perpendicular projection $u_{\perp}^{Z}$ satisfies $< u_{\perp}^{Z} >= 0$ and its width provides an estimate of the recoil resolution. For W-boson events, the parallel and perpendicular

[2]Different definitions of the hadronic recoil will be discussed in Section 5.3.

projections are defined onto the axes parallel and perpendicular to the reconstructed charged lepton transverse momentum. The magnitude and direction of the transverse momentum vector of the decay neutrino $\vec{p}_{\mathrm{T}}^{\,\nu}$, are inferred from the vector of the missing transverse energy $\vec{E}_{\mathrm{T}}^{\,\mathrm{miss}}$, which corresponds to the momentum imbalance in the transverse plane and is defined as:

$$\vec{E}_{\mathrm{T}}^{\,\mathrm{miss}} = -\left(\sum_{i=1}^{N} \vec{p}_{\mathrm{T},\,i}^{\,\ell} + \vec{u}_{\mathrm{T}}\right), \tag{3.5}$$

where $N = 1$ for W-boson events and $N = 2$ for Z-boson events. This definition of $E_{\mathrm{T}}^{\mathrm{miss}}$ does not involve the explicit reconstruction of particles and jets, thus it avoids possible threshold effects. The recoil based definition of $E_{\mathrm{T}}^{\mathrm{miss}}$ is applicable only for Z- and W-boson events, allowing straightforward and precise calibration for the W-boson mass measurement. Detailed description of the hadronic recoil, its performance and calibration, is given in Chapter 5.

3.5 W-BOSON EVENT SELECTION

The W-boson candidates are required to have at least one electron or muon candidate and a large missing transverse energy, as illustrated in Figure 3.3.

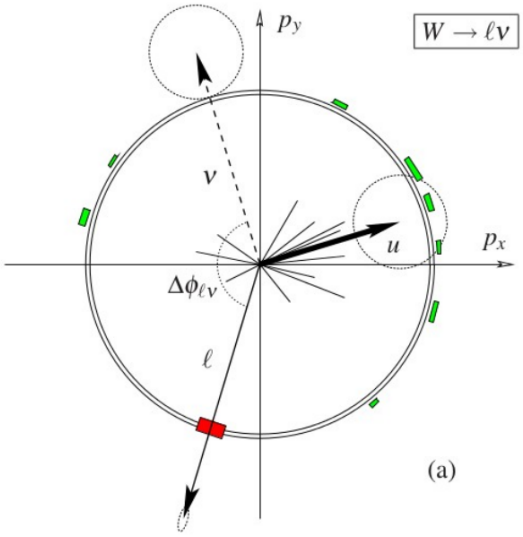

Figure 3.3: The transverse view of a W-boson candidate with the electron or the muon candidate denoted as ℓ, the neutrino ν and the hadronic recoil u_{T}. The circles around the objects represent the energy deposited in the calorimeters.

The candidates are selected by applying set of selection requirements on the event variables, these cuts are applied in sequence, one given cut is applied to the events passing the one immediately before. In the following, each step of the selection is described and a summary of the selection requirements for the W-boson candidates is given in Table 3.4.

First, for data, events has to pass the GRL requirement, as explained in Section 3.2. Then, the W-boson candidates are selected with triggers requiring at least one muon candidate with transverse momentum larger than 18 GeV or at least one electron candidate with transverse energy larger than 20 GeV. The transverse energy requirement for the electron candidate was raised to 22 GeV in later data taking periods because of the increased instantaneous luminosity delivered by the LHC. In order to suppress cosmic events and events from non-collision background, only events with a reconstructed primary vertex with at least three associated tracks with $p_{\mathrm{T}} > 500$ MeV are selected. The electron and muon candidates are selected following requirements described in Section 3.4. In addition, selection is requiring exactly one reconstructed electron or muon with $p_{\mathrm{T}}^{\ell} > 30$ GeV. Then, the lepton candidates are matched to the trigger object, so called trigger matching, and only events with $\Delta R < 0.2$ between the two objects are considered. Trigger matching is necessary in order to have reliable estimation of the trigger efficiency. Problems in the calorimeter can lead to energy miss-measurements affecting the hadronic recoil reconstruction. These spurious events are vetoed using standard *cleaning cuts*. The standard procedure for jet cleaning is applied, in order to reject events with fake jets. During one part of the 2011 data-taking, the LAr calorimeter suffered from six dead front end boards, which affected about 20% of the data, so this was incorporated in the simulation. The part of the LAr calorimeter with problems is localised in the region $0 < \eta < 1.475$ and $-0.9 < \varphi < -0.5$, and is referred as LAr hole [77]. This cut is vetoing events if a jet falls inside the LAr hole. In order to reduce the multijet background contribution, and to minimise model uncertainties from W bosons produced at high transverse momentum, the W-boson selection is constricted by three additional requirements: $u_{\mathrm{T}} < 30$ GeV, $E_{\mathrm{T}}^{\mathrm{miss}} > 30$ GeV and $m_{\mathrm{T}} > 60$ GeV. The selection requirements on p_{T}^{ℓ}, m_{T} and $E_{\mathrm{T}}^{\mathrm{miss}}$ illustrate a standard set of kinematical cuts for W-boson selection [169, 175, 183–185]. For the m_W measurement, tighter cuts are imposed with respect to the standard ones: $p_{\mathrm{T}}^{\ell} > 25$ GeV, $E_{\mathrm{T}}^{\mathrm{miss}} > 25$ GeV and $m_{\mathrm{T}} > 40$ GeV, with the purpose to increase suppression of the multijet background. The upper cut on u_{T} also sharpens the Jacobian peak of the p_{T}^{ℓ} and m_{T} distributions.

After all selection criteria applied there is 5.89 and 7.84 million W-boson candidates in electron and muon channel respectively.

Table 3.4: The summary of the W-boson selection requirements.

Cut	$W \to e\nu$	$W \to \mu\nu$
GRL	GRL	
Event selection	primary vertex with at least 3 tracks	
Trigger	one electron $E_{\mathrm{T}} > 20/22$ GeV	one muon $p_{\mathrm{T}} > 18$ GeV
Event cleaning	jet cleaning, LAr veto	
Lepton selection	tight++	combined, ID kinematics, $\lvert z_0\rvert < 10$ mm
	$\lvert\eta\rvert < 1.2$ and $1.8 < \lvert\eta\rvert < 2.4$	$\lvert\eta\rvert < 2.4$
	$p_{\mathrm{T}}^{\ell} > 30$ GeV	
Lepton isolation	$p_{\mathrm{T}}^{\mathrm{cone40}}/p_{\mathrm{T}}$ and $E_{\mathrm{T}}^{\mathrm{cone20}}/E_{\mathrm{T}}$	$p_{\mathrm{T}}^{\mathrm{cone20}}/p_{\mathrm{T}} < 0.1$
W-boson selection	$u_{\mathrm{T}} < 30$ GeV	
	$m_{\mathrm{T}} > 60$ GeV	
	$E_{\mathrm{T}}^{\mathrm{miss}} > 30$ GeV	

4 *Muon Momentum Calibration*

The ATLAS muon system is designed to precisely measure the momentum of muons in an energy range from a few GeV to the TeV scale, as discussed in Chapter 2. Muons pass through the detector, leaving tracks in ID and MS and some minimal amount of energy, typically 3 GeV, in the calorimeters. The MS is designed to provide muon momentum measurement with a relative resolution better than 3% over a wide p_{T} range and up to 10% at $p_{\mathrm{T}} \approx 1$ TeV [76].

Muons play a key role to some of the most important physics results published by the ATLAS experiment. Some of these results are the discovery of the Higgs boson, precise measurement of the W-boson mass and searches for physics beyond SM with muons in final states. Thus, by improving the measurement of muon momentum, one improves measurement of particles that decay into muons.

In this chapter an overview of the calibration of the muon momentum scale and resolution with the ATLAS detector during Run-1 is given. In the first section, the muon reconstruction is introduced. Then, the description of the muon energy loss in the calorimeters is given. Following section explains the muon momentum studies with the J/ψ events, where the detailed description is presented in [186]. Next, the description of the muon momentum scale and resolution corrections is given, which is based on the [187] and [79]. This chapter concludes with an overview of the muon momentum uncertainties for the Higgs boson mass measurement [188], given in [189].

4.1 MUON RECONSTRUCTION AT ATLAS IN RUN-1

Muons are reconstructed independently in the ID and MS. The muon momentum is measured from the curvature of the track in the magnetic field. The inverse momentum P of the muon is proportional to the track curvature (sagitta) s:

$$\frac{1}{P} = \frac{8s}{BL^2}, \tag{4.1}$$

where B is the magnetic field and L is the length of the straight line connecting the two outer segments, as illustrated in Figure 4.1. The sagitta for a 1 TeV muon is approximately 500 μm. Thus, in order to achieve designed transverse momentum relative resolution of 10 % for a 1 TeV muon, the sagitta must be known with an accuracy of 50 μm.

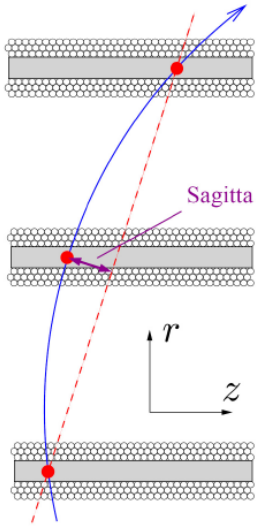

Figure 4.1: Illustration of the muon momentum measurement, using three chambers of the MDT [135].

In the MS, muon reconstruction starts with a search for regions of activity (ROA), defined as a 0.4×0.4 regions in $\Delta\eta \times \Delta\varphi$ with at least one RPC or TGC hit. Then, pattern recognitions algorithms, based on Hough transforms [135], search for hits aligned on a trajectory in the bending plane of the detector in each MDT and near trigger chambers. The MDT segments are composed of hit patterns, defined from straight-line fit to the hits found in each layer. The muon coordinates in the plane orthogonal to the bending plane are measured from RPC or TGC hits. The CSC segments are reconstructed from separate hit search in the η and φ detector planes. The muon track candidates are defined by performing a fits to all hits from segments in different layers. The combination of segments starts from the segments generated in the middle layers of the detector where more trigger hits are available, then, the segments from the outer and inner layers are used. Selection of segments is based on hit multiplicity and fit quality. The matching of segments is defined from its relative position and angles. Every time when a reasonable match is found, the segment is added to the track candidate. At least two matching segments are required to build a track, except in the barrel-endcap transition region where a single high-quality segment with η and φ information can be used to build a track. One segment can be used to build several track candidates. Then, a global χ^2 fit is performed to the hits associated with each track candidate. The track candidates are sorted by quality according to the number of hits and the smallest χ^2/NDF. If hits are shared among track candidates, they are assigned to the track with the highest ranking. Also, hits with large contributions to the χ^2 are removed. Then, the track fit is repeated, if additional hits along the track are found. If the refit fails, the track candidate is dropped. In the last step, the track candidates are extrapolated back to the interaction point while taking into account the geometrical description of the material along the track as well as and the magnetic field inhomogeneities. The reconstruction of tracks in the MS is affected by acceptance losses in two regions: at $\eta \sim 0$, where the MS is only partially equipped with muon chambers in order to provide space for the services for the ID and the calorimeters, and

in the region between the barrel and the positive η end-cap $1.1 < |\eta| < 1.3$, where there are regions in azimuth with only one layer of chambers, since some of the chambers were not yet installed [79]. During the extended shutdown between Run-1 and Run-2 the missing chambers were finally installed.

The reconstruction of tracks in the MS is biased by several effects: (i) muon energy loss in the material in front of the MS, (ii) multiple scattering and energy loss inside the MS, in particular in the coils and in the structure of the toroid magnets, (iii) the alignment of the muon chambers, (iv) the intrinsic resolution of the MDT and CSC. An imperfect knowledge of the magnetic field map may also bias the muon reconstruction since it is to used to convert a measured track curvature to a particle momentum. The muon momentum resolution in MS can be parametrised as quadratic sum of three terms:

$$\frac{\sigma(p_{\mathrm{T}})}{p_{\mathrm{T}}} = \frac{a}{p_{\mathrm{T}}} \oplus b \oplus c\ p_{\mathrm{T}}, \tag{4.2}$$

where a refers to the fluctuations of the muon energy loss in the traversed material, b describes the multiple scattering effect along the muon trajectory and c accounts for the intrinsic resolution of the muon chambers caused by the spatial resolution of the detector components and by any residual misalignment. The contribution of these effects to the designed momentum resolution as a function of the muon transverse momentum is shown in Figure 4.2. For muon tracks in MS with a transverse momenta

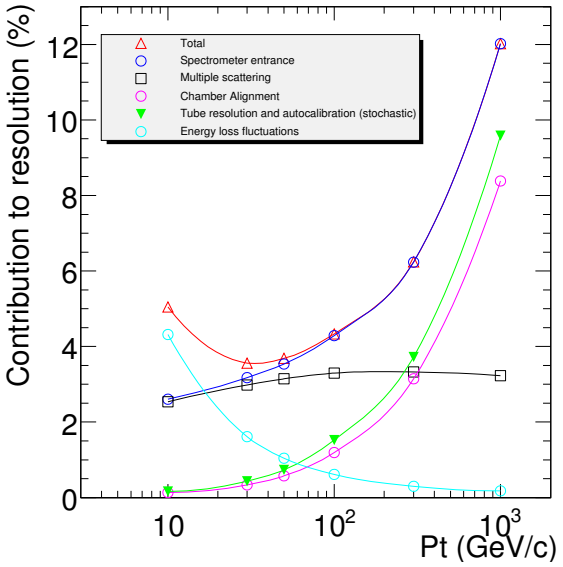

Figure 4.2: Contributions to the designed momentum resolution for muons reconstructed in the MS as a function of transverse momentum for $|\eta| < 1.5$. The alignment curve is for an uncertainty of 30 μm in the chamber positions. [76].

less than 20 GeV energy loss fluctuations in the calorimeters contribute dominantly to the momentum resolution. For muons with transverse momenta in the range between 20 GeV and 200 GeV, the multiple scattering dominates the resolution. And, for very high transverse momentum muons over 200 GeV, the resolution is dominated by the intrinsic MDT tube resolution and chamber alignment.

Muons in the ID are reconstructed as tracks, as explained in Section 3.4. The main track reconstruction algorithm (inside-out) in the ID starts from finding hits in the pixel and SCT, and then the track candidate is extended to TRT. Similarly as in MS, a track is defined from χ^2 fit to the hits in different parts of the ID. In order to indicate that a track candidate originated from a real particle, the tracks are ranked by number of hits and goodness of χ^2 fit. Holes are defined when a track passes through a detector element without producing a hit, and number of holes lowers the track rank. Hits that are shared among tracks are assigned to the one with the highest rank and removed from others. Finally, the track is refitted taking into account the effects coming from the dead material. On average, a track in the ID has 3 pixel hits, 8 hits in the SCT and 30 TRT hits. In the ID the muon momentum resolution can be parametrised by Equation 4.2 with the parameter a set to zero, the parameter b representing the multiple scattering contribution. The parameter c describes the intrinsic resolution caused by the imperfect knowledge of the magnetic field in the ID, by the spatial resolution of the detector components, and by any residual misalignment of the detector components, for $|\eta| > 2$ the parametrisation of the last term is given by $c\,p_{\mathrm{T}}/\tan^2\theta$ [76].

The muon track is characterised in terms of five parameters: transverse and longitudinal impact parameters d_0 and z_0, the polar and azimuthal angles θ and φ and the ratio of the charge to the track momentum q/P. Thus, the track is defined with a vector $\mathbf{P}^T = (d_0, z_0, \varphi, \theta, q/P)$.

In order to provide the best possible muon reconstruction performance, the information about muon tracks provided by the ID, MS, and calorimeters is combined. Four muon types are defined depending on which sub-detectors are used in the reconstruction [79], as illustrated in Figure 4.3:

- Stand-Alone (SA) muons: track is reconstructed only in the MS, without a matching track in the ID. The trajectory is extrapolated back from the MS to the interaction point, while taking into account energy loss in the calorimeters. SA muons are mainly used to extend the acceptance to the range $2.5 < |\eta| < 2.7$ which is not covered by the ID. In general, muon is should cross at least two layers of MS chambers to provide a track measurement. However, for the forward region and in order to increase the purity of the tracks, hits are required in all three layers of the MS.
- Combined (CB) muons: track reconstruction is performed independently in the ID and MS, and a combined track is defined from a successful combination of a MS track with an ID track:

$$\chi^2_{\mathrm{match}} = (\mathbf{P}_{\mathrm{MS}} - \mathbf{P}_{\mathrm{ID}})^T(\mathbf{C}_{\mathrm{MS}} + \mathbf{C}_{\mathrm{ID}})^{-1}(\mathbf{P}_{\mathrm{MS}} - \mathbf{P}_{\mathrm{ID}}), \tag{4.3}$$

  where $\mathbf{P}$ is the vector of the five track parameters in ID and MS, and $\mathbf{C}$ is the covariance matrix in the ID and MS which contains the covariances on the track parameters. This is the main type of reconstructed muons, resulting in higher accuracy of the estimate of the muon candidate kinematics. CB muon candidates have the highest muon purity.
- Segment-tagged (ST) muons: a track in the ID is associated to at least one track segment in the MDT or CSC chambers. ST muons are used to increase the

acceptance in cases in where muon crossed only one layer of MS chambers, either because of its low p_{T} or because it falls in regions with reduced MS acceptance.

- Calorimeter-tagged (CT) muons: a track in the ID is matched to a calorimeter energy deposit corresponding to a minimum ionizing particle. CT muons have the lowest purity of all muon types, but they are used for recovering acceptance in the regions where the MS lacks instrumentation due to the presence of ID and calorimeter services. Therefore, the identification criteria for CT muons is optimised for region $|\eta| < 0.1$ and transverse momentum range 25 GeV $< p_{\mathrm{T}} <$ 100 GeV.

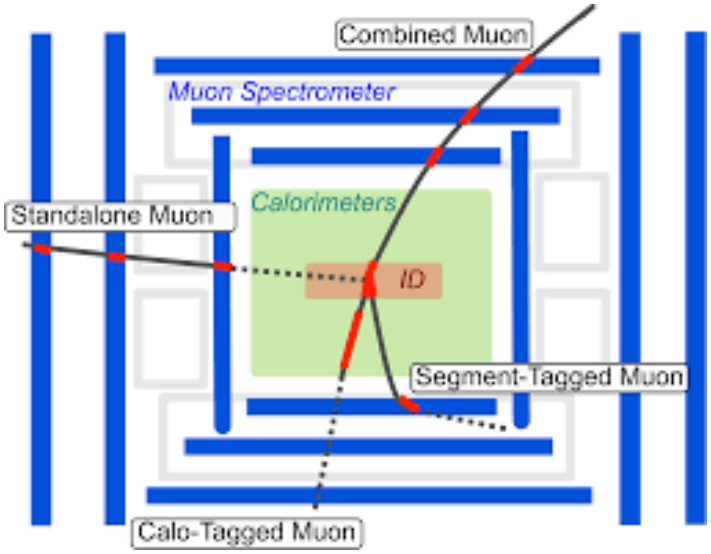

Figure 4.3: The longitudinal view of the ATLAS detector with labeled different muon types: SA, CB, ST and CT.

In the case of overlap among different muon types, if an ID track is shared the preference is given to the CB muon, then to the ST, and the latest to CT, if the MS track is shared the track with larger number of hits is preferred.

The combination of measurements made in MS with the ones from the ID improves the momentum resolution and allows the rejection of muons from secondary interactions as well as the ones from π and K meson in flight decays. The measurement of the activity around the muon track is important to discriminate between processes where isolated muons are produced and background reactions where muons are produced by the semi-leptonic decay of b and c quarks.

During Run-1, depending on the definition of the combined track and the treatment of the muon energy loss though the calorimeters, there are different muon reconstruction algorithms, named *chains* [79], which are described below.

The first chain, known as STACO [179], uses the covariance matrices of the measurements of MS and ID muon tracks to perform statistical combinations of track para-

meters. Then, the combined track parameter is defined as:

$$\mathbf{P} = (\mathbf{C}_{\mathrm{ID}}^{-1} - \mathbf{C}_{\mathrm{MS}}^{-1})^{-1}(\mathbf{C}_{\mathrm{ID}}^{-1}\mathbf{P}_{\mathrm{ID}} + \mathbf{C}_{\mathrm{MS}}^{-1}\mathbf{P}_{\mathrm{MS}}). \tag{4.4}$$

The algorithm combines selected pairs of ID and MS tracks. Then the pairs are ranked according to the matched χ^2 value. A combined muon track candidate is the one with the lowest matching χ^2.

The second chain, known as MUID [190], performs a global refit of muon tracks in the ID and MS. There are two approaches for combined reconstruction and both are used to maximise the efficiency. Outside-in algorithm matches the tracks in MS to the ones in the ID, the disadvantage of this approach is in inefficiency in regions with poor coverage in the MS. Inside-out algorithm extrapolate ID tracks into the MS, with the disadvantage for high pile-up conditions when there is a large number of ID tracks.

A unified reconstruction algorithm (chain 3) has been developed to incorporate the best features of the two chains and has been used, in parallel to the other two, for the reconstruction of 2012 data. For Run-2 and beyond, only chain 3 is used.

4.2 MUON ENERGY LOSS IN THE CALORIMETERS

To reach MS, muons have to pass through approximately 100 radiation lengths of the material [76], since the MS is the outermost layer of the ATLAS detector. Figure 4.4 illustrates the material distribution, expressed in radiation lengths, as a function of pseudorapidity, in front of the pre-sampler, the hadronic calorimeter and the MS. In order to have a correct measurement of the muon momentum, the MS measurement must be corrected for energy losses in the calorimeters and in the inert material in front of the MS.

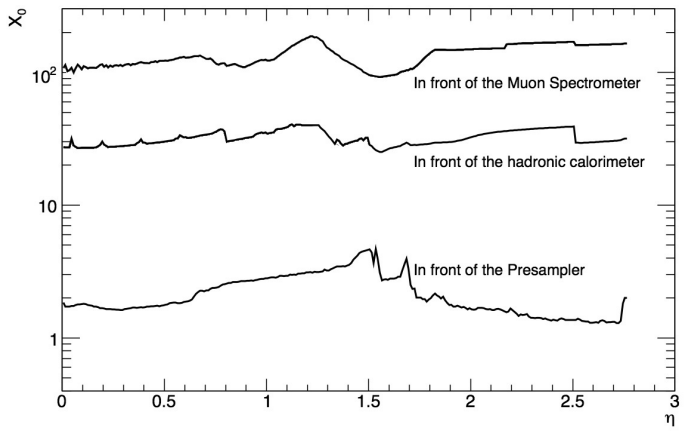

Figure 4.4: Material distribution, expressed in radiation lengths X_0, before the MS as a function of η [76].

Relativistic muons passing through matter lose their energy mostly through electromagnetic processes: ionisation, electron-positron pair production and bremsstrahlung. Then, the total mean energy loss per unit length is:

$$\frac{\mathrm{d}E}{\mathrm{d}x} = \left(\frac{\mathrm{d}E}{\mathrm{d}x}\right)_{\text{ionisation}} + \left(\frac{\mathrm{d}E}{\mathrm{d}x}\right)_{\text{pair production}} + \left(\frac{\mathrm{d}E}{\mathrm{d}x}\right)_{\text{bremsstrahlung}}. \tag{4.5}$$

Energy loss due to ionisation dominates for muons with momenta up to 200 GeV. While higher energy muons lose energy mostly through radiative processes, which is a common name for bremsstrahlung and electron-positron pair production. However, when passing through materials made of high-Z elements, the radiative effects can be already significant for muons of energies 10 GeV [12].

The mean energy loss of muons due to ionisation is given with Bethe-Block formula [12]:

$$\left(\frac{\mathrm{d}E}{\mathrm{d}x}\right)_{\text{ionisation}} = -Kq^2\frac{Z}{A\beta^2}\left(\frac{1}{2}\ln\frac{2mc^2\beta^2\gamma^2E_{\max}}{I^2} - \beta^2 - \frac{\delta(\beta\gamma)}{2}\right), \tag{4.6}$$

where K is a constant, q is the charge of the incident particle, Z is the atomic number of medium, A is the atomic mass of medium, $\beta = p/E$, $\gamma = E/m$, m is the mass of the particle, $E_{\max}$ is the maximal kinetic energy that can be transferred to the medium in a single interaction, I is the mean excitation energy of the medium and $\delta(\beta\gamma)$ is the density effect correction to ionisation energy loss. The Bethe-Block formula describes the mean rate of energy loss due to ionisation for intermediate-Z materials with an accuracy of a few percent [12].

The fluctuations of the muon energy loss due to ionisation in thin layers of material are characterised by Landau distribution [191]. Here, thin layers refer to any amount of material in which muon loses a small percentage of its energy. The Landau distribution is characterised by the most probable value and the width parameter. When radiative effects become dominant processes of energy loss, the tail of the Landau distribution becomes larger. In order to account for the energy loss when extrapolating a muon track from the MS to the IP, one has to add either the most probable energy loss or the mean value of the energy loss. However, these energy loss estimations are statistical quantities which can not take into account the event-by-event energy loss fluctuations.

As mentioned before, there are different algorithms for combining tracks in the ID and MS, with the difference on the treatment of the muon energy loss though the calorimeters. The STACO algorithm uses a momentum dependent parametrisation of energy loss and a detailed geometrical description of the detector outside the ID. In addition the effects of multiple scattering and energy losses fluctuations have been taken into account in the covariance matrix propagation. The track is then propagated down to the closest approach to the beam line accounting for multiple scattering effects in the ID. The parametrisation of the muon energy loss with the STACO algorithm as a function of the pseudorapidity is illustrated in Figure 4.5. On average, muon before entering the MS, lose from 2.5 GeV in barrel region to 4.5 GeV in transition region. The MUID algorithm uses an energy loss measurement obtained either from the observed calorimeter energy deposition or from parametrisation to correct for the

Landau tails of the energy loss distribution. The unified reconstruction algorithm (chain 3) uses the energy loss map from MUID. For Run-2 the calculation of the energy loss in the calorimeter was improved. The average energy loss is parametrised from a detailed description of the detector geometry. The final estimate of the energy loss is obtained by combining the analytic parameterisation with the energy measured in the calorimeter. This method yields a precision on the mean energy loss of about 30 MeV for a 50 GeV muons [192].

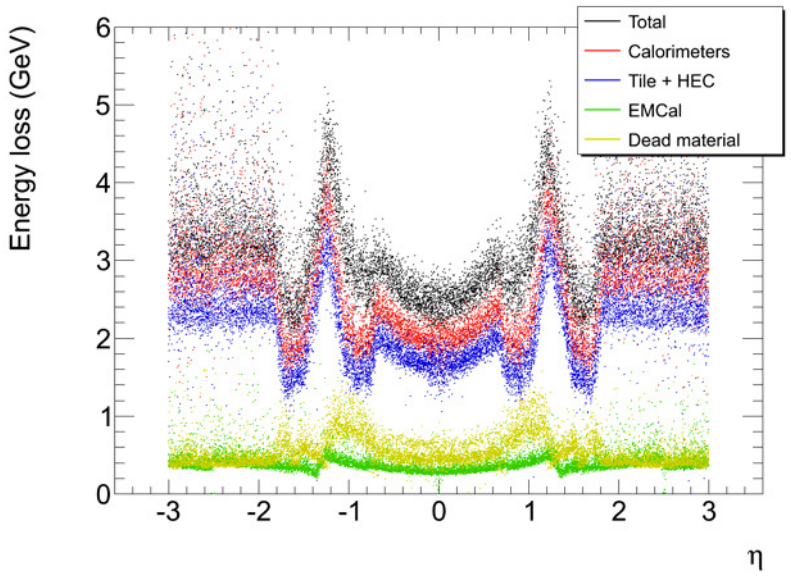

Figure 4.5: Energy loss parameterisation used in the track reconstruction with STACO algorithm as a function of pseudorapidity [189].

4.3 MUON MOMENTUM STUDIES USING J/ψ EVENTS

The J/ψ meson is the first discovered bound state of a charm quark and a charm antiquark $c\bar{c}$ (charmonium) in 1974, simultaneously at Brookhaven National Laboratory [193] and Stanford Linear Accelerator Centre (SLAC) [194]. The world average value for the mass of the J/ψ meson is 3.096900 ± 0.000006 GeV with very narrow decay width 92.9 ± 2.8 keV [12]. In proton–proton collisions at the LHC, the J/ψ mesons can be produced via two mechanisms: *prompt production* where the J/ψ meson is produced directly in the primary interaction and *non-prompt production* where the J/ψ meson is produced in the decays from the b hadrons, which is characterised by a secondary vertex and a longer lifetime. The dominant J/ψ decay mode is into hadrons, while the branching ratio for lepton decays into electron–positron or muon–anti-muon pair is 5.97 % [12]. Since electron and muon decays can be reconstructed with high purity, the J/ψ meson is used for calibration purposes to directly study the detector effects. Furthermore, because of its very narrow decay width, the width of the reconstructed mass distribution of the J/ψ meson comes from the resolution of the measurement of the four-momenta of J/ψ decay products. The event display of a J/ψ meson candidate decay into muons recorded by the ATLAS detector in 2015 is shown in Figure 4.6.

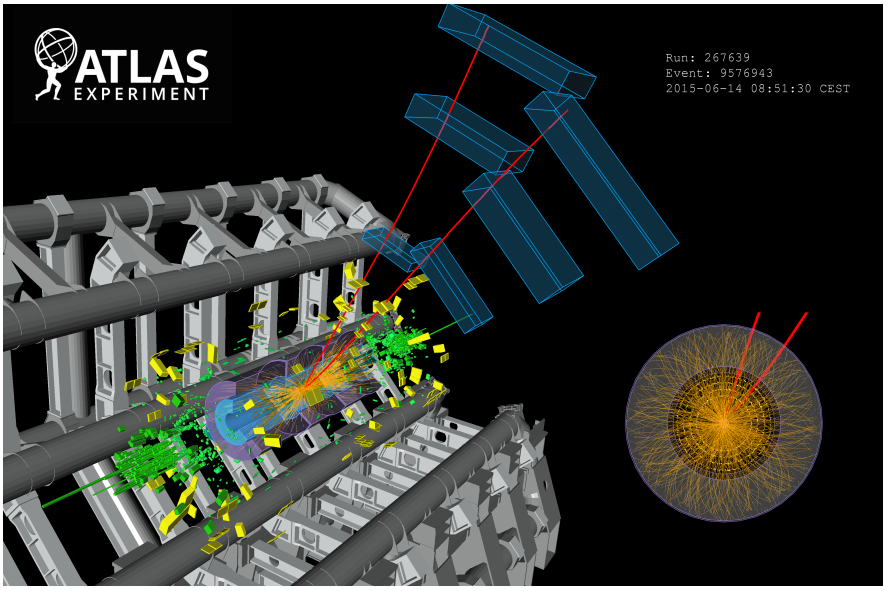

Figure 4.6: Event display of a proton–proton collision event recorded by ATLAS on 14 June 2015 at a collision energy of 13 TeV. Tracks reconstructed from hits in the ID are shown as arcs curving in the solenoidal magnetic field and the blue bars indicate hits in the MS. In this event two muons are identified, and their invariant mass is consistent with that of a J/ψ meson [195].

This section describes the studies of the momentum of the muons from the J/ψ decay reconstructed with the STACO algorithm, a detailed description can be found in [186]. The J/ψ resonance represents a very good probe of the MS track reconstruction. Firstly, the J/ψ mesons are largely produced at the LHC. There are about 7 million events J/ψ candidates in the muon channel collected during 2011 and more then 30 million candidates collected during 2012 data-taking. The J/ψ meson decays represent a very clean sample of muons with relatively low background, and with momentum in the region complementary to the one covered by Z- and W-boson decays. Furthermore, the muons from the J/ψ decay are boosted, leading to small distance between them in the detectors $\eta - \varphi$ space, as illustrated in Figure 4.6. This fact can be exploited with the definition of the fine grid in $\eta - \varphi$ space within the MS where both muons from J/ψ decay end up. Then, the invariant mass of these muon pairs can be used for detection of some local imperfections caused by the magnetic field missmeasurement and for correction of the muon energy loss in the calorimeters. The invariant mass is computed as:

$$m_{\mu\mu} = \sqrt{2E_1E_2(1 - \cos\theta_{12})}, \tag{4.7}$$

where E_1 and E_2 are the energies of the two muons measured by the detector, and θ_{12} is the opening angle between them. A possible inaccuracy in the energy loss calculation, as well as, an inaccuracy of the magnetic field map, is a charge-independent effect. The two can be disentangled by their momentum dependence: the former causes a constant offset, while the contribution of the latter is proportional to the p_{T}. Thus, J/ψ meson events are better suited than Z-boson events for studying energy loss, due to the smaller momentum of the muons.

4.3.1 *Trigger, muon and event selection*

For the muon momentum studies with the J/ψ events, the data from proton–proton collisions at $\sqrt{s} = 7$ TeV and $\sqrt{s} = 8$ TeV is used, collected during 2011 and 2012, respectively. The MC samples used in this study are given in Table 3.3. Only prompt J/ψ production was used, since the samples have higher statistics. The difference in the position of the mass peaks between prompt and non-prompt J/ψ production is found to be less than 1 MeV, therefore it is considered as negligible.

The summary of the J/ψ event selection is given in Table 4.1 for 2011 and 2012 data-taking. For data, events has to pass the GRL requirement, as explained in Section 3.2. Next, the event is required to have a primary vertex with at least three tracks with $p_{\mathrm{T}} > 400$ MeV. Then, the J/ψ candidates are selected with triggers requiring two opposite-charge muon candidates with transverse momentum larger then $p_{\mathrm{T}} > 4$ GeV for 2011 and $p_{\mathrm{T}} > 6$ GeV for 2012 dataset and dimuon invariant mass in range 2.5 GeV $< m_{\mu\mu} <$ 4.5 GeV. With these triggers 16.1 million J/ψ events are collected in 2011 and 37.9 million J/ψ events in 2012 data-taking. Muons have to pass ID hit requirement which are summarised in Table 4.1. Only STACO CB muons are used. It should be stressed that adding ST muons would increase available statistics of the J/ψ candidates by only of 2%. In addition, it is requested that muons are within $|z_0| < 10$ mm from the primary vertex to reduce number of muons arising from the cosmic background. There is no muon isolation requirement applied, since the muons from the J/ψ decay are very close together and it would drastically reduce the acceptance. In order to ensure that muons have sufficiently high momentum to reach the MS, the two most energetic muons are requested to have combined transverse momentum $p_{\mathrm{T}} > 7$ GeV. Finally, in order to reduce the background coming from the DY continuum and muon fakes, the events are requested to have invariant mass of the two most energetic muons around J/ψ peak. Invariant mass is calculated using ID momentum, and it is requested to be 3.0 GeV $< m_{\mu\mu}^{\mathrm{ID}} <$ 3.2 GeV. This selection requirement reduced number of selected events by about 36%, with significant increase in the purity of the sample.

In order to account for already known discrepancy between real data and simulation in terms of momentum scale and resolution, as well as reconstruction efficiency, preliminary corrections [196] are applied to the simulated samples. These preliminary corrections are derived from the Z-boson sample and don't correct for possible energy loss discrepancies. For dimuon J/ψ triggers, there are no official corrections provided. Thus, some remaining discrepancy between efficiency of these triggers in simulated and real data are left uncorrected. It is assumed that these discrepancies should occur mainly in the muons η and φ distributions, having only marginal impact on the studies with the momentum scale.

The cut-flows for data and MC samples are shown in Tables 4.2 and 4.3, respectively. After the full selection, there is 2.2 and 10.7 million J/ψ candidates in 2011 and 2012 data respectively, as well as 4.0 and 18.2 million J/ψ candidates in 2011 and 2012 MC samples, respectively. The differences in the selection between 2011 and 2012 data is

Table 4.1: The summary of the J/ψ event selection requirements.

Cut	2011	2012
GRL	GRL	
Event selection	primary vertex with at least 3 tracks with $p_{\mathrm{T}} > 400$ MeV	
Trigger	two opposite charged muons	
	2.5 GeV $< m_{\mu\mu} <$ 4.5 GeV	
	$p_{\mathrm{T}} > 4$ GeV	$p_{\mathrm{T}} > 6$ GeV
Muon selection	STACO, combined	
	$\lvert\eta\rvert < 2.4$ and $\lvert z_0\rvert < 10$ mm	
ID hits requirement	$N_{\mathrm{pixel}} \geq 1$	$N_{\mathrm{pixel}} \geq 1$
	$N_{\mathrm{pixel}} + N_{\mathrm{dead\ pixel\ sensors}} > 1$	$N_{\mathrm{pixel}} + N_{\mathrm{dead\ pixel\ sensors}} > 0$
	$N_{\mathrm{SCT}} + N_{\mathrm{dead\ SCT\ sensors}} > 5$	$N_{\mathrm{SCT}} + N_{\mathrm{dead\ SCT\ sensors}} > 4$
	$N_{\mathrm{pixel\ holes}} + N_{\mathrm{SCT\ holes}} < 3$	$N_{\mathrm{pixel\ holes}} + N_{\mathrm{SCT\ holes}} < 3$
TRT hits requirement	if $\lvert\eta\rvert < 1.9$:	if $0.1 < \lvert\eta\rvert < 1.9$:
	$N_{\mathrm{TRT}} + N_{\mathrm{TRT\ outliers}} > 5$	$N_{\mathrm{TRT}} + N_{\mathrm{TRT\ outliers}} > 5$
	and $\frac{N_{\mathrm{TRT\ outliers}}}{N_{\mathrm{TRT}}+N_{\mathrm{TRT\ outliers}}} < 0.9$	and $\frac{N_{\mathrm{TRT\ outliers}}}{N_{\mathrm{TRT}}+N_{\mathrm{TRT\ outliers}}} < 0.9$
	if $\lvert\eta\rvert \geq 1.9$:	if $\lvert\eta\rvert \leq 0.1$ or $\lvert\eta\rvert \geq 1.9$:
	$N_{\mathrm{TRT}} + N_{\mathrm{TRT\ outliers}} > 5$	$N_{\mathrm{TRT}} + N_{\mathrm{TRT\ outliers}} > 5$
	if $\frac{N_{\mathrm{TRT\ outliers}}}{N_{\mathrm{TRT}}+N_{\mathrm{TRT\ outliers}}} < 0.9$	if $\frac{N_{\mathrm{TRT\ outliers}}}{N_{\mathrm{TRT}}+N_{\mathrm{TRT\ outliers}}} < 0.9$
J/ψ selection	two muons with opposite charges	
	$p_{\mathrm{T}} > 7$ GeV	
	3.0 GeV $< m_{\mu\mu}^{\mathrm{ID}} <$ 3.2 GeV	

coming from the fact that two muons are required to have $p_{\mathrm{T}} > 7$ GeV and triggers with different thresholds are used for 2011 and 2012 data-taking.

Table 4.2: Cut-flow for the J/ψ event selection in 2011 and 2012 data samples with absolute and relative efficiency.

	2011 data			2012 data		
cut	N_{sel}	eff [%]	rel eff [%]	N_{sel}	eff [%]	rel eff [%]
	54 261 295			159 478 050		
GRL	52 558 322	96.86	96.86	154 898 099	97.13	97.13
Primary Vertex	52 486 676	96.73	99.86	154 780 553	97.05	99.92
Trigger	16 127 654	29.72	30.73	37 872 924	23.75	24.47
Muon Selection	15 269 841	28.14	94.68	34 842 264	21.85	92.00
Two muons	3 539 680	6.52	23.18	16 901 716	10.60	48.51
Invariant Mass	2 237 359	4.12	63.21	10 675 903	6.69	63.16

The invariant mass distribution of the J/ψ candidates after GRL and trigger requirements, collected during 2011 and 2012 are shown in Figure 4.7. The agreement between data and MC is good just around the mass peak. One part of the disagreement is because the background is not subtracted from the data histograms. Another source of the discrepancy is coming from the fact that only prompt production in the MC is used, and the tails of mass distributions are a bit different for prompt and non-prompt production mechanisms. To discard possible bias arising from the reconstruction, the distributions of true muon p_{T} and J/ψ rapidity distributions in MC samples during 2011 and 2012 are checked, for prompt and non-prompt production separately. From the distributions shown in Figure 4.8 one can observe good agreement for non-prompt

Table 4.3: Cut-flow for the J/ψ event selection in 2011 and 2012 MC samples with absolute and relative efficiency.

Cut	2011 MC			2012 MC		
	N_{sel}	eff [%]	rel eff [%]	N_{sel}	eff [%]	rel eff [%]
	43 434 915			66 297 206		
Primary Vertex	43 369 598	99.85	99.85	66 150 883	99.78	99.78
Trigger	22 068 118	50.81	50.88	32 199 426	48.57	48.67
Muon Selection	21 309 378	49.06	96.56	30 996 595	46.75	96.26
Two Muons	4 673 033	10.76	21.93	20 777 953	31.34	67.03
Invariant Mass	4 021 284	9.26	86.05	18 157 219	27.39	87.39

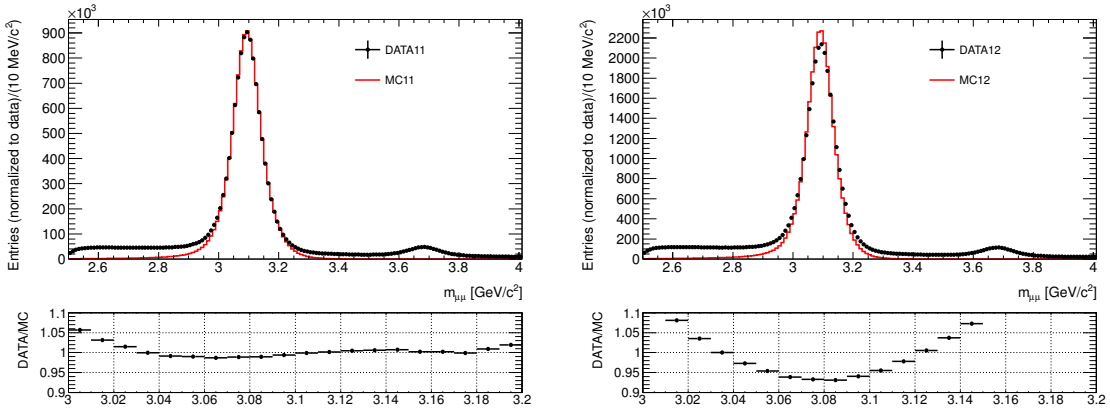

(a) **(b)**

Figure 4.7: The invariant mass distributions of J/ψ candidates collected during (a) 2011 and (b) 2012. Selected candidates pass GRL and trigger requirement. MC is normalised to data for 3.0 GeV $< m_{\mu\mu} <$ 3.2 GeV.

production, while there is a disagreement in the tail of the p_{T} distributions between 2011 and 2012 MC for the prompt J/ψ production. These differences could be caused because Pythia 6 is used for 2011, while Pythia 8 is used for 2012 for the J/ψ modeling in MC. However, the discrepancy is not caused by the differences in the muon reconstruction in 2011 and 2012 datasets.

In order to remove any possible bias in the muon momentum calibration procedure, described in Section 4.4, a set of weights are derived to match the dimuon transverse momentum $p_{\text{T}}(\mu\mu)$ and dimuon rapidity $Y(\mu\mu)$ in data and MC, so called $p_{\text{T}} - Y$ reweighting. The weights are derived in the kinematic region of interest, with muons of $7 < p_{\text{T}} < 80$ GeV and $|\eta| < 2.5$. No other corrections are applied to the simulated sample and no background subtraction is attempted for the calculation of these weights, however tight invariant mass requirement around J/ψ peak is imposed. Figure 4.9 shows the effect on this reweighting on $p_{\text{T}}(\mu\mu)$ and $Y(\mu\mu)$ distributions.

There is also difference in data to MC ratio distributions between 2011 and 2012 samples as shown in Figure 4.7. In order to identify possible biases coming from the

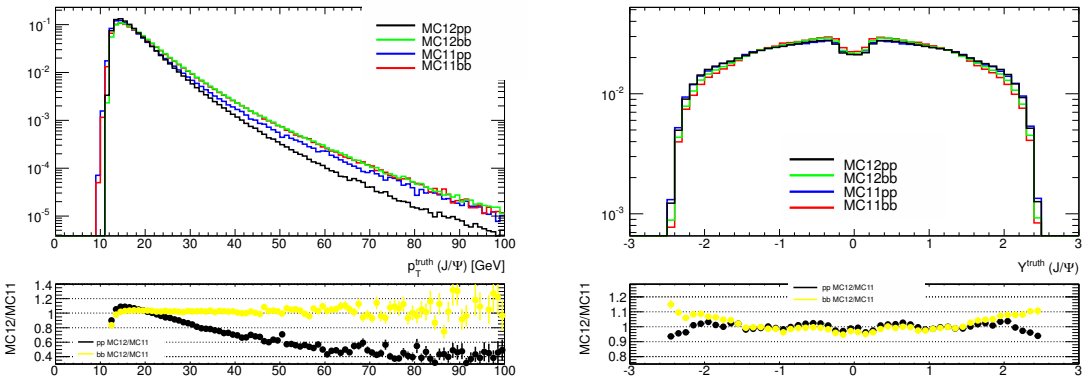

(a) **(b)**

Figure 4.8: The distributions of the true J/ψ (a) p_{T} and (b) rapidity for 2011 and 2012 MC datasets, for prompt (denoted as pp) and non-prompt (denoted as bb) production separately. Histograms are normalised to unity.

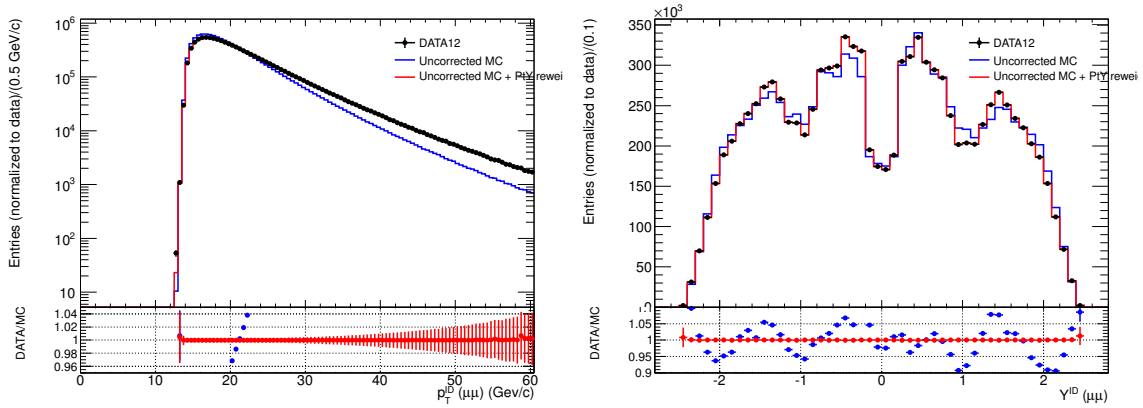

(a) **(b)**

Figure 4.9: Distribution of (a) transverse momentum and (b) rapidity for J/ψ events in data and MC, before and after $p_{\mathrm{T}} - Y$ reweighting. No other corrections are applied to the simulated events.

pile-up conditions which were different during 2011 and 2012 data-taking, for the 2012 data sample, the invariant mass distribution is shown for two ranges of average number of interactions per bunch crossing: $< \mu > < 10$ and $< \mu > > 20$, as illustrated in Figure 4.10. The range $< \mu > < 10$ roughly corresponds to the 2011 pile-up conditions. These distributions indicate that pile-up has a very small effect on the muon reconstruction performance in terms of the scale and resolution. Therefore, the differences between 2011 and 2012 distributions are not due to pileup effects.

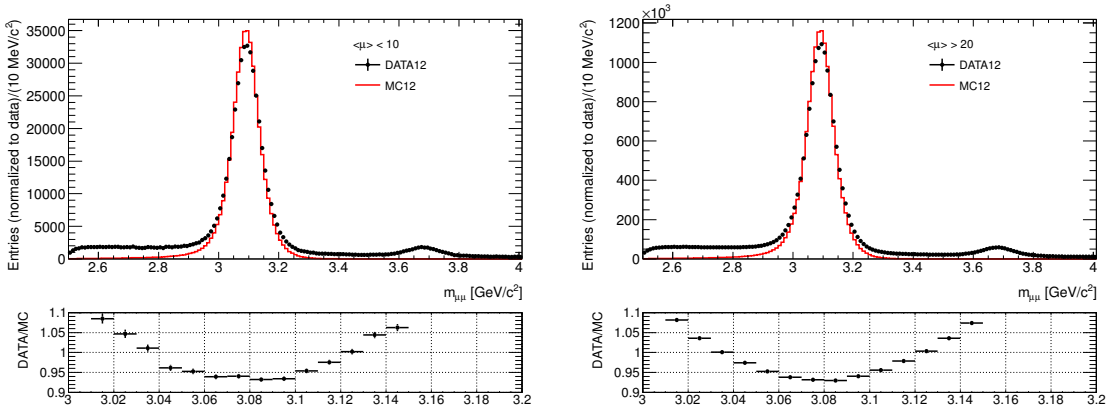

Figure 4.10: The invariant mass distribution of J/ψ candidates collected during 2012 data-taking for (a) $<\mu><10$ and (b) $<\mu>>20$. Events pass GRL and trigger requirement. MC is normalised to data for $3.0\,\text{GeV} < m_{\mu\mu} < 3.2\,\text{GeV}$.

4.3.2 *Mass fits*

One possibility to fix the absolute momentum scale is to use well measured invariant mass of the J/ψ dimuon resonance. For that purpose one can reconstruct invariant mass distribution using muon track momentum variables from different systems: momentum of the ID track, momentum of the MS track extrapolated to the IP with energy loss taken into account refered as ME, and CB momentum. On the other hand, angles can be taken from ID or MS measurement, while combined values are almost identical to the ID, since ID quantities are dominating the measurement. An example of the dimuon invariant mass distribution with different muon track variables is presented in Figure 4.11. The invariant mass from the CB measurement is very close to the ID one, with minimal smearing due to the resolution, while ME measurement is shifted with respect to the one obtained from ID or CB momentum measurements. Using ID angles improves mass resolution significantly for the ME track measurement.

The selection requirement on 3.0 GeV $< m_{\mu\mu}^{\text{ID}} <$ 3.2 GeV increases in the purity of the signal for ME track measurement with ID angles, which is demonstrated in Figure 4.12 for 2011 and 2012 data-taking.

Figure 4.13 shows the mean values of dimuon invariant masses calculated using either muon momentum measured by ID, ME and CB. The masses are calculated in η bins defined by the requirement that both muons from J/ψ decay are occupying the same bin. The muon pseudorapidity is measured by ID. While mass measured by the ID is within few MeV from the world average J/ψ mass measurement (referred as the PDG value), it is obvious that it is not the case for ME measurement, and consequently, for the CB measurement. The mean of the reconstructed invariant mass in barrel is of order 50 MeV away from the PDG value. The CB measurement in the forward region

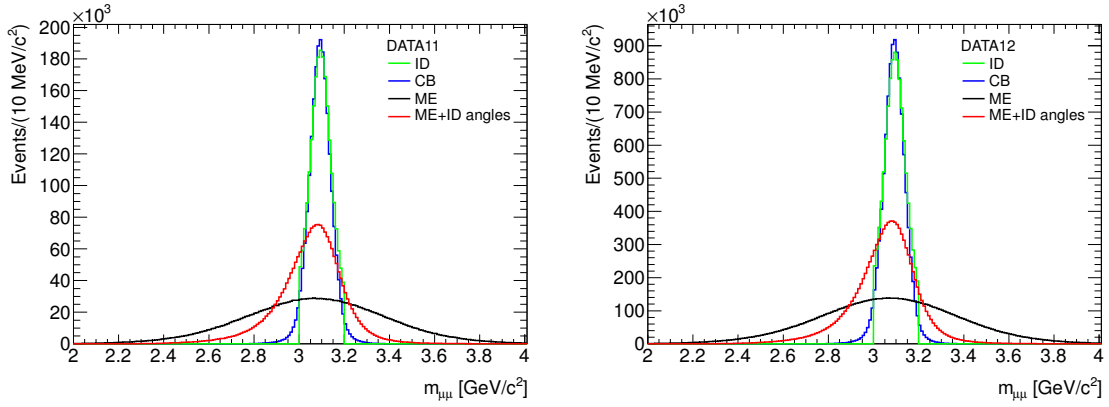

(a) **(b)**

Figure 4.11: The invariant mass distribution calculated using different muon track variables, as indicated on the legend of the plots. The distributions are shown for (a) 2011 and (b) 2012 data-taking. The events pass muon selection requirements and invariant mass cut 3.0 GeV $< m_{\mu\mu}^{\mathrm{ID}} <$ 3.2 GeV calculated with the ID momentum.

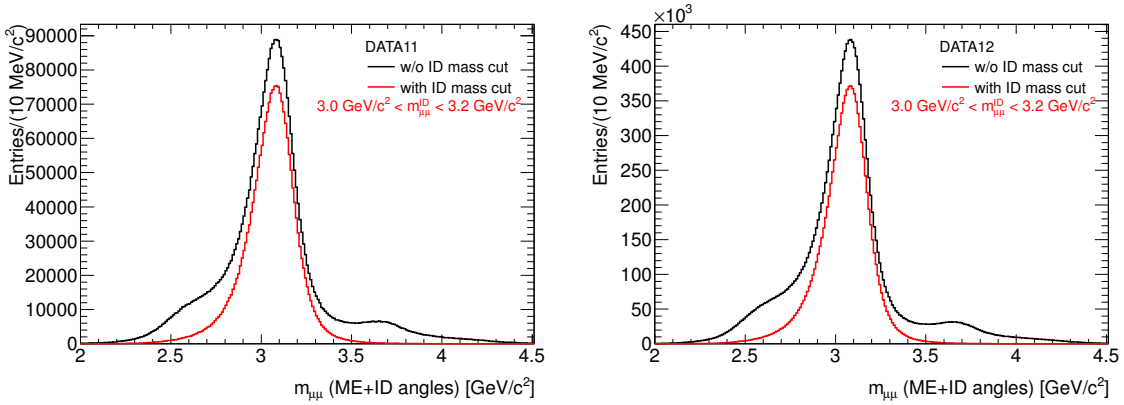

(a) **(b)**

Figure 4.12: The invariant mass distribution calculated using P_{ME} and $\theta_{\mathrm{ID}}, \varphi_{\mathrm{ID}}$ with and without invariant mass requirement 3.0 GeV $< m_{\mu\mu}^{\mathrm{ID}} <$ 3.2 GeV.

is pulled by the momentum measurement in the MS. Also, one can observe that in the forward region there is a discrepancy between data and MC. There is no difference between 2011 and 2012 invariant mass distributions.

Since the mean value of the transverse momenta of the muons from J/ψ decays is around 9 GeV, the offset in the position of the mass peak could originate from the fact that energy loss estimation based on the parametrisation using Landau distribution will not be entirely proper. In order to estimate the size of this effect, the same mass distributions as a function of $\eta$are produced, with the request that both muons have $p_{\mathrm{T}} <$ 15 GeV and $p_{\mathrm{T}} >$ 15 GeV. This is presented in Figure 4.14 for 2012 data and

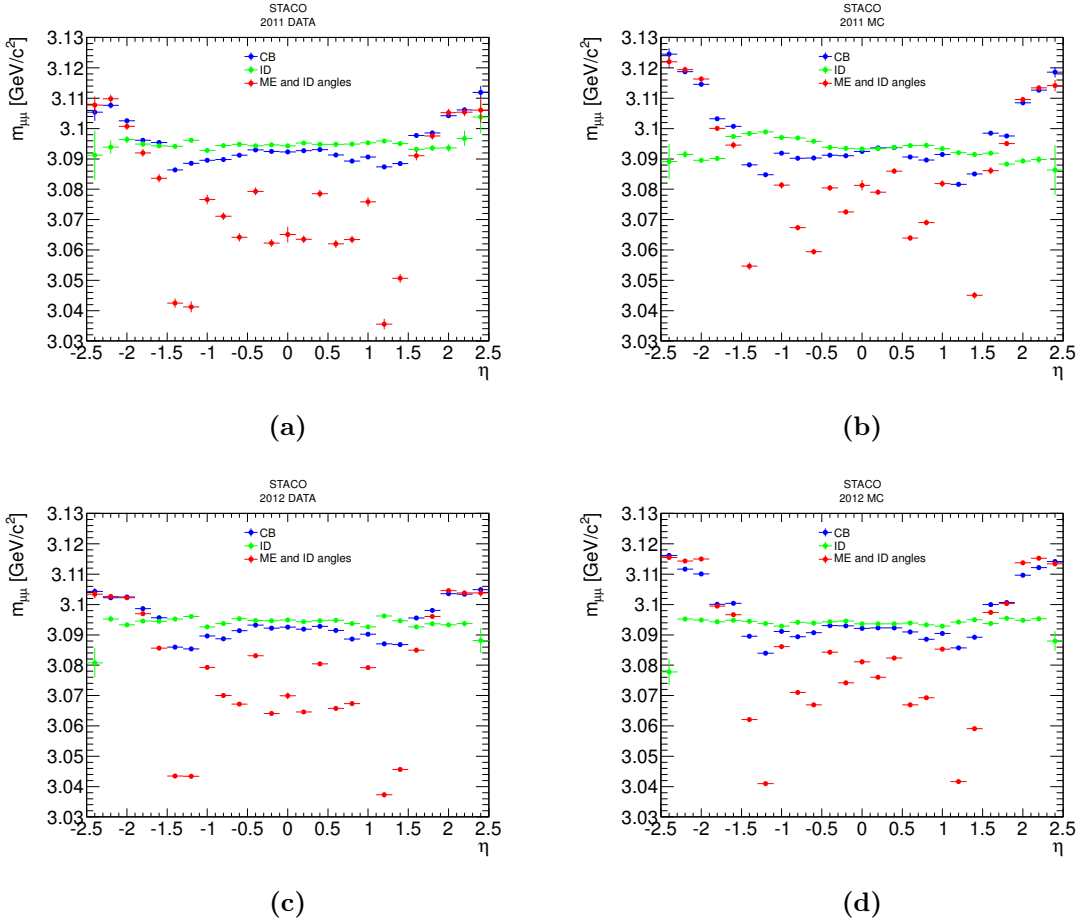

Figure 4.13: Mean the invariant mass distribution for two muons as a function of pseudorapidity, for 2011 real data (a), 2011 MC (b), 2012 real data (c), and 2012 MC (d). η is the center of the pseudorapidity bin in which both muons are reconstructed. Green points represent mass calculated with ID momentum, blue points mass calculated with combined momentum, while red points represent mass calculated with the ME momentum.

simulation. The offset for the events with higher values of the muon momenta are indeed smaller, but still significant, affecting the CB momentum measurement at the same level. This is consistent with the measurement based on the Z-boson events.

The mean value of the reconstructed invariant mass is biased due to the low mass tails. Therefore, in order to precisely quantify the bias in the position of the reconstructed invariant mass peak, fits are performed to the signal and the background. The non resonant dimuon background, coming mainly from heavy-hadron decay and DY production, is parametrised with a second order polynomial function:

$$f(x; p_0, p_1, p_2) = p_0 + p_1 \cdot x + p_2 \cdot x^2. \tag{4.8}$$

The mass peak is fitted with Crystal Ball function with five parameters, it consists of a power law tail stitched to a Gaussian core such that the function and its first derivative

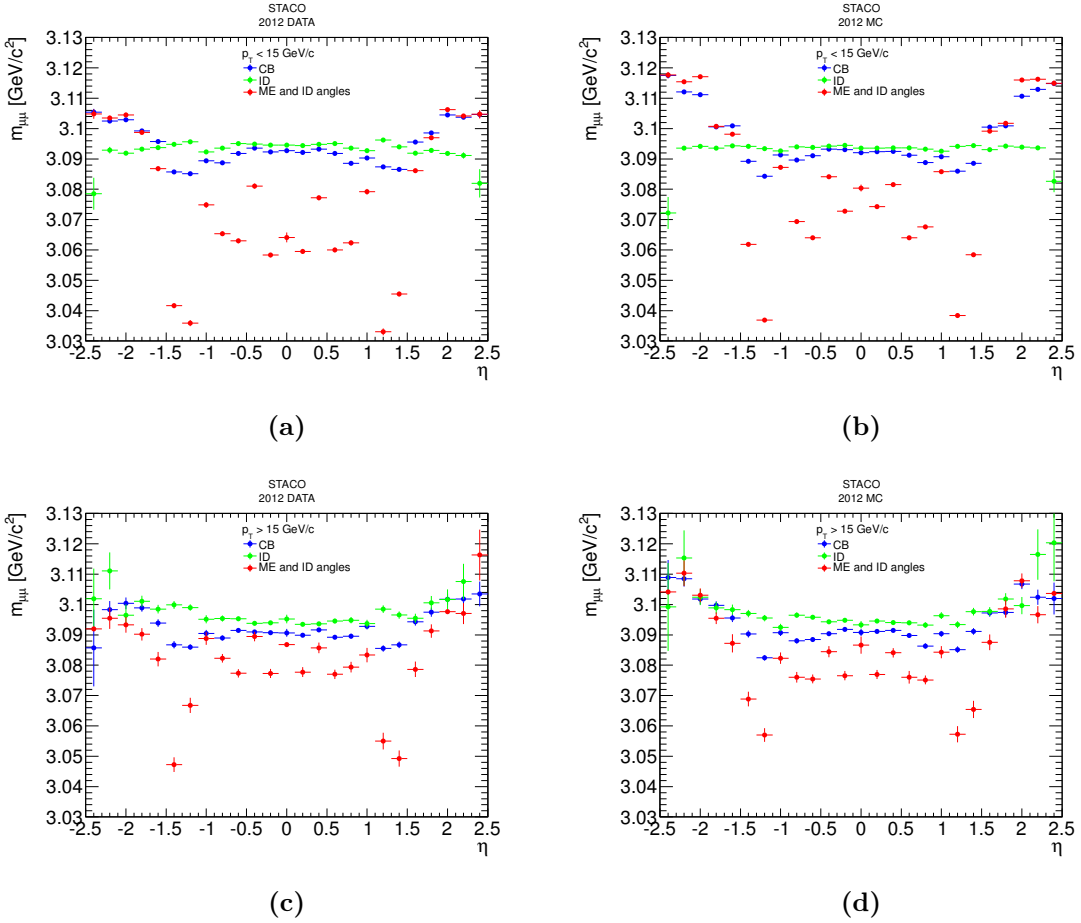

Figure 4.14: Mean of the invariant mass distribution for two muons as a function of pseudorapidity, for 2012 data and simulation. η is the center of the pseudorapidity bin in which both muons are reconstructed. Muons on (a) and (b) plots are requested to have $p_{\mathrm{T}} < 15$ GeV, while on (c) and (d) $p_{\mathrm{T}} < 15$ GeV. The colour code is the same as in previous figure.

are continuous [197]:

$$f(x; N, \alpha, n, \bar{x}, \sigma) = N \begin{cases} \exp\left(-\frac{(x-\bar{x}^2)}{2\sigma^2}\right), & \text{if } \frac{x-\bar{x}}{\sigma} > -\alpha \\ A \cdot \left(B - \frac{x-\bar{x}}{\sigma}\right)^{-n}, & \text{otherwise} \end{cases} \tag{4.9}$$

where $A = (n/|\alpha|)^n \exp\left(-|\alpha|^2/n\right)$ and $B = n/|\alpha| - |\alpha|$, N is the normalisation factor, n is the power law parameter, $\bar{x}$ and σ represent the mean and the standard deviation of the Gaussian core, respectively. Parameters $\alpha, n, \bar{x}, \sigma$ are fitted to the data. Fits are performed in the window of 2× RMS around the pick for combined and ID invariant mass. For ME invariant mass only the pick is fitted 2× RMS around the mean value with Crystal Ball function. The example of the mass peak fits using Crystal Ball function is given in Figure 4.15. The J/ψ mass peak can also be fitted with an iterative Gaussian peak finder, defined as repeated Gaussian fitting within the range $(\bar{x}-\sigma, \bar{x}+\sigma)$

until the fit stabilises, where the Gaussian function is given with:

$$f(x; N, \bar{x}, \sigma) = N \cdot \exp\left(-\frac{(x-\bar{x})^2}{2\sigma^2}\right). \tag{4.10}$$

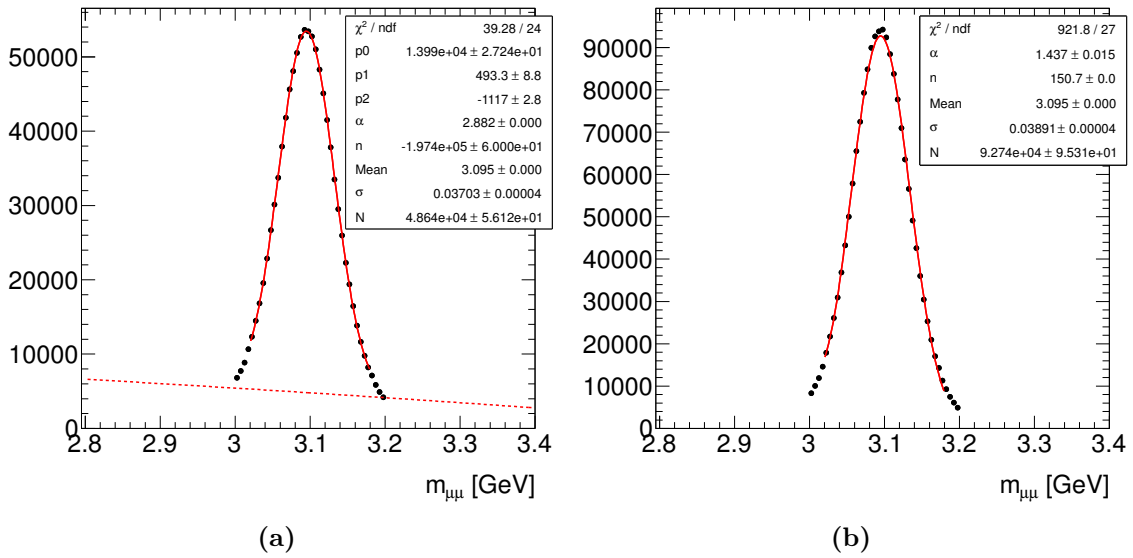

(a) **(b)**

Figure 4.15: The invariant mass fits for the ID momentum for 2011 (a) real data and (b) MC. Both muons are reconstructed in barrel. The dashed line represents the background subtraction.

The relative mass differences for several definitions of the dimuon invariant mass is presented in Figure 4.16. The relative mass difference is presented as a function of the leading muon η. In this way the statistics is increased, and the information is preserved since muons from the J/ψ decay are close. Contrary to the previous distributions where mean value of the mass is shown, mass distributions are fitted with iterative Gaussian (ID and CB) or Crystal Ball (ME). Definitions of the mass differences are indicated on the plots. The distribution for ID show an offset of about 0.5 permile with respect to the PDG, while for ME this goes to about 1% in the barrel. The CB measurement is dominated by the ID, except in the forward region. The relative mass difference that takes into account both data and simulation, show discrepancy up to 0.5% in the forward region. Discrepancy between data and simulation in forward region is probably due to bad description of the material, i.e. missing material in simulation.

In order to discard possible resolution effects, the distribution of mass as a function of muon η is checked with stronger requirement that muon has at least 1 hit in each of the three layers of the MS: inner, middle and outer. The comparison between mean invariant mass distribution calculated with ME momentum for 2012 dataset when there is no hit and with requirement of at least one hit per layer on reconstructed muon track is shown in Figure 4.17. No difference in shape is observed, except in the transition region, where offset with respect to the PDG value is smaller with this additional quality criteria. This confirms that observed effect is mostly coming from energy loss miss modeling.

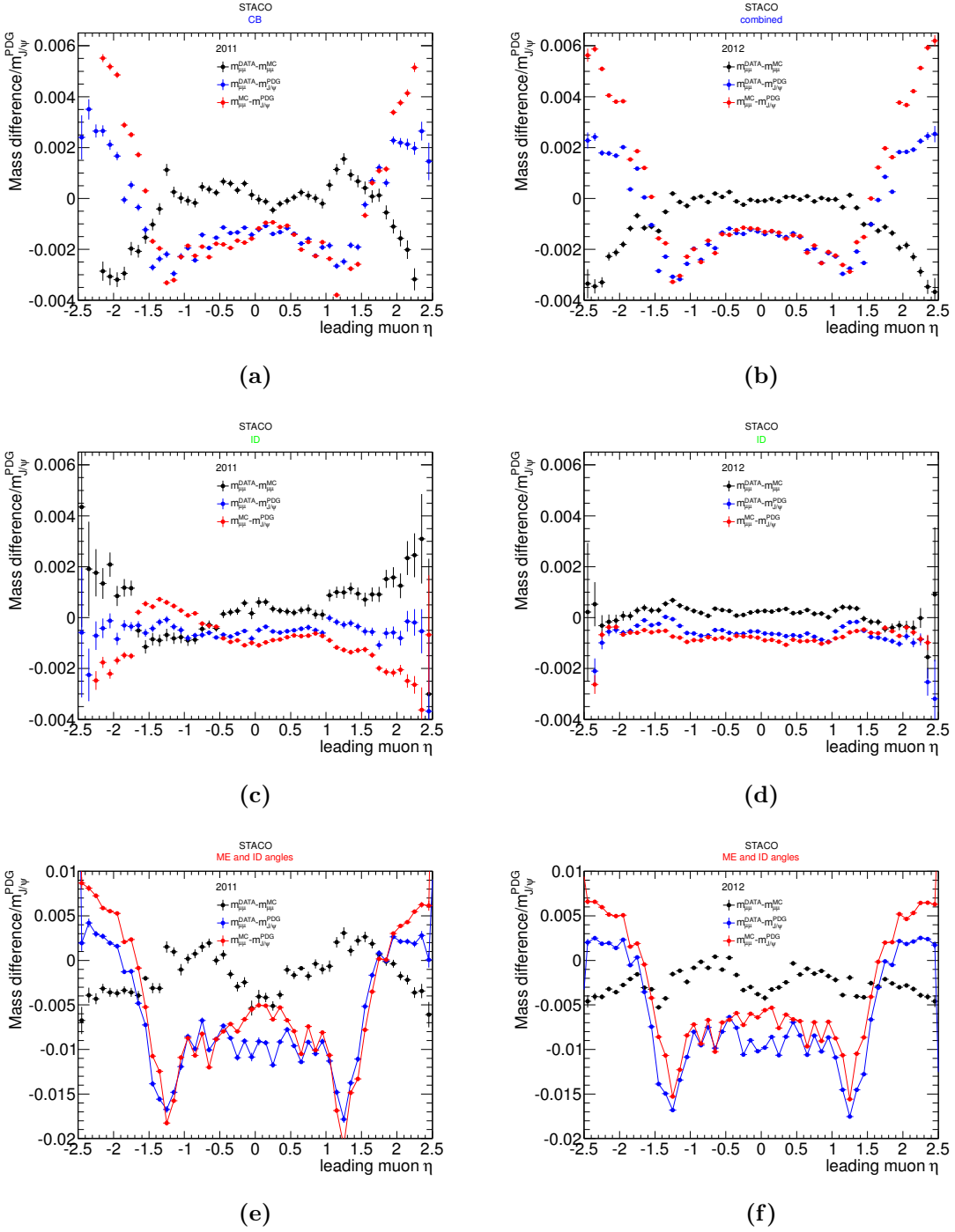

Figure 4.16: The relative mass difference as a function of leading muon pseudorapidity for 2011 (left) and 2012 (right) data-taking for data (black points), simulation (blue points) and difference between data and simulation (red points). The invariant mass is calculated with CB (a) and (b), ID (c) and (d) and ME (e) and (f) momentum. For the CB and ID, iterative Gaussian is used for the fit, while mass calculated with ME momentum is fitted with Crystal Ball.

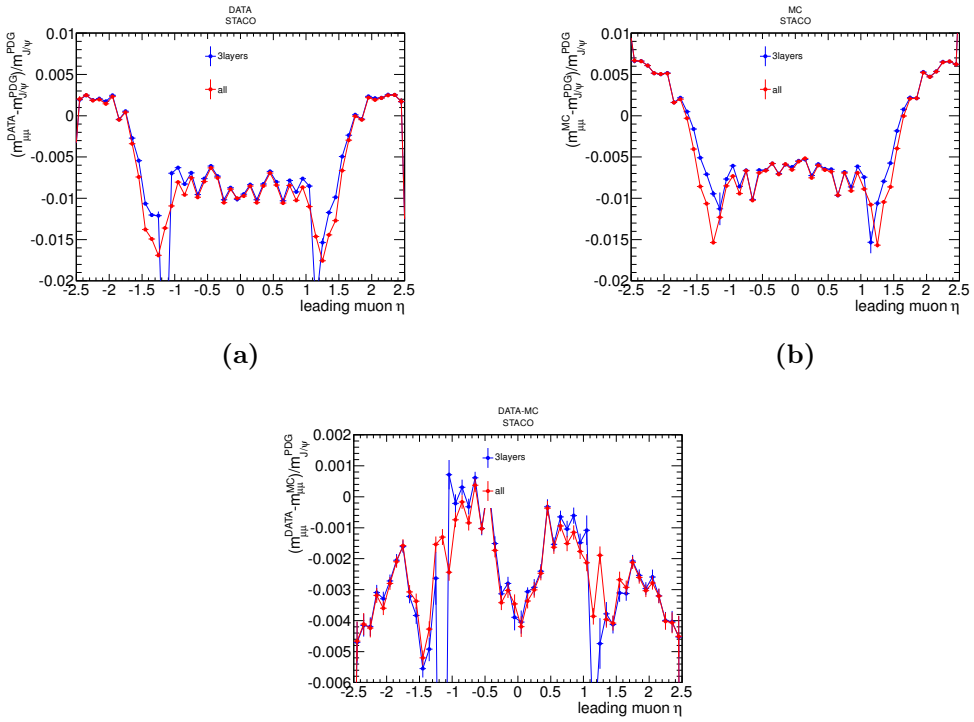

Figure 4.17: The relative mass difference for dimuon invariant mass of the J/ψ resonance as a function of muon η for 2012 (a) data, (b) simulation and (c) difference between data and simulation. Invariant mass is calculated with ME momentum when there is no hit (red points) and with requirement of at least one hit per layer (blue points) on reconstructed muon track.

In order to check the observed effects, similar set of fits are performed on Z-boson dimuon decays. The Z-boson candidates are required to satisfy the same quality criteria as for the selection of good muon candidates from J/ψ decays, as summarised in Table 4.1. Additionally, muons are required to have $p_{\mathrm{T}} > 25$ GeV. Events are required to pass dimuon trigger. Final event selection requires presence of at least two muons, of opposite charge, with invariant mass in the range 66 GeV $< m_{\mu\mu}^{\mathrm{CB}} <$ 116 GeV.

Fits of the data and simulated events for 2011 and 2012 datasets are presented in Figure 4.18. Both muons are required to be in the same η bin. Fitting procedure is the same as for J/ψ except background is neglected since it should be at 0.1% level. Qualitatively, the same shape is observed as for J/ψ as a function of η. However, it is not possible to make direct comparison with the world average value, since position of the Z-boson resonance peak is not possible to match world average value due to effect of FSR, PDFs. Also, due to neglecting the running of the Z-boson width in the POWHEG MC sample, position of the Z-boson peak is biased by $25 - 30$ MeV downwards with respect to the true value. Lineshape reweighting tool used to fix this feature in POWHEG is not applied on the 2012 sample, which causes slight bias in the discrepancy between data and simulation, as discussed in Chapter 3

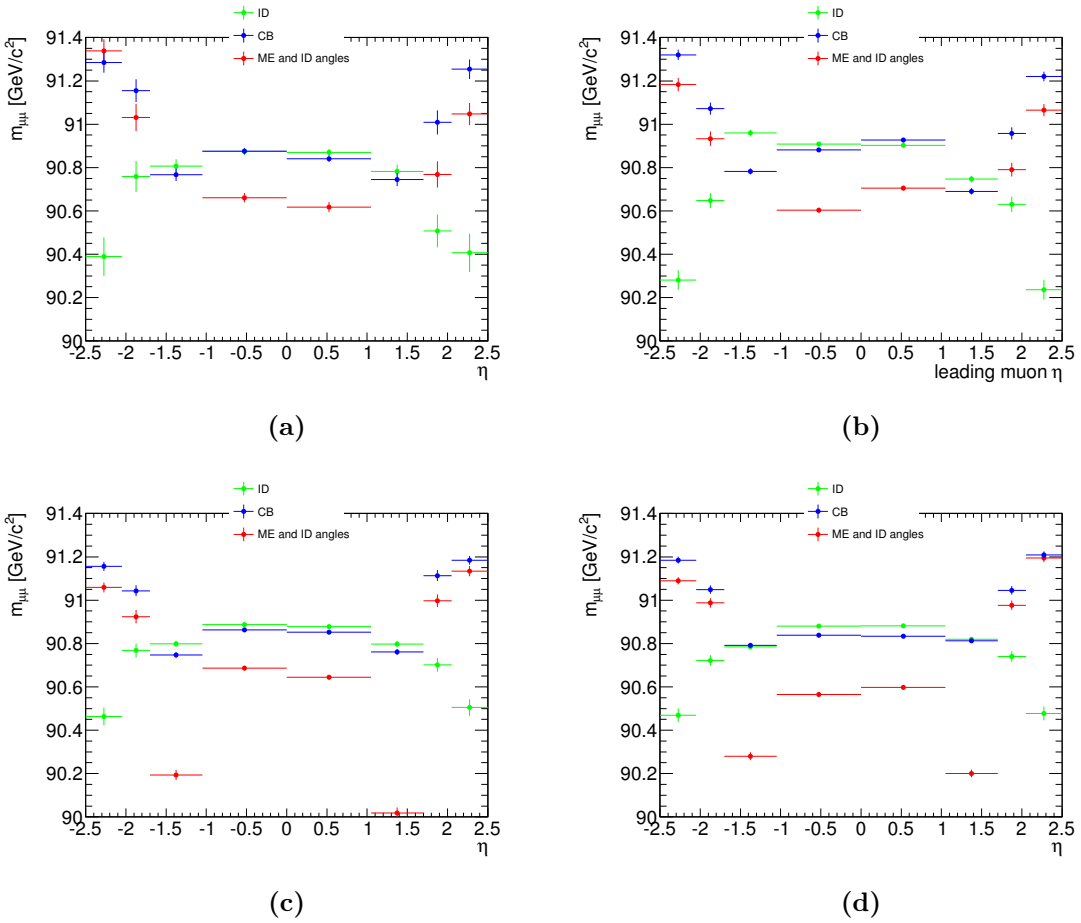

Figure 4.18: The mean of the fit of the invariant mass distribution for two muons as a function of pseudorapidity, for (a) 2011 real data, (b) 2011 MC, (c) 2012 real data and (d) 2012 MC. The η corresponds to the the centre of the pseudorapidity bin in which both muons are reconstructed.

For the J/ψ resonance, the mean fitted invariant mass reconstructed with ME momentum is approximately 30 MeV different from the PDG value in barrel. This corresponds to $\sim$ 1% effect on J/ψ invariant mass. And, 1% on muons transverse momentum from the J/ψ resonance is approximately 100 MeV, since the mean transverse momentum for muons from J/ψ resonance is around 10 GeV which indicates about 100 MeV missing energy loss. For the Z-boson resonance mean ME invariant mass is approximately 200 MeV different from with respect to the mean invariant mass calculated with ID momentum in barrel. This effect is approximately 0.2 % on Z-boson invariant mass and it corresponds to 80 MeV missing energy loss, since the mean transverse momentum for muons from Z-boson decay is around 40 GeV. This rough estimation shows that the missing energy loss is coherent between Z-boson and J/ψ resonance. It also explains the shape of mean CB invariant mass as a function of muon pseudorapidity.

4.3.3 *Momentum fits*

Another way to study energy loss corrections is to use high statistics the J/ψ resonance and study the difference between ME and ID momentum per muon as a function of muon η and/or φ. This allows to directly compare results with the mass fits, minimise the potential backgrounds, as well as investigate possible differences between muons and anti-muons. In order to check energy loss behaviour, Figure 4.19(b) shows an absolute energy loss $P_{\mathrm{ID}} - P_{\mathrm{MS}}$ for 2012 data and simulation as a function of muon pseudorapidity. When comparing absolute energy loss with cumulative amount of material in front of MS, shown in Figure 4.19(a), there are four different regions:

- barrel: the energy loss proportional to $1/\sin(\theta)$;
- $\eta \approx 0.8$: the services and the material in the electromagnetic calorimeter change its width from 1.53 mm to 1.15 mm;
- $1.1 < \eta < 1.4$: the extended tile calorimeter corner;
- $\eta \approx 1.6$: the end of extended tile calorimeter and services with density smaller than iron.

There is also globally good agreement between the absolute energy loss and the GEANT 4 information, with a small shift in barrel observed as expected.

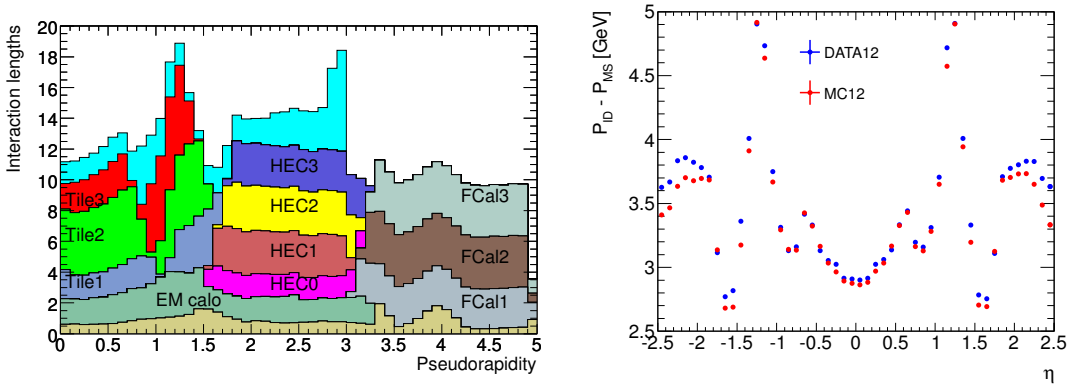

(a) **(b)**

Figure 4.19: (a) Cumulative amount of material, in units of interaction length X_0, as a function of absolute pseudorapidity, in front of the electromagnetic calorimeters, in the electromagnetic calorimeters themselves, in each hadronic compartment, and the total amount at the end of the active calorimetry [76]. For completeness, the total amount of material in front of the first active layer of the MS up to $|\eta| < 0.3$ is also shown. (b) The absolute energy loss for 2012 data and simulation as a function of muon pseudorapidity.

Distributions of $P_{\mathrm{ME}} - P_{\mathrm{ID}}$ are studied in η and P_{CB} bins. The ID track momentum is taken as reference, assuming its miss-calibration is at the permile level, as shown with the mass fits previously. The momentum fits are performed in $\Delta\eta = 0.1$ and variable

ΔP_{CB} bin size to minimise the statistical uncertainty. The $P_{\mathrm{ME}} - P_{\mathrm{ID}}$ distributions are fitted using Crystal Ball function. Other fitting functions, like, the double Gaussian and iterative Gaussian core fit have shown worse quality of the fits. The example of the fits performed on the 2012 data for several η bins and for several P_{CB} bins are shown in Figure 4.20. The overall quality of the fit is good, allowing to extract the peak position with good accuracy.

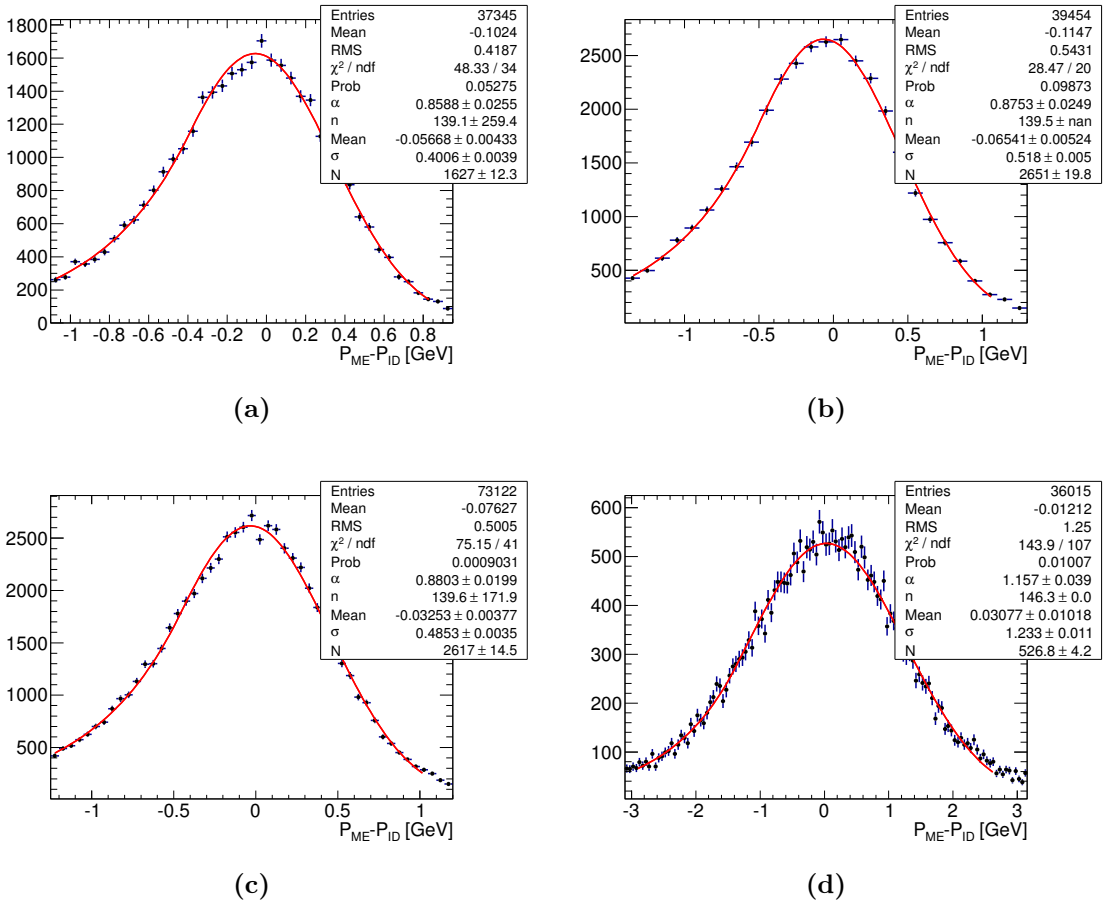

Figure 4.20: The examples of Crystal Ball fits of $P_{\mathrm{ME}} - P_{\mathrm{ID}}$ for 2012 data. Muons satisfy: (a) $|\eta| < 0.1$ and $10 < P_{\mathrm{CB}} < 11$ GeV, (b) $0.2 < |\eta| < 0.3$ and $15 < P_{\mathrm{CB}} < 16$ GeV, (c) $0.5 < |\eta| < 0.6$ and $12 < P_{\mathrm{CB}} < 13$ GeV, and (d) $1.6 < |\eta| < 1.7$ and $23 < P_{\mathrm{CB}} < 24$ GeV.

After performing fits in each of the η, P_{CB} bins and extracting mean value of the $P_{\mathrm{ME}} - P_{\mathrm{ID}}$ distributions, this mean value is fitted as function of CB momentum for a given η assuming the linear dependence:

$$P_{\mathrm{ME}} - P_{\mathrm{ID}} = a + b \cdot P_{\mathrm{CB}}. \tag{4.11}$$

If the miss-calibration of the ME muon momentum track is entirely due to missmodeling of the energy loss, it would be expected that parameter $b \approx 0$, while parameter a represents the energy loss correction. It is noticed that the first point, with the lowest

P_{CB}, is always separated from the rest of the points, thus it is excluded from the fit. The quality of the fits is chaining going from barrel to the forward region. While in the forward region linear function fits the points very well, in the barrel deviation from the linear function is noticed especially around $P_{\mathrm{CB}} = 12 - 14$ GeV. This is observed in both, data and simulated events, hence the potential influence of the background is discarded. Also, there is no particular η or φ dependence of this effect, nor difference between small and large sectors or positively and negatively charged muons. Figure 4.21 shows the obtained fitted parameter values for 2011 and 2012, real data and simulation. There is a good agreement between 2011 and 2012 results, which indicates

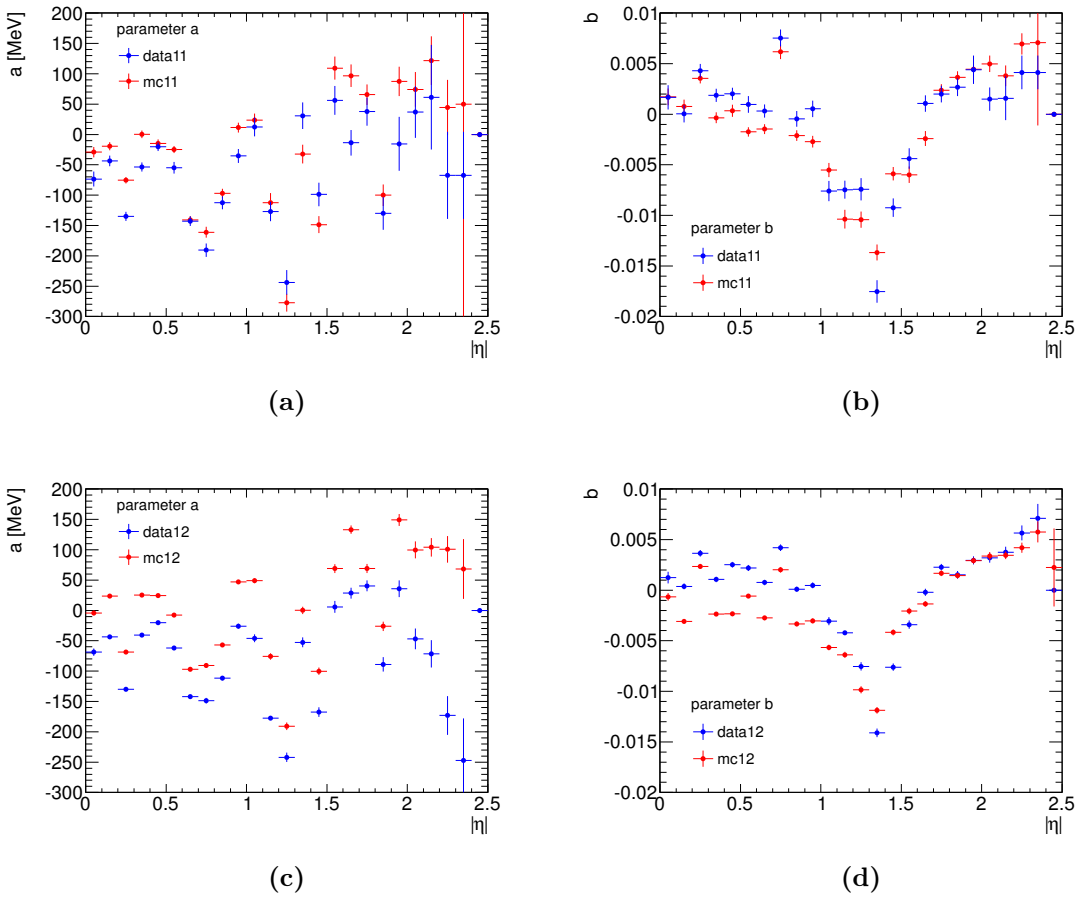

Figure 4.21: Obtained values of the parameters according to the Equation 4.11 as a function of pseudorapidity for 2011 (a) a and (b) b, and 2012 (c) a and (d) b, data (blue points) and simulation (red points).

the same underlying feature that causes the shift of the ME muon momentum with respect the momentum from the ID. There is a difference between data and simulation, represented as constant shift $\Delta a = a^{\mathrm{data}} - a^{\mathrm{MC}}$. The constant offset of parameter a for data in the barrel is around $50 - 100$ MeV, which is consistent with the observed mass offset with respect to the J/ψ PDG value estimated in Section 4.3.2. Value of the parameter b is ~ 0 in the barrel, and reaches around 1 % in the transition region. This momentum dependence indicates that the wrong estimation of the energy loss is

not the only reason for the observed offset with respect to the ID track. The values of parameter b in data and simulation have a constant shift in the barrel, but quite good agreement in the end-cap and forward region. The results of parameters a and b are summarised in the Tables 4.4 and 4.5 for 2011 and 2012 data-taking respectively.

Table 4.4: Values of the parameters a and b for 2011 data and simulation.

	2011 simulation				2011 data			
η	a [MeV]	δa [MeV]	b	δb	a [MeV]	δa [MeV]	b	δb
(0.0,0.1)	-29.2	8.6	0.0017	0.0008	-73.5	12.4	0.0017	0.0012
(0.1,0.2)	-19.3	6.8	0.0008	0.0007	-43.5	8.7	0.0001	0.0008
(0.2,0.3)	-75.4	5.1	0.0035	0.0005	-135.0	7.4	0.0043	0.0007
(0.3,0.4)	0.3	6.1	-0.0003	0.0005	-53.5	7.4	0.0019	0.0006
(0.4,0.5)	-14.9	6.6	0.0003	0.0006	-20.2	7.0	0.0020	0.0006
(0.5,0.6)	-24.8	5.7	-0.0017	0.0005	-54.7	9.6	0.0010	0.0008
(0.6,0.7)	-141.0	6.2	-0.0015	0.0005	-142.9	8.0	0.0003	0.0006
(0.7,0.8)	-161.1	9.0	0.0062	0.0007	-190.6	11.0	0.0075	0.0008
(0.8,0.9)	-96.9	7.3	-0.0021	0.0005	-112.6	10.5	-0.0004	0.0008
(0.9,1.0)	11.4	8.1	-0.0027	0.0006	-35.4	11.6	0.0005	0.0008
(1.0,1.1)	23.6	10.9	-0.0055	0.0007	12.5	15.6	-0.0076	0.0010
(1.1,1.2)	-112.6	15.9	-0.0104	0.0009	-126.8	16.0	-0.0074	0.0009
(1.2,1.3)	-277.3	14.6	-0.0104	0.0008	-243.8	20.4	-0.0074	0.0011
(1.3,1.4)	-32.2	15.6	-0.0137	0.0008	30.8	21.9	-0.0175	0.0011
(1.4,1.5)	-148.7	14.0	-0.0059	0.0007	-98.8	19.4	-0.0092	0.0009
(1.5,1.6)	109.3	19.0	-0.0060	0.0008	56.3	23.9	-0.0044	0.0010
(1.6,1.7)	96.7	18.5	-0.0024	0.0007	-13.6	21.0	0.0011	0.0008
(1.7,1.8)	65.7	16.9	0.0024	0.0006	37.6	23.2	0.0020	0.0008
(1.8,1.9)	-100.1	17.9	0.0036	0.0006	-130.2	26.8	0.0027	0.0009
(1.9,2.0)	87.5	24.3	0.0045	0.0007	-15.5	44.5	0.0044	0.0014
(2.0,2.1)	74.2	28.5	0.0050	0.0008	36.9	42.6	0.0015	0.0011
(2.1,2.2)	121.7	39.9	0.0038	0.0010	61.3	86.2	0.0016	0.0022
(2.2,2.3)	44.6	45.4	0.0070	0.0010	-67.2	71.8	0.0041	0.0017
(2.3,2.4)	49.9	374.6	0.0071	0.0082	0	0	0	0
(2.4,2.5)	0	0	0	0	0	0	0	0

In addition, the parameter values are extracted as defined in Equation 4.11 by separating positive and negative muons as well as large and small sectors in the MS, and the obtained values of the fitted parameters are in agreement with the ones shown in Figure 4.21.

The difference in the fitted values of parameter a in data and simulation $\Delta a = a^{\text{data}} - a^{\text{MC}}$ can be used to correct the observed difference in the mass scale between data and simulation, especially for the high η region. The values of Δa are shown in Figure 4.22 and Table 4.6, there is a good agreement between 2011 and 2012 datasets. The effect of this correction is demonstrated in Figure 4.23 on the mass obtained with corrected CB muon momentum $P_{\text{CB}}^{\text{corr}}$. The CB muon track is recalculated using $P_{\text{ME}}^{\text{corr}}$ and leaving all other covariant matrix elements unchanged in Equation 4.4.

Table 4.5: Values of the parameters a and b for 2012 data and simulation.

	2012 simulation				2012 data			
η	a [MeV]	δa [MeV]	b	δb	a [MeV]	δa [MeV]	b	δb
(0.0,0.1)	-4.2	3.9	-0.0006	0.0004	-68.7	6.0	0.0012	0.0006
(0.1,0.2)	23.7	2.4	-0.0031	0.0002	-43.4	3.2	0.0004	0.0003
(0.2,0.3)	-68.5	2.5	0.0023	0.0002	-130.2	3.4	0.0036	0.0003
(0.3,0.4)	25.3	2.1	-0.0024	0.0002	-40.7	2.9	0.0011	0.0003
(0.4,0.5)	24.4	2.5	-0.0023	0.0002	-20.2	3.3	0.0025	0.0003
(0.5,0.6)	-7.9	2.6	-0.0006	0.0002	-61.8	3.5	0.0022	0.0003
(0.6,0.7)	-97.1	2.6	-0.0027	0.0002	-142.2	3.2	0.0008	0.0002
(0.7,0.8)	-90.7	3.6	0.0020	0.0003	-148.8	4.4	0.0042	0.0003
(0.8,0.9)	-57.0	3.1	-0.0033	0.0002	-111.5	3.7	0.0001	0.0002
(0.9,1.0)	47.2	3.4	-0.0030	0.0002	-25.9	4.2	0.0005	0.0003
(1.0,1.1)	49.0	4.2	-0.0057	0.0003	-45.9	6.4	-0.0031	0.0004
(1.1,1.2)	-75.9	5.1	-0.0064	0.0003	-177.7	0.01	-0.0042	0.0001
(1.2,1.3)	-190.9	6.4	-0.0098	0.0004	-242.1	7.6	-0.0075	0.0004
(1.3,1.4)	0.1	6.0	-0.0119	0.0003	-52.6	8.3	-0.0141	0.0004
(1.4,1.5)	-100.2	6.0	-0.0042	0.0003	-167.6	7.9	-0.0076	0.0004
(1.5,1.6)	69.0	7.3	-0.0020	0.0003	5.7	9.8	-0.0034	0.0004
(1.6,1.7)	133.0	6.9	-0.0014	0.0003	28.5	9.0	-0.0002	0.0003
(1.7,1.8)	69.1	7.6	0.0017	0.0003	40.5	9.0	0.0023	0.0003
(1.8,1.9)	-26.2	7.8	0.0014	0.0003	-88.9	12.0	0.0015	0.0004
(1.9,2.0)	149.0	9.8	0.0029	0.0003	35.7	13.7	0.0029	0.0004
(2.0,2.1)	99.7	14.1	0.0034	0.0004	-46.9	17.1	0.0032	0.0005
(2.1,2.2)	104.0	15.2	0.0034	0.0004	-71.6	22.4	0.0038	0.0006
(2.2,2.3)	100.7	21.9	0.0042	0.0005	-173.1	31.83	0.0057	0.0007
(2.3,2.4)	68.3	49.2	0.0058	0.0010	-247.2	69.4	0.0071	0.0014
(2.4,2.5)	327.8	195.7	0.0022	0.0039	0	0	0	0

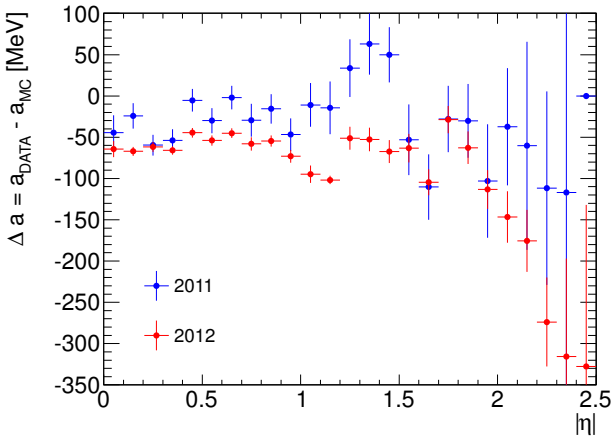

Figure 4.22: The difference of parameter a between data and simulation $\Delta a = a^{\text{data}} - a^{\text{MC}}$ for 2011 (blue points) and 2012 (red points).

Table 4.6: The difference of parameter a between data and simulation $\Delta a = a^{\text{data}} - a^{\text{MC}}$ for 2011 and 2012 data-taking.

	2011		2012	
η	Δa [MeV]	$\delta(\Delta a)$ [MeV]	Δa [MeV]	$\delta(\Delta a)$ [MeV]
(0.0,0.1)	-44.3	21.0	-64.4	9.9
(0.1,0.2)	-24.2	15.3	-67.1	5.6
(0.2,0.3)	-59.6	12.5	-61.7	6.0
(0.3,0.4)	-53.8	13.5	-66.0	5.0
(0.4,0.5)	-5.3	13.6	-44.6	5.8
(0.5,0.6)	-29.9	15.3	-53.9	6.1
(0.6,0.7)	-1.9	14.3	-45.1	5.8
(0.7,0.8)	-29.4	20.0	-58.1	8.0
(0.8,0.9)	-15.6	17.9	-54.5	6.8
(0.9,1.0)	-46.8	19.7	-73.1	7.7
(1.0,1.1)	-11.0	26.5	-94.9	10.5
(1.1,1.2)	-14.2	31.9	-101.8	5.1
(1.2,1.3)	33.6	34.9	-51.2	14.0
(1.3,1.4)	63.1	37.5	-52.7	14.3
(1.4,1.5)	49.9	33.5	-67.3	13.9
(1.5,1.6)	-53.1	42.9	-63.3	17.2
(1.6,1.7)	-110.4	39.5	-104.5	15.9
(1.7,1.8)	-28.0	40.1	-28.6	16.6
(1.8,1.9)	-30.0	44.7	-62.7	19.8
(1.9,2.0)	-103.0	68.8	-113.4	23.5
(2.0,2.1)	-37.3	71.1	-146.6	31.2
(2.1,2.2)	-60.4	126.2	-175.6	37.6
(2.2,2.3)	-111.8	117.2	-273.8	53.8
(2.3,2.4)	-49.9	374.6	-315.6	118.5
(2.4,2.5)	0	0	-327.8	195.7

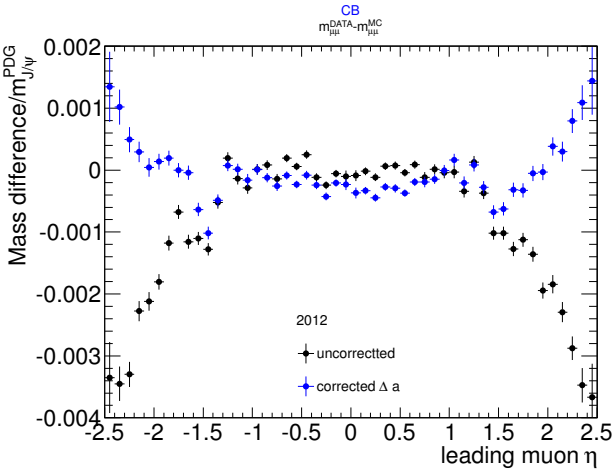

Figure 4.23: Relative mass difference between data and MC of the mean of the fitted J/ψ invariant mass distributions with CB muon momentum without any correction (black points), and with corrections as $P_{\text{ME}}^{\text{corr}} = P_{\text{ME}} - \Delta a$ (blue points). Combined muon is recalculated using $P_{\text{ME}}^{\text{corr}}$ leaving all other covariant matrix elements unchanged.

4.3.4 *Energy loss corrections*

The study performed in Section 4.3.3 is used to derive corrections that are applied to the ME muon momentum, and consequently to correct the CB muon momentum. A set of corrections, Δa, has been derived and tested in order to improve agreement between data and simulation. Also, a possibility of correcting both data and simulation in order to improve momentum calibration using the ID momentum as reference is studied. The corrections are derived as a function of the muon pseudorapidity, assuming that imperfection in φ are covered by the additional curvature smearing in the official smearing package.

Two approaches for the correction are considered:

- Use only parameter a from Equation 4.11 as an energy loss correction and apply it to the ME muon momentum:

$$P_{\mathrm{ME}}^{\mathrm{corr}} = P_{\mathrm{ME}} - a. \tag{4.12}$$

  Non-zero value for parameter b outside of barrel could be caused by the magnetic field, or any other effect which is not understood in detail, therefore it should be ignored from the correction procedure.

- Use the full correction from Equation 4.11 and apply it to the ME momentum:

$$P_{\mathrm{ME}}^{\mathrm{corr}} = P_{\mathrm{ME}} - (a + b \cdot P_{\mathrm{CB}}). \tag{4.13}$$

After the ME momentum is corrected, the CB muon momentum is recalculated from the covariance matrix, as defined in Equation 4.4, leaving all other elements of the covariance matrix unchanged, which is a reasonable approximation since the overall corrections are small. Both possibilities are tested, on the J/ψ and Z-boson events, in data and MC samples. Additional test is performed on the $Z' \to \mu\mu$ MC sample.

Figure 4.24 shows the results of the corrections on ME muon momentum applied on 2011 and 2012 data samples, the invariant mass is calculated with $P_{\mathrm{ME}}^{\mathrm{corr}}$ and the angles are taken from the ID, and then the mean of the Crystal Ball fit is shown as a function of muon pseudorapidity. Applying only parameter a obtained from momentum fits with data is correcting invariant mass distribution in barrel while having a small impact outside the barrel. However, the increasing bias in the regions with $|\eta|$ >2 remains uncorrected. Applying the full effective corrections, with parameters a and b from momentum fits with data show significant improvement in the whole η range. The effect of the corrections on the invariant mass calculated using CB momentum is shown in Figure 4.25 for 2011 and 2012 data samples. As for the ME momentum, using the full correction is decreasing the bias with respect to the PDG value for the entire η range.

The relative difference of the mean of iterative Gauss fit on J/ψ invariant mass calculated with the CB momentum for both approaches to the correction is shown

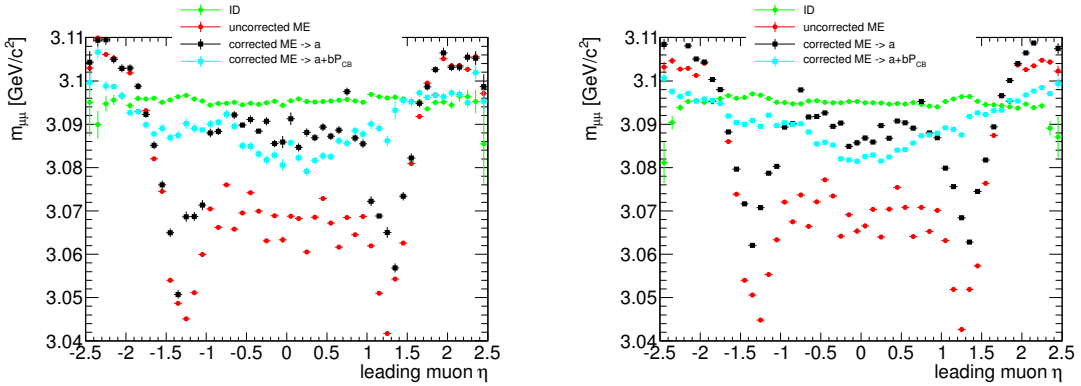

(a) **(b)**

Figure 4.24: Mean of the Crystal Ball fit on the J/ψ invariant mass distribution calculated with ME momentum without any correction (red points), and with corrections defined from 4.12 (black points) and 4.13 (cyan points) as a function of the leading muon pseudorapidity for (a) 2011 and (b) 2012 data samples. The green points represent the mean of the iterative Gaussian fit of the J/ψ invariant mass calculated with the ID momentum, shown for reference.

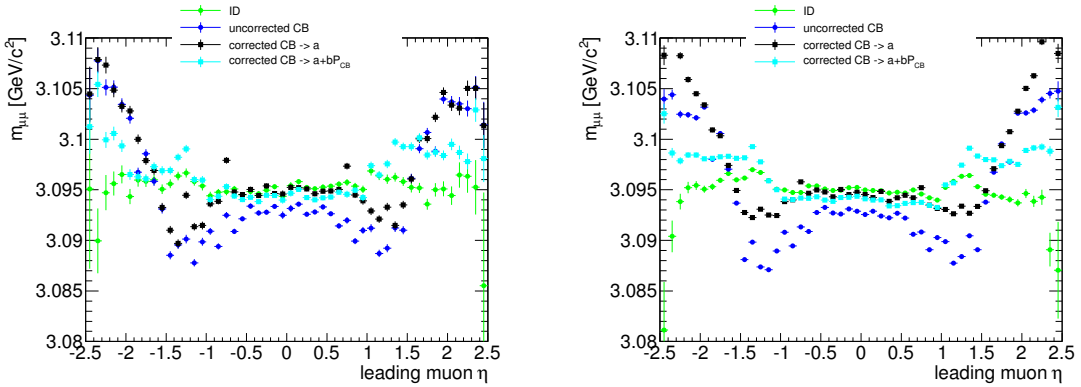

(a) **(b)**

Figure 4.25: Mean of the iterative Gauss fit on the J/ψ invariant mass distributions calculated with CB muon momentum without any correction (blue points), and with corrections defined from 4.12 (black points) and 4.13 (cyan points) as a function of the leading muon pseudorapidity for (a) 2011 and (b) 2012 data samples. The green points represent the mean of the iterative Gaussian fit of the J/ψ invariant mass calculated with the ID momentum, shown for reference. The CB momentum is recalculated using only $P_{\mathrm{ME}}^{\mathrm{corr}}$ while leaving all other covariant matrix elements unchanged.

in Figure 4.26 for 2012 data-taking, and similar results are obtained for 2011 data-taking. The discrepancy between data and simulation increased in the barrel for the full

momentum dependent corrections. It should be noted that here the Δa correction is not applied. Distributions of relative mass scale for data and MC show improvement in the region up to $|\eta|$ <2, when parameter b is taken to be 0. In the forward region, the mass seems to be degraded for the data but not for MC. The relative mass difference between data and MC is not affected in the forward region after applying the corrections. Applying full correction with non zero b term flattens the mass scale against η, with slight degradation of the relative mass scale between data and simulation in the barrel. With the proposed corrections, absolute mass scale is stabilised to be within 0.001% of the PDG value.

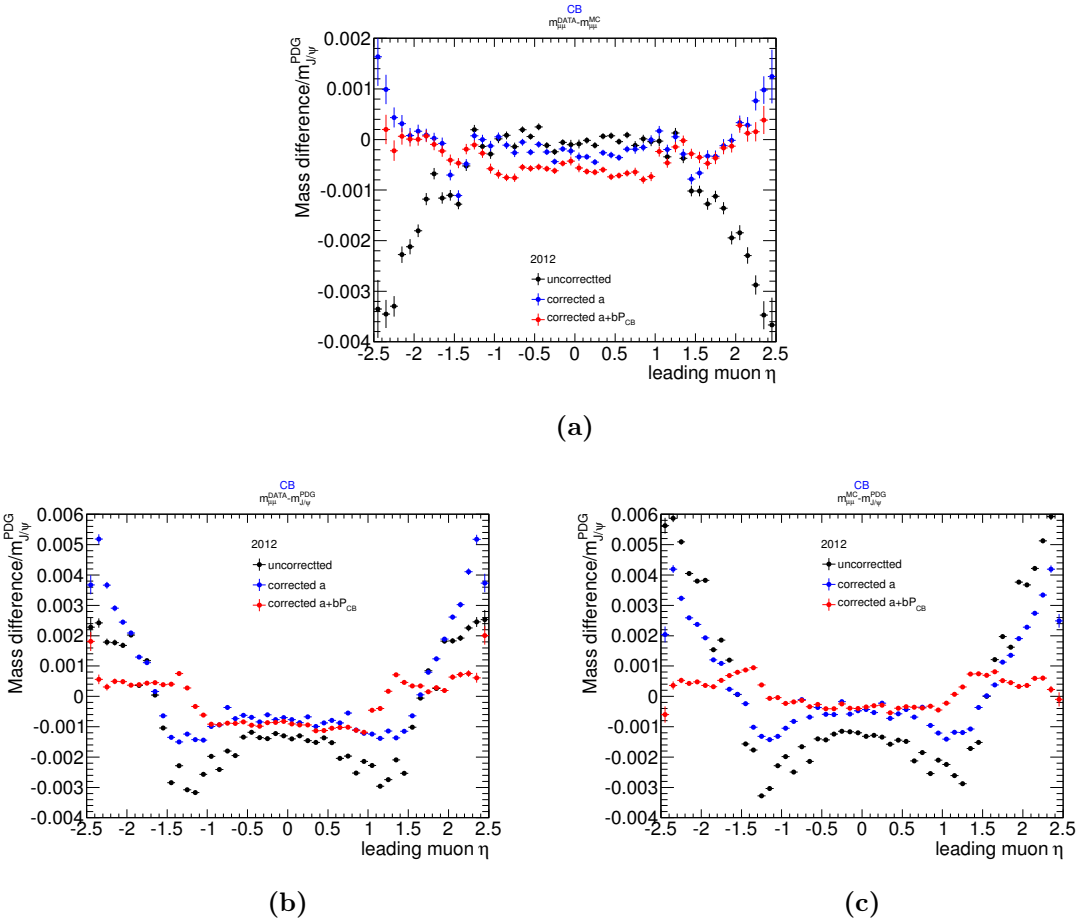

Figure 4.26: The relative difference of the mean of iterative Gauss fit on J/ψ invariant mass calculated with the CB momentum during 2012 data-taking without any correction (black points), and with corrections defined from 4.12 (blue points) and 4.13 (red points) as a function of the leading muon pseudorapidity between (a) data and MC, (b) data and PDG value, and (c) MC and PDG value, the definition of the mass difference is indicated on the plots.

The corrections are tested also on $Z \to \mu\mu$ events, as illustrated in Figure 4.27 for 2012 data samples, and similar results are obtained for 2011 data-taking. Similar results are obtained as for the J/ψ. Applying only constant shift improves mass scale in the barrel, but slightly in the transition and end-caps regions. In the forward region

applying only parameter a increases the bias in the peak position. The results of the full correction applied on data are showing almost uniform value of the invariant mass across the whole η region.

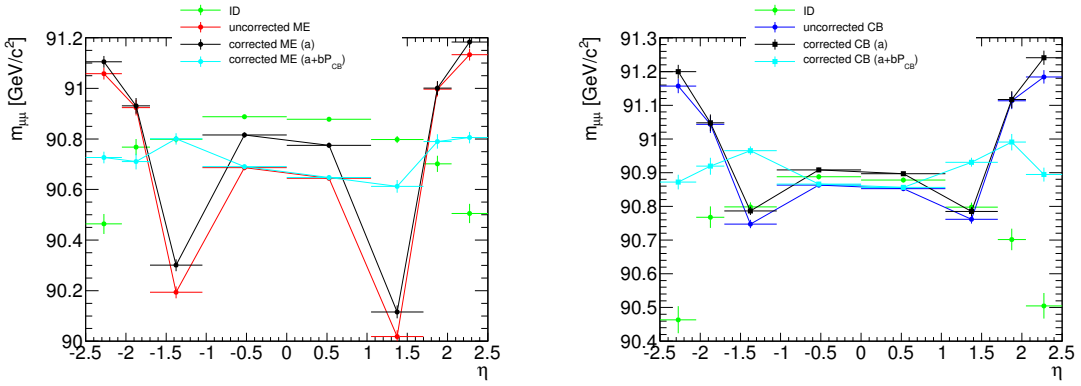

(a) **(b)**

Figure 4.27: The most probable value of the $Z \to \mu\mu$ invariant mass distributions calculated with (a) ME and (b) CB muon momentum without any correction, and with corrections defined from 4.12 (black points) and 4.13 (cyan points) as a function of muon pseudorapidity for 2012 data samples. The η corresponds to the the centre of the pseudorapidity bin in which both muons are reconstructed. The CB muon is recalculated using $P_{\mathrm{ME}}^{\mathrm{corr}}$ while leaving all other covariant matrix elements unchanged.

The corrections are also tested on simulated $Z' \to \mu\mu$ events with ($m_{Z'} = 2$ TeV) events, as illustrated in Figure 4.28. The Z' invariant mass is calculated with CB momentum. Even though the correction is momentum dependent, there is no visible effect on the peak position of the reconstructed resonance, and the average muon transverse momentum is ~ 1 TeV in this sample. Also, there is an improvement in the resolution of the invariant mass distribution after the correction.

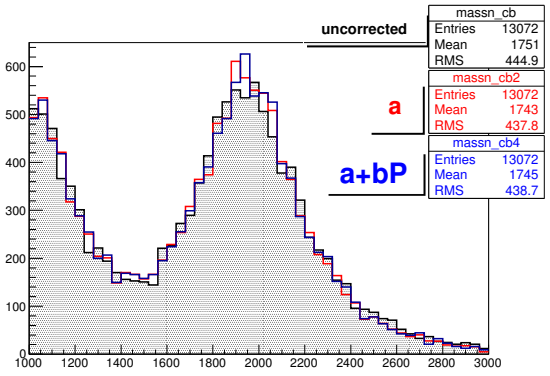

Figure 4.28: $Z' \to \mu\mu$ invariant mass distribution calculated with CB muon momentum without any correction (black line), and with corrections defined from 4.12 (red line) and 4.13 (blue line). The CB muon is recalculated using $P_{\mathrm{ME}}^{\mathrm{corr}}$ while leaving all other covariant matrix elements unchanged.

4.4 MUON MOMENTUM CALIBRATION IN RUN-1

The MC simulation includes a precise description of the detector geometry, material distribution and physics model approximations, nevertheless additional correction is needed to accurately describe the characteristics of the muon momentum reconstructed in experimental data. The standard method to determine scale and resolution corrections is to study the well defined resonances, like J/ψ, Υ and Z-boson dimuon decays. Then, the muon momentum is parametrised and corrections are extracted for the two subdetectors used in the muon momentum reconstruction, the ID and the MS. The desired precision is to describe the muon momentum scale to the per-mile level and the muon momentum resolution to the percent level.

The resolution of the dimuon resonances incorporates the muon momentum resolution effects of both muons from the decay. Figure 4.29 illustrates the resolution of the J/ψ, Υ and Z-boson dimuon resonances as a function of pseudorapidity of the highest p_{T} muon, measured in data during 2012. For all three resonances there is a difference in resolution of ID, CB and MS muons. For central pseudorapidity, the CB muon resolution is dominated by the ID measurement, while for the high pseudorapidity region the resolution in MS is better. Since the resolution of the CB momentum is the best for the full pseudorapidity range, it is very important to simultaneously use and correct both, the measurements in the ID and the MS.

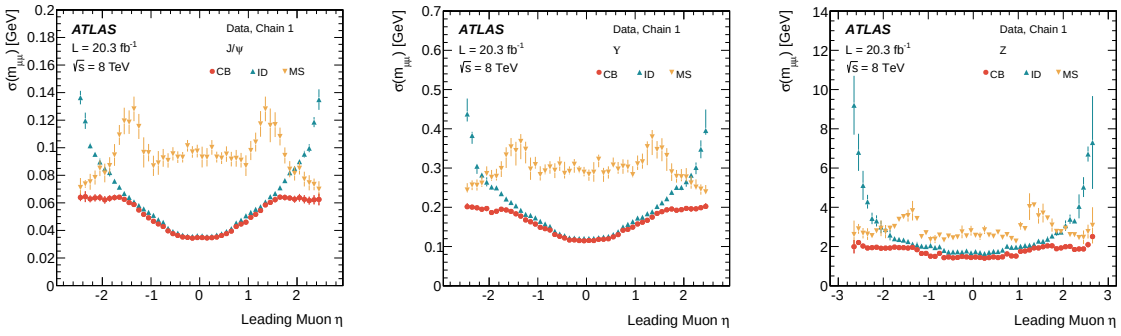

(a) **(b)** **(c)**

Figure 4.29: Dimuon invariant mass resolution for CB, MS and ID muon reconstruction for (a) J/ψ, (b) Υ and (c) Z events measured in data during 2012 as a function of the pseudorapidity of the highest p_{T} muon [79].

This section describes the muon momentum corrections used in Run-1, based on large statistics samples of J/ψ and Z-boson dimuon decays. The full procedure for the muon reconstruction performance with the ATLAS detector is defined in [187] and [79]. Moreover, these are the first studies which are using J/ψ resonance for the muon momentum calibration, in 2010 the muon momentum was calibrated using only the Z decay [196]. The use of both, J/ψ and Z-boson dimuon decays, allows the sensitivity to the reconstructed muon momentum in the range from a few to approximately 100 GeV.

4.4.1 *Muon momentum scale and resolution corrections evaluated from $J/\psi \to \mu\mu$ and $Z \to \mu\mu$ decays*

The simulated muon transverse momentum reconstructed in the ID and in the MS subdetectors $p_{\mathrm{T}}^{\mathrm{corr\,Det}}$ with Det = ID, MS, is parametrised by the following equation [79]:

$$p_{\mathrm{T}}^{\mathrm{corr\,Det}} = \frac{p_{\mathrm{T}}^{\mathrm{MC,Det}} + s_0^{\mathrm{Det}}(\eta,\varphi) + s_1^{\mathrm{Det}}(\eta,\varphi)p_{\mathrm{T}}^{\mathrm{MC,Det}}}{1 + \frac{\Delta r_0^{\mathrm{Det}}(\eta,\varphi)g_0}{p_{\mathrm{T}}^{\mathrm{MC,Det}}} + \Delta r_1^{\mathrm{Det}}(\eta,\varphi)g_1 + \Delta r_2^{\mathrm{Det}}(\eta,\varphi)p_{\mathrm{T}}^{\mathrm{MC,Det}}g_2}, \tag{4.14}$$

with $s_0^{\mathrm{ID}} = 0$ and $\Delta r_0^{\mathrm{ID}} = 0$, where

- g_i $(i = 0, 1, 2)$ are normally distributed random variables with zero mean and unit width,
- $s_i^{\mathrm{Det}}(\eta,\varphi)$ $(i = 0, 1)$ are scale correction terms applied to a specific detector region,
- $\Delta r_i^{\mathrm{Det}}(\eta,\varphi)$ $(i = 0, 1, 2)$ are momentum resolution smearing correction terms applied to a specific detector region.

The corrections described with Equation 4.14 are defined up to $|\eta| < 2.7$ in 18 η sectors of sizes $\Delta\eta$ from 0.2 to 0.4 for both the MS and the ID. The MS is additionally separated into φ to account for small and large sectors in the MS. The sector boundaries are listed in Table 2.3 where the odd numbered sectors are large and even numbered are small. The variations of the corrections between different regions is expected to be small.

The term s_0^{MS} model the p_{T} scale dependence observed in the MS momentum reconstruction due to differences between data and MC in the energy loss of muons passing through the calorimeter and other materials between the interaction point and the MS. These energy loss effects are observed with preceding J/ψ studies described in Section 4.3. Since the energy loss between the interaction point and the ID is negligible (about 1 MeV per silicon layer), the term is fixed to be $s_0^{\mathrm{ID}} = 0$. The term s_1^{Det} corrects the imperfect knowledge of the magnetic field integral and of the radial dimension of the detector.

The muon momentum resolution smearing correction terms can be related to different sources of experimental resolution by comparing the coefficient of the p_{T} powers in the Equation 4.2. The energy loss term Δr_0^{ID} is fix to zero, while Δr_0^{MS} is not, in order to account for energy loss fluctuations in the calorimeter material present in front of the MS.

The separate corrections of ID and MS momentum reconstruction are extracted and a corrected CB momentum is obtained using a weighted average:

$$p_{\mathrm{T}}^{\mathrm{corr\,CB}} = f p_{\mathrm{T}}^{\mathrm{corr\,ID}} + (1-f) p_{\mathrm{T}}^{\mathrm{corr\,MS}}, \tag{4.15}$$

where f is derived weight for each muon taken from the CB muon transverse momentum before corrections, extracted from:

$$p_{\mathrm{T}}^{\mathrm{MC,\,CB}} = f p_{\mathrm{T}}^{\mathrm{MC,\,ID}} + (1-f) p_{\mathrm{T}}^{\mathrm{MC,\,MS}}. \tag{4.16}$$

The Equation 4.14 contains three parameters for the ID and five for the MS momentum, which gives total of eight parameters that need to be extracted from the experimental data. The parameters are extracted comparing the data to the templates from the MC simulation using a maximum likelihood fit of the invariant mass distribution in J/ψ and Z-boson dimuon candidate events. For the muon momentum calibration procedure it is assumed that all differences between data and MC simulation are due to miscalibration of the muon momentum and the impact of an inaccurate measurement of the angles is neglected.

The J/ψ and Z candidates are selected by requiring exactly two opposite charged CB muons which need to satisfy the track quality criteria described in Table 4.1. In order to suppress the backgrounds, muons from the Z-boson decays are required to be isolated from neighbouring activity. Muons are isolated if they have a sum of transverse momenta measured in the ID around the muon less then 10% of the muon p_{T}. No isolation criterion is imposed on muons from the J/ψ decays. Muons for ID parameter extraction are required to have 8 GeV $< p_{\mathrm{T}}^{\mathrm{ID}} <$ 17 GeV and 2.76 GeV $< m_{\mu\mu}^{\mathrm{ID}} <$ 3.6 GeV for J/ψ candidates and 26 GeV $< p_{\mathrm{T}}^{\mathrm{ID}} <$ 300 GeV and 76 GeV $< m_{\mu\mu}^{\mathrm{ID}} <$ 96 GeV for Z-boson candidates, where the lower boundary for the sub-leading muon p_{T} from Z-boson decay is set to a smaller value of 15 GeV. In order to improve the sensitivity to the p_{T} dependent correction effects, the invariant mass is classified according to the p_{T} of the muons. For the J/ψ candidates there are three bins with lower thresholds at $p_{\mathrm{T}}^{\mathrm{ID}} = 8$, 9, 11 GeV of the sub-leading muon, and for the Z candidates the lower thresholds are set to $p_{\mathrm{T}}^{\mathrm{ID}} = 26$, 47, 70 GeV of the leading muon. The muon selection for MS parameter extraction is the same as for the ID with one additional variable sensitive to the momentum scale and resolution, reconstructed only for Z-boson candidates defined as:

$$\rho = \frac{p_{\mathrm{T}}^{\mathrm{MS}} - p_{\mathrm{T}}^{\mathrm{ID}}}{p_{\mathrm{T}}^{\mathrm{ID}}}. \tag{4.17}$$

which represents the p_{T} imbalance between the measurement in the ID and in the MS. This variable is binned with lower thresholds set to $p_{\mathrm{T}}^{\mathrm{MS}} = 20$, 30, 35, 40, 45, 55, 70 GeV. The non-resonant background for J/ψ decay coming from decays of light and heavy hadrons and from DY production, is about 15 % from selected candidates and it is not possible to accurately simulate it. Therefore, for J/ψ extraction of the background a data-driven method is used: the invariant mass distribution is fitted with Crystal Ball function for the ID fits and a Gaussian distribution convoluted with a Landau in the MS fits, added to an exponential background. The background for the Z-boson decay is extracted from simulation, and yields only 0.1 %.

The templates of $m_{\mu\mu}^{\mathrm{ID}}$ and $m_{\mu\mu}^{\mathrm{MS}}$ are built from the simulation with added background using J/ψ and Z candidates, as well as for ρ using only the Z candidates. The fitting procedure is done in several steps. First, a likelihood function $\mathcal{L}$ is defined in order to compare the data to the final signal plus background templates. Then modified templates are generated by varying the correction parameters in Equation 4.14 and applying them to the muon momentum in simulation. The last step is minimisation of the $-2\ln\mathcal{L}$ between data and the modified templates. This procedure is iterated for all regions (η, φ and p_{T}), the first fit is done using only events with both muons in the same region, while the following fits also allow one of the muons in a previously

analysed region. When all regions are analysed, the fit procedure is iterated twice to improve the stability of the results. The corrections are extracted first for the ID and then for the MS so that the $p_{\mathrm{T}}^{\mathrm{ID}}$ in ρ is kept as constant.

The sensitivity of the resolution parameters Δr_0^{MS} and Δr_2^{MS} as a function of p_{T} is bad because of limited statistics for low p_{T} from the J/ψ and at high p_{T} from the Z candidates. Since the energy loss correction parameter Δr_0^{MS} for $|\eta| < 0.8$ don't show significant disagreement between data and MC, it is fixed to zero in this region. The effect of the misalignment of MS chambers in real data is already taken into account in the simulation, therefore the parameter Δr_2^{MS} is also fixed to zero. Possible deviations from zero for these two parameters is covered by the systematic uncertainties.

Systematic uncertainties are applied to cover the imperfections in the model used for the muon momentum parametrisation and in the fit procedure used for the extraction of the correction parameters. Configurations that are used for the evaluation of the systematic uncertainties are described below.

• *Z-boson mass range*: To cover resolution differences between data and MC for non-Gaussian smearing effects, the variation of ±5 GeV in the dimuon invariant mass range for Z-boson events is applied. This is one of the largest systematic uncertainties on the resolution corrections, with an average effect approximately 10 % on the Δr_1^{ID}, Δr_2^{ID} and Δr_1^{MS} parameters.

• *J/ψ background and p_T selection*: The alternative J/ψ background parametrisation is done with linear function for the MS fits and linear-times-exponential function for the ID fits. The minimal p_{T} cut is increased to 10 GeV which reduces the weight of low p_{T} momentum corrections since the J/ψ sample is smaller. The effect on the resolution parameters is about 10 % on Δr_1^{ID} and Δr_1^{MS}, while the effect on scale parameters is about 0.01 GeV and $4 \cdot 10^{-4}$ for s_0^{MS} and s_1^{MS} respectively.

• *Non-linearity of ID scale*: ID parameters are also extracted using only J/ψ or only Z events. Due to reduced statistics, only parameter s_1^{ID} is left free in the fit with the resolution correction terms fixed to nominal values. The obtained uncertainty yields from 0.01 % to 0.05 % from the central to the forward region of the ID.

• *Energy loss resolution parameter*: Instead of fixing the parameter Δr_0^{MS} to zero for $|\eta| < 0.8$, it is left free for all regions. The largest variation of 0.08 GeV is applied as an additional systematic uncertainty on this parameter.

• *Misalignment effects*: The MS parameters are extracted from a special Z-boson sample with ideal geometry, where there is no simulation of the misalignment of the MS chambers. The largest variation of 0.012 for Δr_1^{MS} is applied as an additional systematic uncertainty for $0.4 < |\eta| < 1.25$.

• *Z background*: The normalisation factor for the MC samples in the Z-boson background estimate is variated by factors of 0.5 and 2. This systematic uncertainty is small except for $|\eta| > 2.0$ where this effect is comparable to the other uncertainties.

• *Excess of material in ID*: In the MC simulation there is an excess of material in the ID for $|\eta| > 2.3$ which is affecting the muon momentum resolution. Systematic uncertainty is added for $|\eta| > 2.3$ to cover for this effect, $2 \cdot 10^{-3}$ and 0.01 for s_1^{ID} and

Δr_1^{ID}, respectively. This is the largest source of uncertainty for ID parameters.

• η *binning*: The position of the Z-boson mass peak is checked in finer η bins and additional systematics of $2 \cdot 10^{-4}$ to the s_1^{ID} parameter is added to cover for the observed differences.

• *Muon track angle*: Increasing the track angular resolution by 40 % in MC simulation for J/ψ events is used to check the effect of an additional correction on the angle of the muon track. The largest difference of 0.001 is added as an uncertainty to the Δr_1^{ID} parameter.

• *MS alignment*: The alignment of MS chambers is checked with special runs when the toroid magnetic field is turned off. The systematics on Δr_2^{MS} parameter is defined as the difference between these special runs and the nominal data.

All sources are added in quadrature to obtain the final uncertainty for eight correction parameters. In order to simplify the procedure for use in physics analysis, four systematics variations are provided: global upper and lower scale variations and independent resolution variations for the ID and the MS. The upper and lower scale variations are defined as a simultaneous variation of all scale or resolution correction parameters by $1\,\sigma$. The parametrisation in Equation 4.14 is invalid when the resolution in experimental data is smaller than in the MC simulation. This is covered by including the amount of resolution that should be subtracted in quadrature from the simulation to reproduce the data in the positive resolution parameter variations.

A summary of the correction parameter values is shown in Tables 4.7 and 4.8 for ID and MS respectively, after averaging over the three main detector regions. Figure 4.30 shows ID, and Figures 4.31 and 4.32 show MS parameter values, the total systematic and statistical uncertainty are added in quadrature and shown as a yellow band around the nominal values.

Table 4.7: Summary of ID scale and resolution parameters with their total uncertainty averaged over three main detector regions.

Region	s_1^{ID}	Δr_1^{ID}	Δr_2^{ID} [TeV^{-1}]
$\lvert\eta\rvert < 1.05$	$-0.92^{+0.26}_{-0.22} \cdot 10^{-3}$	$0.0068^{+0.0010}$	$0.146^{+0.039}$
$1.05 \leq \lvert\eta\rvert < 2.0$	$-0.86^{+0.30}_{-0.35} \cdot 10^{-3}$	$0.0105^{+0.0018}$	$0.302^{+0.046}$
$\lvert\eta\rvert \geq 2.0$	$-0.49^{+1.17}_{-1.63} \cdot 10^{-3}$	$0.0069^{+0.0121}$	$0.088^{+0.084}$

The ID scale correction is always below 0.1% with an uncertainty in the range from 0.02% for $|\eta| < 1$ to 0.2% for $|\eta| > 2.3$. The MS scale correction is less than 0.1% except for the large MS sectors in the barrel region of the detector where the correction is 0.3% and for $1.25 < |\eta| < 1.5$ where correction is about -0.4%. The MS energy loss correction is approximately 30 MeV, which corresponds to the 1% of the total energy loss in the calorimeter and in the dead material in front of the MS and is compatible with the accuracy of the material budget used in the simulation. The total resolution correction is below 10% and 15% for ID and MS parameters respectively.

Table 4.8: Summary of MS scale and resolution parameters with their total uncertainty for small (s) and large (l) MS sectors averaged over three main detector regions.

Region	s_0^{MS} [GeV]	s_1^{MS}	Δr_0^{MS} [GeV]	Δr_1^{MS}	Δr_2^{MS} [TeV^{-1}]
$\lvert\eta\rvert < 1.05$ (s)	$-0.035^{+0.017}_{-0.011}$	$+3.57^{+0.38}_{-0.60} \cdot 10^{-3}$	$0.115^{+0.083}$	$0.0030^{+0.0079}$	$0^{+0.21}$
$\lvert\eta\rvert < 1.05$ (l)	$-0.022^{+0.007}_{-0.014}$	$-0.22^{+0.37}_{-0.24} \cdot 10^{-3}$	$0.101^{+0.090}$	$0.0034^{+0.0081}$	$0^{+0.11}$
$1.05 \leq \lvert\eta\rvert < 2.0$ (s)	$-0.032^{+0.017}_{-0.016}$	$-1.07^{+0.77}_{-0.93} \cdot 10^{-3}$	$0^{+0.080}$	$0.0171^{+0.0059}$	$0^{+0.22}$
$1.05 \leq \lvert\eta\rvert < 2.0$ (l)	$-0.026^{+0.009}_{-0.017}$	$-1.46^{+0.45}_{-0.57} \cdot 10^{-3}$	$0^{+0.080}$	$0.0190^{+0.0047}$	$0^{+0.17}$
$\lvert\eta\rvert \geq 2.0$ (s)	$-0.031^{+0.029}_{-0.031}$	$-0.91^{+1.62}_{-0.91} \cdot 10^{-3}$	$0^{+0.080}$	$0.0022^{+0.0075}$	$0^{+0.06}$
$\lvert\eta\rvert \geq 2.0$ (l)	$-0.057^{+0.019}_{-0.021}$	$+0.40^{+1.23}_{-0.50} \cdot 10^{-3}$	$0^{+0.080}$	$0.0171^{+0.0052}$	$0^{+0.29}$

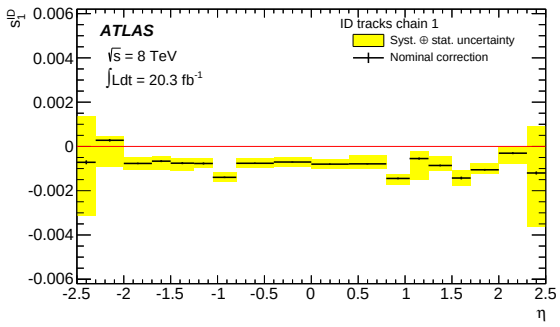

(a)

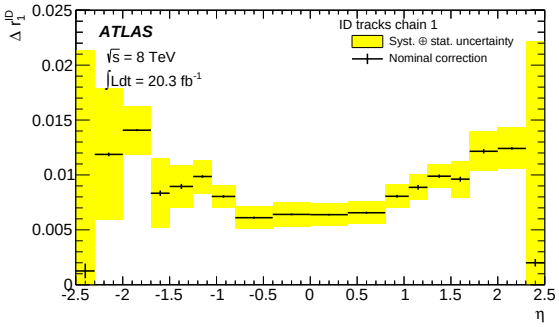

(b)

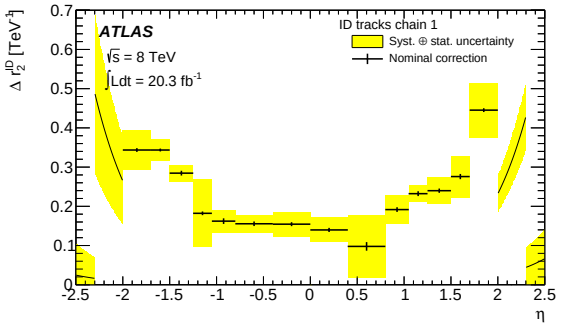

(c)

Figure 4.30: The ID correction parameters as a function of pseudorapidity: (a) scale correction s_1^{ID}, (b) resolution parameter Δr_1^{ID} and (c) resolution parameter Δr_2^{ID}. The parameter Δr_2^{ID} for $|\eta| > 2.0$ appear as a curved line because the correction is weighted by $1/\tan^2\theta$ which follows the steep resolution change in that region. The black lines show the nominal correction values, while the total systematic and statistical uncertainty added in quadrature are shown as a yellow band around the nominal values.

The same procedure is repeated for 2011 data-taking and similar results are obtained but with larger uncertainties since the sample is smaller.

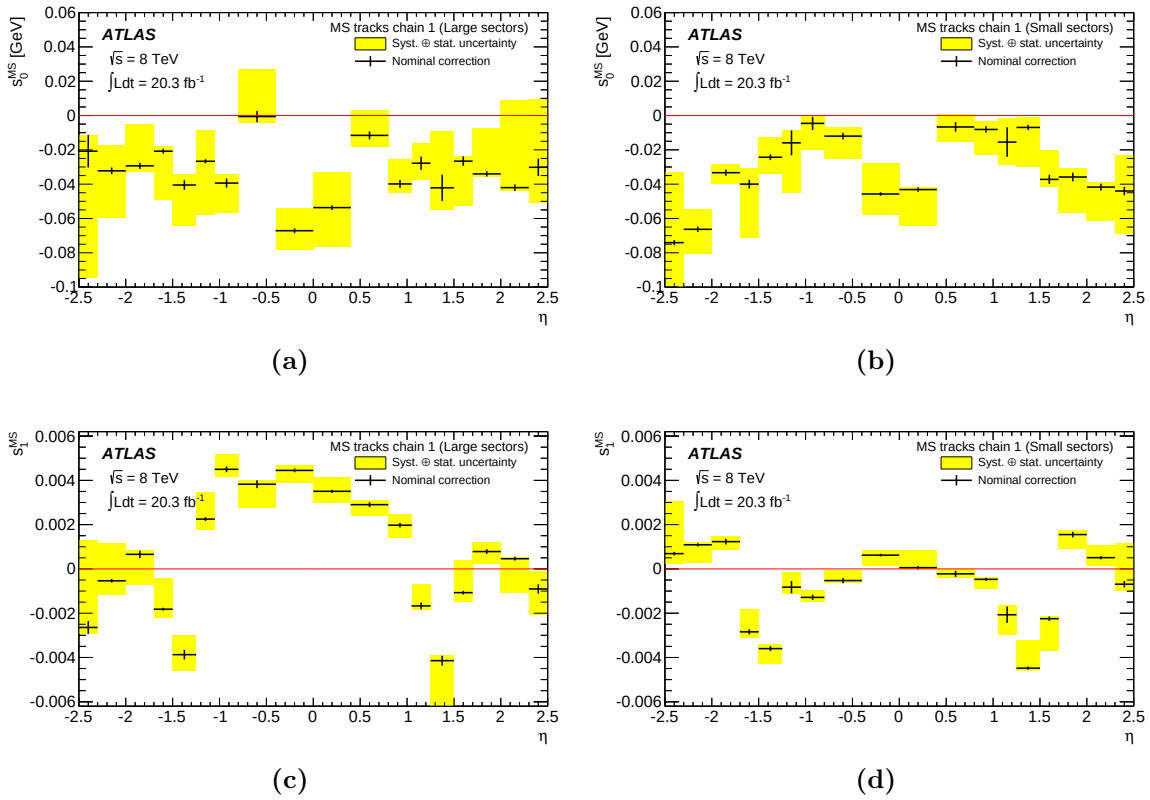

Figure 4.31: The MS scale correction parameters for large (left) and small (right) sectors as a function of pseudorapidity: (a) and (b) s_0^{MS}, and (c) and (d) s_1^{MS}. The black lines show the nominal correction values, while the total systematic and statistical uncertainty added in quadrature are shown as a yellow band around the nominal values.

4.4.2 *Validation of the muon momentum scale and resolution corrections with $J/\psi \to \mu\mu$ decay*

The validation of the momentum scale and resolution corrections is obtained by studying dimuon decays of J/ψ, Υ and Z resonances with a different methodology than the one used for the parameter extraction. The Υ dimuon decay represents an independent validation. The corrected MC is in very good agreement with the data. In the next part only the validation with the J/ψ decay is shown. The validation with Υ and Z resonances can be found in [79].

The J/ψ events are selected as described in Table 4.1, the only difference is in the last cut which is not applied here. After selection there are about 17 million events in real data and about 20 million simulated events. The J/ψ background is obtained using a second order polynomial fit in the two sideband regions outside the mass peak: 2.55 GeV $< m_{\mu\mu} <$ 2.9 GeV and 3.3 GeV $< m_{\mu\mu} <$ 4.0 GeV. The background is then subtracted from the signal mass window.

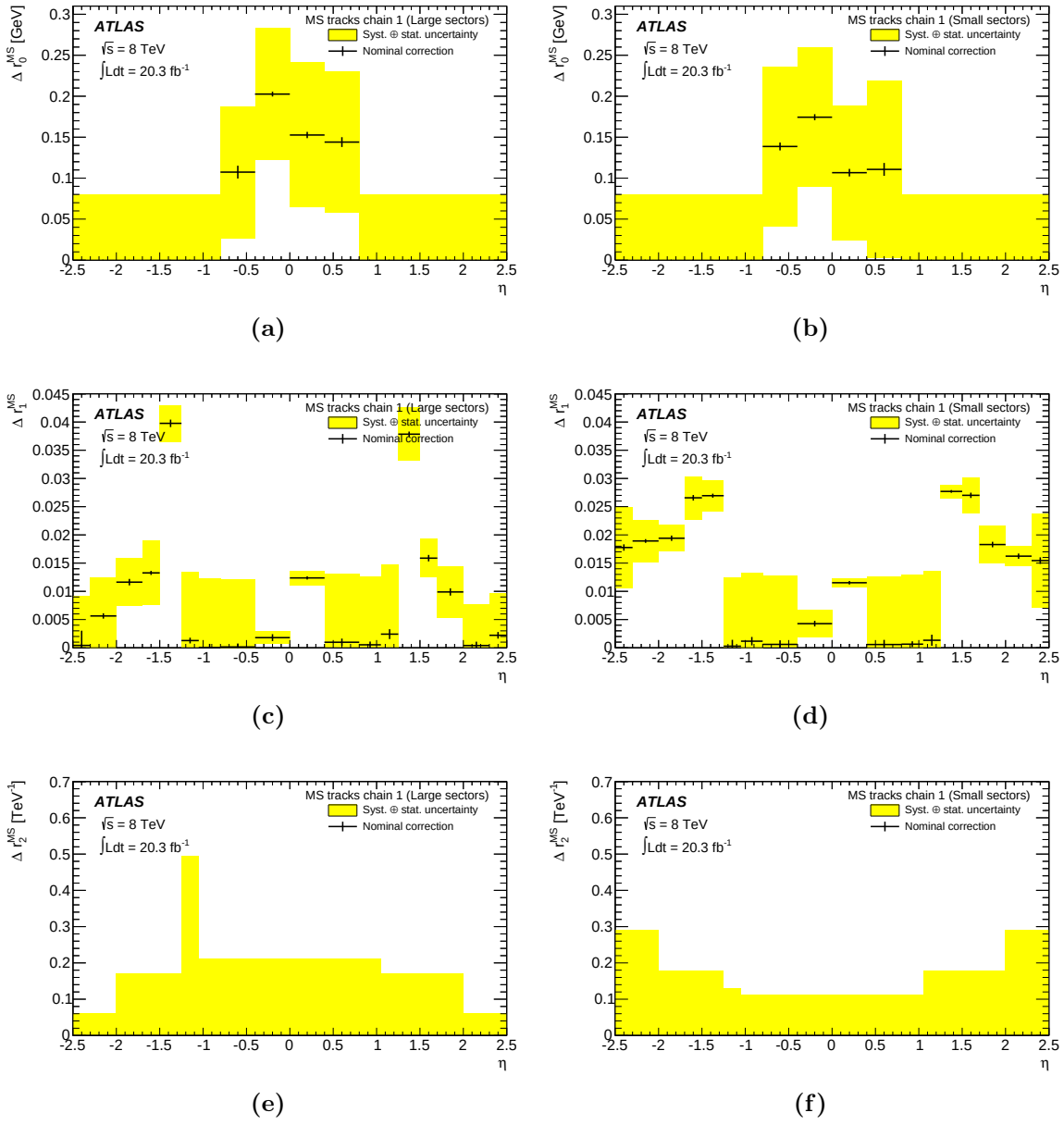

Figure 4.32: The MS resolution correction parameters for large (left) and small (right) sectors as a function of pseudorapidity: (a) and (b) Δr_0^{MS}, (c) and (d) Δr_1^{MS}, and (e) and (f) Δr_2^{MS}. The black lines show the nominal correction values, while the total systematic and statistical uncertainty added in quadrature are shown as a yellow band around the nominal values.

The invariant mass distribution for J/ψ resonance is shown in Figure 4.33, comparing the MC simulation before and after correction with the data. The background estimate is added to the signal simulation and the sum of background and signal MC is normalized to the data. The invariant mass distribution before corrections is narrower and slightly shifted with respect to data. After corrections, the J/ψ lineshape agree very well with the data.

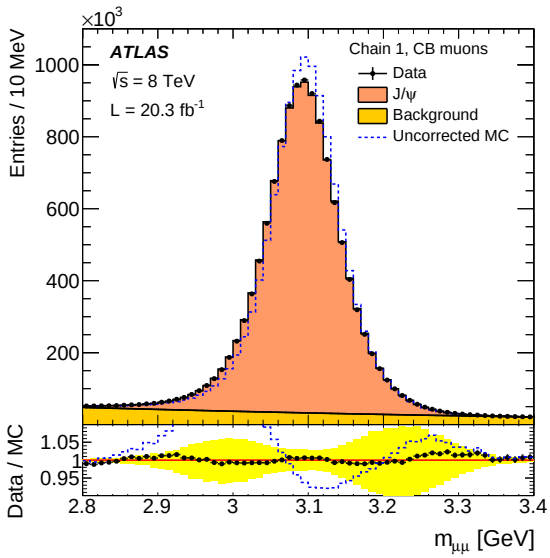

Figure 4.33: Dimuon invariant mass distribution of J/ψ resonance reconstructed with CB muons. The upper panel shows the invariant mass distribution for data and for the signal MC simulation plus the background estimate. The points show the data, the filled histograms show the MC simulation when momentum corrections are applied and the dashed histogram shows the MC simulation when no correction is applied. The lower panel shows the Data/MC ratio and the yellow band represents the systematic uncertainties on the momentum corrections.

A better estimate of the scale corrections is obtained by comparing the mean of the invariant mass peak as a function of η and p_{T}. The mean of the J/ψ invariant mass is extracted with a iterative Gaussian fit (as explained in Section 4.3.2) of the background subtracted signal distribution in the range $< m_{\mu\mu} > \pm 1.5 \cdot \mathrm{RMS}(m_{\mu\mu})$. Figure 4.34 shows the data to MC ratio of the mean mass of J/ψ resonance as a function of the pseudorapidity of the highest-p_{T} muon of the CB muon pair. Before the momentum corrections there is a large discrepancy, up to 5 %, between data and MC for high $|\eta|$ region. This discrepancy is due to imperfections in the MC simulation of the muon energy loss that have larger effect at low p_{T} and in the forward η region where the MS measurement has a larger weight in the MS and ID combination. The corrected MC is

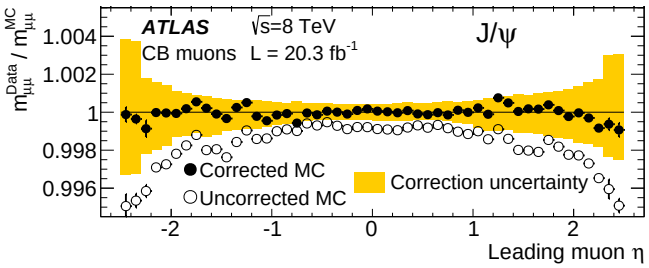

Figure 4.34: Ratio of the fitted J/ψ mean mass for data and corrected MC as a function of the pseudorapidity of the highest-p_{T} muon. The ratio shows corrected MC (filled symbols) and uncorrected MC (empty symbols). The error bars represent the statistical and the systematic uncertainty on the mass fits added in quadrature. The band shows the uncertainty on the momentum corrections.

in very good agreement with the data, well within the scale systematics uncertainties. Figure 4.35 shows the mean of the iterative Gaussian fit of invariant mass distribution of the dimuon J/ψ resonance (marked with blue triangles) as a function of $< p_{\mathrm{T}} >$ defined as average momentum of the two muons from the J/ψ decay for three pseudorapidity bins. Figure 4.35 also shows the results with Υ and Z resonances. The momentum scale is well known and within the uncertainties in the whole p_{T} range.

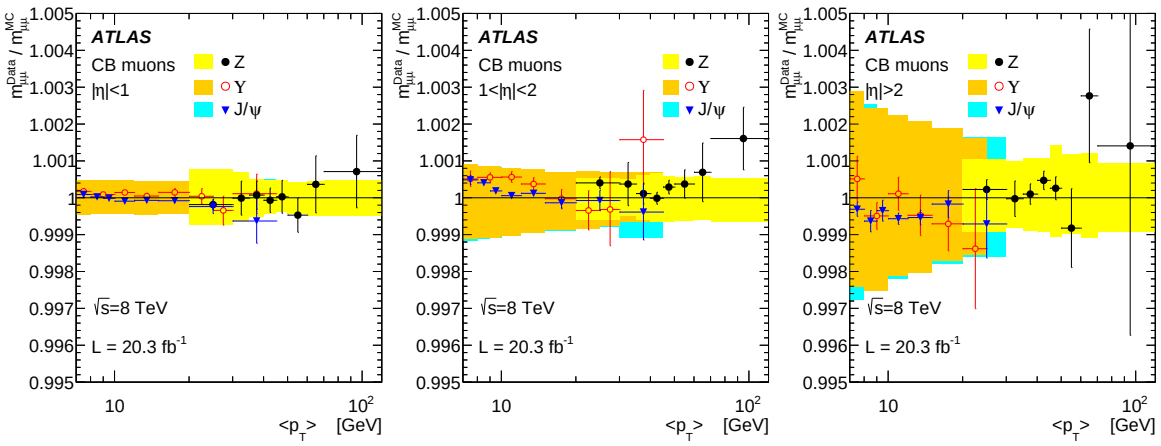

(a) **(b)** **(c)**

Figure 4.35: Ratio of the fitted mean mass of data and corrected MC from J/ψ, Υ and Z events as a function of the average transverse momentum in three pseudorapidity ranges: (a) $|\eta| < 1.0$, (b) $1.0 < |\eta| < 2.0$ and (c) $|\eta| > 2.0$, using CB muons. Both muons are required to be in the same η range. The error bars represent the statistical uncertainty and the systematic uncertainty is shown as a band.

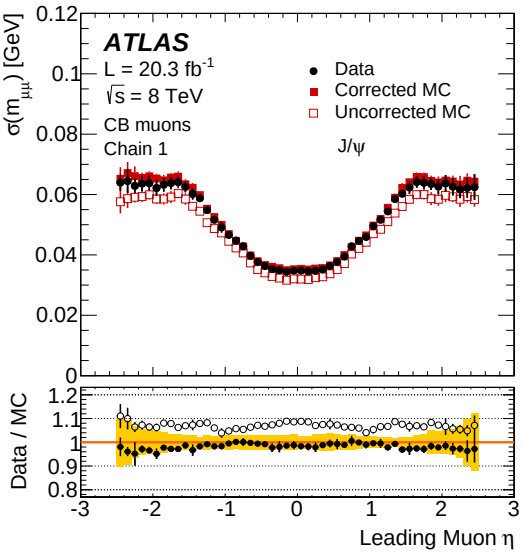

Figure 4.36: J/ψ dimuon invariant mass resolution for CB muons as a function of the pseudorapidity of the highest-p_{T} muon. The upper plot shows the fitted resolution parameter for data, uncorrected MC and corrected MC, while the lower panel shows the data to MC ratio. The error bars represent the statistical uncertainty and the systematic uncertainty is shown as a band.

The dimuon mass width for CB muons is shown as a function of the leading muon η in Figure 4.36 for the J/ψ resonance. The width is estimated from the iterative Gaussian fit as explained previously. Before corrections, the mass width in MC is up to 10% smaller than in the data, while after corrections there is very good agreement with the data.

Energy loss estimation from the momentum fits

In order to further test the energy loss correction parameters defined with Equation 4.14, the momentum fits with the J/ψ events are performed, as explained in Section 4.3.3. The muon momentum difference between ID and MS is fitted using Crystal ball function in bins of $\Delta\eta = 0.2$. The difference with Equation 4.11 is in the CB momentum, here the transverse momentum $p_{\mathrm{T,\,CB}}$ is used. The parameters a and b are extracted from linear fits in data and MC simulation before and after the momentum corrections. The demonstration of the effectiveness of the momentum calibration is obtained by comparing the difference in parameters a and b between data and MC simulation before and after the corrections: $\Delta a = a^{\mathrm{data}} - a^{\mathrm{MC}}$ and $\Delta b = b^{\mathrm{data}} - b^{\mathrm{MC}}$. Figure 4.37 shows the dependence of Δa and Δb as a function of pseudorapidity before and after momentum corrections. Before the momentum corrections there is an offset in the barrel region of about 50 to 100 MeV which is larger for high $|\eta|$ region, while after the corrections the overall difference between data and MC is consistent with zero and the biggest improvement is observed in high $|\eta|$ region. Also, there is visible improvement between data and MC for parameter b after the momentum corrections for full η region.

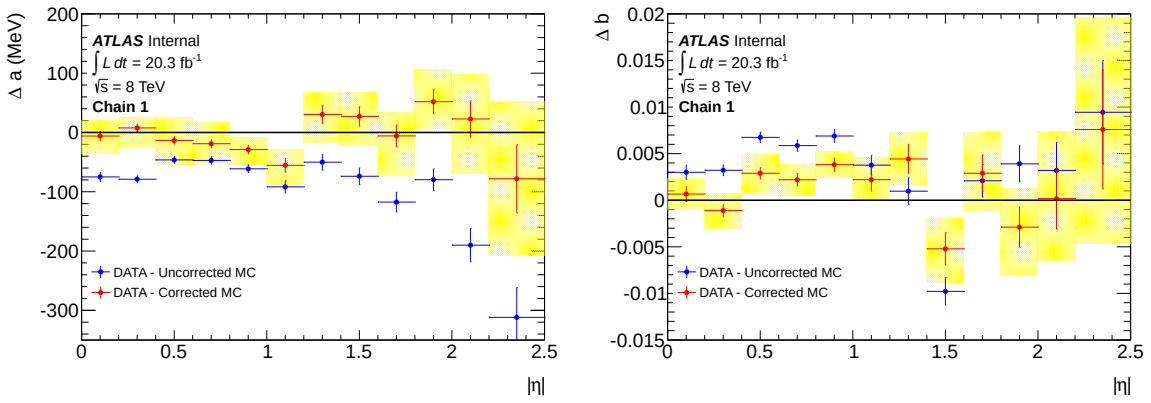

(a) **(b)**

Figure 4.37: Difference of the parameters (a) a and (b) b between the data and MC simulation before (blue points) and after (red points) the momentum corrections as a function of $|\eta|$. The error bars on the points represent the statistical uncertainty of the fit, while the yellow band represents statistical uncertainty of the fit added in quadrature to the systematic uncertainty from the scale variations.

Muon momentum scale in small and large MS sectors

Muon momentum reconstruction is expected to have different performance for large and small MS sectors due to material distribution, alignment of the components, magnetic filed integral, etc. However, the observed data to MC difference of about 0.3 % in MS scale correction in the barrel region, as shown in Figure 4.31 (c) and (d), is an unexpected feature which is investigated. There are two variables that are sensitive to the MS scale difference between large and small sectors:

- Relative mass difference $\Delta m/m_{\text{ref}}$ defined as the data to MC difference divided by the mass value in PDG. The mass peak position is extracted with an iterative Gaussian fit.
- Difference between small and large sectors in ρ defined with Equation 4.17. The ρ peak position is extracted with an iterative Gaussian fit.

These two variables are checked on J/ψ and Z events which are selected requiring two oppositely charged CB muons in the barrel. The muon transverse momentum is required to be in the range $7.5 < p_{\text{T}} < 20$ GeV and $25 < p_{\text{T}} < 100$ GeV for J/ψ and Z candidates, respectively. Selected candidates have invariant mass in range $3.0 < m_{\mu\mu} < 3.2$ GeV and $86.2 < m_{\mu\mu} < 96.2$ GeV for J/ψ and Z decays, respectively. Since the point of this study is comparison between small and large sectors, there is no background estimation.

Figure 4.38 shows relative mass difference for J/ψ and Z events for 16 MS sectors separated by the leading muon. There is about 0.2 % difference between large and small sectors in data to MC simulation before the momentum corrections difference. Since the subleading muon from the decay can be reconstructed in a different sector, the estimation is not very precise.

Figure 4.39 shows the comparison between large and small sectors in ρ as a function of leading muon p_{T}. Events with $|\rho| < 0.15$ are only selected. The peak position is extracted with iterative Gaussian fit in each p_{T} bin, and then the obtained values are subtracted for large and small sectors. Now, a more quantitative estimate of the muon momentum scale differences between data and MC is possible. An energy loss effect would cause a difference between data and MC which decreases with p_{T}, while a multiplicative scale factor would induce a constant difference. There is about 0.3 % difference between data and MC which is constant as a function of p_{T}, indicating the presence of the the multiplicative scale effect.

Finally, the crosscheck is performed to test whether the difference between large and small MS sectors is caused by the magnetic field integral. Since the small sectors include the toroid coils, the expansion or shrinking of the coil geometry of the order of 0.2 % is not excluded with Run-1 data, a toy model study of this effect on the magnetic field integral has been done [187]. A toy model assumes a simple detector geometry, with 16 MS sectors corresponding to the large and small segmentation and seven wide barrel regions. The magnetic field integral is evaluated in each of these regions along the radial direction when the coils are expanded or shrunk by 5 mm which corresponds to 0.2 %. Figure 4.40 (a) shows the effect of the modified coils

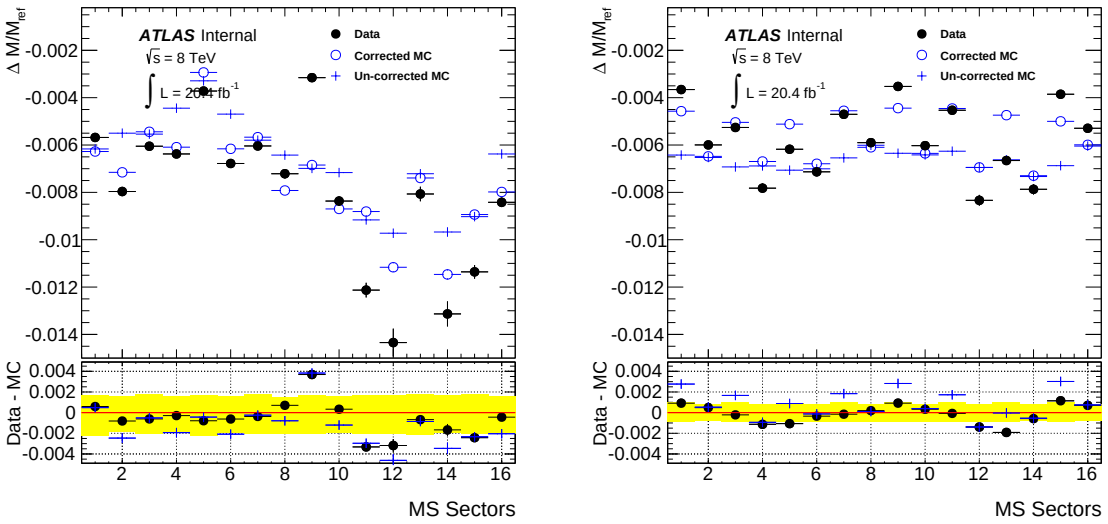

Figure 4.38: The relative mass difference for (a) J/ψ and (b) Z events as a function of MS sector depending on the leading muon φ, for data and MC simulation before and after muon momentum corrections. The yellow band in the bottom panel corresponds to the systematics uncertainties of the momentum corrections.

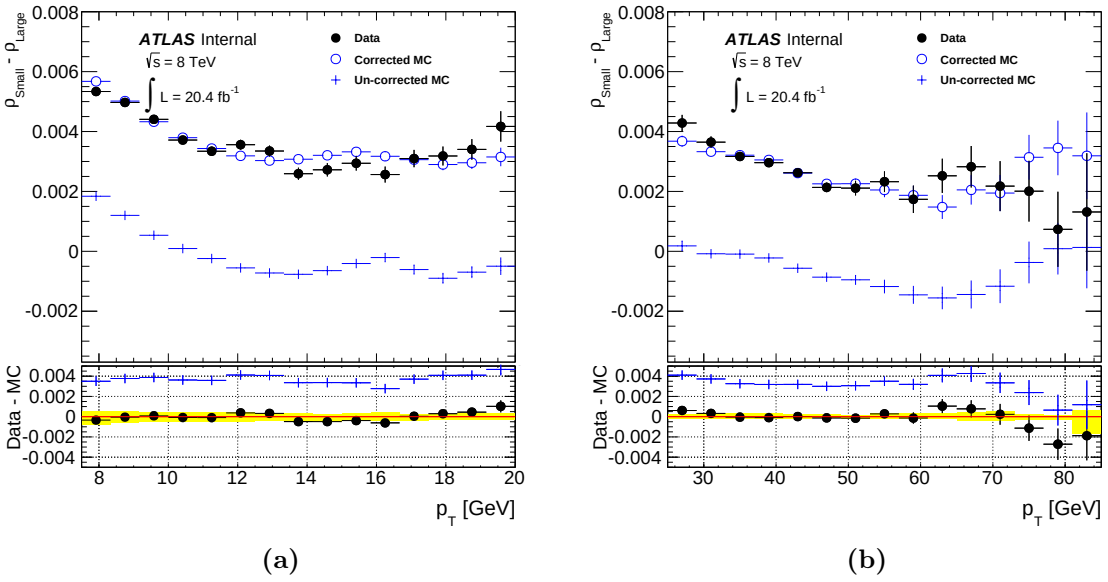

Figure 4.39: The difference in ρ for small and large MS sectors for (a) J/ψ and (b) Z events as a function of leading muon p_{T}, for data and MC simulation before and after muon momentum corrections. The yellow band in the bottom panel corresponds to the systematics uncertainties of the momentum corrections.

geometry as a correction to the magnetic field integral in each of the 16 MS sectors. This toy model can be compared to the data by analysing the ρ variable as a function

of $\hat{\varphi} = \varphi \mod \pi/4$. Variable $\hat{\varphi}$ folds the MS detector in one distribution overlaying all the large MS sectors around $\hat{\varphi} = 0$ and small sectors around $\hat{\varphi} = \pm\pi/8$. Figure 4.40 (b) and (c) shows ρ as a function of $\hat{\varphi}$ for J/ψ and Z events, respectively, in data and MC before and after momentum corrections. The structure expected from the toy study is reproduced, at least qualitatively, by the difference between the data and MC simulation before the momentum corrections.

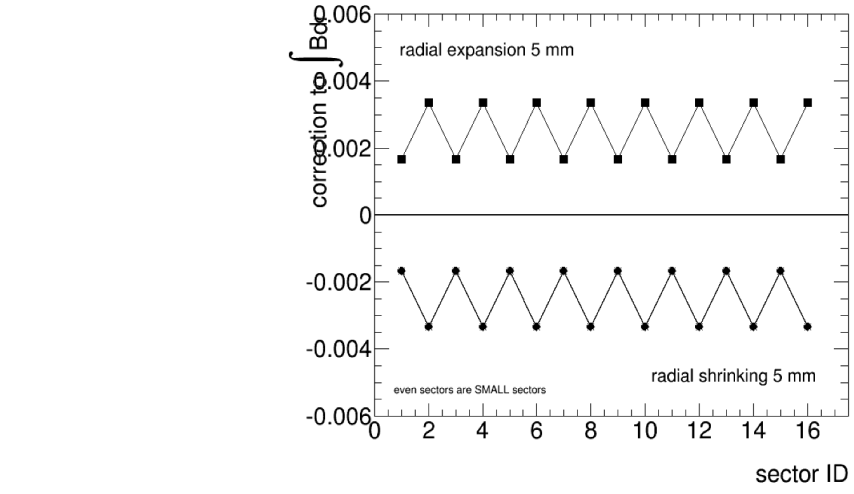

(a)

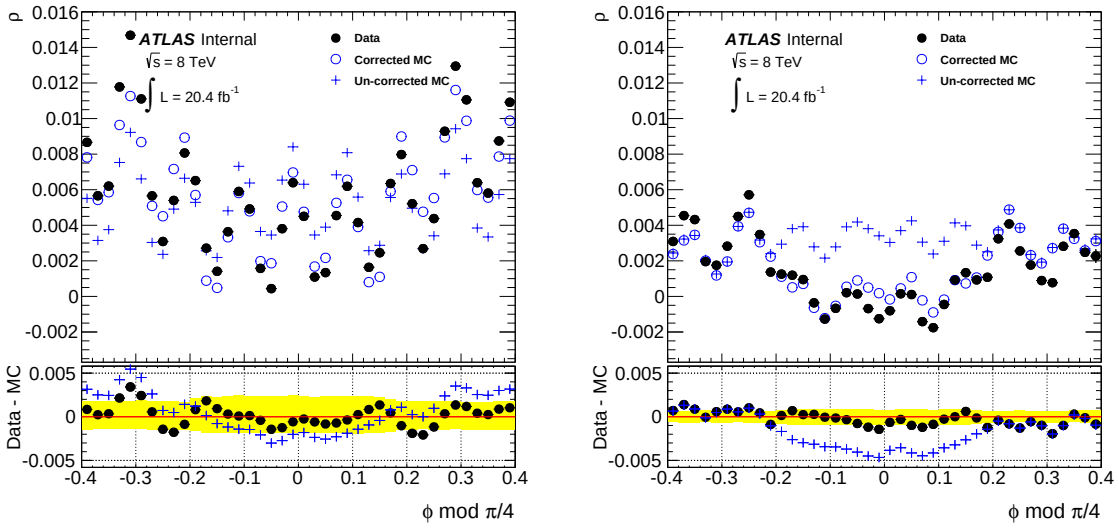

(b) (c)

Figure 4.40: (a) A toy model of the ATLAS MS geometry when a magnetic field integral is changed by expansing or shrinking the toroid coils by 5 mm. The dependence of ρ as a function of $\hat{\varphi}$ for (b) J/ψ and (c) Z events, for data and MC simulation before and after muon momentum corrections. The yellow band in the bottom panel corresponds to the systematics uncertainties of the momentum corrections.

Angular distributions in J/ψ events

The $p_{\mathrm{T}}-Y$ reweighting, described in 4.3.1, affects the opening angle between two muons from the J/ψ decay $\cos\theta(\mu_1,\mu_2)$, as shown in Figure 4.41 for four pseudorapidity regions. The blue histograms show MC events without reweighting, while the red histogram show MC events after the reweighting is applied, both muons are required to be the same $|\eta|$ bin indicated on the plots. Distributions obtained from real data contain background events as well, although the impact of the background should be small since tight invariant mass requirement is imposed. The distributions show that applied reweighting fixes the difference between the opening angle in data and MC. Also, the distributions show that opening angle between the muons is small, decreasing with the muon η.

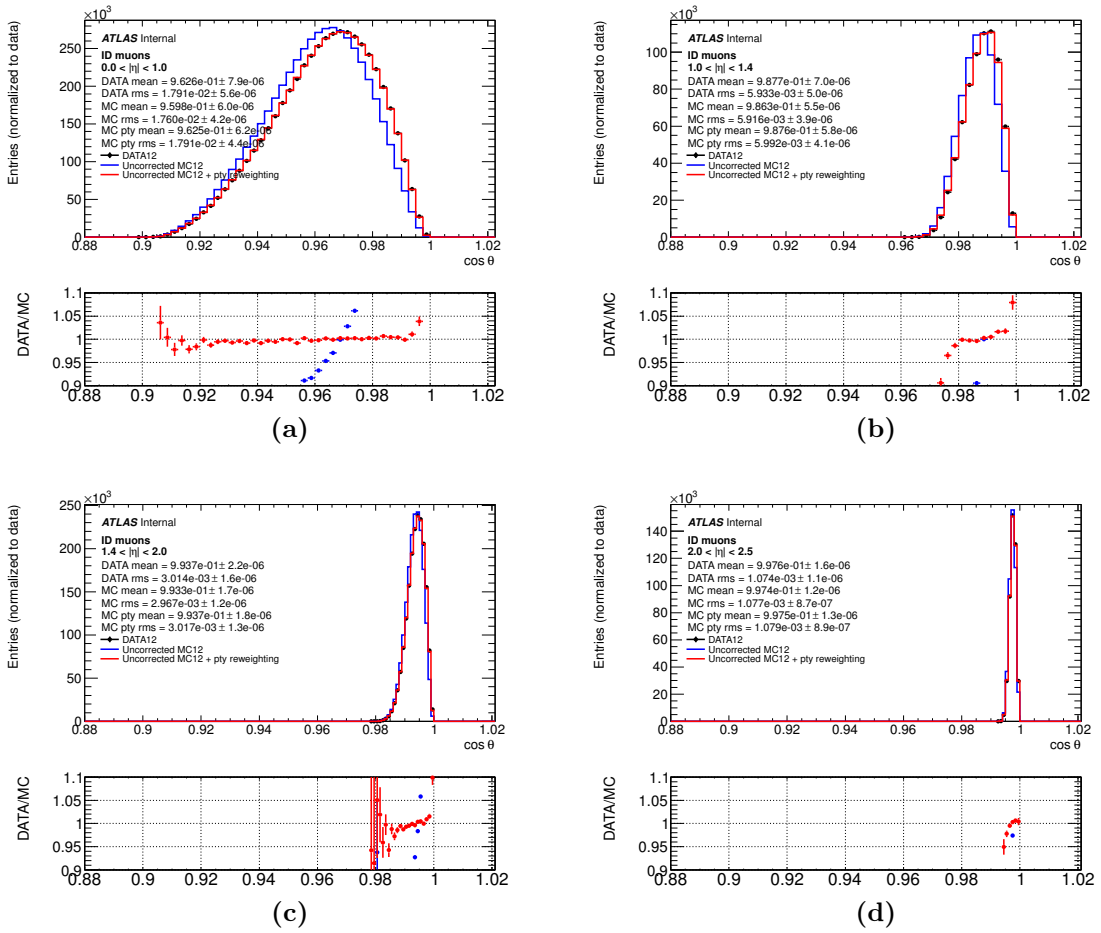

Figure 4.41: Distribution of the opening angle $\cos\theta(\mu_1,\mu_2)$ between the muons from the J/ψ decay for data (black points) and MC before (blue line) and after (red line) reweighting. Both muons are required to be in the same pseudorapidity bin: (a) $|\eta| < 1.0$, (b) $1.0 < |\eta| < 1.4$, (c) $1.4 < |\eta| < 2.0$ and $|\eta| > 2.0$.

The effect of the reweighting on the dimuon invariant mass calculated using ID, CB, and MS muon momentum is shown in Figure 4.42 (a), (b) and (c), respectively. The

effect on the mass distribution is at the % level. Figure 4.42 (d) shows the effect of the reweighting on the ID momentum scale correction s_1^{ID} as a difference of the calculated scale with and without reweighting applied as a function of detector region. The effect of the reweighting is bellow 10^{-4} except for two endcap regions where the difference is at the level of 0.04 % and in one CSC region with the difference of 0.1 %. Since the effect of this reweighting is small no additional systematic uncertainty is assigned to the muon momentum corrections.

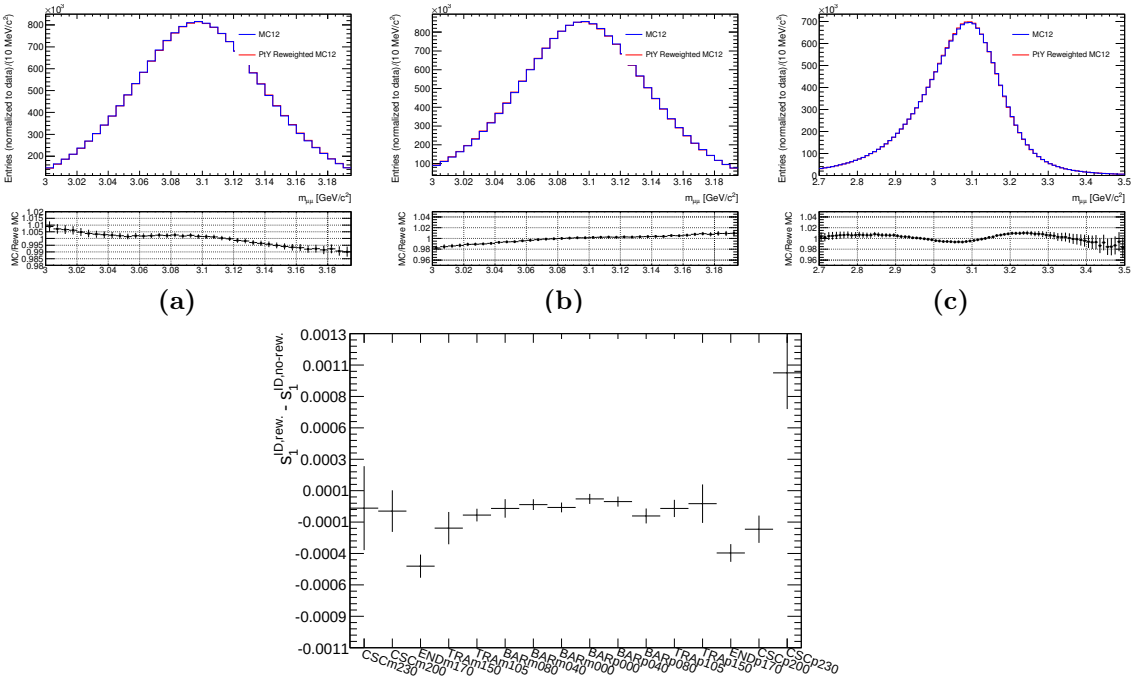

Figure 4.42: The invariant mass distribution calculated using (a) ID, (b) CB and (c) MS muons in the J/ψ MC sample, blue histogram is before while red histogram is after reweighting. The ratio of reweighted and unreweighted events is shown in the bottom part of each histogram. (d) The difference of the scale correction s_1^{ID} with and without reweighting applied as a function of a detector region.

The impact of the the additional material that might be present in the ID on the measurement of the muon angles θ and φ is also studied. The width of the reconstructed J/ψ invariant mass peak is affected by the momentum resolution and also, to a smaller extent, by the angular resolution. The effect of angular resolution has been neglected and all the difference in resolution between data and MC has been absorbed into the additional smearing of the momentum. The impact of the angular resolution on the invariant mass measurement increases as the opening angle of the muon pair decreases. Therefore it is expected to have larger impact on the J/ψ rather that on the Z events. In the region of the J/ψ measurement, the angular resolution is dominated by the multiple scattering. Then, additional material may affect the width of the J/ψ invariant mass distribution in two ways: through the degradation of the angular resolution and through the degradation of the momentum resolution.

In order to check if an increase of the angular resolution due to an increase of multiple scattering can have a significant impact on the scale and on the resolution parameters, following study has been performed. The possible effect of material on the angular resolution is studied by comparing the reconstructed θ and φ angles to the MC truth for each muon in J/ψ decay samples with nominal and distorted geometry. The sample produced with distorted geometry has 10 % additional material uniformly distributed across the ID. Figures 4.43 and 4.44 show the difference between reconstructed and truth muon θ and φ, respectively, in J/ψ events for MC samples corresponding to the nominal and distorted geometry is four pseudorapidity regions. The truth muons are matched with reconstructed CB muons for $p_{\mathrm{T}} > 7$ GeV with a matching requirement of $\Delta R < 0.02$. The effect of 10 % additional material would introduce a negligible bias of the angular measurements, at a level of 10^{-6}, as shown by the differences in the means in Figures 4.43 and 4.44. Also, the angular resolution increases, with an increase of the RMS of the distributions at the level of 5 - 7 %, except for the θ measurement in the barrel where the increase is at the level of 2 - 3 %.

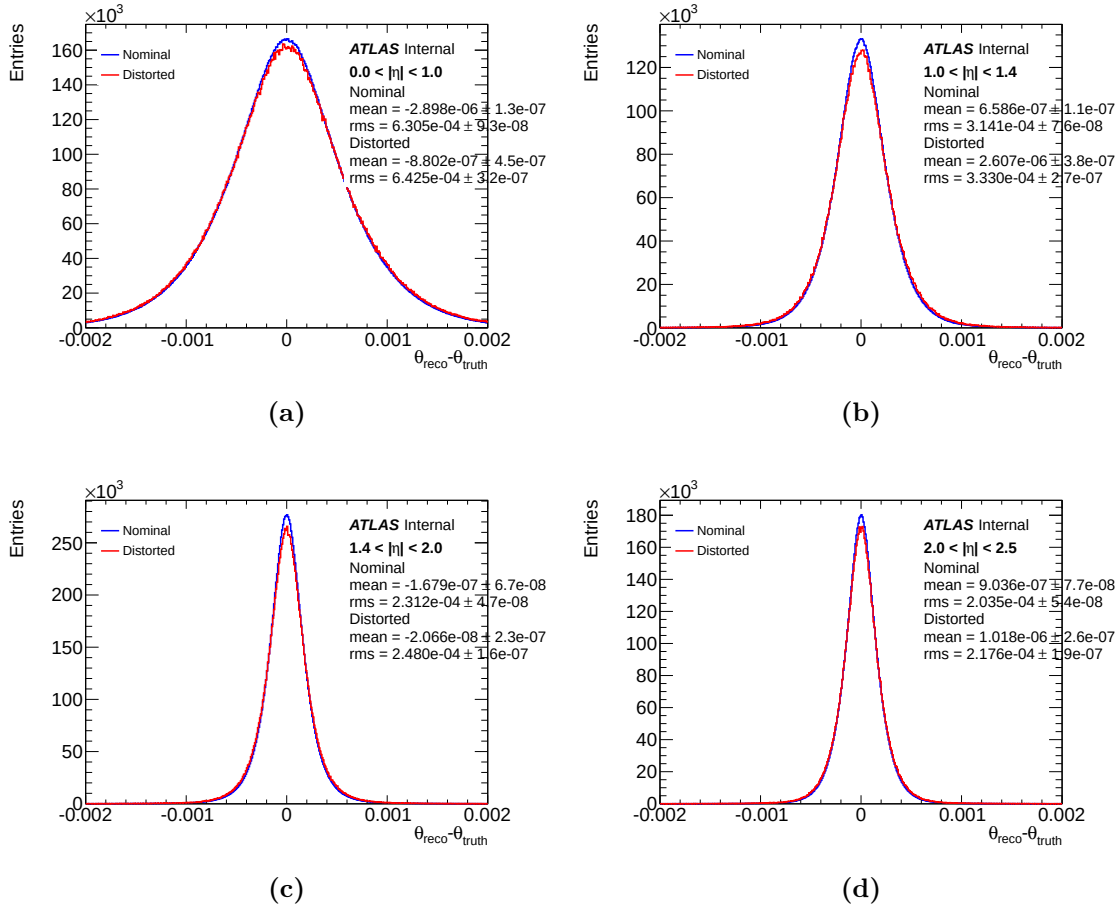

Figure 4.43: The difference between reconstructed and truth muon θ in J/ψ events for MC samples corresponding to the nominal and distorted geometry, in pseudorapidity bins: (a) $|\eta| < 1.0$, (b) $1.0 < |\eta| < 1.4$, (c) $1.4 < |\eta| < 2.0$ and $|\eta| > 2.0$.

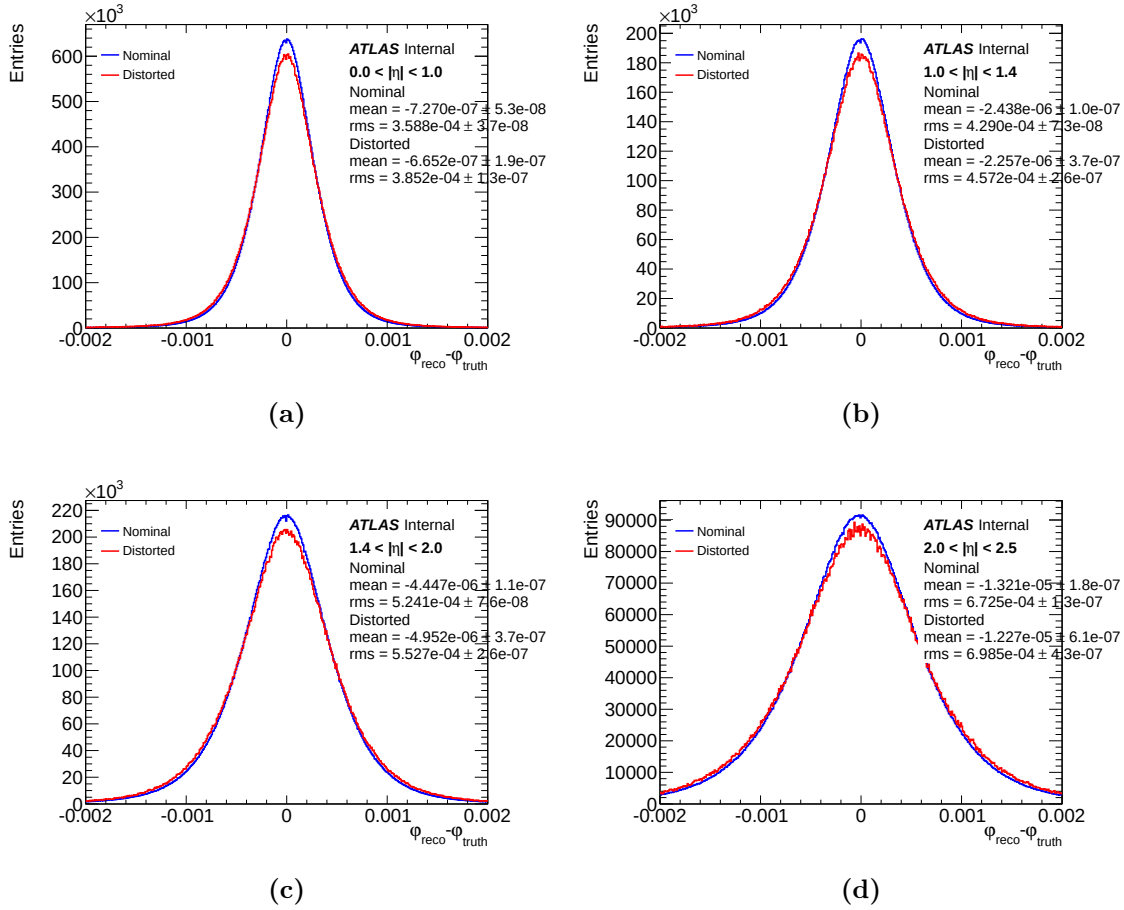

Figure 4.44: The difference between reconstructed and truth muon φ in J/ψ events for MC samples corresponding to the nominal and distorted geometry, in pseudorapidity bins: (a) $|\eta| < 1.0$, (b) $1.0 < |\eta| < 1.4$, (c) $1.4 < |\eta| < 2.0$ and $|\eta| > 2.0$.

To study the impact of the angular measurement on the mass scale and resolution, the reconstructed θ and φ angles of the nominal MC sample have been smeared by 100 % of the RMS shown in Figures 4.43 and 4.44, corresponding to an increase of the angular resolution by a factor of 2. No significant change is observed in the mean reconstructed invariant mass. Figure 4.45 shows the effect of the smearing of the angles on the width of the reconstructed invariant mass. The largest effect is observed in the barrel, in which the resolution changes by 1.5 %. Since in this study the increase of the angular resolution was more than 10 times larger than what is expected from an excess of material by 10 %, any realistic angular resolution degradation should be much less than what is obtained in this exercise. Since this level of smearing is already covered by the systematic uncertainty on the Δr_1^{ID} term, there is no need for an additional smearing of the measured muon angles and the effect of a difference between data and MC in the angular resolutions can be neglected.

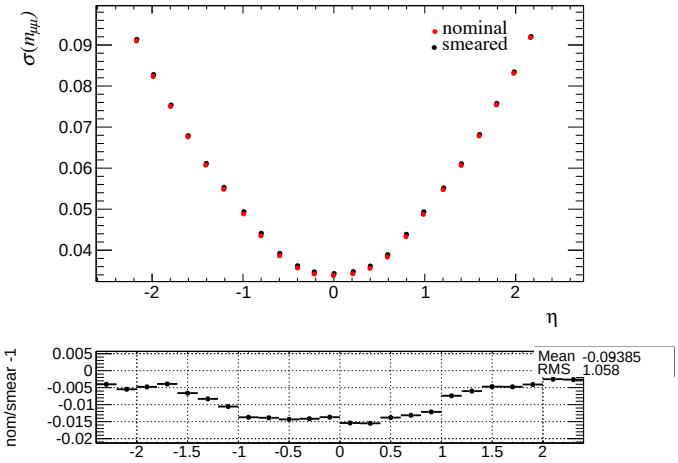

Figure 4.45: The width of the J/ψ invariant mass distribution for the nominal geometry sample with θ and φ angles smeared by 100 % RMS of their resolution (black points) compared to the unsmeared events (red points), with the relative ratio shown in the bottom panel. Since the realistic smearing due to additional material is more then 10 times smaller with respect to the one applied, the effect on the mass resolution is negligible.

4.5 MUON MOMENTUM UNCERTAINTIES IN THE HIGGS BOSON MASS MEASUREMENT

The Higgs boson is discovered in 2012 by the ATLAS and CMS collaboration at the LHC [30, 31]. The measurement of the mass of the Higgs boson is based on fitting the mass spectra of the two decay modes $H \to \gamma\gamma$ and $H \to ZZ^* \to 4\ell$, where ℓ refers to electron or muon [188]. These two channels have a narrow mass peak over a smooth background, from which the mass can be extracted without any assumption on the signal production and decay. The results are based on the data from proton–proton collisions collected during 2011 and 2012 corresponding to the 4.6 fb^{-1} and 20.3 fb^{-1}, respectively. The Higgs boson mass measurement is described in detail in [188]. The detailed discussion of the uncertainties is given in [189]. In this section only the impact of the muon momentum correction uncertainties, described in Section 4.4, on the Higgs boson mass measurement is described.

A summary of the muon momentum corrections and their uncertainties is shown in Figure 4.46. Figure 4.46 (a) shows the ratio of the reconstructed dimuon invariant mass in data to the corrected mass in simulation for J/ψ, Υ and Z-boson events as a function of leading muon η, while Figure 4.46 (b) shows the same ratio as a function of the average transverse momentum of the two muons. The momentum resolution ranges from 1.7 % at central pseudorapidity and for transverse momentum $p_{\mathrm{T}} = 10$ GeV, to 4 % at large pseudorapidity and $p_{\mathrm{T}} = 100$ GeV, while the momentum scale is known with an uncertainty of 0.05 % to 0.2 % depending on pseudorapidity.

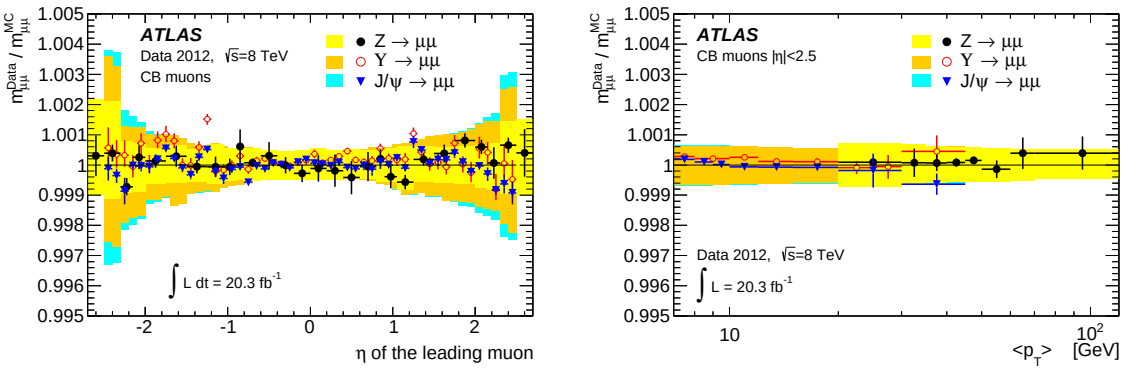

(a) **(b)**

Figure 4.46: Ratio of the reconstructed dimuon invariant mass for data to the corrected mass in simulation for J/ψ, Υ and Z-boson events as a function of (a) leading muon η and (b) average p_{T} of the two muons. The shaded areas show the systematic uncertainty on the simulation corrections for each of the three samples. The error bars on the points show the combined statistical and systematic uncertainty. Plots are taken from [188].

The $H \to ZZ^* \to 4\ell$ channel provides good sensitivity of the measurement of the Higgs boson properties due to its high signal-to-background ratio, which is about two in the signal mass window $120 - 130$ GeV, and its excellent mass resolution, for each of the four final states: $\mu^+\mu^-\mu^+\mu^-$ (4μ), $\mu^+\mu^-e^+e^-$ $(2\mu 2e)$, $e^+e^-\mu^+\mu^-$ $(2e2\mu)$ and $e^+e^-e^+e^-$ $(4e)$, where the first pair is defined to be the one with the dilepton mass closest to the Z-boson mass. The typical mass resolution varies from 1.6 GeV for the 4μ final state to 2.2 GeV for the $4e$ final state. For a SM Higgs boson with a mass of about 125 GeV, the dominant background is the production of Z-boson pairs $(Z^*/\gamma^*)(Z^*/\gamma^*)$ process, referred as ZZ^*. A smaller contribution is expected from the Z +jets, where jets are misidentified as electrons, or contain muons from decays of heavy flavor particles inside jets, and top production processes. The ZZ^* background is estimated from simulation and normalised to NLO calculation, while the Z +jets and top backgrounds are estimated with data-driven methods. Further description of the background determination is beyond the scope of this thesis.

The Higgs boson candidates in four lepton channel are selected with a single- and dilepton triggers (single electron, single muon and dimuon, dielectron and mixed electron and muon topologies). Muon tracks are required to have a minimal number of hits in the ID, or hits in all muon stations for SA muons as listed in Table 4.1. All four types of muons are allowed with at most one SA or CT muon per event. Each muon must have $p_{\mathrm{T}} > 6$ GeV in the pseudorapidity range $|\eta| < 2.7$. Electrons are selected do satisfy loose identification criteria, as discussed in Section 3.4, with $E_{\mathrm{T}} > 7$ GeV and $|\eta| < 2.7$. The highest p_{T} lepton in the quadruplet must satisfy $p_{\mathrm{T}} > 20$ GeV, and the second and third lepton in p_{T} order must satisfy $p_{\mathrm{T}} > 15$ GeV and $p_{\mathrm{T}} > 10$ GeV, respectively. The leptons are required to be separated from each other by $\Delta R > 0.1$ and $\Delta R > 0.2$ for same and different flavor, respectively. All selected leptons must be isolated. Further details about the selection can be found in [188].

The Higgs boson mass in the $H \to ZZ^* \to 4\ell$ channel is extracted from a two-dimensional fit to the $m_{4\ell}$. The invariant mass distribution $m_{4\ell}$ for four different final states is shown in Figure 4.47.

All sources of the systematics uncertainties are implemented in the signal and background models and evaluated using MC studies to determine the impact of the systematic uncertainties on the final fit. The impact of the muon momentum scale and resolution correction uncertainties on the Higgs boson mass measurement in four different final states is shown in Table 4.9. The up and down variation corresponds to $+1\sigma$ and -1σ, respectively. The difference in mean reconstructed masses with the nominal and varied parameters is used as a systematic uncertainty on $m_{4\ell}$, taking that the uncertainties are fully correlated across the whole pseudorapidity. The total systematic uncertainties of the muon momentum on $m_{4\ell}$ for the $m_H = 125$ GeV signal are 0.044 %, 0.018 % and 0.026 % for 4μ, $2\mu 2e$ and $2e2\mu$ final states, respectively. When all the final states are combined together, the uncertainty on m_H from the muon momentum scale and resolution is 0.03 %.

Table 4.9: The impact of the muon momentum scale and resolution correction uncertainties on the Higgs boson mass measurement in MeV.

Parameter	4μ		$2\mu 2e$		$2e2\mu$		$4e$	
	Up	Down	Up	Down	Up	Down	Up	Down
Scale	54	-55	32	-32	21	-25	-	-
Resolution ID	0	0	2	-2	-1	1	-	-
Resolution MS	4	-4	2	-2	1	-1	-	-

Table 4.10 shows the observed and expected number of events for $\sqrt{s} = 7$ TeV and $\sqrt{s} = 8$ TeV data in a mass window corresponding to $\pm 2\sigma_{m_{4\ell}}$.

Table 4.10: The number of events expected and observed for $m_H = 125$ GeV hypothesis for the four lepton final states.

Final state	Signal	ZZ^*	Z +jets, top	s/b	Expected	Observed
4μ	6.20 ± 0.61	2.82 ± 0.14	0.79 ± 0.13	1.7	9.81 ± 0.64	14
$2\mu 2e$	4.04 ± 0.40	1.99 ± 0.10	0.69 ± 0.11	1.5	6.72 ± 0.42	9
$2e2\mu$	3.15 ± 0.32	1.38 ± 0.08	0.72 ± 0.12	1.5	5.24 ± 0.35	6
$4e$	2.77 ± 0.27	1.22 ± 0.08	0.76 ± 0.11	1.4	4.75 ± 0.32	8
Total	16.2 ± 1.6	7.41 ± 0.40	2.95 ± 0.33	1.6	26.5 ± 1.7	37

The measured Higgs boson mass in the $H \to ZZ^* \to 4\ell$ decay channel yields:

$$m_H = 124.51 \pm 0.52 \text{ (stat.)} \pm 0.06 \text{ } syst \text{ GeV} = 124.51 \pm 0.52 \text{ GeV}. \quad (4.18)$$

The systematic uncertainty is obtained from the quadrature subtraction of the fit uncertainty evaluated with and without the systematic uncertainties fixed at their best fit values. Due to the excellent calibration of the muon momentum, systematic uncertainty on the Higgs boson mass in the four lepton channel is completely dominated by the statistics of the given sample. Due to the large difference between the magnitude of

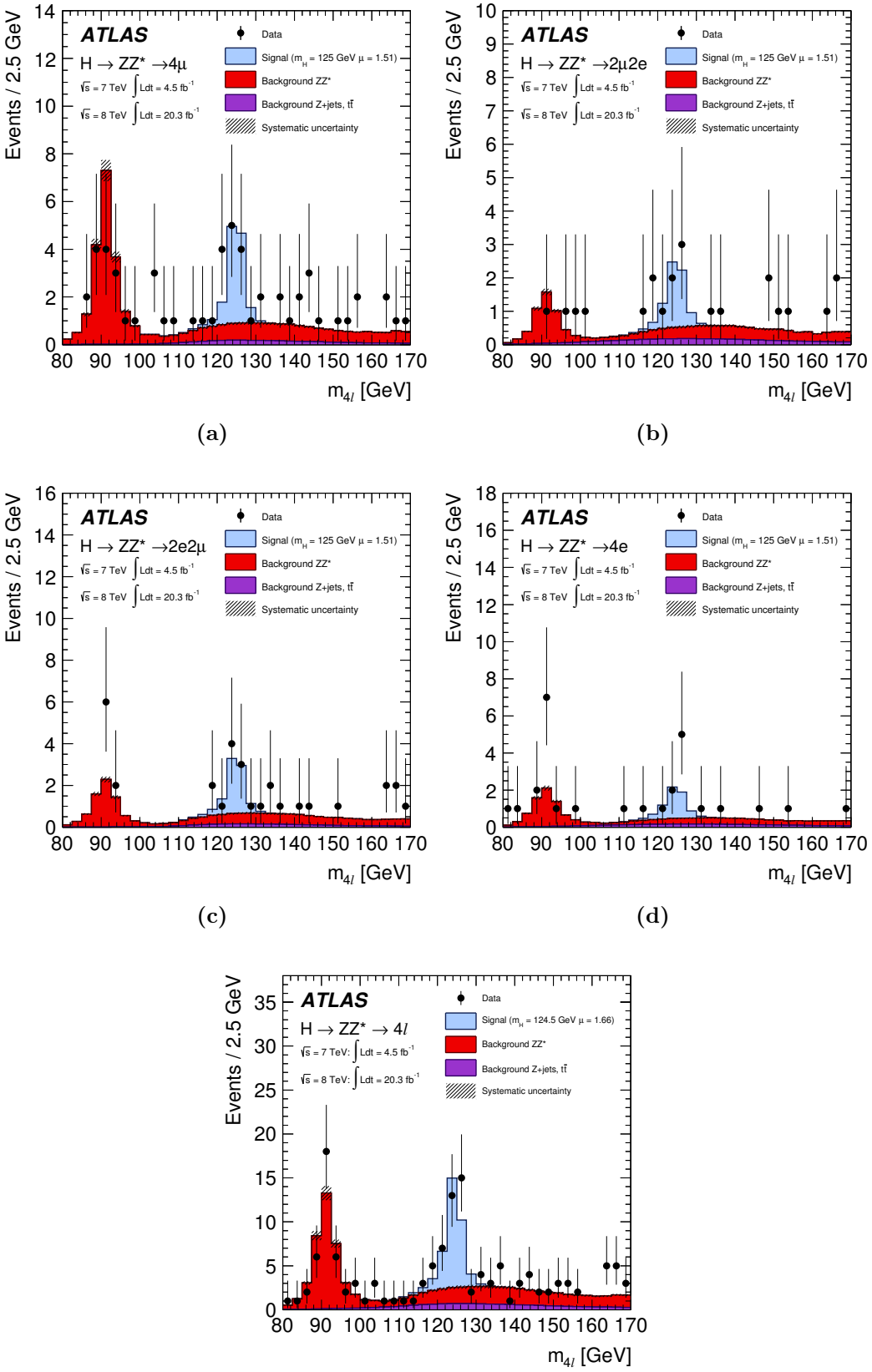

Figure 4.47: The invariant mass distribution $m_{4\ell}$ for four different final states: (a) 4μ, (b) $2\mu 2e$, (c) $2e2\mu$, (d) 4μ and (e) their combination. The signal expectation is shown in blue, while the data is represented with black points.

the statistical and systematic uncertainties, the numerical precision on the quadrature subtraction is estimated to be of the order of 10 MeV.

The combined mass measurement from the $H \to \gamma\gamma$ and $H \to ZZ^* \to 4\ell$ channels gives:

$$m_H = 125.36 \pm 0.37 \text{ (stat.)} \pm 0.18 \text{ (syst.) GeV} = 125.36 \pm 0.41 \text{ GeV}. \quad (4.19)$$

The contribution of the muon momentum scale, as a dominating source of uncertainty from Table 4.9, to the combined mass measurement is only 10 MeV from the total of 180 MeV.

The combined measurement of the Higgs boson mass between ATLAS and CMS experiments from the $H \to \gamma\gamma$ and $H \to ZZ^* \to 4\ell$ channels is [45]:

$$m_H = 125.09 \pm 0.21 \text{ (stat.)} \pm 0.11 \text{ (syst.) GeV} = 125.09 \pm 0.24 \text{ GeV}. \quad (4.20)$$

The results are obtained from a simultaneous fit to the reconstructed invariant mass peaks in the two channels and for the two experiments. The muon momentum scale and resolution uncertainties are smaller for the ATLAS measurement, and contributes with less than 10 MeV in the combination, compared to the CMS whose contribution is 50 MeV [45]. The measured masses from the individual channels and the two experiments are found to be consistent among themselves. Figure 4.48 shows the summary of the Higgs boson mass measurements from the individual analyses of ATLAS and CMS and from the combined analysis.

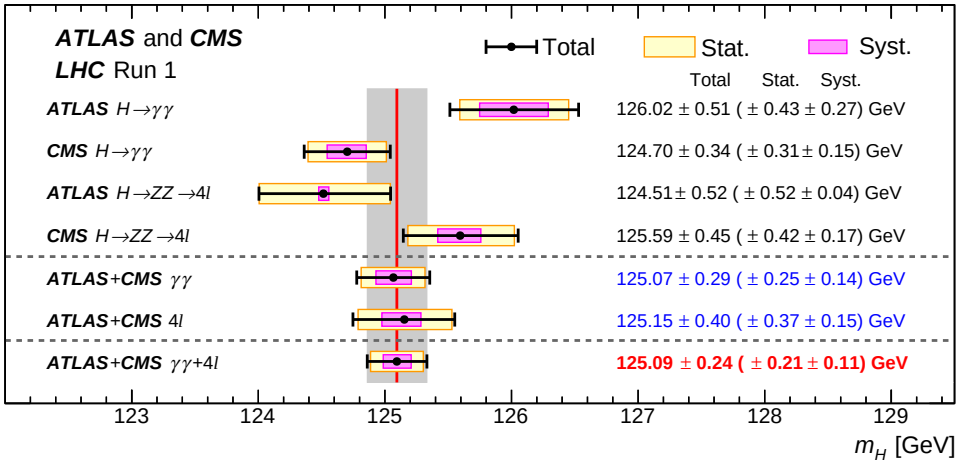

Figure 4.48: Summary of the Higgs boson mass measurements from the individual analyses of ATLAS and CMS and from the combined analysis [45]. The systematic (narrower, magenta-shaded bands), statistical (wider, yellow-shaded bands), and total (black error bars) uncertainties are indicated. The (red) vertical line and corresponding (gray) shaded column indicate the central value and the total uncertainty of the combined measurement, respectively.

5

Performance of the Hadronic Recoil Reconstruction

For the W-boson mass measurement, the magnitude and direction of the neutrino transverse energy is estimated from the charged lepton transverse momentum and the hadronic recoil, as discussed in Section 3.4. Thus, the hadronic recoil defined as the energy deposited in the calorimeters excluding energy deposits associated with the charged leptons in the transverse plane, becomes the fundamental quantity which should be calibrated. The calibration of the hadronic recoil affects the measurement of the W-boson mass through its impact on the transverse mass distribution used for the mass extraction. Furthermore, the hadronic recoil calibration influences the p_{T}^{ℓ} distribution through the event selection requirements on u_{T}, m_{T} and $E_{\mathrm{T}}^{\mathrm{miss}}$, which are presented in Section 3.5.

In this chapter performance of the hadronic recoil reconstruction is described. First, basic variables are introduced. Then, definition of the cluster based algorithm is given, followed by other definitions of the hadronic recoil. The chapter concludes with the detailed description of the correction procedure as well as the propagation of the corresponding uncertainties to the W-boson mass measurement. The hadronic recoil reconstruction described in this chapter is based on [198], while the hadronic recoil calibration is based on [199].

5.1 INTRODUCTION

The transverse momentum of the vector boson in a proton–proton collisions is induced by initial gluon or quark radiation in the transverse plane, as discussed in Chapter 1. Since the produced Z and W bosons recoil against this ISR, then the transverse momentum of the Z or W boson can be defined as:

$$\vec{p}_{\mathrm{T}}^{\,\mathrm{Z/W}} = -\sum \vec{p}_{\mathrm{T}}^{\,\mathrm{ISR\ quarks,\ gluon}}, \tag{5.1}$$

where $\vec{p}_{\mathrm{T}}^{\,\mathrm{Z/W}}$ is the transverse momentum of the Z or W bosons and $\sum \vec{p}_{\mathrm{T}}^{\,\mathrm{ISR\ quarks,\ gluon}}$ accounts for all transverse momenta of the partons from ISR. These quarks and gluons fragment into hadrons which deposit their energies in the calorimeters. Therefore, the transverse momentum of the W boson can be reconstructed from the hadronic recoil [175]. For the Z-boson events, since the detector response to the hadronic energy is

very different than the response to the lepton energy, the hadronic recoil is relatively poor measurement of the Z-boson transverse momentum.

For the W-boson mass measurement, the hadronic recoil is measured from the vector sum of all reconstructed transverse energies of topo-clusters in the calorimeter system:

$$\vec{u}_{\mathrm{T}} = \sum_{i=0}^{N_{\mathrm{topo}}} \vec{E}_{\mathrm{T}}^{\,\mathrm{topo}}, \tag{5.2}$$

while the scalar sum of all transverse energies of topo-clusters represents the hadronic activity of the event:

$$\Sigma E_{\mathrm{T}} = \sum_{i=0}^{N_{\mathrm{topo}}} E_{\mathrm{T}}^{\mathrm{topo}}, \tag{5.3}$$

where topo-clusters close to the reconstructed electron or muon candidates are excluded. This exclusion ensures that the energy deposits originating from the charged lepton or from accompanying photons from FSR or Bremsstrahlung do not contribute to the hadronic recoil measurement. The $\Delta R = 0.2$ cone around the lepton direction is excluded from the calculation and replaced with randomly chosen topo-cluster activity far away from the lepton and the hadronic activity, further than $\Delta\varphi = \pi/3$, i.e. the same η but different φ region. The exclusion and replacement procedure is repeated for every event. This procedure ensures that there is no difference in the reconstruction of the hadronic recoil for electron and muon channels, so that it is possible to use the same calibration applied to both channels. More details about this definition of the hadronic recoil, referred as cluster-based, is given in Section 5.2. Also, there are other definitions of the hadronic recoil which are discussed in Section 5.3.

In addition to the hadronic activity, there is one more important quantity, the soft ΣE_{T}, defined as the difference between scalar sum of all topo-cluster energies that are used for the calculation of hadronic recoil and the magnitude of the vector of hadronic recoil: $\Sigma E_{\mathrm{T}} - u_{\mathrm{T}}$. The $\Sigma E_{\mathrm{T}} - u_{\mathrm{T}}$ quantity is less correlated with the hadronic recoil than the ΣE_{T} and better represents the event activity related to the pile-up and to the UE.

The reconstructed hadronic recoil can be decomposed into a parallel and a perpendicular component to the projection of the transverse momentum of the vector boson, as shown in Figure 5.1:

$$u_{\parallel} = \vec{u}_{\mathrm{T}} \cdot \vec{v}_{\mathrm{T}} \quad \text{and} \quad u_{\perp} = u_x v_y - u_y v_x, \tag{5.4}$$

where the $\vec{v}_{\mathrm{T}}$ is the unit vector of the transverse momentum of the vector boson, and the u_x and u_y are projections of the recoil onto axes of the transverse plane in the ATLAS coordinate system, defined in Chapter 2. The parallel and perpendicular axes are defined to be orthogonal to each other in the transverse plane with the parallel axis having the direction of true boson vector. Since the perpendicular component is a consequence of limited detector resolution, it is expected that the parallel component is maximal on the parallel axis, and minimal on the perpendicular. On average, the perpendicular component should be zero, and its width provides an estimate of the

recoil resolution. The parallel component should be equal to the absolute value of the vector boson transverse momentum.

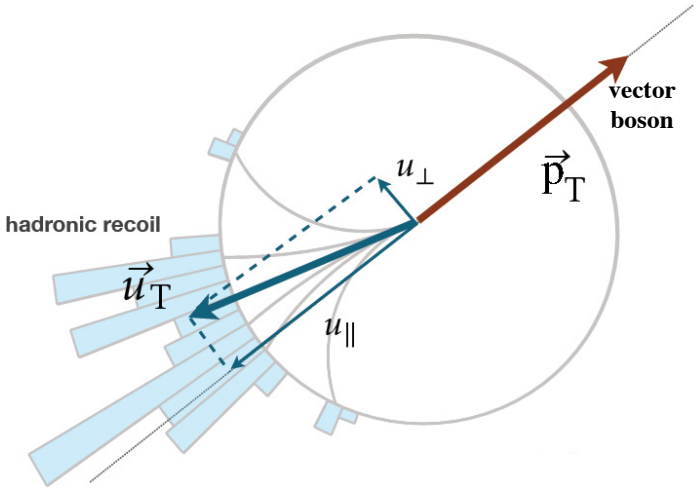

Figure 5.1: Parallel and perpendicular projection of the hadronic recoil with respect to the transverse momentum of the vector boson.

It is very important to calibrate the hadronic recoil as precisely as possible for the W-boson mass measurement, since the transverse mass is strongly correlated with the parallel projection of the W-boson transverse momentum on the lepton transverse momentum, as shown with Equation 1.57, and any bias in the $u_\parallel$ distribution will introduce a bias in the transverse mass measurement. In order to measure the W-mass with an uncertainty of about 10 MeV, coming only from the hadronic recoil m_T measurement, the hadronic recoil has to be measured with a precision of about half of a percent.

For the W-boson mass measurement presented in this thesis the calibration of the hadronic recoil is performed using the $Z \to \mu\mu$ events. The method of using the $Z \to \ell\ell$ events to model the hadronic recoil in the $W \to \ell\nu$ events ($\ell = e, \mu$) was first used by the D0 collaboration [200]. The advantages of using the Z-boson events for the hadronic recoil calibration are coming from very low background contamination and from similar production and decay kinematics as the W-boson events. The Z-boson candidates used for the calibration are selected with the same trigger as used for the W-boson selection, described in Section 3.4, with exactly two reconstructed leptons with opposite charge with $p_\mathrm{T}^\ell > 25\,\mathrm{GeV}$ and invariant mass $66\,\mathrm{GeV} < m_{\ell\ell} < 166\,\mathrm{GeV}$. The calibration procedure is performed into two steps. First, the recoil resolution missmodeling is addressed by correcting the modeling of the event activity in the MC simulation. Then, the residual differences in the recoil response and resolution are corrected. The second step is particularly important, since the corrections are derived using the Z-boson events and then transferred to the W-boson events, where the possible difference in the recoil resolution coming from two and one removed charged leptons, for the Z- and W-boson events respectively, is accounted as a systematics uncertainty. The full procedure for hadronic recoil calibration is described in Section 5.5.

5.2 CLUSTER BASED HADRONIC RECOIL

As a basic concept defined with Equation 3.4, the hadronic recoil is computed as the vector sum of all energy deposited in the calorimeters, i.e. as a sum of the energies reconstructed in topo-clusters defined in Section 3.4. Each topo-cluster is defined with its polar and azimuth coordinate, η^{topo} and φ^{topo}, and transverse energy $E_{\text{T}}^{\text{topo}}$. If the hadronic recoil is calculated from all topo-clusters in the calorimeters, then the transverse energy of electrons and muon energy loss in the calorimeters is calculated twice in Equation 3.5. This double counting creates a bias in the measurement of $E_{\text{T}}^{\text{miss}}$. The double counting problem is solved by excluding the topo-clusters in the cone of size ΔR around the lepton [201]. The cone size is defined as:

$$\Delta R = \sqrt{(\eta^{\text{topo}} - \eta^{\ell})^2 + (\varphi^{\text{topo}} - \varphi^{\ell})^2}, \tag{5.5}$$

where η^{ℓ} and φ^{ℓ} are the lepton angles. The performance of $E_{\text{T}}^{\text{miss}}$ has been studied with different cone sizes in [201]. For a cone size of $\Delta R = 0.05$ the double counting problem is still present, while for cones of sizes above 0.1 the leptons are completely excluded, but the $E_{\text{T}}^{\text{miss}}$ resolution degrades when more information is removed from the recoil measurement. In general, there are deposits in the calorimeter near the lepton which are unrelated to the lepton, like the ISR of quarks and gluons the underlaying event effects described in Section 1.3.1. Thus, the degradation with larger cone sizes is present because the underlying event within the cone ΔR is removed together with the lepton. The chosen cone size with the best performance is $\Delta R = 0.2$.

In order to recover the recoil energy, the excluded clusters coming from the underlying event have to be compensated. The procedure is illustrated in Figure 5.2. For each event, there are three components which can be identified as:

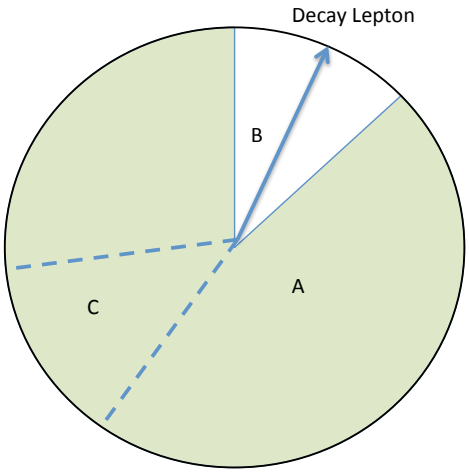

Figure 5.2: Definition of different zones for the calculation of the cluster-based hadronic recoil.

- zone A: all clusters in the calorimeter except the cone around the lepton, so called raw recoil,
- zone B: the part of clusters in a cone around the lepton, so called removed cone,
- zone C: clusters in a cone of the same size as the removed cone, taken from a similar detector region, but far from the lepton, so called the replacement cone.

The replacement cone is defined for each event at the same pseudorapidity region as the removed lepton $\eta^{\text{cone}} = \eta^{\ell}$ since the lepton energy is η dependent, but randomly chosen in azimuth so that it does not overlap with the removed cone $\Delta\varphi(\ell, \text{recoil}) > \pi/3$ and to be far from the direction of the raw recoil $\Delta\varphi(\text{raw recoil}, \text{recoil}) > 0.6$. Therefore, the hadronic recoil is calculated as a sum of clusters in zone A and zone C rotated to the position of the zone B. For events with non isolated leptons, this recoil energy correction has poor performance since it replaces a region around the lepton, which contains a lot of calorimeter activity, with a region from the detector specifically picked to have no hard calorimeter activity. Moreover, the isolation of electrons is based on ID and calorimeter based variables, while the isolation of muons is defined from ID only, as explained in Section 3.4.

In summary, the cluster-based hadronic recoil measurements involves three steps:

1. vector sum of the E_{T} of all topo-clusters deposited in the calorimeters;
2. remove the clusters in a $\Delta R = 0.2$ cone around the lepton to avoid the double counting problem;
3. compensate the underlying event excluded in the cone to correct the recoil energy.

The recoil energy correction is needed because the recoil behaviour in Z- and W-boson events has to be similar, and the number of exclusion cones which is equal to the number of leptons in the final states is different for these events.

5.3 OTHER DEFINITIONS OF THE HADRONIC RECOIL RECONSTRUCTION

In order to test the performance of the hadronic recoil, and its sensitivity to different pile-up conditions various definitions of the hadronic recoil are studied. In this section three more definitions of the hadronic recoil will be described: track based, improved track based and calculated from the standard definition of $E_{\text{T}}^{\text{miss}}$ in the ATLAS experiment defined in Section 3.4. The performance of the different hadronic recoil definitions is studied in MC only.

The *track based* hadronic recoil is calculated from the vector sum of transverse momenta of the selected ID tracks. The track reconstruction is given in Section 3.4. The tracks satisfy following requirements: $p_{\text{T}} > 500$ MeV, $|\eta| < 2.5$, $|d_0| < 1.5$ mm, $|z_0 \sin\theta| < 1.5$ mm, where θ is the polar angle of the track. The ID tracks are selected with at least one pixel hit and at least six SCT hits, while the requirement on the

track p_{T} ensures selection of tracks which extend through to the outer layers of the ID. Furthermore, the reconstruction of very low p_{T} tracks is difficult due to their large curvature and high degree of multiple scattering within the detector. The requirements on the number of hits in the pixel and SCT ensures good calculation of the track momentum from the reconstruction algorithms. These track requirements are needed in order to select primary tracks that can be associated to the production vertex of the vector boson. The tracks from the leptons and pile-up vertices are not considered in the calculation. Thus, only a small dependence on the number of reconstructed vertices is expected. The track based hadronic recoil neglects contributions from all tracks outside the acceptance $|\eta| < 2.5$ and all neutral particles, which degrades the resolution of the hadronic recoil.

The improved cluster based hadronic recoil algorithm combines the advantages of the cluster based and track based algorithm, i.e. the *track-cluster* hadronic recoil. This definition excludes the contribution from topo-clusters which are not associated to the vector boson production vertex. As for the track based case, the primary tracks must satisfy: $p_{\mathrm{T}} > 500$ MeV, $|\eta| < 2.5$, $|d_0| < 1.5$ mm, $|z_0 \sin\theta| < 1.5$ mm, where θ is the polar angle of the track, with at least one pixel hit and at least six SCT hits. All other tracks are defined as secondary tracks. The track-cluster hadronic recoil is based on track and cluster association method which consists from three steps:

1. each track is extrapolated to the second layer of the calorimeter, where the seed of the cluster is usually formed,
2. a cone ΔR(track, cluster) for the extrapolated track and the reconstructed cluster position is defined,
3. a track is associated to a cluster if ΔR(track, cluster) < 0.15, this threshold has been optimised with MC studies.

Then, the clusters are categorised in three categories: clusters that have only associated primary tracks, clusters that have no associated tracks and clusters that have at least one associated, secondary track. The track-cluster based hadronic recoil is restricted only to clusters that do not have associated secondary track. In this way, beside the clusters with associated primary tracks, clusters that have no associated tracks are taken into account, which solves the main problem with track based algorithm. The track-cluster hadronic recoil follows the same exclusion of the replacement cone as described in Section 5.2.

The hadronic recoil is defined from the standard definition of the missing transverse energy in the ATLAS experiment, as described in Section 3.4. Thus, instead of calculating hadronic recoil directly from the hadronic activity, it is calculated from the missing transverse energy and lepton transverse momentum as:

$$\vec{u}_{\mathrm{T}} = -\vec{E}_{\mathrm{T}}^{\mathrm{miss}} - \sum \vec{p}_{\mathrm{T}}^{\,\ell}, \tag{5.6}$$

where $\ell = e, \mu$. This definition of hadronic recoil, denoted as *METRefFinal* hadronic recoil is defined only for comparison with other hadronic recoil definitions.

The performance of these four realisations of hadronic recoil is compared using $Z \to \mu\mu$ MC events. The dependence of $u_{\parallel} - p_{\mathrm{T}}^{\ell\ell}$ as a function of $p_{\mathrm{T}}^{\ell\ell}$ for four definitions

is shown in Figure 5.3. The track based algorithm shows the largest bias, followed by the track-cluster based algorithm. The best performance is shown by the METRefFinal method, closely followed by the cluster-based method. The resolution dependence of $u_{\parallel} - p_{\mathrm{T}}^{\ell\ell}$ and $u_{\perp}$ on the number of reconstructed collision vertices (N_{vtx}) is shown in Figure 5.4. While the METRefFinal approach and the cluster based method show a similar performance, the resolution of the track-cluster based method shows a significantly weaker dependence. Only a relatively small dependence can be observed for the track-based method. It should be noted, that the resolution of $u_{\parallel} - p_{\mathrm{T}}^{\ell\ell}$ and $u_{\perp}$ is similar for all methods expect the track based approach, which shows a significantly better resolution for $u_{\perp}$.

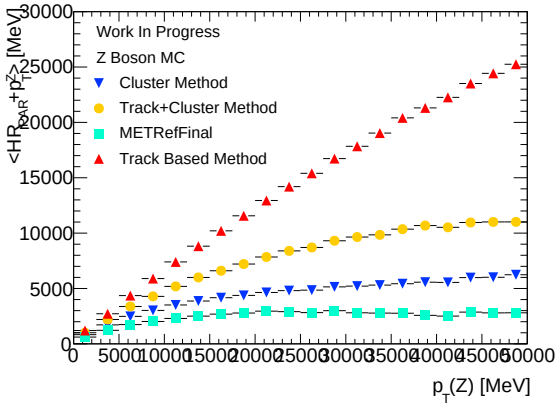

Figure 5.3: Comparison of the $Z \to \mu\mu$ MC predictions for several different hadronic recoil methods. The dependence of the mean value of $u_{\parallel} - p_{\mathrm{T}}^{\ell\ell}$ as a function on the dilepton transverse momentum is shown.

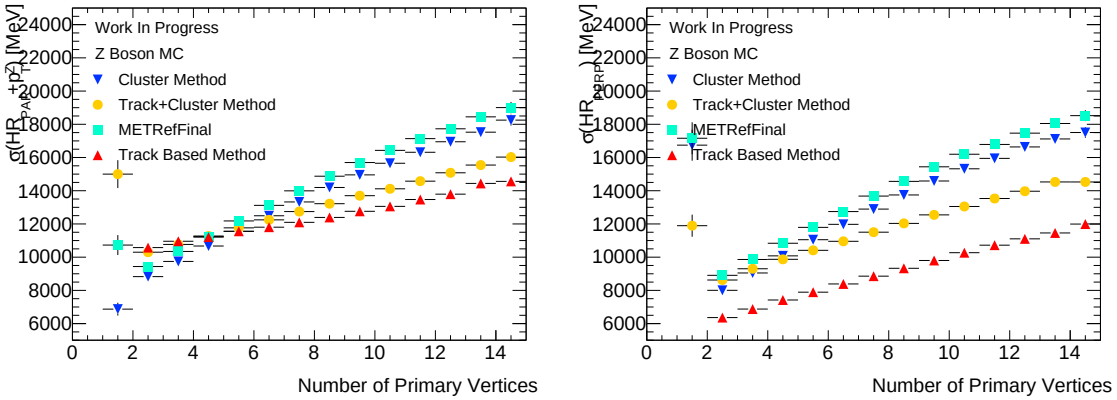

(a) **(b)**

Figure 5.4: Comparison of the $Z \to \mu\mu$ MC predictions for several different hadronic recoil methods. The dependence of the resolution of the (a) parallel $\sigma(u_{\parallel} + p_{\mathrm{T}}^{\ell\ell})$ and (b) perpendicular $\sigma(u_{\perp})$ hadronic recoil on the number of reconstructed primary vertices is shown.

In summary, the purely track-based algorithm has a too poor sensitivity on the vector boson transverse momentum, as shown in Figure 5.3. The METRefFinal approach

leads to the worse recoil resolution from all recoil definitions, with a significantly weaker dependence of $u_{\parallel} - p_{\mathrm{T}}^{\ell\ell}$ as a function of $p_{\mathrm{T}}^{\ell\ell}$, and the associated calibration would be very complex and leads to several correlated effects during a W-boson mass fit which are difficult to disentangle. Hence, the focus is only on the simple cluster based approach and the combined track-cluster based approach.

The optimal resolution of the perpendicular component of the hadronic recoil can be achieved by rescaling the parallel and the perpendicular component by an arbitrary factor α, the rescaling is defined as:

$$u'_{\perp} = \alpha \cdot u_{\perp}, \qquad u'_{\parallel} = \alpha \cdot u_{\parallel}. \tag{5.7}$$

In this way, the rescaled hadronic recoil projections will have an improved resolution, but with no real gain on a the measurement. Furthermore, this rescaling would degrade the sensitivity of the parallel component of the hadronic recoil on the vector boson p_{T}. Since the bias for different definitions of the hadronic recoil is not the same, as seen in Figure 5.3, in order to have a fair comparison of the cluster and truck-cluster methods, it was chosen to rescale the measured $u'_{\perp}$ and $u_{\parallel}$ such, that they show the same bias for both methods. Figure 5.5 shows a good agreement of the bias for both methods versus $p_{\mathrm{T}}^{\ell\ell}$ when choosing a scaling factor of $\alpha \approx 1.2$. Significant differences for the resulting bias dependence on ΣE_{T} is seen. This is expected, as the ΣE_{T} was not rescaled accordingly.

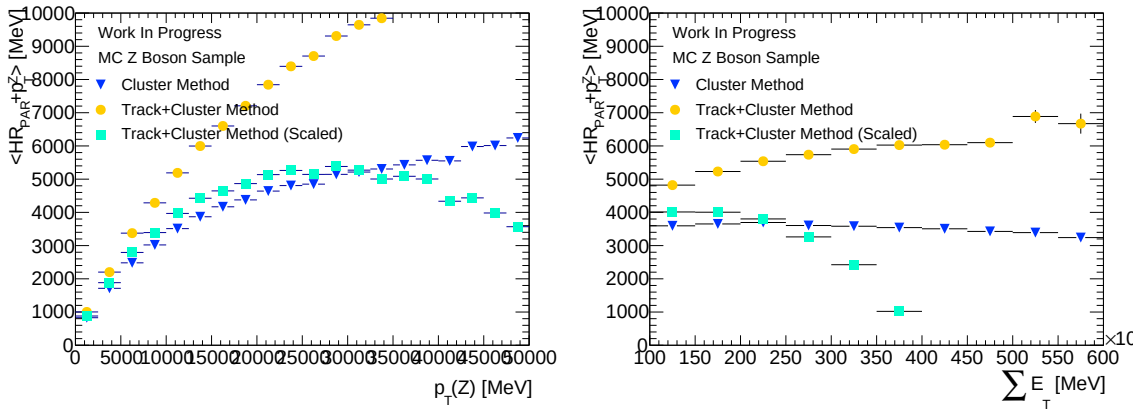

(a) **(b)**

Figure 5.5: Comparison of the $Z \to \mu\mu$ MC predictions for cluster based hadronic recoil algorithm and the corrected track-cluster based hadronic recoil algorithm. The dependence of the bias of $u_{\parallel} - p_{\mathrm{T}}^{\ell\ell}$ on (a) the dilepton transverse momentum and (b) the ΣE_{T} of the event is shown.

The resulting resolutions for the rescaled observables $u'_{\parallel} - p_{\mathrm{T}}^{\ell\ell}$ and $u_{\perp}$ are shown in Figure 5.6. Before the rescaled, the resolution of the track-cluster based method was better for $N_{\mathrm{vtx}} > 5$, while now the break-even point increased to $N_{\mathrm{vtx}} \approx 11$. The average number of reconstructed collision vertices is $< N_{\mathrm{vtx}} > \approx 5$ for the LHC run in 2011. Hence the simple cluster based hadronic recoil calculation shows the best performance and will be used in the W-boson mass measurement. It should be noted, for the 2012 dataset, $< N_{\mathrm{vtx}} > \approx 15$, due to the increase of pile-up events.

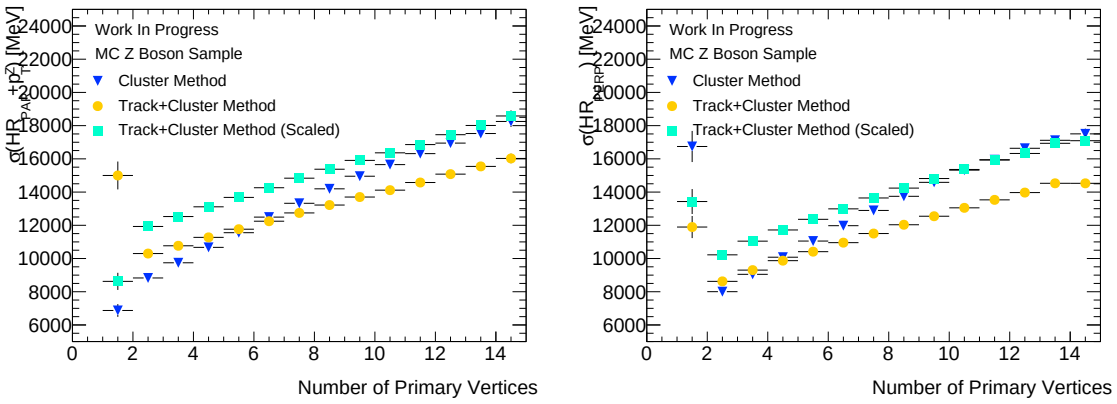

(a) **(b)**

Figure 5.6: Comparison of the $Z \to \mu\mu$ MC predictions for cluster based hadronic recoil algorithm and the corrected track-cluster based hadronic recoil algorithm. The dependence of the resolution of (a) the parallel and (b) perpendicular hadronic recoil on the number of reconstructed primary vertices is shown.

Since there is a higher sensitivity of the METRefFinal algorithm on the vector boson transverse momentum compared to the cluster based algorithm, a correction factor α from Equation 5.7 is applied, so that the sensitivity of both algorithm agrees. It was found, that a value of $\alpha \approx 0.9$ applied on the METRefFinal observables, leads to a comparable sensitivity, as shown in Figure 5.7. A relatively good agreement can be observed.

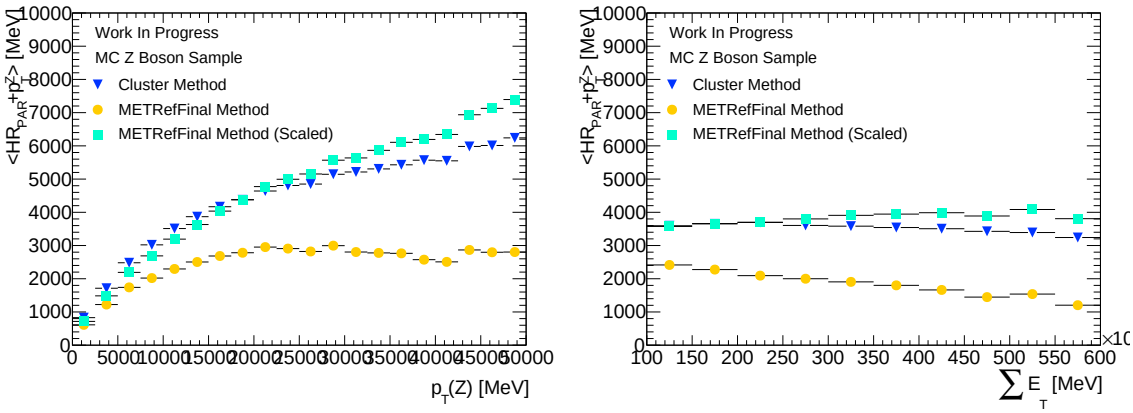

(a) **(b)**

Figure 5.7: Comparison of the $Z \to \mu\mu$ MC predictions for cluster based hadronic recoil algorithm and the scaled METRefFinal algorithm. The dependence of the bias of $u_{\parallel} - p_{\mathrm{T}}^{\ell\ell}$ on (a) the dilepton transverse momentum and (b) the ΣE_{T} of the event is shown.

The resulting comparison of the resolutions are shown in Figure 5.8. A slight improvement of the resolution of the scaled METRefFinal algorithm is observed, however, at the cost of a reduced sensitivity on the vector boson transverse momentum. This is

expected as the scaling factor α had to be chosen to be < 1.

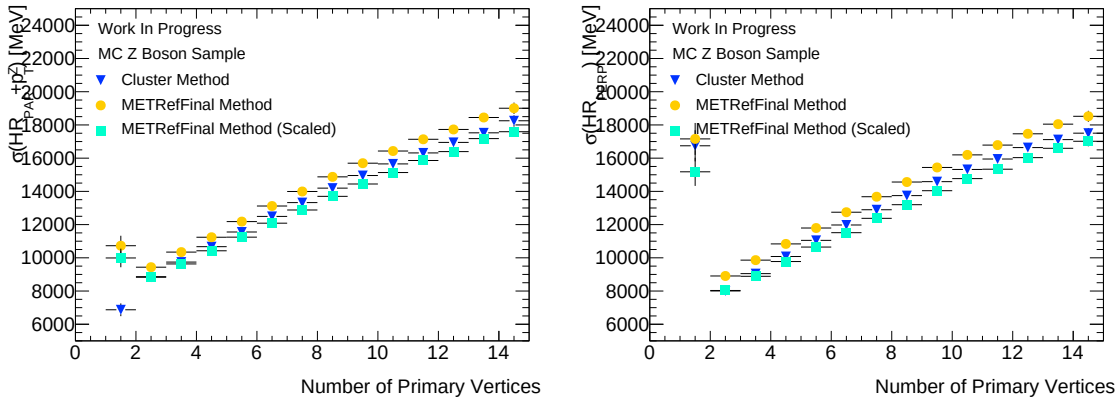

(a) **(b)**

Figure 5.8: Comparison of the $Z \to \mu\mu$ MC predictions for cluster based hadronic recoil algorithm and the scaled METRefFinal algorithm. The dependence of the resolution of (a) the parallel and (b) perpendicular hadronic recoil on the number of reconstructed primary vertices is shown.

5.4 INITIAL PERFORMANCE OF THE HADRONIC RECOIL

For the W-boson mass measurement, the cluster based hadronic recoil is used. In this section comparison between the data and MC for Z-boson events and cluster based hadronic recoil after the pile-up corrections is shown. The pile-up is modeled with PYTHIA 8 A2 tune, as described in Section 3.2. In order to reproduce the distribution of the average number of interactions per bunch crossing ($< \mu >$) observed in data, the events in MC need to be reweighted [202]. However, this reweighting corrects only the in-time pile-up, and the out-of-time pile-up remains uncorrected, which is represented with a disagreement in the number of primary vertices (N_{vxt}) between data and MC. In order to correct the out-of-time pile-up, the $< \mu >$ distribution has to be rescaled.

The distribution of mean number of interactions per bunch crossing, number of primary vertices and the scalar sum of transverse energies of all clusters are shown in Figure 5.9 for the Z-boson events in data and MC after pile-up corrections but without any rescaling of the $< \mu >$ distribution. Since only the in-time pile-up is corrected, there is a significant discrepancy between data and MC for N_{vxt} distribution, which is also reflected the ΣE_{T} and $\Sigma E_{\text{T}} - u$ distribution.

The hadronic recoil distribution, as well as its parallel and perpendicular projections with respect to the dilepton transverse momentum $p_{\text{T}}^{\ell\ell}$ in data and MC for Z-boson events are shown in Figure 5.10. As MC does not describe the data, corrections for the hadronic recoil are needed.

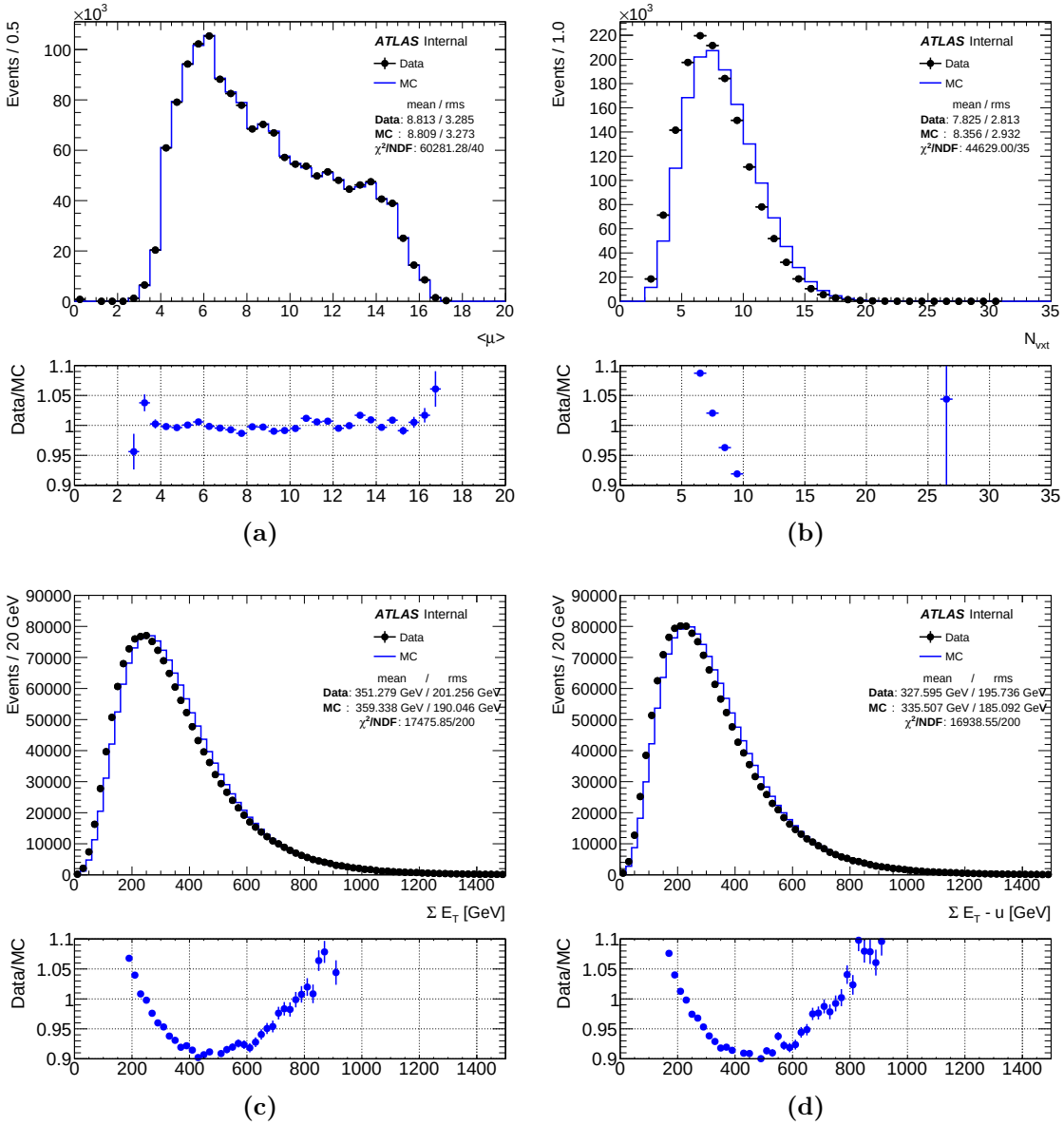

Figure 5.9: (a) Mean number of interactions per bunch crossing, (b) number of vertices, (c) ΣE_{T} distribution and (d) $\Sigma E_{\mathrm{T}} - u$ distribution in data (points) and MC (solid line) in $Z \to \mu\mu$ events after pile-up reweighting and without rescaling the $< \mu >$ distribution.

5.5 CALIBRATION OF THE HADRONIC RECOIL

The calibration procedure of the hadronic recoil consists of two steps. First, the dominant part of the recoil resolution mismodeling is addressed by correcting the modelling of the overall event activity in the simulation. These corrections are derived separately in the Z- and W-boson events. Second, the corrections for residual differences in the recoil response and resolution are derived using Z-boson events in data, and transferred

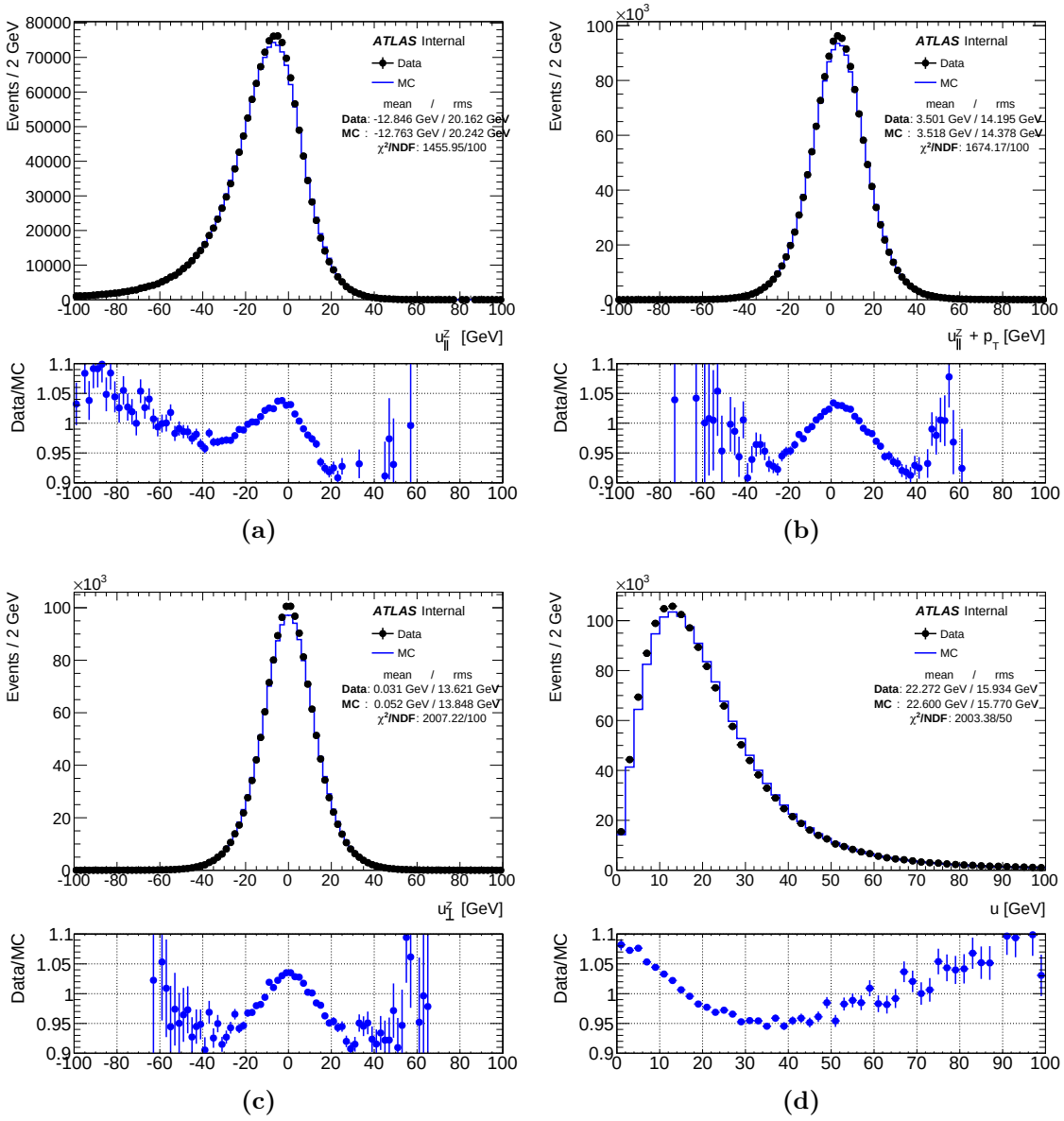

Figure 5.10: Hadronic recoil distribution in data (points) and MC (solid line) in $Z \to \mu\mu$ events: (a) parallel projection of the hadronic recoil on the dilepton transverse momentum, (b) parallel projection of the hadronic recoil plus the dilepton transverse momentum, (c) perpendicular projection of the hadronic recoil on the dilepton transverse momentum, (d) hadronic recoil distribution. Distributions are obtained after the pile-up reweighting and without rescaling the $< \mu >$ distribution.

to the W-boson events. The event activity corrections consist of the rescaling of the $< \mu >$ distribution and correcting the $\Sigma E_{\mathrm{T}} - u$ distribution, while the residual response corrections contain the calibration of the φ distribution of the hadronic recoil and an additional correction for the mean and resolution of the hadronic recoil distribution based on the parameter extraction from mean and width comparisons.

5.5.1 *Pile-up modeling*

The pile-up has significant effect on the reconstruction of $E_{\mathrm{T}}^{\mathrm{miss}}$ and ΣE_{T}. In order to account for mismodeling of vertex multiplicity in data and MC, as observed in Figure 5.9, a scale factor on $<\mu>$ should be applied. Then the MC will be able to reproduce the average activity of the event in a sence that each event in MC with a certain $<\mu>$ will have a number of primary vertices comparable to the one in data with a scaled $<\mu>\approx$ ScaleFactor $\times <\mu>$. The scale factor for PYTHIA 8 tune is 1.11 ± 0.03 [203]. This scale factor is calculated by comparing the ratio between the visible cross section with the total inelastic cross section for data and simulation. Also, the final scale factor is corrected to match the visible cross section within the ATLAS ID acceptance. The uncertainty is calculated from the quadrature sum of the uncertainties in the cross section measurements, and an uncertainty in the extrapolation from 7 to 8 TeV and to the ID acceptance [203].

In order to check the value of scaling factor for the m_W measurement, the scaling factor was obtained by scanning its impact on the data to MC agreement in the ΣE_{T}, $\Sigma E_{\mathrm{T}} - u$, $u_{\parallel}$, $u_{\parallel} + p_{\mathrm{T}}^{\ell\ell}$, $u_{\perp}$ and u_{T} distribution in Z-boson events. The results of these scans are shown in Figure 5.11. As one can observe ΣE_{T}, $u_{\parallel} + p_{\mathrm{T}}^{Z}$, and $u_{\perp}$ distributions (sensitive to resolution) prefer lower value of the $<\mu>$ scale factor. On the other hand $u_{\parallel}$ and u distributions (sensitive to the boson p_{T}) prefer higher value of the scale factor. The idea of scanning is to optimise the scale factor for the hadronic recoil observables.

Finally, the value $1.10^{+0.04}_{-0.03}$ is adopted, mainly to match u and $u_{\parallel}$ distributions and to cover the uncertainty from the visible cross section measurement and preferred value for $u_{\perp}$ and $\Sigma E_{\mathrm{T}} - u$ distribution. The $<\mu>$ distribution in data is continuous, while in MC is discrete, therefore the rescaling of $<\mu>$ is done on data, simply by dividing the distribution $<\mu>/1.1$.

The mean number of interactions per bunch crossing and number of vertices after reweighting and rescaling by 1.10 are shown in Figure 5.12. The overall agreement between data and MC is good, especially the vertex multiplicity is in much better agreement after rescaling. The pile-up is also affecting the distribution of the scalar sum of transverse energy in the calorimeter (ΣE_{T} and $\Sigma E_{\mathrm{T}} - u$), which are still showing residual disagreement between data and MC after rescaling the $<\mu>$ distribution.

After the rescaling, a significant difference is still present for the ΣE_{T} and $\Sigma E_{\mathrm{T}} - u$ distribution in MC and data, although the peaks of the distributions are more aligned. The hadronic recoil distributions in data and MC projected on the reconstructed transverse momentum of the dilepton system are shown in Figure 5.13, where the data to MC agreement is much better.

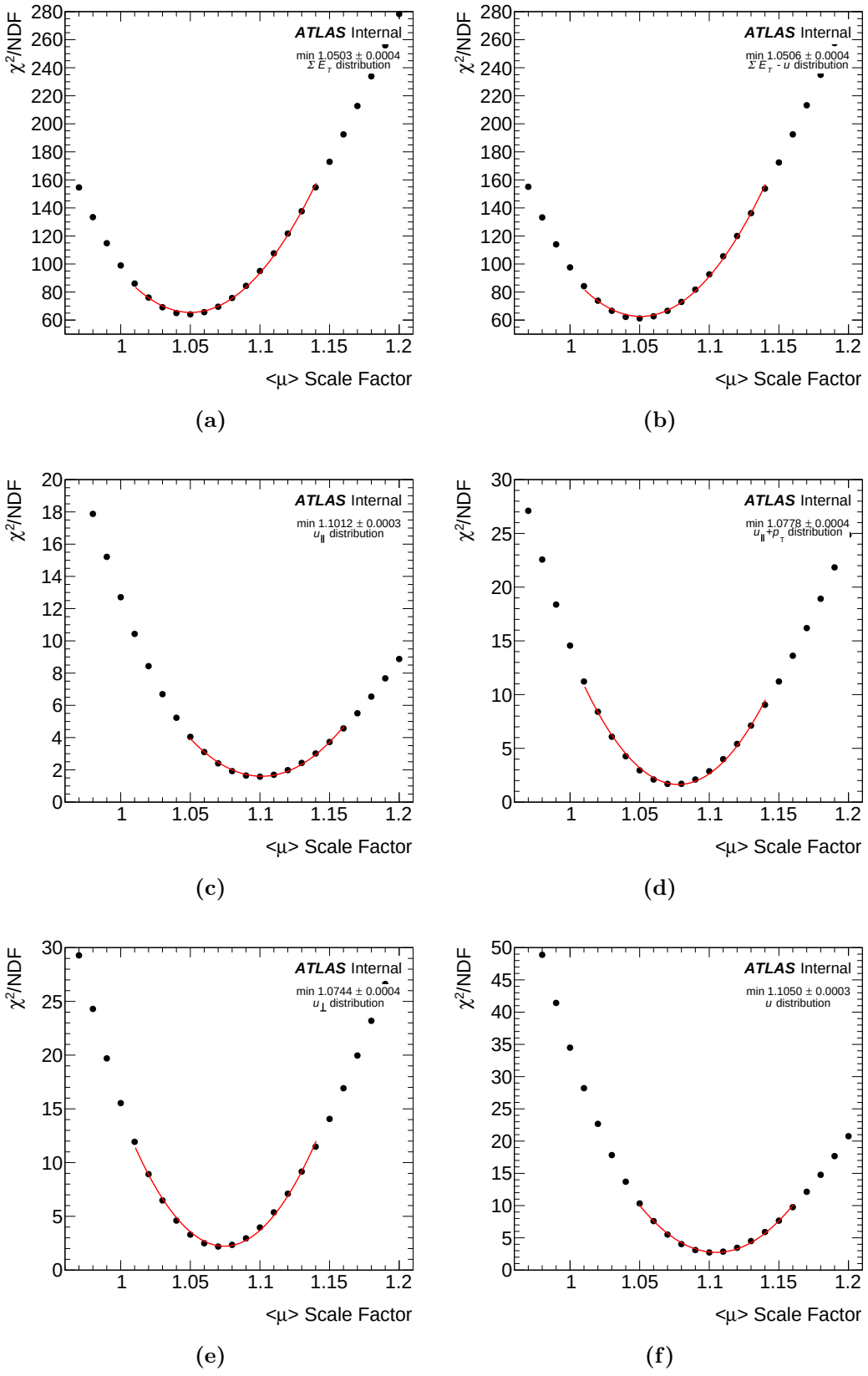

Figure 5.11: The results of the scanning the $< \mu >$ scale factor on agreement between data and MC in $Z \to \mu\mu$ events. The scans are performed for the following distributions: (a) ΣE_{T}, (b) $\Sigma E_{\mathrm{T}} - u$, (c) $u_{\parallel}$, (d) $u_{\parallel} + p_{\mathrm{T}}^{\ell\ell}$, (e) $u_{\perp}$ and (f) u distribution.

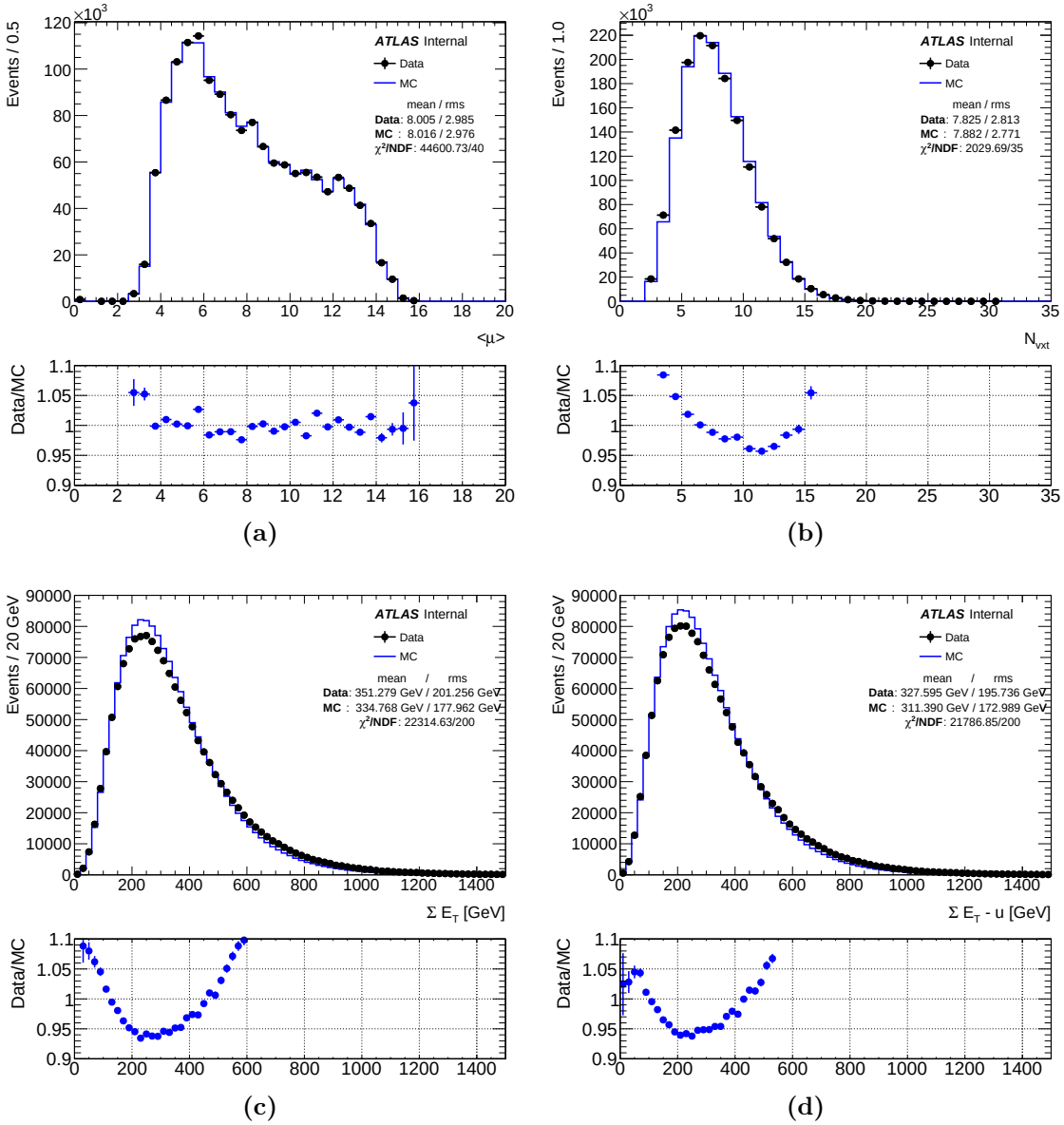

Figure 5.12: (a) Mean number of interactions per bunch crossing, (b) number of vertices, (c) ΣE_{T} distribution and (d) $\Sigma E_{\mathrm{T}} - u$ distribution in data (points) and MC (solid line) in $Z \to \mu\mu$ events after pile-up reweighting and rescaling the $< \mu >$ distribution by 1.1.

5.5.2 *Event activity correction*

The residual data to MC differences for $\Sigma E_{\mathrm{T}} - u$ distribution are responsible for the most of the remaining recoil resolution mismodeling. The $\Sigma E_{\mathrm{T}} - u$ distribution in MC is corrected by means of the *Smirnov transform*. This transformation is extracted from the Smirnov inverse probability integral transform [204]. It goes beyond a simple Gaussian smearing correction and can in principle transform one histogram to another,

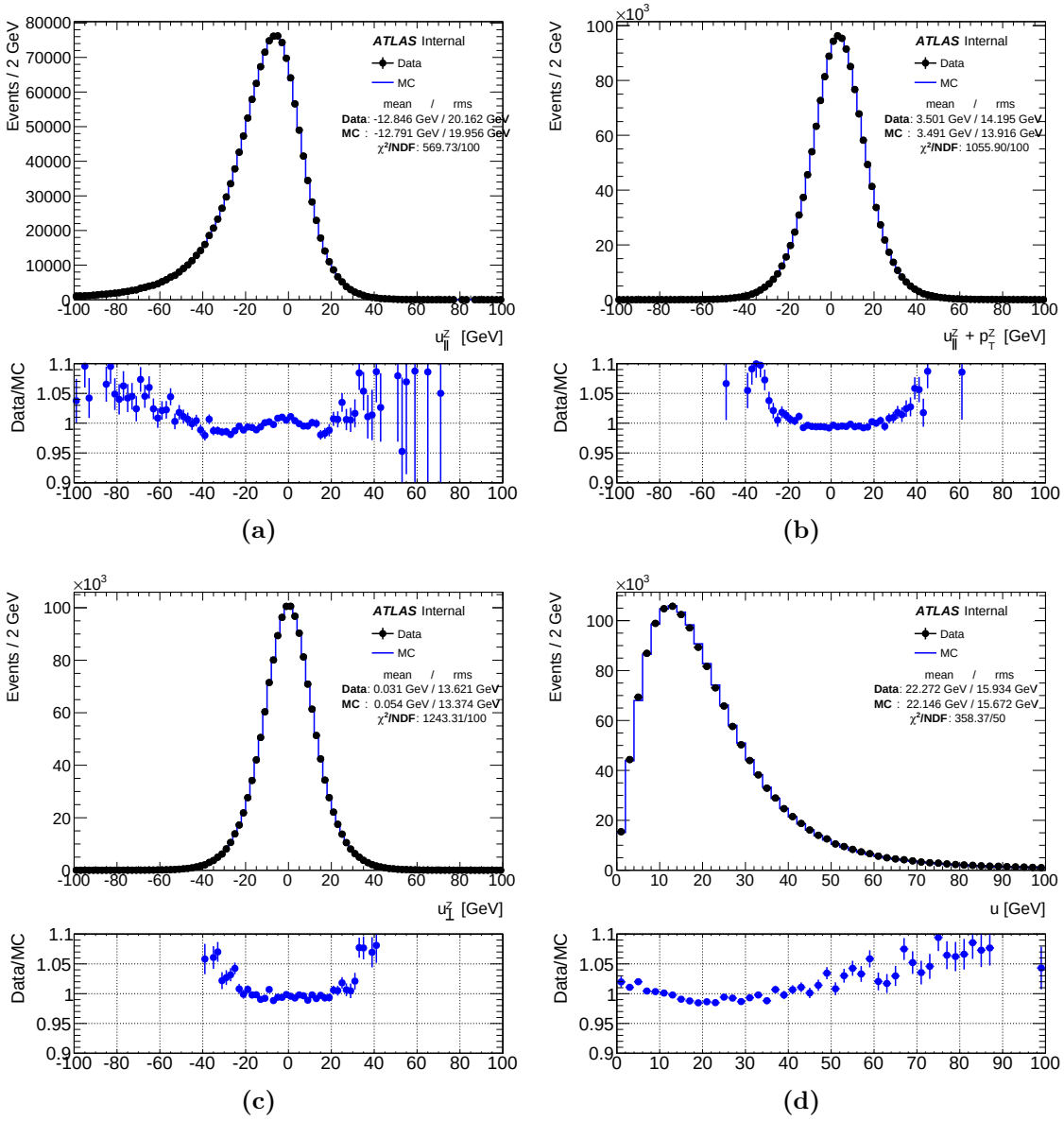

Figure 5.13: Hadronic recoil distribution in data (points) and MC (solid line) in $Z \to \mu\mu$ events: (a) parallel projection of the hadronic recoil on the dilepton transverse momentum, (b) parallel projection of the hadronic recoil plus the dilepton transverse momentum, (c) perpendicular projection of the hadronic recoil on the dilepton transverse momentum, (d) hadronic recoil distribution. Distributions are obtained after the pile-up reweighting and rescaling the $< \mu >$ distribution by 1.1.

barring issues with numerical stability, empty bins and low statistics. This transformation was used in shower shape analysis of unconverted photons [205]. If a given variable x is distributed according to the probability distribution function $h_{\text{data}}(x)$ in data, and

according to $h_{\mathrm{MC}}(x)$ in MC, the respective cumulative distribution functions are:

$$\begin{aligned} H_{\mathrm{data}}(x) &= \int_{-\infty}^{x} h_{\mathrm{data}}(t)\,\mathrm{d}t; \\ H_{\mathrm{MC}}(x) &= \int_{-\infty}^{x} h_{\mathrm{MC}}(t)\,\mathrm{d}t. \end{aligned} \tag{5.8}$$

The Smirnov transform function is mapping, in MC, the $\Sigma E_{\mathrm{T}} - u$ variable to a transformed variable $(\Sigma E_{\mathrm{T}} - u)^{\mathrm{tr}}$, that is by construction distributed as $\Sigma E_{\mathrm{T}} - u$ in data. It is defined as:

$$(\Sigma E_{\mathrm{T}} - u)^{\mathrm{tr}} = H^{-1}_{\mathrm{data}}[H_{\mathrm{MC}}(\Sigma E_{\mathrm{T}} - u)], \tag{5.9}$$

and the distribution h' of this variable satisfies

$$h'_{\mathrm{MC}}((\Sigma E_{\mathrm{T}} - u)^{\mathrm{tr}}) \equiv h_{\mathrm{data}}(\Sigma E_{\mathrm{T}} - u). \tag{5.10}$$

Figure 5.14 shows an example of this procedure for $\Sigma E_{\mathrm{T}} - u$. The result of the transformation, for $\Sigma E_{\mathrm{T}} - u$ distribution is shown in Figure 5.15.

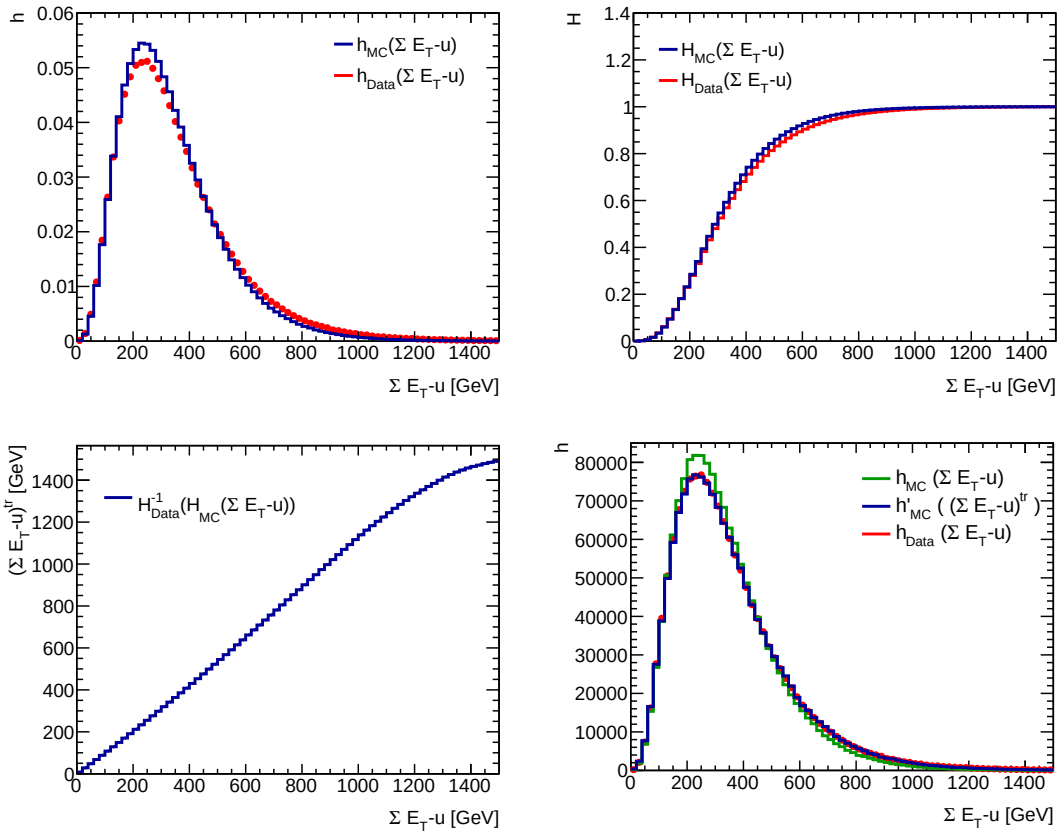

Figure 5.14: An example of the Smirnov transform procedure for $\Sigma E_{\mathrm{T}} - u$ distribution for the bin $10 < p_{\mathrm{T}}^{\ell\ell} < 20$ GeV in $Z \to \mu\mu$ events.

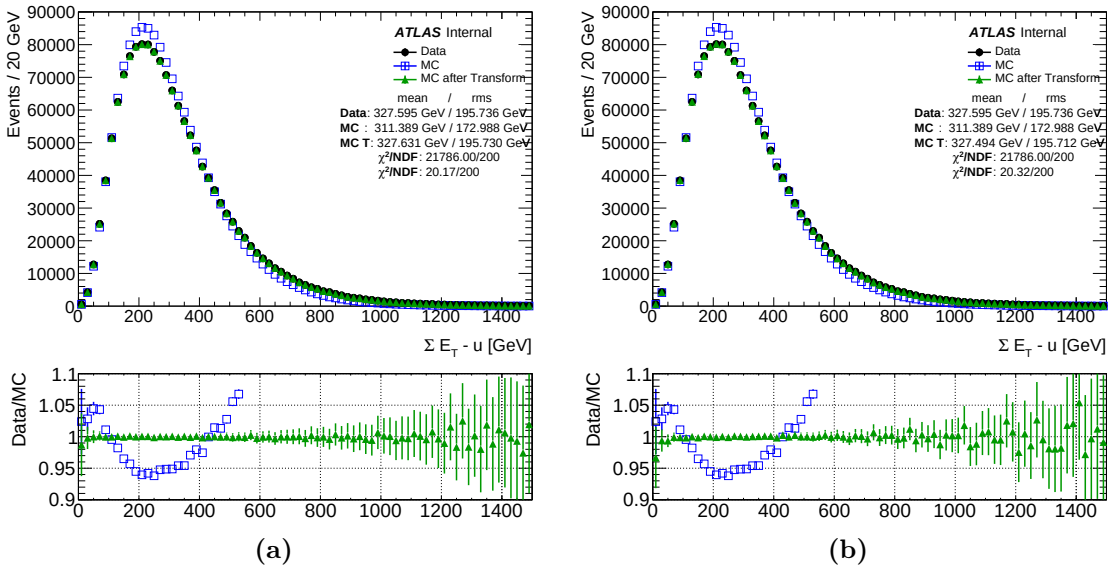

Figure 5.15: $\Sigma E_{\mathrm{T}} - u$ distribution in data and MC in $Z \to \mu\mu$ events before and after the transformation as described in the text, where MC T in the legend denotes the transformed $\Sigma E_{\mathrm{T}} - u$ distribution. The Smirnov transform is defined (a) inclusively in $p_{\mathrm{T}}^{\ell\ell}$ and (b) in bins of $p_{\mathrm{T}}^{\ell\ell}$.

The Smirnov transform can be defined inclusively or in bins of boson p_{T}. In Z-boson events, the $\Sigma E_{\mathrm{T}} - u$ data to MC discrepancy is observed to depend on the p_{T} of the boson, and incorporating this dependence results in better performance of the correction, as shown in Figure 5.16, where the distributions are shown after the full procedure for the recoil corrections.

The p_{T}-independent Smirnov transform can be defined directly on W-boson events, comparing data and MC:

$$h^{W}_{\mathrm{MC}}(\Sigma E_{\mathrm{T}} - u) \;\to\; h'^{W}_{\mathrm{MC}}((\Sigma E_{\mathrm{T}} - u)^{\mathrm{tr}}) \;\equiv\; h^{W}_{\mathrm{data}}(\Sigma E_{\mathrm{T}} - u), \tag{5.11}$$

but a p_{T}-dependent Smirnov transform on W-boson events has to be defined indirectly from Z-boson events, since the boson p_{T} is measured with poor resolution in the W-boson events. For this purpose the following approximation is used:

$$\tilde{h}^{W}_{\mathrm{data}}(\Sigma E_{\mathrm{T}} - u; p_{\mathrm{T}}) \equiv h^{Z}_{\mathrm{data}}(\Sigma E_{\mathrm{T}} - u; p_{\mathrm{T}}) \times \frac{\frac{h^{W}_{\mathrm{data}}(\Sigma E_{\mathrm{T}} - u)}{h^{W}_{\mathrm{MC}}(\Sigma E_{\mathrm{T}} - u)}}{\frac{h^{Z}_{\mathrm{data}}(\Sigma E_{\mathrm{T}} - u)}{h^{Z}_{\mathrm{MC}}(\Sigma E_{\mathrm{T}} - u)}}, \tag{5.12}$$

where the double ratio accounts for the overall data/MC difference between Z- and W-boson events, but assumes the p_{T} dependence of the discrepancy follows the behaviour seen in Z-boson events. The p_{T}-dependent transform is defined as:

$$h^{W}_{\mathrm{MC}}(\Sigma E_{\mathrm{T}} - u; p_{\mathrm{T}}) \;\to\; h'^{W}_{\mathrm{MC}}((\Sigma E_{\mathrm{T}} - u)^{\mathrm{tr}}; p_{\mathrm{T}}) \;\equiv\; \tilde{h}^{W}_{\mathrm{data}}(\Sigma E_{\mathrm{T}} - u; p_{\mathrm{T}}). \tag{5.13}$$

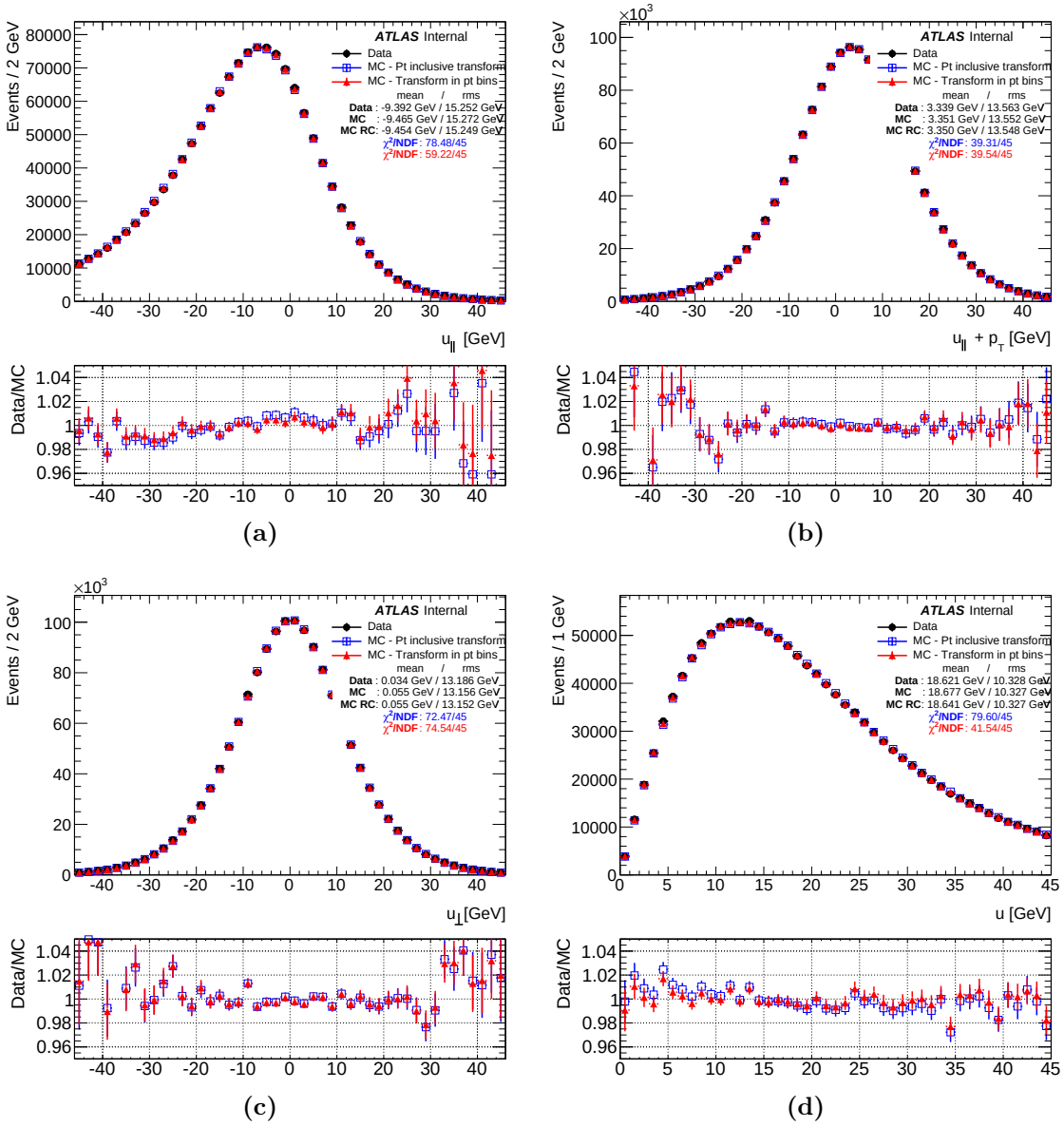

Figure 5.16: The impact of the p_{T}-dependence of the Smirnov transform on the hadronic recoil corrections. The hadronic recoil distribution in data (black points) and MC in $Z \to \mu\mu$ events after recoil corrections with Smirnov transform defined inclusively in p_{T} (blue points) and in p_{T} bins (red points). (a) Parallel projection of the hadronic recoil on the dilepton transverse momentum, (b) parallel projection of the hadronic recoil plus the dilepton transverse momentum, (c) perpendicular projection of the hadronic recoil on the dilepton transverse momentum, (d) hadronic recoil distribution.

5.5.3 *Azimuthal corrections*

The hadronic recoil vector is expected to have no preferred φ direction. However, the non-uniformity of the calorimeter, with the places where the density is lower or

higher then the average, will cause the observed missmodelng of the φ distribution of the hadronic recoil. The movement of the beam position, i.e. any an offset from the detector centre is resulting that some clusters which are closer to the interaction point have a larger averaged measured energy, also affects the φ distribution. Figure 5.17 shows x and y component of the hadronic recoil, as well as φ distribution marked in blue.

This missmodeling of the $\varphi(u)$ distribution can be corrected by shifting the mean of u_{X} and u_{Y} distributions. The corrections are obtained by studying the slopes of the mean of u_{X} and u_{Y} distributions as a function of $\Sigma E_{\mathrm{T}} - u$ and the azimuth of the dimuon system $\varphi_{\mu\mu}$ in the $Z \to \mu\mu$ events which is illustrated in Figure 5.18, marked in blue.

The corrections are applied to the u_{X} and u_{Y} distributions in MC according to data to MC difference shown in Figure 5.18 (a) and (b) with blue points as a function of $\Sigma E_{\mathrm{T}} - u$:

$$\begin{aligned} u'_{\mathrm{X}} &= u_{\mathrm{X}} + (< u_{\mathrm{X}} >_{\mathrm{data}} - < u_{\mathrm{X}} >_{\mathrm{MC}}); \\ u'_{\mathrm{Y}} &= u_{\mathrm{Y}} + (< u_{\mathrm{Y}} >_{\mathrm{data}} - < u_{\mathrm{Y}} >_{\mathrm{MC}}). \end{aligned} \tag{5.14}$$

The effect of these corrections in the $Z \to \mu\mu$ events is illustrated in Figure 5.17 for x and y component of the hadronic recoil, as well as φ distribution, Figure 5.18 for the mean of u_{X} and u_{Y} as a function of $\Sigma E_{\mathrm{T}} - u$ and the azimuth of the dimuon system $\varphi_{\mu\mu}$, and Figure 5.19 for the hadronic recoil distribution as well as its parallel and perpendicular projection with respect to the dilepton transverse momentum.

5.5.4 *Residual recoil corrections*

After previously described corrections: the rescaling the $< \mu >$ distribution by 1.1, the transform of the $\Sigma E_{\mathrm{T}} - u$ distribution and the correction of the $\varphi(u)$ missmodeling, there are still differences between data and MC for hadronic recoil in Z-boson events, as illustrated in Figure 5.19. The recoil distributions as well as their projections are not affected by the Smirnov transform of the $\Sigma E_{\mathrm{T}} - u$ distribution. The mean and width of $u_{\perp}$ and $u_{\parallel} + p_{\mathrm{T}}^{\ell\ell}$ as a function of $\Sigma E_{\mathrm{T}} - u$ are shown in Figure 5.20 respectively. In order to correct for the remaining differences between simulation and data, an additional correction to the hadronic recoil is nedded.

The mean and the width of the projection of hadronic recoil with respect to boson p_{T} are corrected in bins of boson p_{T} and $\Sigma E_{\mathrm{T}} - u$. The dependence of ΣE_{T} and $\Sigma E_{\mathrm{T}} - u$ as a function of p_{T} is shown in Figure 5.21. Since the boson p_{T} and ΣE_{T} are correlated, it is better to derive the corrections as a function of $\Sigma E_{\mathrm{T}} - u$. Corrections are derived from $Z \to \mu\mu$ events. By using correction factors that depend explicitly on boson p_{T} and $\Sigma E_{\mathrm{T}} - u$, all remaining differences between Z- and W-boson events are taken into account and therefore the derived residual correction factors can be applied directly on simulated W-boson events. Remaining differences between data and MC for u_{T} and

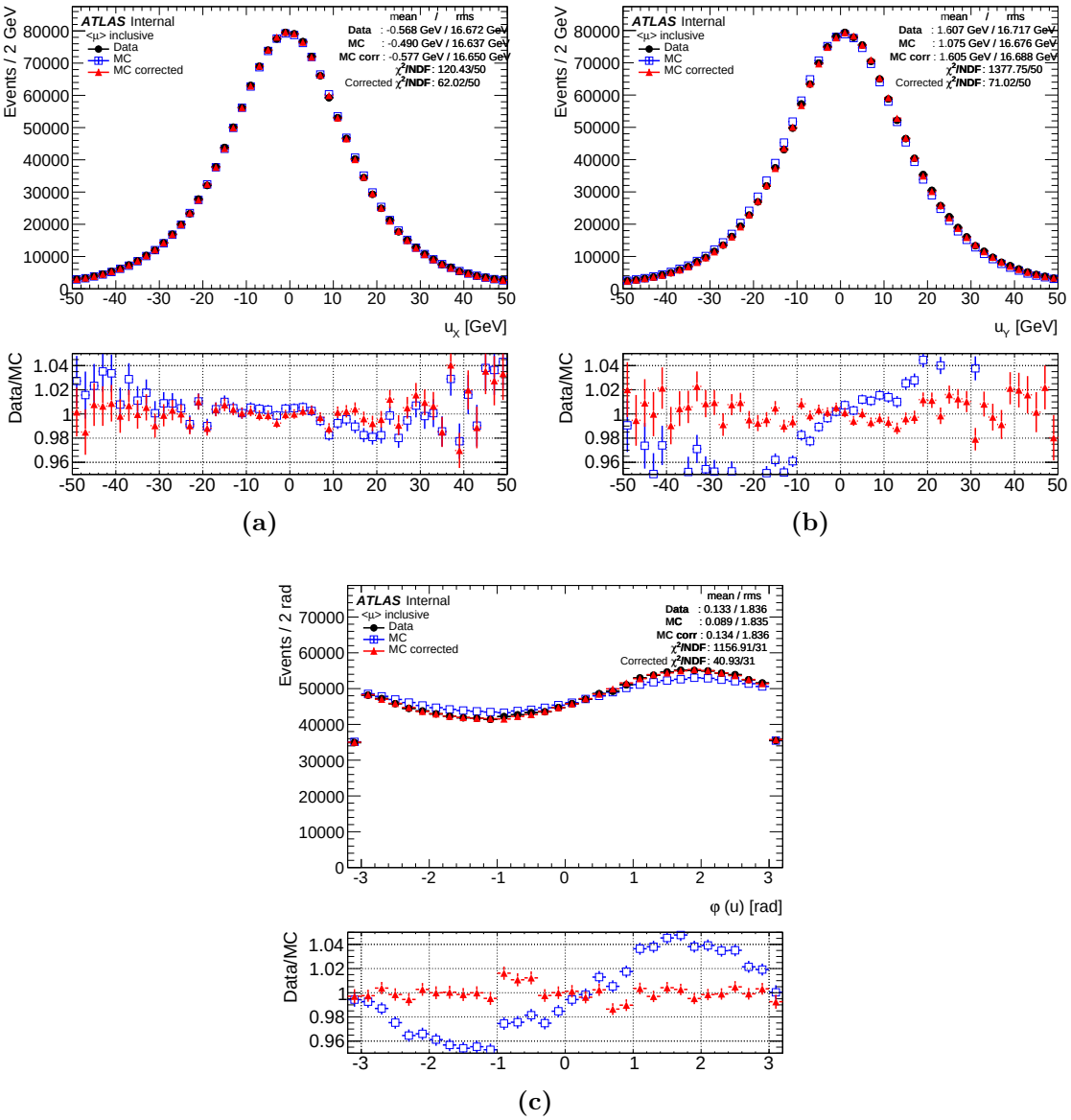

Figure 5.17: Hadronic recoil distribution in data (black points), MC (blue points) and corrected MC (red points) in $Z \to \mu\mu$ events: (a) x-component of the hadronic recoil, (b) y-component of the hadronic recoil, (c) φ distribution of the hadronic recoil. Distributions are obtained after the pile-up reweighting, rescaling the $< \mu >$ distribution by 1.1 and applying the u_{X} and u_{Y} correction.

$\Sigma E_{\mathrm{T}} - u$ in W-boson events can be corrected independently from the residual hadronic recoil corrections. This correction is applied on MC to the mean and width of parallel and perpendicular projection of the hadronic recoil with respect to true boson p_{T}, in this way the correction is universal.

The correction procedure is schematically shown in Figure 5.22 (a). The first step is to define different resolution curves as a functions of $\Sigma E_{\mathrm{T}} - u$ and p_{T} (Figure 5.22

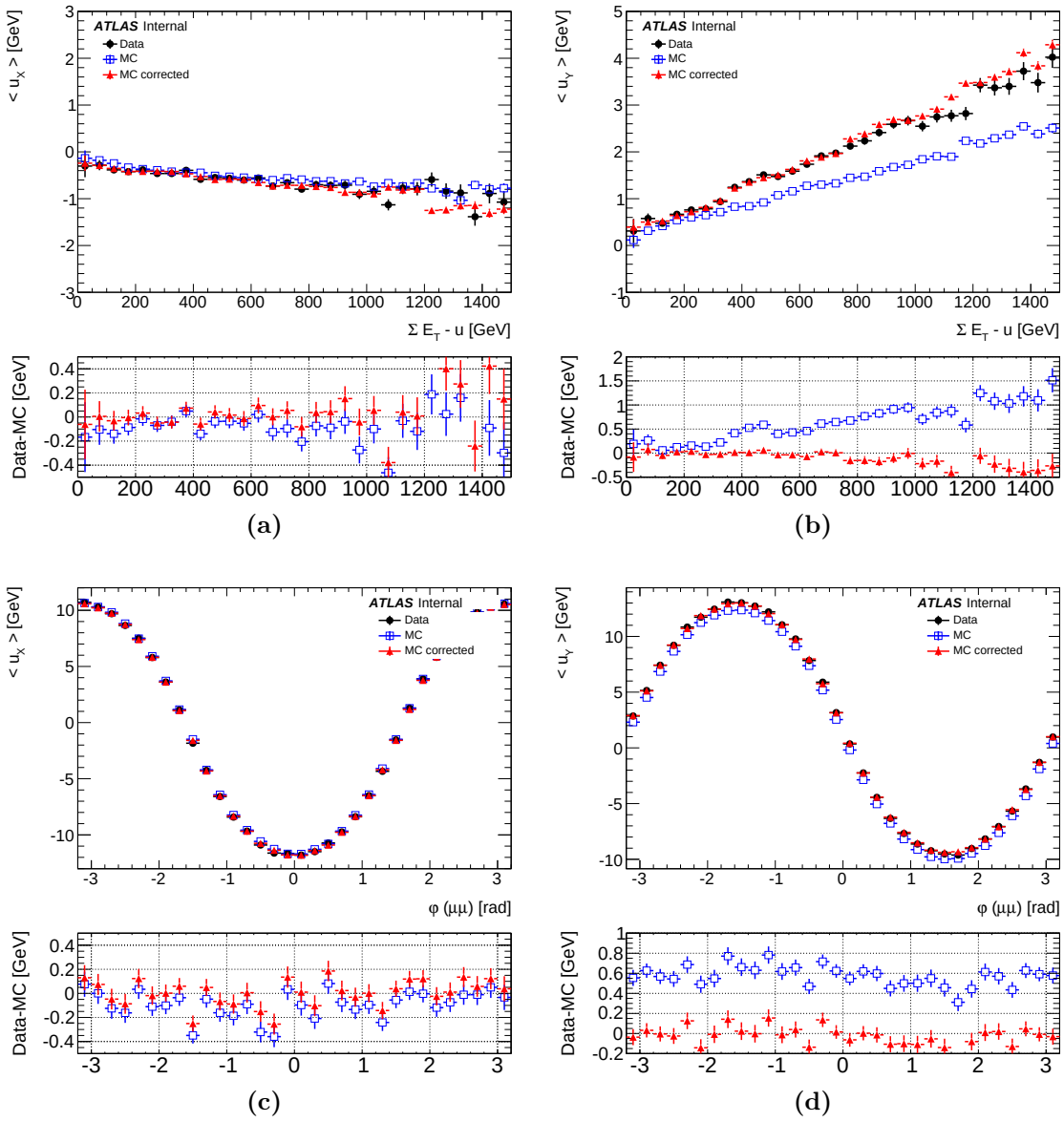

Figure 5.18: Mean of u_{X} and u_{Y} distributions in data (black points), MC (blue points) and corrected MC (red points) in $Z \to \mu\mu$ events: (a) and (b) as a function of $\Sigma E_{\mathrm{T}} - u$, (c) and (d) as a function of φ of the di-muon system. Distributions are obtained after the pile-up reweighting, rescaling the $< \mu >$ distribution by 1.1 and applying the u_{X} and u_{Y} correction.

(a) is showing only as a function of $\Sigma E_{\mathrm{T}} - u$) for data, MC and $(\Sigma E_{\mathrm{T}} - u)^{\mathrm{tr}}$ in MC. One part of the difference in resolution between data and MC comes from mismodeling of the $\Sigma E_{\mathrm{T}} - u$ distribution, this is accounted for with the transform, step from (1) to (2) in Figure 5.22 (a). Therefore, the correction for the resolution is defined from the difference in resolution between data and MC evaluated at $(\Sigma E_{\mathrm{T}} - u)^{\mathrm{tr}}$, for a given

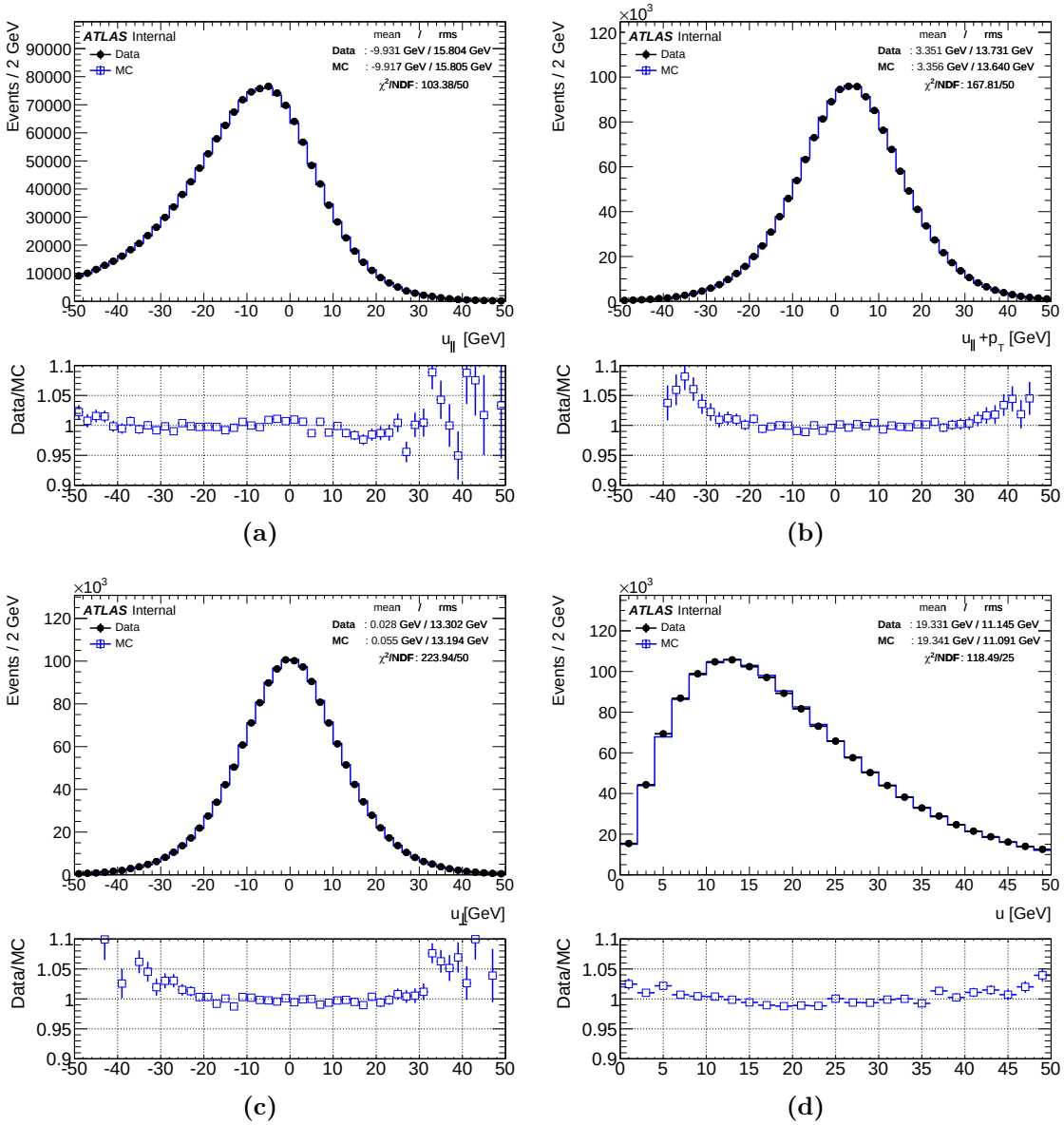

Figure 5.19: Hadronic recoil distribution in data (points) and MC (solid line) in $Z \to \mu\mu$ events: (a) parallel projection of the hadronic recoil on the dilepton transverse momentum, (b) sum of parallel projection of the hadronic recoil and the dilepton transverse momentum, (c) perpendicular projection of the hadronic recoil on the dilepton transverse momentum, (d) hadronic recoil distribution. Distributions are obtained after the pile-up reweighting, rescaling the $< \mu >$ distribution by 1.1 and applying the u_{X} and u_{Y} correction.

$\Sigma E_{\mathrm{T}} - u$ value, the difference between (2) and (3) in Figure 5.22 (a):

$$r = \frac{(3)}{(2)} = \frac{\sigma^{\mathrm{data}}_{u_\perp}((\Sigma E_{\mathrm{T}} - u)^{\mathrm{tr}})}{\sigma'^{\mathrm{MC}}_{u_\perp}((\Sigma E_{\mathrm{T}} - u)^{\mathrm{tr}})}, \qquad \sigma'^{\mathrm{MC}}_{u_\perp}((\Sigma E_{\mathrm{T}} - u)^{\mathrm{tr}}) \equiv \sigma^{\mathrm{MC}}_{u_\perp}(\Sigma E_{\mathrm{T}} - u). \quad (5.15)$$

This procedure accounts both for possible data to MC differences in the resolution

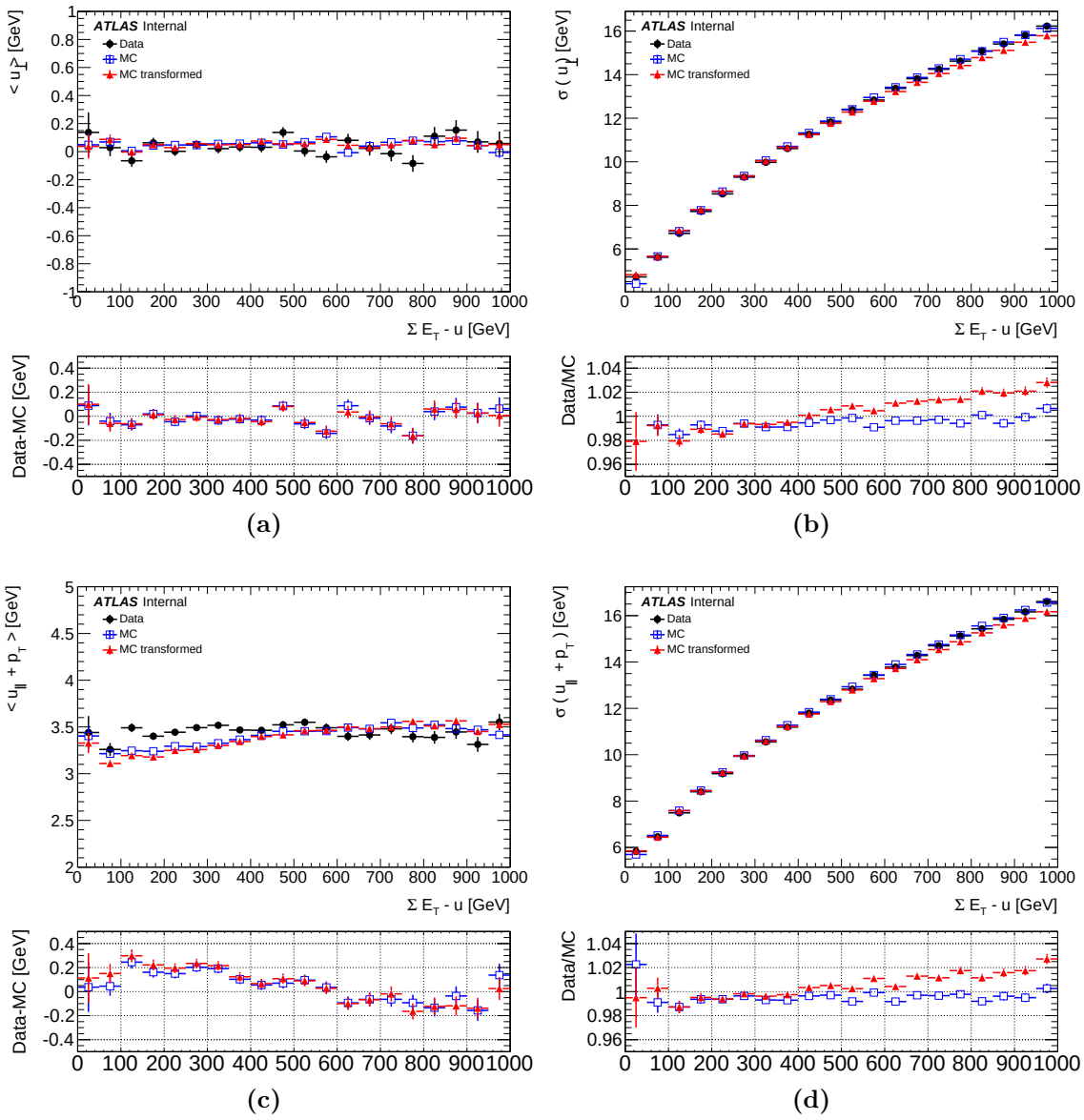

Figure 5.20: (a) Mean and (b) width of $u_\perp$, (c) mean and (d) width of $u_\parallel + p_{\mathrm{T}}^{\ell\ell}$ of the hadronic recoil projections distributions as a function of $\Sigma E_{\mathrm{T}} - u$ in data and MC for $Z \to \mu\mu$ events, the blue points are representing function of $\Sigma E_{\mathrm{T}} - u$, while red points as a function of transformed $\Sigma E_{\mathrm{T}} - u$.

curves as a function of $\Sigma E_{\mathrm{T}} - u$, and for differences in the $\Sigma E_{\mathrm{T}} - u$ distribution itself.

The correction for the mean of the parallel projection of hadronic recoil with respect to boson p_{T} is defined in the same way, from the difference in mean for $u_\parallel + p_{\mathrm{T}}^{\ell\ell}$ in data and transformed MC. This method allows the mean and resolution to be evaluated at the same value of $\Sigma E_{\mathrm{T}} - u$. It is possible to use a different approach for this method, instead of calculating additional resolution curve, to calculate the difference between data and MC but for two different values of $\Sigma E_{\mathrm{T}} - u$ and transformed $\Sigma E_{\mathrm{T}} - u$,

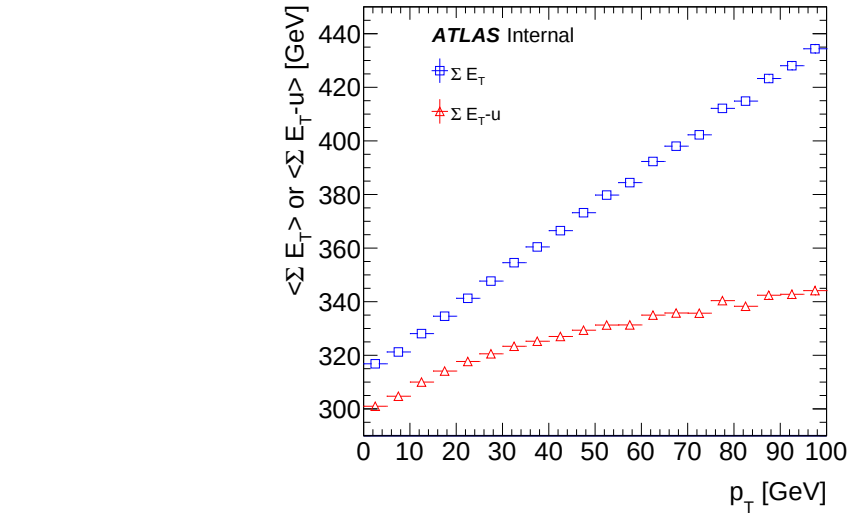

(a)

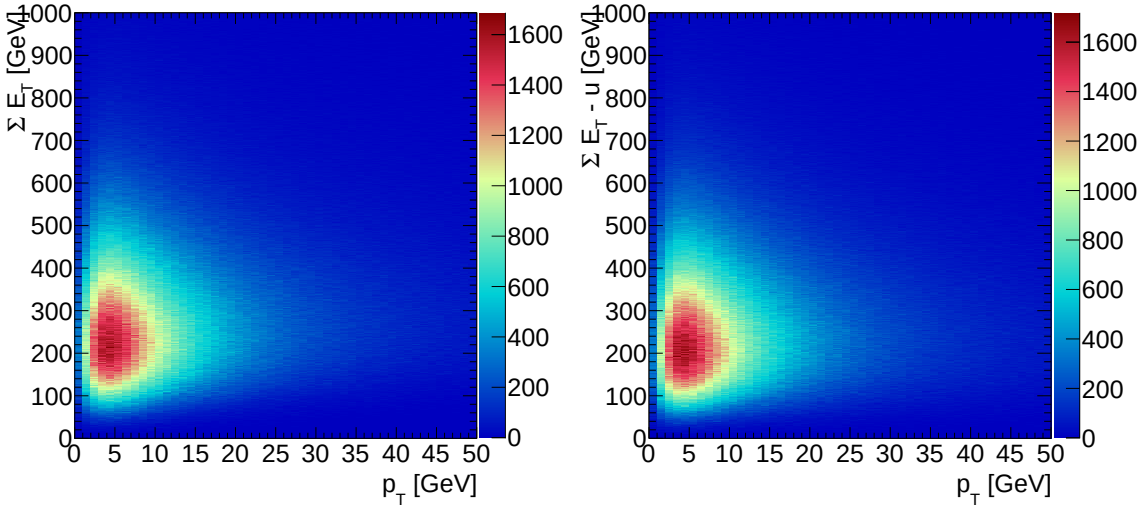

(b) (c)

Figure 5.21: Correlation between ΣE_{T} and $p_{\mathrm{T}}^{\mathrm{Z}}$ and $\Sigma E_{\mathrm{T}} - u$ and $p_{\mathrm{T}}^{\mathrm{Z}}$ in $Z \to \mu\mu$ events. (a) Mean of ΣE_{T} and $\Sigma E_{\mathrm{T}} - u$ as a function of $p_{\mathrm{T}}^{\mathrm{Z}}$. (b) Two dimensional plot ΣE_{T} vs $p_{\mathrm{T}}^{\mathrm{Z}}$, with the correlation coefficient of 0.8. (c) Two dimensional plot $\Sigma E_{\mathrm{T}} - u$ vs $p_{\mathrm{T}}^{\mathrm{Z}}$, with the correlation coefficient of 0.3.

as illustrated in Figure 5.22 (b). Step form (1) to (2) is the correction of the ΣE_T discrepancy (i.e. transform), and from (2) to (3) is correction for the resolution for a given value of ΣE_T. In this case correction for the resolution is defined as a difference between (1) and (3):

$$\mathbf{r} = \frac{(3)}{(1)} = \frac{\sigma_{u_\perp}^{DATA}(\Sigma E_T^{tr/V})}{\sigma_{u_\perp}^{MC}(\Sigma E_T)}$$

These two approaches are equivalent and give the same result. The only difference is that with approach with three resolution curves corrections are defined at same value

of ΣE_T, while for the approach with two resolution curves corrections are defined for two different values of ΣE_T - original and transformed.

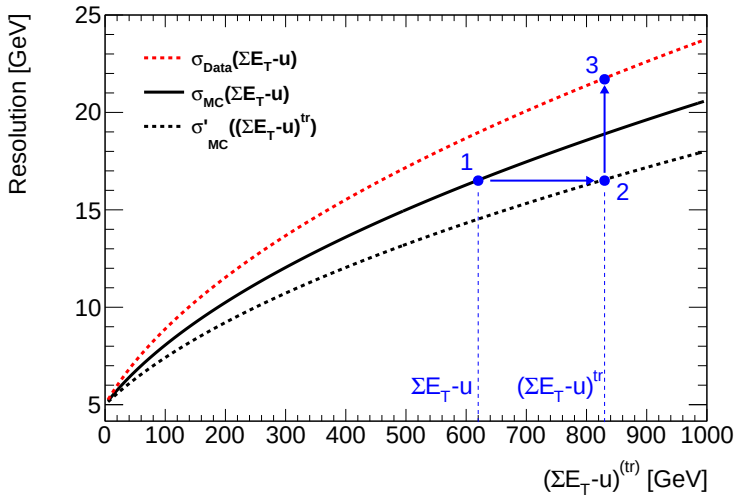

(a)

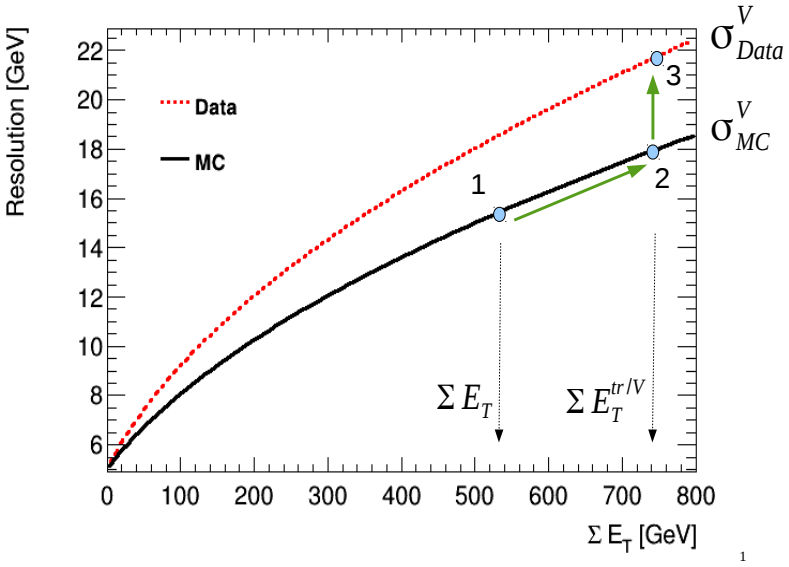

(b)

Figure 5.22: Schematic view of the correction procedure: resolution of $u_\perp$ as a function of $\Sigma E_\mathrm{T} - u$. There are (a) three and (b) two resolution curves: data in dotted red (σ_{data}), MC in solid black (σ_{MC}) and MC as a function of $(\Sigma E_\mathrm{T} - u)^\mathrm{tr}$ in dotted black (σ'_{MC}). Step $1 \rightarrow 2$ represents the transformation of $\Sigma E_\mathrm{T} - u$ in MC; step $2 \rightarrow 3$ is the actual resolution correction (difference in resolution between data and MC for a given value of $(\Sigma E_\mathrm{T} - u)^\mathrm{tr}$.

In order to derive correction factors for mean and resolution for parallel and perpendicular component of the hadronic recoil, mean and RMS of the corresponding distributions are extracted from data and MC in bins of $\Sigma E_\mathrm{T} - u$ and p_T. The par-

allel component of the hadronic recoil is corrected for mean and resolution, while the perpendicular component is corrected only for resolution. Parallel and perpendicular component of the hadronic recoil (with respect to the boson p_{T}) are corrected in MC according to the equations:

$$u'_{\parallel} = b(p_{\mathrm{T}}, (\Sigma E_{\mathrm{T}} - u)^{\mathrm{tr}}) + < u_{\parallel} >_{\mathrm{data}} + (u_{\parallel} - < u_{\parallel} >_{\mathrm{data}}) \cdot r(p_{\mathrm{T}}, (\Sigma E_{\mathrm{T}} - u)^{\mathrm{tr}}), \quad (5.16)$$

$$u'_{\perp} = u_{\perp} \cdot r(p_{\mathrm{T}}, (\Sigma E_{\mathrm{T}} - u)^{\mathrm{tr}}), \quad (5.17)$$

where correction for the mean is the difference in the means for $u_{\parallel} + p_{\mathrm{T}}$ in data and MC:

$$b = < u_{\parallel} + p_{\mathrm{T}} >^{\mathrm{data}} - < u_{\parallel} + p_{\mathrm{T}} >^{\mathrm{MC}}, \quad (5.18)$$

and the resolution correction $r(p_{\mathrm{T}}, (\Sigma E_{\mathrm{T}} - u)^{\mathrm{tr}})$ is the ratio of the $u_{\perp}$ distributions RMS in data and MC, as defined in Equation 5.15.

The correction for the resolution is derived from $u_{\perp}$ and applied to both parallel and perpendicular component of the hadronic recoil. The mean is only corrected for the $u_{\parallel}$ component of the recoil. The correction presented with previous equations is applied event by event.

The resolution of $u_{\perp}$ depends on the pile-up and therefore the $< \mu >$ distribution. The resolution of $u_{\perp}$ as a function of $< \mu >$ is illustrated in Figure 5.23. In order to gain sensitivity, this correction procedure is defined in three $< \mu >$ bins, i.e. for low pile-up for $< \mu > \in (2.5, 6.5)$, medium for $< \mu > \in (6.5, 9.5)$ and high pile-up for $< \mu > \in (9.5, 16.0)$, the sample approximately corresponds to 40%, 30% and 30% of the events for the 3 $< \mu >$ bins respectevly. The correction values for these three $< \mu >$ bins are shown in Figure 5.24.

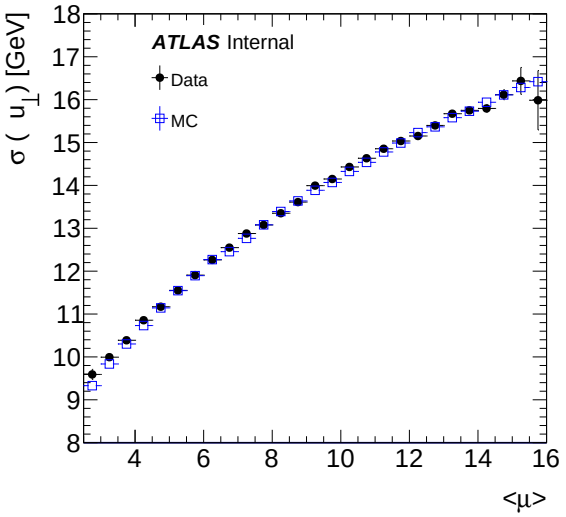

Figure 5.23: The RMS of $u_{\perp}$ as a function of $< \mu >$ in $Z \to \mu\mu$ events for data and MC.

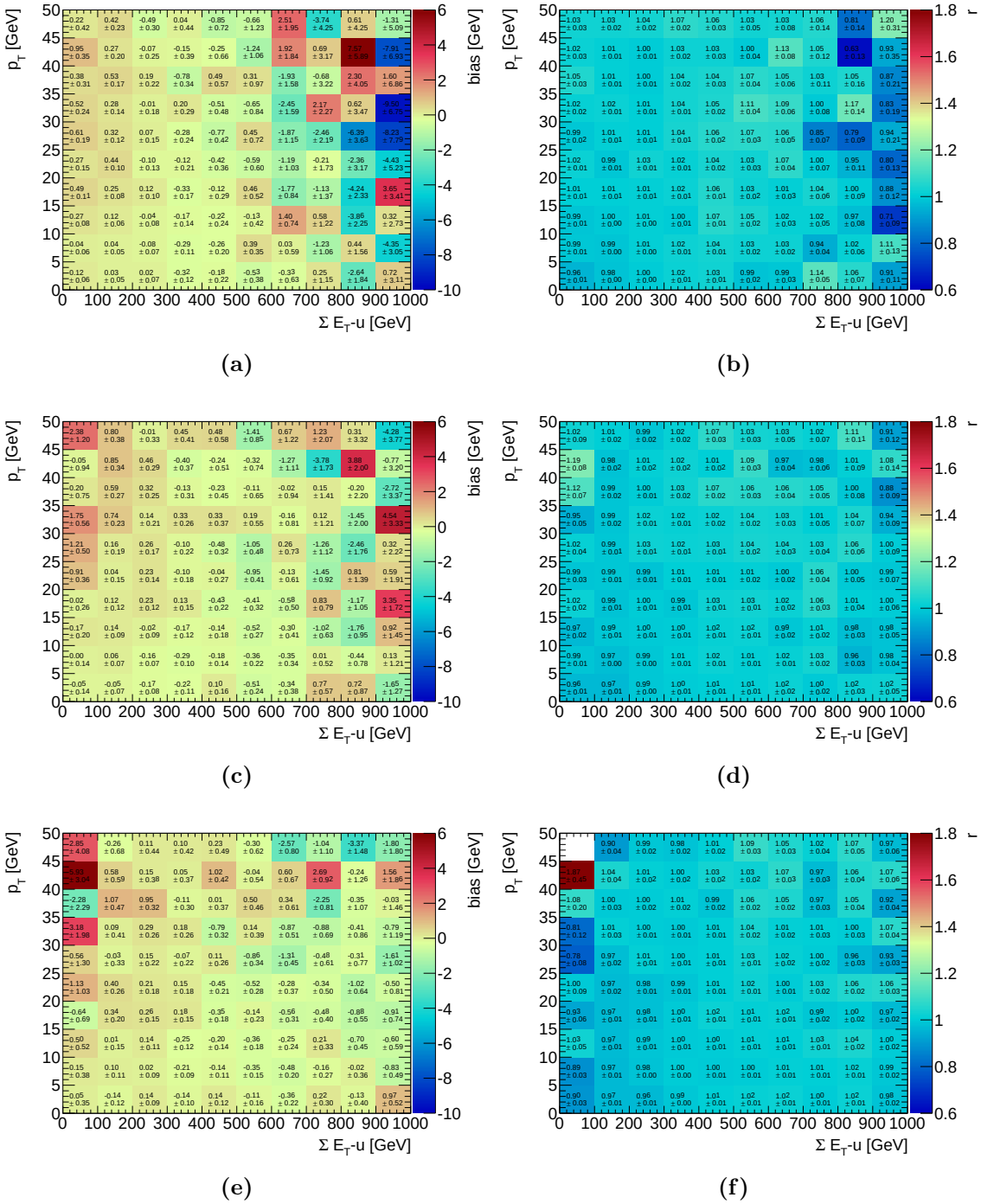

Figure 5.24: Values of the parameters b (left) and r (right) for (a), (b) low, (c), (d) medium and (e), (f) high pile-up in bins of $\Sigma E_{\mathrm{T}} - u$ and boson p_{T} . Only statistical uncertainty is shown.

5.6 VALIDATION OF THE CORRECTED HADRONIC RECOIL IN Z- AND W-BOSON EVENTS

5.6.1 *Validation with the Z-boson events*

The effect of the described procedure for correction of the hadronic recoil is shown in Figure 5.25 for the hadronic recoil distribution and its parallel and perpendicular projection inclusively in $< \mu >$. After corrections there is a very good agreement between data and MC. The improvement can be quantified with the decreasing χ^2/NDF for each distribution which takes only statistical uncertainty into account. Mean of the $u_{\parallel} + p_{\mathrm{T}}^{\ell\ell}$ and RMS of the $u_{\perp}$ as a function of the dilepton transverse momentum $p_{\mathrm{T}}^{\ell\ell}$ and $\Sigma E_{\mathrm{T}} - u$ are shown in Figures 5.26 and 5.27, respectively, and there is much better agreement between data and MC after the hadronic recoil corrections, the resolution is modeled within less than 1%.

Since the hadronic recoil corrections are derived only from $Z \to \mu\mu$ events, it is very important to validate the corrections on the $Z \to ee$ events. The hadronic recoil distribution and its parallel and perpendicular projection with respect to the dilepton transverse momentum is shown in Figure 5.28 inclusively in $< \mu >$. After the corrections there is good agreement between data and MC, allowing the application of the correction in both, electron and muon, channels.

An important quantity that can be calculated from the Z-boson events, to test the goodness of the recoil correction to the W-boson events is the pseudo-transverse mass. The Z-boson pseudo-transverse mass is defined with analogy to the W-boson transverse mass defined with Equation 1.54 when treating one of the charged leptons from the Z-boson decay as the neutrino and ignoring its transverse momentum when defining the event kinematics. There are two pseudo-transverse masses, one calculated with the positive and one with the negative lepton, as shown in Figure 5.29 in $Z \to \mu\mu$ and in Figure 5.30 in $Z \to ee$ events for inclusive $< \mu >$ distribution.

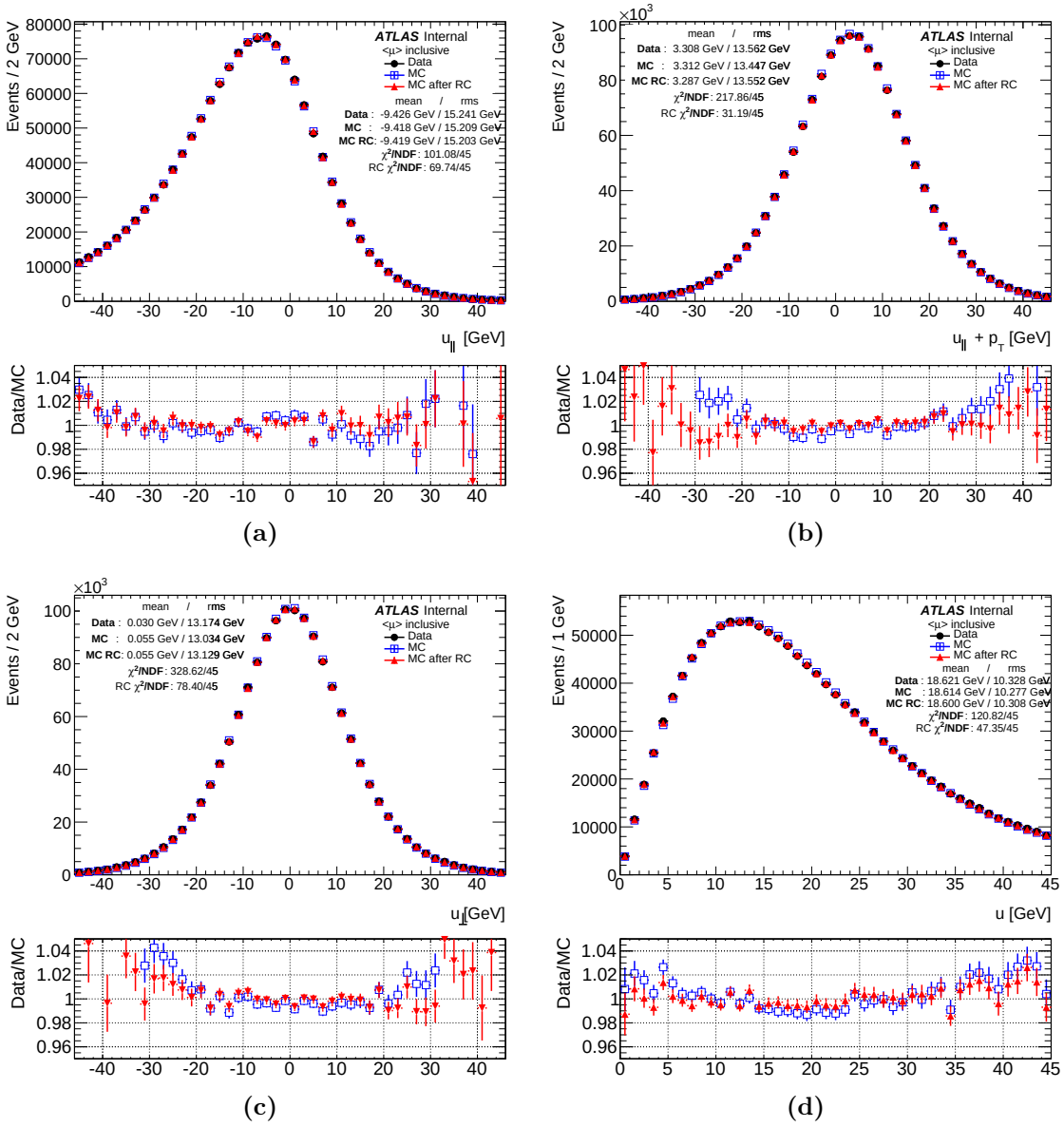

Figure 5.25: Hadronic recoil distribution in data and MC before (blue points) and after (red points) the hadronic recoil corrections in $Z \to \mu\mu$ events inclusive in $< \mu >$. (a) Projection of the hadronic recoil to the parallel to the dilepton transverse momentum. (b) Sum of parallel projection of the hadronic recoil to the dilepton transverse momentum and the dilepton transverse momentum. (c) Projection of the hadronic recoil to the perpendicular to the dilepton transverse momentum. (d) Hadronic recoil distribution. The lower panels show the data to MC ratio, with the error bars showing only the statistical uncertainty. The χ^2/NDF does not account the systematics uncertainties.

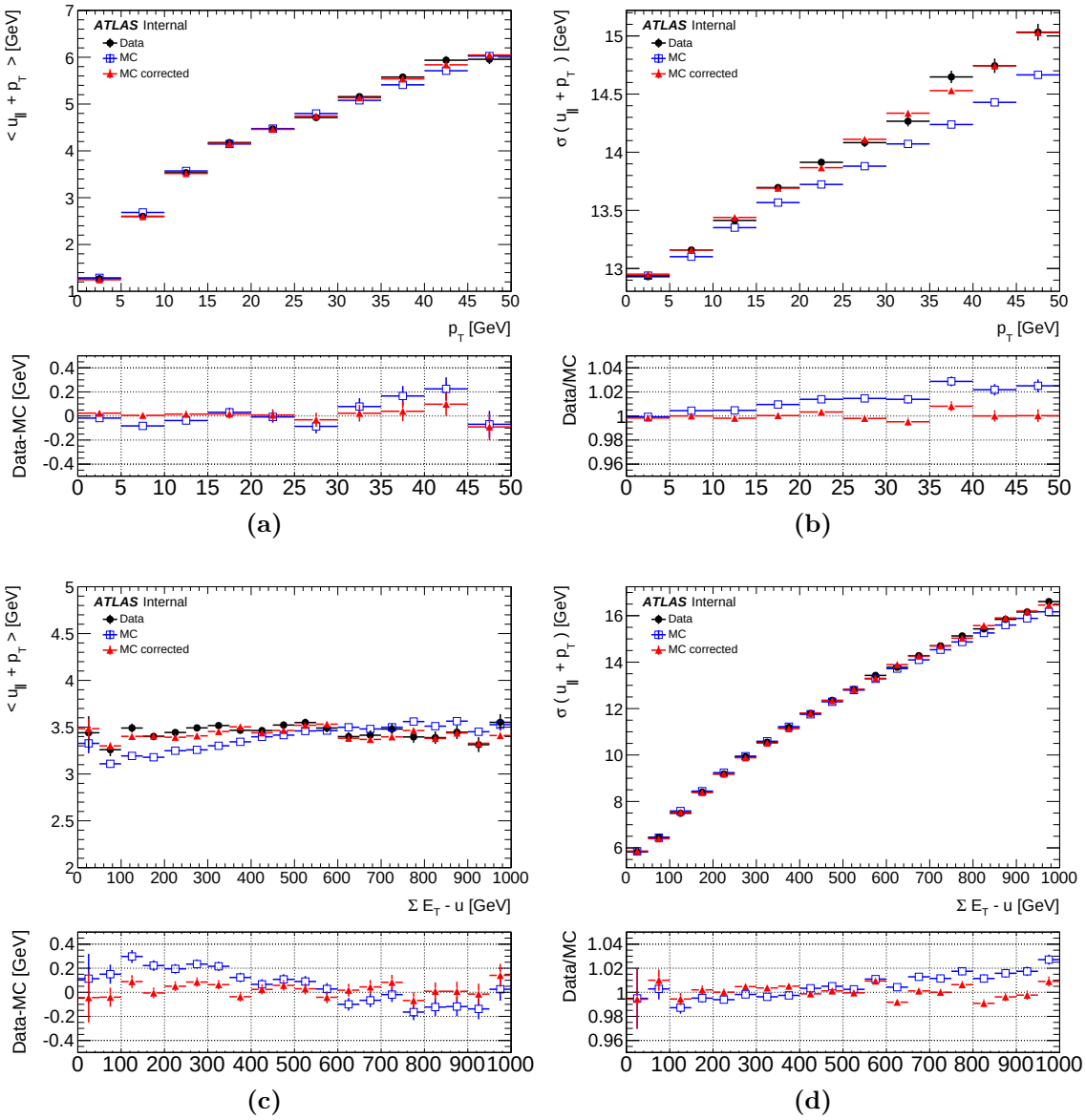

Figure 5.26: Mean and RMS of the $u_{\parallel} + p_{\mathrm{T}}^{\ell\ell}$ of the hadronic recoil projections distributions as a function of $p_{\mathrm{T}}^{\ell\ell}$ (a and b) and $\Sigma E_{\mathrm{T}} - u$ (c and d) in data and MC in $Z \to \mu\mu$ events before (blue) and after (red) the hadronic recoil correction. The lower panels show the data to MC ratio, with the error bars showing only the statistical uncertainty.

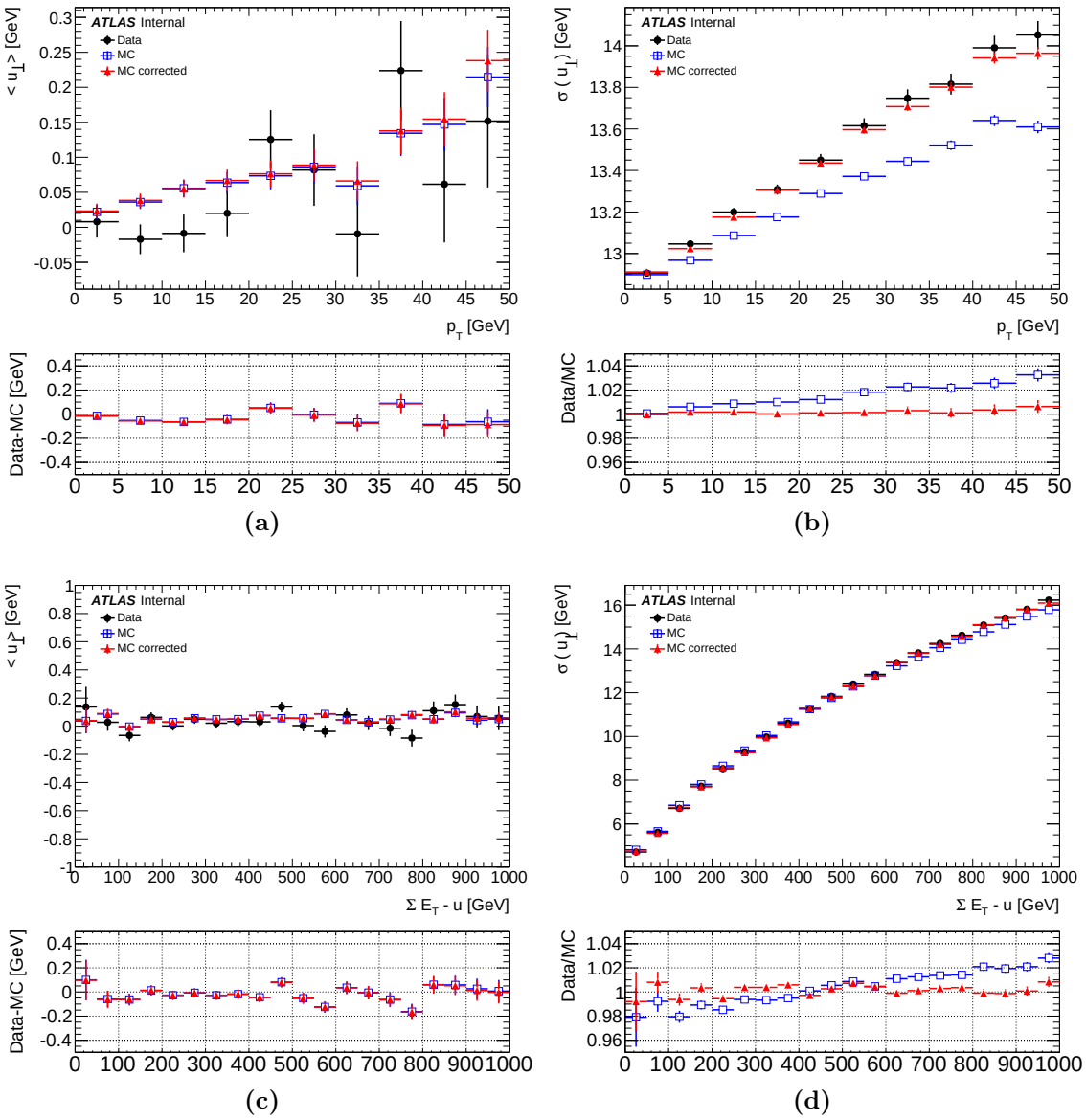

Figure 5.27: Mean and RMS of the $u_\perp$ of the hadronic recoil projections distributions as a function of $p_{\mathrm{T}}^{\ell\ell}$ (a and b) and $\Sigma E_{\mathrm{T}} - u$ (c and d) in data and MC in $Z \to \mu\mu$ events before (blue) and after (red) the hadronic recoil correction. The lower panels show the data to MC ratio, with the error bars showing only the statistical uncertainty.

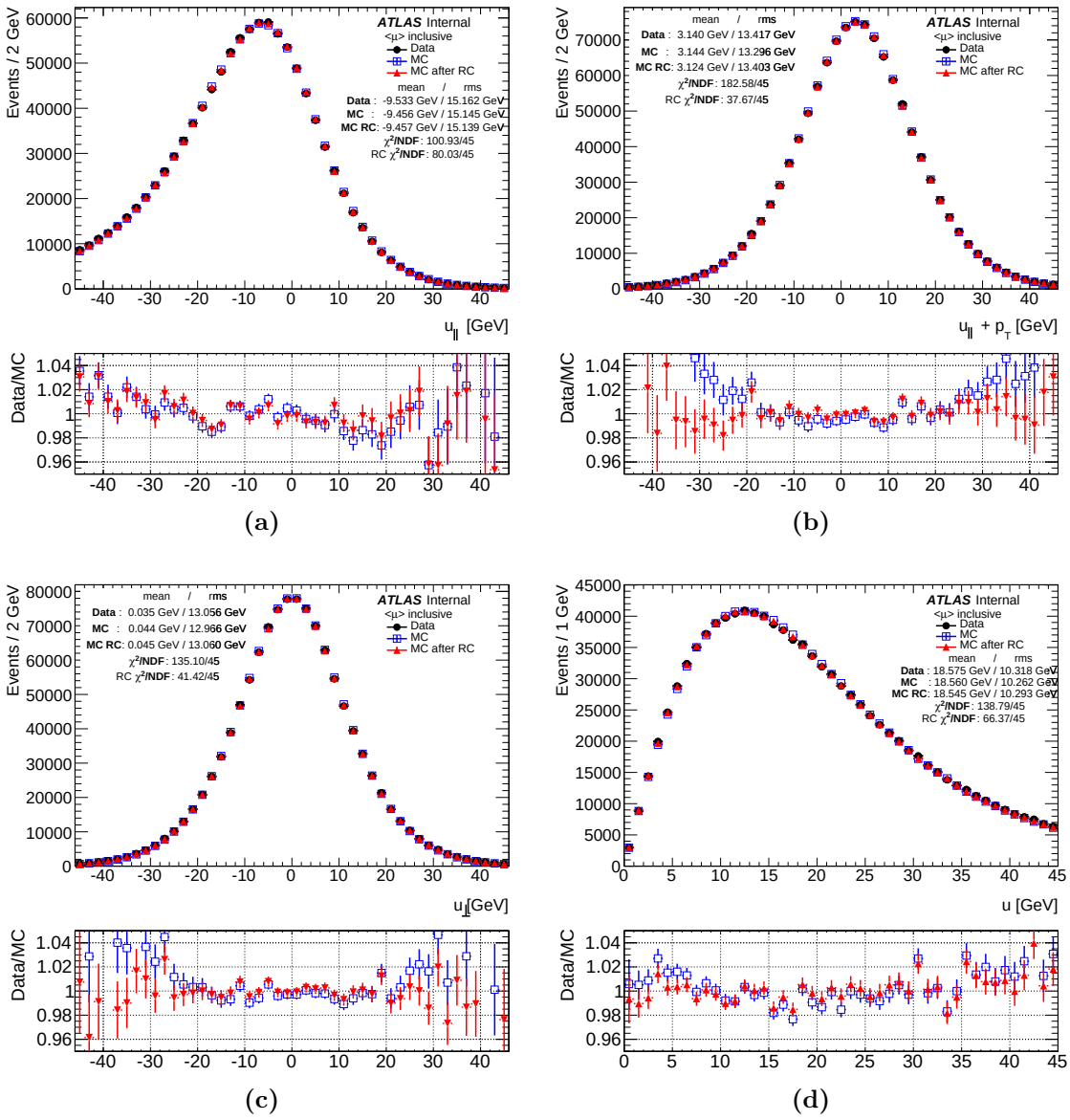

Figure 5.28: Hadronic recoil distribution in data and MC before (blue) and after (red) the hadronic recoil corrections in $Z \to ee$ events inclusive in $< \mu >$. (a) Projection of the hadronic recoil to the parallel to the dilepton transverse momentum. (b) Sum of parallel projection of the hadronic recoil to the dilepton transverse momentum and the dilepton transverse momentum. (c) Projection of the hadronic recoil to the perpendicular to the dilepton transverse momentum. (d) Hadronic recoil distribution. The lower panels show the data to MC ratio, with the error bars showing only the statistical uncertainty. The χ^2/NDF does not account the systematics uncertainties.

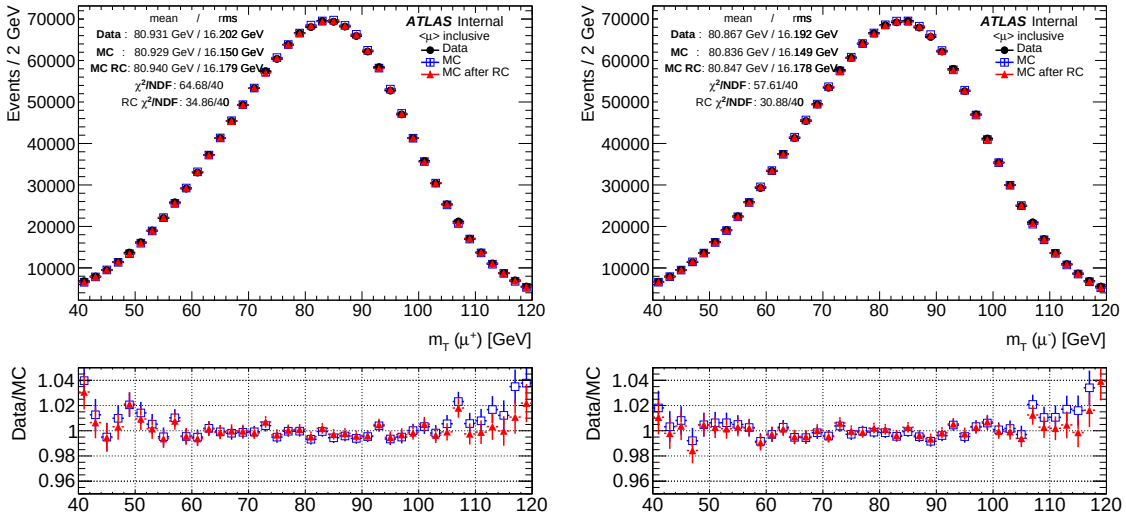

(a) **(b)**

Figure 5.29: Pseudo-transverse mass when only (a) positive or (b) negative lepton is taken into account in data and MC before (blue) and after (red) the hadronic recoil corrections in $Z \to \mu\mu$ events inclusively in $< \mu >$. The lower panels show the data to MC ratio, with the error bars showing only the statistical uncertainty. The χ^2/NDF does not account the systematics uncertainties.

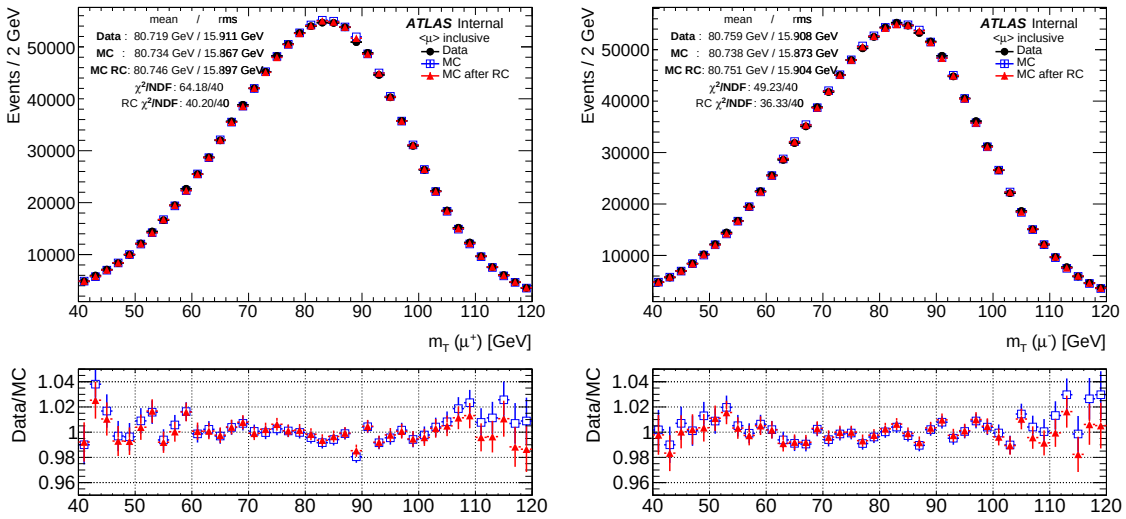

(a) **(b)**

Figure 5.30: Pseudo-transverse mass when only (a) positive or (b) negative lepton is taken into account in data and MC before (blue) and after (red) the hadronic recoil corrections in $Z \to ee$ events inclusively in $< \mu >$. The lower panels show the data to MC ratio, with the error bars showing only the statistical uncertainty. The χ^2/NDF does not account the systematics uncertainties.

5.6.2 *Validation with the W-boson events*

The $W \to \mu\nu$ distributions for recoil, parallel and perpendicular projection with respect to the lepton p_{T} before the recoil corrections are shown in Figure 5.31.

The results after applying corrections derived with the Z-boson events, to the W-boson events in the muon channel are shown in Figure 5.32. There is a discrepancy between data and MC after application of these correction. One of the reasons for this discrepancy is because the $\Sigma E_{\mathrm{T}} - u$ distribution itself is different between Z, W^+ and W^- boson events, as illustrated in Figure 5.42. Therefore the $\Sigma E_{\mathrm{T}} - u$ transform derived only from the Z-boson events will not be fully correct when applied to the W-boson events. There is approximately 20 GeV difference in mean and about 10 GeV difference in RMS between $\Sigma E_T - u$ in Z- and W-boson events. Furthermore, there is a difference between W^+ and W^- boson events. Therefore, the hadronic recoil corrections derived with the transformation of $\Sigma E_{\mathrm{T}} - u$ from the Z-boson events does not give good results when applied to the W-boson events.

When applying the correction procedure to the W-boson events, a new $\Sigma E_{\mathrm{T}} - u$ transformation is defined, one for W^+ and one for W^-, after the final selection. After the transformation, the $\Sigma E_{\mathrm{T}} - u$ distribution in data and MC agree by construction.

After defining the new transformation for W^+ and W^- boson events, the calibration procedure is repeated, and a new corrections to the mean and resolution are derived. The correction parameters for the mean and resolution of the parallel and perpendicular component of the hadronic recoil are extracted from Z-boson events, while from the W-boson events only the definition of Smirnov transform for $\Sigma E_{\mathrm{T}} - u$ is taken. Now, there are two different corrections, one for W^+ and one for W^- boson events. The result of applying this correction on W-boson events in muon channel is shown in Figure 5.33 with the hadronic recoil distribution and its parallel and perpendicular projection with respect to the lepton p_{T}^{ℓ} inclusively in $< \mu >$. These distributions are shown for illustration of the effect from the hadronic recoil corrections and the W-boson mass is unknown at this stage, the application of other corrections and background processes is described in Chapter 6. There is a very good agreement between data and MC after this corrections. When comparing the effects of defining the Smirnov transform directly on W-boson events with the correction based on Smirnov transform on Z-boson events, there is much better agreement between data and MC for W^+ and W^-, while for $W^{\pm}$ combined there is no significant difference.

The result of application this correction on $W \to e\nu$ events is shown in Figure 5.34 with the hadronic recoil distribution, its parallel and perpendicular projection with respect to the lepton p_{T}^{ℓ} inclusively in $< \mu >$. There is very good agreement between data and MC after this corrections.

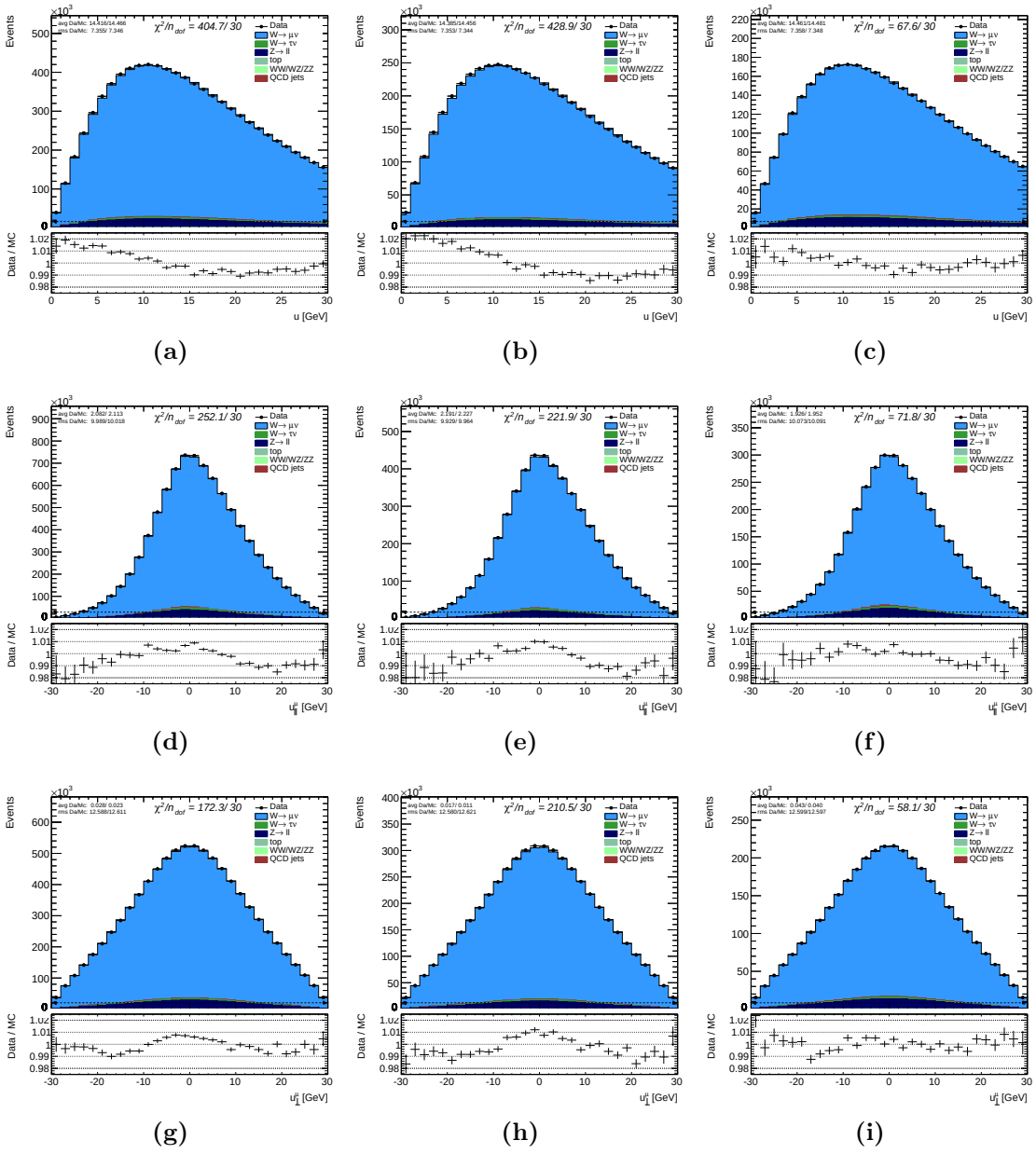

Figure 5.31: Hadronic recoil distribution in (a) $W^{\pm}$, (b) W^{+} and (c) W^{-}, parallel component of the hadronic recoil distribution with respect to lepton p_{T}^{ℓ} in (d) $W^{\pm}$, (e) W^{+} and (f) W^{-} and perpendicular component of the hadronic recoil distribution with respect to lepton p_{T}^{ℓ} in (g) $W^{\pm}$, (h) W^{+} and (i) W^{-} before recoil corrections for the muon channel. The lower panels show the data to MC ratio, with the error bars showing only the statistical uncertainty. The χ^2/NDF does not account the systematics uncertainties.

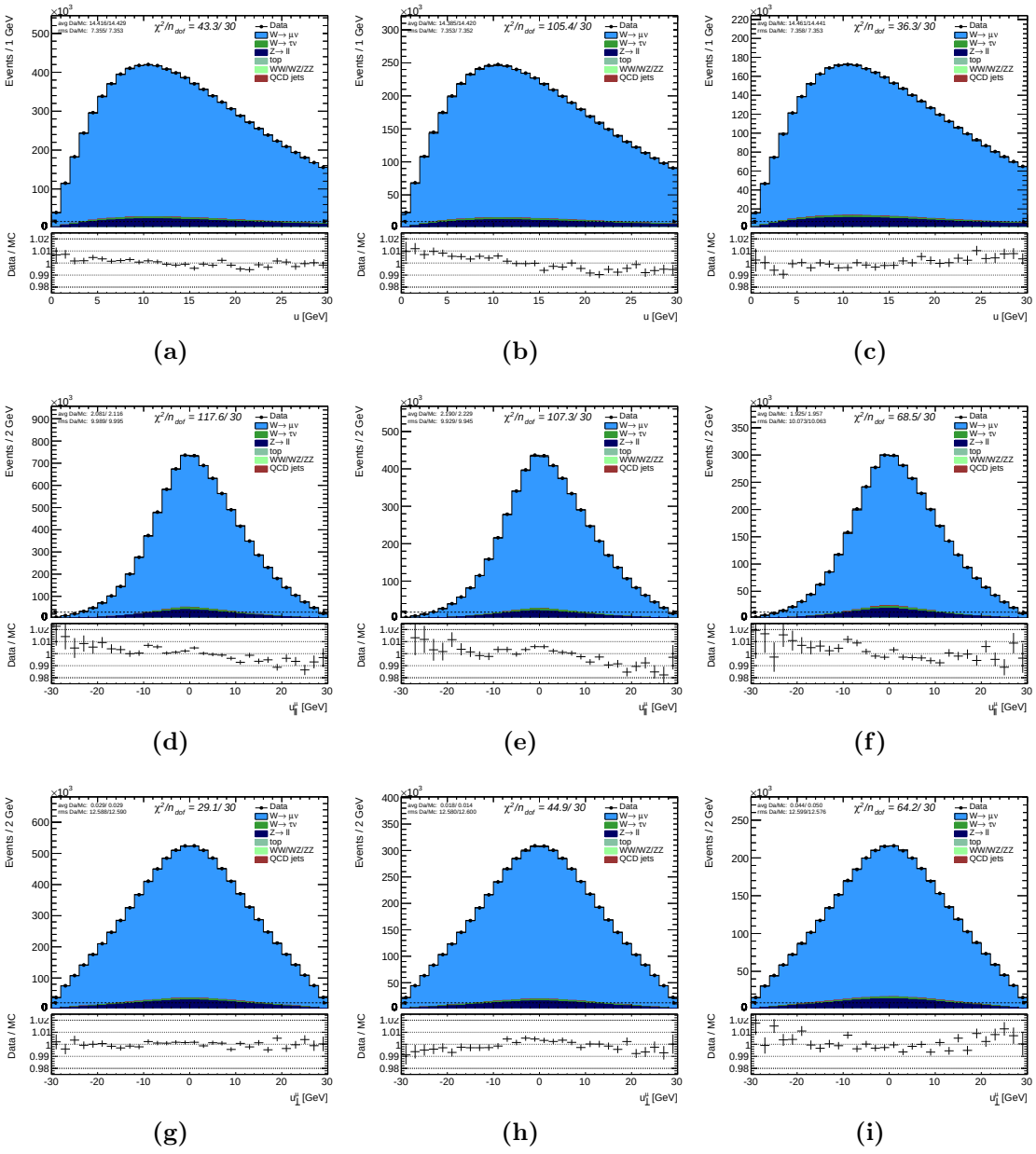

Figure 5.32: Hadronic recoil distribution in (a) $W^{\pm}$, (b) W^{+} and (c) W^{-}, parallel component of the hadronic recoil distribution with respect to lepton p_{T}^{ℓ} in (d) $W^{\pm}$, (e) W^{+} and (f) W^{-} and perpendicular component of the hadronic recoil distribution with respect to lepton p_{T}^{ℓ} in (g) $W^{\pm}$, (h) W^{+} and (i) W^{-} after recoil corrections derived only from Z-boson events for the muon channel. The lower panels show the data to MC ratio, with the error bars showing only the statistical uncertainty. The χ^2/NDF does not account the systematics uncertainties.

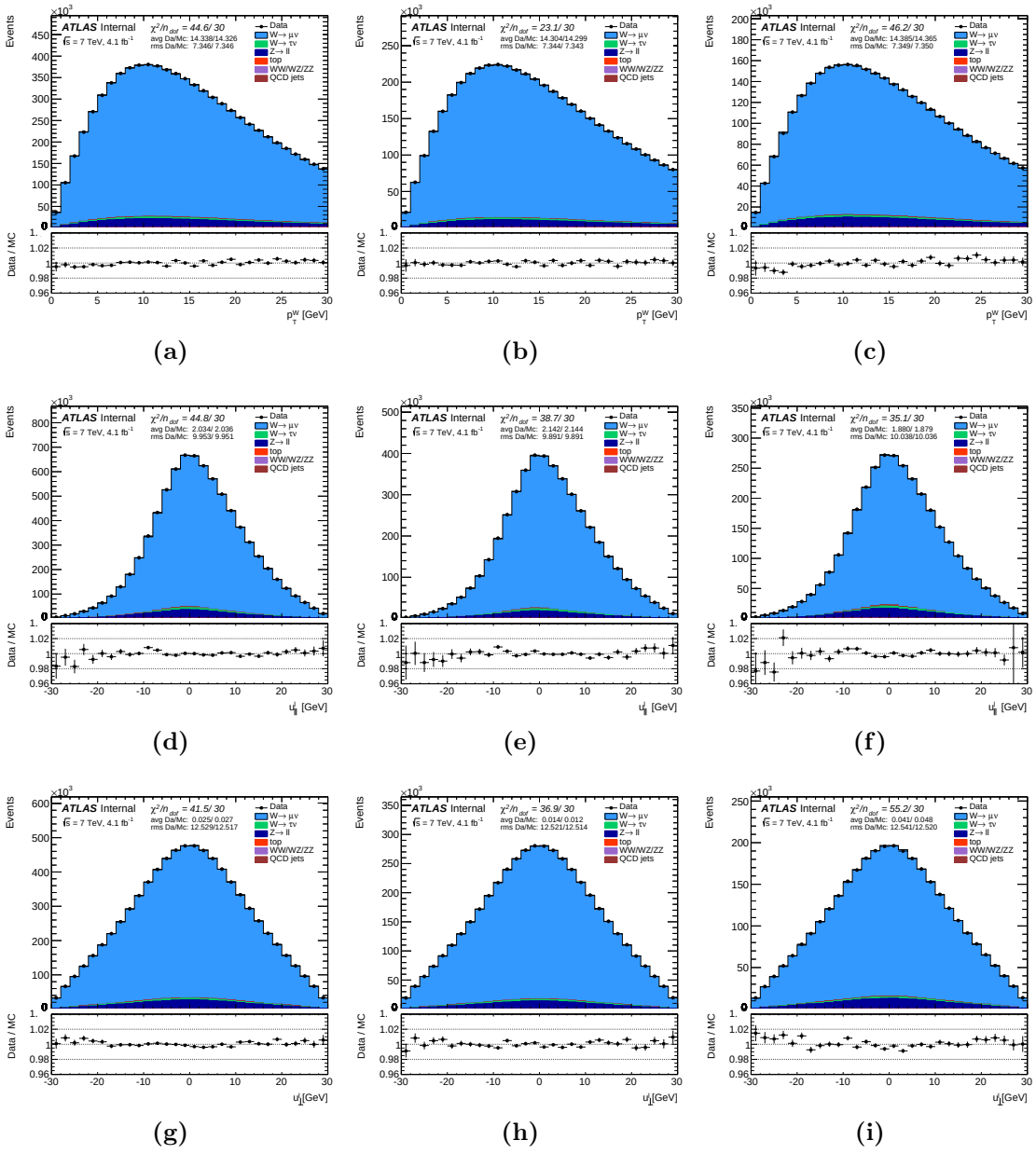

Figure 5.33: Hadronic recoil distribution in (a) $W^{\pm}$, (b) W^{+} and (c) W^{-}, parallel component of the hadronic recoil distribution with respect to lepton p_{T}^{ℓ} in (d) $W^{\pm}$, (e) W^{+} and (f) W^{-} and perpendicular component of the hadronic recoil distribution with respect to lepton p_{T}^{ℓ} in (g) $W^{\pm}$, (h) W^{+} and (i) W^{-} after the recoil corrections for the muon channel. The lower panels show the data to MC ratio, with the error bars showing only the statistical uncertainty. The χ^2/NDF does not account the systematics uncertainties.

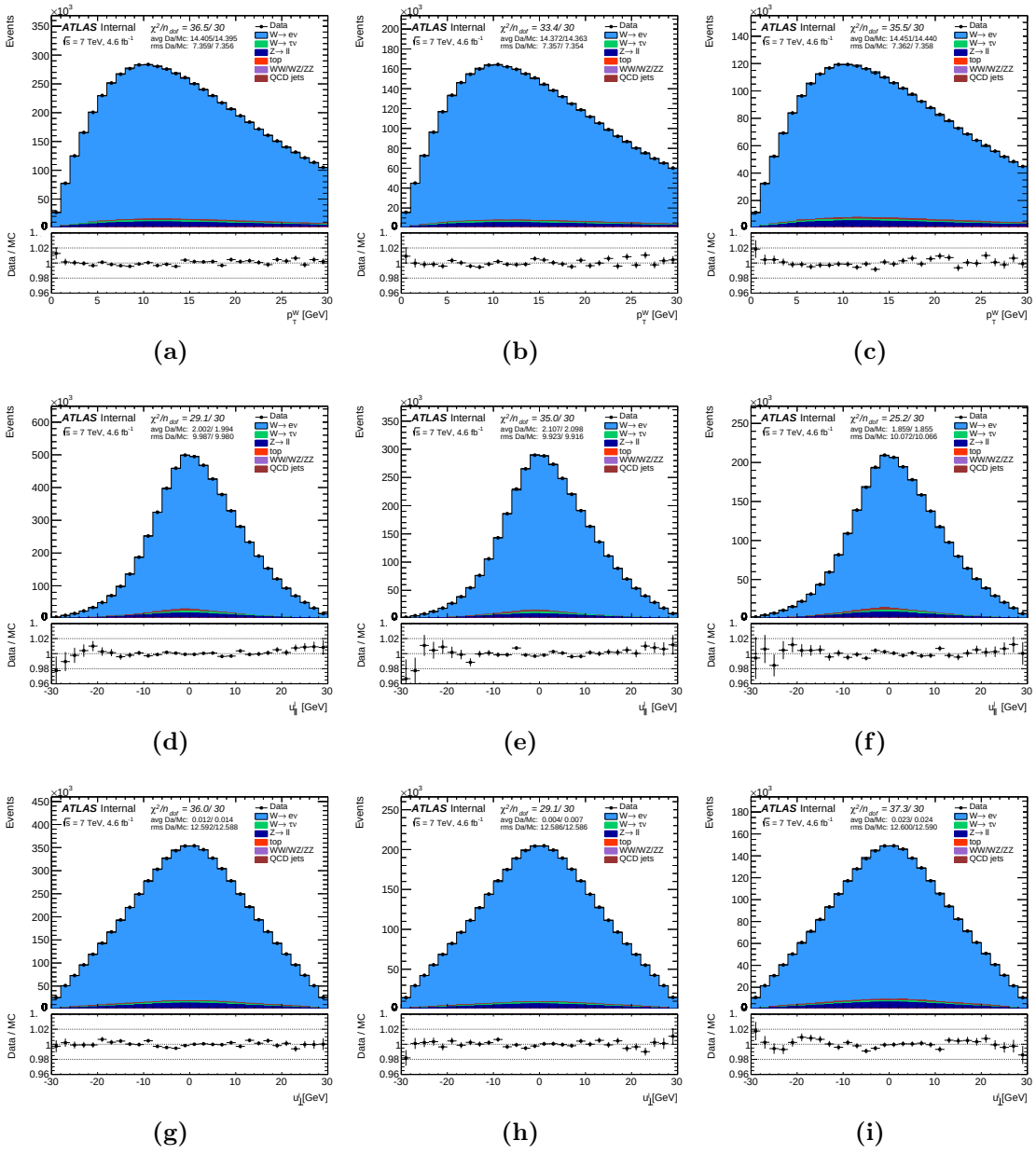

Figure 5.34: Hadronic recoil distribution in (a) $W^{\pm}$, (b) W^{+} and (c) W^{-}, parallel component of the hadronic recoil distribution with respect to lepton p_{T}^{ℓ} in (d) $W^{\pm}$, (e) W^{+} and (f) W^{-} and perpendicular component of the hadronic recoil distribution with respect to lepton p_{T}^{ℓ} in (g) $W^{\pm}$, (h) W^{+} and (i) W^{-} after the recoil corrections for the electron channel. The lower panels show the data to MC ratio, with the error bars showing only the statistical uncertainty. The χ^2/NDF does not account the systematics uncertainties.

5.6.3 *Closure test of the hadronic recoil correction procedure*

A closure test on the full hadronic recoil correction procedure was performed using the PowhegPythia as nominal MC-Sample, while a PowhegHerwig was used as pseudo-data. Both processes, W- and Z-bosons, have been simulated at NLO but with a different parton-shower and underlying event model. While the PowhegPythia sample was tuned to data, the PowhegHerwig was not tuned. The list of samples used is summarised in Table 3.2. Figure 5.35 shows the difference between the two Z-boson samples for the $p_{\mathrm{T}}^{\ell\ell}$ and ΣE_{T} distributions. Figure 5.36 shows several hadronic recoil distributions for both samples; while the difference for most distributions could be explained by the difference in the p_{T}^{Z} modeling, the difference in the $u_{\perp}$ distribution indicates that there are also differences in the hadronic recoil reconstruction resolution itself. The dependence of the $< \Sigma E_{\mathrm{T}} >$ and the perpendicular hadronic recoil resolution, $\sigma(u_{\perp})$, vs. the dimuon p_{T} are shown in Figure 5.37.

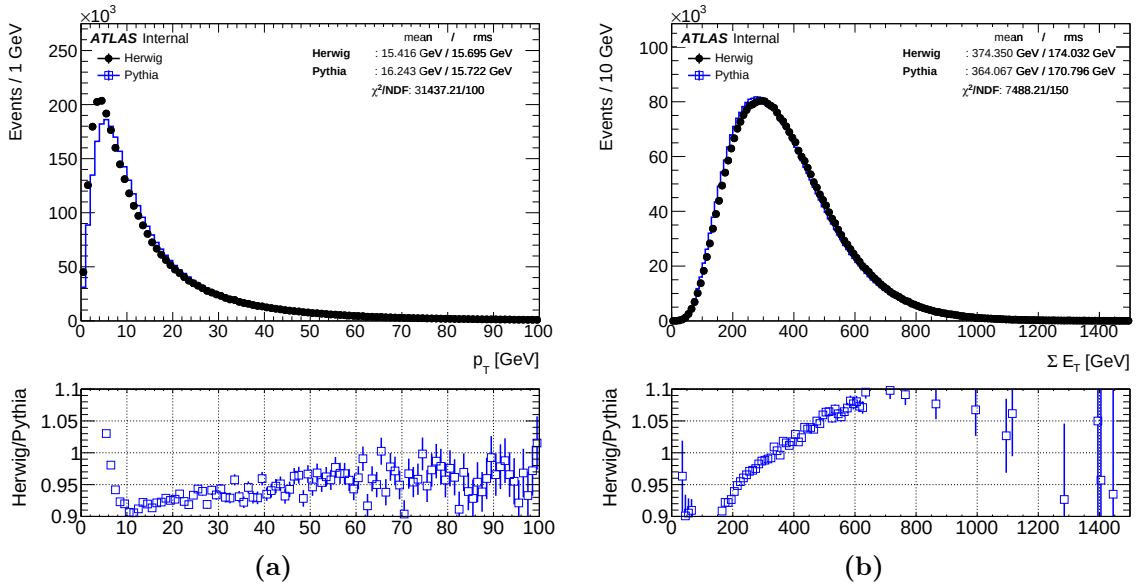

Figure 5.35: Comparison of the (a) $p_{\mathrm{T}}^{\ell\ell}$ and (b) $\sum E_{\mathrm{T}}$ distributions in $Z \to \mu\mu$ events predicted by PowhegHerwig and PowhegPythia before any correction procedure. The lower panels show the PowhegHerwig to PowhegPythia ratio, with the error bars showing only the statistical uncertainty. The χ^2/NDF does not account the systematics uncertainties.

The observed differences between the nominal MC sample and the PowhegHerwig sample are significantly larger than what is seen between PowhegPythia and data. We therefore consider the PowhegHerwig as a conservative test-sample for a closure test of the hadronic recoil correction.

The following correction steps are applied on the nominal PowhegPythia MC samples and compared afterwards to the predicted PowhegHerwig distributions:

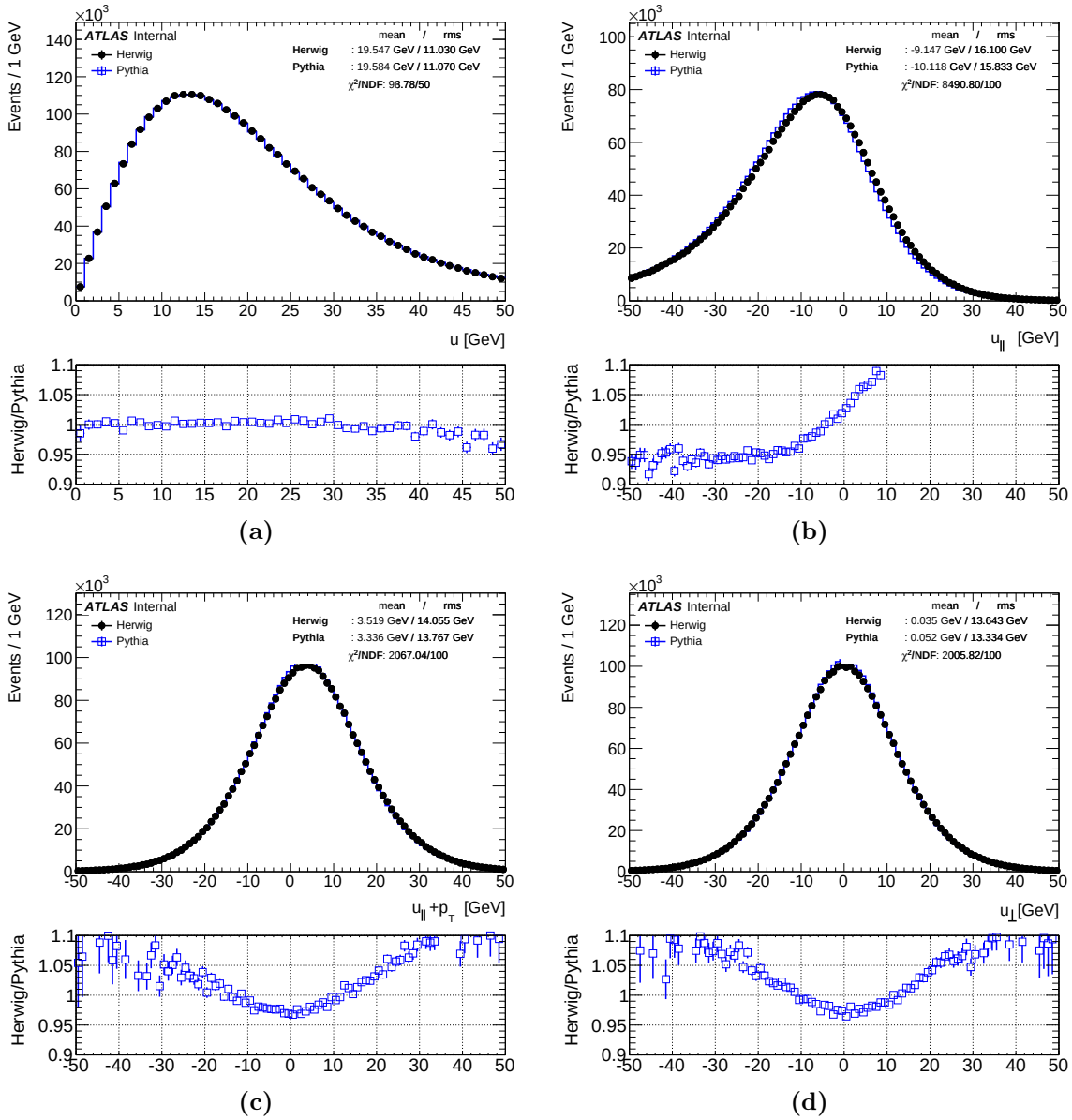

Figure 5.36: Comparison of the (a) u, (b) $u_{||}$, (c) $u_{||} + p_{\mathrm{T}}$ and (d) $u_{\perp}$ distributions in $Z \to \mu\mu$ events, predicted by PowhegHerwig and PowhegPythia before any correction procedure. The lower panels show the PowhegHerwig to PowhegPythia ratio, with the error bars showing only the statistical uncertainty. The χ^2/NDF does not account the systematics uncertainties.

- Reweighting of the truth $p_{\mathrm{T}}^{\mathrm{Z/W}}$ distribution in bins of y, of sizes 0.1, for Z, W^+ and W^- boson events. It should be noted, that this reweighing corresponds to the tuning of the baseline MC to data and isolates the effect of the recoil corrections in order to test the closure. It was tested in addition, that the double ratio of p_{T}

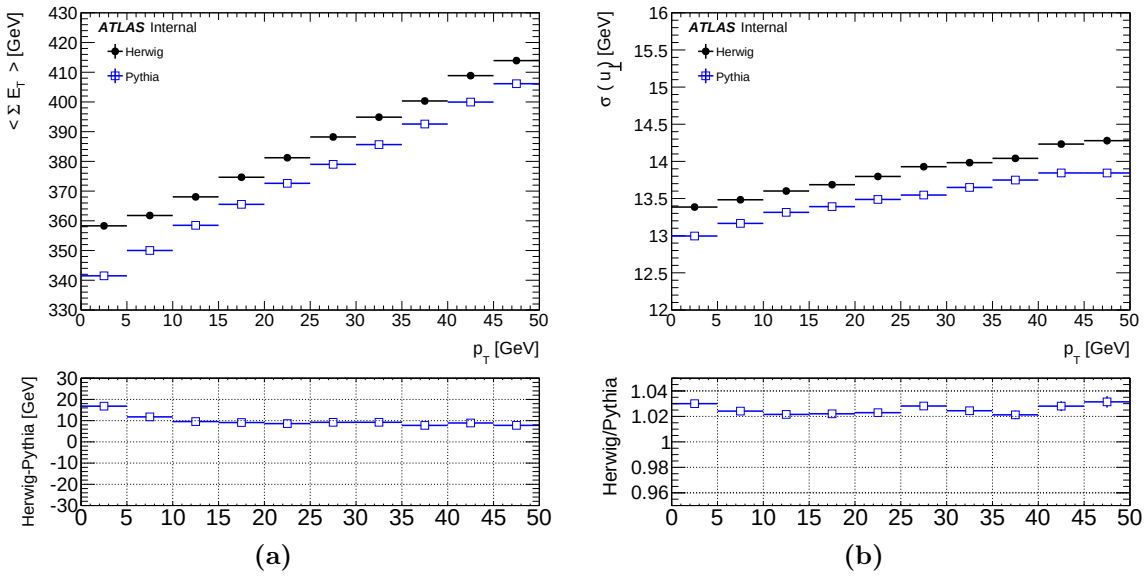

Figure 5.37: Comparison of the (a) $< \Sigma E_{\mathrm{T}} >$ and (b) $\sigma(u_{\perp})$ dependence on $p_{\mathrm{T}}^{\ell\ell}$ in $Z \to \mu\mu$ events predicted by PowhegHerwig and PowhegPythia before any correction procedure. The lower panels show the PowhegHerwig to PowhegPythia ratio, with the error bars showing only the statistical uncertainty.

distributions for W and Z bosons on MC truth level of both generators, i.e.

$$\frac{p_{\mathrm{T}}^{\mathrm{Pythia}}(Z)/p_{\mathrm{T}}^{\mathrm{Herwig}}(Z)}{p_{\mathrm{T}}^{\mathrm{Pythia}}(W)/p_{\mathrm{T}}^{\mathrm{Herwig}}(W)} = 1, \tag{5.19}$$

within the statistical uncertainties. This implies that the reweighting can also be solely derived via the Z boson sample.

- Derivation of the hadronic recoil corrections treating Herwig as data and Pythia as MC:

  - Pile-up reweighting; but, the pile-up is already the same for both MC samples.

  - Definition of the Smirnov transform for $\Sigma E_{\mathrm{T}} - u$ in p_{T} bins for Z, W^+ and W^- boson events.

  - Correction of the u_{x} and u_{y} distributions, which does not apply for the comparison between two MC samples.

  - Derivation of the residual bias and resolution corrections as a function of $\Sigma E_{\mathrm{T}} - u$ in p_{T}.

The resulting, corrected PowhegPythia-distributions $(u, u_{||}, u_{||} + p_{\mathrm{T}}, u_{\perp})$ for the Z- and W-boson events are shown in Figure 5.38 and 5.39, respectively, in comparison to the corresponding PowhegHerwig distributions. The $u_{||}$ and $u_{\perp}$ distributions

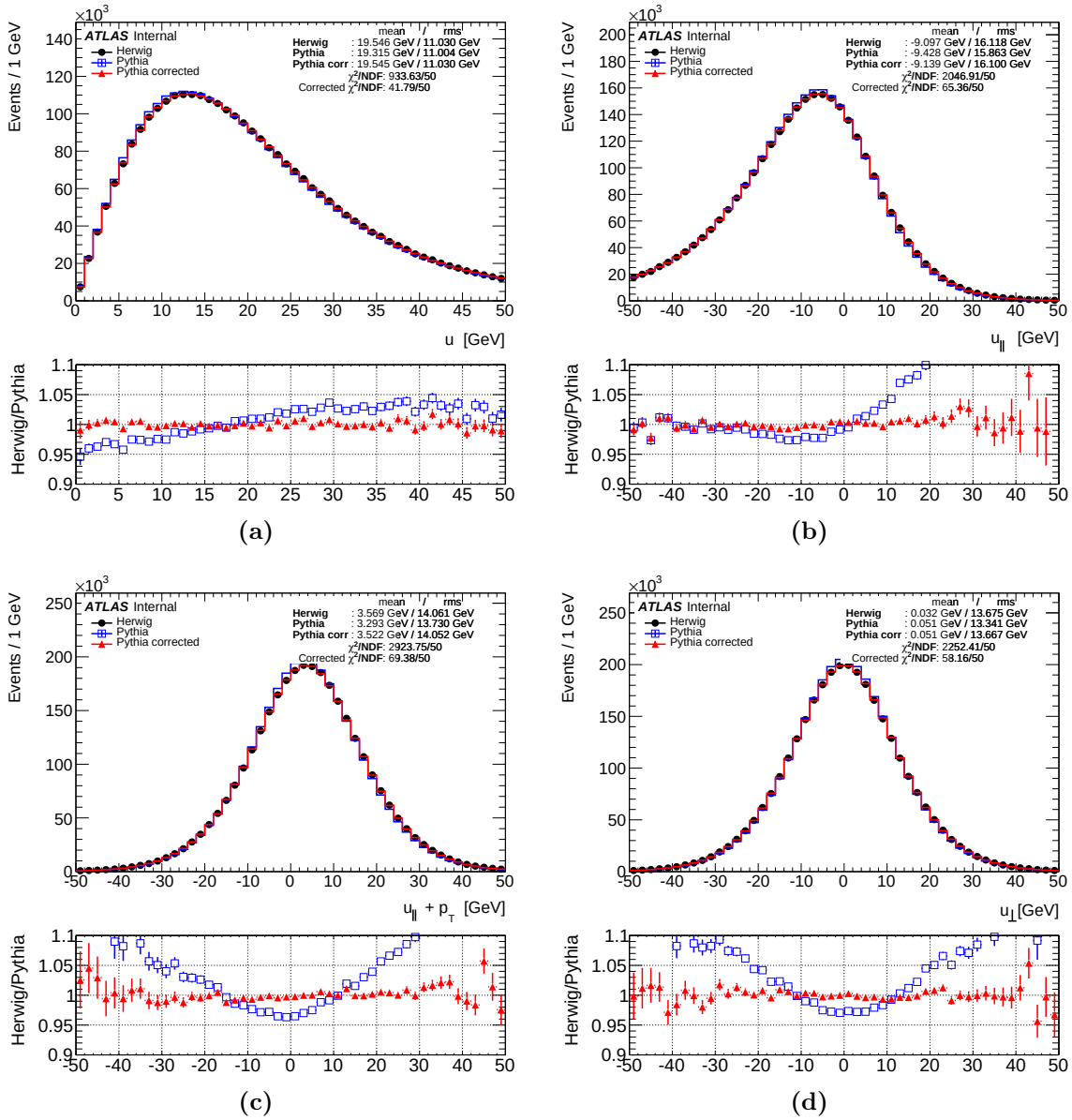

Figure 5.38: Comparison of the (a) u, (b) $u_{||}$, (c) $u_{||} + p_{\mathrm{T}}$ and (d) $u_{\perp}$ distributions in $Z \to \mu\mu$ events, predicted by PowhegHerwig and PowhegPythia after the full correction procedure. The lower panels show the PowhegHerwig to PowhegPythia ratio, with the error bars showing only the statistical uncertainty. The χ^2/NDF does not account the systematics uncertainties.

are shown here again for the projection in the truth boson kinematics. A very good agreement can be seen, validating the developed correction procedure.

In order to increase the statistical precision and to stress-test the correction procedure even further, we remove the selection cuts on $E_{\mathrm{T}}^{\mathrm{miss}}$ and m_{T}, but apply the full derived corrections. The resulting comparisons between the corrected PowhegPythia distributions and the PowhegHerwig predictions are shown in Figure 5.40.

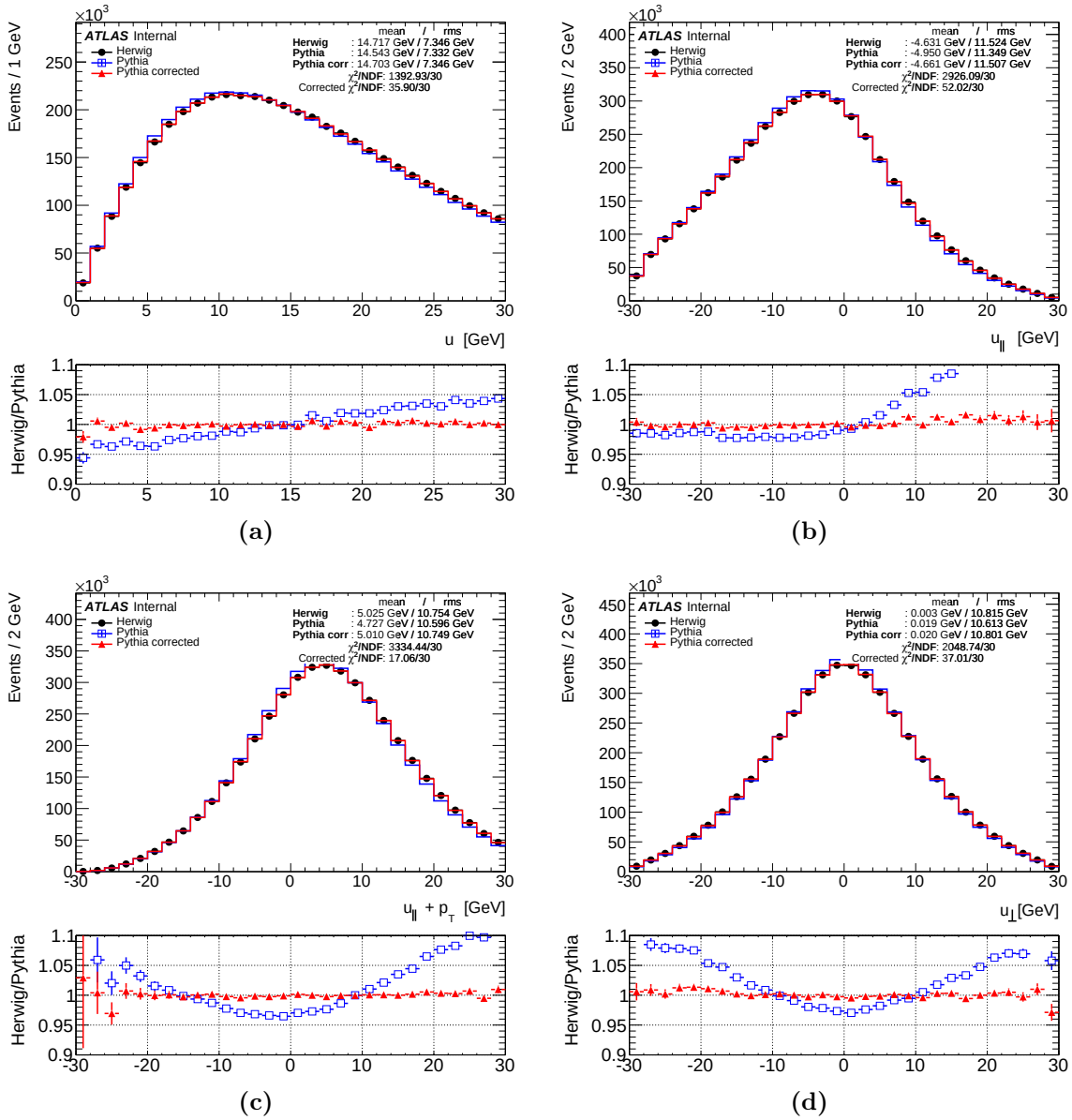

Figure 5.39: Comparison of the (a) u, (b) $u_{||}$, (c) $u_{||} + p_{\mathrm{T}}$ and (d) $u_{\perp}$ distributions in $W^{\pm}$ boson events, predicted by PowhegHerwig and PowhegPythia after the full correction procedure. The lower panels show the PowhegHerwig to PowhegPythia ratio, with the error bars showing only the statistical uncertainty. The χ^2/NDF does not account the systematics uncertainties.

Also here, a perfect closure can be seen.

Figure 5.41 shows the comparison of the $u_{||}$ distribution for the nominal W boson selection and the loose W boson selection between the corrected PowhegPythia distributions and the PowhegHerwig predictions, where the hadronic recoil was projected on one decay lepton. Of special importance is the $u_{||}$ distribution (projected on leptons) for W-boson events between -30 and -15 GeV, as it is very sensitive to

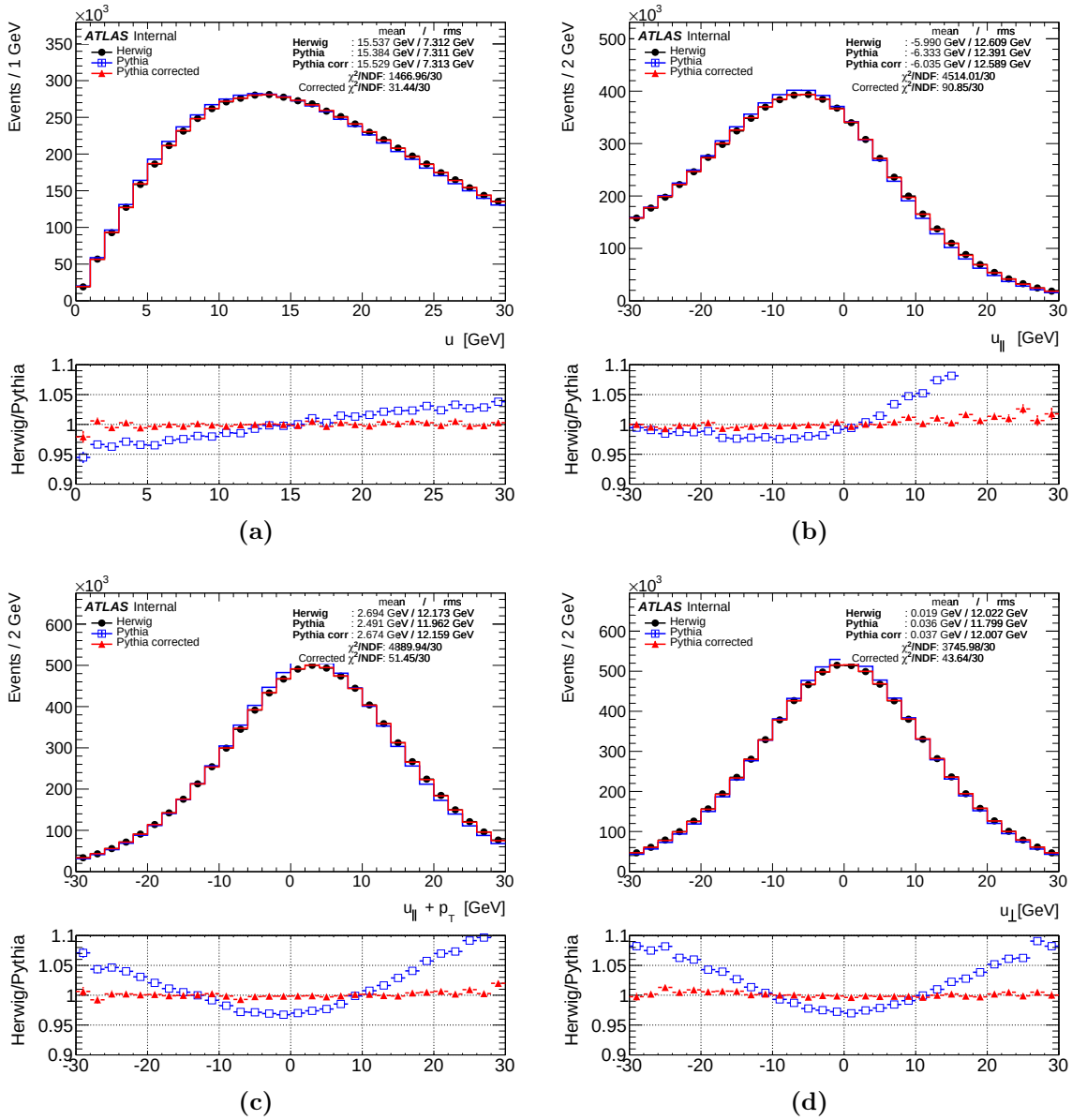

Figure 5.40: Comparison of the (a) u, (b) $u_{||}$, (c) $u_{||} + p_{\mathrm{T}}$ and (d) $u_{\perp}$ distributions in $W^{\pm}$ boson events without selection cuts on $E_{\mathrm{T}}^{\mathrm{miss}}$ and m_{T}, predicted by PowhegHerwig and PowhegPythia after the full correction procedure. The lower panels show the PowhegHerwig to PowhegPythia ratio, with the error bars showing only the statistical uncertainty. The χ^2/NDF does not account the systematics uncertainties.

the modeling of the $p_{\mathrm{T}}(W)$. In this region, we observe that the fraction of events in the $u_{||}$ distribution which have $-30\,\mathrm{GeV} < u_{||} < -15\,\mathrm{GeV}$ is agreeing within 0.998(3) and 0.999(1) after corrections, i.e. a closure to per-mill level, for the nominal and the relaxed selection cuts, respectively. Values for the fraction of events between -30 and -15 GeV for PowhegHerwig, PowhegPythia before and after corrections is summarised in Table 5.1.

Table 5.1: Fraction of events in range $-30\,\text{GeV} < u_{\parallel} < -15\,\text{GeV}$ for PowhegHerwig, PowhegPythia before and after corrections.

	PowhegHerwig	PowhegPythia before recoil corrections	PowhegPythia after recoil corrections
Nominal selection	0.03708(9)	0.03733(7)	0.03716(7)
Relaxed selection cuts	0.18700(15)	0.18583(12)	0.18727(12)

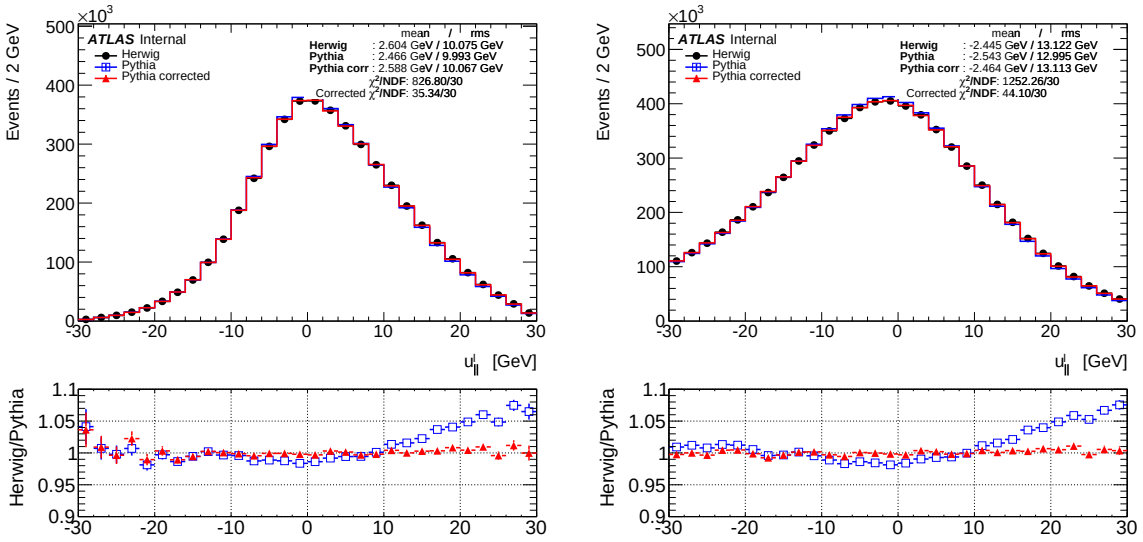

Figure 5.41: Comparison of the $u_{||}$ distributions, where the hadronic recoil was projected on the charged lepton, in W-boson events with the nominal selection (left) and without selection cuts on $E_{\text{T}}^{\text{miss}}$ and m_{T} (right), predicted by PowhegHerwig and PowhegPythia after the full correction procedure. The lower panels show the PowhegHerwig to PowhegPythia ratio, with the error bars showing only the statistical uncertainty. The χ^2/NDF does not account the systematics uncertainties.

5.7 PROPAGATION OF THE SYSTEMATICS UNCERTAINTIES TO THE W-BOSON MASS MEASUREMENT

In this section the systematic uncertainties from the hadronic recoil calibration procedure are discussed. The propagation of the systematic uncertainties to the W-boson mass measurement is described in Section 1.4.3. The recoil calibration procedure is sensitive to the uncertainty of the scale factor applied to the $< \mu >$ distribution, the uncertainty due to $\Sigma E_{\mathrm{T}} - u$ transformation, the uncertainties in the correction of the φ of the hadronic recoil, the statistical uncertainties in the residual corrections, and the expected differences in the recoil response between Z- and W-boson events.

The statistical uncertainty is estimated with toy MC method. A 100 toy MC are defined with the hadronic recoil corrected with randomly chosen correction values within their statistical uncertainties, in the range $(b-\delta b, b+\delta b)$ for the correction of the mean of $u_{\parallel}$, and in the range $(r-\delta r, r+\delta r)$ for the correction of the recoil resolution. The b and r values with their statistical uncertainties are shown in Figure 5.24. These toys are compared to the nominal sample and the statistical uncertainty is extracted from the RMS of the spread of the toys.

$< \mu >$ *scale factor uncertainty*

The procedure for rescaling $< \mu >$ distribution is described in Section 5.5.1. The low boundary for $< \mu >$ scale factor is 1.07 and the high boundary for $< \mu >$ scale factor is 1.14, this values were chosen to cover the uncertainty from official recommendation and preferred value for $u_{\perp}$ distribution, see Figure 5.11. For these two variations of scale factor, all steps for derivation of the hadronic recoil corrections are repeated, i.e. rescaling of $< \mu >$ distribution, $\Sigma E_{\mathrm{T}} - u$ transform, u_{X} and u_{Y} corrections and additional corrections for mean and resolution.

$\Sigma E_{\mathrm{T}} - u$ *correction uncertainty*

The systematic uncertainty on the $\Sigma E_{\mathrm{T}} - u$ correction method is estimated by comparing the p_{T}-dependent and p_{T}-independent $\Sigma E_{\mathrm{T}} - u$ transform. In the Z-boson events, the $\Sigma E_{\mathrm{T}} - u$ data to MC discrepancy is observed to be p_{T} boson dependent, and the Smirnov transform gives better results when defined in bins of p_{T} rather than inclusively. The p_{T} dependence can be mapped accurately in Z-boson events, thanks to the reconstructed lepton pair transverse momentum.

As discussed in Section 5.5.2, the p_{T}-dependent Smirnov transform in the W-boson events has to be defined indirectly using the Z-boson events, since the boson p_{T} is measured with poor resolution in the W-boson events. The following approximation is

used:

$$\tilde{h}^{W}_{\text{data}}(\Sigma E_{\text{T}} - u; p_{\text{T}}) \equiv h^{Z}_{\text{data}}(\Sigma E_{\text{T}} - u; p_{\text{T}}) \times \frac{\frac{h^{W}_{\text{data}}(\Sigma E_{\text{T}} - u)}{h^{W}_{\text{MC}}(\Sigma E_{\text{T}} - u)}}{\frac{h^{Z}_{\text{data}}(\Sigma E_{\text{T}} - u)}{h^{Z}_{\text{MC}}(\Sigma E_{\text{T}} - u)}}, \tag{5.20}$$

where the double ratio represent the ratio of the data to MC $\Sigma E_{\text{T}} - u$ distribution in W- and Z-boson events defined inclusively in p_{T}. Then, the p_{T}-dependent transform is defined such that

$$h^{W}_{\text{MC}}(\Sigma E_{\text{T}} - u; p_{\text{T}}) \rightarrow h'^{W}_{\text{MC}}((\Sigma E_{\text{T}} - u)^{\text{tr}}; p_{\text{T}}) \equiv \tilde{h}^{W}_{\text{data}}(\Sigma E_{\text{T}} - u; p_{\text{T}}). \tag{5.21}$$

This approximation is based on an assumption that the p_{T}-dependence of the $\Sigma E_{\text{T}} - u$ is the same in Z- and W-boson events. Also, it allows for a precise mapping of the p_{T} dependence of the correction, but can only be verified in broad recoil bins. The associated systematic uncertainties are described below.

The $\Sigma E_{\text{T}} - u$ distribution and its data/MC discrepancies differ for Z- and W-boson events, as shown in Figures 5.42 and 5.43. Figure 5.42 shows the data to MC ratio of $\Sigma E_{\text{T}} - u$ distribution for W^+, W^-, $W^{\pm}$ and Z events, for the full recoil range and in coarse recoil bins: $0\,\text{GeV} < u < 10\,\text{GeV}$, $10\,\text{GeV} < u < 20\,\text{GeV}$, and $20\,\text{GeV} < u < 30\,\text{GeV}$. While Figure 5.43 shows the corresponding double Z/W data to MC ratios. Similar behaviour is observed as in Z-boson events. Different behaviour for Z- and W-boson events is observed only for relatively small values of the $\Sigma E_{\text{T}} - u$ distribution ($\Sigma E_{\text{T}} - u < 200\,\text{GeV}$) where the double ratio deviates from one. The two figures show results for the inclusive $< \mu >$, and similar behaviour is observed for low, medium and high pile-up conditions, as defined in Section 5.5.4.

When applying the hadronic recoil corrections to the W-boson events, the $\Sigma E_{\text{T}} - u$ transform is defined for W^+ and W^- boson events, and thus incorporates p_{T} dependence as discussed above. In order to estimate the systematic uncertainty arising from this prescription, one can compare behaviour of the $\Sigma E_{\text{T}} - u$ distribution in recoil bins and inclusively as illustrated in Figure 5.44. The relative difference in the p_{T}-dependence between the Z- and the W-boson events is taken as systematic uncertainty. One can estimate this difference by comparing the $\Sigma E_{\text{T}} - u$ distribution in recoil bins (Figure 5.44). The biggest difference is observed in the first and third recoil bin, therefore by comparing this two recoil bins (as shown in Figure 5.45) the difference between the W- and Z-boson events for $\Sigma E_{\text{T}} - u$ distribution can be quantified. By fitting the difference between W- and Z-boson events to the difference of Z-boson events from 1 with a constant as a function of $\Sigma E_{\text{T}} - u$ one can find a fraction which corresponds to the p_{T} dependence observed in the W-boson events relative to the one seen in the Z-boson events. The result of the constant fits are shown in Table 5.2 for W^+, W^- boson events and combined for the $W^{\pm}$ boson events in $< \mu >$ bins.

In order to account for maximal difference in p_{T} dependence of $\Sigma E_{\text{T}} - u$ distribution between W and Z events, the fractions for estimation of the systematics is taken as a residual difference (from the one in Table 5.2) with errors as shown in Table 5.3.

The systematics for the p_{T}-dependence of $\Sigma E_{\text{T}} - u$ distribution in the W-boson events is calculated as a fraction noted in Table 5.3 from the full difference between

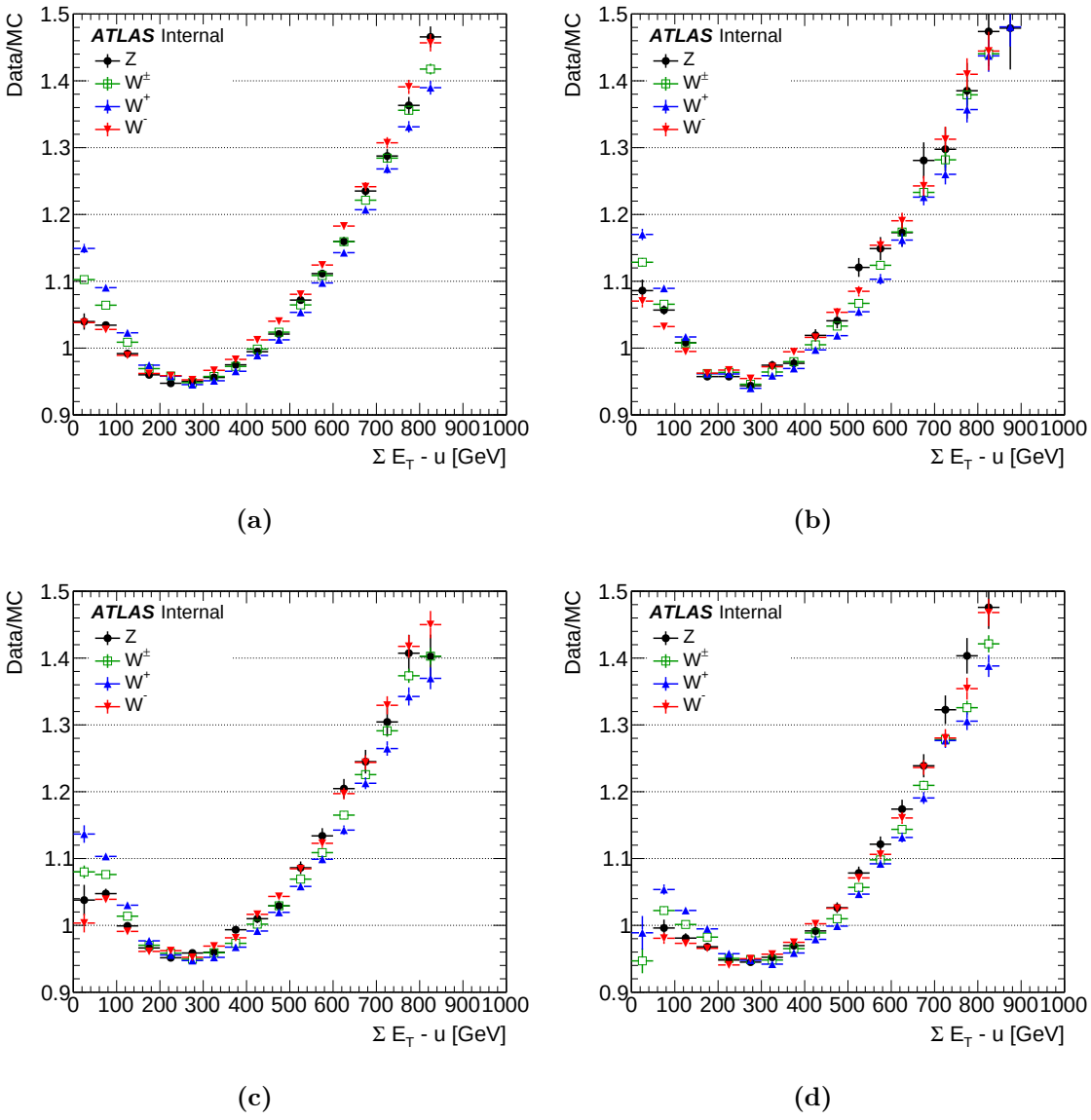

Figure 5.42: data to MC ratio of $\Sigma E_{\mathrm{T}} - u$ distribution for $W^+ \to \mu\nu$ (blue points), $W^- \to \mu\nu$ (red points), $W^\pm \to \mu\nu$ (green points) and $Z \to \mu\mu$ (black points) where (a) is for full recoil range, (b) is for the first recoil bin $0\,\mathrm{GeV} < u < 10\,\mathrm{GeV}$, (c) is for the second recoil bin $10\,\mathrm{GeV} < u < 20\,\mathrm{GeV}$ and (d) is for the third recoil bin $20\,\mathrm{GeV} < u < 30\,\mathrm{GeV}$.

p_{T}-dependent and p_{T}-independent $\Sigma E_{\mathrm{T}} - u$ transform. This fraction is depending on the pile-up and it is different for W^+ and W^- boson events.

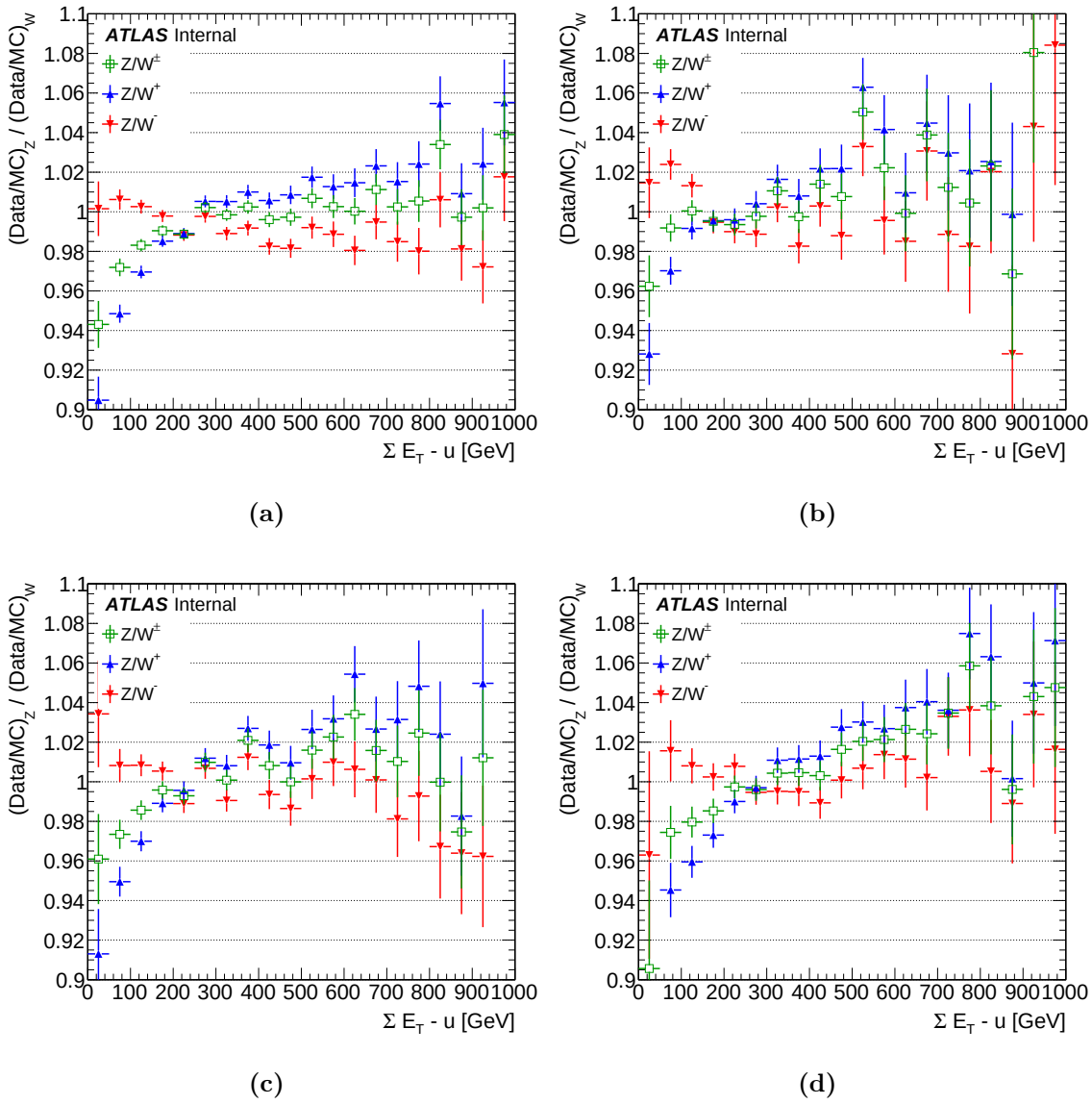

Figure 5.43: Data to MC double ratio of $\Sigma E_{\mathrm{T}} - u$ distribution for $Z \to \mu\mu$ to $W^+ \to \mu\nu$, $W^- \to \mu\nu$ and $W^\pm \to \mu\nu$ (a) for full recoil range, (b) for the first recoil bin $0\,\mathrm{GeV} < u < 10\,\mathrm{GeV}$, (c) for the second recoil bin $10\,\mathrm{GeV} < u < 20\,\mathrm{GeV}$ and (d) for the third recoil bin $20\,\mathrm{GeV} < u < 30\,\mathrm{GeV}$.

Azimuthal correction uncertainty

The overall value of the u_{Y} correction is $\approx 600\,\mathrm{MeV}$. There are 32 φ bins, with an average uncertainty of $\approx 70\,\mathrm{MeV}$, as seen in Figure 5.18 (d). The accuracy of the correction thus corresponds to about 2% of the overall size of the effect. The systematics coming from this correction is thus defined as 2% of the full difference when the corrections are defined with and without u_{Y} corrections.

Table 5.2: The result of the constant fits as a function of $\Sigma E_{\mathrm{T}} - u$.

$<\mu>$ bin	W^+	W^-	$W^{\pm}$
$<\mu> \in (2.5, 6.5)$	0.44±0.09	0.64±0.12	0.48±0.09
$<\mu> \in (6.5, 9.5)$	0.39±0.12	0.49±0.14	0.41±0.10
$<\mu> \in (9.5, 16.0)$	0.44±0.13	0.54±0.15	0.47±0.11
Inclusive	0.46±0.08	0.61±0.11	0.47±0.08

Table 5.3: The fraction used to calculate the systematics for p_{T}-dependence of $\Sigma E_{\mathrm{T}} - u$ distribution in W events compared to the dependence observed in Z events.

$<\mu>$ bin	W^+	W^-	$W^{\pm}$
$<\mu> \in (2.5, 6.5)$	0.65	0.48	0.61
$<\mu> \in (6.5, 9.5)$	0.73	0.65	0.69
$<\mu> \in (9.5, 16.0)$	0.69	0.61	0.64
Inclusive	0.62	0.50	0.61

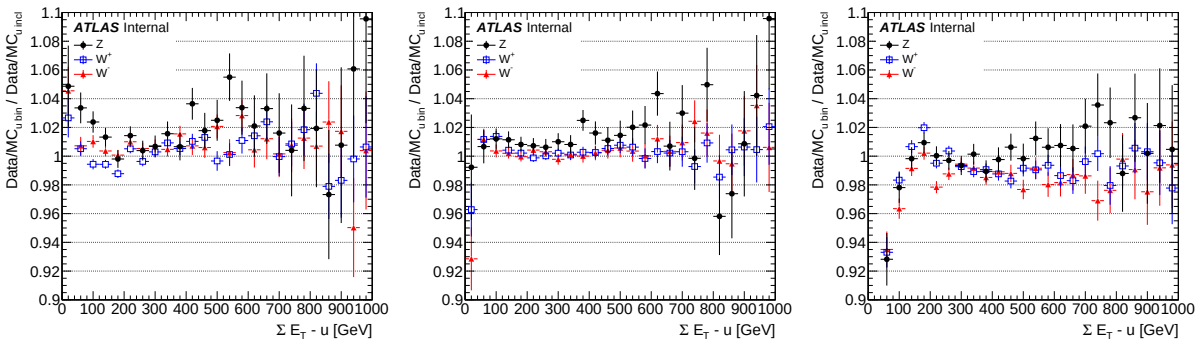

(a) **(b)** **(c)**

Figure 5.44: Data to MC double ratio of $\Sigma E_{\mathrm{T}} - u$ distribution for $W^+ \to \mu\nu$, $W^- \to \mu\nu$ and $Z \to \mu\mu$ (a) for the first recoil bin $0\,\mathrm{GeV} < u_{\mathrm{T}} < 10\,\mathrm{GeV}$, (b) for the second recoil bin $10\,\mathrm{GeV} < u_{\mathrm{T}} < 20\,\mathrm{GeV}$ and (c) for the third recoil bin $20\,\mathrm{GeV} < u_{\mathrm{T}} < 30\,\mathrm{GeV}$ compared to the inclusive recoil bin.

Residual correction uncertainties

Since the correction factors for bias and resolution are derived on Z-boson events and applied to the W-boson events, possible differences between the Z and W^+ and W^- boson events for the recoil response should be considered as an additional source of the systematic uncertainty. One part of the difference in resolution comes from different $\Sigma E_{\mathrm{T}} - u$ distributions in W- and Z-boson events, as illustrated in Figure 5.42. The resolution can be compared, after $\Sigma E_{\mathrm{T}} - u$ reweighting, in data and MC for Z-boson events, as illustrated in Figure 5.46 (a), and between Z, W^+ and W^- boson events in simulation, as illustrated in Figure 5.47.

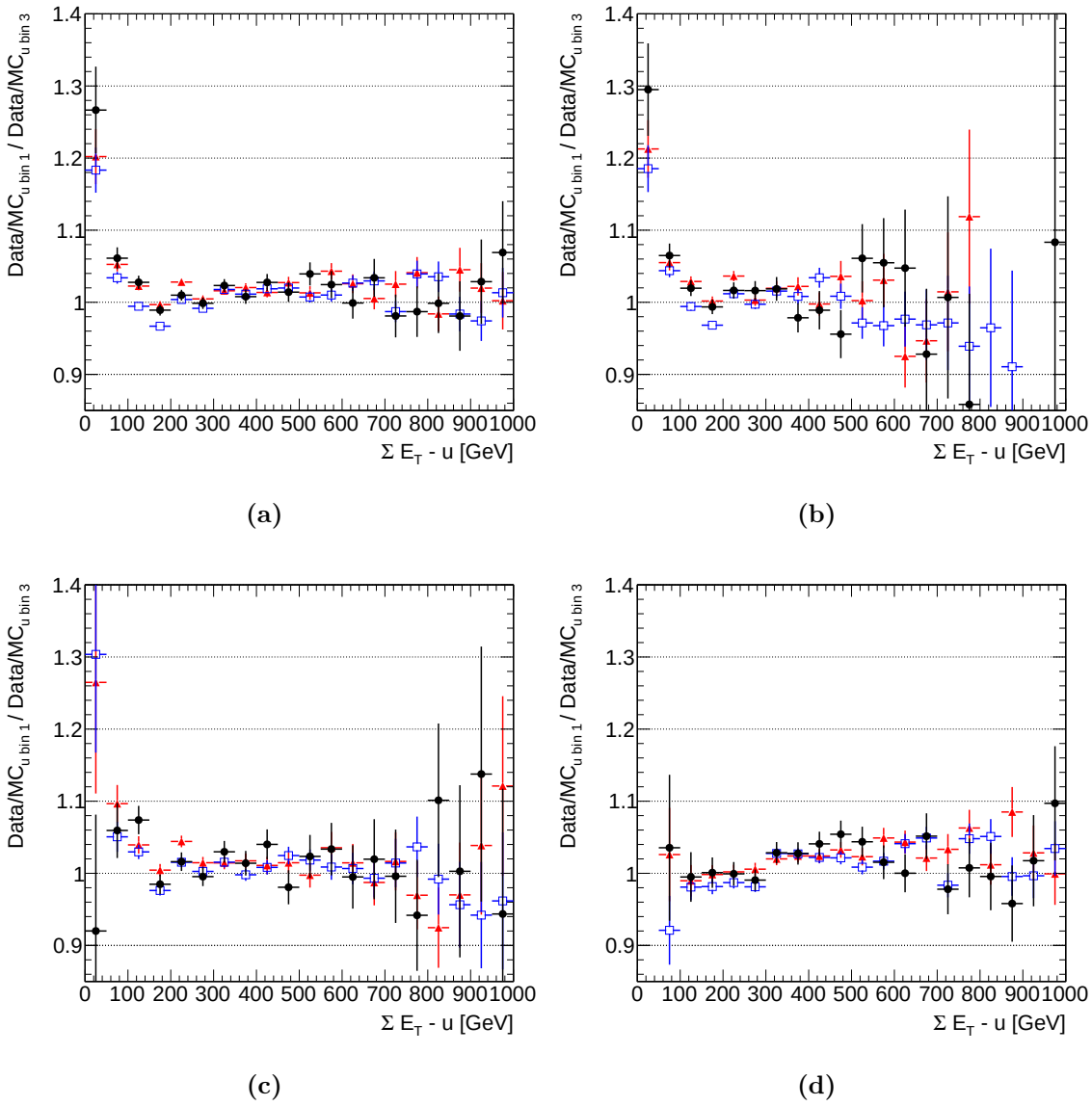

Figure 5.45: Data to MC double ratio of $\Sigma E_{\mathrm{T}} - u$ distribution for $W^+ \to \mu\nu$ (blue points), $W^- \to \mu\nu$ (red points) and $Z \to \mu\mu$ (black points) for the first recoil bin $0\,\mathrm{GeV} < u_{\mathrm{T}} < 10\,\mathrm{GeV}$, compared with the third recoil bin $20\,\mathrm{GeV} < u_{\mathrm{T}} < 30\,\mathrm{GeV}$ (a) inclusive in $< \mu >$, (b) for low pile-up, (c) for medium pile-up, (d) for high pile-up.

When comparing the $u_{\perp}$ in the W- and Z-boson MC events, it is possible to observe a difference in resolution, which is parametrised as: $\sigma_{\mathrm{W}} = \sigma_{\mathrm{Z}} + \Delta\sigma$. This difference in recoil resolution can originate from genuine differences in the boson kinematic between Z- and W-boson events, or can be the consequence of different selection criteria as described in Section 3.5. In order to study the effect of the different number of leptons and replacement cones for W- and Z-boson events, it is possible to use in the calculation of the hadronic recoil with the truth-level leptons. One feature of the hadronic recoil algorithm is that it can accept a variety of physics objects as lepton seeds. In particular, it is possible to run the algorithm using as seeds for the removal and replacement cones

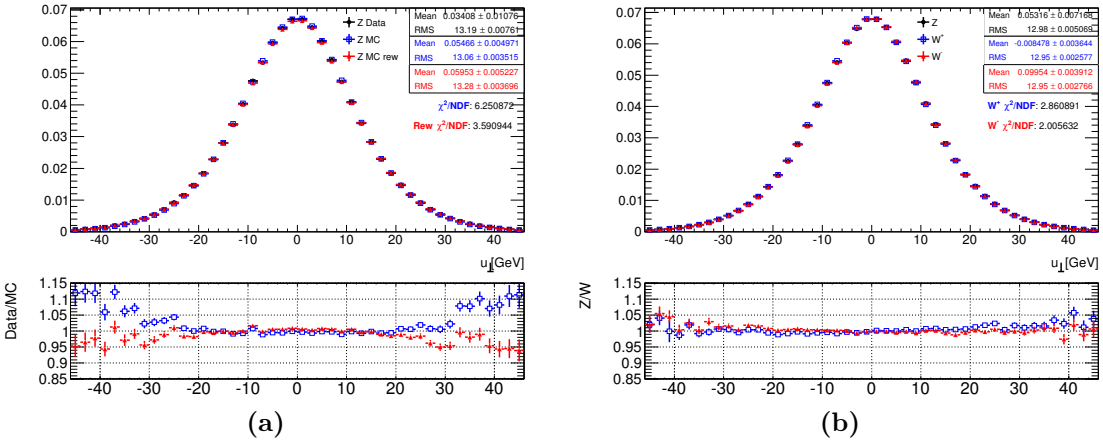

Figure 5.46: Perpendicular component of hadronic recoil distribution in (a) data and MC for Z-boson events and (b) MC for Z, W^+ and W^- boson events, after ΣE_{T} reweighting.

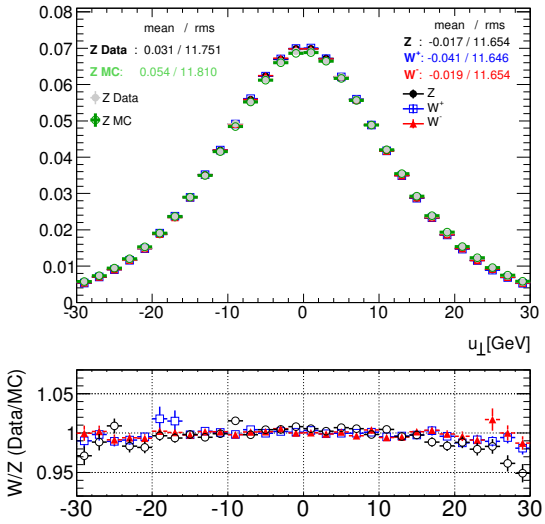

Figure 5.47: The perpendicular component of hadronic recoil distribution in Z, W^+ and W^- boson events, black points represents the data to MC ratio for the Z-boson events, while blue and red points are showing the W- to Z-boson ratio in MC.

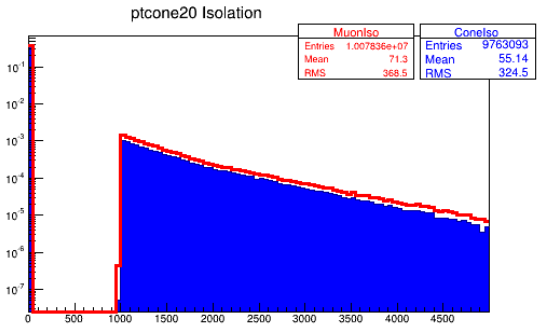

Figure 5.48: Sum of the p_{T} of the tracks in a cone of $\Delta R = 0.2$ around the muon (red line) and around the direction chosen for the replacement cone (solid blue histogram).

the truth level leptons. By doing that is possible to treat in the same way both the charged lepton and the neutrino, i.e. using two removal and two replacement cones both in the W- and Z-boson events.

For this study the hadronic recoil algorithm was configured to remove a cone around both neutrinos and charged leptons satisfying the requirements: $|\eta| < 2.5$ and $p_{\mathrm{T}}^{\ell} > 20$ GeV. The truth leptons have also to be isolated. This study was performed using the W- and Z-boson samples with muons in final states. In this case the isolation is the relative track isolation in a cone $\Delta R = 0.2$ around the truth lepton direction, taking as denominator in one case the p_{T} of the reconstructed muon track and in the other case the truth-level neutrino p_{T}. Another source of bias could be due to the different choice of the replacement cone, depending on the isolation of the lepton. In fact, if the lepton is isolated, the replacement cone is randomly taken at same η of the lepton and a random φ, while, when the lepton is not isolated, as replacement we use the value of the lepton isolation. In order to reduce the effect of this choice, events will be selected only if the lepton is isolated and if the replacement cone satisfies the same requirement, i.e. the sum of the p_{T} of the tracks in the replacement cone divided by the lepton p_{T} satisfies the same isolation requirements used for the lepton. The distribution of the sum of the p_{T} of the tracks around the muon and around the direction chosen for the replacement cone are shown in Figure 5.48. To reduce other differences due to the differences in the p_{T} distribution of W- and Z-boson events, the W-boson events are reweighted to match the p_{T} distribution in the Z-boson events, as shown in Figure 5.49.

The difference of the $u_{\perp}$ resolution in W- and Z-boson events will be shown using the ratio between W- and Z-boson events, which can be fitted using the functional form: $e^{(-x^2 \cdot p_0) \cdot (1+p_1)}$, where the difference in resolution $\Delta\sigma$ can be directly calculated as: $\Delta\sigma = 0.5 \cdot p_0 \cdot \sigma^3$, with σ the $u_{\perp}$ resolution, which is approximately 14 GeV. In Figure 5.50(a) the ratio of W- and Z-boson events is shown as a function of $u_{\perp}$, together with the fitted values. For the W^+ boson the fit returns $p_0 = (-15.8 \pm 1.5) \times 10^{-12}$, while for W^- boson the fit returns $p_0 = (-19.8 \pm 1.4) \times 10^{-12}$, which corresponds to $\Delta\sigma = 20 \pm 3$ MeV. The effect of the difference between the W- and Z-boson events

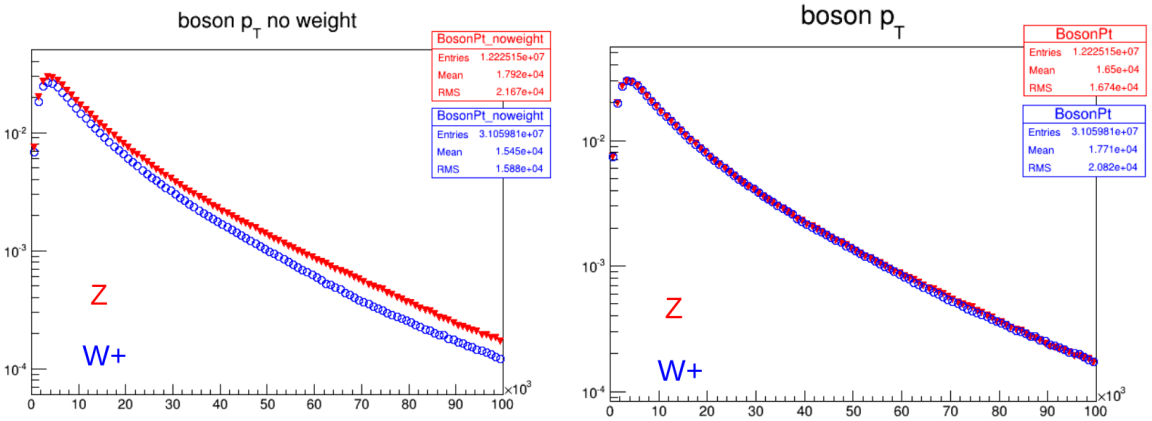

(a) **(b)**

Figure 5.49: Boson p_{T} distribution (a) before and (b) after reweighting.

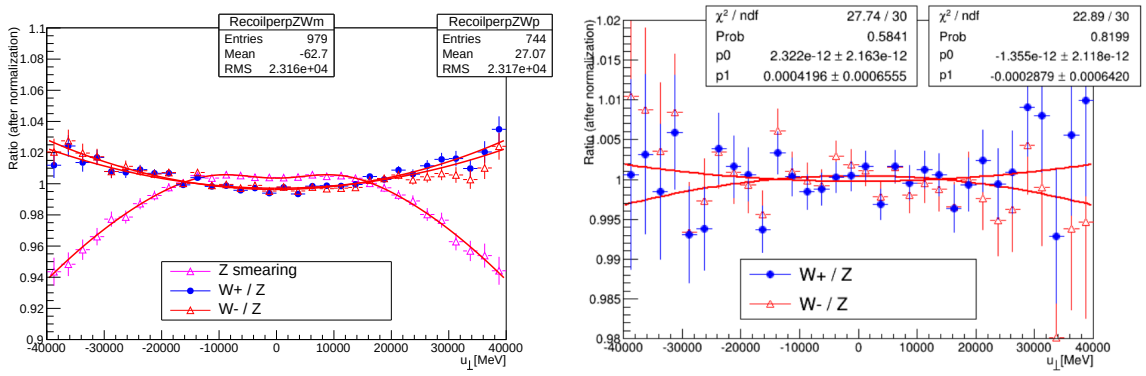

(a) **(b)**

Figure 5.50: (a) Ratio of $u_{\perp}$ in W- and Z-boson events. (b) Ratio of $u_{\perp}$ in W- and Z-boson events requesting a photon veto at truth level

can be compared with the effect of smearing of Z-boson events, which is done in order to have the MC reproducing the data, as shown in Figure 5.50(a). In this case $p_0 = (48.7 \pm 1.4) \times 10^{-12}$, and $\Delta\sigma = 50 \pm 3$ MeV. In order to reduce the effect on the recoil of ISR/FSR and decouple the effect from the genuine W- and Z-boson differences, a cut was applied at truth level vetoing on photons in the event. The efficiency of this cut is roughly of 50%. A similar cut can also be applied at reconstruction level requesting no photon in the event with p_{T} above 100 MeV. The difference between the truth-level and the reconstruction level cut were estimated to have a negligible effect on the W- and Z-boson differences. In Figure 5.50(b) the ratio of $u_{\perp}$ in the W- and Z-boson events is shown. The overall effect for W^+ (W^-) events is $\Delta\sigma = -2 \pm 3$ MeV ($\Delta\sigma = 3 \pm 3$ MeV), which is extremely small compared to the effect of the smearing in the Z-boson events shown above. The values of the W- and Z-boson events smearing can also be compared with the effect of the statistical error on the Z-events smearing, which is calculated

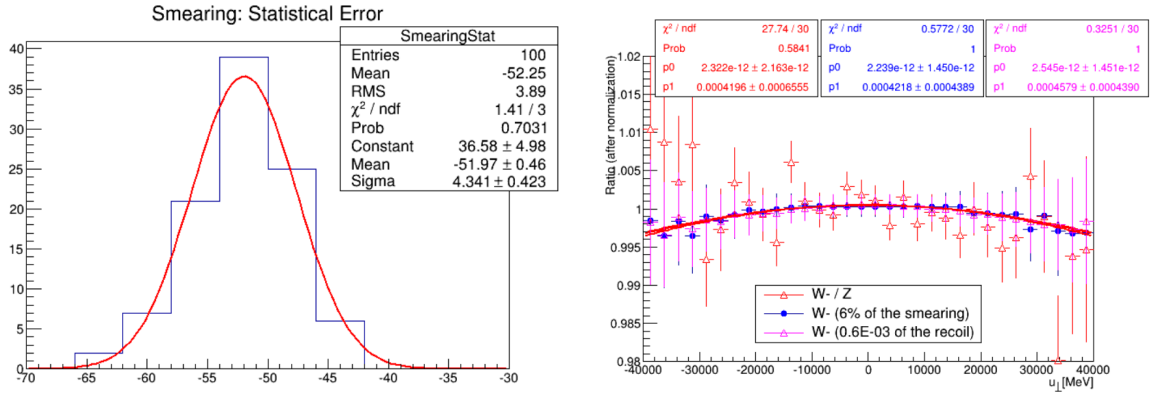

(a) **(b)**

Figure 5.51: (a) Effect of the statistical error on the smearing of Z-boson events. (b) Effect of smearing the recoil in W-boson events by an overall 6% of the Z-boson smearing (blue dots) and by $6 \times 10^{-4} \cdot u_{\perp}$ (magenta triangles).

using the bootstrap method [206]. In Figure 5.51(a) the effect on the resolution of $u_{\perp}$ due to the statistical error on the smearing correction in Z-boson events is shown. The effect corresponds roughly to 4 MeV. Finally, the effect of the W- and Z-boson differences with two possible working cases is compared: smearing $u_{\perp}$ in the W-boson events overall (for each value of $u_{\perp}$) by 6% of the smearing correction, smearing $u_{\perp}$ in the W-boson events by a value of $6 \times 10^{-4} \cdot u_{\perp}$. Those two cases are shown in Figure 5.51(b). Comparing the RMS of the $u_{\perp}$ distribution, as illustrated in Figure 5.47), the W- and Z-boson difference in MC is approximately 6% of the difference between data and MC for Z events:

$$\frac{1 - \frac{\sigma(u_{\perp})_{\text{MC W}}}{\sigma(u_{\perp})_{\text{MC Z}}}}{1 - \frac{\sigma(u_{\perp})_{\text{data Z}}}{\sigma(u_{\perp})_{\text{MC Z}}}}.$$

Therefore, 6% of the value of the smearing correction is considered as systematic uncertainty.

Systematics on the m_W

To estimate the impact of the hadronic recoil corrections on the m_W measurement, template fits are performed for p_{T}^{ℓ}, m_{T} and $E_{\text{T}}^{\text{miss}}$ distributions. The nominal recoil corrections are used for the templates, while pseudo-data are produced including correction variations, with only signal samples variated. The ranges for the fitting are: $30 - 50$ GeV for p_{T}^{ℓ}, $60 - 100$ GeV for m_{T} and $30 - 60$ GeV for $E_{\text{T}}^{\text{miss}}$.

The expected statistical uncertainties form MC are given in Table 5.4 for different $< \mu >$ bins.

The results obtained from the $< \mu >$ scale factor variation as described in this section are given in Table 5.5.

Table 5.4: Expected statistical uncertainty form MC. The values are given in MeV.

Bin	$p_{\mathrm{T}}^{\ell+}$	$p_{\mathrm{T}}^{\ell-}$	$p_{\mathrm{T}}^{\ell\pm}$	m_{T}^{W+}	m_{T}^{W-}	$m_{\mathrm{T}}^{W\pm}$	$E_{\mathrm{T}}^{\mathrm{miss}+}$	$E_{\mathrm{T}}^{\mathrm{miss}-}$	$E_{\mathrm{T}}^{\mathrm{miss}\pm}$
$<\mu>\in(2.5,6.5)$	9.3	10.5	7.0	11.2	12.8	8.4	21.5	24.5	16.3
$<\mu>\in(6.5,9.5)$	9.6	10.7	7.2	13.1	14.9	9.8	27.8	32.0	21.1
$<\mu>\in(9.5,16.0)$	8.7	10.0	6.6	13.5	15.1	10.1	32.9	32.0	23.9
Inclusive	5.4	6.1	4.1	7.3	8.2	5.5	15.4	17.2	11.4

Table 5.5: The systematics form low and high variation of the $<\mu>$ scale factor. The values are given in MeV.

Bin	$p_{\mathrm{T}}^{\ell+}$	$p_{\mathrm{T}}^{\ell-}$	$p_{\mathrm{T}}^{\ell\pm}$	m_{T}^{W+}	m_{T}^{W-}	$m_{\mathrm{T}}^{W\pm}$	$E_{\mathrm{T}}^{\mathrm{miss}+}$	$E_{\mathrm{T}}^{\mathrm{miss}-}$	$E_{\mathrm{T}}^{\mathrm{miss}\pm}$
	low variation ($<\mu>$ scale factor is 1.07)								
$<\mu>\in(2.5,6.5)$	0.1	0.2	0.0	1.8	-0.7	1.1	-0.2	1.1	0.7
$<\mu>\in(6.5,9.5)$	-0.2	1.3	0.1	-1.5	-2.6	-2.1	-1.1	-6.9	-5.0
$<\mu>\in(9.5,16.0)$	-0.4	-0.1	-0.2	-1.3	1.2	-0.4	-0.1	-8.6	-2.8
Inclusive	-0.2	0.5	0.0	-0.1	-0.7	-0.2	-0.4	-4.0	-2.0
	high variation ($<\mu>$ scale factor is 1.14)								
$<\mu>\in(2.5,6.5)$	0.7	-0.7	0.3	0.6	3.3	1.3	3.7	1.0	3.0
$<\mu>\in(6.5,9.5)$	0.5	-1.0	0.1	2.8	2.1	3.4	5.4	4.3	4.9
$<\mu>\in(9.5,16.0)$	1.4	0.7	1.1	-0.5	1.3	0.8	-5.3	1.9	-1.7
Inclusive	0.8	-0.4	0.5	0.9	2.4	1.8	1.6	2.2	2.2

The full difference between p_{T} dependent and p_{T} independent Smirnov transform of the $\Sigma E_{\mathrm{T}} - u$ distribution is given in Table 5.6. However, in order to properly estimate the systematic uncertainty which is coming from the p_{T} dependence of the Smirnov transform, the full difference is multiplied by the fractions given in Table 5.3 as described in this section.

Table 5.6: The full difference between p_{T} dependent and p_{T} independent Smirnov transform of the $\Sigma E_{\mathrm{T}} - u$ distribution. The values are given in MeV.

Bin	$p_{\mathrm{T}}^{\ell+}$	$p_{\mathrm{T}}^{\ell-}$	$p_{\mathrm{T}}^{\ell\pm}$	m_{T}^{W+}	m_{T}^{W-}	$m_{\mathrm{T}}^{W\pm}$	$E_{\mathrm{T}}^{\mathrm{miss}+}$	$E_{\mathrm{T}}^{\mathrm{miss}-}$	$E_{\mathrm{T}}^{\mathrm{miss}\pm}$
$<\mu>\in(2.5,6.5)$	0.9	2.0	1.4	30.6	23.3	27.9	74.3	45.0	62.0
$<\mu>\in(6.5,9.5)$	0.8	1.9	1.3	15.2	20.3	17.6	22.3	37.5	30.6
$<\mu>\in(9.5,16.0)$	3.2	2.9	3.2	5.7	1.6	4.1	-4.4	-7.6	-6.2
Inclusive	1.5	2.2	1.9	20.6	17.9	19.6	46.4	32.7	40.1

The full difference between the hadronic recoil corrections with and without u_{Y} correction is given in the Table 5.7. As discussed in this section for the estimation of uncertainty coming from u_{Y} correction is taken to be 2% from the full difference.

The systematic uncertainties arising from the residual bias and resolution corrections is described in this part. Since bias and resolution corrections are defined as a function of $\Sigma E_{\mathrm{T}} - u$ (in 100 GeV bins) and boson p_{T} (in 5 GeV bins) the variation from the interpolation of the bin values are taken into account. The nominal recoil corrections are taking the value which is in corresponding ($\Sigma E_{\mathrm{T}} - u$,$p_{\mathrm{T}}$) bin, while the

Table 5.7: The full difference between the hadronic recoil corrections with and without u_{Y} correction. The values are given in MeV.

Bin	$p_{\mathrm{T}}^{\ell+}$	$p_{\mathrm{T}}^{\ell-}$	$p_{\mathrm{T}}^{\ell\pm}$	m_{T}^{W+}	m_{T}^{W-}	$m_{\mathrm{T}}^{W\pm}$	$E_{\mathrm{T}}^{\mathrm{miss}+}$	$E_{\mathrm{T}}^{\mathrm{miss}-}$	$E_{\mathrm{T}}^{\mathrm{miss}\pm}$
$<\mu>\in(2.5,6.5)$	1.4	0.0	0.8	11.1	10.1	10.7	32.1	21.6	26.4
$<\mu>\in(6.5,9.5)$	0.7	0.4	0.7	13.4	8.0	12.2	41.0	24.1	26.3
$<\mu>\in(9.5,16.0)$	2.4	1.7	0.7	23.0	13.0	19.2	72.4	24.1	60.0
Inclusive	1.5	0.3	0.7	15.2	9.9	13.4	41.5	29.1	35.2

varied one is taking the interpolated value among the neghibouring bins.

The results of variation due to the $<\mu>$ scale factor, p_{T} dependence of the Smirnov transform, interpolation of the corrections values and due to resolution difference between Z- and W-boson samples are summarised in Table 5.8. The total uncertainty is given in Table 5.9. As can be seen, the largest contributions are from the p_{T} dependence of the $\Sigma E_{\mathrm{T}} - u$ distribution.

The $E_{\mathrm{T}}^{\mathrm{miss}}$ has the poorest resolution, therefore the cut on this quantity introduces the biggest uncertainty. The effect of relaxed $E_{\mathrm{T}}^{\mathrm{miss}}$ cut (this cut is removed from selection) is shown in Table 5.10 and the total uncertainty is given in Table 5.11. The ranges for the fitting in this case are the same for p_{T}^{ℓ} and m_{T} and for $E_{\mathrm{T}}^{\mathrm{miss}}$ is $20 - 60\,\mathrm{GeV}$. Relaxing this cut improves the systematic on the p_{T}^{ℓ} fit, but does not significantly affect the $E_{\mathrm{T}}^{\mathrm{miss}}$ and m_{T} fits.

A refinement of the systematics can be defined by checking the expected difference between W^+ and W^- and/or $<\mu>$ bins, if no difference is observed then averaging by charge and/or in $<\mu>$ bins is performed:

- **Effective corrections: statistical uncertainty**: there is no difference between charges, therefore averaging by charges is done, however correction is different for $<\mu>$ bins.
- $<\mu>$ **scale factor variation**: no difference between charges or in $<\mu>$ bins is observed, therefore averaging by charge and $<\mu>$ bins is done.
- p_{T} **dependence of the** $\Sigma E_{\mathrm{T}} - u$ **distribution**: there is difference between charges for the first $<\mu>$ bin, for the second and third bin averaging by charges is done.
- u_Y **correction**: since the effect of this correction is always less then 1 MeV this systematics is neglected.
- **Effective corrections:** $Z \to W$ **extrapolation**: there is difference between charges for the first $<\mu>$ bin, for the second and third bin averaging by charges is done.
- **Effective corrections: binned vs interpolated**: no difference between charges or in $<\mu>$ bins is observed, therefore averaging by charge and $<\mu>$ bins is done.

Table 5.8: Summarised results of variation due to variation of scale factor, p_{T} dependence of the $\Sigma E_{\mathrm{T}} - u$, interpolation and resolution difference. The systematics on m_W are given in MeV.

Bin	$p_{\mathrm{T}}^{\ell+}$	$p_{\mathrm{T}}^{\ell-}$	$p_{\mathrm{T}}^{\ell\pm}$	m_{T}^{W+}	m_{T}^{W-}	$m_{\mathrm{T}}^{W\pm}$	$E_{\mathrm{T}}^{\mathrm{miss}+}$	$E_{\mathrm{T}}^{\mathrm{miss}-}$	$E_{\mathrm{T}}^{\mathrm{miss}\pm}$
	$<\mu>$ scale factor variation								
$<\mu>\in(2.5, 6.5)$	-0.3	0.5	-0.1	0.6	-2.0	-0.1	-1.9	0.1	-1.2
$<\mu>\in(6.5, 9.5)$	-0.4	1.2	0.0	-2.1	-2.4	-2.7	-3.2	-5.6	-4.9
$<\mu>\in(9.5, 16.0)$	-0.9	-0.4	-0.7	-0.4	0.0	-0.6	2.6	-5.3	-0.5
Inclusive	-0.5	0.4	-0.2	-0.5	-1.5	-1.0	-1.0	-3.1	-2.1
	$\Sigma E_{\mathrm{T}} - u$ correction systematic uncertainties								
$<\mu>\in(2.5, 6.5)$	0.6	1.0	0.9	19.9	11.2	17.0	48.3	21.6	37.8
$<\mu>\in(6.5, 9.5)$	0.6	1.2	0.9	11.1	13.2	12.1	16.3	24.4	21.1
$<\mu>\in(9.5, 16.0)$	2.2	1.7	2.0	4.0	1.0	2.6	-3.0	-4.7	-4.0
Inclusive	1.0	1.3	1.2	12.7	8.9	11.4	24.0	14.9	20.8
	Effective corrections: u_Y correction								
$<\mu>\in(2.5, 6.5)$	0.0	0.0	0.0	0.2	0.2	0.2	0.6	0.4	0.5
$<\mu>\in(6.5, 9.5)$	0.0	0.0	0.0	0.3	0.2	0.2	0.8	0.5	0.5
$<\mu>\in(9.5, 16.0)$	0.0	0.0	0.0	0.5	0.3	0.4	1.4	0.5	1.2
Inclusive	0.0	0.0	0.0	0.3	0.2	0.3	0.8	0.6	0.7
	Effective corrections: statistical uncertainty								
$<\mu>\in(2.5, 6.5)$	1.3	0.9	2.0	3.9	2.5	2.9	4.6	3.1	3.7
$<\mu>\in(6.5, 9.5)$	1.3	0.9	1.7	3.2	3.3	2.4	7.5	5.8	4.7
$<\mu>\in(9.5, 16.0)$	1.6	1.8	2.3	2.1	3.2	2.8	6.4	6.5	4.4
Inclusive	1.4	1.2	2.0	3.2	2.9	2.7	6.0	4.9	4.2
	Effective corrections: $Z \to W$ extrapolation								
$<\mu>\in(2.5, 6.5)$	0.7	0.7	0.7	4.7	1.2	3.2	18.2	7.4	13.4
$<\mu>\in(6.5, 9.5)$	0.1	0.2	0.1	6.5	4.3	5.7	23.2	13.1	17.9
$<\mu>\in(9.5, 16.0)$	-1.0	-0.3	-0.7	8.4	5.6	7.3	28.3	20.2	24.3
Inclusive	0.1	0.3	0.1	6.3	3.4	5.1	22.6	12.8	17.9
	Effective corrections: binned vs interpolated								
$<\mu>\in(2.5, 6.5)$	0.9	1.8	1.3	2.8	5.6	3.8	9.3	11.6	10.0
$<\mu>\in(6.5, 9.5)$	1.7	2.1	1.8	3.5	6.3	4.4	7.4	10.5	9.3
$<\mu>\in(9.5, 16.0)$	1.0	1.4	1.1	1.3	2.4	0.9	-5.1	-3.0	-2.8
Inclusive	1.2	1.8	1.4	2.6	4.9	3.1	4.6	7.1	6.1

Table 5.9: Summarised results of total uncertainty. The systematics on m_W are given in MeV.

Bin	$p_{\mathrm{T}}^{\ell+}$	$p_{\mathrm{T}}^{\ell-}$	$p_{\mathrm{T}}^{\ell\pm}$	m_{T}^{W+}	m_{T}^{W-}	$m_{\mathrm{T}}^{W\pm}$	$E_{\mathrm{T}}^{\mathrm{miss}+}$	$E_{\mathrm{T}}^{\mathrm{miss}-}$	$E_{\mathrm{T}}^{\mathrm{miss}\pm}$
$<\mu>\in(2.5, 6.5)$	1.8	2.4	2.6	21.0	13.0	18.0	52.7	25.8	41.5
$<\mu>\in(6.5, 9.5)$	2.3	2.9	2.6	13.9	15.8	14.6	30.4	30.7	30.0
$<\mu>\in(9.5, 16.0)$	3.2	2.9	3.4	9.6	6.9	8.3	29.7	22.6	25.2
Inclusive	2.2	2.5	2.7	14.8	11.2	13.2	33.8	21.6	28.5

Table 5.10: Summarised results of variation due to scale factor, p_{T} dependence of the $\Sigma E_{\mathrm{T}} - u$, interpolation and resolution difference with relaxed $E_{\mathrm{T}}^{\mathrm{miss}}$ cut. The systematics on m_W are given in MeV.

Bin	$p_{\mathrm{T}}^{\ell+}$	$p_{\mathrm{T}}^{\ell-}$	$p_{\mathrm{T}}^{\ell\pm}$	m_{T}^{W+}	m_{T}^{W-}	$m_{\mathrm{T}}^{W\pm}$	$E_{\mathrm{T}}^{\mathrm{miss}+}$	$E_{\mathrm{T}}^{\mathrm{miss}-}$	$E_{\mathrm{T}}^{\mathrm{miss}\pm}$
	$< \mu >$ scale factor variation								
$< \mu > \in (2.5, 6.5)$	0.8	-0.5	0.5	-0.9	1.1	-0.5	1.4	-1.0	0.7
$< \mu > \in (6.5, 9.5)$	1.1	-1.3	0.5	2.0	3.0	2.8	1.9	5.7	3.9
$< \mu > \in (9.5, 16.0)$	-0.1	0.2	-0.1	-0.2	1.3	0.8	-1.1	4.6	0.8
Inclusive	0.6	-0.5	0.3	0.1	1.7	0.8	0.8	2.6	1.7
	$\Sigma E_{\mathrm{T}} - u$ correction systematic uncertainties								
$< \mu > \in (2.5, 6.5)$	4.5	3.1	4.2	16.0	9.3	13.9	38.4	16.6	29.5
$< \mu > \in (6.5, 9.5)$	3.4	4.1	3.7	8.9	11.0	10.1	11.3	21.9	17.3
$< \mu > \in (9.5, 16.0)$	4.0	3.2	3.7	3.1	-1.4	1.1	-2.8	-6.3	-5.4
Inclusive	4.0	3.4	3.9	10.2	6.7	9.1	18.5	11.6	15.8
	Effective corrections: u_Y correction								
$< \mu > \in (2.5, 6.5)$	0.0	0.0	0.0	0.4	0.2	0.3	0.7	0.4	0.6
$< \mu > \in (6.5, 9.5)$	0.1	0.0	0.1	0.2	0.2	0.2	0.5	0.5	0.3
$< \mu > \in (9.5, 16.0)$	0.0	0.1	0.0	0.4	0.3	0.4	1.3	0.5	1.2
Inclusive	0.1	0.0	0.0	0.3	0.2	0.3	0.6	0.6	0.6
	Effective corrections: statistical uncertainty								
$< \mu > \in (2.5, 6.5)$	1.3	0.9	2.0	3.9	2.5	2.9	4.6	3.1	3.7
$< \mu > \in (6.5, 9.5)$	1.3	0.9	1.7	3.2	3.3	2.4	7.5	5.8	4.7
$< \mu > \in (9.5, 16.0)$	1.6	1.8	2.3	2.1	3.2	2.8	6.4	6.5	4.4
Inclusive	1.4	1.2	2.0	3.2	2.9	2.7	6.0	4.9	4.2
	Effective corrections: $Z \to W$ extrapolation								
$< \mu > \in (2.5, 6.5)$	0.6	0.0	0.4	3.5	-0.2	2.0	14.5	4.2	10.1
$< \mu > \in (6.5, 9.5)$	0.8	0.4	0.6	5.9	4.0	5.2	21.8	11.5	16.3
$< \mu > \in (9.5, 16.0)$	1.3	0.8	1.1	8.8	5.8	7.6	26.5	16.9	22.3
Inclusive	0.9	0.4	0.7	6.1	3.0	4.9	21.4	10.9	16.6
	Effective corrections: binned vs interpolated								
$< \mu > \in (2.5, 6.5)$	1.2	2.5	1.8	2.3	4.1	2.9	9.2	9.1	9.0
$< \mu > \in (6.5, 9.5)$	2.4	1.3	1.9	4.3	5.4	4.3	6.4	6.5	6.6
$< \mu > \in (9.5, 16.0)$	1.3	1.6	1.4	2.1	1.4	0.9	-1.8	-2.4	-1.1
Inclusive	1.6	1.9	1.7	2.8	3.7	2.7	5.2	5.0	5.4

Table 5.11: Summarised results of total uncertainty with relaxed $E_{\mathrm{T}}^{\mathrm{miss}}$ cut. The systematics on m_W are given in MeV.

Bin	$p_{\mathrm{T}}^{\ell+}$	$p_{\mathrm{T}}^{\ell-}$	$p_{\mathrm{T}}^{\ell\pm}$	m_{T}^{W+}	m_{T}^{W-}	$m_{\mathrm{T}}^{W\pm}$	$E_{\mathrm{T}}^{\mathrm{miss}+}$	$E_{\mathrm{T}}^{\mathrm{miss}-}$	$E_{\mathrm{T}}^{\mathrm{miss}\pm}$
$< \mu > \in (2.5, 6.5)$	4.9	4.1	5.0	17.0	10.5	14.6	42.3	19.7	32.6
$< \mu > \in (6.5, 9.5)$	4.5	4.6	4.6	12.1	13.6	12.7	26.5	26.9	25.4
$< \mu > \in (9.5, 16.0)$	4.7	4.1	4.7	9.8	7.0	8.3	27.5	19.8	23.4
Inclusive	4.7	4.1	4.8	12.6	8.9	11.0	29.4	17.6	24.0

The uncertainties after the refinement for the nominal selection are given in Table 5.12 for each source separately and the total uncertainty. The uncertainty from the $< \mu >$ scale factor variation has less than 1 MeV impact on the m_W determination. The uncertainty related to the $\Sigma E_{\mathrm{T}} - u$ correction dependence on boson p_{T} has 1.2 MeV and 11.4 MeV impact on the m_W determination from p_{T}^{ℓ} and m_{T}, respectively, which represents the largest source of uncertainties on the m_W from the hadronic recoil calibration procedure. The statistical uncertainty of the residual correction factors is estimated to 2.0 MeV and 2.7 MeV on the m_W determination from p_{T}^{ℓ} and m_{T}, respectively. The uncertainty coming from the $Z \to W$ extrapolation is negligible for the p_{T}^{ℓ} distribution, and 5 MeV for the m_{T} distribution. The uncertainty on the residual recoil corrections from the interpolation is estimated to 1.4 MeV and 3.1 MeV on the m_W determination from p_{T}^{ℓ} and m_{T}, respectively. The total uncertainty from the hadronic recoil calibration is estimated to 2.7 MeV from p_{T}^{ℓ} and 13.2 MeV from m_{T} on the m_W determination.

Table 5.12: Summarised results of variation due to variation of scale factor, p_{T} dependence of the $\Sigma E_{\mathrm{T}} - u$, interpolation, resolution difference and the total uncertainty after the refinement. The systematics on m_W are given in MeV.

Bin	$p_{\mathrm{T}}^{\ell+}$	$p_{\mathrm{T}}^{\ell-}$	$p_{\mathrm{T}}^{\ell\pm}$	m_{T}^{W+}	m_{T}^{W-}	$m_{\mathrm{T}}^{W\pm}$	$E_{\mathrm{T}}^{\mathrm{miss}+}$	$E_{\mathrm{T}}^{\mathrm{miss}-}$	$E_{\mathrm{T}}^{\mathrm{miss}\pm}$
	$< \mu >$ scale factor variation								
All	0.2	0.2	0.2	1.0	1.0	1.0	2.1	2.1	2.1
	$\Sigma E_{\mathrm{T}} - u$ correction systematic uncertainties								
$< \mu > \in (2.5, 6.5)$	0.6	1.0	0.9	19.9	11.2	17.0	48.3	21.6	37.8
$< \mu > \in (6.5, 9.5)$	0.9	0.9	0.9	12.1	12.1	12.1	21.1	21.1	21.1
$< \mu > \in (9.5, 16.0)$	2.0	2.0	2.0	2.6	2.6	2.6	4.0	4.0	4.0
Inclusive	1.1	1.2	1.2	12.6	9.0	11.4	27.5	16.4	20.8
	Effective corrections: statistical uncertainty								
$< \mu > \in (2.5, 6.5)$	2.0	2.0	2.0	2.9	2.9	2.9	3.7	3.7	3.7
$< \mu > \in (6.5, 9.5)$	1.7	1.7	1.7	2.4	2.4	2.4	4.7	4.7	4.7
$< \mu > \in (9.5, 16.0)$	2.3	2.3	2.3	2.8	2.8	2.8	4.4	4.4	4.4
Inclusive	2.0	2.0	2.0	2.7	2.7	2.7	4.2	4.2	4.2
	Effective corrections: $Z \to W$ extrapolation								
$< \mu > \in (2.5, 6.5)$	0.7	0.7	0.7	4.7	1.2	3.2	18.2	7.4	13.4
$< \mu > \in (6.5, 9.5)$	0.1	0.1	0.1	5.7	5.7	5.7	17.9	17.9	17.9
$< \mu > \in (9.5, 16.0)$	0.7	0.7	0.7	7.3	7.3	7.3	24.3	24.3	24.3
Inclusive	0.1	0.1	0.1	5.8	4.3	5.1	19.9	15.4	17.9
	Effective corrections: binned vs interpolated								
All	1.4	1.4	1.4	3.1	3.1	3.1	6.1	6.1	6.1
	Total								
$< \mu > \in (2.5, 6.5)$	2.6	2.7	2.7	21.0	12.2	17.9	52.4	24.6	41.1
$< \mu > \in (6.5, 9.5)$	2.4	2.4	2.4	14.1	14.1	14.1	29.2	29.2	29.2
$< \mu > \in (9.5, 16.0)$	3.4	3.4	3.4	9.0	9.0	9.0	26.3	26.3	26.4
Inclusive	2.7	2.7	2.7	14.5	10.8	13.2	34.8	23.8	28.5

The uncertainties after the refinement with relaxed $E_{\mathrm{T}}^{\mathrm{miss}}$ cut are given in Table 5.13 for each source separately and the total uncertainty. There results are similar as for the nominal case. As expected the uncertainty on the m_{T} determination is smaller, with the total uncertainty from the hadronic recoil calibration estimated to 4.8 MeV from p_{T}^{ℓ} and 11.0 MeV from m_{T} on the m_W determination.

Table 5.13: Summarised results of variation due to scale factor, p_{T} dependence of the $\Sigma E_{\mathrm{T}} - u$, interpolation, resolution difference and the total uncertainty with relaxed $E_{\mathrm{T}}^{\mathrm{miss}}$ cut after refinement. The systematics on m_W are given in MeV.

Bin	$p_{\mathrm{T}}^{\ell+}$	$p_{\mathrm{T}}^{\ell-}$	$p_{\mathrm{T}}^{\ell\pm}$	m_{T}^{W+}	m_{T}^{W-}	$m_{\mathrm{T}}^{W\pm}$	$E_{\mathrm{T}}^{\mathrm{miss}+}$	$E_{\mathrm{T}}^{\mathrm{miss}-}$	$E_{\mathrm{T}}^{\mathrm{miss}\pm}$
	$<\mu>$ scale factor variation								
All	0.3	0.3	0.3	0.8	0.8	0.8	1.7	1.7	1.7
	$\Sigma E_{\mathrm{T}} - u$ correction systematic uncertainties								
$<\mu>\in(2.5, 6.5)$	4.5	3.1	4.2	16.0	9.3	13.9	38.4	16.6	29.5
$<\mu>\in(6.5, 9.5)$	3.7	3.7	3.7	10.1	10.1	10.1	17.3	17.3	17.3
$<\mu>\in(9.5, 16.0)$	3.7	3.7	3.7	1.1	1.1	1.1	-5.4	-5.4	-5.4
Inclusive	4.0	3.5	3.9	10.0	7.2	9.1	19.5	10.5	15.8
	Effective corrections: statistical uncertainty								
$<\mu>\in(2.5, 6.5)$	2.0	2.0	2.0	2.9	2.9	2.9	3.7	3.7	3.7
$<\mu>\in(6.5, 9.5)$	1.7	1.7	1.7	2.4	2.4	2.4	4.7	4.7	4.7
$<\mu>\in(9.5, 16.0)$	2.3	2.3	2.3	2.8	2.8	2.8	4.4	4.4	4.4
Inclusive	2.0	2.0	2.0	2.7	2.7	2.7	4.2	4.2	4.2
	Effective corrections: $Z \to W$ extrapolation								
$<\mu>\in(2.5, 6.5)$	0.6	0.0	-0.4	3.5	-0.2	2.0	14.5	4.2	10.1
$<\mu>\in(6.5, 9.5)$	0.6	0.6	0.6	5.2	5.2	5.2	16.3	16.3	16.3
$<\mu>\in(9.5, 16.0)$	1.1	1.1	1.1	7.6	7.6	7.6	22. 3	22.3	22.3
Inclusive	0.9	0.4	0.7	6.1	3.0	4.9	21.4	10.9	16.6
	Effective corrections: binned vs interpolated								
All	1.7	1.7	1.7	2.7	2.7	2.7	5.4	5.4	5.4
	Total								
$<\mu>\in(2.5, 6.5)$	5.3	4.1	4.9	16.9	10.1	14.6	41.6	18.4	31.9
$<\mu>\in(6.5, 9.5)$	4.5	4.5	4.5	12.0	12.0	12.0	24.9	24.9	24.9
$<\mu>\in(9.5, 16.0)$	4.8	4.8	4.8	8.7	8.7	8.7	24.0	24.0	24.0
Inclusive	4.9	4.4	4.8	12.3	8.7	11.0	29.8	16.7	24.0

The m_W determination from p_{T}^{ℓ} measurement is only slightly affected, because of the selection requirements on u_{T}, m_{T} and $E_{\mathrm{T}}^{\mathrm{miss}}$. In general, the systematics uncertainties are larger for W^+ than for W^- bosons, since the $\Sigma E_{\mathrm{T}} - u$ distribution in W^- boson events is closer to the corresponding distribution in the Z-boson events.

Compared to the hadronic recoil uncertainties of the m_W measurement at the Tevatron, shown in Tables 1.2 and 1.3 for the CDF and D0 experiments, the obtained uncertainty is smaller for the p_{T}^{ℓ} and larger for the m_{T} distribution. Smaller uncertainty on the p_{T}^{ℓ} reflect the different selection of the W-boson candidates, while the larger m_{T} uncertainty corresponds to the higher pile-up conditions at the LHC.

6

Measurement of the W-boson Mass with the 7 TeV Data

In this chapter the measurement of the W-boson mass is described and the results with 2011 data are presented. The results shown in this chapter are based on [80] and [81]. In the first part of the chapter the final experimental and theoretical corrections are described, as well as the background determination. The first part concludes with the description of the systematics uncertainties and an overview of the control distributions. The second part is dedicated to the extraction of the W-boson mass and the combination of obtained results, it concludes with the final results obtained for this measurement. The third and last part of this chapter is devoted to the prospect for the future W-boson mass measurements, with the special emphasis on the direct measurement of the p_{T}^{W} distribution, which can be used to reduce systematics uncertainties on the future W-boson mass measurements.

6.1 W-BOSON EVENTS

The W-boson event selection is presented in Chapter 3.5. The final measured value of the W-boson mass is obtained from the combination of various measurements performed in the electron and muon decay channels, and in charge- and $|\eta|$-dependent categories, as defined in Table 6.1. The pseudorapidity boundaries are driven by experimental and statistical constraints. The $1.2 < |\eta| < 1.8$ range missing in the electron channel, because the amount of the passive material in front of the calorimeter is largest in this region, as explained in Section 3.4. The measurement of the m_W in different categories is important in order to test the consistency and the understanding of experimental and theoretical uncertainties. Since in proton–proton collisions, there are more W^+ than W^- bosons, as explained in Section 1.3.2, the m_W measurement is performed separately for W^+ and W^- bosons. Measurement in both, electron and muon decay channels provides an additional test on the experimental calibration, e.g. the agreement between m_{W^+} and m_{W^-} in the muon channel but not in the electron channel, would point to an experimental problem in electron calibration. Furthermore, the consistency between charges and pseudorapidity categories allows testing of the theoretical corrections, e.g. a consistent charge dependency of m_W would point to a problem of the underlying physics model. The m_W measurement in pseudorapidity categories allows to test the consistency for PDF and angular coefficients uncertainties.

The number of selected events in each category in data is given in Table 6.2. For the final measurement only combination of the p_{T} and m_{T} distribution is used, since the measurement based on $E_{\mathrm{T}}^{\mathrm{miss}}$ distribution has significantly lower precision.

Table 6.1: Summary of categories and kinematic distributions used for the m_W measurement for the electron and muon decay channels.

Decay channel	$W \to e\nu$	$W \to \mu\nu$
Kinematic distributions	p_{T}^{ℓ}, m_{T}	p_{T}^{ℓ}, m_{T}
Charge categories	W^+, W^-	W^+, W^-
$\lvert\eta_\ell\rvert$ categories	$[0, 0.6]$, $[0.6, 1.2]$, $[1.8, 2.4]$	$[0, 0.8]$, $[0.8, 1.4]$, $[1.4, 2.0]$, $[2.0, 2.4]$

Table 6.2: Numbers of selected W^+ and W^- boson events in the different decay channels in data, inclusively and for the various $|\eta_\ell|$ categories.

$\lvert\eta_\ell\rvert$ range	0–0.8	0.8–1.4	1.4–2.0	2.0–2.4	Inclusive
$W^+ \to \mu^+\nu$	1 283 332	1 063 131	1 377 773	885 582	4 609 818
$W^- \to \mu^-\bar{\nu}$	1 001 592	769 876	916 163	547 329	3 234 960
$\lvert\eta_\ell\rvert$ range	0–0.6	0.6–1.2		1.8–2.4	Inclusive
$W^+ \to e^+\nu$	1 233 960	1 207 136		956 620	3 397 716
$W^- \to e^-\bar{\nu}$	969 170	908 327		610 028	2 487 525

6.1.1 *Final experimental and theoretical corrections*

The electron energy corrections are mostly based on the ATLAS Run-1 electron and photon calibration result [78]. The correction procedure starts with the intercalibration of the first and second layers of the EM calorimeter for minimum ionising particles, using the energy deposits of muons in Z decays. After the intercalibration of the calorimeter layers, the longitudinal energy profiles of electrons and photons are used to determine the presampler energy scale and probe the passive material in front of the EM calorimeter, leading to an improved description of the detector material distribution and providing estimates of the residual passive material uncertainty. Finally, a non-linearity of the energy measurement at the cell level is observed and corrected for. After these preliminary corrections, an overall energy scale correction is determined as a function of pseudorapidity from the Z-boson decays to electrons, by comparing the reconstructed mass distributions in data and simulation. Simultaneously, an effective constant term for the calorimeter energy resolution is extracted by adjusting the width of the reconstructed dielectron invariant mass distribution in simulation to match the distribution in data.

Azimuthal variations of the electron energy response are expected from the mechanical deformation under gravity of the EM calorimeter, and observed especially in the endcaps, as illustrated in Figure 6.1. Although this modulation does not affect

the average response in the Z-boson sample, a small residual effect is expected when applying the Z-boson calibration to the selected W-boson sample, where the electron azimuthal distribution is not perfectly uniform, as discussed in Chapter 5. A dedicated correction is derived using the azimuthal dependence of the mean of the electron energy/momentum ratio, $< E/p >$, after correcting p for the momentum scale and curvature bias. The effect of this correction is a relative change of the average energy response of 3.8×10^{-5} in the W-boson events.

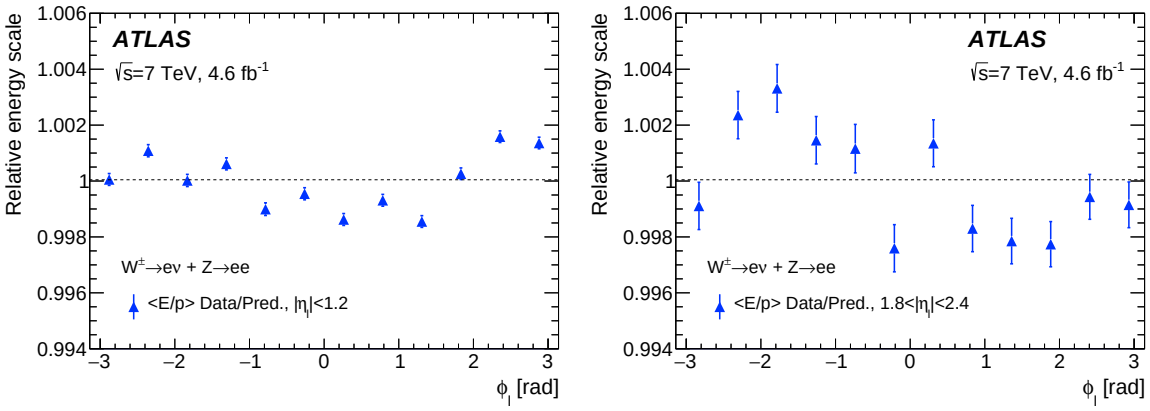

Figure 6.1: Azimuthal variation of the data-to-prediction ratio of $< E/p >$ in W- and Z-boson events, for electrons in (a) $|\eta| < 1.2$ and (b) $1.8 < |\eta| < 2.4$. The electron energy calibration based on $Z \to ee$ events is applied, and the track p is corrected for the momentum scale, resolution and sagitta bias. The mean for the E/p distribution integrated in φ is normalised to unity. The error bars are statistical only.

The result of the complete calibration procedure is illustrated in Figure 6.2(a), which shows the comparison of the dielectron invariant mass distribution for $Z \to ee$ events in data and simulation.

Electron efficiency corrections are determined using samples of $W \to e\nu$, $Z \to ee$, and $J/\psi \to ee$ events, and measured separately for electron reconstruction, identification and trigger efficiencies [77], as a function of electron η and p_{T}. Figure 6.2(b) compares the η distribution in data and simulation for $Z \to ee$ events, after applying the efficiency corrections discussed above.

Muon momentum scale and resolution corrections are derived using $Z \to \mu\mu$ decays, following the method described in Section 4.4. There are two types of possible biases in the reconstructed muon track momenta radial and sagitta biases. The radial biases originate from detector movements along the particle trajectory and can be corrected by an η-dependent, charge-independent momentum scale correction. The sagitta biases originate from curl distortions or linear twists of the detector around the z-axis [207], and can be corrected with η-dependent correction factors proportional to $q \cdot p_{\mathrm{T}}$, where q is the charge of the muon. The overall momentum correction is parameterised as

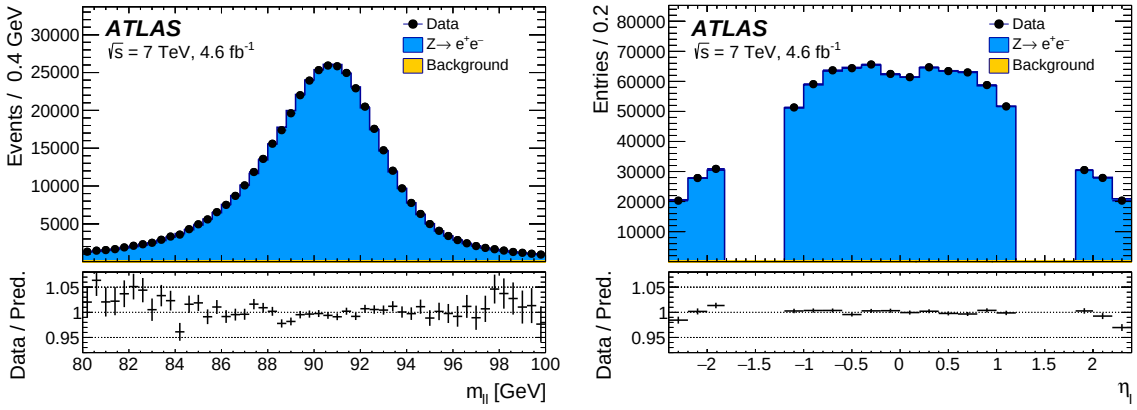

(a) **(b)**

Figure 6.2: (a) Dielectron invariant mass and (b) reconstructed electrons η distribution in $Z \to ee$ events. The data is compared to the simulation including signal and backgrounds. Corrections for energy resolution, and for reconstruction, identification, isolation and trigger efficiencies are applied to the simulation; energy-scale corrections are applied to the data. Background events contribute less than 0.2% of the observed distribution. The lower panel shows the data-to-prediction ratio, with the error bars showing the statistical uncertainty.

follows:

$$
\begin{aligned}
p_{\mathrm{T}}^{\mathrm{MC,corr}} &= p_{\mathrm{T}}^{\mathrm{MC}} \times [1 + \alpha(\eta, \phi)] \times \left[1 + \beta_{\mathrm{curv}}(\eta) \cdot G(0,1) \cdot p_{\mathrm{T}}^{\mathrm{MC}}\right], \\
p_{\mathrm{T}}^{\mathrm{data,corr}} &= \frac{p_{\mathrm{T}}^{\mathrm{data}}}{1 + q \cdot \delta(\eta, \phi) \cdot p_{\mathrm{T}}^{\mathrm{data}}},
\end{aligned}
$$

where $p_{\mathrm{T}}^{\mathrm{data,MC}}$ is the uncorrected muon transverse momentum in data and simulation, $G(0,1)$ are normally distributed random variables with mean zero and unit width, and α, β_{curv}, and δ represent the momentum scale, intrinsic resolution and sagitta bias corrections, respectively. Since the multiple scattering contribution to the resolution are relevant at low p_{T}, this correction is neglected. Template histograms of the dimuon invariant mass are constructed from the simulated event samples, including momentum scale and resolution corrections in narrow steps within a range covering the expected uncertainty. The optimal values of α and β_{curv} are determined by means of a χ^2 minimisation, comparing data and simulation in the range of twice the standard deviation on each side of the mean value of the invariant mass distribution. In the first step, the corrections are derived by averaging over φ, and for 24 pseudorapidity bins in the range $-2.4 < \eta_\ell < 2.4$. In the second iteration, φ-dependent correction factors are evaluated in coarser bins of η_ℓ. The typical size of α varies from -0.0005 to -0.0015 depending on η_ℓ, while β_{curv} values increase from 0.2 TeV^{-1} in the barrel to 0.6 TeV^{-1} in the high η_ℓ region. Before the correction, the φ-dependence has an amplitude at the level of 0.1%.

Two methods are used for the determination of the sagitta bias corrections δ. The first method exploits $Z \to \mu\mu$ events. Muons are categorised according to their charge

and pseudorapidity, and for each of these categories, the position of the peak in the dimuon invariant mass distribution is determined for data and simulation. The procedure allows the determination of the charge dependence of the momentum scale for p_{T} values of approximately 42 GeV, which corresponds to the average transverse momentum of muons from Z-boson decays. The second method exploits identified electrons in a sample of $W \to e\nu$ decays. It is based on the ratio of the measured electron energy deposited in the calorimeter, E, to the electron momentum, p, measured in the ID. A clean sample of $W \to e\nu$ events with tightly identified electrons [77] is selected. Assuming that the response of the electromagnetic calorimeter is independent of the charge of the incoming particle, charge-dependent ID track momentum biases are extracted from the average differences in E/p for electrons and positrons [207]. This method benefits from a larger event sample compared to the $Z \to \mu\mu$ sample used in the first method, and allows the determination of charge-dependent corrections for p_{T} values of approximately 38 GeV, which corresponds to the average transverse momentum of muons in W-boson decays. The correction factors are derived in 40 η bins and 40 φ bins. Sagitta bias corrections are derived using both methods separately. Both results are found to agree within uncertainties and are combined, as illustrated in Figure 6.3(a). Figure 6.3(b) shows the dimuon invariant mass distribution of $Z \to \mu\mu$ decays in data and simulation, after applying all corrections.

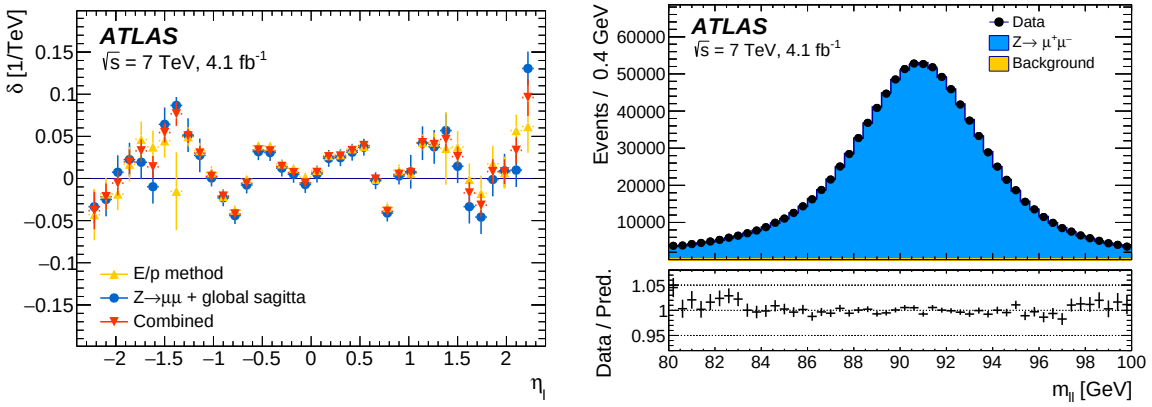

(a) **(b)**

Figure 6.3: (a) Sagitta bias, δ, as a function of η_ℓ averaged over φ_ℓ. The results are obtained with the $Z \to \mu\mu$ and E/p methods and the combination of the two. The results obtained with the $Z \to \mu\mu$ method are corrected for the global sagitta bias. The E/p method uses electrons from $W \to e\nu$ decays. The two measurements are combined assuming they are uncorrelated. The error bars on the points show statistical uncertainties only. (b) Dimuon invariant mass distribution in $Z \to \mu\mu$ events. The data are compared to the simulation including signal and background contributions. Corrections for momentum scale and resolution, and for reconstruction, isolation, and trigger efficiencies are applied to the muons in the simulated events. Background events contribute less than 0.2% of the observed distribution. The lower panel shows the data-to-prediction ratio, with the error bars showing the statistical uncertainty.

Corrections to the muon reconstruction, trigger and isolation efficiencies are estimated by applying the tag-and-probe method [79] to $Z \to \mu\mu$ events in data and simulation. Efficiency corrections are defined as the ratio of efficiencies evaluated in data to efficiencies evaluated in simulated events. The corrections are evaluated as functions of two variables, p_{T}^{ℓ} and $u_{\parallel}^{\ell}$, and in various regions of the detector. The detector is segmented into regions corresponding to the η and φ coverage of the MS. The subdivision accounts for the geometrical characteristics of the detector, such as the presence of uninstrumented or transition regions. The quality of the efficiency corrections is evaluated by applying the corrections to the $Z \to \mu\mu$ simulated sample, and comparing the simulated kinematic distributions to the corresponding distributions in data. The dependence of the efficiencies on $u_{\parallel}^{\ell}$ agree in data and simulation. Therefore the muon efficiency corrections are evaluated only as a function of p_{T}^{ℓ} and η, separately for positive and negative muon charges. The final efficiency correction factors are linearly interpolated as a function of muon p_{T}. No significant p_{T}-dependence of the corrections is observed in any of the detector regions. The resulting scale factors are shown as a function of p_{T} and averaged over η_{ℓ} in Figure 6.4(a). The quality of the efficiency corrections is evaluated by applying the corrections to the $Z \to \mu\mu$ events in simulation, and comparing the simulated kinematic distributions to the corresponding distributions in data. Figure 6.4(b) illustrates the η_{ℓ} distribution after applying described corrections.

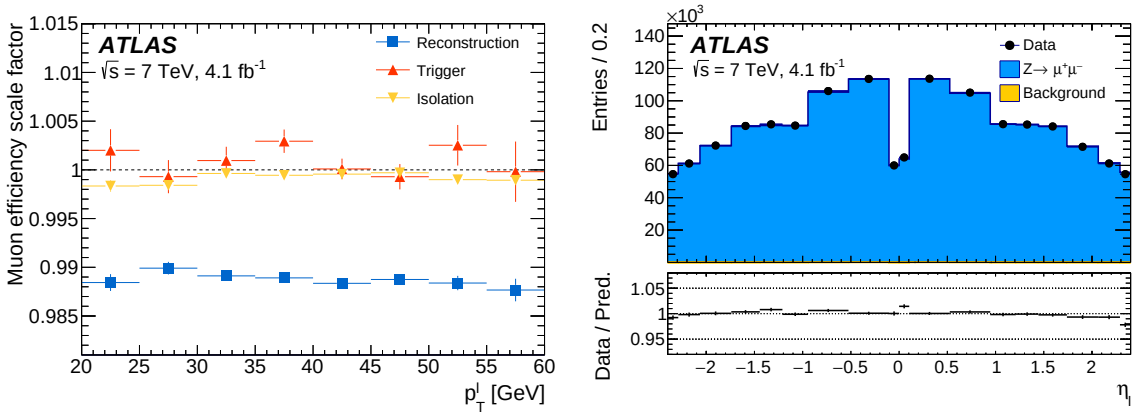

(a) **(b)**

Figure 6.4: (a) Scale factors for the muon reconstruction, trigger and isolation efficiency obtained with the tag and probe method as a function of the muon p_{T}. Scale factors for the trigger efficiency are averaged over two data-taking periods as explained in the text. The error bars on the points show statistical uncertainties only. (b) Distribution of the reconstructed muons η in $Z \to \mu\mu$ events. The data are compared to the simulation including signal and background contributions. Corrections for momentum scale and resolution, and for reconstruction, isolation, and trigger efficiencies are applied to the muons in the simulated events. Background events contribute less than 0.2% of the observed distribution. The lower panel shows the data-to-prediction ratio, with the error bars showing the statistical uncertainty.

The calibration of the hadronic recoil is described in detail in Chapter 5. The theoretical corrections to the W-boson production and decay are described in Section 3.3. It is important to distinguish the effect of the hadronic recoil corrections and the modeling of the p_{T}^{W} distribution. This is illustrated in Figure 6.5, by comparing the recoil distributions in the POWHEG+PYTHIA8 and POWHEG+HERWIG6 samples, before and after the corrections described in Section 5.5 with different p_{T}^{W} distribution. As can be seen, the recoil corrections and the different p_{T}^{W} distributions have a comparable effect on the u_{T} distribution. In contrast, the effect of the recoil corrections is small at negative values of $u_{\parallel}^{\ell}$, whereas the difference in the p_{T}^{W} distributions has a large impact in this region. Therefore, the sensitivity of the $u_{\parallel}^{\ell}$ distribution can be used to test the modeling of the p_{T}^{W} distribution. This validation test supports the PYTHIA 8 AZ prediction for the p_{T}^{W} distribution, which is described in Section 3.3.3.

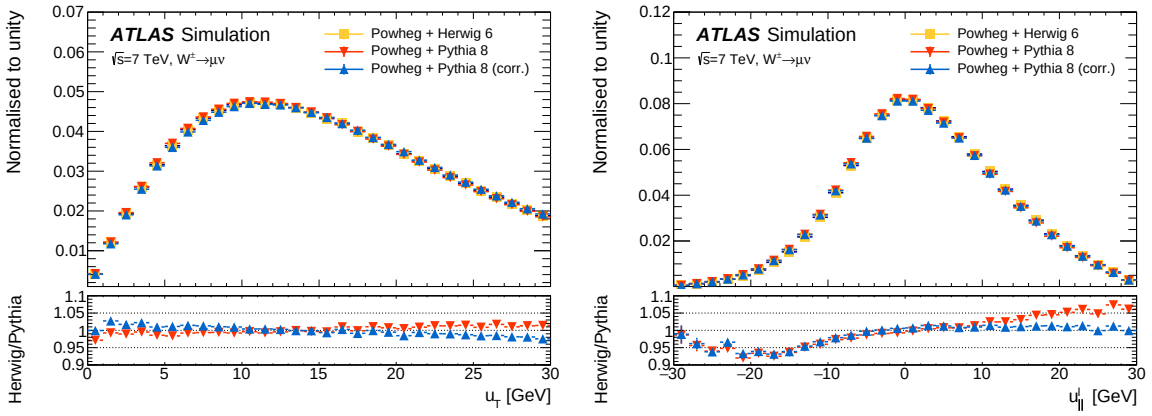

(a) **(b)**

Figure 6.5: Distribution of (a) u_{T} and (b) $u_{\parallel}^{\ell}$ in W-boson events simulated with POWHEG+PYTHIA8 and POWHEG+HERWIG6 after all analysis selection cuts are applied. The POWHEG+PYTHIA8 distributions are shown before and after correction to the hadronic recoil in POWHEG+HERWIG6. The lower panels show the ratios of POWHEG+HERWIG6 and POWHEG+PYTHIA8, with and without the hadronic recoil correction. The discrepancy remaining after recoil corrections reflects the different p_{T}^{W} distributions.

In summary, following experimental and theoretical corrections are applied to the simulated signal and background samples:

- Electron energy and muon momentum scale and resolution, and efficiency (reconstruction, identification, trigger and isolation) corrections.
- Hadronic recoil correction with the pile-up reweighting and $< \mu >$ rescaling.
- Line-shape reweighting, incorporating EW corrections.
- Reweighting the vector boson p_{T}^{V} in bins of y^{V} according to the PYTHIA8 AZ tune.
- Reweighting the rapidity distribution following a fixed order NNLO prediction and the CT10NNLO PDF set.
- Reweighting the QCD angular coefficients A_i in bins of y^{V}, m and $p_{\mathrm{T}}^{\mathrm{V}}$ according to the fixed order DYNNLO prediction.

6.1.2 *Z-boson based cross checks*

The $Z \to \ell\ell$ sample allows several validation and consistency tests for the W-boson mass measurement. As already shown in Section 5.6.1, by treating one of the charged leptons from the Z-boson decay as a neutrino, a pseudo m_{T} distribution is defined in Z-boson events. Similarly, as for the W-boson case, the mass of the Z boson is extracted with template fits to the $m_{\ell\ell}$, p_{T}^{ℓ} and m_{T} kinematic distributions. The extraction of the Z-boson mass from the dilepton invariant mass distribution is expected to yield, by construction, the value of m_Z used as input for the muon-momentum and electron-energy calibrations, providing a closure test of the lepton calibration procedures. The p_{T}^{ℓ} distribution is very sensitive to the physics modeling corrections. The comparison of the value of m_Z extracted from the p_{T}^{ℓ} distribution to the value used as input for the calibration provides a stringent test of the physics modellng. Finally, the extraction of m_Z from the m_{T} distribution provides a test of the recoil calibration. The ranges used for the extraction are $[80, 100]$ GeV for the $m_{\ell\ell}$ distributions, $[30, 55]$ GeV for the p_{T}^{ℓ} distribution, and $[40, 120]$ GeV for the m_{T} distribution.

The Z-boson mass fits are performed using the m_{T} and p_{T}^{ℓ} distributions in the electron and muon decay channels, inclusively in η^{ℓ} and separately for positive and negative leptons. The results of the fits are summarised in Figure 6.6.

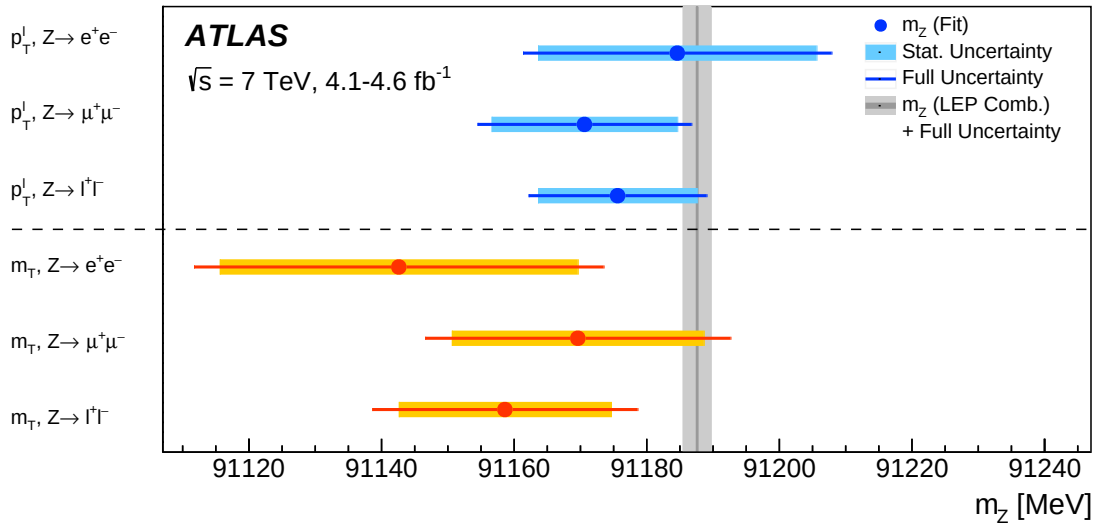

Figure 6.6: Summary of the m_Z extraction from the p_{T}^{ℓ} and m_{T} distributions in the muon and electron decay channels. The LEP combined value of m_Z [40], which is used as input for the detector calibration, is also indicated. The horizontal and vertical bands show the uncertainties of the m_Z determinations and of the LEP combined value, respectively.

The value of m_Z measured from positive leptons is correlated with the corresponding extraction from the negative leptons. The p_{T}^{ℓ} distributions for positive and negative leptons are statistically independent, but the m_{T} distributions share the same reconstructed recoil event by event, and are statistically correlated. In both cases, the decay

of the Z-boson induces a kinematical correlation between the distributions of positive and negative leptons. The correlation is estimated by constructing two-dimensional ℓ^+ and ℓ^- distributions, separately for p_{T}^{ℓ} and m_{T}, fluctuating the bin contents of these distributions within their uncertainties, and repeating the fits for each pseudodata sample. The correlation values are -7% for the p_{T}^{ℓ} distributions, and -12% for the m_{T} distributions.

The combined extraction of m_Z from the p_{T}^{ℓ} distribution yields a result compatible with the reference value within 0.9 standard deviations. The difference between the m_Z extractions from positive and negative lepton distributions is compatible with zero within 1.4 standard deviations. For the extraction from the m_{T} distribution, the compatibility with the reference value of m_Z is at the level of 1.5 standard deviations. Fits using the lepton pair invariant mass distribution agree with the reference, yielding $\Delta m_Z = 1 \pm 3$ MeV in the muon channel and $\Delta m_Z = 3 \pm 5$ MeV in the electron channel, as expected from the calibration procedure. In summary, the consistency tests based on the Z-boson sample agree with the expectations within the uncertainties. More details about the Z-boson based cross checks can be found in [80].

6.1.3 *Background determination*

The W-boson event sample includes events from various background processes. Background contributions from Z-boson, $W \to \tau\nu$, boson pair, and top-quark production are estimated using simulation. Contributions from multijet production are estimated with data-driven techniques.

The dominant sources of background contribution in the $W \to \ell\nu$ sample are $Z \to \ell\ell$ events, in which one of the two leptons escapes detection, and $W \to \tau\nu$ events, where the τ decays to an electron or muon. These background contributions are estimated using the POWHEG+PYTHIA 8 samples after applying the modelling corrections discussed in Section 3.3, which include NNLO QCD corrections to the angular coefficients and rapidity distributions, and corrections to the vector-boson transverse momentum. The $Z \to ee$ background represents 2.9% of the $W^+ \to e\nu$ sample and 4.0% of the $W^- \to e\nu$ sample. In the muon channel, the $Z \to \mu\mu$ background represents 4.8% and 6.3% of the $W^+ \to \mu\nu$ and $W^- \to \mu\nu$ samples, respectively. The $W \to \tau\nu$ background represents 1.0% of the selected sample in both channels, and the $Z \to \tau\tau$ background contributes approximately 0.12%. The normalisation of these processes relative to the W-boson signal and the corresponding uncertainties are discussed in Section 3.2. In the determination of the W-boson mass, the variations of m_W are propagated to the $W \to \tau\nu$ background templates in the same way as for the signal.

Similarly, backgrounds involving top-quark (top-quark pairs and single top-quark) production, and boson-pair production are estimated using simulation, and normalisation uncertainties are assigned as discussed in Section 3.2. These processes represent 0.11% and 0.07% of the signal event selection, respectively.

Inclusive multijet production in strong-interaction processes constitutes a significant source of background. A fraction of multijet events contains semileptonic decays of bottom and charm hadrons to muons or electrons and neutrinos, and can pass the W-boson signal selection. In addition, inclusive jet production contributes to the background if one jet is misidentified as electron or muon, and sizeable missing transverse momentum is reconstructed in the event. In-flight decays of pions or kaons within the tracking region can mimic the W-boson signal in the muon channel. In the electron channel, events with photon conversions and hadrons misidentified as electrons can be selected as W-boson events. Due to the small selection probability for multijet events, their large production cross section, and the relatively complex modelling of the hadronisation processes, the multijet background contribution cannot be estimated precisely using simulation, and a data-driven method is used instead.

The estimation of the multijet background contribution follows similar procedures in the electron and muon decay channels, and relies on template fits to kinematic distributions in background-dominated regions. The analysis uses the distributions of $E_{\mathrm{T}}^{\mathrm{miss}}$, m_{T}, and the $p_{\mathrm{T}}^{\ell}/m_{\mathrm{T}}$ ratio, where jet-enriched regions are obtained by relaxing a subset of the signal event-selection requirements. The first kinematic region, denoted FR1, is defined by removing the $E_{\mathrm{T}}^{\mathrm{miss}}$ and m_{T} requirements from the event selection. A second kinematic region, FR2, is defined in the same way as FR1, but by also removing the requirement on u_{T}. Multijet background events, which tend to have smaller values of $E_{\mathrm{T}}^{\mathrm{miss}}$ and m_{T} than the signal, are enhanced by this selection. The $p_{\mathrm{T}}^{\ell}/m_{\mathrm{T}}$ distribution is sensitive to the angle between the p_{T}^{ℓ} and $E_{\mathrm{T}}^{\mathrm{miss}}$ vectors in the transverse plane. Whereas W-boson events are expected to peak at values of $p_{\mathrm{T}}^{\ell}/m_{\mathrm{T}} = 0.5$, relatively large tails are observed for multijet events.

Templates of the multijet background distributions for these observables are obtained from data by inverting the lepton energy-isolation requirements. Contamination of these control regions by EW and top production is estimated using simulation and subtracted. In the muon channel, the anti-isolation requirements are defined from the ratio of the scalar sum of the p_{T} of tracks in a cone of size $\Delta R < 0.2$ around the reconstructed muon to the muon p_{T}. The isolation variable $p_{\mathrm{T}}^{\mu,\mathrm{cone}}$, introduced in Section 3.4, is required to satisfy $c_1 < p_{\mathrm{T}}^{\mu,\mathrm{cone}}/p_{\mathrm{T}}^{\ell} < c_2$, where the anti-isolation boundaries c_1 and c_2 are varied as discussed below. In order to avoid overlap with the signal region, the lower boundary c_1 is always larger than 0.1. In the electron channel, the scalar sum of the p_{T} of tracks in a cone of size $\Delta R < 0.4$ around the reconstructed electron, defined as $p_{\mathrm{T}}^{e,\mathrm{cone}}$ in Section 3.4, is used to define the templates, while the requirements on the calorimeter isolation are omitted.

The multijet background normalisation is determined by fitting each of the $E_{\mathrm{T}}^{\mathrm{miss}}$, m_{T}, and $p_{\mathrm{T}}^{\ell}/m_{\mathrm{T}}$ distributions in the two kinematic regions FR1 and FR2, using templates of these distributions based on multijet events and obtained with several ranges of the anti-isolation variables. The multijet background in the signal region is determined by correcting the multijet fraction fitted in the FR1 and FR2 for the different efficiencies of the selection requirements of the signal region. In the electron channel, c_1 is varied from 4GeV to 9GeV in steps of 1 GeV, and c_2 is set to $c_2 = c_1 + 1$ GeV. In the muon channel, c_1 is varied from 0.1 to 0.37 in steps of 0.03, and c_2 is set to

$c_2 = c_1 + 0.03$. The results corresponding to the various observables and to the different kinematic regions are linearly extrapolated in the isolation variables to the signal regions, denoted by $c_1 = 0$. Figure 6.7 illustrates the extrapolation procedure.

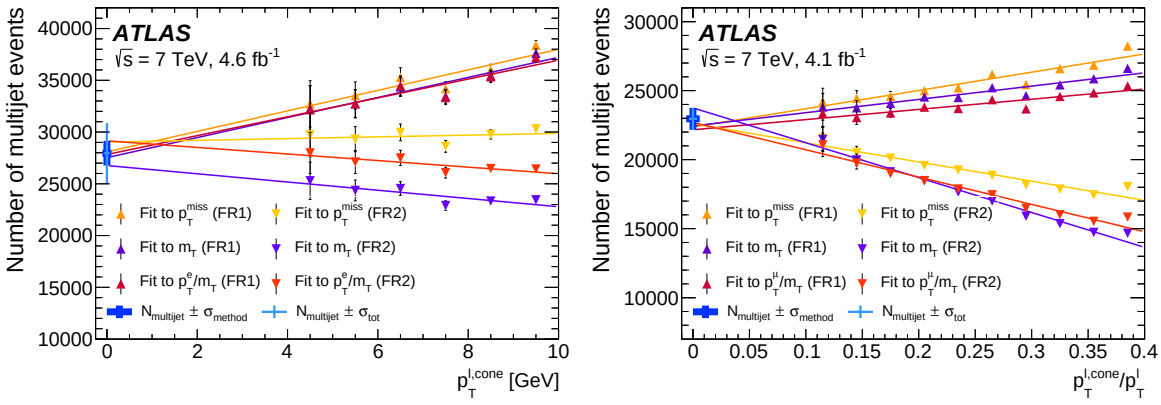

(a) **(b)**

Figure 6.7: Estimated number of multijet-background events as a function of the lower bound of the isolation-variable range used to define the control regions, for (a) electron and (b) muon decay channel. The estimation is performed for the two regions FR1 and FR2 and three distributions $E_{\mathrm{T}}^{\mathrm{miss}}$, m_{T}, and $p_{\mathrm{T}}^{\ell}/m_{\mathrm{T}}$, as described in the text. The linear extrapolations are indicated by the solid lines. The thick crosses show the results of the linear extrapolation of the background estimate to the signal region, including uncertainties from the extrapolation only. The thin crosses also include the uncertainty induced by the contamination of the control regions by EW and top-quark processes.

Corrections to the shape of the multijet background contributions in the distributions used to measure the W-boson mass are estimated with a similar procedure. The kinematic distributions in the control regions are obtained for a set of anti-isolation ranges, and parameterised with linear functions of the lower bound of the anti-isolation requirement. The distributions are extrapolated to the signal regions accordingly.

Table 6.3 shows the summary of the background fractions in % for different $W \to \ell\nu$ event selection categories. The number of the W-boson events after each selection requirement described in Section 3.5 for the data and MC signal are shown in Tables A.1 and A.3 for the electron and muon channels respectively, while the selection on backround samples is shown in Tables A.2 and A.4 for the electron and muon channels respectively.

6.1.4 *Systematics uncertainties*

In this section a summary of the systematics uncertainties from the experimental and theoretical corrections for the W-boson mass measurement is given, the detailed dis-

Table 6.3: Background fractions in % for different $W \to \ell\nu$ event selection categories.

$W \to \mu\nu$						
Category	$W \to \tau\nu$	$Z \to \mu\mu$	$Z \to \tau\tau$	Top	Dibosons	Multijet
$W^{\pm}$ $0.0 < \lvert\eta\rvert < 0.8$	1.04	2.83	0.12	0.16	0.08	0.72
$W^{\pm}$ $0.8 < \lvert\eta\rvert < 1.4$	1.01	4.44	0.11	0.12	0.07	0.57
$W^{\pm}$ $1.4 < \lvert\eta\rvert < 2.0$	0.99	6.78	0.11	0.07	0.06	0.51
$W^{\pm}$ $2.0 < \lvert\eta\rvert < 2.4$	1.00	8.50	0.10	0.04	0.05	0.50
$W^{\pm}$ all η bins	1.01	5.41	0.11	0.10	0.06	0.58
W^{+} all η bins	0.99	4.80	0.10	0.09	0.06	0.51
W^{-} all η bins	1.04	6.28	0.14	0.12	0.08	0.68
$W \to e\nu$						
Category	$W \to \tau\nu$	$Z \to ee$	$Z \to \tau\tau$	Top	Dibosons	Multijet
$W^{\pm}$ $0.0 < \lvert\eta\rvert < 0.6$	1.02	3.34	0.13	0.15	0.08	0.59
$W^{\pm}$ $0.6 < \lvert\eta\rvert < 1.2$	1.00	3.48	0.12	0.13	0.08	0.76
$W^{\pm}$ $1.8 < \lvert\eta\rvert < 2.4$	0.97	3.23	0.11	0.05	0.05	1.74
$W^{\pm}$ all η bins	1.00	3.37	0.12	0.12	0.07	1.00
W^{+} all η bins	0.98	2.92	0.10	0.11	0.06	0.84
W^{-} all η bins	1.04	3.98	0.14	0.13	0.08	1.21

cussion for each source individually is beyond the scope of this thesis and can be found in [80].

Systematics uncertainties due to the electron corrections

Uncertainties in the electron energy response corrections arise from the limited size of the $Z \to ee$ sample, from the physics modelling of the resonance and from the calibration algorithm itself. The physics modeling uncertainties include uncertainties from missing higher-order EW corrections (dominated by the absence of lepton-pair emissions in the simulation) and from the experimental uncertainty in m_Z; these effects are taken as fully correlated with muon channel. Background contributions are small and the associated uncertainty is considered to be negligible. Uncertainties related to the calibration procedure are estimated by varying the invariant mass range used for the calibration, and with a closure test. For the closure test, a pseudodata sample of $Z \to ee$ events is obtained from the nominal sample by rescaling the electron energies by known η-dependent factors; the calibration algorithm is then applied, and the measured energy corrections are compared with the input rescaling factors. These sources of uncertainty constitute a subset of those listed in [78], where additional variations were considered in order to generalise the applicability of the Z-boson calibration results to electrons and photons spanning a wide energy range. The effect of these uncertainties is averaged within the different η_ℓ categories. The overall relative energy-scale uncertainty, averaged over η_ℓ, is 9.4×10^{-5} for electrons from Z-boson decays. Furthermore, possible differences in the energy response between electrons from Z-boson and W-boson decays constitute a significant source of uncertainty. The linearity of the response is affected by uncertainties in the intercalibration of the layers and in the passive material and calorimeter read-out corrections. Additional uncertainties are assigned

to cover imperfect electronics pedestal subtraction affecting the energy measurement in the cells of the calorimeter, and to the modelling of the interactions between the electrons and the detector material in GEANT4. The contribution from these sources to the relative energy-scale uncertainty is (3–12) $\times 10^{-5}$ in each η bin, and 5.4×10^{-5} when averaged over the full η range after taking into account the correlation between the η bins.

The reconstruction and identification efficiency corrections have a typical uncertainty of 0.1–0.2% in the barrel, and 0.3% in the endcap. The trigger efficiency corrections have an uncertainty smaller than 0.1%, and are weakly dependent on p_{T}^{ℓ}. The energy-isolation efficiency corrections have an uncertainty smaller than 0.2% on average.

The charge mismeasurement is accounted as an additional source of uncertainty. The rate of electron charge mismeasurement in simulated events rises from about 0.2% in the barrel to 4% in the endcap. Since, estimation of charge mismeasurement in data confirms these predictions within better than 0.1%, apart from the high $|\eta_\ell|$ region where differences up to 1% are observed.

Systematics uncertainties due to the muon corrections

Uncertainties due to muon momentum scale and resolution corrections arise from the choice of the fitting range, methodological biases, background contributions, theoretical modelling of Z-boson production, non-linearity of the corrections, and material distribution in the ID. The uncertainty due to the choice of fitting range is estimated by varying the range by ±10%, and repeating the correction procedure. The uncertainty due to the fit methodology is estimated by comparing the template fit results with an alternative approach, based on an iterative χ^2 minimisation. Background contributions from gauge-boson pair and top-quark pair production are estimated using the simulation. The uncertainty in these background contributions is evaluated by varying their normalisation within the theoretical uncertainties on the production cross sections. The uncertainty in the theoretical modelling of Z-boson production is evaluated by propagating the effect of EW corrections to QED FSR, QED radiation of fermion pairs, and other NLO EW corrections described in Section 3.3.1. The experimental uncertainty in the value of the Z-boson mass used as input is also accounted for. These sources of uncertainty are summed in quadrature, yielding an uncertainty $\delta\alpha$ in the muon momentum scale correction of approximately 0.5×10^{-4}. The systematic uncertainty in the muon momentum scale due to the extrapolation from the $Z \to \mu\mu$ momentum range to the $W \to \mu\nu$ momentum range is estimated by evaluating momentum scale corrections as a function of $1/p_{\mathrm{T}}$ for muons in various $|\eta|$ ranges. The extrapolation uncertainty $\delta\alpha$ is parameterised as follows:

$$\delta\alpha = p_0 + \frac{p_1}{\left\langle p_{\mathrm{T}}^{\ell}(W) \right\rangle},$$

where $\left\langle p_{\mathrm{T}}^{\ell}(W) \right\rangle$ is the average p_{T} of muons in W-boson events, and p_0 and p_1 are free parameters. If the momentum-scale corrections are independent of $1/p_{\mathrm{T}}$, the fitting parameters are expected to be $p_0 = p_1 = 0$. Deviations of p_1 from zero indicate

a possible momentum dependence. The fitted values of p_1 are consistent with zero, within two standard deviations of the statistical error. The corresponding systematic uncertainty in m_W is defined assuming, in each bin of $|\eta|$, a momentum non-linearity given by the larger of the fitted value of p_1 and its uncertainty. Uncertainties due to imperfect knowledge of the material in the ID, and due to imperfect knowledge of the detector geometry, are found to be small in comparison and considered negligible. The dominant systematic uncertainty in the momentum scale is due to the extrapolation of the correction from the Z-boson momentum range to the W-boson momentum range. The extrapolation uncertainty $\delta\alpha$ is (2–5) $\times 10^{-5}$ for $|\eta_\ell| < 2.0$, and (4–7) $\times 10^{-4}$ for $|\eta_\ell| > 2.0$. Systematic uncertainties from other sources are relatively small. The systematic uncertainty of the resolution corrections is dominated by the statistical uncertainty of the Z-boson event sample, and includes a contribution from the imperfect closure of the method. The latter is defined from the residual difference between the standard deviations of the dimuon invariant mass in data and simulation, after applying resolution corrections.

The dominant source of uncertainty in the determination of the muon efficiency corrections is the statistical uncertainty of the Z-boson data sample. The largest sources of systematic uncertainty are the multijet background contribution and the momentum-scale uncertainty. The ID tracking efficiencies for muon candidates are above 99.5% without any significant p_{T} dependence, and the associated uncertainties are not considered further.

Systematics uncertainties due to the hadronic recoil corrections

The systematics uncertainties from the hadronic recoil calibration procedure are discussed in detail in Section 5.7.

Systematics uncertainties due to backgrounds

The uncertainties on EW and top-quark background estimation are arising from the fraction and shape uncertainties. An uncertainty of 1.8% and 2.3% are assigned to the W^+/Z and W^-/Z production cross-section ratios, respectively [169]. A relative uncertainty of 0.2% is assigned to the normalisation of the $W \to \tau\nu$ samples with respect to the W-boson signal sample, to account for the uncertainty in the τ-lepton branching fractions to electrons and muons. The normalisation uncertainty for the $t\bar{t}$ sample is 3.9%, while 7% for the single top production processes. The samples of events with massive gauge-boson pair production have an uncertainty of 10% to cover the differences to the NNLO predictions. The shape uncertainties for boson-pair production and top-quark production are considered negligible compared to the uncertainties in their cross sections, given the small contributions of these processes to the signal event selection, see Table 6.3.

The systematic uncertainty in the multijet background fraction is defined as half of the largest difference between the results extrapolated from the different kinematic regions and observables, as illustrated in Figure 6.7. The multijet background contribution is estimated separately in all measurement categories. Uncertainties to the

shape of the multijet background contributions in the distributions used to measure the W-boson mass are estimated with a similar procedure.

Systematics uncertainties from higher order EW corrections

The uncertainty in the modelling of QED FSR is evaluated by comparing distributions obtained using the default LO photon emission matrix elements with predictions obtained using NLO matrix elements, as well as by comparing PHOTOS with an alternative implementation available in WINHAC. The differences are small in both cases, and the associated uncertainty is considered negligible.

Other sources of EW corrections which are not included in the simulated event samples, the interference between ISR and FSR QED corrections (IFI), pure weak corrections due to virtual-loop and box diagrams, and final-state emission of lepton pairs, are considered as systematic uncertainties. The NLO EW corrections are estimated using WINHAC. The corresponding uncertainties are evaluated comparing the final state distributions obtained including QED FSR only with predictions using the complete NLO EW corrections in the $\alpha(0)$ and G_μ renormalisation schemes. The latter predicts the larger correction and is used to define the systematic uncertainty.

Final-state lepton pair production, through $\gamma^* \to \ell\ell$ radiation, is formally a higher-order correction but constitutes a significant additional source of energy loss for the W-boson decay products. This process is not included in the event simulation, and the impact on the determination of m_W is evaluated at particle level with PHOTOS and SANC.

Systematics uncertainties due to the QCD modelling

The impact of the perturbative and non-perturbative modelling of the strong interaction on the extraction of the W-boson mass is assessed through variations of the model parameters of the predictions for the differential cross sections as functions of the boson rapidity, transverse-momentum spectrum at a given rapidity, and angular coefficients, which correspond to the second, third, and fourth terms of the decomposition of Equation 3.1, respectively. The parameter variations used to estimate the uncertainties are propagated to the simulated event samples by means of the reweighting procedure described in Section 3.3.

The imperfect knowledge of the PDFs affects the differential cross section as a function of boson y, A_i, and the p_{T}^W distribution. The PDF contribution to the prediction uncertainty is estimated with the CT10NNLO PDF set by using the Hessian method [67]. There are 25 error eigenvectors, and a pair of PDF variations associated with each eigenvector. Each pair corresponds to positive and negative 90% CL excursions along the corresponding eigenvector. Symmetric PDF uncertainties are defined as the mean value of the absolute positive and negative excursions corresponding to each pair of PDF variations. The overall uncertainty of the CT10NNLO PDF set is scaled to 68% CL by applying a multiplicative factor of 1/1.645. The effect of PDF variations on the y distributions and A_i are evaluated with DYNNLO, while their impact on the W-boson p_{T} distribution is evaluated using PYTHIA 8 and by reweighting

event-by-event the PDFs of the hard-scattering process, which are convolved with the LO matrix elements. Only relative variations of the p_{T}^{W} and p_{T}^{Z} distributions induced by the PDFs are considered. The PDF variations are applied simultaneously to the boson y, A_i, and p_{T} distributions, and the overall PDF uncertainty is evaluated with the Hessian method as described above. As an additional PDF uncertainty other PDF sets are considered and the envelope of values of m_W extracted with the MMHT2014 and CT14 NNLO PDF sets is added in quadrature after combining the W^+ and W^- categories.

The effect of missing higher-order corrections on the NNLO predictions of the rapidity distributions of Z bosons, and the pseudorapidity distributions of the decay leptons of W bosons, is estimated by varying the renormalisation and factorisation scales by factors of 0.5 and 2.0 with respect to their nominal value $\mu_{\mathrm{R}} = \mu_{\mathrm{F}} = m_V$ in the DYNNLO predictions. The corresponding relative uncertainty in the normalised distributions is of the order of 0.1–0.3%, and significantly smaller than the PDF uncertainties. These uncertainties are expected to have a negligible impact on the measurement of m_W, and are not considered further.

The effect of the LHC beam-energy uncertainty of 0.65% [208] on the fixed-order predictions is studied. Relative variations of 0.65% around the nominal value of 3.5TeV are considered, yielding variations of the inclusive W^+ and W^- cross sections of 0.6% and 0.5%, respectively. No significant dependence as a function of lepton pseudorapidity is observed in the kinematic region used for the measurement, and the dependence as a function of p_{T}^{ℓ} and m_{T} is expected to be even smaller. This uncertainty is not considered further.

The uncertainties in the Pythia 8 AZ tune parameters, are propagated to the p_{T}^{W} predictions through the variations of the orthogonal eigenvector components of the parameters error matrix [165]. The uncertainties due to model variations are largely correlated between p_{T}^{W} and p_{T}^{Z} and they are canceled.

Uncertainties due to variations of parton shower parameters that are not fitted to the p_{T}^{Z} measurement include variations of the masses of the charm and bottom quarks, and variations of the factorisation scale used for the QCD ISR. The mass of the charm quark is varied in Pythia 8, conservatively, by ± 0.5 GeV around its nominal value of 1.5 GeV. The mass of the bottom quark is varied in Pythia 8, conservatively, by ± 0.8 GeV around its nominal value of 4.8 GeV. The resulting variations have a negligible impact on the transverse-momentum distributions of Z- and W-bosons, and are not considered further.

The uncertainty due to higher-order QCD corrections to the parton shower is estimated through variations of the factorisation scale, μ_{F}, in the QCD ISR by factors of 0.5 and 2.0 with respect to the central choice $\mu_{\mathrm{F}}^2 = p_{\mathrm{T},0}^2 + p_{\mathrm{T}}^2$, where $p_{\mathrm{T},0}$ is an infrared cut-off, and p_{T} is the evolution variable of the parton shower [209]. Variations of the renormalisation scale in the QCD ISR are equivalent to a redefinition of the initial value of the strong coupling constant at the Z-boson mass used for the QCD ISR, which is fixed from the fits to the p_{T}^{Z} data. As a consequence, variations of the ISR

renormalisation scale do not apply when estimating the uncertainty in the predicted p_{T}^{W} distribution. Higher-order QCD corrections are expected to be largely correlated between W-boson and Z-boson production induced by the light quarks, u, d, and s, in the initial state. However, a certain degree of decorrelation between W- and Z-boson transverse-momentum distributions is expected, due to the different amounts of heavy-quark-initiated production, where heavy refers to charm and bottom flavours. The physical origin of this decorrelation can be ascribed to the presence of independent QCD scales corresponding to the three-to-four flavours and four-to-five flavours matching scales μ_c and μ_b in the variable-flavour-number scheme PDF evolution [210], which are of the order of the charm- and bottom-quark masses, respectively. To assess this effect, the variations of μ_{F} in the QCD ISR are performed simultaneously for all light-quark $q\bar{q} \to W, Z$ processes, with $q = u, d, s$, but independently for each of the $c\bar{c} \to Z$, $b\bar{b} \to Z$, and $c\bar{q} \to W$ processes, where $q = d, s$. The effect of the $c\bar{q} \to W$ variations on the determination of m_W is reduced by a factor of two, to account for the presence of only one heavy-flavour quark in the initial state. Since the μ_{F} variations affect all the branchings of the shower evolution and not only vertices involving heavy quarks, this procedure yields a conservative estimate of the decorrelation between W- and Z-boson transverse-momentum distributions arising from the independent μ_c and μ_b scales in the PDF evolution.

The parton shower PDF uncertainty is estimated by comparing CT14, MMHT2014 and NNPDF2.3 of the LO PDF sets used in the parton shower The PDFs which give the largest deviation from the nominal ratio of the p_{T}^{W} and p_{T}^{Z} distributions are used to estimate the uncertainty.

Two sources of uncertainty affecting the modelling of the angular coefficients are considered. One source is defined from the experimental uncertainty of the Z-boson measurement of the angular coefficients which is used to validate the NNLO predictions. The uncertainty in the corresponding W-boson predictions is estimated by propagating the experimental uncertainty of the Z-boson measurement as follows. A set of pseudodata distributions are obtained by fluctuating the angular coefficients within the experimental uncertainties, preserving the correlations between the different measurement bins for the different coefficients. For each pseudo-experiment, the differences in the A_i coefficients between fluctuated and nominal Z-boson measurement results are propagated to the corresponding coefficient in W-boson production. The corresponding uncertainty is defined from the standard deviation of the m_W values as estimated from the pseudodata distributions. The other source of uncertainty is considered to account for the disagreement between the measurement and the NNLO QCD predictions observed for the A_2 angular coefficient as a function of the Z-boson p_{T}, as discussed in Section 3.3.2. The corresponding uncertainty in m_W is estimated by propagating the difference in A_2 between the Z-boson measurement and the theoretical prediction to the corresponding coefficient in W-boson production.

6.1.5 *Control distributions*

The detector calibration and the physics modelling are validated by comparing data with simulated W-boson signal and backgrounds for several kinematic distributions that are insensitive to the W-boson mass. The comparison is based on a χ^2 compatibility test, including statistical and systematic uncertainties, and the bin-to-bin correlations induced by the latter. The systematic uncertainty comprises all sources of experimental uncertainty related to the lepton and recoil calibration, and to the background subtraction, as well as sources of modelling uncertainty associated with EW corrections, or induced by the helicity fractions of vector-boson production, the vector-boson transverse-momentum distribution, and the PDFs. Comparisons of data and simulation for the η_ℓ, u_{T}, and $u_{\parallel}^{\ell}$ distributions, in positive and negative W-boson events, are shown in Figures 6.8 and 6.9 for the electron and muon decay channels, respectively. Data and simulation agree for all distributions.

The comparison of data and simulation for kinematic distributions sensitive to the value of m_W provides further validation of the detector calibration and physics modelling. The comparison is performed in all measurement categories. The η-inclusive p_{T}^{ℓ}, m_{T} and $E_{\mathrm{T}}^{\mathrm{miss}}$ distributions for positive and negative W bosons are shown in Figures 6.10 and 6.11 for the electron and muon decay channels, respectively. The value of m_W used in the predictions is set to the overall measurement result presented in the next section. The χ^2 values quantifying the comparison between data and prediction are calculated over the full histogram range and account for all sources of uncertainty. The bin-to-bin correlations induced by the experimental and physics-modelling systematic uncertainties are also accounted for. Overall, satisfactory agreement is observed. The deficit of data visible for $p_{\mathrm{T}}^{\ell} \sim 40$–$42$ GeV in the $W^+ \to e^+\nu$ channel does not strongly affect the mass measurement, as the observed effect differs from that expected from m_W variations. Cross-checks of possible sources of this effect were performed, and its impact on the mass determination was shown to be within the corresponding systematic uncertainties.

6.2 MASS FITS

This section presents the determination of the mass of the W boson from template fits to the kinematic distributions of the W-boson decay products, as described in Section 1.4.3. Measurements of m_W are performed using the p_{T}^{ℓ} and m_{T} distributions, separately for positive and negative W bosons, in three bins of $|\eta_\ell|$ in the electron decay channel, and in four bins of $|\eta_\ell|$ in the muon decay channel, leading to a total of 28 m_W determinations. In each category, the value of m_W is determined by a χ^2 minimisation, comparing the p_{T}^{ℓ} and m_{T} distributions in data and simulation for different values of m_W. The templates are generated with values of m_W in steps of 1 to 10 MeV within a range of ± 400 MeV, centred around the reference value of $80399 + b$ MeV used in the MC signal samples, where b is an unknown blinding value. The statistical uncertainty

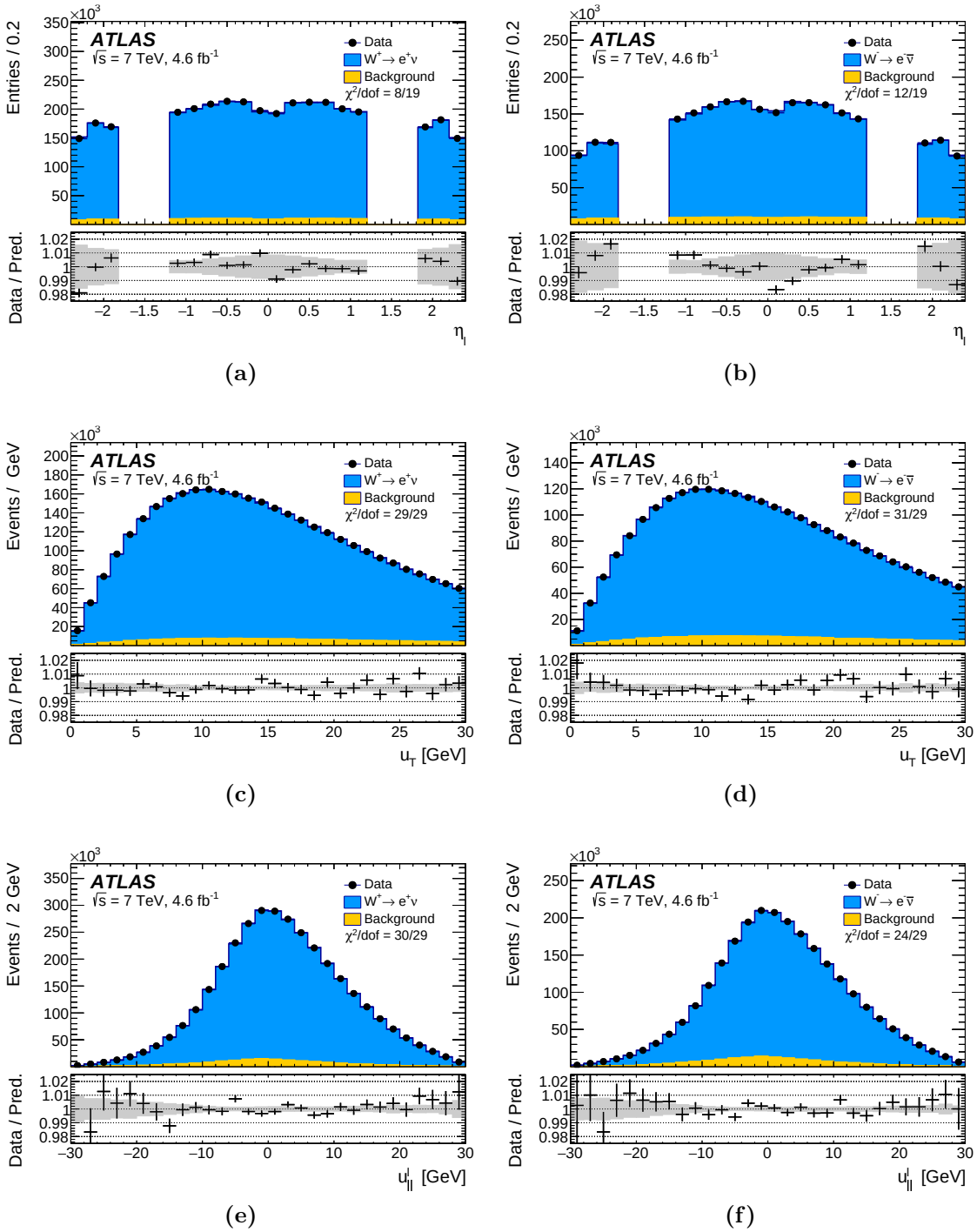

Figure 6.8: The (a,b) η_ℓ, (c,d) u_{T}, and (e,f) $u_{\parallel}^{\ell}$ distributions for (a,c,e) W^+ events and (b,d,f) W^- events in the electron decay channel. The data are compared to the simulation including signal and background contributions. Detector calibration and physics-modelling corrections are applied to the simulated events. The lower panels show the data-to-prediction ratios, the error bars show the statistical uncertainty, and the band shows the systematic uncertainty of the prediction. The χ^2 values displayed in each figure account for all sources of uncertainty and include the effects of bin-to-bin correlations induced by the systematic uncertainties.

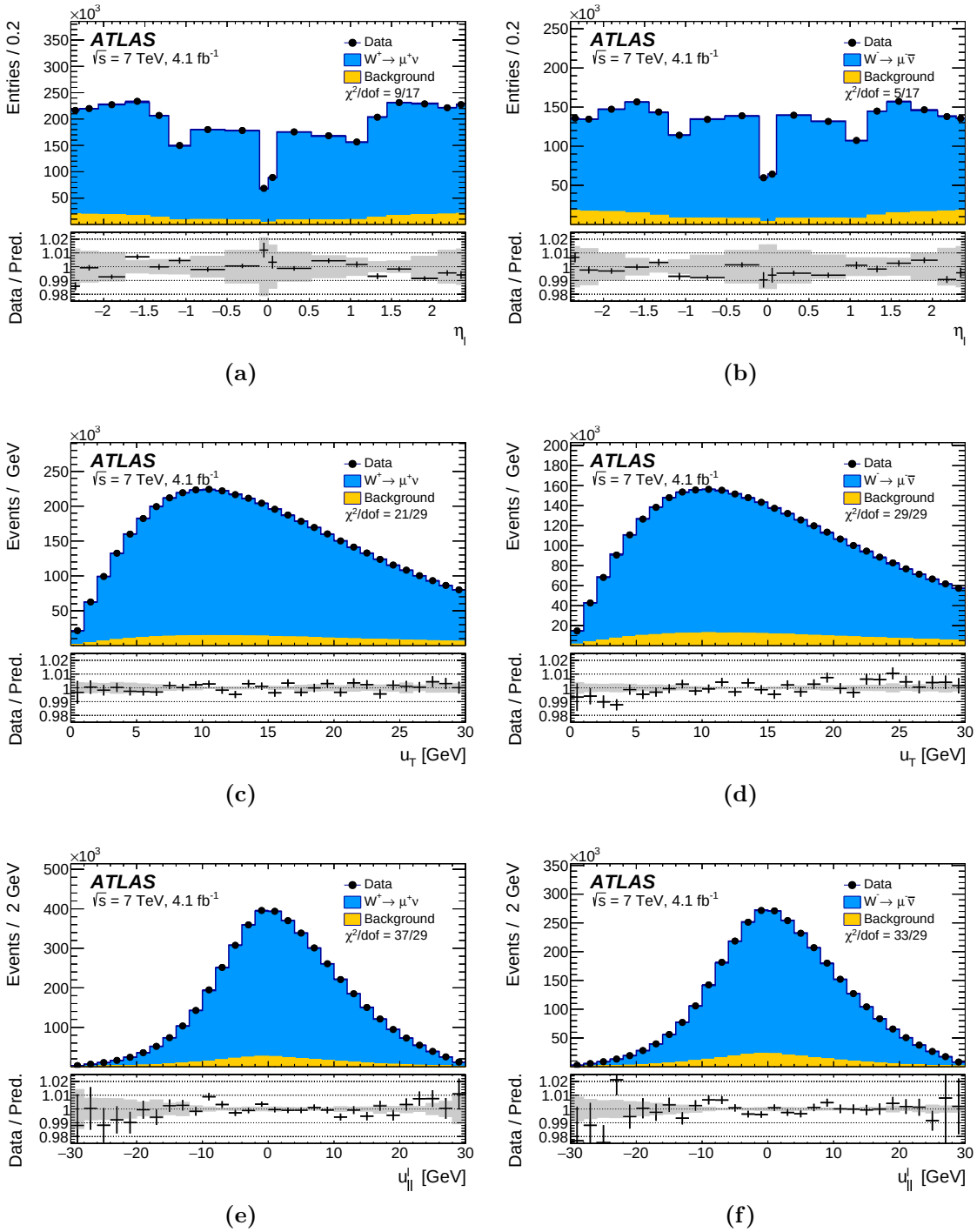

Figure 6.9: The (a,b) η_ℓ, (c,d) u_{T}, and (e,f) $u_{\parallel}^{\ell}$ distributions for (a,c,e) W^+ events and (b,d,f) W^- events in the muon decay channel. The data are compared to the simulation including signal and background contributions. Detector calibration and physics-modelling corrections are applied to the simulated events. The lower panels show the data-to-prediction ratios, the error bars show the statistical uncertainty, and the band shows the systematic uncertainty of the prediction. The χ^2 values displayed in each figure account for all sources of uncertainty and include the effects of bin-to-bin correlations induced by the systematic uncertainties.

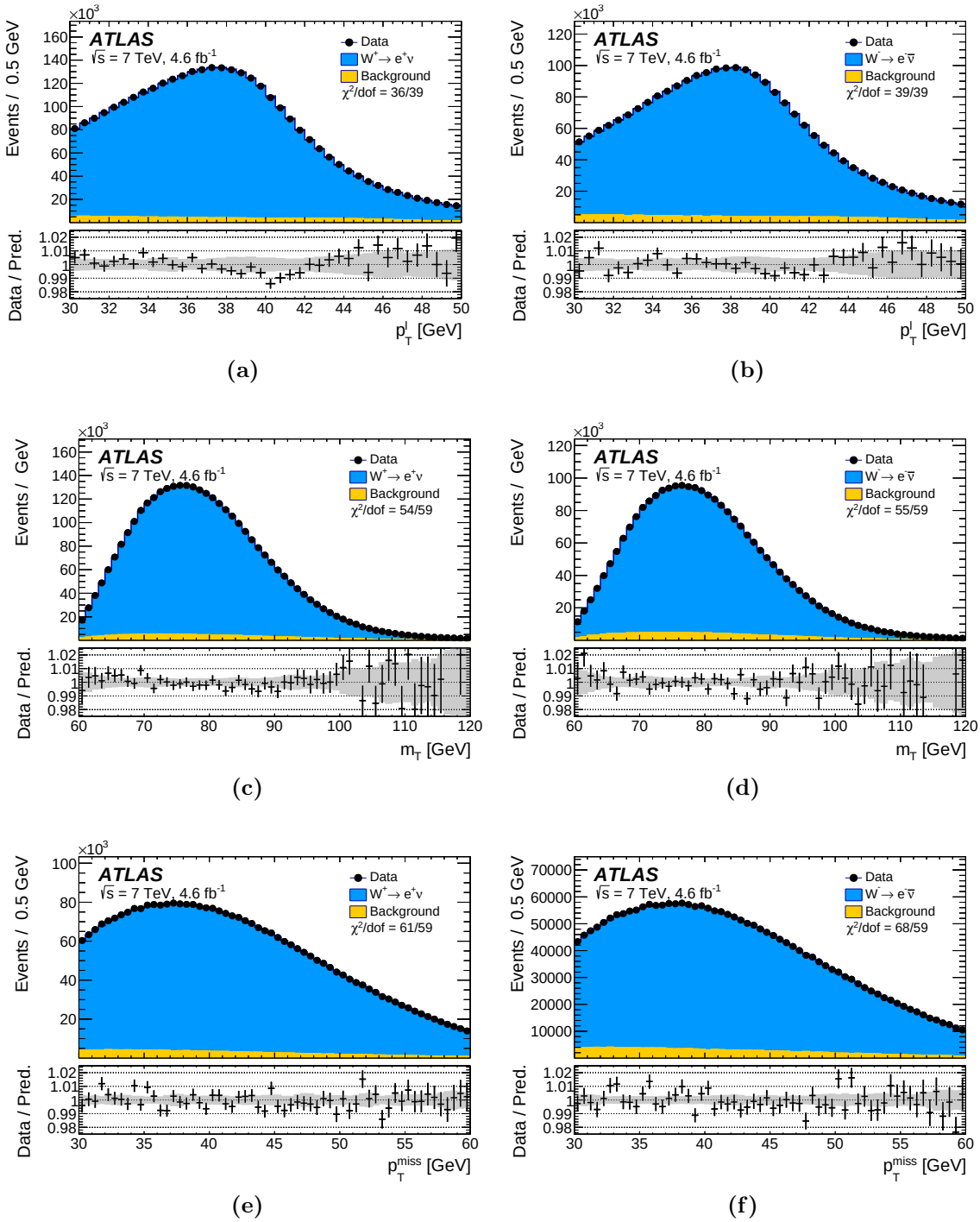

Figure 6.10: The (a,b) p_{T}^{ℓ}, (c,d) m_{T}, and (e,f) $E_{\mathrm{T}}^{\mathrm{miss}}$ distributions for (a,c,e) W^+ events and (b,d,f) W^- events in the electron decay channel. The data are compared to the simulation including signal and background contributions. Detector calibration and physics-modelling corrections are applied to the simulated events. For all simulated distributions, m_W is set according to the overall measurement result. The lower panels show the data-to-prediction ratios, the error bars show the statistical uncertainty, and the band shows the systematic uncertainty of the prediction. The χ^2 values displayed in each figure account for all sources of uncertainty and include the effects of bin-to-bin correlations induced by the systematic uncertainties.

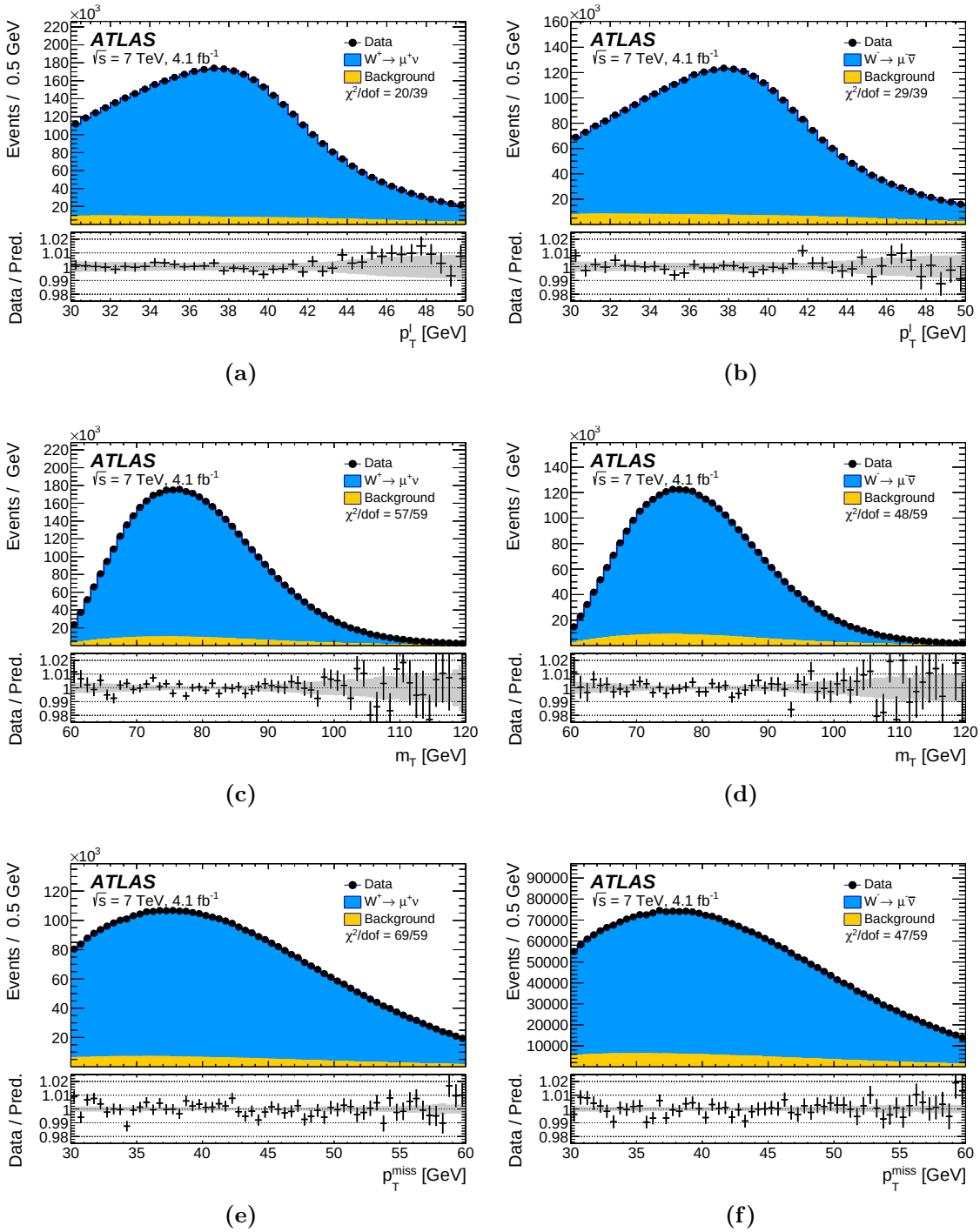

Figure 6.11: The (a,b) p_{T}^{ℓ}, (c,d) m_{T}, and (e,f) $E_{\mathrm{T}}^{\mathrm{miss}}$ distributions for (a,c,e) W^+ events and (b,d,f) W^- events in the muon decay channel. The data are compared to the simulation including signal and background contributions. Detector calibration and physics-modelling corrections are applied to the simulated events. For all simulated distributions, m_W is set according to the overall measurement result. The lower panels show the data-to-prediction ratios, the error bars show the statistical uncertainty, and the band shows the systematic uncertainty of the prediction. The χ^2 values displayed in each figure account for all sources of uncertainty and include the effects of bin-to-bin correlations induced by the systematic uncertainties.

is estimated from the half width of the χ^2 function at the value corresponding to one unit above the minimum.

Experimentally, the p_{T} and m_{T} distributions are affected by the lepton energy calibration. The m_{T} distribution is also affected by the calibration of the recoil. The p_{T} distribution is broadened by the W-boson transverse-momentum distribution, and are sensitive to the proton PDFs. Compared to p_{T}, the m_{T} distribution has larger uncertainties due to the recoil, but smaller sensitivity to such physics modelling effects. Imperfect modelling of these effects can distort the template distributions, and constitutes a significant source of uncertainties for the determination of m_W.

In order to be sensitive to the Jacobian peak, and at the same time minimising a possible bias from misprediction of the multijet background, the initial fitting ranges are chosen to be $30-50$ GeV for p_{T}^{ℓ} and $65-100$ GeV for m_{T}. The first step is to check the consistency between electron and muon channels, charges and pseudorapidity categories. The W-boson mass blinding is removed when the overall consistency between different measurement categories is observed, as described in Section 1.4.3.

Figure 6.12 illustrates the p_{T} and m_{T} fit results as a function of lepton pseudorapidity for electron and muon channels. The first point corresponds to h inclusive result. The error bars correspond to statistical uncertainties only. Already without taking into account the systematic uncertainties, a very good compatibility across channels and categories can be seen.

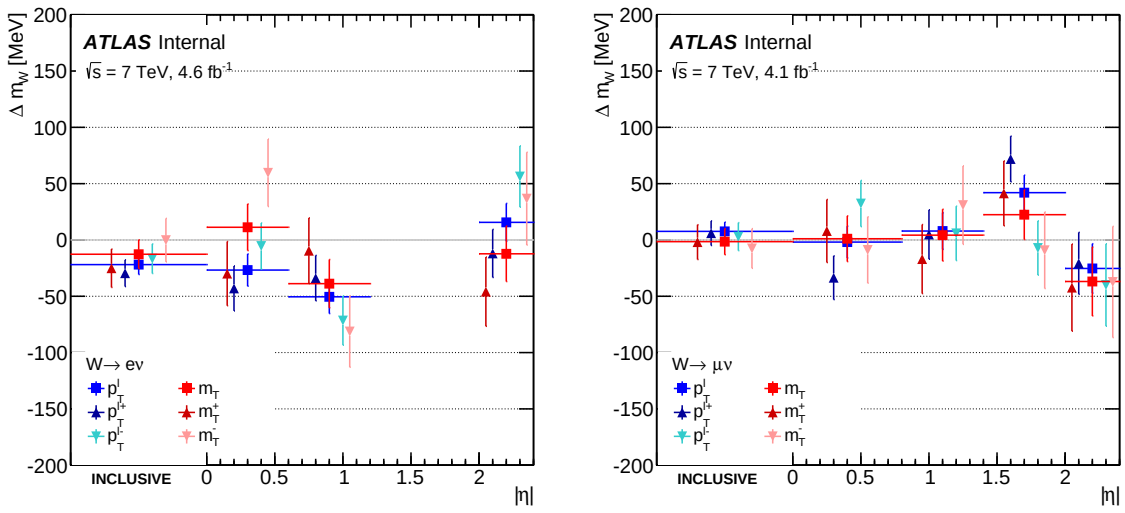

(a) **(b)**

Figure 6.12: Blinded p_{T} and m_{T} fit results as a function of lepton pseudorapidity for (a) electron and (b) muon channel, with the nominal event selection. Error bars are statistical only. The result is given as a shift with respect to the assumed value of m_W in the MC, plus an unknown offset.

6.2.1 *Correlation between the fitting observables*

To estimate the statistical correlation between the m_W values extracted from the fit to the p_{T}^{ℓ} and m_{T} distributions, a study with 1000 pseudo-datasets created from $W \to \mu\nu$ events in MC is performed. This information is needed for the combination of the m_W value obtained with the two measurements. A pseudo-dataset is obtained by weighting each MC event by a random sample from a Poisson distribution with mean one. Figure 6.13 plots the m_W value obtained from the fit of the m_{T} against the fit to the p_{T}^{ℓ} distribution, for each of the 1000 pseudo-datasets

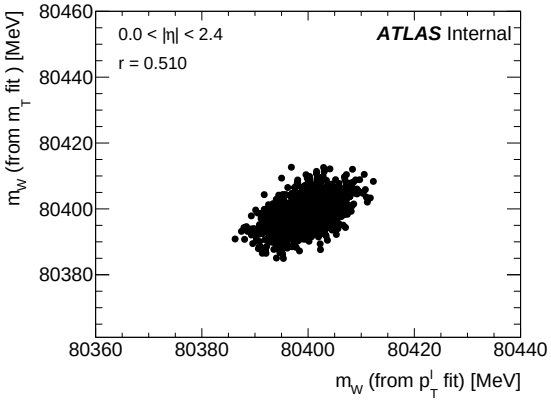

Figure 6.13: The m_W value obtained from a fit to the m_{T} distribution against the m_W value obtained from a fit to the p_{T}^{ℓ} distribution for 1000 pseudo-datasets.

One can see qualitatively that there is positive correlation between the two fitting distributions, as expected. The sample correlation coefficient r, between sample pairs (X_i, Y_i) is defined with:

$$r = \frac{\sum_{i=1}^{N}(X_i - \bar{X})(Y_i - \bar{Y})}{\sqrt{\sum_{i=1}^{N}(X_i - \bar{X})^2}\sqrt{\sum_{i=1}^{N}(Y_i - \bar{Y})^2}} \tag{6.1}$$

The sample pairs in Figure 6.13 give $r = 0.51 \pm 0.02$, where the uncertainty arises from the limited number of pseudo-datasets. The corresponding histograms for fits in different lepton $|\eta|$ ranges are given in Figure 6.14. Both, the pseudo-datasets and the MC used for fitting, have the requirement on $|\eta|$.

A further study is performed to investigate how much can be gained in statistical precision from the combination of the m_W value from the p_{T}^{ℓ} and m_{T} fits. The motivation is that a second measurement can appear to be decorrelated from the first, without adding additional information, so called fake decorrelation. The extreme example would be a measurement of p_{T}^{ℓ} (X) and of p_{T}^{ℓ} plus a noise term (Y). In this scenario the correlation r would be equal to σ_X/σ_Y, but the uncertainty on the combination would be no smaller than σ_X.

The two methods used to estimate the statistical uncertainty on the combination are now described and are found to give consistent results. Note that in the following

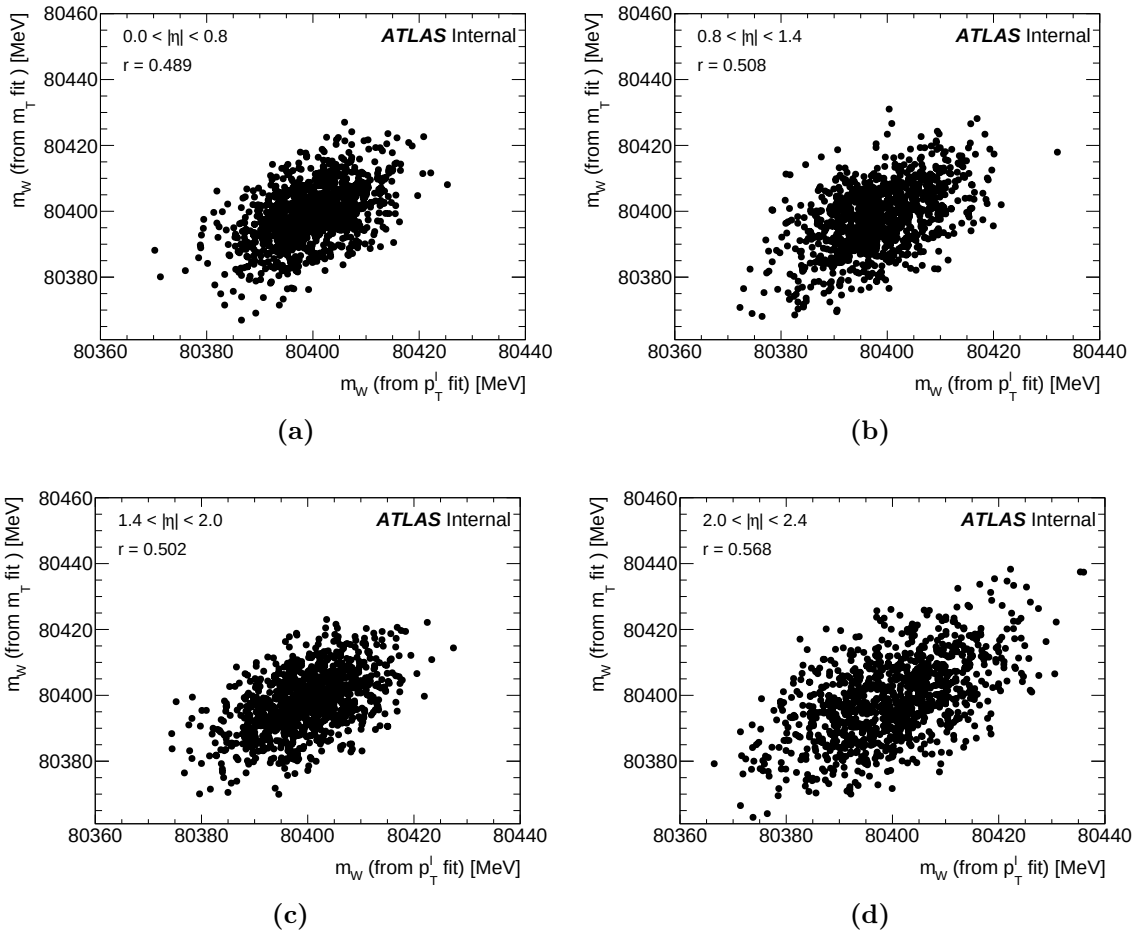

Figure 6.14: The m_W value obtained from a fit to the m_{T} distribution against the m_W value obtained from a fit to the p_{T}^{ℓ} distribution for 1000 pseudo-datasets. Each plot corresponds to a different selection requirement on the lepton $|\eta|$ with ranges indicated on each plot.

the m_W value from the p_{T}^{ℓ} and m_{T} fits are denoted as A and B respectively and their combined value is denoted as C. The value of C is given by:

$$C = wA + (1 - w)B\,, \tag{6.2}$$

where w is a weight to be determined. The error on C squared, σ_C^2, is given with:

$$\sigma_C^2 = w^2\sigma_A^2 + 2rw(1 - w)\sigma_A\sigma_B + (1 - w)^2\sigma_B^2\,, \tag{6.3}$$

where r is the correlation value calculated previously. Equation 6.3 can be minimised to get the value of w which gives the smallest uncertainty on the combination:

$$w = \frac{\sigma_B^2 - r\sigma_A\sigma_B}{\sigma_A^2 - 2r\sigma_A\sigma_B + \sigma_B^2}. \tag{6.4}$$

The example calculation used here is for the $0.0 < |\eta| < 2.4$ category, where $r = 0.524$, $\sigma_A = 3.93$ MeV for p_{T}^{ℓ} fit, and $\sigma_B = 4.83$ MeV for m_{T} fit. Therefore $w = 0.71$ and $\sigma_C = 3.727$.

A second way of calculating the value of σ_C is to again create a set of 1000 pseudo-datasets from $W \to \mu\nu$ MC events and to combine the values of A and B for each pseudo-dataset. This creates a set of 1000 combined values. There are two possible choices for the values of σ_A and σ_B in this case, the first being the statistical uncertainty on the fit to each pseudo-dataset. However since some events are lost when the Poisson weight is set to 0, this is larger than the statistical uncertainty on the nominal MC. Therefore a better value to use is the RMS of the 1000 pseudo-datasets.

An estimate for σ_C is given by the RMS of the set of 1000 values of C. Using again the same $|\eta|$ category and therefore with the same value of w as previously described, the RMS of the set of 1000 values of C is 3.721, which is very similar to the direct calculation.

The conclusion of this study is that a reduction in the statistical uncertainty from 3.93, taking the result from the p_{T}^{ℓ} fit only to 3.72 from the combination of the p_{T}^{ℓ} and m_{T} fits, is small, given a correlation, r, of only $\approx 50\%$. This suggests there is indeed some small level of fake decorrelation between the p_{T}^{ℓ} and m_{T} fits.

6.2.2 *Combination procedure*

χ^2 definition and least squares solution

The method described here is referred to as the BLUE method [12], summarized for the case of N independent measurements of a single physical parameters. The χ^2 to be minimized is defined as:

$$\chi^2 = (X - \bar{X})^T C^{-1} (X - \bar{X}) \tag{6.5}$$

where the vector $X = \{X_1^e, ..., X_m^e; X_1^\mu, ..., X_n^\mu\}$ represents the measured values of m_W in the $m+n = N$ electron and muon channels and categories; $\bar{X} = \{\bar{X}, ..., \bar{X}\}$ contains N times the average value to be determined, and C^{-1} is the full $N \times N$ covariance matrix.

The χ^2 minimization and combined uncertainty calculation is performed analytically. The solution is:

$$\bar{X} = (H^T C^{-1} H)^{-1} H^T C^{-1} X, \tag{6.6}$$

where H is, in the case of a single parameter of interest, a unit vector of size N:

$$H = \begin{pmatrix} 1 \\ \vdots \\ 1 \end{pmatrix} \tag{6.7}$$

Finally, the combined covariance matrix is:

$$\bar{C} = (H^T C^{-1} H)^{-1}. \tag{6.8}$$

Construction of the covariance matrices

The total covariance matrix can be written as:

$$C = C^{\text{stat}} + \sum_{\alpha} C^{\alpha}. \tag{6.9}$$

C^{stat} is a diagonal matrix containing the measurements statistical uncertainties, i.e. $C^{\text{stat}}_{k,k} = \delta X_k$, and $C^{\text{stat}}_{k\neq l} = 0$. The C^{α} are systematic uncertainty contributions.

Most systematic sources are described by a single nuisance parameter, which can affect one or a larger subset of the measurements X_k. In this case, the covariance matrix is constructed from the differences:

$$\delta X^{\alpha}_k = X^{\alpha}_k - X^{\text{nom}}_k, \tag{6.10}$$

where α labels the sources of uncertainty and k the measurements, and δX^{α}_k reflects the impact of the uncertainty variation α on measurement k. Finally,

$$C^{\alpha}_{k,l} = \delta X^{\alpha}_k \times \delta X^{\alpha}_l \tag{6.11}$$

describes the covariance of measurements k, l under this variation.

In some special cases, where a given class of uncertainty source involves a large number of nuisance parameters, it is more practical to propagate the uncertainties with the toy MC method, where all nuisance parameters of the class are varied simultaneously. The random variations follow a gaussian distribution of mean zero and width equal to the nuisance parameters uncertainties, and preserve correlations among them if applicable. The uncertainty on each measurement is estimated from the spread of the measurement results under the toy variations, and the covariance is calculated explicitly:

$$C^{\alpha}_{k,l} = \frac{1}{n_{\text{toys}}} \sum_{i=1}^{n_{\text{toys}}} (X^{\alpha,i}_k - X^{\text{nom}}_k)(X^{\alpha,i}_l - X^{\text{nom}}_l). \tag{6.12}$$

Correlations between uncertainties

The systematic uncertainties have specific correlation patterns across the m_W measurement categories. Muon-momentum and electron-energy calibration uncertainties are uncorrelated between the different decay channels, but largely correlated between the p^{ℓ}_{T} and m_{T} distributions. Recoil calibration uncertainties are correlated between electron and muon decay channels, and they are small for p^{ℓ}_{T} distributions. Uncertainties in the normalisation of multijet, EW, and top-quark background processes are considered correlated across decay channels, boson charges and rapidity bins, whereas the uncertainty in the shape of multijet background is considered uncorrelated between decay channels and boson charges. The FSR theoretical uncertainties, and smaller effects such as fermion pair radiation, ISR/FSR interference corrections and pure higher-order weak (non QED) corrections are taken fully correlated between all categories. The PDF uncertainties are largely correlated between electron and muon decay channels,

but significantly anti-correlated between positive and negative W bosons. The anti-correlation of the PDF uncertainties is due to the fact that the total light quark sea PDF is constrained by the DIS experiments, while the u, d and s quark decomposition of the sea is less precisely known. The experimental uncertainties of the AZ tune parameters, the variation of the c quark mass and the factorisation scale variation are taken as fully correlated between the electron and the muon channels, positive and negative W bosons and the pseudorapidity categories. The parton shower PDF uncertainty is anti-correlated between positive and negative W bosons. The correlation between p_{T}^{ℓ} and m_{T} is taken from Section 6.2.1. The overall measurement includes 117 separate sources of uncertainty.

Due to the different balance of systematic uncertainties and to the variety of correlation patterns, a significant reduction of the uncertainties in the measurement of m_W is achieved by combining the different decay channels and the charge and $|\eta_\ell|$ categories. The measurement combination is performed in several ways:

- combining all measurement categories, separately for p_{T}^{ℓ} and m_{T} fits;
- combining the electron and muon channel results separately;
- combining all W^+ and W^- results separately;
- combining all measurement categories, including p_{T}^{ℓ} and m_{T} fits.

6.2.3 *Results with the initial fitting range*

The fitted m_W values are given with respect to the MC W-boson mass plus an unknown blinding value b, i.e. $80399 + b$ MeV. The fit results for all individual categories and channels, including all uncertainties are given in Table 6.4 with the initial fitting range $30 - 50$ GeV for p_{T}^{ℓ} and $65 - 100$ GeV for m_{T}. In order to test the BLUE combination method has been used, s cross-check these results is performed with the HERAverager framework [211]. Both combinations yield equivalent results with $\chi^2/\mathrm{NDF} = 30.5/27$, i.e. a very good agreement of all individual measurements is observed. While the PDF uncertainties for each individual measurement are in the order of $20 - 35$ MeV, a significant reduction in the combined fit can be observed, coming from different impacts of PDF uncertainty eigenvectors in the different categories and fit observables. In order to test the compatibility of all channels, fit observables and categories further, several combinations individually are shown in Table 6.5. All individual combinations have very good χ^2/NDF values, all close to one σ deviation. Moreover, all combined values are consistent with each other. The good consistency between the electron and the muon channel results indicate a correct modeling of the detector response, while the agreement between the results for W^+ and W^- bosons are an additional confirmation of the underlying physics modeling. The agreement between the p_{T}^{ℓ} and m_{T} fits tests both, the physics and the detector response modeling.

Table 6.4: Results of the fitted mass values given with respect to the MC W-boson mass plus an unknown blinding value b in the electron and muon decay channels, for positive and negative W bosons, in different lepton-$|\eta|$ ranges, using the m_{T} and p_{T}^{ℓ} distributions in the initial fitting range. The table shows the statistical uncertainties, together with all experimental uncertainties, divided into muon-, electron-, recoil- and background-related uncertainties, and all modelling uncertainties, separately for QCD modelling including scale variations, parton shower and angular coefficients, EW corrections, and PDFs. All uncertainties are given in MeV.

Channel m_{T}-Fit	Value [MeV]	Stat. Unc.	Muon Calib.	Elec. Calib.	Recoil Calib.	Back-grd.	QCD	EW	PDF's	Total Unc.
$W^+ \to \mu\nu, \lvert\eta\rvert < 0.8$	7.9	28.0	13.6	0.0	14.3	7.4	10.0	3.4	29.1	46.8
$W^+ \to \mu\nu, 0.8 < \lvert\eta\rvert < 1.4$	-17.0	30.6	19.4	0.0	11.1	6.1	9.7	3.4	23.9	46.4
$W^+ \to \mu\nu, 1.4 < \lvert\eta\rvert < 2.0$	41.4	28.8	34.4	0.0	13.5	6.6	9.4	3.4	27.6	55.7
$W^+ \to \mu\nu, 2.0 < \lvert\eta\rvert < 2.4$	-42.3	38.7	113.9	0.0	13.7	9.0	8.5	3.4	33.4	126.2
$W^- \to \mu\nu, \lvert\eta\rvert < 0.8$	-8.9	29.5	12.8	0.0	10.6	7.7	9.6	3.4	31.5	48.0
$W^- \to \mu\nu, 0.8 < \lvert\eta\rvert < 1.4$	30.9	34.8	19.5	0.0	10.8	6.7	9.9	3.4	22.6	48.7
$W^- \to \mu\nu, 1.4 < \lvert\eta\rvert < 2.0$	-9.1	34.0	34.8	0.0	10.1	6.8	9.9	3.4	23.6	56.4
$W^- \to \mu\nu, 2.0 < \lvert\eta\rvert < 2.4$	-37.3	49.4	122.8	0.0	11.0	9.9	9.9	3.4	34.6	138.0
$W^+ \to e\nu, \lvert\eta\rvert < 0.6$	-25.5	28.2	0.0	22.7	13.4	15.2	10.0	3.4	29.2	51.8
$W^+ \to e\nu, 0.6 < \lvert\eta\rvert < 1.2$	-0.7	29.1	0.0	24.4	14.2	13.4	9.7	3.4	23.9	50.0
$W^+ \to e\nu, 1,8 < \lvert\eta\rvert < 2.4$	-40.7	30.9	0.0	32.7	14.0	32.2	8.5	3.4	27.8	64.1
$W^- \to e\nu, \lvert\eta\rvert < 0.6$	57.9	30.1	0.0	19.3	10.1	14.8	9.6	3.4	32.1	52.3
$W^- \to e\nu, 0.6 < \lvert\eta\rvert < 1.2$	-85.9	31.5	0.0	22.8	9.8	12.0	9.9	3.4	24.3	49.5
$W^- \to e\nu, 1.8 < \lvert\eta\rvert < 2.4$	43.4	40.9	0.0	36.2	11.4	35.0	9.9	3.4	28.8	72.7
p_{T}^{ℓ}-Fit										
$W^+ \to \mu\nu, \lvert\eta\rvert < 0.8$	-33.5	19.4	13.0	0.0	1.2	6.0	13.4	6.0	28.6	40.3
$W^+ \to \mu\nu, 0.8 < \lvert\eta\rvert < 1.4$	4.8	21.9	19.5	0.0	0.6	5.1	13.5	6.0	24.6	41.4
$W^+ \to \mu\nu, 1.4 < \lvert\eta\rvert < 2.0$	71.9	20.3	34.6	0.0	1.0	5.3	12.6	6.0	29.3	51.8
$W^+ \to \mu\nu, 2.0 < \lvert\eta\rvert < 2.4$	-20.8	27.5	113.9	0.0	0.6	4.3	10.4	6.0	35.6	123.1
$W^- \to \mu\nu, \lvert\eta\rvert < 0.8$	32.3	20.5	12.2	0.0	1.4	5.8	12.1	6.0	31.2	42.0
$W^- \to \mu\nu, 0.8 < \lvert\eta\rvert < 1.4$	5.9	24.2	18.9	0.0	0.9	5.4	12.2	6.0	23.1	41.1
$W^- \to \mu\nu, 1.4 < \lvert\eta\rvert < 2.0$	-7.1	24.1	35.2	0.0	1.3	5.5	12.5	6.0	24.1	51.2
$W^- \to \mu\nu, 2.0 < \lvert\eta\rvert < 2.4$	-40.0	36.6	120.5	0.0	1.8	8.2	13.0	6.0	37.1	132.4
$W^+ \to e\nu, \lvert\eta\rvert < 0.6$	-34.7	19.7	0.0	24.4	1.1	7.9	13.4	5.3	28.7	45.6
$W^+ \to e\nu, 0.6 < \lvert\eta\rvert < 1.2$	-31.2	20.0	0.0	27.1	1.6	7.8	13.5	5.3	24.0	44.6
$W^+ \to e\nu, 1,8 < \lvert\eta\rvert < 2.4$	-11.6	21.3	0.0	37.9	1.4	15.0	10.4	5.3	28.6	55.4
$W^- \to e\nu, \lvert\eta\rvert < 0.6$	-8.0	20.5	0.0	22.8	1.6	8.0	12.1	5.3	31.9	46.8
$W^- \to e\nu, 0.6 < \lvert\eta\rvert < 1.2$	-73.3	21.8	0.0	24.7	1.6	7.7	12.2	5.3	25.1	44.2
$W^- \to e\nu, 1.8 < \lvert\eta\rvert < 2.4$	54.5	27.1	0.0	38.2	1.6	14.4	13.0	5.3	27.2	57.8
Combined	0.6	5.7	7.6	6.6	3.8	5.5	11.8	5.0	10.1	21.1

In summary, the measured W-boson mass yields a value of:

$$\begin{aligned} m_W &= 80399 + 0.6 + b \ \pm 5.7\ (\text{stat.}) \pm 12.0\ (\text{exp. syst.}) \pm 16.3\ (\text{mod. syst.})\ \text{MeV} \\ &= 80399 + 0.6 + b \ \pm 21.1\ \text{MeV}. \end{aligned}$$

where the first uncertainty is statistical, the second corresponds to the experimental systematic uncertainty, and the third to the physics modelling systematic uncertainty.

Table 6.5: Results of the m_W measurements for various combinations of categories. The result is given with respect to the MC W-boson mass plus an unknown blinding value b. The table shows the statistical uncertainties, together with all experimental uncertainties, divided into muon-, electron-, recoil- and background-related uncertainties, and all modelling uncertainties, separately for QCD modelling including scale variations, parton shower and angular coefficients, EW corrections, and PDFs. All uncertainties are given in MeV.

Combination of	Value [MeV]	Stat. Unc.	Muon Calib.	Elec. Calib.	Recoil Calib.	Back-grd.	QCD	EW	PDF's	Total Unc.	χ^2/NDF of Comb.
m_{T}-Fit (W^+)	-7.1	11.8	8.7	7.3	13.3	9.2	9.6	3.4	17.1	30.5	2.1/6
m_{T}-Fit (W^-)	1.1	13.3	9.2	7.0	10.5	9.4	9.8	3.4	16.4	29.8	8.6/6
m_{T}-Fit ($W^\pm$)	-1.0	9.4	8.2	5.6	11.6	8.2	9.7	3.4	10.3	24.5	14.4/13
p_{T}^ℓ-Fit (W^+)	-11.5	8.5	7.4	9.4	1.1	5.5	12.6	5.7	16.9	27.0	3.8/6
p_{T}^ℓ-Fit (W^-)	6.0	9.5	8.0	8.9	1.2	5.7	12.4	5.7	15.9	26.7	8.0/6
p_{T}^ℓ-Fit ($W^\pm$)	-1.1	6.5	7.4	7.1	1.1	5.2	12.6	5.8	10.1	21.6	16.6/13
p_{T}^ℓ-Fit (e)	-22.0	8.8	0	17.6	1.4	6.8	12.5	5.3	9.8	26.8	6.4/5
m_{T}-Fit (e)	-9.9	12.9	0	15.8	12.0	13.1	9.7	3.4	10.9	30.9	11.5/5
p_{T}^ℓ-Fit (μ)	6.4	8.8	11.4	0	1.0	4.7	12.7	6.0	11.7	23.8	4.2/7
m_{T}-Fit (μ)	2.8	12.5	11.9	0	11.6	5.9	9.8	3.4	11.3	26.5	2.2/7
Combined-Fit (W^+)	-11.4	7.3	7.7	8.8	4.1	6.2	11.8	5.0	16.9	26.4	6.9/13
Combined-Fit (W^-)	6.1	8.1	8.3	8.5	3.9	6.6	11.7	4.9	15.8	30.0	14.1/13
Combined-Fit ($W^\pm$)	0.6	5.7	7.6	6.6	3.8	5.5	11.8	5.0	10.1	21.1	30.5/27

6.2.4 *Consistency checks*

Measurements of m_W based on the $E_{\mathrm{T}}^{\mathrm{miss}}$ distributions are performed only as consistency test. Further consistency tests are performed by repeating the measurement in three intervals of $< \mu >$ to check the stability of the result with respect to different pile-up conditions. This categorisation also tests the stability of m_W with respect to data-taking periods, as the later data-taking periods have on average more pile-up due to the increasing LHC luminosity. The calibration of the recoil and the modelling of the p_{T}^W distribution are tested by performing m_W fits in two intervals of p_{T}^W and $u_{\parallel}^\ell$.The analysis is also repeated with the $E_{\mathrm{T}}^{\mathrm{miss}}$ requirement removed from the signal selection, leading to a lower recoil modelling uncertainty but a higher multijet background contribution. This consistency tests for the m_{W} measurement are summarised in Table 6.6 for the η-inclusive measurements using p_{T}^ℓ and m_{T} fits in the electron and muon decay channel. Only statistical uncertainties are shown. Consistent results are observed in all measurement categories.

6.2.5 *Optimisation of the fitting range*

The stability of the m_W for different fitting ranges has been studied, by changing the upper and lower fit ranges of p_{T}^ℓ and m_{T} by up to 5 GeV in steps of 1 GeV. The extreme cases are therefore:

Table 6.6: Summary of consistency tests for the determination of m_W in several additional measurement categories. The Δm_W values correspond to the difference between the result for each category and the inclusive result for the corresponding observable (p_{T}^{ℓ} or m_{T}). The uncertainties correspond to the statistical uncertainty of the fit to the data of each category alone. Fitting ranges of $30 < p_{\mathrm{T}}^{\ell} < 50$ GeV and $65 < m_{\mathrm{T}} < 100$ GeV are used.

Decay channel	$W \to e\nu$		$W \to \mu\nu$		Combined	
Kinematic distribution	p_{T}^{ℓ}	m_{T}	p_{T}^{ℓ}	m_{T}	p_{T}^{ℓ}	m_{T}
$<\mu>$ in $[2.5, 6.5]$	8 ± 14	14 ± 18	-21 ± 12	0 ± 16	-9 ± 9	6 ± 12
$<\mu>$ in $[6.5, 9.5]$	-6 ± 16	6 ± 23	12 ± 15	-8 ± 22	4 ± 11	-1 ± 16
$<\mu>$ in $[9.5, 16]$	-1 ± 16	3 ± 27	25 ± 16	35 ± 26	12 ± 11	20 ± 19
u_{T} in $[0, 15]$GeV	0 ± 11	-8 ± 13	5 ± 10	8 ± 12	3 ± 7	-1 ± 9
u_{T} in $[15, 30]$GeV	10 ± 15	0 ± 24	-4 ± 14	-18 ± 22	2 ± 10	-10 ± 16
$u_{\parallel}^{\ell} < 0$ GeV	8 ± 15	20 ± 17	3 ± 13	-1 ± 16	5 ± 10	9 ± 12
$u_{\parallel}^{\ell} > 0$ GeV	-9 ± 10	1 ± 14	-12 ± 10	10 ± 13	-11 ± 7	6 ± 10
No $E_{\mathrm{T}}^{\mathrm{miss}}$-cut	14 ± 9	-1 ± 13	10 ± 8	-6 ± 12	12 ± 6	-4 ± 9

- p_{T}^{ℓ} fit ranges (nominal $30-50$ GeV): $30-45$ GeV...,$35-45$ GeV,...$35-50$ GeV
- m_{T} fit ranges (nominal $65-100$ GeV): $65-90$ GeV...,$70-90$ GeV,...$70-100$ GeV

To compare the results obtained from different fitting ranges, the uncertainty on the difference needs to be evaluated. This is done by calculating, for each source of uncertainty, the quadratic difference between the two results for the statistical or systematic dominated by the statistical effects: polarisation and multi-jet shape uncertainty, and the linear difference for all other sources, and then summing quadratically over all sources:

$$\delta(m_W^i - m_W^j) = \left(\sum_k \left[(\delta m_W^{i,k})^2 - (\delta m_W^{j,k})^2 \right] + \sum_l \left[(\delta m_W^{i,l}) - (\delta m_W^{j,l}) \right]^2 \right)^{1/2} \tag{6.13}$$

where i, j label fit ranges, k the uncertainty sources for statistical, polarisation and multi-jet shape, and l the other uncertainty sources. It should be noted, that highly asymmetric fitting ranges, e.g. $30-45$ GeV in p_{T}^{ℓ}, are unnatural, as they potentially enhance effects which would otherwise affect symmetrically the Jacobian peak of the distributions.

The full scan of the fitting ranges is shown in Appendix B in Figures B.1 – B.4 with the total uncertainty as a function of the fitting ranges and in Figures B.5 – B.8 for the differences between the ranges. Figure 6.15 shows the dependence of the statistical and systematic uncertainties on the fitting range for the fully combined result when only p_{T}^{ℓ} or m_{T} range is variated. The dominating source of uncertainty is from the $p_{\mathrm{T}}^{\mathrm{W}}$ modeling which is becoming smaller when reducing the p_{T}^{ℓ} range as can be observed on the left plot of Figure 6.15. The fit results are stable when symmetric variation of the fitting range, i.e. going from $[30, 50]$ to e.g. $[32, 48]$ is applied. This scenario seems to be the most relevant one, as potential resolution effects are expected to similarly impact both

sides of the p_{T}^{ℓ} distribution. In addition, this scenarios always keep the Jacobean peak position and therefore the most sensitive area in the center of the fitting range. In addition, it is observed that the fit stability is also within expected uncertainties when raising the lower bound of the fitting range by up to 5 GeV. For all the fitting ranges the fully combined measurement result is within $\approx 2\sigma$ with respect to the nominal value.

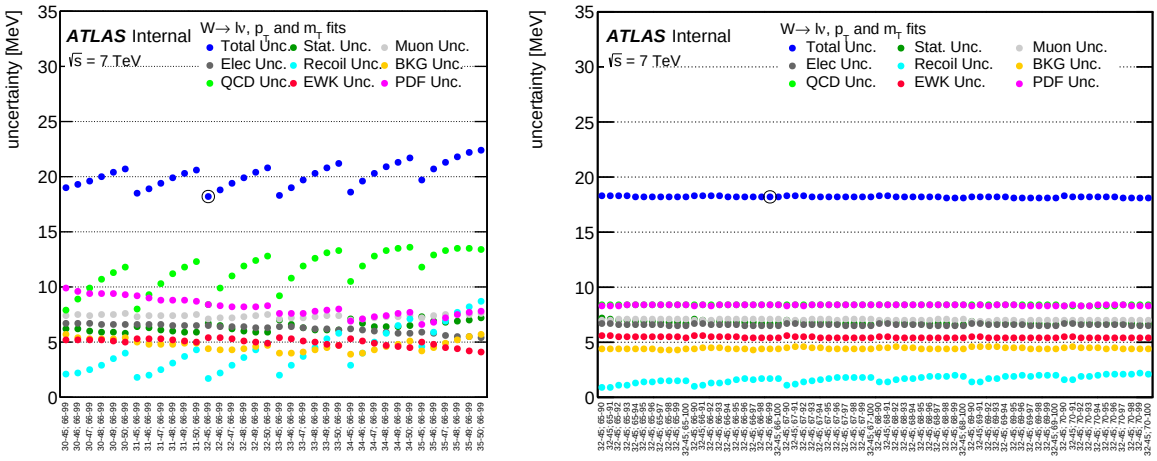

(a) **(b)**

Figure 6.15: Dependence of the statistical and systematic uncertainties on the fitting ranges for the fully combined value of m_W when only (a) p_{T}^{ℓ} range and when only (b) m_{T} range is variated. The total uncertainty is represented with blue points.

The smallest value of the total uncertainty for the symmetric ranges is found to be ≈ 18.5 MeV for p_{T}^{ℓ} range $[32, 45]$ for all m_{T} ranges. The fully combined measurement for the p_{T}^{ℓ} range $[32, 45]$ and m_{T} range $[66, 99]$ is giving -11.6 ± 18.5 MeV with $\chi^2/\mathrm{NDF} = 29.1/27$, while for the nominal fit range we measure 0.6 ± 21.1 MeV with $\chi^2/\mathrm{NDF} = 30.5/27$. Then, the optimal fitting range, p_{T}^{ℓ} range $[32, 45]$ and m_{T} range $[66, 99]$ is chosen as a reference for comparing the differences between the different fitting ranges.

Figure 6.16 shows measured values of m_W for selected ranges of the p_{T}^{ℓ} and m_{T} distributions, where only the uncorrelated statistical and systematic uncertainties with respect to the optimal range are shown. The observed variations are all within two standard deviations of the uncorrelated uncertainties, and small compared to the overall uncertainty of the measurement, which is illustrated by the band on Figure 6.16. The largest dependence on the kinematic ranges used for the fits is observed for variations of the upper bound of the p_{T}^{ℓ} distribution in the $W^+ \to e^+\nu$ channel, and is related to the shape of the data-to-prediction ratio for this distribution in the region $40 < p_{\mathrm{T}}^{\ell} < 42$ GeV, as discussed in Section 6.1.5.

6.2.6 *Final results*

After good performance of the m_W measurement in different categories, the compatibility between the electron and muon channel, as well as W^+ and W^- with p_{T}^{ℓ} and m_{T}

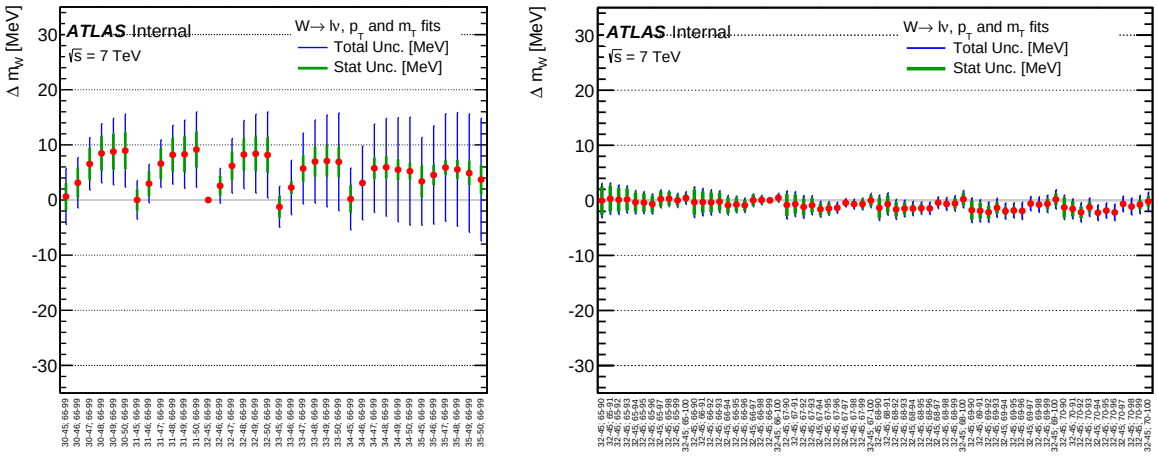

(a) **(b)**

Figure 6.16: Stability of the combined measurement of m_W with respect to variations of the fitting ranges of (a) p_{T}^{ℓ} and (b)m_{T} used for the template fits. The optimal m_{T} range is used for the p_{T}^{ℓ} variations, and the optimal p_{T}^{ℓ} range is used for the m_{T} variations. The uncorrelated statistical uncertainties are indicated with green line, while the total uncorrelated uncertainties between the different fitting ranges are shown as blue line. The difference is calculated comparing to the optimal fitting range.

fits, the stability in the different $< \mu >$, u_{T} and $u_{\parallel}$ bins and after choosing the fit range with minimal uncertainty, the unblinding is performed. The random off-set parameter is $b = -17.9$ MeV. Results in this section are shown with the unblinded results in the range $32 < p_{\mathrm{T}}^{\ell} < 45$ GeV and $66 < m_{\mathrm{T}} < 99$ GeV.

The determination of m_W from the p_{T}^{ℓ} and m_{T} distributions in the various categories is summarised in Table 6.7, including an overview of statistical and systematic uncertainties. The results are also shown in Figure 6.17. No significant differences in the values of m_W corresponding to the different decay channels and to the various charge and $|\eta_{\ell}|$ categories are observed.

Lepton-calibration uncertainties are the dominant sources of experimental systematic uncertainty for the extraction of m_W from the p_{T}^{ℓ} distribution. These uncertainties vary from about 15 MeV to about 35 MeV for most measurement categories, except the highest $|\eta|$ bin in the muon channel where the total uncertainty of about 120 MeV is dominated by the muon momentum linearity uncertainty. The uncertainty in the calibration of the recoil is the largest source of experimental systematic uncertainty for the m_{T} distribution, with a typical contribution of about 15 MeV for all categories. The final measurement uncertainty is dominated by modelling uncertainties, with typical values in the range 25–35 MeV for the various charge and $|\eta_{\ell}|$ categories.

An overview of the m_W measurement combinations are summarised in Table 6.8 and illustrated in Figure 6.18. In the first step, determinations of m_W in the electron and muon decay channels from the m_{T} distribution are combined separately for the positive- and negative-charge categories, and together for both W-boson charges. The

Table 6.7: Results of the m_W measurements in the electron and muon decay channels, for positive and negative W bosons, in different lepton-$|\eta|$ ranges, using the m_{T} and p_{T}^{ℓ} distributions in the optimised fitting range. The table shows the statistical uncertainties, together with all experimental uncertainties, divided into muon-, electron-, recoil- and background-related uncertainties, and all modelling uncertainties, separately for QCD modelling including scale variations, parton shower and angular coefficients, EW corrections, and PDFs. All uncertainties are given in MeV.

Channel m_{T}-Fit	m_W [MeV]	Stat. Unc.	Muon Unc.	Elec. Unc.	Recoil Unc.	Bckg. Unc.	QCD Unc.	EW Unc.	PDF Unc.	Total Unc.
$W^+ \to \mu\nu, \lvert\eta\rvert < 0.8$	80371.3	29.2	12.4	0.0	15.2	8.1	9.9	3.4	28.4	47.1
$W^+ \to \mu\nu, 0.8 < \lvert\eta\rvert < 1.4$	80354.1	32.1	19.3	0.0	13.0	6.8	9.6	3.4	23.3	47.6
$W^+ \to \mu\nu, 1.4 < \lvert\eta\rvert < 2.0$	80426.3	30.2	35.1	0.0	14.3	7.2	9.3	3.4	27.2	56.9
$W^+ \to \mu\nu, 2.0 < \lvert\eta\rvert < 2.4$	80334.6	40.9	112.4	0.0	14.4	9.0	8.4	3.4	32.8	125.5
$W^- \to \mu\nu, \lvert\eta\rvert < 0.8$	80375.5	30.6	11.6	0.0	13.1	8.5	9.5	3.4	30.6	48.5
$W^- \to \mu\nu, 0.8 < \lvert\eta\rvert < 1.4$	80417.5	36.4	18.5	0.0	12.2	7.7	9.7	3.4	22.2	49.7
$W^- \to \mu\nu, 1.4 < \lvert\eta\rvert < 2.0$	80379.4	35.6	33.9	0.0	10.5	8.1	9.7	3.4	23.1	56.9
$W^- \to \mu\nu, 2.0 < \lvert\eta\rvert < 2.4$	80334.2	52.4	123.7	0.0	11.6	10.2	9.9	3.4	34.1	139.9
$W^+ \to e\nu, \lvert\eta\rvert < 0.6$	80352.9	29.4	0.0	19.5	13.1	15.3	9.9	3.4	28.5	50.8
$W^+ \to e\nu, 0.6 < \lvert\eta\rvert < 1.2$	80381.5	30.4	0.0	21.4	15.1	13.2	9.6	3.4	23.5	49.4
$W^+ \to e\nu, 1,8 < \lvert\eta\rvert < 2.4$	80352.4	32.4	0.0	26.6	16.4	32.8	8.4	3.4	27.3	62.6
$W^- \to e\nu, \lvert\eta\rvert < 0.6$	80415.8	31.3	0.0	16.4	11.8	15.5	9.5	3.4	31.3	52.1
$W^- \to e\nu, 0.6 < \lvert\eta\rvert < 1.2$	80297.5	33.0	0.0	18.7	11.2	12.8	9.7	3.4	23.9	49.0
$W^- \to e\nu, 1.8 < \lvert\eta\rvert < 2.4$	80423.8	42.8	0.0	33.2	12.8	35.1	9.9	3.4	28.1	72.3
p_{T}-Fit										
$W^+ \to \mu\nu, \lvert\eta\rvert < 0.8$	80327.7	22.1	12.2	0.0	2.6	5.1	9.0	6.0	24.7	37.3
$W^+ \to \mu\nu, 0.8 < \lvert\eta\rvert < 1.4$	80357.3	25.1	19.1	0.0	2.5	4.7	8.9	6.0	20.6	39.5
$W^+ \to \mu\nu, 1.4 < \lvert\eta\rvert < 2.0$	80446.9	23.9	33.1	0.0	2.5	4.9	8.2	6.0	25.2	49.3
$W^+ \to \mu\nu, 2.0 < \lvert\eta\rvert < 2.4$	80334.1	34.5	110.1	0.0	2.5	6.4	6.7	6.0	31.8	120.2
$W^- \to \mu\nu, \lvert\eta\rvert < 0.8$	80427.8	23.3	11.6	0.0	2.6	5.8	8.1	6.0	26.4	39.0
$W^- \to \mu\nu, 0.8 < \lvert\eta\rvert < 1.4$	80395.6	27.9	18.3	0.0	2.5	5.6	8.0	6.0	19.8	40.5
$W^- \to \mu\nu, 1.4 < \lvert\eta\rvert < 2.0$	80380.6	28.1	35.2	0.0	2.6	5.6	8.0	6.0	20.6	50.9
$W^- \to \mu\nu, 2.0 < \lvert\eta\rvert < 2.4$	80315.2	45.5	116.1	0.0	2.6	7.6	8.3	6.0	32.7	129.6
$W^+ \to e\nu, \lvert\eta\rvert < 0.6$	80336.5	22.2	0.0	20.1	2.5	6.4	9.0	5.3	24.5	40.7
$W^+ \to e\nu, 0.6 < \lvert\eta\rvert < 1.2$	80345.8	22.8	0.0	21.4	2.6	6.7	8.9	5.3	20.5	39.4
$W^+ \to e\nu, 1,8 < \lvert\eta\rvert < 2.4$	80344.7	24.0	0.0	30.8	2.6	11.9	6.7	5.3	24.1	48.2
$W^- \to e\nu, \lvert\eta\rvert < 0.6$	80351.0	23.1	0.0	19.8	2.6	7.2	8.1	5.3	26.6	42.2
$W^- \to e\nu, 0.6 < \lvert\eta\rvert < 1.2$	80309.8	24.9	0.0	19.7	2.7	7.3	8.0	5.3	20.9	39.9
$W^- \to e\nu, 1.8 < \lvert\eta\rvert < 2.4$	80413.4	30.1	0.0	30.7	2.7	11.5	8.3	5.3	22.7	51.0
Combined	80369.5	6.8	6.6	6.4	2.9	4.5	8.3	5.5	9.2	18.5

results are compatible, and the positively charged, negatively charged, and charge-inclusive combinations yield values of χ^2/dof corresponding to 2/6, 7/6, and 11/13, respectively. Compatibility of the results is also observed for the corresponding combinations from the p_{T}^{ℓ} distribution, with values of χ^2/dof of 5/6, 10/6, and 19/13, for positively charged, negatively charged, and charge-inclusive combinations, respectively. The χ^2 compatibility test validates the consistency of the results in the $W \to e\nu$ and $W \to \mu\nu$ decay channels. The precision of the determination of m_W from the m_{T} distribution is slightly worse than the result obtained from the p_{T}^{ℓ} distribution, due to the

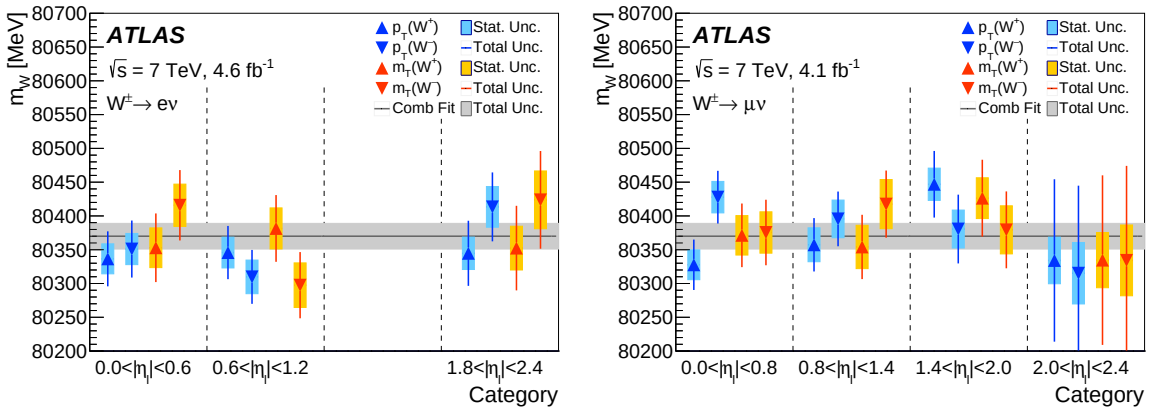

(a) **(b)**

Figure 6.17: Overview of the m_W measurements in the (a) electron and (b) muon decay channels. Results are shown for the p_{T}^{ℓ} and m_{T} distributions, for W^+ and W^- boson events in the different $|\eta_\ell|$ categories. The coloured bands and solid lines show the statistical and total uncertainties, respectively. The horizontal line and band show the fully combined result and its uncertainty.

larger uncertainty induced by the recoil calibration. In addition, the impact of PDF- and p_{T}^{W}-related uncertainties on the p_{T}^{ℓ} fits is limited by the optimisation of the fitting range. In the second step, determinations of m_W from the p_{T}^{ℓ} and m_{T} distributions are combined separately for the electron and the muon decay channels. The results are compatible, with values of χ^2/NDF of 4/5 and 8/5 in the electron channel for the p_{T}^{ℓ} and m_{T} distributions, respectively, and values of 7/7 and 3/7 in the muon channel for the p_{T}^{ℓ} and m_{T} distributions, respectively. The m_W determinations in the electron and in the muon channels agree, further validating the consistency of the electron and muon calibrations. Agreement between the m_W determinations from the p_{T}^{ℓ} and m_{T} distributions supports the calibration of the recoil, and the modelling of the transverse momentum of the W boson.

The combination of all the determinations of m_W shown in Table 6.7 has a value of χ^2/NDF of 29/27, and yields a final result of

$$\begin{aligned} m_W &= 80369.5 \pm 6.8\ \text{MeV(stat.)} \pm 10.6\ \text{MeV(exp. syst.)} \pm 13.6\ \text{MeV(mod. syst.)} \\ &= 80369.5 \pm 18.5\ \text{MeV}, \end{aligned}$$

where the first uncertainty is statistical, the second corresponds to the experimental systematic uncertainty, and the third to the physics-modelling systematic uncertainty. The latter dominates the total measurement uncertainty, and it itself dominated by strong interaction uncertainties. The experimental systematic uncertainties are dominated by the lepton calibration; backgrounds and the recoil calibration have a smaller impact. In the final combination, the muon decay channel has a weight of 57%, and the p_{T}^{ℓ} fit dominates the measurement with a weight of 86%. Finally, the charges contribute similarly with a weight of 52% for W^+ and of 48% for W^-.

Table 6.8: Results of the m_W measurements for various combinations of categories. The table shows the statistical uncertainties, together with all experimental uncertainties, divided into muon-, electron-, recoil- and background-related uncertainties, and all modelling uncertainties, separately for QCD modelling including scale variations, parton shower and angular coefficients, EW corrections, and PDFs. All uncertainties are given in MeV.

Combined categories	Value [MeV]	Stat. Unc.	Muon Unc.	Elec. Unc.	Recoil Unc.	Bckg. Unc.	QCD Unc.	EW Unc.	PDF Unc.	Total Unc.	χ^2/NDF of Comb.
m_{T}, W^+, e-μ	80370.0	12.3	8.3	6.7	14.5	9.7	9.4	3.4	16.9	30.9	2/6
m_{T}, W^-, e-μ	80381.1	13.9	8.8	6.6	11.8	10.2	9.7	3.4	16.2	30.5	7/6
m_{T}, $W^\pm$, e-μ	80375.7	9.6	7.8	5.5	13.0	8.3	9.6	3.4	10.2	25.1	11/13
p_{T}^ℓ, W^+, e-μ	80352.0	9.6	6.5	8.4	2.5	5.2	8.3	5.7	14.5	23.5	5/6
p_{T}^ℓ, W^-, e-μ	80383.4	10.8	7.0	8.1	2.5	6.1	8.1	5.7	13.5	23.6	10/6
p_{T}^ℓ, $W^\pm$, e-μ	80369.4	7.2	6.3	6.7	2.5	4.6	8.3	5.7	9.0	18.7	19/13
p_{T}^ℓ, $W^\pm$, e	80347.2	9.9	0.0	14.8	2.6	5.7	8.2	5.3	8.9	23.1	4/5
m_{T}, $W^\pm$, e	80364.6	13.5	0.0	14.4	13.2	12.8	9.5	3.4	10.2	30.8	8/5
m_{T}-p_{T}^ℓ, W^+, e	80345.4	11.7	0.0	16.0	3.8	7.4	8.3	5.0	13.7	27.4	1/5
m_{T}-p_{T}^ℓ, W^-, e	80359.4	12.9	0.0	15.1	3.9	8.5	8.4	4.9	13.4	27.6	8/5
m_{T}-p_{T}^ℓ, $W^\pm$, e	80349.8	9.0	0.0	14.7	3.3	6.1	8.3	5.1	9.0	22.9	12/11
p_{T}^ℓ, $W^\pm$, μ	80382.3	10.1	10.7	0.0	2.5	3.9	8.4	6.0	10.7	21.4	7/7
m_{T}, $W^\pm$, μ	80381.5	13.0	11.6	0.0	13.0	6.0	9.6	3.4	11.2	27.2	3/7
m_{T}-p_{T}^ℓ, W^+, μ	80364.1	11.4	12.4	0.0	4.0	4.7	8.8	5.4	17.6	27.2	5/7
m_{T}-p_{T}^ℓ, W^-, μ	80398.6	12.0	13.0	0.0	4.1	5.7	8.4	5.3	16.8	27.4	3/7
m_{T}-p_{T}^ℓ, $W^\pm$, μ	80382.0	8.6	10.7	0.0	3.7	4.3	8.6	5.4	10.9	21.0	10/15
m_{T}-p_{T}^ℓ, W^+, e-μ	80352.7	8.9	6.6	8.2	3.1	5.5	8.4	5.4	14.6	23.4	7/13
m_{T}-p_{T}^ℓ, W^-, e-μ	80383.6	9.7	7.2	7.8	3.3	6.6	8.3	5.3	13.6	23.4	15/13
m_{T}-p_{T}^ℓ, $W^\pm$, e-μ	80369.5	6.8	6.6	6.4	2.9	4.5	8.3	5.5	9.2	18.5	29/27

The presented results can be used to derive a measurement of the mass difference between the positive and negative W bosons, $m_{W^+} - m_{W^-}$. Starting from the m_W measurement results in the 28 categories described above, 14 measurements of $m_{W^+} - m_{W^-}$ can be constructed by subtraction of the results obtained from the W^+ and W^- samples in the same decay channel and $|\eta|$ category. In practice, the m_W values measured in W^+ and W^- events are subtracted linearly, as are the effects of systematic uncertainties on these measurements, while the uncertainty contributions of a statistical nature are added in quadrature. Contrarily to the m_W measurement discussed above, no blinding procedure was applied for the measurement of $m_{W^+} - m_{W^-}$. The uncertainties that are anti-correlated between W^+ and W^- and largely cancel for the m_W measurement become dominant when measuring $m_{W^+} - m_{W^-}$. On the physics-modelling side, the fixed-order PDF uncertainty and the parton shower PDF uncertainty give the largest contributions, while other sources of uncertainty only weakly depend on charge and tend to cancel. Among the sources of uncertainty related to lepton calibration, the track sagitta correction dominates in the muon channel, whereas several residual uncertainties contribute in the electron channel. Most lepton and recoil calibration uncertainties tend to cancel. Background systematic uncertainties contribute as the Z and multijet background fractions differ in the W^+ and W^- channels. The dominant statistical uncertainties arise from the size of the data and MC signal samples, and of the control samples used to derive the multijet background. The fully combined result

is:

$$\begin{aligned} m_{W^+} - m_{W^-} &= -29.2 \pm 12.8\text{MeV(stat.)} \pm 7.0\text{MeV(exp. syst.)} \pm 23.9\text{MeV(mod. syst.)} \\ &= -29.2 \pm 28.0\text{MeV}, \end{aligned}$$

where the first uncertainty is statistical, the second corresponds to the experimental systematic uncertainty, and the third to the physics-modelling systematic uncertainty. The current world average result is $m_{W^+} - m_{W^-} = -0.2 \pm 0.6$ GeV [12]. This results is the most precise measurement of the $m_{W^+} - m_{W^-}$.

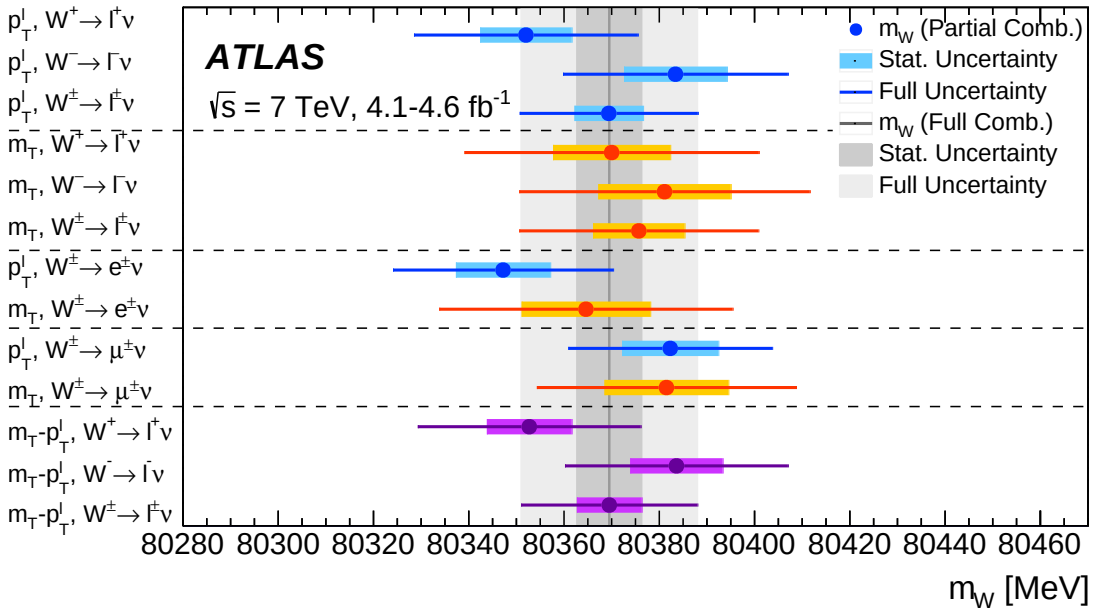

Figure 6.18: Overview of the m_W determinations from the p_{T}^{ℓ} and m_{T} distributions, and for the combination of the p_{T}^{ℓ} and m_{T} distributions, in the muon and electron decay channels and for W^+ and W^- events. The horizontal lines and bands show the statistical and total uncertainties of the individual m_W determinations. The combined result for m_W and its statistical and total uncertainties are also indicated (vertical line and bands).

6.2.7 *Discussion*

Obtained result for the W-boson mass measurement with the ATLAS experiment is:

$$m_W = 80370 \pm 19 \text{ MeV},$$

which is in agreement with the current world average value of $m_W = 80385 \pm 15$ MeV [12], and has a precision comparable to the currently most precise single measurements of the CDF and D0 collaborations [56, 57], which are presented in Section 1.2.3.

When comparing the m_W measurement with the ATLAS and CDF experiments, see Tables 6.7 and 1.2, the total uncertainty is 19 MeV in both measurements. The difference in the W-boson event selection is in the cut on the hadronic recoil distribution which is $u_{\mathrm{T}} < 15$ GeV and $u_{\mathrm{T}} < 30$ GeV in the CDF and ATLAS measurements respectively, the recoil resolution is worse in the ATLAS measurement due to larger pile-up. The ATLAS measurement is mainly done using the p_{T}^{ℓ} distribution, with the weight of 86%, while the CDF measurement is mainly done with the m_{T} distribution with the weight of 53% and it also uses the $E_{\mathrm{T}}^{\mathrm{miss}}$ distribution with the weight of 16%. The fitting ranges for the CDF measurement are $32 < p_{\mathrm{T}}^{\ell} < 48$ GeV and $65 < m_{\mathrm{T}} < 90$ GeV, while for the ATLAS measurement are $32 < p_{\mathrm{T}}^{\ell} < 45$ GeV and $66 < m_{\mathrm{T}} < 99$ GeV. Because of the larger sample, the ATLAS measurement has smaller statistical uncertainty. The uncertainties due to PDF and lepton calibration are similar in both measurements, while the uncertainty due to hadronic recoil is bigger for the ATLAS m_{T} measurement.

An overview of the different m_W measurements is shown in Figure 6.19. The compatibility of the measured value of m_W in the context of the global electroweak fit is illustrated in Figures 6.20 and 6.21. Figure 6.20 compares the present measurement with earlier results, and with the SM prediction updated with regard to [39] using recent measurements of the top quark and Higgs boson masses, $m_t = 172.84 \pm 0.70$ GeV [43] and $m_H = 125.09 \pm 0.24$ GeV [45]. This update gives a numerical value for the SM prediction of $m_W = 80356 \pm 8$ MeV. The corresponding two-dimensional 68% and 95% confidence limits for m_W and m_t are shown in Figure 6.21, and compared to the present measurement of m_W and the average of the top-quark mass determinations performed by ATLAS [43].

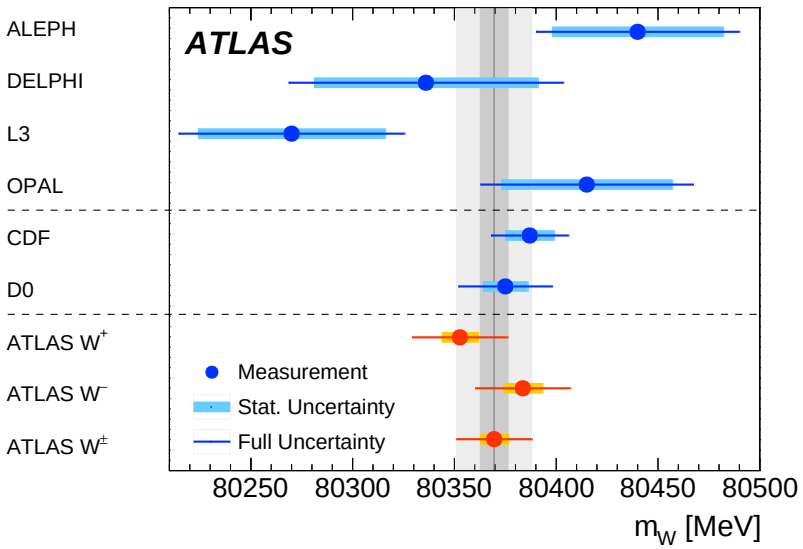

Figure 6.19: The measured value of m_W is compared to other published results, including measurements from the LEP experiments ALEPH, DELPHI, L3 and OPAL [51–54], and from the Tevatron collider experiments CDF and D0 [56, 57]. The vertical bands show the statistical and total uncertainties of the ATLAS measurement, and the horizontal bands and lines show the statistical and total uncertainties of the other published results. Measured values of m_W for positive and negative W bosons are also shown.

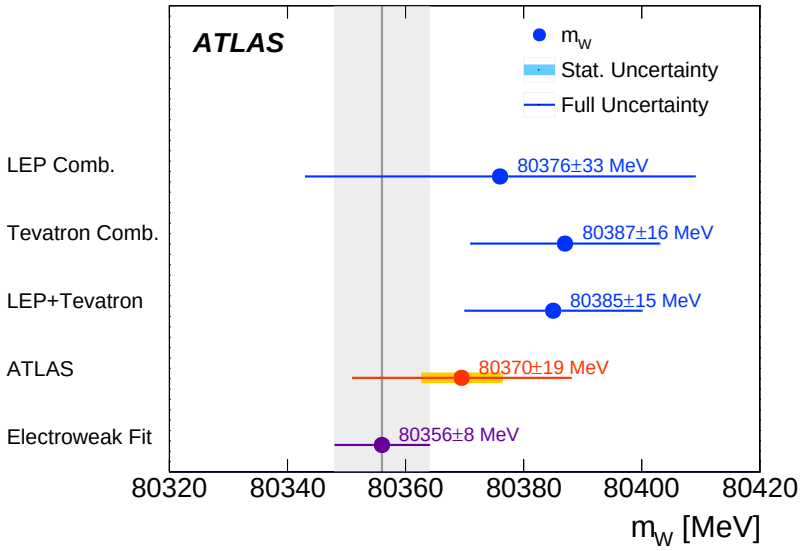

Figure 6.20: The present measurement of m_W is compared to the SM prediction from the global electroweak fit [39] updated using recent measurements of the top-quark and Higgs-boson masses, $m_t = 172.84 \pm 0.70$ GeV [43] and $m_H = 125.09 \pm 0.24$ GeV [45], and to the combined values of m_W measured at LEP [55] and at the Tevatron collider [58].

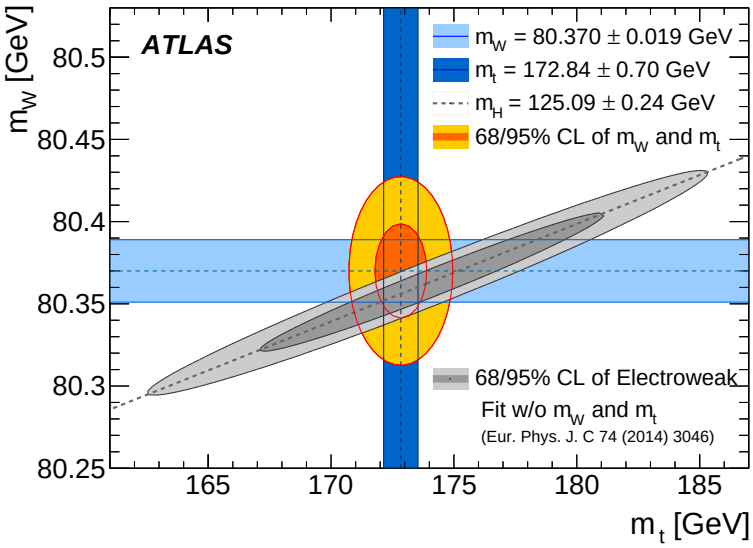

Figure 6.21: The 68% and 95% confidence-level contours of the m_W and m_t indirect determination from the global electroweak fit [39] are compared to the 68% and 95% confidence-level contours of the ATLAS measurements of the top-quark and W-boson masses. The determination from the electroweak fit uses as input the LHC measurement of the Higgs-boson mass, $m_H = 125.09 \pm 0.24$ GeV [45].

6.3 PROSPECTS FOR THE FUTURE

The result of the W-boson mass measurement is presented in previous section. For presented measurement only a part of the data collected during Run-1 is used. The m_W uncertainty from the global electroweak fit is 8 MeV, which represents a natural target for the precision of the experimental measurement of the mass of the W boson. The current measurement of m_W is dominated by the theoretical uncertainty. The PDF uncertainties can be reduced when including precision inclusive rapidity measurement of the Z and W bosons [169], which is in the $\sqrt{s} = 7$ TeV measurement used only for validation. Improved QCD and EW predictions for DY production, are crucial for the future measurements of the m_W.

6.3.1 *Prospects for the W-boson mass measurement using 8 TeV and 13 TeV data*

Large samples of data are collected by the ATLAS experiment during 2012 data-taking at $\sqrt{s} = 8$ TeV, almost four time more data than in 2011, as shown in Chapter 2. During Run-2, at $\sqrt{s} = 13$ TeV, in 2015 and 2016, even more data is collected, corresponding to an integrated luminosity of 36.1 fb^{-1}, additional 45 fb^{-1} is planed to be collected per year during 2017 and 2018 data-taking. The collected data can be used for new m_W measurements. Since at $\sqrt{s} = 8$ TeV and $\sqrt{s} = 13$ TeV the number of collected W- and Z-boson candidates is much higher, with a higher statistics calibration samples there is a possible reduction of experimental systematics uncertainties. However, the pile-up for the data collected at $\sqrt{s} = 8$ TeV and during 2016 at $\sqrt{s} = 13$ TeV is higher than for the $\sqrt{s} = 7$ TeV, as shown in Chapter 2, the average $< \mu >$ is $< \mu >= 9.1$ and $< \mu >= 20.7$ for the data collected at $\sqrt{s} = 7$ TeV and $\sqrt{s} = 8$ TeV, respectively, while $< \mu >= 13.7$ and $< \mu >= 24.2$ for the data collected a $\sqrt{s} = 13$ TeV, during 2015 and 2016 respectively.

Due to higher pile-up, for the future m_W measurement at $\sqrt{s} = 8$ TeV and $\sqrt{s} = 13$ TeV different hadronic recoil algorithm must be used. The performance of different hadronic recoil algorithms is shown in Chapter 5. Another improvement for the hadronic recoil is possible by using the particle flow algorithm which showed good performance in high pile-up conditions [212]. The calibration procedure will the same as for the $\sqrt{s} = 7$ TeV m_W measurement described in Section 5.5. Therefore, the m_{T} distribution will be more affected than the p_{T}^{ℓ} distribution. As a consequence, the precise electron and muon calibration is more important at $\sqrt{s} = 8$ TeV and $\sqrt{s} = 13$ TeV m_W measurements.

In summary, measurements of m_W with 8 TeV and 13 TeV data, will reduce the statistical uncertainty, but due to higher pile-up the hadronic recoil and the background will be more challenging to control. On the other hand, the m_W measurement at $\sqrt{s} = 13$ TeV probes a different region of the PDFs, and there is a small correlation with

the $\sqrt{s} = 7$ TeV measurement, therefore a possible reduction of the total uncertainty is in the combination of the m_W measurements at $\sqrt{s} = 7$ TeV and $\sqrt{s} = 13$ TeV.

6.3.2 *Direct measurement of the W-boson transverse momentum with low pile-up data*

As demonstrated, one of the main contributions to the m_W uncertainty arises from the modeling of the p_{T}^W. The low p_{T}^W region is sensitive to the ISR and non perturbative effects while the high p_{T}^W region is more sensitive to the perturbative effects, as discussed in Section 3.3.3. The last measurement of the W-boson transverse momentum was with the data collected during 2010 by the ATLAS detector at the LHC [175]. For this p_{T}^W measurement, there is only 2-3 bins for the low p_{T}^W part of the distribution as shown in Figure 3.1, which is the most relevant for the m_W measurement. The $\sqrt{s} = 7$ TeV m_W measurement uses the W- to Z-boson p_{T} ratio to model the p_{T}^W, as described in Section 3.3. A percent level accuracy is needed for the low p_{T}^W region in order to improve theoretical prediction of the W- to Z-boson ratio. For future m_W measurements, in order to reduce the total uncertainty, a precise measurement of the p_{T}^W distribution is needed. The standard unfolding method leads to higher uncertainties of 3 to 5 % and coarse p_{T}^W bins [175]. The reduction of uncertainties is possible with the direct measurement of the p_{T}^W by finding a 3 of 4 parameter function to fit the p_{T}^W distribution. On the other hand, the p_{T}^W distribution is very sensitive to the pile-up conditions, as discussed in Chapter 5. Therefore, one can benefit from the measurement of the $p_{\mathrm{T}}^{\mathrm{W}}$ in low pile-up conditions.

As discussed in Chapter 5, the hadronic recoil distribution is reconstructed from energies in topo-clusters. The basic observable controlling the topo-cluster formation is the cell signal significance which is defined as the ratio of the cell signal to the average expected noise in this cell estimated for each run year independently. The cell noise thresholds are set to an average of $\mu = 0$, $\mu = 8$ and $\mu = 30$ additional proton–proton interactions per bunch crossing during 2010, 2011 and 2012 data-taking, respectively [180]. These configurations are choices based on the expected average $< \mu >$ for the run year. They are needed to be made before the data-taking has started, to allow for a fast reconstruction of the collected data. With the change of $< \mu >$ during the data-taking period, this threshold is only optimal for the small subset of recorded data with $< \mu >= \mu$. If $< \mu >< \mu$ the calorimeter sensitivity is reduced because the noise threshold is too large. On the other hand, if $< \mu >> \mu$, the noise suppression is not optimal, leading to more noise contributions to the topo-cluster signals. Therefore, the main question is how to optimise the parameters of a low luminosity running period, since there is the trade-off between the value $< \mu >$ and the running time needed to accumulate a given integrated luminosity for precise enough measurement. To understand this, 1 million Z- and W-boson decays to electrons and muons are simulated in different pile-up conditions. These events have been digitised with a $\mu = 0.01$, 1, 2, 4, 8 pile-up events superimposed. All of these files have been finally reconstructed using reconstruction optimised for $< \mu > = 0.01$, 1, 2, 4, 8,

leading to a final set of 25 combinations of μ values at the digitisation stage and at the reconstruction stage. For each of there 25 combination the performance of the hadronic recoil is studied. Figure 6.22 shows the recoil distribution for the Z-boson events with all 25 combinations of the μ values. The resolution of the hadronic recoil is very sensitive to the pile-up conditions and for $< \mu >= 8$ the recoil distribution is too wide, results are similar for the W-boson events. While the recoil resolution is very sensitive to the reconstructed $< \mu >$, the variation of the cell noise threshold μ does not affect the recoil resolution. The optimal conditions for the $p_{\mathrm{T}}^{\mathrm{W}}$ measurement can be achieved with $< \mu >= 4$. Integrated luminosity of $150 - 200$ pb^{-1} corresponds to about 1 million W-boson candidates, which can be collected during about 10 days of data-taking at $\sqrt{s} = 13$ TeV with $\mu = 4$.

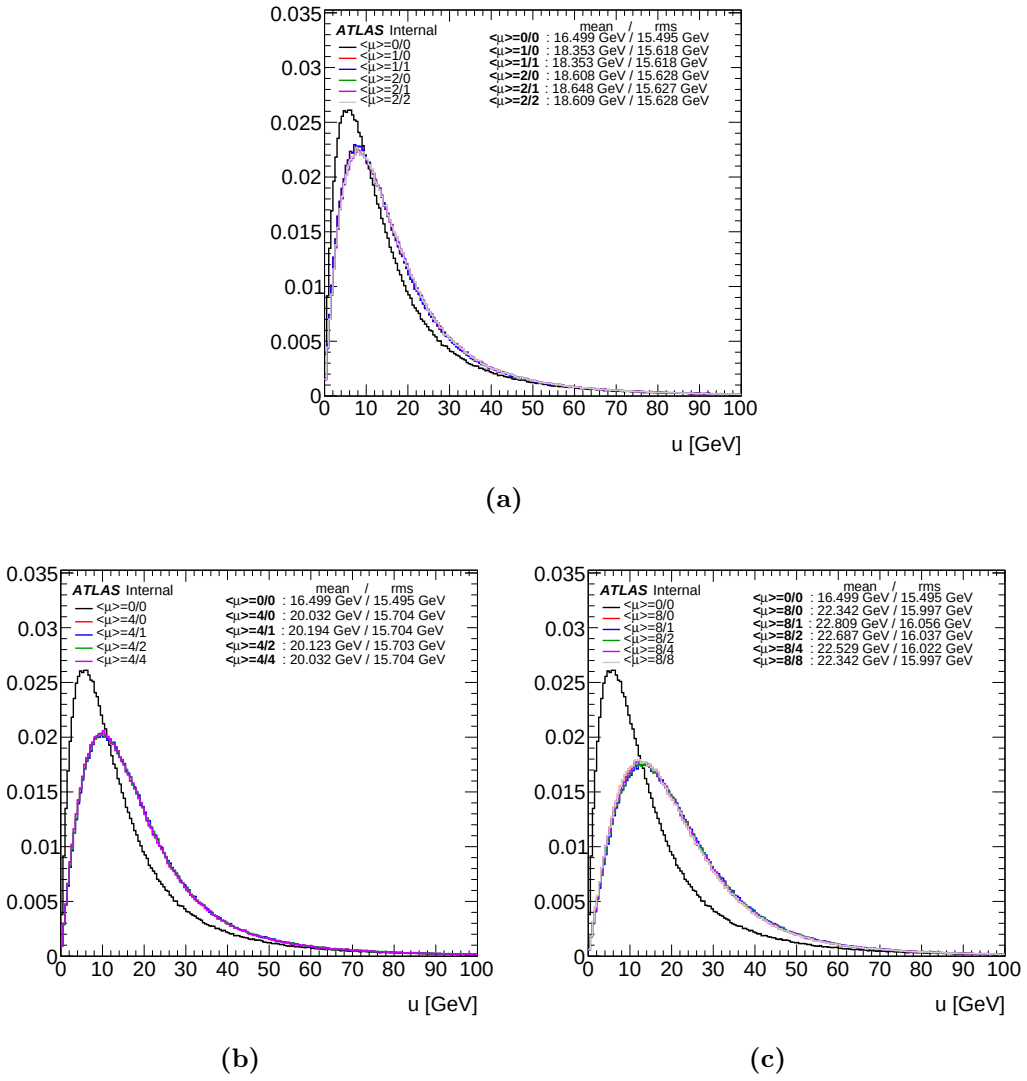

Figure 6.22: The hadronic recoil distribution for Z boson events in different pile-up conditions: (a) $< \mu >= 1$ and $< \mu >= 2$ (b) $< \mu >= 4$ and (c) $< \mu >= 8$. The cell noise threshold μ is varied for each value of reconstructed $< \mu >$. The black line represents, as a reference, the hadronic recoil distribution with $\mu = 0$. The mean and RMS values are indicated on the plots.

Conclusion

This thesis describes the W-boson mass measurement with data collected during 2011 in proton–proton collisions at a centre-of-mass energy of $\sqrt{s} = 7$ TeV at the LHC with the ATLAS detector. The W-boson events are detected through their leptonic decay in electron and muon channels. The W-boson candidates are selected by requiring exactly one lepton (electron or muon) with high transverse momentum and the presence of the large missing transverse energy in the event, originating from the neutrino. The mass of the W boson (m_W) is measured from sensitive observables which have a sharp Jacobian peak: the lepton transverse momentum (p_{T}^{ℓ}) and the W-boson transverse mass (m_{T}). The χ^2 minimisation is used to determine the W-boson mass by comparing p_{T}^{ℓ} and m_{T} distributions in the data to the set of corresponding template distributions generated from the simulation with different values of m_W.

The muon momentum calibration is performed with the data collected in proton–proton collisions at $\sqrt{s} = 7$ TeV and $\sqrt{s} = 8$ TeV with the ATLAS detector. The muon momentum scale and resolution is studied in detail with a large calibration samples of $J/\psi \to \mu\mu$ and $Z \to \mu\mu$ decays. The $J/\psi \to \mu\mu$ studies show the importance of the energy loss corrections. The correction procedure is based on the template fitting of the $J/\psi \to \mu\mu$ and $Z \to \mu\mu$ invariant mass distributions in bins of pseudorapidity (η) to extract the inner detector muon momentum corrections, while the muon spectrometer momentum corrections have been extracted by fitting the invariant mass distributions and the inner detector and muon spectrometer relative momentum difference in bins of muon pseudorapidity, separately for large and small sectors in the muon spectrometer. The corrections have been derived for the momentum measurements in the inner detector and in the muon spectrometer separately. The corrections for the combined muons are then obtained by combining the corrections for inner detector and muon spectrometer momentum according to their relative weight in the determination of the combined momentum. The obtained results are validated with independent analysis using $J/\psi \to \mu\mu$, $\Upsilon \to \mu\mu$ and $Z \to \mu\mu$ decays in bins of muon pseudorapidity, azimuth and transverse momentum. The uncertainties on the muon momentum scale increase with $|\eta|$. The combined muon momentum scale is measured with a precision of a 0.05% for $|\eta| < 1$, which changes up to 0.2% for $|\eta| > 2.3$. The dimuon resolution is from 1.2% for low p_{T} up to 2% for $p_{\mathrm{T}} = 100$ GeV for the central region ($|\eta| < 1$), while for $|\eta| > 1$ the dimuon resolution is in range from 2% for low p_{T} up to 3% for $p_{\mathrm{T}} = 100$ GeV. The relative uncertainty on the measured dimuon resolution is from 3% to 10% depending on the pseudorapidity and transverse momentum.

The muon momentum calibration is used for the Higgs-boson mass measurement based on the data from proton-proton collisions during 2011 and 2012. Due to an excellent calibration of the muon momentum (as well as electron energy), the total

uncertainty for the Higgs-boson mass measurement is completely dominated by the statistics of a given sample, yielding to a muon momentum uncertainty of 10 MeV from the total of 180 MeV.

An important quantity for the W-boson mass measurement is the hadronic recoil, from which the magnitude and the direction of the neutrino form the W-boson decay can be estimated. The hadronic recoil represents the vector sum of all energy depositions in the calorimeter except the energy associated to the charged lepton. The calibration of the hadronic recoil is performed in the following way. First, the modeling of the overall event activity in the simulation is corrected, then the residual differences in the recoil response and resolution are derived using Z-boson events in data, and transferred to the W-boson sample. The calibration is performed in bins of boson transverse momentum and the total reconstructed transverse energy in the calorimeter. The hadronic recoil calibration procedure is sensitive to the uncertainty on the scale factor applied to the average number of proton–proton interactions per bunch crossing, uncertainties due to the W-boson transverse momentum dependence of the Smirnov transform of the total reconstructed transverse energy in the calorimeter, uncertainties on the correction of the average value of the x and y component of the hadronic recoil and the expected differences in the recoil response between Z- and W-boson events. The total uncertainty due to hadronic recoil calibration is about 3 MeV for the p_{T}^{ℓ} measurement and about 13 MeV for the m_{T} measurement, which gives 3 MeV uncertainty to the final W-boson mass measurement after combining p_{T}^{ℓ} and m_{T} measurements for electron and muon channels.

The final experimental corrections and the physics modeling are applied to the W-boson candidates. The W-boson mass measurement is obtained from the combination of various measurements performed in the electron and muon decay channels, and in charge- and pseudorapidity-dependent categories. Then, an optimal fitting range is found by minimising the total expected measurement uncertainty. For the final result, the fit ranges of $32 < p_{\mathrm{T}}^{\ell} < 45$ GeV and $66 < m_{\mathrm{T}} < 99$ GeV are used. The individual measurements of the extracted W-boson mass are found to be consistent and their combination yields a value of

$$\begin{aligned} m_W &= 80369.5 \pm 6.8\ \text{MeV(stat.)} \pm 10.6\ \text{MeV(exp. syst.)} \pm 13.6\ \text{MeV(mod. syst.)} \\ &= 80370 \pm 19\ \text{MeV}, \end{aligned}$$

where the first uncertainty is statistical, the second corresponds to the experimental systematic uncertainty, and the third to the physics modeling systematic uncertainty. The obtained result is in agreement with the current world average value of $m_W = 80385 \pm 15$ MeV, and with the Standard Model prediction form the global electroweak fit $m_W = 80358 \pm 8$ MeV. The ATLAS measurement is at the same level of precision as the CDF and D0 measurements at the Tevatron. The dominate source of uncertainty is due to the modeling of the W-boson transverse momentum. Further improvement in the precision of the W-boson mass measurement is possible by constraining the parton distribution function uncertainty with the precise measurements of Z- and W-boson rapidity distributions, and the measurement of the W-boson transverse momentum, especially the low-p_{T} region.

References

[1] D. J. Griffiths, *Introduction to elementary particles; 2nd rev. version*, Physics textbook, Wiley, 2008, URL: https://cds.cern.ch/record/111880.

[2] D. H. Perkins, *Introduction to high-energy physics; 4th ed.* Cambridge Univ. Press, 2000, URL: https://cds.cern.ch/record/396126.

[3] F. Halzen and A. D. Martin, *Quarks and leptons: an introductory course in modern particle physics*, Wiley, 1984, URL: https://cds.cern.ch/record/100339.

[4] A. Djouadi, *The Anatomy of electro-weak symmetry breaking. I: The Higgs boson in the standard model*, Phys. Rept. **457** (2008) 1, arXiv: hep-ph/0503172 [hep-ph].

[5] A. Djouadi, *The Anatomy of electro-weak symmetry breaking. II. The Higgs bosons in the minimal supersymmetric model*, Phys. Rept. **459** (2008) 1, arXiv: hep-ph/0503173 [hep-ph].

[6] A. Purcell, *Go on a particle quest at the first CERN webfest. Le premier webfest du CERN se lance Ãă la conquÃłte des particules*, (2012) 10, URL: https://cds.cern.ch/record/1473657.

[7] S. Weinberg, *The Quantum Theory of Fields*, The Quantum Theory of Fields 3 Volume Hardback Set Volume 1, Cambridge University Press, 1995, ISBN: 9780521550017, URL: https://books.google.rs/books?id=doeDB3_WLvwC.

[8] E. Noether, *Invariant Variation Problems*, Gott. Nachr. **1918** (1918) 235, [Transp. Theory Statist. Phys.1,186(1971)], arXiv: physics/0503066 [physics].

[9] T. W. B. Kibble, *Symmetry breaking in nonAbelian gauge theories*, Phys. Rev. **155** (1967) 1554.

[10] N. Cabibbo, *Unitary Symmetry and Leptonic Decays*, Phys. Rev. Lett. **10** (1963) 531, [,648(1963)].

[11] M. Kobayashi and T. Maskawa, *CP Violation in the Renormalizable Theory of Weak Interaction*, Prog. Theor. Phys. **49** (1973) 652.

[12] C. Patrignani et al., *Review of Particle Physics*, Chin. Phys. **C40** (2016) 100001.

[13] P. A. M. Dirac, *A Theory of Electrons and Protons*, Proc. Roy. Soc. Lond. **A126** (1930) 360.

[14] F. J. Dyson, *The Radiation Theories of Tomonaga, Schwinger, and Feynman*, Phys. Rev. **75** (3 1949) 486, URL: http://link.aps.org/doi/10.1103/PhysRev.75.486.

[15] C.-N. Yang and R. L. Mills, *Conservation of Isotopic Spin and Isotopic Gauge Invariance*, Phys. Rev. **96** (1954) 191.

[16] S. L. Glashow, *Partial Symmetries of Weak Interactions*, Nucl. Phys. **22** (1961) 579.

[17] A. Salam and J. C. Ward, *Electromagnetic and weak interactions*, Phys. Lett. **13** (1964) 168.

[18] S. Weinberg, *A Model of Leptons*, Phys. Rev. Lett. **19** (1967) 1264.

[19] S. L. Glashow, J. Iliopoulos and L. Maiani, *Weak Interactions with Lepton-Hadron Symmetry*, Phys. Rev. **D2** (1970) 1285.

[20] D. J. Gross and F. Wilczek, *Asymptotically Free Gauge Theories. 1*, Phys. Rev. **D8** (1973) 3633.

[21] H. D. Politzer, *Reliable Perturbative Results for Strong Interactions?*, Phys. Rev. Lett. **30** (1973) 1346.

[22] H. D. Politzer, *Asymptotic Freedom: An Approach to Strong Interactions*, Phys. Rept. **14** (1974) 129.

[23] K. G. Wilson, *Confinement of Quarks*, Phys. Rev. **D10** (1974) 2445, [,45(1974)].

[24] P. W. Higgs, *Broken symmetries, massless particles and gauge fields*, Phys. Lett. **12** (1964) 132.

[25] F. Englert and R. Brout, *Broken Symmetry and the Mass of Gauge Vector Mesons*, Phys. Rev. Lett. **13** (1964) 321.

[26] P. W. Higgs, *Broken Symmetries and the Masses of Gauge Bosons*, Phys. Rev. Lett. **13** (1964) 508.

[27] G. 't Hooft, *Renormalization of Massless Yang-Mills Fields*, Nucl. Phys. **B33** (1971) 173.

[28] G. 't Hooft and M. J. G. Veltman, *Regularization and Renormalization of Gauge Fields*, Nucl. Phys. **B44** (1972) 189.

[29] W. Heisenberg, *Zur Theorie des Ferromagnetismus*, Zeit. Phys. **49** (1928) 619.

[30] ATLAS Collaboration, *Observation of a new particle in the search for the Standard Model Higgs boson with the ATLAS detector at the LHC*, Phys. Lett. B **716** (2012) 1, arXiv: 1207.7214 [hep-ex].

[31] CMS Collaboration, *Observation of a new boson at a mass of 125 GeV with the CMS experiment at the LHC*, Phys. Lett. **B716** (2012) 30, arXiv: 1207.7235 [hep-ex].

[32] 'Summary plots from the ATLAS Standard Model physics group', URL: https://atlas.web.cern.ch/Atlas/GROUPS/PHYSICS/CombinedSummaryPlots/SM/index.html#ATLAS_a_SMSummary_TotalXsect.

[33] J. Ellis, *Searching for Particle Physics Beyond the Standard Model at the LHC and Elsewhere*, AIP Conf. Proc. **1446** (2012) 9, arXiv: 1102.5009 [hep-ph].

[34] J. Wess and B. Zumino, *Supergauge Transformations in Four-Dimensions*, Nucl. Phys. **B70** (1974) 39.

[35] A. Sirlin, *Radiative Corrections in the SU(2)-L x U(1) Theory: A Simple Renormalization Framework*, Phys. Rev. **D22** (1980) 971.

[36] M. Awramik et al., *Precise prediction for the W boson mass in the standard model*, Phys. Rev. **D69** (2004) 053006, arXiv: hep-ph/0311148 [hep-ph].

[37] A. Freitas, *Numerical multi-loop integrals and applications*, Prog. Part. Nucl. Phys. **90** (2016) 201, arXiv: 1604.00406 [hep-ph].

[38] S. Heinemeyer et al., *Implications of LHC search results on the W boson mass prediction in the MSSM*, JHEP **12** (2013) 084, arXiv: 1311.1663 [hep-ph].

[39] M. Baak et al., *The global electroweak fit at NNLO and prospects for the LHC and ILC*, Eur. Phys. J. **C74** (2014) 3046, arXiv: 1407.3792 [hep-ph].

[40] S. Schael et al., *Precision electroweak measurements on the Z resonance*, Phys. Rept. **427** (2006) 257, arXiv: hep-ex/0509008 [hep-ex].

[41] LEP Electroweak Working Group, *Precision Electroweak Measurements and Constraints on the Standard Model*, (2010), arXiv: 1012.2367 [hep-ex].

[42] ATLAS, CDF, CMS and D0 Collaboration, *First combination of Tevatron and LHC measurements of the top-quark mass*, (2014), arXiv: 1403.4427 [hep-ex].

[43] ATLAS Collaboration, *Measurement of the top quark mass in the $t\bar{t} \to$ dilepton channel from $\sqrt{s} = 8$ TeV ATLAS data*, Phys. Lett. **B761** (2016) 350, arXiv: 1606.02179 [hep-ex].

[44] C. Collaboration, *Measurement of the top quark mass using proton-proton data at $\sqrt{(s)} = 7$ and 8 TeV*, Phys. Rev. **D93** (2016) 072004, arXiv: 1509.04044 [hep-ex].

[45] ATLAS and CMS Collaborations, *Combined Measurement of the Higgs Boson Mass in pp Collisions at $\sqrt{s} = 7$ and 8 TeV with the ATLAS and CMS Experiments*, Phys. Rev. Lett. **114** (2015) 191803, arXiv: 1503.07589 [hep-ex].

[46] A. Akhundov et al., *The ZFITTER project*, Phys. Part. Nucl. **45** (2014) 529, arXiv: 1302.1395 [hep-ph].

[47] M. Baak et al., *The Electroweak Fit of the Standard Model after the Discovery of a New Boson at the LHC*, Eur. Phys. J. **C72** (2012) 2205, arXiv: 1209.2716 [hep-ph].

[48] J. de Blas et al., *Electroweak precision observables and Higgs-boson signal strengths in the Standard Model and beyond: present and future*, JHEP **12** (2016) 135, arXiv: 1608.01509 [hep-ph].

[49] G. Arnison et al., *Experimental Observation of Isolated Large Transverse Energy Electrons with Associated Missing Energy at s**(1/2) = 540-GeV*, Phys. Lett. **122B** (1983) 103, [,611(1983)].

[50] M. Banner et al., *Observation of Single Isolated Electrons of High Transverse Momentum in Events with Missing Transverse Energy at the CERN anti-p p Collider*, Phys. Lett. **122B** (1983) 476.

[51] ALEPH Collaboration, *Measurement of the W boson mass and width in e^+e^- collisions at LEP*, Eur. Phys. J. **C47** (2006) 309, arXiv: hep-ex/0605011 [hep-ex].

[52] DELPHI Collaboration, *Measurement of the Mass and Width of the W Boson in e^+e^- Collisions at $\sqrt{s}$ = 161-GeV - 209-GeV*, Eur. Phys. J. **C55** (2008) 1, arXiv: 0803.2534 [hep-ex].

[53] L3 Collaboration, P. Achard et al., *Measurement of the mass and the width of the W boson at LEP*, Eur. Phys. J. C **45** (2006) 569, arXiv: hep-ex/0511049.

[54] OPAL Collaboration, *Measurement of the mass and width of the W boson*, Eur. Phys. J. **C45** (2006) 307, arXiv: hep-ex/0508060 [hep-ex].

[55] DELPHI, OPAL, LEP Electroweak, ALEPH, L3 Collaboration, *Electroweak Measurements in Electron-Positron Collisions at W-Boson-Pair Energies at LEP*, Phys. Rept. **532** (2013) 119, arXiv: 1302.3415 [hep-ex].

[56] CDF Collaboration, *Precise measurement of the W-boson mass with the CDF II detector*, Phys. Rev. Lett. **108** (2012) 151803, arXiv: 1203.0275 [hep-ex].

[57] D0 Collaboration, *Measurement of the W boson mass with the D0 detector*, Phys. Rev. **D89** (2014) 012005, arXiv: 1310.8628 [hep-ex].

[58] CDF and D0 Collaborations, *Combination of CDF and D0 W-Boson Mass Measurements*, Phys. Rev. **D88** (2013) 052018, arXiv: 1307.7627 [hep-ex].

[59] ATLAS Collaboration, *Re-evaluation of the LHC potential for the measurement of Mw*, Eur. Phys. J. **C57** (2008) 627, arXiv: 0805.2093 [hep-ex].

[60] S. D. Drell and T.-M. Yan, *Massive Lepton Pair Production in Hadron-Hadron Collisions at High-Energies*, Phys. Rev. Lett. **25** (1970) 316, [Erratum: Phys. Rev. Lett.25,902(1970)].

[61] R. P. Feynman, *The behavior of hadron collisions at extreme energies*, Conf. Proc. **C690905** (1969) 237.

[62] J. M. Campbell, J. W. Huston and W. J. Stirling, *Hard Interactions of Quarks and Gluons: A Primer for LHC Physics*, Rept. Prog. Phys. **70** (2007) 89, arXiv: hep-ph/0611148 [hep-ph].

[63] G. Altarelli and G. Parisi, *Asymptotic Freedom in Parton Language*, Nucl. Phys. **B126** (1977) 298.

[64] Y. L. Dokshitzer, *Calculation of the Structure Functions for Deep Inelastic Scattering and e+ e- Annihilation by Perturbation Theory in Quantum Chromodynamics.*, Sov. Phys. JETP **46** (1977) 641, [Zh. Eksp. Teor. Fiz.73,1216(1977)].

[65] V. N. Gribov and L. N. Lipatov, *Deep inelastic e p scattering in perturbation theory*, Sov. J. Nucl. Phys. **15** (1972) 438, [Yad. Fiz.15,781(1972)].

[66] M. Schott and M. Dunford, *Review of single vector boson production in pp collisions at $\sqrt{s} = 7$ TeV*, Eur. Phys. J. **C74** (2014) 2916, arXiv: 1405.1160 [hep-ex].

[67] J. Pumplin et al., *Uncertainties of predictions from parton distribution functions. 2. The Hessian method*, Phys. Rev. **D65** (2001) 014013, arXiv: hep-ph/0101032 [hep-ph].

[68] P. Nadolsky et al., 'Progress in CTEQ-TEA PDF Analysis', *Proceedings, 20th International Workshop on Deep-Inelastic Scattering and Related Subjects (DIS 2012): Bonn, Germany, March 26-30, 2012*, [,417(2012)], 2012 417, arXiv: 1206.3321 [hep-ph], URL: http://inspirehep.net/record/1118434/files/arXiv:1206.3321.pdf.

[69] A. D. Martin et al., *Parton distributions for the LHC*, Eur. Phys. J. **C63** (2009) 189, arXiv: 0901.0002 [hep-ph].

[70] R. D. Ball et al., *Parton distributions for the LHC Run II*, JHEP **04** (2015) 040, arXiv: 1410.8849 [hep-ph].

[71] S. Dulat et al., *New parton distribution functions from a global analysis of quantum chromodynamics*, Phys. Rev. **D93** (2016) 033006, arXiv: 1506.07443 [hep-ph].

[72] J. C. Collins, D. E. Soper and G. F. Sterman, *Factorization of Hard Processes in QCD*, Adv. Ser. Direct. High Energy Phys. **5** (1989) 1, arXiv: hep-ph/0409313 [hep-ph].

[73] A. D. Martin et al., *Parton distributions and the LHC: W and Z production*, Eur. Phys. J. **C14** (2000) 133, arXiv: hep-ph/9907231 [hep-ph].

[74] J. C. Collins and D. E. Soper, *Angular Distribution of Dileptons in High-Energy Hadron Collisions*, Phys. Rev. **D16** (1977) 2219.

[75] ATLAS Collaboration, *Studies of theoretical uncertainties on the measurement of the mass of the W boson at the LHC*, ATL-PHYS-PUB-2014-015, 2014, URL: https://cds.cern.ch/record/1956455.

[76] ATLAS Collaboration, *Expected performance of the ATLAS experiment: detector, trigger and physics*, 2009, URL: https://cds.cern.ch/record/1125884.

[77] ATLAS Collaboration, *Electron reconstruction and identification efficiency measurements with the ATLAS detector using the 2011 LHC proton–proton collision data*, Eur. Phys. J. C **74** (2014) 2941, arXiv: 1404.2240 [hep-ex].

[78] ATLAS Collaboration, *Electron and photon energy calibration with the ATLAS detector using LHC Run 1 data*, Eur. Phys. J. C **74** (2014) 3071, arXiv: 1407.5063 [hep-ex].

[79] ATLAS Collaboration, *Measurement of the muon reconstruction performance of the ATLAS detector using 2011 and 2012 LHC proton–proton collision data*, Eur. Phys. J. C **74** (2014) 3130, arXiv: 1407.3935 [hep-ex].

[80] ATLAS Collaboration, *Measurement of the W-boson mass in pp collisions at $\sqrt{s} = 7$ TeV with the ATLAS detector*, (2017), arXiv: 1701.07240 [hep-ex].

[81] N. Andari, M. Boonekamp, S. Camarda, A. Dimitrievska, R. Hanna, O. Kivernyk, M. Schott, R. Stroehmer, N. Vranjes, S. Webb, C. Zimmermann, et al., *Measurement of m_W with 7 TeV data: W-boson mass measurement*, (2014), ATLAS Internal documentation: ATL-COM-PHYS-2014-1569, URL: https://cds.cern.ch/record/1976186.

[82] G. Brianti et al., *Summary report*, (1984) 78 p, URL: https://cds.cern.ch/record/151593.

[83] H. Edwards, *The Tevatron Energy Doubler: A Superconducting Accelerator*, Ann. Rev. Nucl. and Part. Sci **35** (1985) 605.

[84] 'HERA', URL: http://www.desy.de/research/facilities__projects/hera/index_eng.html.

[85] T. Behnke et al., *The International Linear Collider Technical Design Report - Volume 1: Executive Summary*, (2013), arXiv: 1306.6327 [physics.acc-ph].

[86] C.-S. S. Group, *CEPC-SPPC Preliminary Conceptual Design Report. 1. Physics and Detector*, (2015).

[87] M. Benedikt and F. Zimmermann, *Future Circular Colliders*, (2015).

[88] J. P. Delahaye, *The CLIC study of a multi-TeV linear collider*, Mod. Phys. Lett. **A26** (2011) 2997.

[89] S. Geer, *Muon Colliders and Neutrino Factories*, Ann. Rev. Nucl. Part. Sci. **59** (2009) 347.

[90] O. S. Bruning et al., *LHC Design Report Vol.1: The LHC Main Ring*, (2004).

[91] O. Buning et al., *LHC Design Report. 2. The LHC infrastructure and general services*, (2004).

[92] M. Benedikt et al., *LHC Design Report*, CERN, 2004, URL: https://cds.cern.ch/record/823808.

[93] L. R. Evans and P. Bryant, *LHC Machine*, J. Instrum. **3** (2008) S08001. 164 p, This report is an abridged version of the LHC Design Report (CERN-2004-003), URL: https://cds.cern.ch/record/1129806.

[94] E. A. Mobs, *The CERN accelerator complex. Complexe des accÃľlÃľrateurs du CERN*, (2016), General Photo, URL: https://cds.cern.ch/record/2225847.

[95] P. Grafstrom and W. Kozanecki, *Luminosity determination at proton colliders*, Prog. Part. Nucl. Phys. **81** (2015) 97.

[96] S van der Meer, 'Calibration of the effective beam height in the ISR', tech. rep. CERN-ISR-PO-68-31. ISR-PO-68-31, CERN, 1968, URL: https://cds.cern.ch/record/296752.

[97] ALICE Collaboration, *The ALICE experiment at the CERN LHC*, JINST **3** (2008) S08002.

[98] ATLAS Collaboration, *The ATLAS Experiment at the CERN Large Hadron Collider*, JINST **3** (2008) S08003.

[99] CMS Collaboration, *The CMS experiment at the CERN LHC*, JINST **3** (2008) S08004.

[100] LHCb Collaboration, *The LHCb Detector at the LHC*, JINST **3** (2008) S08005.

[101] LHCf Collaboration, *The LHCf detector at the CERN Large Hadron Collider*, JINST **3** (2008) S08006.

[102] MoEDAL Collaboration, *Technical Design Report of the MoEDAL Experiment*, (2009).

[103] TOTEM Collaboration, *The TOTEM experiment at the CERN Large Hadron Collider*, JINST **3** (2008) S08007.

[104] R. Bruce et al., 'LHC Run 2: Results and Challenges ', tech. rep. CERN-ACC-2016-0103, CERN, 2016, URL: https://cds.cern.ch/record/2201447.

[105] 'The LHC parameters during 2011 and 2012 data taking', Public Plots, URL: https://twiki.cern.ch/twiki/bin/view/AtlasPublic/LuminosityPublic\-Results.

[106] ATLAS Collaboration, *Improved luminosity determination in pp collisions at $\sqrt{s} = 7$ TeV using the ATLAS detector at the LHC*, Eur. Phys. J. C **73** (2013) 2518, arXiv: 1302.4393 [hep-ex].

[107] ATLAS Collaboration, *Luminosity determination in pp collisions at $\sqrt{s} = 8$ TeV using the ATLAS detector at the LHC*, Eur. Phys. J. C **76** (2016) 653, arXiv: 1608.03953 [hep-ex].

[108] 'The LHC parameters during 2015 and 2016 data taking', Public Plots, URL: https://twiki.cern.ch/twiki/bin/view/AtlasPublic/Luminosity\-PublicResultsRun2.

[109] *The High-Luminosity LHC*, (2015), URL: https://cds.cern.ch/record/2114693.

[110] 'Long term LHC schedule', Public Plots, URL: http://hilumilhc.web.cern.ch/about/hl-lhc-project.

[111] J. Pequenao, 'Computer generated image of the whole ATLAS detector', 2008, URL: https://cds.cern.ch/record/1095924.

[112] J. Pequenao and P. Schaffner, 'An computer generated image representing how ATLAS detects particles', 2013, URL: https://cds.cern.ch/record/1505342.

[113] ATLAS Collaboration, *ATLAS central solenoid: Technical Design Report*, Technical Design Report ATLAS, Electronic version not available, CERN, 1997, URL: https://cds.cern.ch/record/331067.

[114] ATLAS Collaboration, *ATLAS barrel toroid: Technical Design Report*, Technical Design Report ATLAS, Electronic version not available, CERN, 1997, URL: https://cds.cern.ch/record/331065.

[115] ATLAS Collaboration, *ATLAS end-cap toroids: Technical Design Report*, Technical Design Report ATLAS, Electronic version not available, CERN, 1997, URL: https://cds.cern.ch/record/331066.

[116] ATLAS Collaboration, *ATLAS inner detector: Technical Design Report, 1*, Technical Design Report ATLAS, CERN, 1997, URL: https://cds.cern.ch/record/331063.

[117] ATLAS Collaboration, *ATLAS inner detector: Technical Design Report, 2*, Technical Design Report ATLAS, CERN, 1997, URL: https://cds.cern.ch/record/331064.

[118] J. Pequenao, 'Computer generated image of the ATLAS inner detector', 2008, URL: https://cds.cern.ch/record/1095926.

[119] ATLAS Collaboration, *ATLAS pixel detector: Technical Design Report*, Technical Design Report ATLAS, CERN, 1998, URL: https://cds.cern.ch/record/381263.

[120] ATLAS Collaboration, *ATLAS pixel detector electronics and sensors*, J. Instrum. **3** (2008) P07007, URL: https://cds.cern.ch/record/1119279.

[121] ATLAS Collaboration, 'The Barrel Modules of the ATLAS SemiConductor Tracker', tech. rep. ATL-INDET-PUB-2006-005. ATL-COM-INDET-2006-009. CERN-ATL-COM-INDET-2006-009, CERN, 2006, URL: https://cds.cern.ch/record/974073.

[122] ATLAS Collaboration, *The ATLAS semiconductor tracker end-cap module*, Nucl. Instrum. Methods Phys. Res., A **575** (2007) 353, URL: https://cds.cern.ch/record/1063618.

[123] ATLAS Collaboration, *The Silicon Microstrip Sensors of the ATLAS SemiConductor Tracker*, (2007), URL: https://cds.cern.ch/record/1019885.

[124] ATLAS Collaboration, *The ATLAS TRT Barrel Detector*, J. Instrum. **3** (2008) P02014, URL: https://cds.cern.ch/record/1094548.

[125] ATLAS Collaboration, *The ATLAS TRT end-cap detectors*, J. Instrum. **3** (2008) P10003, URL: https://cds.cern.ch/record/1151338.

[126] ATLAS Collaboration, *The ATLAS Transition Radiation Tracker (TRT) proportional drift tube: design and performance*, J. Instrum. **3** (2008) P02013, URL: https://cds.cern.ch/record/1094549.

[127] ATLAS Collaboration, 'ATLAS Insertable B-Layer Technical Design Report', tech. rep. CERN-LHCC-2010-013. ATLAS-TDR-19, 2010, URL: https://cds.cern.ch/record/1291633.

[128] ATLAS Collaboration, *Study of the mechanical stability of the ATLAS Insertable B-Layer*, ATL-INDET-PUB-2015-001, 2015, URL: https://cds.cern.ch/record/2022587.

[129] ATLAS Collaboration, *The Optimization of ATLAS Track Reconstruction in Dense Environments*, ATL-PHYS-PUB-2015-006, 2015, URL: https://cds.cern.ch/record/2002609.

[130] ATLAS Collaboration, *Expected performance of the ATLAS b-tagging algorithms in Run-2*, ATL-PHYS-PUB-2015-022, 2015, URL: https://cds.cern.ch/record/2037697.

[131] ATLAS Collaboration, *ATLAS calorimeter performance: Technical Design Report*, Technical Design Report ATLAS, CERN, 1996, URL: https://cds.cern.ch/record/331059.

[132] ATLAS Collaboration, *ATLAS liquid-argon calorimeter: Technical Design Report*, Technical Design Report ATLAS, CERN, 1996, URL: https://cds.cern.ch/record/331061.

[133] ATLAS Collaboration, *ATLAS tile calorimeter: Technical Design Report*, Technical Design Report ATLAS, CERN, 1996, URL: https://cds.cern.ch/record/331062.

[134] J. Pequenao, 'Computer Generated image of the ATLAS calorimeter', 2008, URL: http://cds.cern.ch/record/1095927.

[135] ATLAS Collaboration, *ATLAS muon spectrometer: Technical Design Report*, Technical Design Report ATLAS, CERN, 1997, URL: https://cds.cern.ch/record/331068.

[136] J. Pequenao, 'Computer generated image of the ATLAS Muons subsystem', 2008, URL: http://cds.cern.ch/record/1095929.

[137] ATLAS Collaboration, *Construction and Test of MDT Chambers for the ATLAS Muon Spectrometer*, vol. 461, arXiv:1604.02000. MPP-2016-071. MPI-PHE-2000-11, 2016 17, URL: https://cds.cern.ch/record/2145043.

[138] ATLAS Collaboration, *Cathode strip chambers in ATLAS: Installation, commissioning and in situ performance*, vol. 56, 2009 1568.

[139] ATLAS Collaboration, *Commissioning of the ATLAS Muon Spectrometer with cosmic rays*, Eur. Phys. J. C **70** (2010) 875, arXiv: 1006.4384 [hep-ex].

[140] ATLAS Collaboration, *The RPC first level muon trigger in the barrel of the ATLAS experiment*, vol. 158, 2006 11, URL: https://cds.cern.ch/record/1043004.

[141] ATLAS Collaboration, *A thin multiwire chamber operating in the high multiplication mode*, vol. 217, 1983 265, URL: https://cds.cern.ch/record/149171.

[142] J Wotschack, *ATLAS Muon Chamber Construction Parameters for CSC, MDT, and RPC chambers*, ATL-MUON-PUB-2008-006. ATL-COM-MUON-2008-008, Back-up document for the ATLAS Detector Paper, 2008, URL: https://cds.cern.ch/record/1099400.

[143] ATLAS Collaboration, *ATLAS high-level trigger, data-acquisition and controls: Technical Design Report*, Technical Design Report ATLAS, CERN, 2003, URL: https://cds.cern.ch/record/616089.

[144] ATLAS Collaboration, *Performance of the ATLAS Trigger System in 2010*, Eur. Phys. J. C **72** (2012) 1849, arXiv: 1110.1530 [hep-ex].

[145] ATLAS Collaboration, *2015 start-up trigger menu and initial performance assessment of the ATLAS trigger using Run-2 data*, ATL-DAQ-PUB-2016-001, 2016, URL: https://cds.cern.ch/record/2136007/.

[146] ATLAS Collaboration, *The ATLAS Simulation Infrastructure*, Eur. Phys. J. C **70** (2010) 823, arXiv: 1005.4568 [hep-ex].

[147] R. Brun and F. Rademakers, *ROOT - An object oriented data analysis framework*, Nucl. Instrum. Meth. **A389** (1997) 81, ISSN: 0168-9002, URL: http://www.sciencedirect.com/science/article/pii/S016890029700048X.

[148] ATLAS Collaboration, *ATLAS Computing: technical design report*, Technical Design Report ATLAS, CERN, 2005, URL: https://cds.cern.ch/record/837738.

[149] S. A. et al., *Geant4 - a simulation toolkit*, Nucl. Instrum. Meth. **A506** (2003) 250, ISSN: 0168-9002, URL: http://www.sciencedirect.com/science/article/pii/S0168900203013688.

[150] T. Sjostrand, S. Mrenna and P. Z. Skands, *PYTHIA 6.4 Physics and Manual*, JHEP **05** (2006) 026, arXiv: hep-ph/0603175 [hep-ph].

[151] G. Corcella et al., *HERWIG 6: An Event generator for hadron emission reactions with interfering gluons (including supersymmetric processes)*, JHEP **01** (2001) 010, arXiv: hep-ph/0011363 [hep-ph].

[152] J. M. Butterworth, J. R. Forshaw and M. H. Seymour, *Multiparton interactions in photoproduction at HERA*, Z. Phys. **C72** (1996) 637, arXiv: hep-ph/9601371 [hep-ph].

[153] S. Frixione, P. Nason and C. Oleari, *Matching NLO QCD computations with Parton Shower simulations: the POWHEG method*, JHEP **11** (2007) 070, arXiv: 0709.2092 [hep-ph].

[154] S. Frixione and B. R. Webber, *Matching NLO QCD computations and parton shower simulations*, JHEP **06** (2002) 029, arXiv: hep-ph/0204244 [hep-ph].

[155] R. Gavin et al., *FEWZ 2.0: A code for hadronic Z production at next-to-next-to-leading order*, Comput. Phys. Commun. **182** (2011) 2388, arXiv: 1011.3540 [hep-ph].

[156] R. Boughezal et al., *Color singlet production at NNLO in MCFM*, Eur. Phys. J. **C77** (2017) 7, arXiv: 1605.08011 [hep-ph].

[157] S. Catani et al., *Vector boson production at hadron colliders: a fully exclusive QCD calculation at NNLO*, Phys. Rev. Lett. **103** (2009) 082001, arXiv: 0903.2120 [hep-ph].

[158] S. Catani et al., *Vector boson production at hadron colliders: transverse-momentum resummation and leptonic decay*, JHEP **12** (2015) 047, arXiv: 1507.06937 [hep-ph].

[159] G. A. Ladinsky and C. P. Yuan, *The Nonperturbative regime in QCD resummation for gauge boson production at hadron colliders*, Phys. Rev. **D50** (1994) R4239, arXiv: hep-ph/9311341 [hep-ph].

[160] C. Balazs and C. P. Yuan, *Soft gluon effects on lepton pairs at hadron colliders*, Phys. Rev. **D56** (1997) 5558, arXiv: hep-ph/9704258 [hep-ph].

[161] K. Hamilton, P. Nason and G. Zanderighi, *MINLO: Multi-Scale Improved NLO*, JHEP **10** (2012) 155, arXiv: 1206.3572 [hep-ph].

[162] E. Barberio, B. van Eijk and Z. Was, *PHOTOS: A Universal Monte Carlo for QED radiative corrections in decays*, Comput. Phys. Commun. **66** (1991) 115.

[163] W. PÅĆaczek, S. Jadach and M. W. Krasny, *Drell-Yan processes with WINHAC*, Acta Phys. Polon. **B44** (2013) 2171, arXiv: 1310.5994 [hep-ph].

[164] A. Arbuzov et al., *One-loop corrections to the Drell-Yan process in SANC. I. The Charged current case*, Eur. Phys. J. **C46** (2006) 407, [Erratum: Eur. Phys. J.C50,505(2007)], arXiv: hep-ph/0506110 [hep-ph].

[165] ATLAS Collaboration, *Measurement of the Z/γ^* boson transverse momentum distribution in pp collisions at $\sqrt{s} = 7$ TeV with the ATLAS detector*, JHEP **09** (2014) 145, arXiv: 1406.3660 [hep-ex].

[166] H.-L. Lai et al., *New parton distributions for collider physics*, Phys. Rev. **D82** (2010) 074024, arXiv: 1007.2241 [hep-ph].

[167] J. Pumplin et al., *New generation of parton distributions with uncertainties from global QCD analysis*, JHEP **07** (2002) 012, arXiv: hep-ph/0201195 [hep-ph].

[168] ATLAS Collaboration, *Summary of ATLAS Pythia 8 tunes*, ATL-PHYS-PUB-2012-003, 2012, URL: https://cds.cern.ch/record/1474107.

[169] ATLAS Collaboration, *Precision measurement and interpretation of inclusive W^+, W^- and Z/γ^* production cross sections with the ATLAS detector*, (2016), arXiv: 1612.03016 [hep-ex].

[170] ATLAS Collaboration, *Measurement of the $t\bar{t}$ production cross-section using $e\mu$ events with b-tagged jets in pp collisions at $\sqrt{s} = 7$ and 8 TeV with the ATLAS detector*, Eur. Phys. J. C **74** (2014) 3109, arXiv: 1406.5375 [hep-ex].

[171] J. M. Campbell and R. K. Ellis, *An Update on vector boson pair production at hadron colliders*, Phys. Rev. **D60** (1999) 113006, arXiv: hep-ph/9905386 [hep-ph].

[172] N. Andari, M. Boonekamp, S. Camarda, R. Hanna, *Measurement of m_W at 7 TeV: Physics modeling*, (2014), ATLAS Internal documentation: ATL-COM-PHYS-2014-1436, URL: https://cds.cern.ch/record/1966965.

[173] ATLAS Collaboration, *Measurement of the angular coefficients in Z-boson events using electron and muon pairs from data taken at $\sqrt{s} = 8$ TeV with the ATLAS detector*, JHEP **08** (2016) 159, arXiv: 1606.00689 [hep-ex].

[174] J. Gao et al., *CT10 next-to-next-to-leading order global analysis of QCD*, Phys. Rev. **D89** (2014) 033009, arXiv: 1302.6246 [hep-ph].

[175] ATLAS Collaboration, *Measurement of the transverse momentum distribution of W bosons in pp collisions at $\sqrt{s} = 7$ TeV with the ATLAS detector*, Phys. Rev. D **85** (2012) 012005, arXiv: 1108.6308 [hep-ex].

[176] ATLAS Collaboration, *Performance of the ATLAS Inner Detector Track and Vertex Reconstruction in High Pile-Up LHC Environment*, ATLAS-CONF-2012-042, 2012, URL: https://cds.cern.ch/record/1435196.

[177] ATLAS Collaboration, *Alignment of the ATLAS Inner Detector and its Performance in 2012*, ATLAS-CONF-2014-047, 2014, URL: https://cds.cern.ch/record/1741021.

[178] M. Boonekamp, JB. Blanchard, *Measurement of m_W at 7 TeV: Electron performance corrections and uncertainties*, (2014), ATLAS Internal documentation: ATL-COM-PHYS-2014-1434, URL: https://cds.cern.ch/record/11966963.

[179] Nicolaidou, R. and Chevalier, L. and Hassani, S. and Laporte, J. F. and Le Menedeu, E. and Ouraou, A., *Muon identification procedure for the ATLAS detector at the LHC using Muonboy reconstruction package and tests of its performance using cosmic rays and single beam data*, J. Phys. Conf. Ser. **219** (2010) 032052.

[180] ATLAS Collaboration, *Topological cell clustering in the ATLAS calorimeters and its performance in LHC Run 1*, (2016), arXiv: 1603.02934 [hep-ex].

[181] ATLAS Collaboration, *Jet energy measurement and its systematic uncertainty in proton–proton collisions at $\sqrt{s} = 7$ TeV with the ATLAS detector*, Eur. Phys. J. C **75** (2015) 17, arXiv: 1406.0076 [hep-ex].

[182] ATLAS Collaboration, *Performance of missing transverse momentum reconstruction in proton–proton collisions at $\sqrt{s} = 7$ TeV with ATLAS*, Eur. Phys. J. C **72** (2012) 1844, arXiv: 1108.5602 [hep-ex].

[183] ATLAS Collaboration, *Measurement of the $W \to \ell\nu$ and $Z/\gamma^* \to \ell\ell$ production cross sections in proton–proton collisions at $\sqrt{s} = 7$ TeV with the ATLAS detector*, JHEP **12** (2010) 060, arXiv: 1010.2130 [hep-ex].

[184] ATLAS Collaboration, *Measurement of the inclusive $W^\pm$ and Z/γ^* cross sections in the e and μ decay channels in pp collisions at $\sqrt{s} = 7$ TeV with the ATLAS detector*, Phys. Rev. D **85** (2012) 072004, arXiv: 1109.5141 [hep-ex].

[185] ATLAS Collaboration, *Measurement of $W^\pm$ and Z-boson production cross sections in pp collisions at $\sqrt{s} = 13$ TeV with the ATLAS detector*, Phys. Lett. B **759** (2016) 601, arXiv: 1603.09222 [hep-ex].

[186] L. Chevalier, A. Dimitrievska, N. Vranjes, *Muon performance studies using $J/\psi \to \mu^+\mu^-$ at $\sqrt{s} = 7$ TeV and $\sqrt{s} = 8$ TeV of pp collisions*, (2013), URL: https://cds.cern.ch/record/1596789.

[187] G. Artoni, M. Corradi, A. Dimitrievska, F. Sforza, N. Vranjes, P. Fleischmann, *Muon momentum scale and resolution corrections evaluated with $Z \to \mu\mu$ and $J/\psi \to \mu\mu$ decays on Run I ATLAS data*, (2014), Preliminary version of MCP scale and momentum corrections for 2012 data, URL: https://cds.cern.ch/record/1643495.

[188] ATLAS Collaboration, *Measurement of the Higgs boson mass from the $H \to \gamma\gamma$ and $H \to ZZ^* \to 4\ell$ channels in pp collisions at center-of-mass energies of 7 and 8 TeV with the ATLAS detector*, Phys. Rev. D **90** (2014) 052004, arXiv: 1406.3827 [hep-ex].

[189] T. Adye, ..., A. Dimitrievska, ..., N. Vranjes, et al., *Higgs mass measurements and uncertainties in 2011 and 2012 data*, (2012), URL: https://cds.cern.ch/record/1498240.

[190] T Lagouri et al., *A Muon Identification and Combined Reconstruction Procedure for the ATLAS Detector at the LHC at CERN*, (2003), revised version number 1 submitted on 2003-10-30 18:34:15, URL: https://cds.cern.ch/record/681410.

[191] L. Landau, *On the energy loss of fast particles by ionization*, J. Phys.(USSR) **8** (1944) 201.

[192] ATLAS Collaboration, *Muon reconstruction performance of the ATLAS detector in proton–proton collision data at* $\sqrt{s} = 13$ *TeV*, Eur. Phys. J. C **76** (2016) 292, arXiv: 1603.05598 [hep-ex].

[193] J. J. Aubert et al., *Experimental Observation of a Heavy Particle J*, Phys. Rev. Lett. **33** (1974) 1404.

[194] J. E. Augustin et al., *Discovery of a Narrow Resonance in* e^+e^- *Annihilation*, Phys. Rev. Lett. **33** (1974) 1406, [Adv. Exp. Phys.5,141(1976)].

[195] A. Collaboration, 'ATLAS event at 13 TeV - JPsi candidate - run: 265545, lb: 68, event: 1020606', General Photo, 2015, URL: https://cds.cern.ch/record/2019362.

[196] ATLAS Collaboration, *Muon reconstruction efficiency and momentum resolution of the ATLAS experiment in proton–proton collisions at* $\sqrt{s} = 7$ *TeV in 2010*, Eur. Phys. J. C **74** (2014) 3034, arXiv: 1404.4562 [hep-ex].

[197] J. E. Gaiser, 'Charmonium Spectroscopy From Radiative Decays of the J/ψ and ψ'', PhD thesis: SLAC, 1982, URL: http://www-public.slac.stanford.edu/sciDoc/docMeta.aspx?slacPubNumber=slac-r-255.html.

[198] M. Schott, G. Siragusa, J. Cuth, T. Lin, *Measurement of* m_W *at 7 TeV: Reconstruction of the hadronic recoil*, (2014), URL: https://cds.cern.ch/record/1966964.

[199] A. Dimitrievska, N. Vranjes, M. Schott, M. Boonekamp, *Measurement of* m_W *at 7 TeV: Hadronic recoil corrections*, (2015), URL: https://cds.cern.ch/record/2013274.

[200] D0 Collaboration, *A Novel method for modeling the recoil in W boson events at hadron collider*, Nucl. Instrum. Meth. **A609** (2009) 250, arXiv: 0907.3713 [hep-ex].

[201] T.H.L. Nguyen, N. Besson, M. Boonekamp, *ETmiss from the reconstruction and calibration of the hadronic recoil*, (2010), URL: https://cds.cern.ch/record/1241042.

[202] ATLAS Collaboration, *Using Event Weights to account for differences in Instantaneous Luminosity and Trigger Prescale in Monte Carlo and Data*, ATL-COM-SOFT-2015-119, 2015, URL: https://cds.cern.ch/record/2014726.

[203] ATLAS Collaboration, *Reconstruction of primary vertices at the ATLAS experiment in Run 1 protonâĂŞproton collisions at the LHC*, Eur. Phys. J. **C77** (2017) 332, arXiv: 1611.10235 [physics.ins-det].

[204] L. Devroye, *"Non-Uniform Random Variate Generation"*, Available at http://www.eirene.de/Devroye.pdf, Springer-Verlag, 1986.

[205] ATLAS Collaboration, *Measurements of the photon identification efficiency with the ATLAS detector using* 4.9 fb^{-1} *of pp collision data collected in 2011*, ATLAS-CONF-2012-123, 2012, URL: https://cds.cern.ch/record/1473426.

[206] B. Efron, *Bootstrap Methods: Another Look at the Jackknife*, The Annals of Statistics **7** (1979) 1, ISSN: 00905364, URL: http://www.jstor.org/stable/2958830.

[207] ATLAS Collaboration, *Study of alignment-related systematic effects on the ATLAS Inner Detector track reconstruction*, ATLAS-CONF-2012-141, 2012, URL: https://cds.cern.ch/record/1483518.

[208] J Wenninger, 'Energy Calibration of the LHC Beams at 4 TeV', tech. rep. CERN-ATS-2013-040, CERN, 2013, URL: https://cds.cern.ch/record/1546734.

[209] T. Sjostrand and P. Z. Skands, *Transverse-momentum-ordered showers and interleaved multiple interactions*, Eur. Phys. J. **C39** (2005) 129, arXiv: hep-ph/0408302 [hep-ph].

[210] M. Bonvini, A. S. Papanastasiou and F. J. Tackmann, *Matched predictions for the $b\bar{b}H$ cross section at the 13 TeV LHC*, JHEP **10** (2016) 053, arXiv: 1605.01733 [hep-ph].

[211] F. D. Aaron et al., *Measurement of the Inclusive ep Scattering Cross Section at Low Q^2 and x at HERA*, Eur. Phys. J. **C63** (2009) 625, arXiv: 0904.0929 [hep-ex].

[212] ATLAS Collaboration, *Jet reconstruction and performance using particle flow with the ATLAS Detector*, (2017), arXiv: 1703.10485 [hep-ex].

Appendix

A

Cut-flow tables for the W-boson event selection

The cut-flows for data and MC signal samples, based on the event selection described in Section 3.5, are shown in Tables A.1 and A.3 for the electron and muon channels respectively. The cut-flows for MC background samples are shown in Tables A.2 and A.4 for the electron and muon channels respectively. All MC cut-flows are scaled to an integrated luminosity of 4.6 fb^{-1} and 4.1 fb^{-1} for electron and muon channel respectively. The muon isolation cut is shown as part of muon selection while for the electron the isolation is explicitly shown. After all selection criteria applied there is 5.89 and 7.84 million W-boson candidates in electron and muon channel respectively.

Table A.1: Cut-flow in the $W \to e\nu$ channel in the signal region.

Cut	Data	$W^+ \to e\nu$		$W^- \to e\nu$	
	N_{evt}	N_{evt}	Cut efficiency [%]	N_{evt}	Cut efficiency [%]
No cut	185039772	29129499	100.000	20092555	100.000
Primary Vertex	184249665	28998609	99.551	20014265	99.610
GRL	167449232	28998609	99.551	20014265	99.610
Trigger	153832216	13838494	47.507	8929879	44.444
$p_{\text{T}}^{\text{e}} > 30$ GeV	22902461	7589574	26.055	5292189	26.339
Veto tight++	16902915	6077780	20.865	4295834	21.380
One tight++	16233973	6077664	20.864	4295749	21.380
Trigger Matching	16164844	6077518	20.864	4295640	21.379
Jet Cleaning	16147902	6075311	20.856	4294135	21.372
LAr simple veto	16105063	6069418	20.836	4289625	21.349
Isolation (calorimeter)	14198159	5998321	20.592	4237721	21.091
Isolation (track)	12830863	5866093	20.138	4145913	20.634
$u_{\text{T}} < 30$ GeV	8390077	4405066	15.122	3090832	15.383
$m_{\text{T}} > 60$ GeV	6681997	3699439	12.700	2637380	13.126
$E_{\text{T}}^{\text{miss}} > 30$ GeV	5885241	3278533	11.255	2335603	11.624

Table A.2: Cut-flow in the $W \to e\nu$ channel for background processes. The numbers represents number of events normalised according to the cross sections listed in Table 3.1 and normalised to the integrated luminosity of the data sample.

Cut	$W \to \tau\nu$	$Z \to ee$	top	WW/WZ/ZZ	$Z \to \tau\tau$
No cut	7041098	4546477	871755	134852	1195589
Primary Vertex	7003917	4525771	871377	134588	1191224
GRL	7003917	4525771	871377	134588	1191224
Trigger	848239	3163313	217990	44386	173267
$p_{\mathrm{T}}^{\mathrm{e}} > 30$ GeV	238701	2101526	147363	29192	56279
Veto tight++	193059	1562570	124684	23224	45550
One tight++	193044	929921	120716	20395	44636
Trigger Matching	193038	924780	120679	20374	44629
Jet Cleaning	192957	924096	120529	20348	44559
LAr simple veto	192533	914458	118669	20197	44365
Isolation (calorimeter)	190571	901816	114706	19761	43890
Isolation (track)	186783	880120	106641	18904	42965
$u_{\mathrm{T}} < 30$ GeV	106568	332214	11833	5979	17372
$m_{\mathrm{T}} > 60$ GeV	67357	229545	10319	5172	8438
$E_{\mathrm{T}}^{\mathrm{miss}} > 30$ GeV	58453	196292	9317	4654	6855

Table A.3: Cut-flow in the $W \to \mu\nu$ channel in the signal region.

Cut	Data	$W^+ \to \mu\nu$		$W^- \to \mu\nu$	
	N_{evt}	N_{evt}	Cut efficiency [%]	N_{evt}	Cut efficiency [%]
No cut	154532753	29129499	100.000	20092555	100.000
GRL	140976111	29129499	100.000	20092555	100.000
Primary Vertex	139003866	28956395	99.406	19991586	99.497
Trigger	116109480	14838771	50.941	9035835	44.971
Muon Selection	42951700	12713212	43.644	7903333	39.335
Muon Veto	41153751	12713068	43.643	7903195	39.334
Trigger Matching	41044423	12710370	43.634	7901520	39.326
Jet Cleaning	40996618	12705864	43.619	7898825	39.312
LAr simple veto	40915645	12694963	43.581	7891061	39.274
$p_{\mathrm{T}}^{\mu} > 30$ GeV and remove L3+L4	16077674	7670767	26.333	5181689	25.789
$u_{\mathrm{T}} < 30$ GeV	10811788	5814759	19.962	3894645	19.384
$m_{\mathrm{T}} > 60$ GeV	8851402	4885304	16.771	3322739	16.537
$E_{\mathrm{T}}^{\mathrm{miss}} > 30$ GeV	7844778	4342572	14.908	2950049	14.682

Table A.4: Cut-flow in the $W \to \mu\nu$ channel for background processes. The numbers represents number of events normalised according to the cross sections listed in Table 3.1 and normalised to the integrated luminosity of the data sample

Cut	$W \to \tau\nu$	$Z \to \mu\mu$	top	WW/WZ/ZZ	$Z \to \tau\tau$
No cut	7041098	4546477	871755	134852	1195589
GRL	7041098	4546477	871755	134852	1195589
Primary Vertex	7003914	4519068	871377	134588	1191224
Trigger	1319622	3304329	230939	45372	249997
Muon Selection	912106	3102010	181127	38989	179908
Muon Veto	912084	1423848	172580	34813	175628
Trigger Matching	911863	1369356	170252	34646	175123
Jet Cleaning	911546	1365933	170045	34604	174768
LAr simple veto	910452	1364188	167347	34396	174181
$p_{\mathrm{T}}^{\mu} > 30$ GeV and remove L3+L4	242669	839816	118148	23370	54751
$u_{\mathrm{T}} < 30$ GeV	142062	577069	13784	7688	22405
$m_{\mathrm{T}} > 60$ GeV	90351	476111	11859	6652	10715
$E_{\mathrm{T}}^{\mathrm{miss}} > 30$ GeV	78674	420111	10666	5971	8721

B

Fitting range scans

Figures B.1 – B.4 present a systematic study of the fully combined measurement result when scanning the fitting ranges in steps of 1 GeV as follows:

- $30 - 35$ GeV for the lower boundary of the p_{T}^{ℓ} fits
- $45 - 50$ GeV for the upper boundary of the p_{T}^{ℓ} fits
- $65 - 70$ GeV for the lower boundary of the m_{T} fits
- $90 - 100$ GeV for the upper boundary of the m_{T} fits

The fitting range with the smallest overall uncertainty is chosen as a optimal. The statistical and total uncertainty is evaluated comparing to the optimal fitting range and calculated with Equation 6.13. The difference between the fitting ranges is shown on Figures B.5 – B.8.

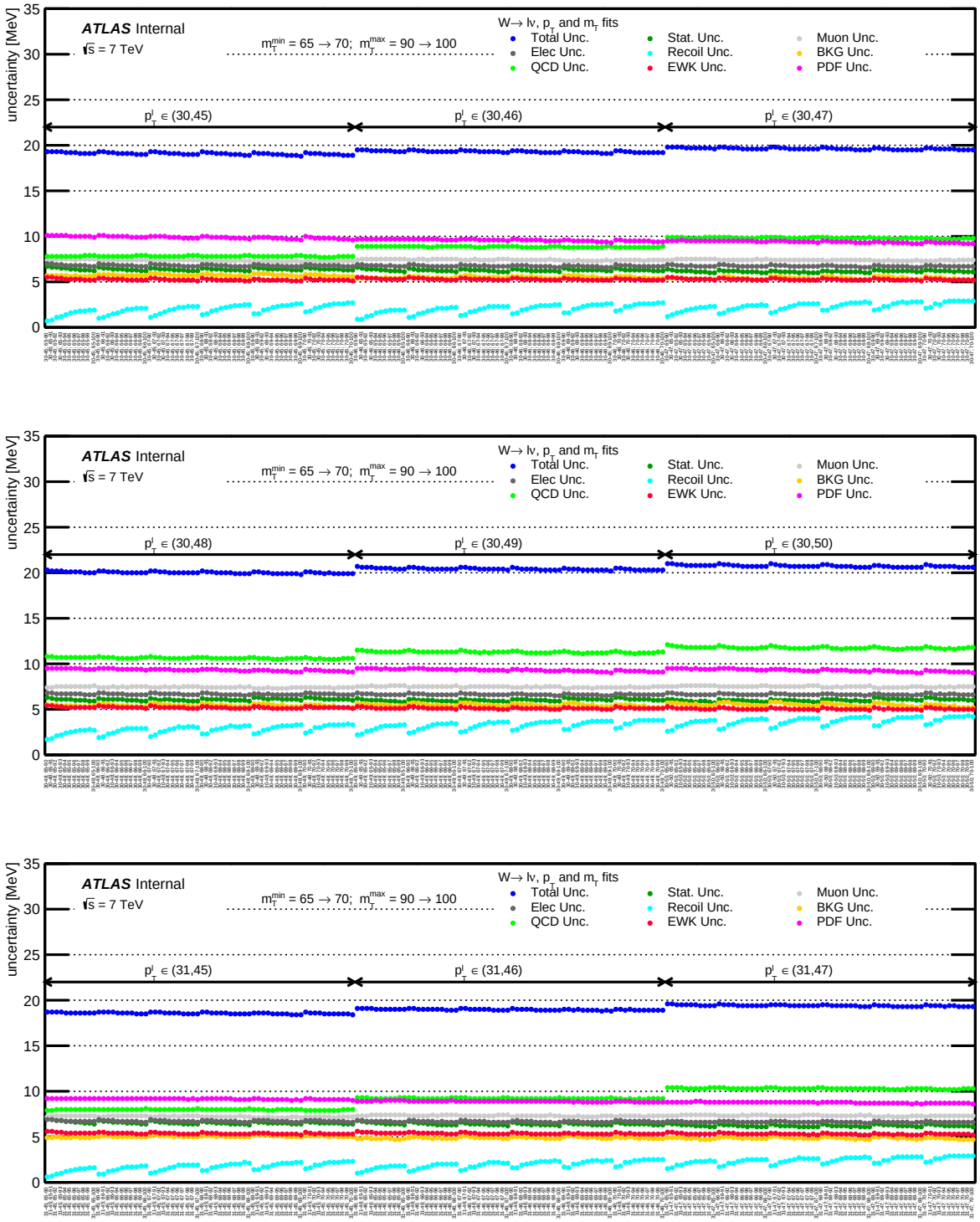

Figure B.1: Dependence of the statistical and systematic uncertainties on the fitting ranges for the fully combined measurement.

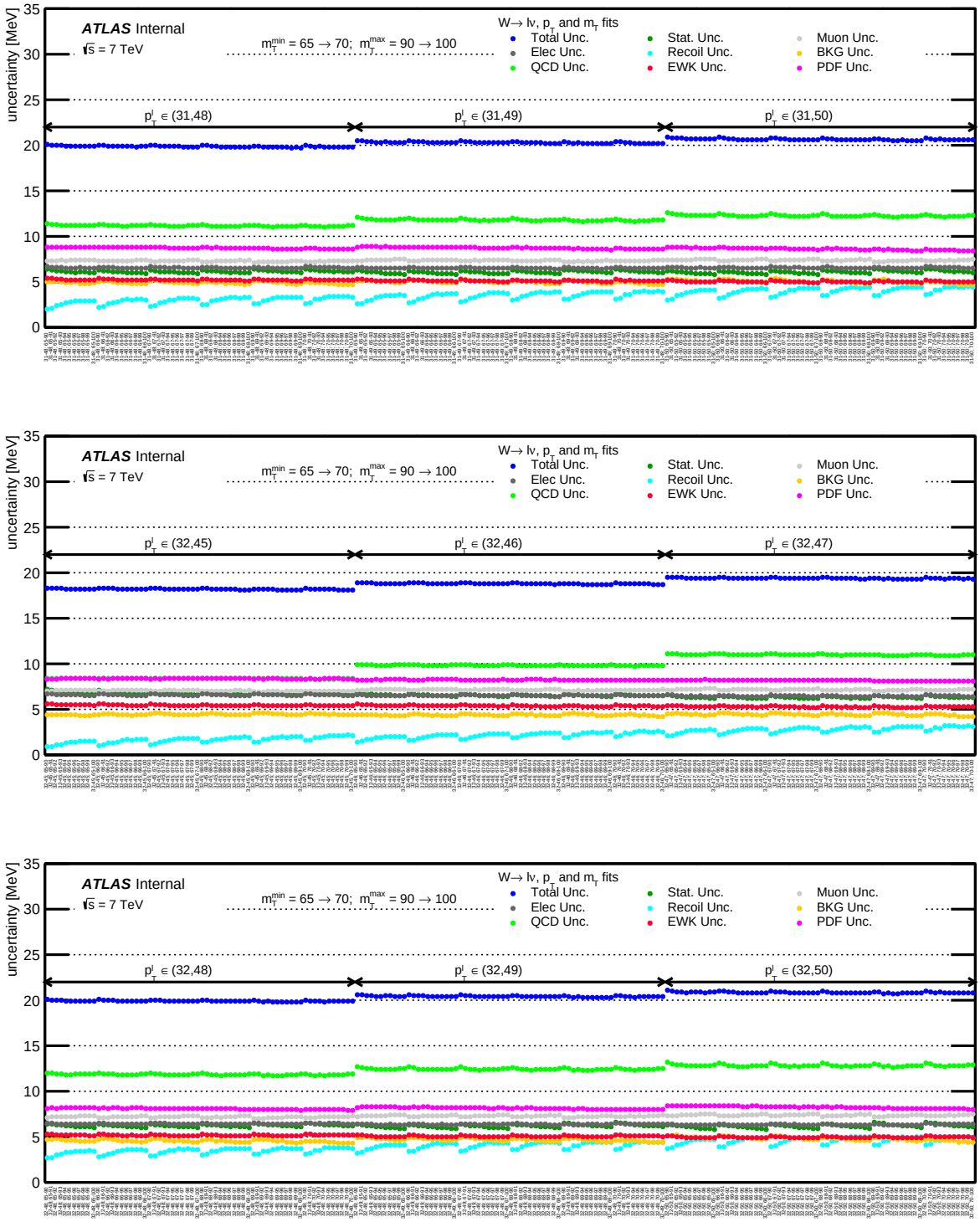

Figure B.2: Dependence of the statistical and systematic uncertainties on the fitting ranges for the fully combined measurement.

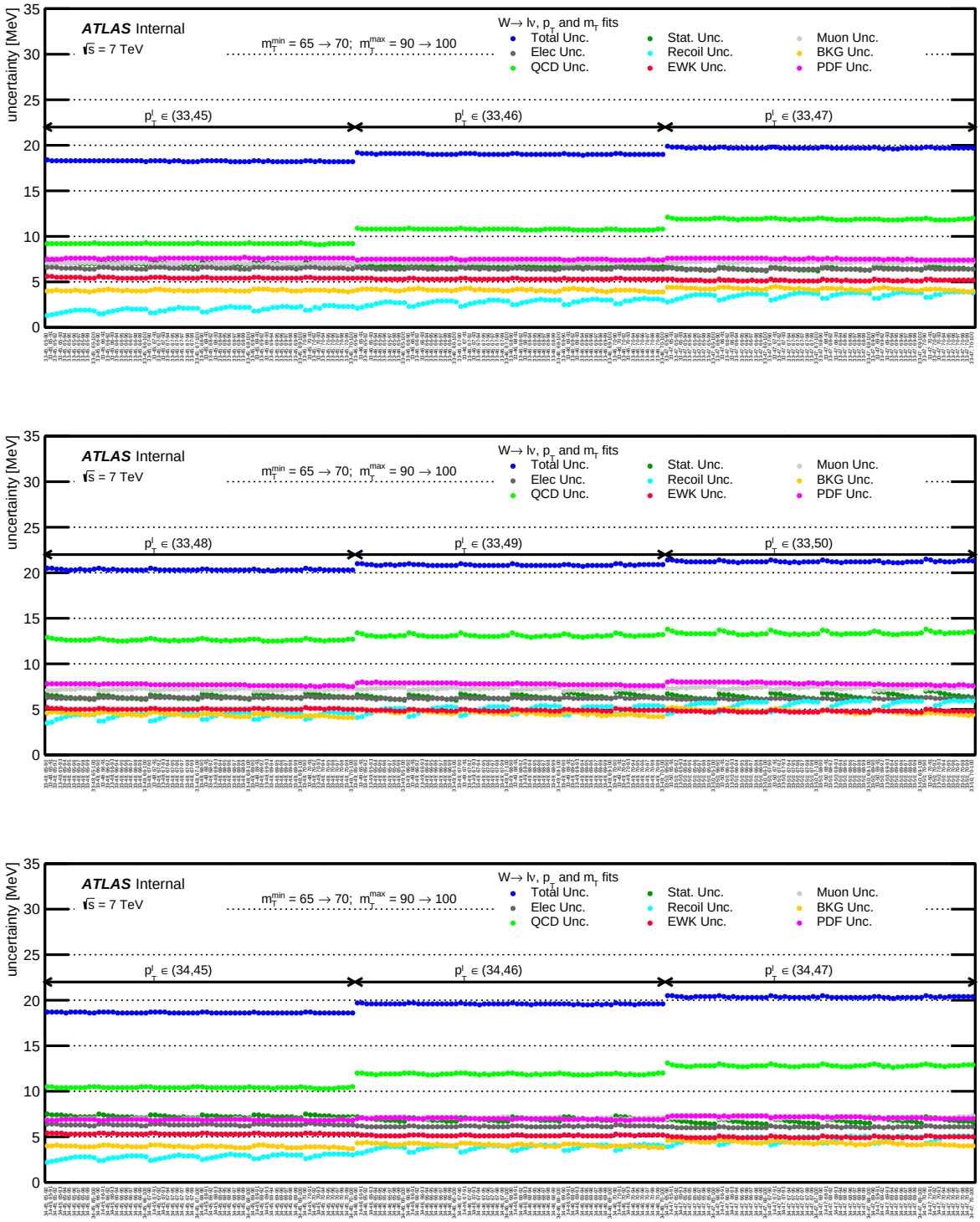

Figure B.3: Dependence of the statistical and systematic uncertainties on the fitting ranges for the fully combined measurement.

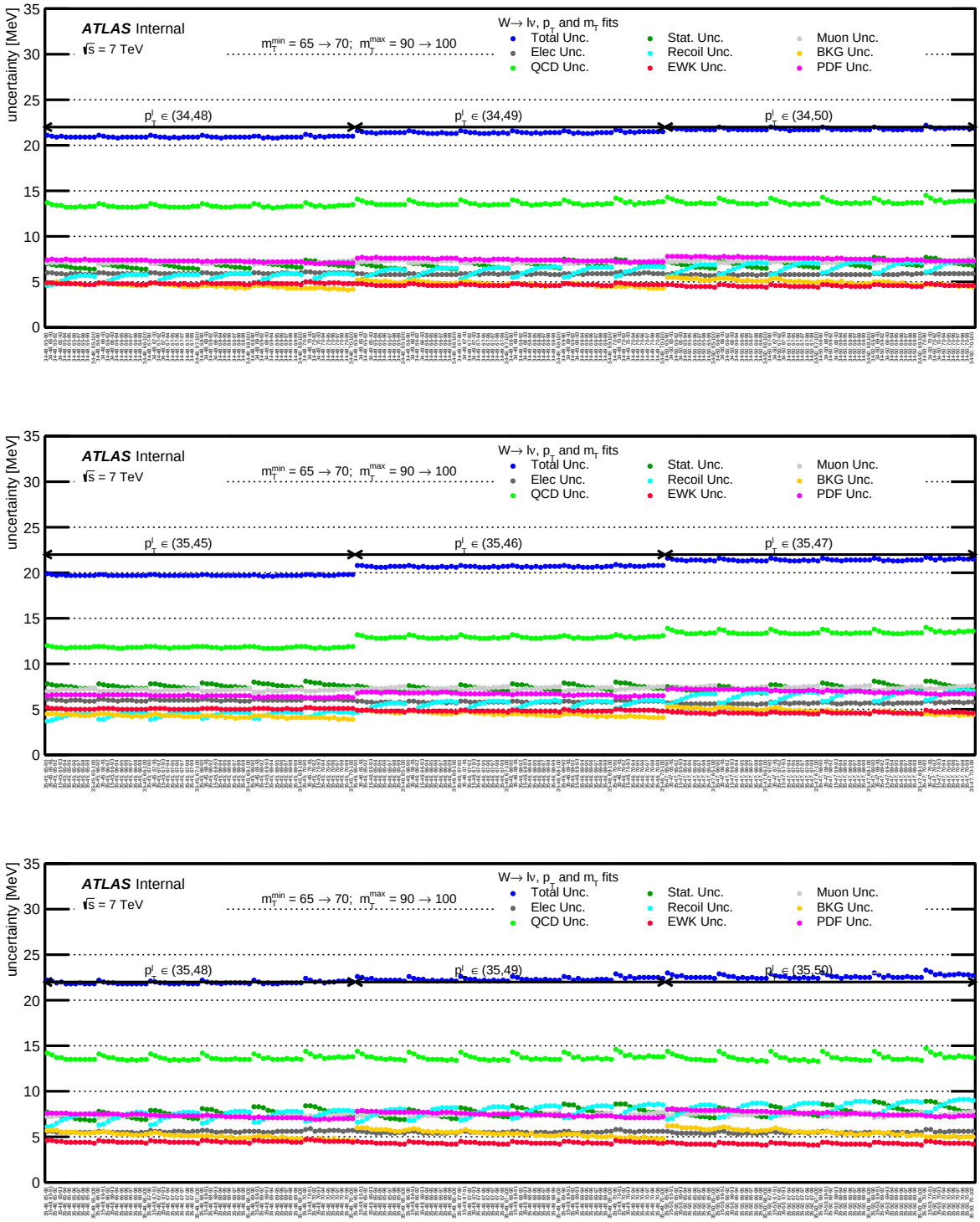

Figure B.4: Dependence of the statistical and systematic uncertainties on the fitting ranges for the fully combined measurement.

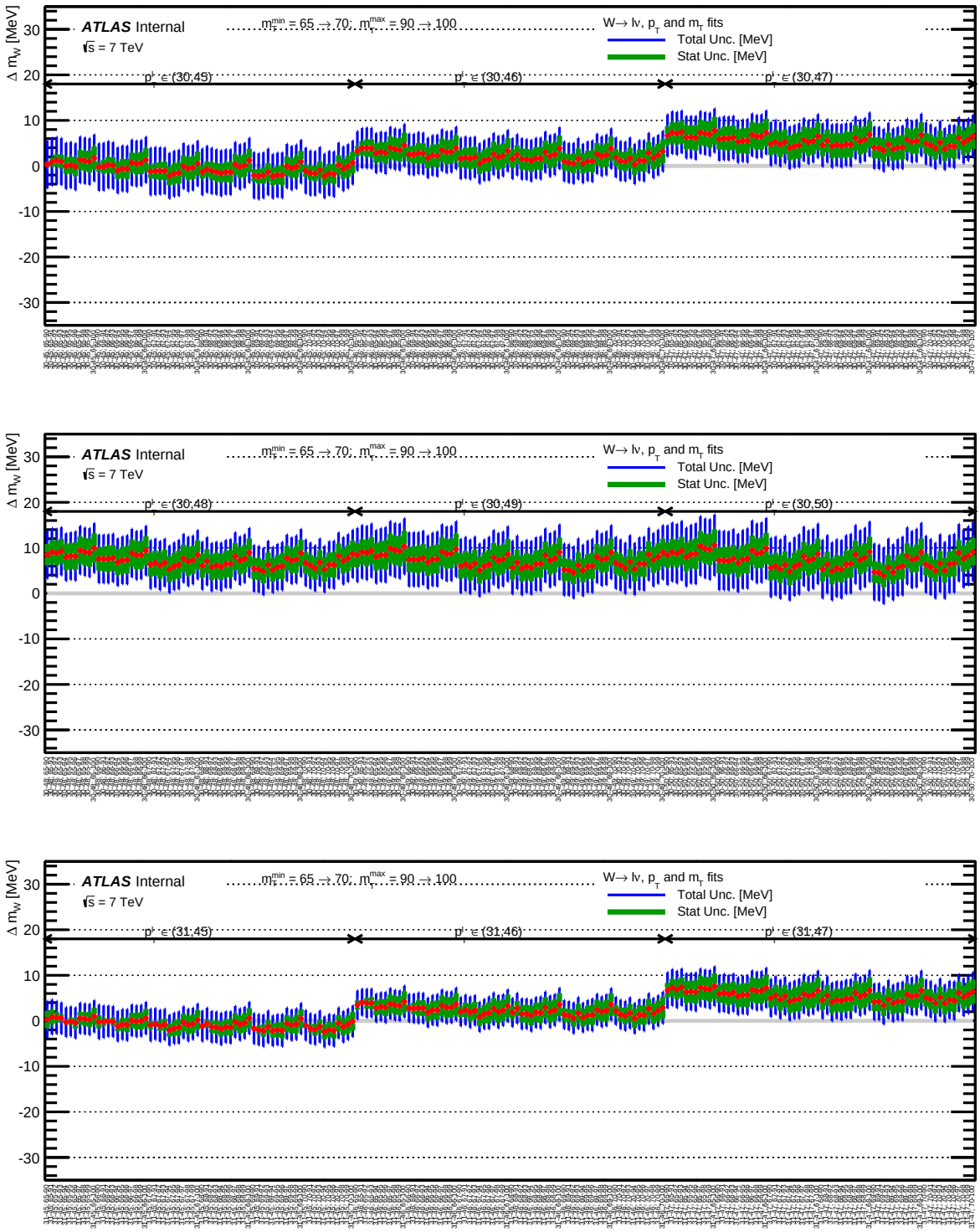

Figure B.5: Fit results for different fitting ranges using the fully combined measurement. The uncorrelated statistical uncertainties are indicated in green, the total uncorrelated uncertainties between the different fitting ranges are shown as blue line. As reference, the optimal fitting range is chosen.

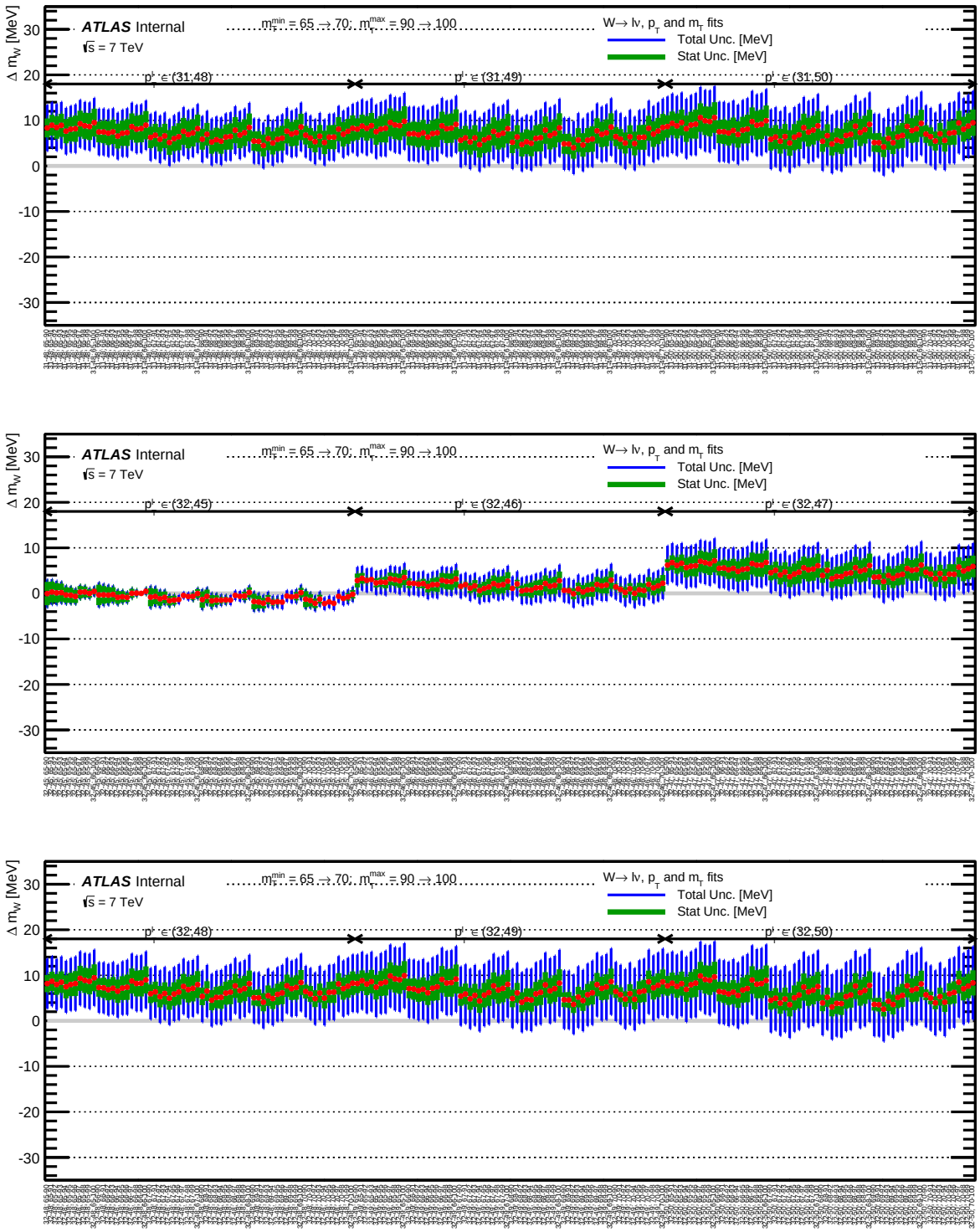

Figure B.6: Fit results for different fitting ranges using the fully combined measurement. The uncorrelated statistical uncertainties are indicated in green, the total uncorrelated uncertainties between the different fitting ranges are shown as blue line. As reference, the optimal fitting range is chosen.

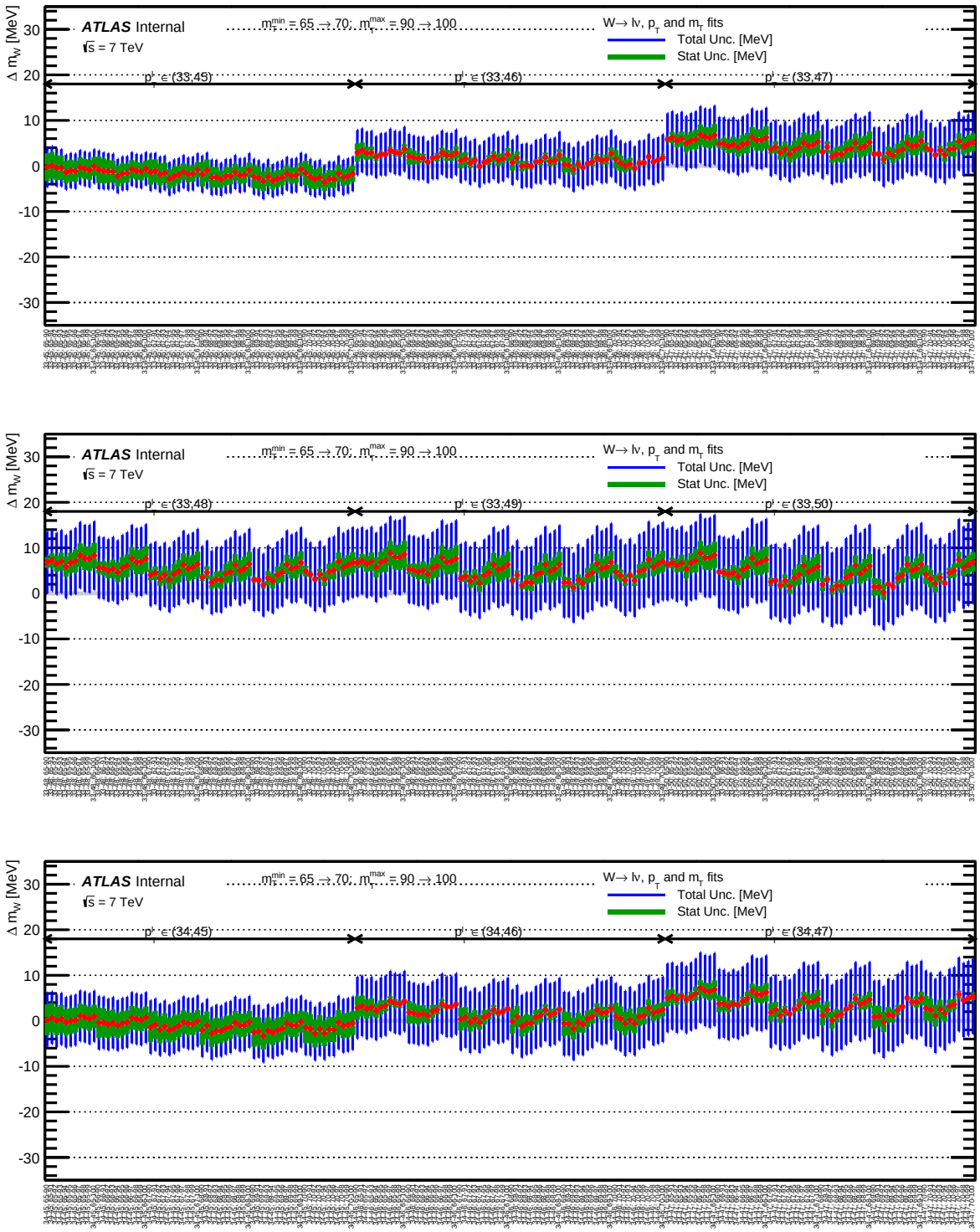

Figure B.7: Fit results for different fitting ranges using the fully combined measurement. The uncorrelated statistical uncertainties are indicated in green, the total uncorrelated uncertainties between the different fitting ranges are shown as blue line. As reference, the optimal fitting range is chosen.

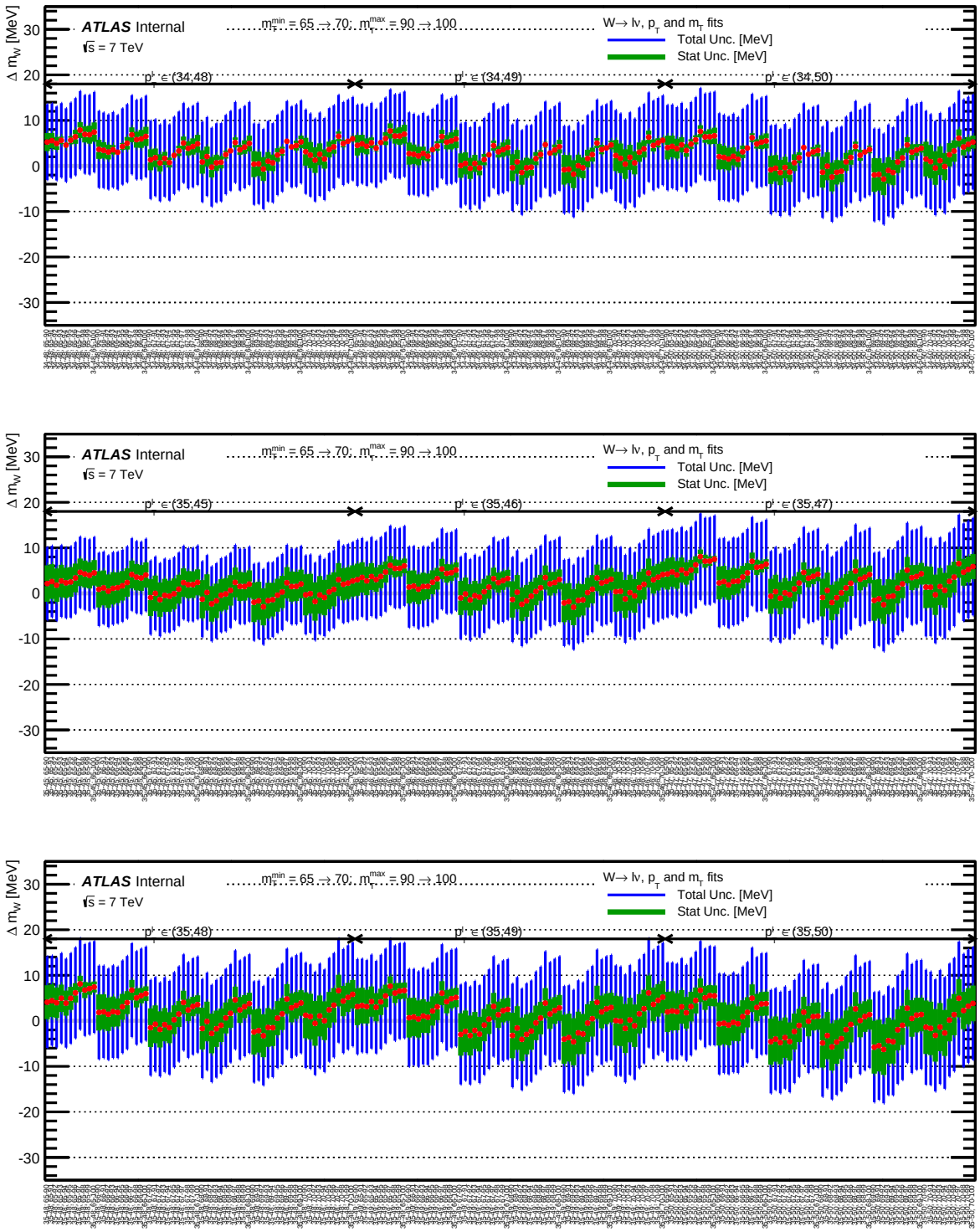

Figure B.8: Fit results for different fitting ranges using the fully combined measurement. The uncorrelated statistical uncertainties are indicated in green, the total uncorrelated uncertainties between the different fitting ranges are shown as blue line. As reference, the optimal fitting range is chosen.

ACKNOWLEDGEMENTS

First, I like to thank my thesis advisor Dr. Nenad Vranješ for the continuous support of my PhD study and related research, and his dedication and patience. Also, I thank all committee members, for accepting to review my work, Dr. Petar Adžić, Dr. Maja Burić and Dr. Maarten Boonekamp. And particulary Dr. Lidija Živković for taking the time to read, comment and evaluate the quality of my thesis.

This dissertation could not have been completed without the great support of Dr. Maarten Boonekamp (CEA-Saclay). I appreciate all the discussions, ideas, and enthusiasm for the W-boson mass measurement, and for providing me the funding for my internships at CERN and Saclay. I am especially grateful to Dr. Laurent Chevalier for introducing me to a wonderful world of muons. A very special gratitude goes out to all the members of the W-boson mass group, it was fantastic to have the opportunity to work with all of you.

I am also grateful to the members of the ATLAS group at the Institute of Physics in Belgrade: Prof. Djordje Šijački, Dr. Ljiljana Simić, Dr. Jelena Krstić and Dr. Marija Vranješ Milosavljević for their support and assistance. I would like to mention the late Prof. Dragan Popović, and express my gratitude for his support and encouragement.

And finally, last but by no means least, I would like to thank my friends and colleagues: Marija, Petar, Branka, Nancy, Oleh, Remie, Tanja, Danijela, thank you for your support during these years. Though we are dispersing around the world, I am looking forward to our future meetings over coffee and good laughs over the past time.

Прилог 1.

Изјава о ауторству

Потписани-а Александра Димитриевска

број уписа 31д / 2011

Изјављујем

да је докторска дисертација под насловом

Measurement of the W boson mass and the calibration of the muon momentum with the ATLAS detector

- резултат сопственог истраживачког рада,
- да предложена дисертација у целини ни у деловима није била предложена за добијање било које дипломе према студијским програмима других високошколских установа,
- да су резултати коректно наведени и
- да нисам кршио/ла ауторска права и користио интелектуалну својину других лица.

Потпис докторанда

У Београду, 7. јул 2017.

ADimitrievska

Прилог 2.

Изјава о истоветности штампане и електронске верзије докторског рада

Име и презиме аутора Александра Димитриевска

Број уписа 31д / 2011

Студијски програм Физика језгара и честица

Наслов рада Measurement of the W boson mass and the calibration of the muon momentum with the ATLAS detector

Ментор др Ненад Врањеш

Потписани _____

изјављујем да је штампана верзија мог докторског рада истоветна електронској верзији коју сам предао/ла за објављивање на порталу **Дигиталног репозиторијума Универзитета у Београду.**

Дозвољавам да се објаве моји лични подаци везани за добијање академског звања доктора наука, као што су име и презиме, година и место рођења и датум одбране рада.

Ови лични подаци могу се објавити на мрежним страницама дигиталне библиотеке, у електронском каталогу и у публикацијама Универзитета у Београду.

Потпис докторанда

У Београду, 7. јул 2017.

ADimitrievska

Прилог 3.

Изјава о коришћењу

Овлашћујем Универзитетску библиотеку „Светозар Марковић“ да у Дигитални репозиторијум Универзитета у Београду унесе моју докторску дисертацију под насловом:

Measurement of the W boson mass and the calibration of the muon momentum with the ATLAS detector

која је моје ауторско дело.

Дисертацију са свим прилозима предао/ла сам у електронском формату погодном за трајно архивирање.

Моју докторску дисертацију похрањену у Дигитални репозиторијум Универзитета у Београду могу да користе сви који поштују одредбе садржане у одабраном типу лиценце Креативне заједнице (Creative Commons) за коју сам се одлучио/ла.

1. Ауторство

2. Ауторство - некомерцијално

3. Ауторство – некомерцијално – без прераде

4. Ауторство – некомерцијално – делити под истим условима

5. Ауторство – без прераде

6. Ауторство – делити под истим условима

(Молимо да заокружите само једну од шест понуђених лиценци, кратак опис лиценци дат је на полеђини листа).

Потпис докторанда

У Београду, 7. јул 2017.

ADimitrievska

1. Ауторство - Дозвољавате умножавање, дистрибуцију и јавно саопштавање дела, и прераде, ако се наведе име аутора на начин одређен од стране аутора или даваоца лиценце, чак и у комерцијалне сврхе. Ово је најслободнија од свих лиценци.

2. Ауторство – некомерцијално. Дозвољавате умножавање, дистрибуцију и јавно саопштавање дела, и прераде, ако се наведе име аутора на начин одређен од стране аутора или даваоца лиценце. Ова лиценца не дозвољава комерцијалну употребу дела.

3. Ауторство - некомерцијално – без прераде. Дозвољавате умножавање, дистрибуцију и јавно саопштавање дела, без промена, преобликовања или употребе дела у свом делу, ако се наведе име аутора на начин одређен од стране аутора или даваоца лиценце. Ова лиценца не дозвољава комерцијалну употребу дела. У односу на све остале лиценце, овом лиценцом се ограничава највећи обим права коришћења дела.

4. Ауторство - некомерцијално – делити под истим условима. Дозвољавате умножавање, дистрибуцију и јавно саопштавање дела, и прераде, ако се наведе име аутора на начин одређен од стране аутора или даваоца лиценце и ако се прерада дистрибуира под истом или сличном лиценцом. Ова лиценца не дозвољава комерцијалну употребу дела и прерада.

5. Ауторство – без прераде. Дозвољавате умножавање, дистрибуцију и јавно саопштавање дела, без промена, преобликовања или употребе дела у свом делу, ако се наведе име аутора на начин одређен од стране аутора или даваоца лиценце. Ова лиценца дозвољава комерцијалну употребу дела.

6. Ауторство - делити под истим условима. Дозвољавате умножавање, дистрибуцију и јавно саопштавање дела, и прераде, ако се наведе име аутора на начин одређен од стране аутора или даваоца лиценце и ако се прерада дистрибуира под истом или сличном лиценцом. Ова лиценца дозвољава комерцијалну употребу дела и прерада. Слична је софтверским лиценцама, односно лиценцама отвореног кода.